

DOTTORATO DI RICERCA IN
FISICA
Ciclo XXXIV

Settore Concorsuale: 02/A1 - Fisica Sperimentale delle Interazioni Fondamentali
Settore Scientifico Disciplinare: FIS/01 - Fisica Sperimentale

**Measurement of
 CP violation with $B_{(s)}^0 \rightarrow h^+ h'^-$ decays,
 $|V_{cb}|$ with $B_s^0 \rightarrow D_s^{(*)-} \mu^+ \nu_\mu$ decays,
and simulation and
characterisation of the
LHCb Upgrade II ECAL**

Presentata da: Daniele Manuzzi

Coordinatore Dottorato
Prof. Michele Cicoli

Supervisore
Prof. Angelo Carbone

Co-supervisor
Dott. Stefano Perazzini
Dott. Fabio Ferrari

Esame finale anno 2022

Abstract

The LHCb experiment is designed to perform flavour-physics measurements at the Large Hadron Collider. In the Standard Model (SM) of particle physics the transitions between quarks of different flavour are ruled by the Cabibbo-Kobayashi-Maskawa (CKM) matrix and involve violation of the CP symmetry. This sector can provide stringent test of the SM internal consistency and includes excellent probes for indirect search for physics beyond the SM.

In this Thesis, the time-dependent CP asymmetries of the $B^0 \rightarrow \pi^+\pi^-$ and $B_s^0 \rightarrow K^+K^-$ decays are measured, as well as the time-integrated CP asymmetries of the $B^0 \rightarrow K^+\pi^-$ and $B_s^0 \rightarrow \pi^+K^-$ decays, using a sample of p - p collision data collected with the LHCb detector at a centre-of-mass energy of $\sqrt{s} = 13$ TeV, and corresponding to a total integrated luminosity of 5 fb^{-1} . The results are compatible with previous determinations of these quantities from LHCb, except for the CP -violation parameters of the $B_s^0 \rightarrow K^+K^-$ decays, that show a discrepancy exceeding 3 standard deviations between different data-taking periods. The status-of-the art of the investigations being conducted to understand the discrepancy is documented.

The measurement of the CKM matrix element $|V_{cb}|$ using exclusive semileptonic decays of the B_s^0 meson is also reported in this Thesis, using a sample of p - p collision data collected with the LHCb detector at a centre-of-mass energy of 7 and 8 TeV, and corresponding to an integrated luminosity of 3 fb^{-1} . The measurement involves the parametrisation of the hadronic form factors proposed by Caprini, Lellouch and Neubert, and leads to

$$|V_{cb}| = (41.4 \pm 0.6 \text{ (stat)} \pm 0.9 \text{ (syst)} \pm 1.2 \text{ (ext)}) \times 10^{-3},$$

where the first uncertainty is statistical, the second is systematic, and the third is due to limited knowledge of the external inputs. This measurement is compatible with the world averages obtained from decays of B^+ and B^0 mesons and constitutes the first measurement of $|V_{cb}|$ at a hadron collider and the absolute first one with decays of the B_s^0 meson. The analysis also provides the very first measurements of the branching ratio and form factors parameters of the signal decay modes.

The study of the characteristics ruling the response of an electromagnetic calorimeter (ECAL) to profitably operate in the high luminosity regime foreseen for the Upgrade II of LHCb is reported in the final part of this Thesis. A fast and flexible simulation framework is developed to this purpose. Physics performance of different configurations of the ECAL are evaluated using samples of fully simulated $B^0 \rightarrow \pi^+\pi^-\pi^0$ and $B^0 \rightarrow K^{*0}e^+e^-$ decays produced in p - p collisions at a centre-of-mass energy of 14 TeV and at an instantaneous luminosity up to $1.5 \times 10^{34} \text{ cm}^{-2} \text{ s}^{-1}$. The study sets the target for the resolution in measuring the time of arrival of particles on the ECAL to be between 10 and 20 ps, in order to recover performance similar to those registered by LHCb during the Run 2. The effects of time resolution and different segmentations of the ECAL on the recovery of bremsstrahlung photons and on the electron-pion discrimination are also studied. The results reported in this Thesis are used to guide the development of the future ECAL and are reported in the Framework Technical Design Report of the LHCb Upgrade II detector.

Contents

Introduction	1
1 <i>CP</i> violation and CKM matrix	5
1.1 The <i>CP</i> violation phenomena	5
1.1.1 Motivations for the neutral meson mixing	5
1.1.2 The two-state system	7
1.1.3 Neutral mesons as a two-state system	10
1.1.4 <i>CP</i> -violation categories	16
1.2 <i>CP</i> violation in the Standard Model	18
1.2.1 Yukawa coupling and flavour transitions	19
1.2.2 Origin of the <i>CP</i> violation	22
1.2.3 Magnitude of the CKM matrix elements	24
1.2.4 Parametrisations of the CKM matrix	26
1.2.5 Unitary Triangles	28
1.2.6 Constraints to the UT	30
1.3 Charmless two-body <i>B</i> decays	32
1.3.1 Topologies contributing to $B_{(s)}^0 \rightarrow h^+h'^-$ decays	32
1.3.2 $B_{(s)}^0 \rightarrow h^+h'^-$ and UT parameters	34
1.4 Semileptonic $B_{(s)}^0$ decays	37
1.4.1 Pseudoscalar final state	37
1.4.2 Vector final state	38
2 The LHCb experiment	41
2.1 The Large Hadron Collider	44
2.2 Tracking system	44
2.2.1 VELO	46
2.2.2 Tracker Turicensis	46
2.2.3 Magnet	48
2.2.4 Tracking stations	49
2.3 Particle identification system	50
2.3.1 Ring Imaging Cherenkov	50
2.3.2 Calorimeters	52
2.3.3 Muon Stations	54
2.4 Trigger	57
2.4.1 Level-0	57
2.4.2 High Level Trigger 1	59
2.4.3 High Level Trigger 2	60

3	Measurements of CP violation with $B_{(s)}^0 \rightarrow h^+h'^-$ decays	61
3.1	Data composition and selection	64
3.1.1	Simulated samples	67
3.1.2	Stripping selection	67
3.1.3	Trigger selection	68
3.1.4	Final selection	69
3.2	PID calibration	78
3.2.1	Maps of PID efficiency	78
3.2.2	PID efficiencies for $B_{(s)}^0 \rightarrow h^+h'^-$ decays	79
3.2.3	Uncertainties on the PID efficiencies	80
3.3	Decay-Time Resolution	85
3.3.1	Prompt- $J/\psi \rightarrow \mu^+\mu^-$ calibration samples	86
3.3.2	Preliminary binned calibration	87
3.3.3	Unbinned calibration	88
3.3.4	Average decay-time resolution	92
3.4	Flavour tagging	93
3.4.1	Calibration of OS taggers	95
3.4.2	Calibration of SS taggers	95
3.4.3	Tagger combination	96
3.5	Decay-time efficiency	98
3.6	Final state asymmetries	103
3.6.1	Asymmetry of detection	104
3.6.2	Asymmetry of the PID efficiencies	104
3.7	Fit strategy	106
3.7.1	Signal model	106
3.7.2	Cross-feed background model	111
3.7.3	Partially-reconstructed background model	113
3.7.4	Combinatorial background model	115
3.7.5	Summary of the fixed parameters	119
3.8	Fit results	120
3.8.1	Fit Cross-Checks	150
4	First measurement of V_{cb} with $B_s^0 \rightarrow D_s^{(*)-} \mu^+ \nu$ decays	153
4.1	Data samples	155
4.2	Simulated samples and their corrections	156
4.2.1	Corrections to the simulation	156
4.2.2	Simulation of signal and reference decays	160
4.2.3	Physics backgrounds	162
4.3	Determination of the parameters of interest	164
4.3.1	The p_{\perp} variable	164
4.3.2	χ^2 fit function	165
4.3.3	Determination of the reference yields	168
4.3.4	Components of the fit to the B_s^0 sample	171
4.3.5	Fit for $ V_{cb} $ in the CLN parametrisation	178
4.3.6	Fit for \mathcal{R} and \mathcal{R}^*	183
4.4	Analysis validation	183
4.4.1	Pseudoexperiments	183

4.4.2	Control sample analysis	187
4.4.3	Allowing different $ V_{cb} $ parameters for $B_s^0 \rightarrow D_s^- \mu^+ \nu_\mu$ and $B_s^0 \rightarrow D_s^{*-} \mu^+ \nu_\mu$	190
4.5	Systematic uncertainties	190
4.5.1	External inputs	191
4.5.2	$D_{(s)}^- \rightarrow K^+ K^- \pi^-$ decay model	191
4.5.3	Background contamination	192
4.5.4	Corrections to the simulation	194
4.5.5	Total uncertainties and correlations	195
4.6	Final results and conclusions	195
5	Simulation and characterization of the LHCb Upgrade II ECAL	201
5.1	Technologies and description of LHCb Upgrade II ECAL	202
5.2	Simulation	207
5.2.1	Generation of p - p collisions	207
5.2.2	Simulation of luminosity conditions in Run 5	208
5.2.3	Simulation of ECAL detector	210
5.3	Reconstruction algorithms	216
5.3.1	Seed finding and cluster reconstruction	216
5.3.2	Energy redistribution and event reconstruction	218
5.3.3	Identification of neutral and charged clusters	222
5.3.4	Reconstruction of π^0	224
5.3.5	Recovery of bremsstrahlung photons	225
5.3.6	Correction to time measurements of the cells	227
5.4	Physics performance studies	233
5.4.1	Study of $B^0 \rightarrow \pi^+ \pi^- \pi^0$ decays	234
5.4.2	Study of $B^0 \rightarrow K^{*0} e^+ e^-$ decays	240
5.5	Summary and conclusions	249
	Conclusions	251
A	CP violation measurements in the decay of $B_{(s)}^0$ mesons to two charged pions and kaons	253
A.1	Background subtraction for $B_{(s)}^0 \rightarrow h^+ h'^-$ decays	254
B	First measurement of V_{cb} with $B_s^0 \rightarrow D_s^{(*)-} \mu^+ \nu$ decays	257
B.1	Lattice data for $B_s^0 \rightarrow D_s^- \mu^+ \nu_\mu$ decays	257
B.2	Data-simulation comparison	259
B.3	Reference sample fit projections	265
B.4	Signal sample fit projections	267
B.5	Control sample fit projections	272
	References	294

Introduction

*If we accept the view
of complete symmetry between
positive and negative electric charge
so far as concerns
the fundamental laws of Nature,
we must regard it rather as an accident
that the Earth, contains
a preponderance of negative electrons
and positive protons.*

P. A. M. Dirac,
Nobel Lecture, 12/12/1933

The discovery of antimatter was a triumph for both theoretical and experimental physics [1, 2]. This breakthrough was based on the exact symmetry – predicted and observed – between a fundamental particle, the electron, and its counter-part with equal mass and opposite electrical charge, the positron. The same idea was immediately extended to all elementary particles, so much so that, in the conclusion of its Noble Lecture, P. A. M. Dirac imagined the existence of stars made of positrons and negative-charged nuclei [3]. However, the current observations strongly exclude the existence of such objects in the visible universe [4]. In facts, the macroscopic dominance of matter over antimatter is still an evident and unresolved question, in our understanding of the cosmos [5–10]. So far, the fundamental symmetry between matter and antimatter has always been confirmed, except for a relatively small phenomenon, called CP violation. This effect was discovered, quite unexpectedly, in 1964 [11]. Since then, CP violation effects have been found only in the charged currents of the weak interactions of quarks. According to the best description to date of the elementary particles and their interactions, namely the Standard Model of particle physics (SM) [12, 13], the only source of asymmetry between matter and antimatter is due to a single complex phase in the so called Cabibbo-Kobayashi-Maskawa (CKM) matrix [14, 15]. The elements of this matrix rule the coupling, namely the fundamental transitions probabilities, between quarks of different flavour [16]. Anyway, it is also well known that the CP violation caused by the CKM matrix alone is not sufficient to quantitatively explain the observed abundance of matter over antimatter [17–20]. This evidence manifests a substantial limit of the Standard Model and call for more insight in the CP -violation and CKM-matrix sectors.

In general, to test the existence of physics beyond the Standard Model (BSM), two complementary approaches are possible. The first one consists in the direct search for the signature of new kind of particles or interactions. The second one is an indirect approach, which is based on the refined verification of the consistency of the SM predictions. Even

if the latter method does not straightforwardly proof the presence of new particles and interactions, it takes advantage from a peculiar aspect of the quantum realm: the mere existence of high-energy phenomena may affect even processes where such energy is not available. More rigorously, transition probability results from the amplitudes of all the consistent Feynman diagrams [21], and Feynman diagrams with loops may involve contributions from virtual processes, whose energy scale is not limited by the energy of the initial state. The amplitudes of diagrams with loop transitions are usually small when compared to those from tree-level diagrams, where no physics beyond the SM is expected. However, in some cases, the amplitudes from loop transitions are relevant, thanks to the specific values of the CKM matrix elements involved. Furthermore, the indirect search for new physics within the CKM sector benefits from another feature of this matrix: the SM assumes it to be unitary. This condition constrains the elements of the matrix, and such relations can be experimentally tested. Since a multitude of different decay processes are connected to the quark-flavour transitions, numerous experimental results can be combined to check the unitarity of the CKM matrix. This diversification reduces the issues related to eventual systematic effects of the measurements, and drastically increases the precision of the SM-consistency tests. This kind of studies are usually referred to as tests of the *Unitary Triangles*.

The Chapter 1 of this Thesis provides details about the concepts outlined so far. It starts with the discussion of the CP -violation phenomena and then describes their implementation within the SM framework. The Chapter is also oriented to introduce the specificities of the physics cases whose measurements are documented in the subsequent Chapters. It shows how the CP violation observables can be combined to produce tests of the Unitary Triangle, and explains the connection between the magnitude of the CKM-matrix element and directly observable decay rates.

The measurements conducted in this Thesis are obtained using data collected by the LHCb experiment, operating at the Large Hadron Collider (LHC) at the CERN laboratory in Geneva. The LHCb detector is the subject of Chapter 2. The detector is characterised by high performance of particle identification and reconstruction, which are fundamental features for its ambitious physics programme, mainly focused on flavour physics. In particular, LHCb is optimised to maximise the collection of hadrons containing b and c quarks. The high energy proton-proton collision of the LHC give LHCb a unique rôle in the sector of the B_s^0 meson and beauty baryons.

The Chapter 3 concerns the measurements of the CP violation observables in the $B^0 \rightarrow \pi^+\pi^-$, $B_s^0 \rightarrow K^+K^-$, $B^0 \rightarrow K^+\pi^-$ and $B_s^0 \rightarrow \pi^+K^-$ decays, also called $B_{(s)}^0 \rightarrow h^+h'^-$ decays. Because of the absence of the c quark in the final states, the tree level contributions to the amplitudes of these processes are reduced, and loop topologies, also called “penguin” topologies [22], are relevant. The LHCb collaboration published the leading measurements in this sector to date [23, 24]. That analysis utilises the p - p collision data collected at centre-of-mass energies of 7, 8 and 13 TeV from 2011 to 2016, namely the Run 1 and the first half of the Run 2 of LHCb, and corresponding to a total integrated luminosity of 5 fb^{-1} . Now 4 more inverse femtobarn are available thanks to the data collected in 2017 and 2018. The analysis reported in this Thesis aims to measure the parameters related to the time-dependent and time integrated CP asymmetries of the $B_{(s)}^0 \rightarrow h^+h'^-$ decays with the full Run 2 dataset. The 2015-2016 data are also analysed again after a reprocessing for consistency check. Several experimental effects are considered and calibrated. The final results are obtained with simultaneous

unbinned maximum-likelihood fits to all the final-state samples. All the aspects of the measurements are accurately investigated to test their robustness against any eventual systematic effect, differentiating the various data-taking periods. They include: the calibration of the determination of the flavour of the B mesons at their production and the calibration of the error in measuring their decay time, the accurate determination of the signal reconstruction efficiency as a function of the decay time, the determination of the differences in the reconstruction efficiencies of the charge-conjugated final states, the accurate modelling of all the components contributing to the final-state samples.

The Chapter 4 reports the first measurement of the magnitude of the CKM matrix elements called V_{cb} from the exclusive $B_s^0 \rightarrow D_s^- \mu^+ \nu_\mu$ and $B_s^0 \rightarrow D_s^{*-} \mu^+ \nu_\mu$ decays. This is the first measurement of this quantity at an hadron collider. The analysis also aims to provide the first determinations ever of branching fractions and form factors of the signal decay modes. An important rôle is also played by the $B^0 \rightarrow D^- \mu^+ \nu_\mu$ and $B^0 \rightarrow D^{*-} \mu^+ \nu_\mu$ decay modes, which are used to normalise the signal yields. The selection of the same final states as for the signal ($D^- (\rightarrow K^+ K^- \pi^-) \mu^+ \nu_\mu$) permits eventual systematic effects in the determination of the selection efficiencies to be abated. The analysis strategy is complicated by the not reconstructible final-state neutrinos. Hence, a corrected version of the invariant mass and a proxy variable for the momentum transferred to the leptonic final state are used. Simulated samples are employed to describe the distributions of these two quantities, after applying data-driven corrections. The whole analysis strategy is finally validated considering a further final state of the normalization channels ($D^- \rightarrow K^+ \pi^- \pi^-$) to measure a ratio of branching fractions compatible with unity and form factors compatible with the current world averages for the semileptonic B^0 decays.

The Chapter 5 illustrates studies for the future Upgrade II of the LHCb experiment. In the Run 5 a factor 40 enhancement of the maximal instantaneous luminosity will be available at the LHCb interaction point. This condition aims to drastically increase the amount of collected statistic to reach unprecedented precision in all the aspects of the flavour-physics field [25]. At the same time, it poses critical challenges for the realisation of new sub-detectors capable to operate in such a demanding environment. Two factors will be critical: the deterioration of the experimental systems because of the high radiation dose to be absorbed, and the increased occupancy, namely the extremely large number of particles to be reconstructed and distinguished. This Chapter is dedicated to the Electromagnetic Calorimeter (ECAL). At this stage of the detector development, one of the essential issues is delineating the target characteristics of the future apparatus. The essential parameters are: the energy resolution, the segmentation *i.e.* the granularity of the detector elements, and the time resolution. In particular, the last feature is new at LHCb and is considered fundamental to resolve the many p - p collision vertices expected in Run 5 conditions. For this reasons, various simulation studies, concerning different physics cases, are conducted. This Thesis focuses on $B^0 \rightarrow \pi^+ \pi^- \pi^0$ and $B^0 \rightarrow K^{*0} e^+ e^-$ decays. They are related to crucial ECAL tasks: the neutral pion reconstruction, the recovery of bremsstrahlung photons, and the electron-pion discrimination. A new simulation framework is developed to estimate the ECAL response to Run 5 conditions, and compare it with the performance achieved in Run 2. Since this is one of the very first approaches to this matter, the current ECAL reconstruction algorithms are reproduced. The effect of using time information is evaluated, providing preliminary, but already effective, results that are used in the Framework Technical Design Report of the LHCb Upgrade II.

Chapter 1

CP violation and CKM matrix

1.1 The CP violation phenomena

The weak interaction maximally violates P and C symmetries. However, combining the two transformations, left-handed particles are substituted with right-handed antiparticles. Hence, the laws of the nature would be exactly the same for matter and antimatter, if CP were an exact symmetry. CP -violation effects in the weak interaction can be experimentally searched for in a variety of processes [4]. On the one hand, the study of the decays of hadrons probes CP violation in flavour transitions. On the other hand, the study of electric dipole moments may find sources of CP violation in flavour-conserving interactions. Besides, the search for CP violation in the neutrino oscillations may provide further insight in the lepton behavior. Finally, thanks to the discovery of the Higgs boson, searches for CP violation are becoming feasible also in this sector.

So far, CP violation effects have been observed only studying bound states of a quark and an anti-quark, called mesons. The violation of CP symmetry can manifest itself in three ways: CP violation *in the decay*, *in the mixing*, and *in the interference between mixing and decay*. The latter two are possible only for pseudoscalar neutral mesons, whose time evolution is marked out by the phenomenon of flavour mixing. The former, instead, occurs also for charged mesons and, according to the SM, is expected also for baryons. A formal description of the CP violation categories is reported in Section 1.1.4, after the introduction of the formalism of the neutral meson mixing (Sections 1.1.1-1.1.3).

As an overview, Tab. 1.1 resumes the status of the CP violation observations for pseudoscalar mesons and Λ baryons. The neutral mesons which carry null flavour quantum numbers (for instance the $\eta^{(\prime)}$) are not considered, because they are their own antiparticle and have definite CP eigenvalue. Hence, the CP violation signature is just the decay in a final state with opposite CP eigenvalue. However, the decays of these mesons are dominated by the electromagnetic and the OZI-suppressed strong interactions, where CP violation has never been observed.

1.1.1 Motivations for the neutral meson mixing

The quark model [16] predicts the existence of meson-antimeson pairs with null electric charge and whose distinction relies only on the opposite flavour quantum numbers. Four such systems, composed by pairs of flavour eigenstates, are observed in nature: K^0 - \bar{K}^0 , D^0 - \bar{D}^0 , B^0 - \bar{B}^0 , B_s^0 - \bar{B}_s^0 . In the following, they are generically referred to as M^0 -

Table 1.1: Summary of the CP violation observations [4, 26]. A five standard deviation (σ) significance threshold is indicated with a \checkmark ; several such observations in different channels are required for a $\checkmark\checkmark$. The symbol \times encodes a current lack of CP violation observations. Particles that do not undergo oscillations may manifest CP violation only in the decay.

	K^0	K^\pm	Λ	D^0	D^\pm	D_s^\pm	Λ_c^+	B^0	B^\pm	B_s^0	Λ_b^0
decay	\checkmark	\times	\times	\checkmark	\times	\times	\times	$\checkmark\checkmark$	$\checkmark\checkmark$	\checkmark	\times
mixing	$\checkmark\checkmark$	–	–	\times	–	–	–	\times	–	\times	–
decay/mixing interf.	\checkmark	–	–	\times	–	–	–	$\checkmark\checkmark$	–	\checkmark	–

\bar{M}^0 systems. Charged mesons are always flavour eigenstates, because the information coming from their mass and electric charge allows their flavour content to be determined unambiguously. On the contrary, the neutral mesons can be experimentally studied both observing or not observing their flavour quantum numbers, namely with *flavour-specific* or *flavor-non-specific* processes. Three reaction categories can be recognized¹:

- A) *flavour-specific production reactions*, like those mediated by the strong interaction; for instance:

$$\begin{aligned}
 D^{*+}(c\bar{d}) &\rightarrow D^0(c\bar{u}) + \pi^+(u\bar{d}), \\
 D^{*-}(\bar{c}d) &\rightarrow \bar{D}^0(\bar{c}u) + \pi^-(\bar{u}d), \\
 p(uud) + \bar{p}(\bar{u}\bar{u}\bar{d}) &\rightarrow B^-(\bar{u}b) + B^0(\bar{b}d) + \pi^+(\bar{d}u),
 \end{aligned}$$

where the electric charges of the final state pions determine the flavour of the neutral mesons. The neutral mesons studied in this thesis are produced by high energy proton-proton collisions (details are in Chapter 2). In this environment, a sure flavour determination at production is not feasible; nevertheless a flavour tag can be associated to the neutral meson candidates with an adequate statistical accuracy [29–32]. Briefly, in processes like:

$$p + p \rightarrow B^- + B_s^0 + K^+ + X$$

information about the flavour of the B_s^0 meson is carried by both the B^- and the K^+ mesons, originated by the hadronization of the second b and s quarks in the event. Even if it is not always possible to identify them among all other particles (X) produced in the collision kinetic and topological considerations can lead to an acceptable mistag rate.

- B) *flavour-specific absorptions or decays*; flavour conserving interactions can constrain the possible absorption processes, depending on the flavour of the neutral meson in the initial state. For instance:

$$\begin{aligned}
 K^0 + p &\rightarrow K^+ + n; & K^0 + p &\not\rightarrow \Sigma^+ + \pi^0; \\
 \bar{K}^0 + p &\not\rightarrow K^+ + n; & \bar{K}^0 + p &\rightarrow \Sigma^+ + \pi^0.
 \end{aligned}$$

¹This classification is useful for the study of flavour at hadron colliders, and it will be frequently exploited in the next. Anyway, other classifications are possible, as for example the distinction between *active* and *passive* flavour measurements, which is necessary to treat the neutral mesons systems as Bell's systems [27, 28].

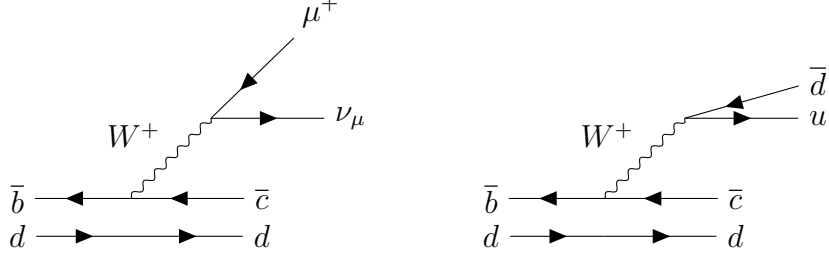


Figure 1.1: Tree-level Feynman diagrams for $B^0 \rightarrow D^- \mu^+ \nu_\mu$ (left) and $B^0 \rightarrow D^- \pi^+$ (right) flavour-specific decays.

These processes are particularly useful for neutral kaons, whose interactions with the ordinary matter can be experimentally studied thanks to their relatively long lifetime. In the B meson sector, instead, only flavour-specific decays can be exploited. Examples are available for both semileptonic and hadronic weak charged-current transitions:

$$\begin{aligned}
 B^0(\bar{b}d) &\rightarrow D^-(\bar{c}d) + \mu^+ + \nu_\mu, \\
 B^0(\bar{b}d) &\rightarrow D^-(\bar{c}d) + \pi^+(\bar{d}u), \\
 B^0(\bar{b}d) &\rightarrow K^+(\bar{s}u) + \pi^-(\bar{u}d).
 \end{aligned}$$

According to the SM, the first two reactions are dominated by the tree-level Feynman diagrams (Figure 1.1), and the electric charge of the final-state muon or pion fixes the flavour of the initial state. The last reaction will be described in detail in Section 1.3.

- C) Decays of opposite flavour eigenstates into common final states are also observed. The *weak transition to common CP eigenstates* are remarkable for this thesis. Some examples are:

$$\begin{aligned}
 K^0 &\leftrightarrow \pi^+\pi^- \leftrightarrow \bar{K}^0; & K^0 &\leftrightarrow \pi^+\pi^-\pi^0 \leftrightarrow \bar{K}^0; \\
 B^0 &\leftrightarrow \pi^+\pi^- \leftrightarrow \bar{B}^0; & B_s^0 &\leftrightarrow K^+K^- \leftrightarrow \bar{B}_s^0;
 \end{aligned}$$

A more formal definition of *flavour-specific* and *flavour-non-specific* decays will be given in section 1.1.3. The key point here is that the processes of type A and B permit the flavour of a neutral meson to be observed at the instants of its creation and decay, respectively. The processes of type C, instead, do not depend on the sign of the flavour quantum numbers.

1.1.2 The two-state system

Several examples of two-state quantum systems can be identified. Some pedagogical ones are: the ammonia molecule, a half-spin particle in a static magnetic field, the polarization of light and even a double slits apparatus [33]. In general, they can be treated as follows.

By definition, any state of the system is the superposition of two orthonormal basis states:

$$|\psi(t)\rangle = |1\rangle c_1(t) + |2\rangle c_2(t), \quad (1.1)$$

where the time-dependent coefficients are the amplitude of the two base states: $c_1(t) = \langle 1|\psi(t)\rangle$, $c_2(t) = \langle 2|\psi(t)\rangle$. The evolution of the system is given by the pair of coupled equations:

$$i\frac{dc_1(t)}{dt} = H_{11}c_1(t) + H_{12}c_2(t), \quad (1.2)$$

$$i\frac{dc_2(t)}{dt} = H_{21}c_1(t) + H_{22}c_2(t). \quad (1.3)$$

where the H_{ij} terms are the matrix elements of the Hamiltonian, \mathbf{H} , of the system. A general proposition of quantum theory [33] states that, in a given base, the Hamiltonian matrix element H_{ij} is proportional to the amplitude that –under the physical conditions described by \mathbf{H} – a base state $|i\rangle$ will transform to a base state $|j\rangle$ during an infinitesimal time dt . Hence, the off-diagonal matrix elements rule the transition between different base states, while the diagonal matrix elements are related to the evolution without transitions.

The uncoupled case The simplest two-state system is provided by two base states which cannot evolve into each other:

$$H_{12} = H_{21} = 0,$$

which produce a diagonal Hamiltonian. Therefore, the Equations (1.2) and (1.3) correspond to two independent Schrödinger equations and the time evolution of the system is given by:

$$|\psi(t)\rangle = |1\rangle a_0 e^{-iH_{11}t} + |2\rangle b_0 e^{-iH_{22}t}, \quad (1.4)$$

where a and b are integration constants, which has to be determined from the initial conditions. For example: $|\psi(t=0)\rangle = |1\rangle$ implies $a_0 = 1$, $b_0 = 0$, $|\psi(t)\rangle = |1\rangle e^{-iH_{11}t}$ and there is no chance to observe the state $|2\rangle$, at any time. In other words, the base states of a diagonal Hamiltonian are independent or uncoupled. The Hamiltonian matrix elements are in general complex numbers. In case of Hermitian Hamiltonian ($\mathbf{H} = \mathbf{H}^\dagger$) the diagonal matrix elements are real and H_{11} and H_{22} are the constant energies of the base states, that coincide with the masses of the base states in the special case of particles at rest.

On the contrary, if the matrix-elements of a diagonal Hamiltonian are complex, the evolution of the system is given by:

$$|\psi(t)\rangle = |1\rangle a_0 e^{-iM_{11}t} e^{-\frac{1}{2}\Gamma_{11}t} + |2\rangle b_0 e^{-iM_{22}t} e^{-\frac{1}{2}\Gamma_{22}t}, \quad (1.5)$$

where $M_{ii} = \mathcal{R}eH_{ii}$, $\Gamma_{ii}/2 = \mathcal{I}mH_{ii}$ with $i = 1, 2$. Thus, the real part of the matrix elements still provides the energy of the base states, while the total probability to observe the system decreases with the time:

$$|\langle\psi(t)|\psi(t)\rangle|^2 = a_0 e^{-\Gamma_{11}t} + b_0 e^{-\Gamma_{22}t}.$$

This corresponds to base states which can disappear like particles which decay [34, 35].

A paradigmatic case. When $H_{12} \neq 0$ and $H_{21} \neq 0$ the variation per time unit of the amplitude of the state $|1\rangle$ depends also on the amplitude of the state $|2\rangle$, and *viceversa*,

hence the two base states are coupled. It is instructive to study the two-state quantum system with a real symmetric Hamiltonian:

$$\mathbf{H} = \begin{pmatrix} M & \Delta \\ \Delta & M \end{pmatrix} \text{ with } \Delta \neq 0.$$

The Hamiltonian is Hermitian, so the probability to observe the system is constant in time, and its symmetry will correspond to a symmetrical behaviour of the base states $|1\rangle$ and $|2\rangle$. Usually, the base states corresponds to physical states, which can be alternatively observable. Nonetheless, it is always possible to perform a formal change of basis to diagonalise the Hamiltonian of the system, and then exploit these new, uncoupled states to get the time evolution of the original coupled states. Solving the characteristic equation $\det(\mathbf{H} - \mathbb{1}\omega) = 0$ the two eigenvalues are

$$\omega_+ = M + |\Delta|, \quad \omega_- = M - |\Delta|,$$

and the equations $\mathbf{H}|\pm\rangle = \omega_{\pm}|\pm\rangle$ provide the following eigenstates:

$$|+\rangle = \frac{1}{\sqrt{2}}(|1\rangle + |2\rangle), \quad |-\rangle = \frac{1}{\sqrt{2}}(|1\rangle - |2\rangle). \quad (1.6)$$

The solution of the Schrödinger equations (1.2)-(1.3) is

$$|\psi(t)\rangle = |+\rangle a_0 e^{-i(M+|\Delta|)t} + |-\rangle b_0 e^{-i(M-|\Delta|)t}, \quad (1.7)$$

where the eigenstates $|+\rangle$ and $|-\rangle$ correspond to specific mixtures of the original eigenstates $|1\rangle$ and $|2\rangle$. The time evolution of these mixtures is analogous to the one for the uncoupled case (compare Equations (1.7) and (1.5)). Therefore, a system prepared in one of the eigenstates reported in Equation (1.6) would evolve in a stationary way. Besides, the difference between the energies of the two uncoupled eigenstates is $\omega_+ - \omega_- = 2|\Delta|$, and the two eigenstates are orthogonal $\langle + | - \rangle = 0$, as required by the spectral theorem.

To study the time evolution of the system, two kinds of initial conditions are explanatory:

- 1) if $|\psi(t=0)\rangle = |+\rangle$, then $a_0 = 1$, $b_0 = 0$ and $|c_1(t)|^2 = |c_2(t)|^2 = 1/2$, therefore the probability to observe $|1\rangle$ or $|2\rangle$ is the same and does not depend on time;
- 2) if $|\psi(t=0)\rangle = |1\rangle$, it is useful to write the initial basis as a function of the eigenstates

$$|1\rangle = \frac{1}{\sqrt{2}}(|+\rangle + |-\rangle), \quad |2\rangle = \frac{1}{\sqrt{2}}(|+\rangle - |-\rangle).$$

Equation (1.7) with $t = 0$ provides: $a_0 = b_0 = 1/\sqrt{2}$, thus the system evolves according to

$$|\psi(t)\rangle = |1\rangle \frac{1}{2} (e^{-i\omega_+ t} + e^{-i\omega_- t}) + |2\rangle \frac{1}{2} (e^{-i\omega_+ t} - e^{-i\omega_- t}),$$

where the base state $|2\rangle$ has appeared, even if it was not present in the initial state. The time-dependent probabilities to observe the base states are

$$|\langle 1 | \psi(t) \rangle|^2 = \cos^2(|\Delta|t), \quad |\langle 2 | \psi(t) \rangle|^2 = \sin^2(|\Delta|t),$$

and it is evident that each one oscillates with period $2\pi/|\Delta|$. Moreover, the two oscillation have a constant phase difference, such that the total probability to observe the system is 1 at any time.

1.1.3 Neutral mesons as a two-state system

The states of definite flavour $|M^0\rangle$, $|\bar{M}^0\rangle$ are considered now as the basis states. They are antiparticle of each other:

$$CP|M^0\rangle = |\bar{M}^0\rangle e^{i\xi_M}, \quad CP|\bar{M}^0\rangle = |M^0\rangle e^{-i\xi_M}, \quad (1.8)$$

where ξ_M is an unobservable real number². The CPT symmetry³ forces the diagonal elements of the Hamiltonian to be equal: $H_{11} = H_{22} \equiv \tilde{H}$ [36]. Moreover, the neutral mesons are observed to decay, therefore a not-Hermitian Hamiltonian is necessary to describe them as a two-state system⁴. Hence, the Hamiltonian describing the system can be written as

$$\mathbf{H} = \begin{pmatrix} \tilde{H} & H_{12} \\ H_{21} & \tilde{H} \end{pmatrix} \equiv \mathbf{M} - \frac{i}{2}\mathbf{\Gamma} = \begin{pmatrix} M & M_{12} \\ M_{12}^* & M \end{pmatrix} - \frac{i}{2} \begin{pmatrix} \Gamma & \Gamma_{12} \\ \Gamma_{12}^* & \Gamma \end{pmatrix}, \quad (1.9)$$

where \mathbf{M} and $\mathbf{\Gamma}$ are Hermitian, their diagonal elements M and Γ are real and their off-diagonal elements are complex conjugated of each other.

Before calculating the time evolution of the system, it is interesting to look at the perturbative expansion of the Hamiltonian matrix elements. According to Ref.s [36, 39]:

$$\begin{aligned} M_{11} &= m_{M^0} + \sum_j \frac{\langle M^0|H_W|j\rangle\langle j|H_W|M^0\rangle}{m_{M^0} - m_j}, & M_{12} &= \sum_j \frac{\langle \bar{M}^0|H_W|j\rangle\langle j|H_W|M^0\rangle}{m_{M^0} - m_j}, \\ M_{21} &= \sum_j \frac{\langle M^0|H_W|j\rangle\langle j|H_W|\bar{M}^0\rangle}{m_{M^0} - m_j}, & M_{22} &= m_{\bar{M}^0} + \sum_j \frac{\langle \bar{M}^0|H_W|j\rangle\langle j|H_W|\bar{M}^0\rangle}{m_{\bar{M}^0} - m_j}, \\ \Gamma_{11} &= 2\pi \sum_f |\langle f|H_W|M^0\rangle|^2 \rho_f, & \Gamma_{12} &= 2\pi \sum_f \langle \bar{M}^0|H_W|f\rangle\langle f|H_W|M^0\rangle \rho_f, \\ \Gamma_{21} &= 2\pi \sum_f \langle M^0|H_W|f\rangle\langle f|H_W|\bar{M}^0\rangle \rho_f, & \Gamma_{22} &= 2\pi \sum_f |\langle f|H_W|\bar{M}^0\rangle|^2 \rho_f, \end{aligned}$$

where H_W stands for the Hamiltonian of the perturbation, which rules the coupling of the flavour eigenstates. In the SM, the expansion of the element M_{11} (M_{22}) is connected to the self-coupling box diagrams reported in Figure 1.2, that contribute to stationary evolution $M^0 \rightarrow M^0$. Instead, the expansions of M_{12} and M_{21} contain the amplitudes responsible for the coupling between the two opposite flavour eigenstates ($M^0 \leftrightarrow \bar{M}^0$) due to the box diagrams of Figure 1.3 that are called *dispersive* (or *off-shell*) virtual transitions. The elements Γ_{12} and Γ_{21} lead as well to meson-antimeson coupling, but they proceed through common virtual decay modes ($M^0 \leftrightarrow f \leftrightarrow \bar{M}^0$), that are referred to as *absorptive* (or *on-shell*) virtual transitions. The elements Γ_{11} and Γ_{22} correspond to the application of

²The arbitrariness of ξ_M correspond to the fact that antiparticles are defined up to a pure phase. Hence, it would be possible to chose $\xi_M = 0$, without loss of generality [36]. We keep this notation to be formally consistent with [4].

³Dissertations, which do not assume CPT invariance, are also possible [4], but they are beyond the scope of this thesis.

⁴The following description actually neglects the internal structure of the neutral mesons. This is the same as assuming that the timescale of the interaction which produces the meson oscillations and decays is much larger than the timescale of the interaction, which rules their internal structure. This description was originally inspired by the work of Weisskopf and Wigner [37, 38].

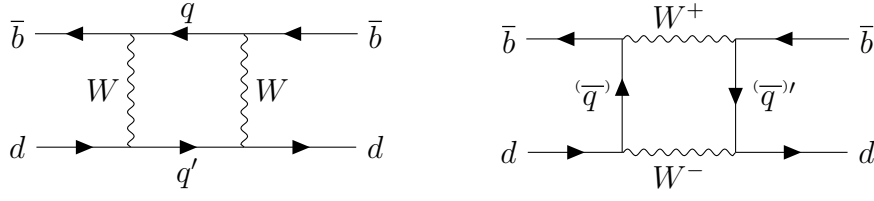


Figure 1.2: Box Feynman diagrams, which contribute to the stationary evolution of neutral mesons. The case of B^0 meson is illustrated as an example. The notations q and q' stand for any up-type quark. The top quark contribution is actually the one which dominates the loops.

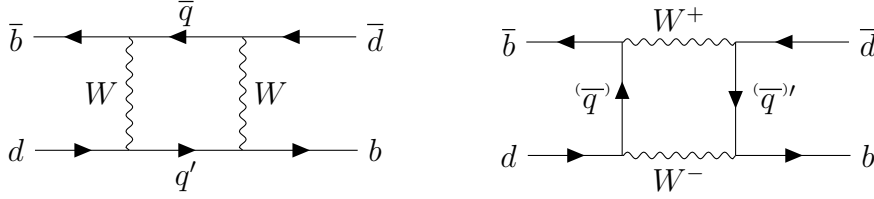


Figure 1.3: Box Feynman diagrams, which generate the dispersive transitions, which responsible for the flavour oscillations. The case of B^0 meson is illustrated as an example. The notations q and q' stand for any up-type quark. The top quark contribution is actually the one which dominates the loops.

the Fermi's golden rule to the flavour eigenstates ($M^0 \rightarrow f$). In conclusion, the flavour eigenstates are coupled if and only if absorptive or dispersive transitions happen, implying that H_W allows for the change of the flavour quantum numbers by one unit to happen.

The calculation of the eigenvalues provides

$$\begin{aligned}\omega_H &= \tilde{H} + \sqrt{H_{12}H_{21}} = M + \mathcal{R}e(\Delta\omega/2) - \frac{i}{2} [\Gamma + \mathcal{I}m(\Delta\omega)], \\ \omega_L &= \tilde{H} - \sqrt{H_{12}H_{21}} = M - \mathcal{R}e(\Delta\omega/2) - \frac{i}{2} [\Gamma - \mathcal{I}m(\Delta\omega)],\end{aligned}$$

where

$$\Delta\omega \equiv \omega_H - \omega_L = 2\sqrt{(M_{12} - \frac{i}{2}\Gamma_{12})(M_{12}^* - \frac{i}{2}\Gamma_{12}^*)}.$$

The respective eigenstates are:

$$|M_H\rangle = |M^0\rangle p + |\bar{M}^0\rangle q, \quad (1.10)$$

$$|M_L\rangle = |M^0\rangle p - |\bar{M}^0\rangle q, \quad (1.11)$$

with

$$|p|^2 + |q|^2 = 1, \quad \frac{q}{p} = \sqrt{\frac{M_{12}^* - \frac{i}{2}\Gamma_{12}^*}{M_{12} - \frac{i}{2}\Gamma_{12}}}. \quad (1.12)$$

According to equation (1.4), the evolution of the system is given by

$$|\psi(t)\rangle = |M_L\rangle a_0 e^{-im_L t} e^{-t\Gamma_L/2} + |M_H\rangle b_0 e^{-im_H t} e^{-t\Gamma_H/2}, \quad (1.13)$$

where the real and imaginary parts of $\omega_{H(L)}$ correspond to the mass and the decay rate of the eigenstate $|M_{H(L)}\rangle$, respectively. The splitting between the two cases is ruled by $\Delta\omega$:

$$m_{\frac{H}{L}} = m_{M^0} \pm \Delta m/2, \quad \Gamma_{\frac{H}{L}} = \Gamma_{M^0} \pm \Delta\Gamma/2,$$

with

$$m_{M^0} = M, \quad \Delta m = \mathcal{R}e[\Delta\omega], \quad \Gamma_{M^0} = \Gamma, \quad \Delta\Gamma = -2\mathcal{I}m[\Delta\omega].$$

For these reasons, the Hamiltonian eigenstates are usually called mass eigenstates or lifetime eigenstates. It is not evident, at this point, whether the eigenstate with higher mass is also the eigenstate with longer lifetime, or not. It depends on the actual values of the complex numbers M_{12}, Γ_{12} . According to the convention adopted here, $\Delta m \equiv m_H - m_L$ is positive, and the subscripts stand for *heavy* and *light*. However, the sign of $\Delta\Gamma$ must be taken from the experiments [36]. In the case of B_s^0 , the heavier mass eigenstate is also the one with the longer lifetime, thus $\Delta\Gamma \equiv \Gamma_H - \Gamma_L < 0$. The same nomenclature is used for B_H^0 and B_L^0 , even if in this case the current measurement of $\Delta\Gamma$ is still compatible with 0. In the case of neutral kaons, the eigenstates are usually distinguished by their very different lifetime. So they are called K_L^0 and K_S^0 , where the subscripts stand for longer and shorter lifetime, respectively. Experimentally the mass of the K_L^0 is heavier than the mass of the K_S^0 .

In general, the two mass eigenstates (1.10) and (1.11) are not guaranteed to be orthogonal,

$$\langle M_L | M_H \rangle = |p|^2 - |q|^2 \neq 0 \Leftrightarrow \left| \frac{q}{p} \right| \neq 1,$$

and the following paragraphs show that such condition is strictly connected with CP conservation or violation. The time evolution of the system is also studied in both cases. In order to do it, it is useful to note that if the system is in a pure M^0 or \bar{M}^0 state at $t = 0$ Equation (1.13) provides $a = b = 1/(2p)$ or $a = b = 1/(2q)$, respectively. Given that, and substituting the mass eigenstates according to (1.10) and (1.11), it is easy to get

$$|M_{\text{phys}}^0(t)\rangle = |M^0\rangle g_+(t) - |\bar{M}^0\rangle g_-(t) \frac{q}{p}, \quad (1.14)$$

$$|\bar{M}_{\text{phys}}^0(t)\rangle = |\bar{M}^0\rangle g_+(t) - |M^0\rangle g_-(t) \frac{p}{q}, \quad (1.15)$$

with

$$g_{\pm}(t) = \frac{1}{2} \left(e^{-im_H t} e^{-t\Gamma_H/2} \pm e^{-im_L t} e^{-t\Gamma_L/2} \right). \quad (1.16)$$

By definition, the ket $|M_{\text{phys}}^0(t)\rangle$ ($|\bar{M}_{\text{phys}}^0(t)\rangle$) stands for the state of the neutral meson system at a generic time t , if at $t = 0$ it was a pure flavour eigenstate $|M^0\rangle$ ($|\bar{M}^0\rangle$).

The neutral mesons with CP conservation. The Hamiltonian conserves CP if and only if $[CP, H] = 0$ or equivalently $H = (CP)^\dagger H (CP)$. In this case the following identity holds:

$$\begin{aligned} M_{12} - \frac{i}{2}\Gamma_{12} &= H_{12} = \\ \langle M^0 | H | \bar{M}^0 \rangle &= \langle M^0 | (CP)^\dagger H (CP) | \bar{M}^0 \rangle = \langle \bar{M}^0 | H | M^0 \rangle e^{-i2\xi_M} = \\ &= H_{21} e^{-i2\xi_M} = (M_{12}^* - \frac{i}{2}\Gamma_{12}^*) e^{-i2\xi_M}. \end{aligned} \quad (1.17)$$

The comparison⁵ between equation (1.17) and Equation (1.12) shows that, if CP is conserved, $(q/p)^2 = e^{i2\xi_M}$ and the mixing factor q/p is a pure arbitrary phase. This implies that

$$|q/p|^2 = 1 \leftrightarrow |p|^2 - |q|^2 = 0 = \langle M_L | M_H \rangle, \quad (1.18)$$

$$\frac{M_{12}}{\Gamma_{12}} = \frac{|M_{12}|e^{i\phi_M}}{|\Gamma_{12}|e^{i\phi_\Gamma}} \text{ is real } \leftrightarrow \sin(\phi_M - \phi_\Gamma) = 0. \quad (1.19)$$

As a result, in the CP -conserving hypothesis, the mass eigenstates are orthogonal and the phase difference between the dispersive and the absorptive matrix elements is null. To facilitate the following considerations, $\xi_M = 0$ is assumed, making both M_{12} and Γ_{12} real. The Hamiltonian eigenvalues become

$$\omega_H = M + M_{12} - \frac{i}{2}(\Gamma + \Gamma_{12}), \quad \omega_L = M - M_{12} - \frac{i}{2}(\Gamma - \Gamma_{12}), \quad (1.20)$$

where the mass and decay-rate splitting clearly coincide with the non-diagonal matrix elements $\Delta m = M_{12}$ and $\Delta\Gamma = \Gamma_{12}$, respectively. Besides, the choice $\xi_M = 0$ implies $p = q = 1/\sqrt{2}$, and the mass eigenstates are also CP eigenstates:

$$|M_H\rangle = \frac{1}{\sqrt{2}} (|M^0\rangle + |\bar{M}^0\rangle), \quad |M_L\rangle = \frac{1}{\sqrt{2}} (|M^0\rangle - |\bar{M}^0\rangle). \quad (1.21)$$

It is instructive to look at the time evolution of the system with two different initial conditions:

- If at $t = 0$ the system is in a pure mass eigenstate $|\psi(t=0)\rangle = |M_L\rangle$, then $a_0 = 1$, $b_0 = 0$, and at any later time $|\psi(t)\rangle = |M_L\rangle e^{-im_L t} e^{-\Gamma_L t} = \frac{1}{\sqrt{2}} (|M^0\rangle + |\bar{M}^0\rangle) e^{-im_L t} e^{-\Gamma_L t}$. Hence, the time-dependent rates to observe the mass and the flavour eigenstates are

$$\Gamma(M_L \rightarrow M_L; t) = e^{-\Gamma_L t}, \quad \Gamma(M_L \rightarrow M_H; t) = 0, \quad (1.22)$$

$$\Gamma(M_L \rightarrow M^0; t) = \frac{1}{2} e^{-\Gamma_L t}, \quad \Gamma(M_L \rightarrow \bar{M}^0; t) = \frac{1}{2} e^{-\Gamma_L t}. \quad (1.23)$$

As expected the probability to observe M_L decreases with decay-rate Γ_L and there is no possibility to observe M_H . Besides, the relations in the second line confirm that M_L is an equal mixture of M^0 and \bar{M}^0 at any time. The total probability to observe the system is the same as the probability to observe M_L :

$$\Gamma(M_L \rightarrow M^0; t) + \Gamma(M_L \rightarrow \bar{M}^0; t) = e^{-\Gamma_L t} = \Gamma(M_L \rightarrow M_L; t). \quad (1.24)$$

Analogous results can be obtained switching the subscripts L and H .

- If at $t = 0$ the system is in a pure flavour eigenstate $|\psi(t=0)\rangle = |M^0\rangle$, Equation (1.14) holds, $a_0 = b_0 = 1/\sqrt{2}$ and

$$|M^0_{\text{phys}}(t)\rangle = |M_L\rangle \frac{1}{\sqrt{2}} e^{-im_L t} e^{-\Gamma_L t} + |M_H\rangle \frac{1}{\sqrt{2}} e^{-im_H t} e^{-\Gamma_H t}. \quad (1.25)$$

⁵At first sight, Equation (1.19) seems to imply that the observable quantities Δm and $\Delta\Gamma$ would depend on the arbitrary phase $e^{i\xi_M}$. However, one can show [36] that also the Hamiltonian matrix elements do depend on $e^{i\xi_M}$ in such a way that the observable quantities are $e^{i\xi_M}$ -independent. Of course, this is true even when CP is not conserved.

Therefore:

$$\Gamma(M^0 \rightarrow M_L; t) = |\langle M_L | M^0_{\text{phys}}(t) \rangle|^2 = \frac{1}{2} e^{-\Gamma_L t}, \quad (1.26)$$

$$\Gamma(M^0 \rightarrow M_H; t) = |\langle M_H | M^0_{\text{phys}}(t) \rangle|^2 = \frac{1}{2} e^{-\Gamma_H t}, \quad (1.27)$$

with the transition rates to the mass eigenstates following their respective decay rate. The total probability to observe the system is the average of these probabilities:

$$\Gamma(M^0 \rightarrow M_L; t) + \Gamma(M^0 \rightarrow M_H; t) = \frac{1}{2} [e^{-\Gamma_L t} + e^{-\Gamma_H t}]. \quad (1.28)$$

The probabilities to observe or not a change of flavour are

$$\Gamma(M^0 \rightarrow \bar{M}^0; t) = |g_-(t)|^2 = \frac{1}{4} [e^{-\Gamma_L t} + e^{-\Gamma_H t} - 2e^{-\Gamma t} \cos(\Delta m t)], \quad (1.29)$$

$$\Gamma(M^0 \rightarrow M^0; t) = |g_+(t)|^2 = \frac{1}{4} [e^{-\Gamma_L t} + e^{-\Gamma_H t} + 2e^{-\Gamma t} \cos(\Delta m t)], \quad (1.30)$$

respectively, where an oscillatory interference term is present. The oscillations have constant period $2\pi/\Delta m$, and their amplitude is damped by the exponential factor $e^{-\Gamma t}$. Analogous results can be obtained switching M^0 and \bar{M}^0 .

The neutral mesons without CP conservation. If CP is not strictly conserved, the mixing factor q/p may alter the mass and decay-time splittings, and therefore the time evolution of the system. Furthermore, CP violation may arise, even if $|q/p| = 1$, either directly in the decay or when an interference occurs between mixing and decay. Details are now provided.

First of all, if the system is prepared in a pure flavour eigenstate at time $t = 0$, the evolution rate into the same flavour at a later time is the same as in the case where CP is conserved,

$$\Gamma(M^0 \rightarrow M^0; t) = \Gamma(\bar{M}^0 \rightarrow \bar{M}^0; t) = |g_+(t)|^2,$$

instead, in general, the flavour oscillation rates can be different:

$$\left(\Gamma(M^0 \rightarrow \bar{M}^0; t) = |g_-(t)|^2 \left| \frac{q}{p} \right|^2 \right) \neq \left(\Gamma(\bar{M}^0 \rightarrow M^0; t) = |g_-(t)|^2 \left| \frac{p}{q} \right|^2 \right). \quad (1.31)$$

In other words, when $|q/p|^2 \neq 1$ the probability of a flavour oscillation is not equal to the probability of the CP -conjugated process. This can be experimentally checked with semileptonic decays, which add a constant factor, *i.e.* their branching fraction, to the two probabilities above. Secondly, if CP is not conserved, the mass eigenstates are no more guaranteed to be CP eigenstates. Furthermore, it is not possible to distinguish them by their decays into CP eigenstate, as was tacitly assumed in the previous paragraph. It is possible, anyway, to predict the time evolution of the neutral-meson system, but the decay to a final state has to be included in the description. In order to do that, the following amplitudes have to be considered:

$$\begin{aligned} A_f &= \langle f | H_W | M^0 \rangle, & \bar{A}_f &= \langle f | H_W | \bar{M}^0 \rangle, \\ A_{\bar{f}} &= \langle \bar{f} | H_W | M^0 \rangle, & \bar{A}_{\bar{f}} &= \langle \bar{f} | H_W | \bar{M}^0 \rangle, \end{aligned}$$

where f is a generic final state with $CP|f\rangle = |\bar{f}\rangle e^{i\xi_f}$ with the arbitrary phase $e^{i\xi_f}$ explicitly reported once more. This notation permits some meaningful, particular cases to be defined:

- if the flavour eigenstate M is directly coupled with a given final state f_{FS} , but it is not coupled with the CP -conjugated final state \bar{f}_{FS} , and the opposite happens for \bar{M} , the decays $M \rightarrow f_{FS}$ and $\bar{M} \rightarrow \bar{f}_{FS}$ are said *flavour-specific* (see Section 1.1.1). Using the notation just introduced:

$$A_{f_{FS}} \neq 0, \quad \bar{A}_{\bar{f}_{FS}} \neq 0 \quad \text{and} \quad \bar{A}_{f_{FS}} = A_{\bar{f}_{FS}} = 0. \quad (1.32)$$

However, the *wrong-sign* decay-rates $\Gamma(M^0 \rightarrow \bar{f}_{FS}; t)$ and $\Gamma(\bar{M}^0 \rightarrow f_{FS}; t)$ are not necessarily null, when the flavour mixing is allowed.

- When the final state is a CP eigenstate, one can assume: $f = \bar{f} \equiv f_{CP}$ and the formal substitutions $A_f = A_{\bar{f}} = A_{f_{CP}}$, $\bar{A}_f = \bar{A}_{\bar{f}} = \bar{A}_{f_{CP}}$ are allowed.
- If CP is a symmetry of H_W , then:

$$|A_f| = |\bar{A}_{\bar{f}}| \quad \text{and} \quad |A_{\bar{f}}| = |\bar{A}_f|; \quad (1.33)$$

while this is not guaranteed, when CP is violated.

If at $t = 0$ the neutral meson system is in a flavour eigenstate M^0 , the decay rate to a generic final state f , at any later time t , is

$$\begin{aligned} \Gamma(M^0 \rightarrow f; t) &= |\langle f | H_W | M^0_{\text{phys}}(t) \rangle|^2 = \left| A_f g_+(t) - \frac{q}{p} \bar{A}_f g_-(t) \right|^2 \\ &= |A_f g_+(t)|^2 + \left| \frac{q}{p} \bar{A}_f g_-(t) \right|^2 - 2\mathcal{R}e \left[A_f^* g_+^*(t) \frac{q}{p} \bar{A}_f g_-(t) \right], \end{aligned}$$

where the three terms are associated with a decay without oscillation, a decay after an oscillation, and the interference between the two cases, respectively. The following definitions

$$\lambda_f \equiv \frac{q \bar{A}_f}{p A_f}, \quad \bar{\lambda}_f \equiv \frac{1}{\lambda_f}, \quad \lambda_{\bar{f}} \equiv \frac{q \bar{A}_{\bar{f}}}{p A_{\bar{f}}}, \quad \bar{\lambda}_{\bar{f}} \equiv \frac{1}{\lambda_{\bar{f}}}, \quad (1.34)$$

are useful to write the following general time-dependent decay rates:

$$\Gamma(M^0 \rightarrow f; t) = |A_f|^2 \left(|g_+(t)|^2 + |\lambda_f|^2 |g_-(t)|^2 - 2\mathcal{R}e[\lambda_f g_+^*(t) g_-(t)] \right), \quad (1.35)$$

$$\Gamma(M^0 \rightarrow \bar{f}; t) = |\bar{A}_{\bar{f}}|^2 \left| \frac{q}{p} \right|^2 \left(|g_-(t)|^2 + |\bar{\lambda}_{\bar{f}}|^2 |g_+(t)|^2 - 2\mathcal{R}e[\bar{\lambda}_{\bar{f}} g_+^*(t) g_-(t)] \right), \quad (1.36)$$

$$\Gamma(\bar{M}^0 \rightarrow f; t) = |A_f|^2 \left| \frac{p}{q} \right|^2 \left(|g_-(t)|^2 + |\lambda_f|^2 |g_+(t)|^2 - 2\mathcal{R}e[\lambda_f g_+^*(t) g_-(t)] \right), \quad (1.37)$$

$$\Gamma(\bar{M}^0 \rightarrow \bar{f}; t) = |\bar{A}_{\bar{f}}|^2 \left(|g_+(t)|^2 + |\bar{\lambda}_{\bar{f}}|^2 |g_-(t)|^2 - 2\mathcal{R}e[\bar{\lambda}_{\bar{f}} g_+^*(t) g_-(t)] \right), \quad (1.38)$$

where

$$|g_{\pm}(t)|^2 = \frac{e^{-\Gamma t}}{2} \left[\cosh\left(\frac{\Delta\Gamma}{2}t\right) \pm \cos(\Delta m t) \right], \quad (1.39)$$

$$g_{\pm}^*(t) g_{\mp}(t) = -\frac{e^{-\Gamma t}}{2} \left[\sinh\left(\frac{\Delta\Gamma}{2}t\right) \pm i \sin(\Delta m t) \right]. \quad (1.40)$$

Combining these expressions, the time-dependent decay rates of neutral mesons can be written:

$$\Gamma(M^0 \rightarrow f; t) = |A_f|^2 (1 + |\lambda_f|^2) \frac{e^{-\Gamma t}}{2} \left[\cosh\left(\frac{\Delta\Gamma}{2}t\right) - A_f^{\Delta\Gamma} \sinh\left(\frac{\Delta\Gamma}{2}t\right) + C_f \cos(\Delta mt) - S_f \sin(\Delta mt) \right], \quad (1.41)$$

$$\Gamma(\bar{M}^0 \rightarrow f; t) = |A_f|^2 \left| \frac{p}{q} \right|^2 (1 + |\lambda_f|^2) \frac{e^{-\Gamma t}}{2} \left[\cosh\left(\frac{\Delta\Gamma}{2}t\right) - A_f^{\Delta\Gamma} \sinh\left(\frac{\Delta\Gamma}{2}t\right) - C_f \cos(\Delta mt) + S_f \sin(\Delta mt) \right], \quad (1.42)$$

with

$$A_f^{\Delta\Gamma} = \frac{-2\mathcal{R}e(\lambda_f)}{1 + |\lambda_f|^2}, \quad C_f = \frac{1 - |\lambda_f|^2}{1 + |\lambda_f|^2}, \quad S_f = \frac{2\mathcal{I}m(\lambda_f)}{1 + |\lambda_f|^2}; \quad (1.43)$$

and by construction

$$(A_f^{\Delta\Gamma})^2 + (C_f)^2 + (S_f)^2 = 1. \quad (1.44)$$

The next sections analyze the concepts introduced here, providing further insight to the meaning of the parameters $A_f^{\Delta\Gamma}$, C_f , S_f .

1.1.4 CP -violation categories

In the previous Section it is shown that CP conservation implies various requirements. However, none of them alone is sufficient for CP conservation. In other words, CP violation may be present, even if some of those conditions are actually satisfied. Depending on the satisfied conditions, different CP -violation categories can be distinguished. They can also be quantified by specific asymmetries, which are going to be introduced.

CP violation in the decay As seen in (1.33), if

$$|\bar{A}_f/A_f| \neq 1,$$

then CP violation occurs. This implicates that the decay rate of a process is not equal to the decay rate of the CP -conjugate process:

$$\Gamma(M \rightarrow f) \neq \Gamma(\bar{M} \rightarrow \bar{f}).$$

Hence, this is called “ CP violation in the decay” and is measured by

$$A_{CP} \equiv \frac{|\bar{A}_f/A_f|^2 - 1}{|\bar{A}_f/A_f|^2 + 1}. \quad (1.45)$$

For flavour-specific decays, it corresponds to the asymmetry of the *right-sign* decay-rates

$$A_{CP} = \frac{\Gamma(\bar{M} \rightarrow \bar{f}_{FS}) - \Gamma(M \rightarrow f_{FS})}{\Gamma(\bar{M} \rightarrow \bar{f}_{FS}) + \Gamma(M \rightarrow f_{FS})}, \quad (1.46)$$

as one can deduce from Equations (1.35) and (1.38), noting that $\lambda_{f_{FS}} = \bar{\lambda}_{\bar{f}_{FS}} = 0$. This is the only possible source of CP violation for electrically charged particles and for baryons, whose mixing is not allowed.

CP-violation in the mixing. As mentioned in (1.18), when

$$|q/p|^2 \neq 1,$$

the Hamiltonian which rules the evolution of the system cannot conserve CP . In particular, it does not conserve CP in the mixing, namely the probabilities of the CP -conjugated flavour oscillation processes are different (see Equation (1.31)):

$$\Gamma(M^0 \rightarrow \bar{M}^0; t) \neq \Gamma(\bar{M}^0 \rightarrow M^0; t).$$

According to the SM –and in most of its reasonable extensions [4]– the charged-current semileptonic neutral meson decays $\bar{M} \rightarrow \ell^\pm X$ are flavour-specific ($A_{\ell^- X} = \bar{A}_{\ell^+ X} = 0$) and do not manifest CP violation in the decay ($|A_{\ell^+ X}| = |\bar{A}_{\ell^- X}|$). Hence, CP violation in the mixing is usually measured by the asymmetry between the decay rates of the oscillation-induced (*wrong-sign*) semileptonic decays

$$A_{SL} = \frac{\Gamma(\bar{M}^0 \rightarrow \ell^+ X) - \Gamma(M^0 \rightarrow \ell^- X)}{\Gamma(\bar{M}^0 \rightarrow \ell^+ X) + \Gamma(M^0 \rightarrow \ell^- X)} = \frac{1 - |q/p|^4}{1 + |q/p|^4}, \quad (1.47)$$

which is easily obtained from the Equations (1.36) and (1.37), where again $\lambda_{\ell^- X} = \bar{\lambda}_{\ell^+ X} = 0$. In the cases of B^0 and B_s^0 mesons, the CP violation in mixing is currently measured to be compatible with 0 with very high precision [4]:

$$\begin{aligned} A_{SL}^d &= -0.0021 \pm 0.0017 & \leftrightarrow & |q/p|_d = 1.0010 \pm 0.0008; \\ A_{SL}^s &= -0.0006 \pm 0.0028 & \leftrightarrow & |q/p|_s = 1.0003 \pm 0.0014; \end{aligned}$$

and consistent with the SM predictions [4]

$$A_{SL}^d = \mathcal{O}[(m_c/m_t)^2 \sin \beta] \lesssim 10^{-3}, \quad A_{SL}^s = \mathcal{O}[(m_c/m_t)^2 \sin \beta_s] \lesssim 10^{-4}.$$

CP-violation in the interference between mixing and decay. CP violation can be observed even if the conditions $|A_f| = |\bar{A}_f|$ and $|q/p| = 1$ are satisfied. This may happen because of the interference of decay without mixing $M^0 \rightarrow f$, and decay with mixing, $M^0 \rightarrow \bar{M}^0 \rightarrow f$. Such decays are necessarily *flavour-non-specific*, namely both M^0 and \bar{M}^0 are directly coupled to f . If CP is not conserved the two time-dependent decay rates are different:

$$\Gamma(M^0 \xrightarrow{(\leftrightarrow \bar{M}^0)} f; t) \neq \Gamma(\bar{M}^0 \xrightarrow{(\leftrightarrow M^0)} f; t).$$

In absence of CP violation in both mixing and decay, this corresponds to the condition [4]:

$$\arg(\lambda_f) + \arg(\lambda_{\bar{f}}) \neq 0. \quad (1.48)$$

All the decays to CP eigenstates are flavour-non-specific, thus the following time-dependent asymmetry is used to quantify the CP violation:

$$A_{f_{CP}}(t) = \frac{\Gamma(\bar{M}^0 \rightarrow f_{CP}; t) - \Gamma(M^0 \rightarrow f_{CP}; t)}{\Gamma(\bar{M}^0 \rightarrow f_{CP}; t) + \Gamma(M^0 \rightarrow f_{CP}; t)}.$$

For B mesons, $|q/p| = 1$ can be assumed [4], therefore, exploiting the Equations (1.41) and (1.42), the time-dependent asymmetry is:

$$A_{f_{CP}}(t) = \frac{S_{f_{CP}} \sin(\Delta mt) - C_{f_{CP}} \cos(\Delta mt)}{\cosh(\Delta \Gamma t/2) - A_{f_{CP}}^{\Delta \Gamma} \sinh(\Delta \Gamma t/2)}. \quad (1.49)$$

The negligible CP violation in the mixing also implies $|\lambda_f|^2 = |\bar{A}_f/A_f|^2$, and therefore $C_{f_{CP}} = A_{CP}$ measures the CP violation in the decay, for B^0 and B_s^0 mesons. By virtue of that, if the CP violation in the decay is also neglected, the remaining conditions to observe CP asymmetry are $\Delta m \neq 0$ and $S_{f_{CP}} \neq 0$, where the former corresponds to the pulsation of the asymmetry oscillations and the latter is the amplitude.

In conclusion, for B^0 and B_s^0 mesons, the parameter S_f measures the CP violation in the interference between mixing and decay. According to the definitions in (1.43), the condition for this kind of CP violation is:

$$\mathcal{I}m(\lambda_{f_{CP}}) \neq 0$$

which is the same as (1.48), but for decays to CP eigenstates.

1.2 CP violation in the Standard Model

All the observations in the CP violation sector are currently consistent with the predictions of the Standard Model [4]. In the SM, CP violation arises because the Yukawa couplings –*i.e.* the parameters which rule the interactions of the Higgs field with the electroweak eigenstates of quark and leptons– are complex numbers. In the basis of the flavour eigenstates of quark and leptons, the matrix of the Yukawa coupling is diagonal and flavour and mass eigenstates coincide for the elementary fermions⁶. In this basis, the Spontaneous Symmetry Breaking (SSB) mechanism [40–44] dynamically explains the origin of the fermion masses. In contrast, the flavour (or mass) eigenstates are distinct from the eigenstates of the electroweak interaction. According to the idea initially proposed by N. Cabibbo [14], the electroweak eigenstates are mixtures of the flavour eigenstates. With this assumption, the SM accommodates the transitions between different flavours and elegantly recovers the universality of the electroweak sector: once the interacting eigenstates are organized into chiral multiplets and singlets, in conformity with the prescriptions of the Glashow-Weinberg-Salam Model [12], the electromagnetic and weak interactions are analogous for all quark and lepton generations. In particular, just two constants, $\alpha_{EM} \simeq 1/137$ and $\theta_W \simeq 30^\circ$, are enough to explain all the couplings. In the case of leptons the flavour and the interaction eigenstates coincide if the neutrino masses are neglected⁷. For quarks, instead, a proper change of basis is unavoidable, and its parameters are encoded by the Cabibbo-Kobayashi-Maskawa matrix (V_{CKM}) [15]. The magnitude of its elements rules the transitions among different quark generations. Since the Yukawa couplings are complex numbers, the V_{CKM} elements are also complex. With three quark generations and without mass degeneration among them –as it is currently observed– a single complex phase in V_{CKM} is enough to generate all the CP violation phenomenology. Two consequences are extremely meaningful: on the one hand, observable CP violation is always connected with the quantum interference of multiple contributions; on the other hand, the same parameters rule a lot of different process, which can be experimentally tested. These arguments make the SM-consistency checks through CP -violation measurements an appealing sector for indirect searches for new

⁶This is different from the case of neutral mesons.

⁷This thesis focuses on the quark sector and neutrino masses are negligible to this respect. Therefore, the following discussion skips the lepton mixing. Reviews of this sector can be found in Ref. [12, 39].

physics. The following sections are going to explain in detail the consideration resumed in this introduction.

1.2.1 Yukawa coupling and flavour transitions

The whole SM Lagrangian is the sum of four terms:⁸

$$\mathcal{L}_{\text{SM}} = \mathcal{L}_{\text{gauge}} + \mathcal{L}_{\text{Higgs}} + \mathcal{L}_{\text{Kin}} + \mathcal{L}_{\text{Yukawa}},$$

that can be briefly introduced as follows. Fermions are encoded by spinor fields ψ , which satisfy the Dirac equation. Their free evolution Lagrangian is

$$\mathcal{L}_{\text{Dirac},\psi} = i\bar{\psi}(\gamma_\mu\partial^\mu)\psi,$$

where $\bar{\psi} \equiv \psi^\dagger\gamma^0$ and the mass terms are not considered, for the moment. The possible spinor fields [45] are organized in three generations (or families), each one with five representations:

$$\begin{aligned} Q_{Li}^I(3, 2, +1/6), \quad u_{Ri}^I(3, 1, +2/3), \quad d_{Ri}^I(3, 1, -1/3), \\ L_{Li}^I(1, 2, -1/2), \quad l_{Ri}^I(1, 1, -1). \end{aligned} \quad (1.50)$$

Each representation encodes multiplets of quarks (first line) or leptons (second line). In this notation, the superscripts I state that the fields are expressed in the interaction basis, the subscripts $i = 1, 2, 3$ distinguish among the different generations, the subscripts L, R indicate the left-handed and right-handed chirality of the fields in the multiplet. The arguments between parentheses fix the dimension of the multiplet for the $SU(3)_C$ group, the dimension of the multiplet for the $SU(2)_L$ group and the hypercharge quantum number, respectively. For example

$$Q_{Li}^I(3, 2, +1/6) = \begin{pmatrix} u_L^I \\ d_L^I \end{pmatrix}_i \in \left\{ \begin{pmatrix} u_L^I \\ d_L^I \end{pmatrix}, \begin{pmatrix} c_L^I \\ s_L^I \end{pmatrix}, \begin{pmatrix} t_L^I \\ b_L^I \end{pmatrix} \right\},$$

where each field is actually a $SU(3)_C$ triplet⁹, and u and d stand for the generic up-type or down-type quark fields. The fermion interactions are introduced by the assumption of local gauge invariance under the transformations of the group $SU(3)_C \times SU(2)_L \times U(1)_Y$. This leads to the necessary substitution of the partial derivative ∂^μ with the covariant derivative D^μ

$$\partial^\mu \rightarrow D^\mu = \partial^\mu + ig_s G_a^\mu L_a + ig W_b^\mu \sigma_b + ig' B^\mu Y,$$

where eight gauge boson fields of the strong interaction, G_a^μ , three gauge boson fields of the weak interaction, W_b^μ , and one boson field of hypercharge appear to preserve the symmetry of the Lagrangian. Besides, L_a are the eight $SU(3)_C$ generators (the 3×3 Gell-Mann matrices); σ_b are the generators of $SU(2)_L$ (the 2×2 Pauli matrices); Y is

⁸The *Lectures Notes on CP Violation* by N. Tuning are the main reference for the composition of this section. Details on all the not mentioned theoretical background and notation definitions can be found in Ref. [12, 13, 39].

⁹With the marginal exception of the interactions with the gluon fields, the following discussion does not depend on the color charges of the strong interaction, so they are not explicitly reported, to keep a lighter notation.

the scalar generator of $U(1)_Y$, and g_s , g and g' are the corresponding coupling constants. With this substitution, the kinetic Lagrangian becomes

$$\mathcal{L}_{\text{Dirac}} \xrightarrow{\partial^\mu \rightarrow D^\mu} \mathcal{L}_{\text{kin}} = \sum_{\psi} i\bar{\psi}(\gamma_\mu D^\mu)\psi,$$

where the sum is over all the multiplets reported in (1.50).

Until no mass contributions are considered, the free dynamics of the gauge bosons is encoded in

$$\mathcal{L}_{\text{gauge}} = -\frac{1}{4}\mathbf{G}_{\mu\nu}^a(\mathbf{G}^a)^{\mu\nu} - \frac{1}{4}\mathbf{W}_{\mu\nu}^b(\mathbf{W}^b)^{\mu\nu} - \frac{1}{4}\mathbf{B}_{\mu\nu}\mathbf{B}^{\mu\nu}, \quad (1.51)$$

where

$$\begin{aligned} \mathbf{G}_{\mu\nu}^a &= \partial_\mu G_{\nu}^a - \partial_\nu G_{\mu}^a + g_s f^{abc} G_{\mu\nu}^b G_{\mu\nu}^c, \\ \mathbf{W}_{\mu\nu}^b &= \partial_\mu W_{\nu}^b - \partial_\nu W_{\mu}^b + g \epsilon^{def} W_{\mu\nu}^e W_{\mu\nu}^f, \\ \mathbf{B}_{\mu\nu} &= \partial_\mu B_{\nu} - \partial_\nu B_{\mu}, \end{aligned}$$

are the strength tensors of the gauge boson fields (details in Ref.s [12, 13]). In the SM, the masses of the fundamental particles dynamically arise because of their interactions with the scalar isospin doublet

$$\phi = \phi(1, 2, +1/2) = \begin{pmatrix} \phi^+ \\ \phi^0 \end{pmatrix}. \quad (1.52)$$

For the fundamental bosons, these couplings are located in the Lagrangian term

$$\mathcal{L}_{\text{Higgs}} = (D_\mu \phi)^\dagger (D^\mu \phi) + \mu^2 \phi^\dagger \phi - \lambda (\phi^\dagger \phi)^2. \quad (1.53)$$

Since the potential $V_\phi = \mu^2 \phi^\dagger \phi - \lambda (\phi^\dagger \phi)^2$ has a non-null point of minimum, the vacuum expectation value (v.e.v.) for the ϕ field can be assumed to be $\langle 0|\phi|0\rangle = (0 \quad v/\sqrt{2})^T$, and the fluctuations about this point can be parametrized by

$$\phi = \begin{pmatrix} 0 \\ \frac{1}{\sqrt{2}}(v + H) \end{pmatrix}. \quad (1.54)$$

By substituting (1.52) with (1.54) in (1.51) and (1.53), the Higgs field H appears as a massive, scalar field, and further mass terms, with consistent strength tensors, appear when the following combinations of the gauge bosons are considered:

$$\begin{aligned} W^{+\mu} &= \frac{1}{\sqrt{2}}(W_1^\mu - iW_2^\mu), & W^{-\mu} &= \frac{1}{\sqrt{2}}(W_1^\mu + iW_2^\mu), \\ \begin{pmatrix} Z^\mu \\ A^\mu \end{pmatrix} &= \begin{pmatrix} \cos \theta_W & -\sin \theta_W \\ \sin \theta_W & \cos \theta_W \end{pmatrix} \begin{pmatrix} W_3^\mu \\ B^\mu \end{pmatrix} & \text{with: } \sin \theta_W &= \frac{g}{\sqrt{g^2 + g'^2}}. \end{aligned}$$

Applying these field redefinitions to \mathcal{L}_{kin} , one can observe that the massive boson fields $W^{\pm\mu}$, Z^μ and the massless field A^μ are coupled with fermionic currents, whose chiralities and coupling constants agree with those observed for the charged weak, neutral weak and electromagnetic interactions, respectively, respectively. In other words they are the physical fields, which mediate the interactions of the electroweak sector¹⁰. This is explicitly shown below for the $W^{\pm\mu}$ case.

¹⁰The gauge bosons of $SU(3)_C$ produce the massless gluons, mediators of the strong interaction. Their case is omitted here for brevity; details can be found in [12, 36].

Remarkably, no new parameters are necessary to explain the masses of the fundamental bosons: the coupling constants g_s , g , g' and the v.e.v. of the Higgs field, v , are sufficient, once the right shape of the Higgs potential is provided. This is not at all the case for fermions. Their coupling with the Higgs field are included in

$$\mathcal{L}_{\text{Yukawa}} = - \sum_{i,j} \left(Y_{ij}^d \bar{Q}_{Li}^I \phi d_{Rj}^I + Y_{ij}^u \bar{Q}_{Li}^I \tilde{\phi} u_{Rj}^I + Y_{ij}^l \bar{L}_{Li}^I \phi l_{Rj}^I + \text{h.c.} \right)$$

where $\tilde{\phi} = i\sigma_2 \phi^*$ is the Higgs charge-conjugated doublet. The complex numbers Y_{ij}^d , Y_{ij}^u , Y_{ij}^l are elements of arbitrary matrices that produce couplings between different generations and are called Yukawa couplings. By applying the SSB formalism, thus writing the ϕ doublet according to (1.54), $\mathcal{L}_{\text{Yukawa}}$ includes

$$\mathcal{L}_{\text{Yukawa}} \supset \mathcal{L}_{\text{Yukawa}}^{\text{quark}} = - \sum_{i,j} \left(Y_{ij}^d \frac{v}{\sqrt{2}} \bar{d}_{Li}^I d_{Rj}^I + Y_{ij}^u \frac{v}{\sqrt{2}} \bar{u}_{Li}^I u_{Rj}^I + \text{h.c.} \right), \quad (1.55)$$

where the leptonic terms and interaction terms between the Higgs boson H and the fermions have been omitted. Proper mass term would appear if the $M^d = Y^d v / \sqrt{2}$, $M^u = Y^u v / \sqrt{2}$ matrices were both diagonal. Indeed, it can be demonstrated¹¹ that they can be made diagonal with positive elements by four different unitary matrices V :

$$M_{diag}^d = V_L^d M^d V_R^{d\dagger}, \quad M_{diag}^u = V_L^u M^u V_R^{u\dagger}.$$

Thanks to the properties of unitary matrices, Equation (1.55) can be rewritten as

$$\begin{aligned} -\mathcal{L}_{\text{Yukawa}}^{\text{quark}} &= \begin{pmatrix} \bar{u}_L^I & \bar{c}_L^I & \bar{t}_L^I \end{pmatrix} V_L^{u\dagger} V_L^u M^u V_R^{u\dagger} V_R^u \begin{pmatrix} u_R^I \\ c_R^I \\ t_R^I \end{pmatrix} + \begin{pmatrix} \bar{d}_L^I & \bar{s}_L^I & \bar{b}_L^I \end{pmatrix} V_L^{d\dagger} V_L^d M^d V_R^{d\dagger} V_R^d \begin{pmatrix} d_R^I \\ s_R^I \\ b_R^I \end{pmatrix} + \text{h.c.} \\ &= \begin{pmatrix} \bar{u}_L^I & \bar{c}_L^I & \bar{t}_L^I \end{pmatrix} V_L^{u\dagger} M_{diag}^u V_R^u \begin{pmatrix} u_R^I \\ c_R^I \\ t_R^I \end{pmatrix} + \begin{pmatrix} \bar{d}_L^I & \bar{s}_L^I & \bar{b}_L^I \end{pmatrix} V_L^{d\dagger} M_{diag}^d V_R^d \begin{pmatrix} d_R^I \\ s_R^I \\ b_R^I \end{pmatrix} + \text{h.c.} \\ &= M_{11}^u \bar{u}u + M_{22}^u \bar{c}c + M_{33}^u \bar{t}t + M_{11}^d \bar{d}d + M_{22}^d \bar{s}s + M_{33}^d \bar{b}b, \end{aligned}$$

where the last line is obtained substituting the interaction basis with the mass (or flavour) basis:

$$\begin{aligned} \mathbf{d}_{Li} &= (V_L^d)_{ij} \mathbf{d}_{Li}^I, & \mathbf{d}_{Ri} &= (V_R^d)_{ij} \mathbf{d}_{Ri}^I, \\ \mathbf{u}_{Li} &= (V_L^u)_{ij} \mathbf{u}_{Li}^I, & \mathbf{u}_{Ri} &= (V_R^u)_{ij} \mathbf{u}_{Ri}^I. \end{aligned} \quad (1.56)$$

Only a small piece¹² of the whole SM Lagrangian permits transitions between different flavours:

$$\mathcal{L}_{\text{kin}} \supset \mathcal{L}_{\text{kin,CC}}^{\text{quark}} = \sum_i \left(\frac{g}{\sqrt{2}} \bar{\mathbf{d}}_{Li}^I \gamma_\mu \mathbf{u}_{Li}^I W^{-\mu} + \frac{g}{\sqrt{2}} \bar{\mathbf{u}}_{Li}^I \gamma_\mu \mathbf{d}_{Li}^I W^{+\mu} \right), \quad (1.57)$$

where the sum is over the three generations. Indeed, using the transformations (1.56) to go from the interaction basis to the mass basis, Equation (1.57) becomes

$$\mathcal{L}_{\text{kin,CC}}^{\text{quark}} = \sum_{ij} \left(\frac{g}{\sqrt{2}} \bar{\mathbf{d}}_{Li} \gamma_\mu (V_L^d V_L^{u\dagger})_{ij} \mathbf{u}_{Lj} W^{-\mu} + \frac{g}{\sqrt{2}} \bar{\mathbf{u}}_{Li} \gamma_\mu (V_L^u V_L^{d\dagger})_{ij} \mathbf{d}_{Lj} W^{+\mu} \right) \quad (1.58)$$

¹¹The Singular Value Decomposition Theorem states that: any complex $m \times n$, ($m \geq n$) matrix A can be diagonalized by $BAC^\dagger = D$; D is a diagonal $n \times n$ matrix with positive diagonal elements, B is an unitary $n \times n$ matrix and C a $n \times m$ matrix that for $n = m$ is unitary [13, 36].

¹²Again, when the neutrino masses are neglected.

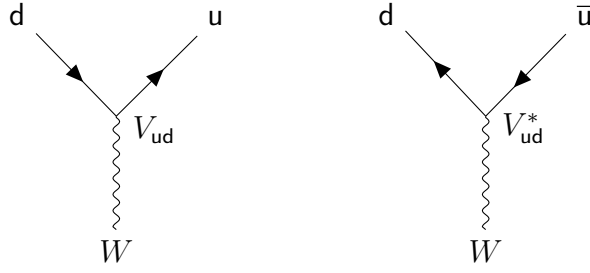


Figure 1.4: Basic vertices of the Feynman diagrams for charged-current weak interaction processes, between up-type (u) and down-type (d) quarks and antiquarks. They are CP conjugated of each other. The charge of the W boson depends on the temporal orientation of the diagram (electric charge conservation). The contribution of each vertex has to be further multiplied by $\frac{g}{\sqrt{2}}\gamma^\mu\frac{1-\gamma^5}{2}$ to complete the Feynman rules.

where the 3×3 unitary matrix

$$V_{\text{CKM}} = V_L^u V_L^{d\dagger} \quad (1.59)$$

is the Cabibbo-Kobayashi-Maskawa matrix [14, 15]. It can be associated equivalently to the up-type or to the down-type quarks. By convention, the interaction eigenstates and the mass eigenstates are chosen to be equal for the up-type quarks, while the down-type quarks are chosen to be rotated, going from one basis to the other according to

$$\mathbf{u}_i^I = \mathbf{u}_i; \quad \mathbf{d}_i^I = (V_{\text{CKM}})_{ij} \mathbf{d}_j.$$

Writing explicitly the left chiral projector $(1 - \gamma_5)/2$, the notorious $V - A$ structure of the weak charged currents is finally obtained:

$$\mathcal{L}_{\text{kin,CC}}^{\text{quark}} = \frac{g}{\sqrt{2}} (\bar{u} \quad \bar{c} \quad \bar{t}) \gamma_\mu \frac{1 - \gamma_5}{2} \begin{pmatrix} V_{ud} & V_{us} & V_{ub} \\ V_{cd} & V_{cs} & V_{cb} \\ V_{td} & V_{ts} & V_{tb} \end{pmatrix} \begin{pmatrix} d \\ s \\ b \end{pmatrix} W^{+\mu} + \text{h.c.} . \quad (1.60)$$

In conclusion, the necessity to diagonalise the Yukawa-coupling matrix produces the CKM matrix, strictly connecting the quark flavours with their masses. Another crucial consequence is that the amplitude of the transition from a down-type quark to an up-type quark is proportional to V_{ud} , whereas the amplitude of the transition from down-type antiquark to an up-type antiquark is proportional to V_{ud}^* . This is resumed by the Feynman diagrams of figure 1.4.

1.2.2 Origin of the CP violation

The CP operation transform spinor bilinear as follows

$$(CP)(\bar{\psi}_{Li} \phi \psi_{Rj}) = \bar{\psi}_{Rj} \phi \psi_{Li}.$$

Hence, $\mathcal{L}_{\text{Yukawa}}$ would remain unchanged under CP if and only if $Y_{ij} = Y_{ij}^*$, namely if the Yukawa couplings were real. Similarly, the Lagrangian of the charged current for quarks,

$$\mathcal{L}_{\text{kin,CC}}^{\text{quark}} = \sum_{ij} \left[(V_{\text{CKM}})_{ij} \frac{g}{\sqrt{2}} \bar{u}_{Li} \gamma_\mu d_{Lj} W^{-\mu} + (V_{\text{CKM}})_{ij}^* \frac{g}{\sqrt{2}} \bar{d}_{Lj} \gamma_\mu u_{Li} W^{+\mu} \right],$$

transforms under CP into

$$(CP) \left(\mathcal{L}_{\text{kin}, CC}^{\text{quark}} \right) = \sum_{ij} \left[(V_{\text{CKM}})_{ij} \frac{g}{\sqrt{2}} \bar{d}_{Lj} \gamma_\mu u_{Li} W^{+\mu} + (V_{\text{CKM}})^*_{ij} \frac{g}{\sqrt{2}} \bar{u}_{Li} \gamma_\mu d_{Lj} W^{-\mu} \right].$$

Therefore, if the V_{CKM} elements are not all real, the SM Lagrangian is not invariant under the CP transformation¹³, and the amplitudes of CP -conjugated processes have opposite complex phases. However, the transition rates are given by the squared module of the amplitudes and this removes the phase difference effects. As a consequence, observable CP violation asymmetries can arise only in presence of quantum interference between different processes with different complex phases.

This point can be clarified by some general arguments. Any amplitude may include two kinds of complex phases. On the one hand, there are the phases that appear in complex conjugated form in the CP -conjugate Lagrangian, like the just mentioned *weak phases*. On the other hand, a second type of phase can appear even when the Lagrangian is real. They originate from the possible contributions from intermediate on-shell states in the decay process. Since such phases are originated by CP -invariant interactions, they do not change between the CP -conjugated amplitudes A_f and $\bar{A}_{\bar{f}}$ [4]. Usually, the dominant rescattering is due to QCD, and thus these phases are called *strong phases*. To sum up, each contribution a_i to the decay amplitude A_f can be written in polar form as: $a_i = |a_i| e^{i(\delta_i + \phi_i)}$, where δ_i and ϕ_i are the strong and the weak phase, respectively. When two contributions are present the total amplitudes become

$$\begin{aligned} A_f &= a_1 + a_2 = |a_1| e^{i(\delta_1 + \phi_1)} + |a_2| e^{i(\delta_2 + \phi_2)}, \\ \bar{A}_{\bar{f}} &= \bar{a}_1 + \bar{a}_2 = |a_1| e^{i(\delta_1 - \phi_1)} + |a_2| e^{i(\delta_2 - \phi_2)}. \end{aligned} \quad (1.61)$$

For neutral mesons, it is convenient to adopt a similar notation for the off-diagonal elements of the Hamiltonian, which rules the evolution of the two-state system:

$$M_{12} = |M_{12}| e^{i\phi_M}, \quad \Gamma_{12} = |\Gamma_{12}| e^{i\phi_\Gamma},$$

where ϕ_M and ϕ_Γ behave like weak phases because the CP -conjugated processes are ruled by the matrix elements M_{12}^* , Γ_{12}^* . Although all cited phases are convention-dependent¹⁴, their combinations may be physical quantities. In particular, $\delta_1 - \delta_2$, $\phi_1 - \phi_2$ and $\phi_M - \phi_\Gamma$ are convention-independent. Indeed, they are strictly related to the three CP violation categories, introduced in Section 1.1.4.

- Inserting the expressions in Equation (1.61) into the asymmetry (1.45), the measurement of the CP violation in the decay becomes:

$$A_{CP} = \frac{2|a_1 a_2| \sin(\delta_2 - \delta_1) \sin(\phi_2 - \phi_1)}{|a_1|^2 + |a_2|^2 + 2|a_1 a_2| \cos(\delta_2 - \delta_1) \cos(\phi_2 - \phi_1)}.$$

This relation shows that CP violation in the decay arises ($A_{CP} \neq 0$) when –at least– two processes contribute to the amplitude of the decay ($|a_1| \neq 0$ and $|a_2| \neq 0$) with

¹³Actually, the phase freedom in the antiparticle definitions might permit to reabsorb the complex phases of V_{CKM} , producing a CP invariant Lagrangian. However, Sect. 1.2.4 explains that it is not possible with three generations of quarks with different masses.

¹⁴For instance, ϕ_M and ϕ_Γ share the common arbitrary term ξ_M introduced in equation (1.8).

different strong and weak phases. Besides, this means that to measure the weak phase difference $\phi_2 - \phi_1$, which is important for theory, the amplitude ratio $|a_1/a_2|$ and the strong phase difference $\delta_2 - \delta_1$ have to be known. Unfortunately, they depend on non-perturbative hadronic parameters, which are difficult to calculate. In particular cases, however, they can be experimentally determined.

- For B^0 and B_s^0 mesons the approximation $|\Gamma_{12}/M_{12}| \ll 1$ holds. This is corroborated by experimental results and consistent with the SM prediction: $|\Gamma_{12}/M_{12}| \sim \mathcal{O}(m_b^2/m_t^2)$ [4, 46]¹⁵. Hence, the CP asymmetry in semileptonic neutral-meson decays (1.47) becomes

$$A_{\text{SL}} = - \left| \frac{\Gamma_{12}}{M_{12}} \right| \sin(\phi_M - \phi_\Gamma).$$

Hence, CP violation in the mixing can be interpreted as a phase difference between the interfering absorptive and dispersive transitions. Again, the weak phase $\phi_M - \phi_\Gamma$ is the one of most interest for theory, but its extraction depends on the knowledge of $|\Gamma_{12}/M_{12}|$, which is difficult to calculate explicitly because it implies hadronic long-distance physics.

- If it is assumed that only one weak phase contributes to a decay into a CP eigenstate, $A_{f_{CP}} = |a_{f_{CP}}| e^{i(\delta_{f_{CP}} + \phi_{f_{CP}})}$, with $|\Gamma_{12}/M_{12}| = 0$ (*i.e.* the CP violation in the decay and in the mixing are both negligible), one obtains $|\lambda_f| = 1$. Consequently, the time-dependent asymmetry (1.49) becomes

$$A_{f_{CP}}(t) = \mathcal{I}m(\lambda_{f_{CP}}) \sin(\Delta mt) \quad \text{with} \quad \mathcal{I}m(\lambda_{f_{CP}}) = \eta_{f_{CP}} \sin(\phi_M + 2\phi_{f_{CP}}),$$

where $\eta_{f_{CP}}$ is the CP eigenvalue of the final state, and only weak phases are involved. As expected this kind of CP violation is related to phases which manifest the interference of mixing and decay processes.

1.2.3 Magnitude of the CKM matrix elements

The following tree-level transitions are usually exploited to directly measure the magnitude of the V_{CKM} elements:

$|V_{ud}|$ - nuclear beta decays ($d \rightarrow ue\bar{\nu}_e$ transitions);

$|V_{us}|$ - semileptonic kaon decays $K \rightarrow \pi l\bar{\nu}$ ($s \rightarrow ul\bar{\nu}$ transitions);

$|V_{ub}|$ - exclusive and inclusive semileptonic B -hadron decays ($b \rightarrow ul\bar{\nu}$ transitions);

$|V_{cd}|$ - semileptonic D -hadron decays $D \rightarrow \pi l\bar{\nu}$ ($c \rightarrow dl\bar{\nu}$ transitions) and charm production from ν interaction with matter;

$|V_{cs}|$ - semileptonic D decays ($c \rightarrow sl\bar{\nu}$ transitions) and leptonic D_s decays ($D_s \rightarrow l\bar{\nu}$);

$|V_{cb}|$ - exclusive and inclusive semileptonic B decays to charm ($b \rightarrow cl\bar{\nu}$ transitions);

¹⁵In [39] a heuristic explanation is provided: “There are a large number of B -meson decay modes, of which only a few are common to both the B^0 and \bar{B}^0 , and the contribution to the effective Hamiltonian of (1.9) from the interference between the decays of the B^0 and \bar{B}^0 can be neglected, $\Gamma_{12} = \Gamma_{21}^* \approx 0$ ”.

CKM matrix element	Experimental value
$ V_{ud} $	0.97370 ± 0.00014
$ V_{us} $	0.2245 ± 0.0008
$ V_{cd} $	0.221 ± 0.004
$ V_{cs} $	0.987 ± 0.011
$ V_{cb} $	0.0410 ± 0.0014
$ V_{ub} $	0.00382 ± 0.00024
$ V_{td} $	0.0080 ± 0.0003
$ V_{ts} $	0.0388 ± 0.0011
$ V_{tb} $	1.013 ± 0.030

Table 1.2: Experimental knowledge of the magnitudes of the CKM matrix elements [4].

$|V_{tb}|$ - branching ratio of $t \rightarrow Wb$ decay (assuming CKM matrix unitarity) and single top-quark-production cross-section.

Since the transitions $t \rightarrow d, s$ are found to be strongly suppressed ($|V_{tb}| \approx 1$), the best strategy to measure $|V_{td}|$ and $|V_{ts}|$ does not exploit tree-level processes. Indeed, the ratio $|V_{td}/V_{ts}|$ is usually determined from the $B^0 - \bar{B}^0$ and the $B_s^0 - \bar{B}_s^0$ oscillations. In the SM, these transitions are mediated by box diagrams (Figure 1.3), which are dominated by the circulation of the top quark as a virtual state.

A summary of the current knowledge about the magnitude of the V_{CKM} elements is reported in Table 1.2. Transitions within the same family have V_{CKM} elements of $\mathcal{O}(1)$, those between the first and second generations are suppressed by a factor $\mathcal{O}(10^{-1})$, those between the second and third generations are suppressed by a factor $\mathcal{O}(10^{-2})$, finally those between the first and third generations are strongly suppressed by a factor $\mathcal{O}(10^{-3})$. These values are illustrated in Figure 1.5 by the size of the red boxes. The figure shows also the

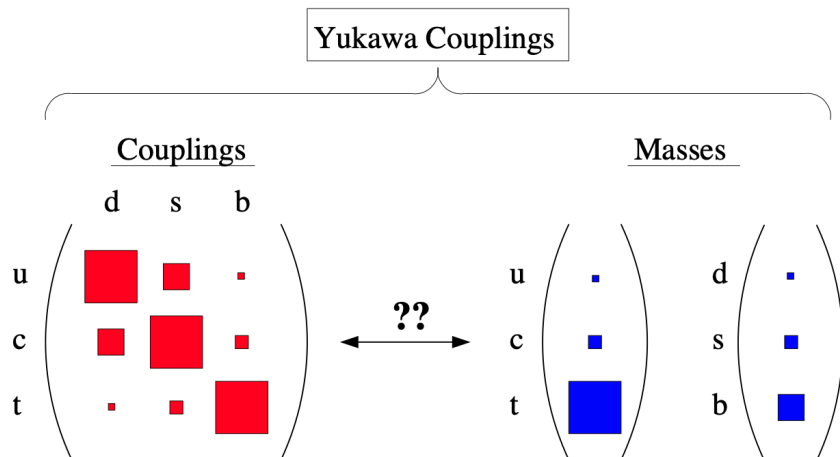


Figure 1.5: Graphical representation of the order of magnitude of the CKM matrix elements and of hierarchy among the quark masses. Further details available in the text.

hierarchy of the quark masses (blue boxes). Both patterns are due to the actual values

of the Yukawa couplings. According to the SM, they are fundamental constants, hence the reason for the depicted configurations is currently unknown. Nonetheless, constraints among the V_{CKM} elements exist, and their verification is needed for the SM internal consistency.

1.2.4 Parametrisations of the CKM matrix

All the elements of the CKM matrix are defined from three real angles and a single complex phase. This can be demonstrated as follows:

- 1) A general $n \times n$ complex matrix has n^2 complex elements, and therefore $2n^2$ real parameters.
- 2) The discussion of Section 1.2.1 explained the reason why V_{CKM} is required to be unitary. This imposes n^2 constraints, namely n conditions for the unity of the diagonal elements of the product $(V_{\text{CKM}})(V_{\text{CKM}})^\dagger = \mathbb{1}$, and $n^2 - n$ conditions for the vanishing of the off-diagonal elements.
- 3) The phase of the quarks can be rotated freely ($u_{Li} \rightarrow e^{i\phi_i^u} d_{Li}$ and $d_{Li} \rightarrow e^{i\phi_i^d} d_{Li}$), since the overall phase is irrelevant; therefore $2n - 1$ relative quarks phase can be removed.

Hence, the total number of free parameters is $2n^2 - n^2 - (2n - 1) = (n - 1)^2$. After that, one can divide such free parameter into Euler angles and phases:

- 4) A general $n \times n$ orthogonal matrix can be constructed from $\frac{1}{2}n(n - 1)$ angles describing rotations among the n dimensions.
- 5) The parameters left are the phases: $(n - 1)^2 - \frac{1}{2}n(n - 1) = \frac{1}{2}(n - 1)(n - 2)$.

As a result, with two families $n = 2$, only one real parameter is necessary. This is the case of the Cabibbo matrix

$$V_C = \begin{pmatrix} \cos \theta_C & \sin \theta_C \\ -\sin \theta_C & \cos \theta_C \end{pmatrix}, \quad (1.62)$$

which accommodates the mixing between the first and the second family of quarks [14]. However, CP violation is not compatible with the absence of complex phases and a single complex phase appears with $n = 3$. This was the original argument that lead Kobayashi and Maskawa to predict the third quark family [15]. Even if the number of free parameters is fixed by the number of families, their organization inside the matrix is not. Therefore, many representations of V_{CKM} are possible. Among them, the one assumed by Ref. [4] has become the standard one:

$$V_{\text{CKM}} = \begin{pmatrix} c_{12}c_{13} & s_{12}c_{13} & s_{13}e^{-i\delta} \\ -s_{12}c_{23} - c_{12}s_{23}s_{13}e^{i\delta} & c_{12}c_{23} - s_{12}s_{23}s_{13}e^{i\delta} & s_{23}c_{13} \\ s_{12}s_{23} - c_{12}c_{23}s_{13}e^{i\delta} & -c_{12}s_{23} - s_{12}c_{23}s_{13}e^{i\delta} & c_{23}c_{13} \end{pmatrix} \quad (1.63)$$

where $s_{ij} \equiv \sin \theta_{ij}$, $c_{ij} \equiv \cos \theta_{ij}$ and δ is the CP violating phase. The θ_{ij} angles can be chosen to lie in the first quadrant ($s_{ij}, c_{ij} \geq 0$). They represent the mixing between different quark generations¹⁶, and their values can be deduced from the magnitudes of the V_{CKM} elements [4].

¹⁶In the case $\theta_{13} = \theta_{23} = 0$, the third generation would decouple and the Cabibbo's matrix would be recovered.

The Jarlskog invariant. The presence of a complex phase is a necessary but not sufficient condition for the violation of the CP symmetry. It can be demonstrated [47] that the fundamental requirement is

$$(m_t^2 - m_c^2) (m_t^2 - m_u^2) (m_c^2 - m_u^2) (m_b^2 - m_s^2) (m_b^2 - m_d^2) (m_s^2 - m_d^2) \times J_{CP} \neq 0 \quad (1.64)$$

where

$$J_{CP} = |\mathcal{I}m (V_{i\alpha} V_{j\beta} V_{i\beta}^* V_{j\alpha}^*)| \quad (i \neq j, \alpha \neq \beta) \quad (1.65)$$

is known as the *Jarlskog parameter*. This condition is related to the fact that it would be possible to remove the V_{CKM} phase if any of two quarks with the same charge were degenerated in mass [36]. Hence, this is another manifestation of the deep connection between origin of CP violation and the origin of quark masses hierarchy. The value of the Jarlskog parameter does not depend on the representation of V_{CKM} , thus it can be used to quantify the entity of the CP violation in the SM. The current experimental results lead to $J_{CP} = \mathcal{O}(10^{-5})$, which allow to assert that CP violation is a small effect in the SM. Exploiting the standard parametrisation in (1.63), J_{CP} can be written as

$$J_{CP} = s_{12}s_{13}s_{23}c_{12}c_{23}c_{13}^2 \sin \delta. \quad (1.66)$$

To conclude, the fundamental requirement (1.64) is equivalent to the following conditions:

1. There should not be mass degeneracy within up-type quarks or down-type quarks.
2. None of the three mixing angle should be 0 or $\pi/2$.
3. The phase should be neither 0 nor π .

The Wolfenstein parametrisation. The observed hierarchy among the magnitude of the V_{CKM} elements can be made more evident with the convenient parametrisation proposed by Wolfenstein [48]. It is related with the standard parametrisation (1.63) by the following definitions:

$$s_{12} = \lambda = \frac{|V_{us}|}{\sqrt{|V_{ud}|^2 + |V_{us}|^2}}, \quad s_{23} = A\lambda^2 = \lambda \left| \frac{V_{cb}}{V_{us}} \right|, \quad s_{13}e^{-i\delta} = A\lambda^3(\rho - i\eta) = V_{ub}, \quad (1.67)$$

where parameters λ , A , ρ and η are all real. The observed experimental condition $s_{13} \ll s_{23} \ll s_{12} \ll 1$ allows V_{CKM} to be written as a power expansion of the parameter $\lambda = \sin \theta_C \approx 0.22$ (where θ_C is the Cabibbo angle defined in (1.62)). As a result the Wolfenstein parametrisation of V_{CKM} is:

$$V_{CKM} = \begin{pmatrix} 1 - \lambda^2/2 & \lambda & A\lambda^3(\rho - i\eta) \\ -\lambda & 1 - \lambda^2/2 & A\lambda^2 \\ A\lambda^3(1 - \rho - i\eta) & -A\lambda^2 & 1 \end{pmatrix} + \mathcal{O}(\lambda^4) \quad (1.68)$$

For certain processes, in particular when CP violation is expected to be very small, it is useful to further expand the parameterization to the subsequent order, obtaining [4]:

$$\begin{aligned}
V_{ud} &= 1 - \frac{1}{2}\lambda^2 - \frac{1}{8}\lambda^4 + \mathcal{O}(\lambda^6), & V_{us} &= \lambda + \mathcal{O}(\lambda^7), & V_{ub} &= A\lambda^3(\rho - i\eta), \\
V_{cd} &= -\lambda + \frac{1}{2}A^2\lambda^5[1 - 2(\rho + i\eta)] + \mathcal{O}(\lambda^7), & V_{cs} &= 1 - \frac{1}{2}\lambda^2 - \frac{1}{8}\lambda^4(1 + 4A^2) + \mathcal{O}(\lambda^6), \\
V_{cb} &= A\lambda^2 + \mathcal{O}(\lambda^8), & V_{td} &= A\lambda^3\left[1 - (\rho + i\eta)\left(1 - \frac{1}{2}\lambda^2\right)\right] + \mathcal{O}(\lambda^7), \\
V_{ts} &= -A\lambda^2 + \frac{1}{2}A\lambda^4[1 - 2(\rho + i\eta)] + \mathcal{O}(\lambda^6), & V_{tb} &= 1 - \frac{1}{2}A^2\lambda^4 + \mathcal{O}(\lambda^6).
\end{aligned} \tag{1.69}$$

With this parametrisation the ‘‘Jarlskog parameter’’ of Eq. (1.66) becomes

$$J_{CP} = \lambda^6 A^2 \eta, \tag{1.70}$$

directly related to the CP violating parameter η . Finally, the following definitions are reported here, for later convenience:

$$\bar{\rho} \equiv \rho \left(1 - \frac{1}{2}\lambda^2\right), \quad \bar{\eta} \equiv \eta \left(1 - \frac{1}{2}\lambda^2\right). \tag{1.71}$$

It can be shown that $\bar{\rho} + i\bar{\eta} = -(V_{ud}V_{ub}^*)/(V_{cd}V_{cb}^*)$ is phase-convention independent and V_{CKM} , written in terms of λ , A , $\bar{\rho}$, and $\bar{\eta}$, is unitary at all orders in λ [4].

1.2.5 Unitary Triangles

The off-diagonal unitary conditions of V_{CKM} are:

$$\underbrace{V_{ud}V_{us}^*}_{\mathcal{O}(\lambda)} + \underbrace{V_{cd}V_{cs}^*}_{\mathcal{O}(\lambda)} + \underbrace{V_{td}V_{ts}^*}_{\mathcal{O}(\lambda^5)} = 0, \tag{1.72}$$

$$\underbrace{V_{us}V_{ub}^*}_{\mathcal{O}(\lambda^4)} + \underbrace{V_{cs}V_{cb}^*}_{\mathcal{O}(\lambda^2)} + \underbrace{V_{ts}V_{tb}^*}_{\mathcal{O}(\lambda^2)} = 0, \tag{1.73}$$

$$\underbrace{V_{ud}V_{ub}^*}_{(\rho+i\eta)A\lambda^3} + \underbrace{V_{cd}V_{cb}^*}_{-A\lambda^3} + \underbrace{V_{td}V_{tb}^*}_{(1-\rho-i\eta)A\lambda^3} = 0, \tag{1.74}$$

$$\underbrace{V_{ud}^*V_{cd}}_{\mathcal{O}(\lambda)} + \underbrace{V_{us}^*V_{cs}}_{\mathcal{O}(\lambda)} + \underbrace{V_{ub}^*V_{cb}}_{\mathcal{O}(\lambda^5)} = 0, \tag{1.75}$$

$$\underbrace{V_{cd}^*V_{td}}_{\mathcal{O}(\lambda^4)} + \underbrace{V_{cs}^*V_{ts}}_{\mathcal{O}(\lambda^2)} + \underbrace{V_{cb}^*V_{tb}}_{\mathcal{O}(\lambda^2)} = 0, \tag{1.76}$$

$$\underbrace{V_{ud}^*V_{td}}_{(1-\rho-i\eta)A\lambda^3} + \underbrace{V_{us}^*V_{ts}}_{-A\lambda^3} + \underbrace{V_{ub}^*V_{tb}}_{(\rho+i\eta)A\lambda^3} = 0. \tag{1.77}$$

They can be represented as triangles in the complex plane, where each $V_{ij}V_{kl}^*$ product depicts a side and the null sums ensure that the triangles are closed. It can be shown [4,36] that the area of all the six unitary triangles is $J_{CP}/2$. The Wolfenstein parametrisation in Eq. (1.68) is useful to show that only two triangles have sides of the same order of

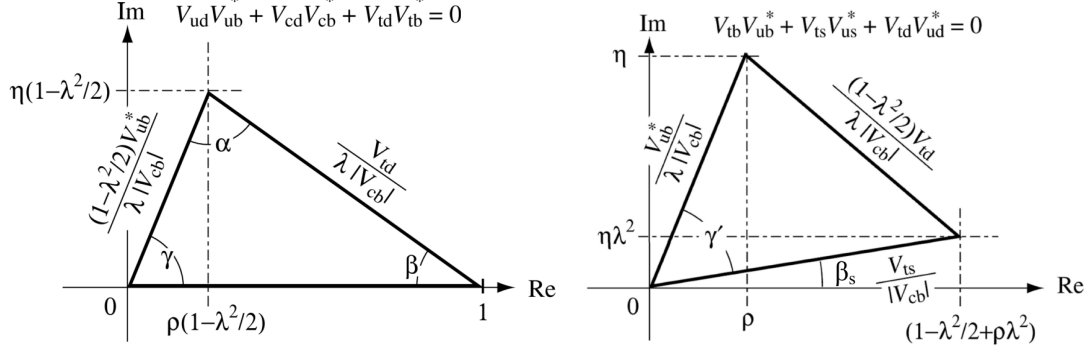


Figure 1.6: Representation in the complex plane of the unitary triangles described in the text: on the left the UT corresponding to Eq. (1.74); on the right the triangle corresponding to Eq. (1.77) is reported.

magnitude. The first one corresponds to equation (1.74), which, using the Wolfenstein parametrisation, becomes

$$[(\rho + i\eta) + (-1) + (1 - \rho - i\eta)] A\lambda^3 = 0, \quad (1.78)$$

or at the next order (Eqs. 1.69):

$$[(\bar{\rho} + i\bar{\eta}) + (-1) + (1 - \bar{\rho} - i\bar{\eta})] A\lambda^3 + \mathcal{O}(\lambda^7) = 0. \quad (1.79)$$

Normalizing to the common factor $A\lambda^3$, one gets “The Unitary Triangle” (UT) of Figure 1.6-(left). Its sides are

$$\begin{aligned} R_b &\equiv \sqrt{\bar{\rho}^2 + \bar{\eta}^2} = \left| \frac{V_{ud}V_{ub}^*}{V_{cd}V_{cb}^*} \right|, \\ R_t &\equiv \sqrt{(1 - \bar{\rho})^2 + \bar{\eta}^2} = \left| \frac{V_{td}V_{tb}^*}{V_{cd}V_{cb}^*} \right|, \end{aligned} \quad (1.80)$$

and its angles are

$$\alpha \equiv \arg \left(-\frac{V_{td}V_{tb}^*}{V_{ud}V_{ub}^*} \right) = \arg \left(-\frac{1 - \bar{\rho} - i\bar{\eta}}{\bar{\rho} + i\bar{\eta}} \right), \quad (1.81)$$

$$\beta \equiv \arg \left(-\frac{V_{cd}V_{cb}^*}{V_{td}V_{tb}^*} \right) = \arg \left(\frac{1}{1 - \bar{\rho} - i\bar{\eta}} \right), \quad (1.82)$$

$$\gamma \equiv \arg \left(-\frac{V_{ud}V_{ub}^*}{V_{cd}V_{cb}^*} \right) = \arg(\bar{\rho} + i\bar{\eta}). \quad (1.83)$$

The γ angle coincide with the CP -violating phase δ of equation (1.63), and the following relations hold:

$$V_{ub} = A\lambda^3 \left(\frac{R_b}{1 - \lambda^2/2} \right) e^{-i\gamma}, \quad (1.84)$$

$$V_{td} = A\lambda^3 R_t e^{-i\beta}. \quad (1.85)$$

Therefore, the angles γ and β are the phases of the two complex elements which appear in Eq. (1.68). The second non-degenerate triangle is provided by equation (1.77) which, in Wolfenstein parametrisation, becomes

$$\left\{ \left[1 - \rho - i\eta - \lambda^2 \left(\frac{1}{2} - \rho - i\eta \right) \right] + \left[-1 + \lambda^2 \left(\frac{1}{2} - \rho - i\eta \right) \right] + [\rho + i\eta] \right\} A\lambda^3 + \mathcal{O}(\lambda^7) = 0. \quad (1.86)$$

Dividing again by the common factor $A\lambda^3$, one obtains the triangle of Figure 1.6-(right). Its apex is located in (ρ, η) (instead of $(\bar{\rho}, \bar{\eta})$), and it is tilted by the angle

$$\beta_s \equiv \phi_s/2 = \arg \left(\frac{V_{ts}V_{tb}^*}{V_{cs}V_{cb}^*} \right), \quad (1.87)$$

with respect to the UT.

1.2.6 Constraints to the UT

Here the various constraints used to determine the UT parameters are summarised.

$|\mathbf{V}_{ub}|/|\mathbf{V}_{cb}|$ - This ratio is proportional to the side of the UT between the α and the γ angles. As reported in section 1.2.3, they can be measured exploiting exclusive and inclusive semileptonic decays of B hadrons.

Δm_d - the mass splitting between mass eigenstates of the $B^0 - \bar{B}^0$ systems rules the flavour oscillations and is proportional to the magnitude of V_{td} . Thus, it measures the side of the UT between the α and the β angles. However, in this case, the extraction of V_{td} is affected by large theoretical uncertainties. This parameter represents the frequency of mixing. It is proportional to the magnitude

$\Delta m_d/\Delta m_s$ - since Δm_s is the equivalent of Δm_d for the $B_s^0 - \bar{B}_s^0$ system, it is proportional to V_{ts} . The relations between $\Delta m_s/\Delta m_d$, V_{ts} and V_{td} permit to reduce the theoretical uncertainties and provide a determination of the UT side more precise than the one from Δm_d alone.

ε_K - This parameter depends on the size of CP violation in the neutral kaon system and carries information on the position of the apex of the UT.

α - The value of this angle can be extracted from $B \rightarrow \pi\pi$ and $B \rightarrow \rho\rho$ decays. Besides, these channels are also related to the sides of the UT because their decay amplitudes and the CP asymmetries depend on the terms $V_{td}V_{tb}^*$ and $V_{ud}V_{ub}^*$.

β - This angle can be extracted from the time-dependent analysis of the $B^0 \rightarrow J/\psi K^0$ decays.

γ - This angle can be derived from $B \rightarrow D^{(*)}K^{(*)}$ decays, because they involve V_{ub} and V_{cb} .

$\sin(2\beta + \gamma)$ - This quantity is proportional to some terms which rule the time-dependent decay rates of $B \rightarrow D^{(*)}\pi$ decays.

In Figure 1.7 [49] the graphical representation of all the above-mentioned constraints is reported. All the constraints are consistent with CKM unitarity, and the corresponding values of the UT apex are

$$\bar{\rho} = 0.148 \pm 0.013, \quad \bar{\eta} = 0.348 \pm 0.010 \quad (1.88)$$

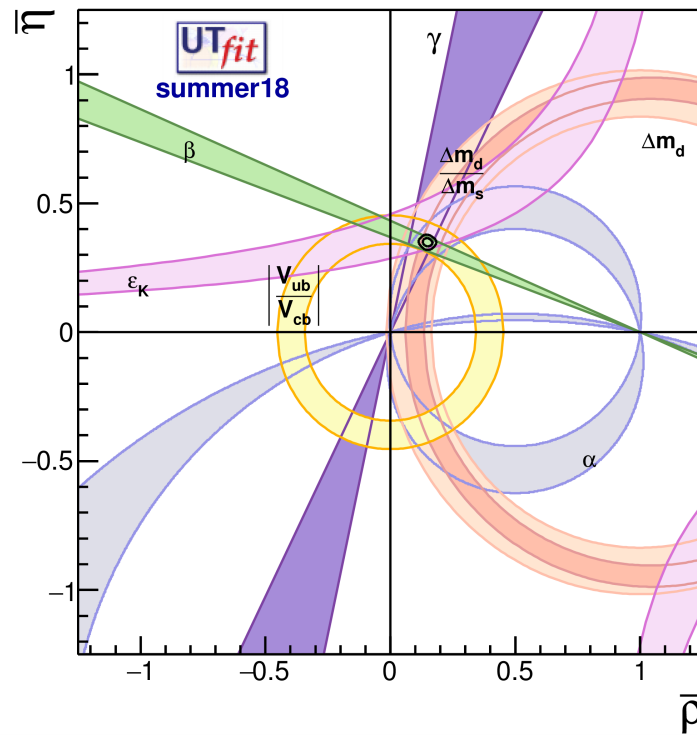


Figure 1.7: Allowed parameter ranges (68% probability regions) for the parameters of the UT obtained from the method described in the text. The 68% and 95% contours for the $\bar{\rho}$ and $\bar{\eta}$ parameters are also shown.

1.3 Charmless two-body B decays

Among the numerous ways for testing the CP -violation sector of the SM, a valuable one is provided by the b quark transitions to charmless hadronic final states. In particular, this thesis will deal with the two-body decays¹⁷ $B^0 \rightarrow \pi^+\pi^-$, $B^0 \rightarrow K^+\pi^-$, $B_s^0 \rightarrow K^+K^-$, $B_s^0 \rightarrow \pi^+K^-$. In the following, they will be generically referred to as $B_{(s)}^0 \rightarrow h^+h'^-$. Besides, the $B^0 \rightarrow K^+K^-$, $B_s^0 \rightarrow \pi^+\pi^-$, $\Lambda_b \rightarrow p\pi^-$ and $\Lambda_b \rightarrow pK^-$ decays will be accounted for, being suppressed but unavoidable backgrounds of the previous signal modes¹⁸.

The $B_{(s)}^0 \rightarrow h^+h'^-$ decays receive contributions by various topologies of Feynman diagrams: from tree-level transitions to sizeable QCD and EW penguin processes. The search for anomalies in this sector is attractive because new particles and interactions, not present in the SM, may appear as virtual contributions inside the loops of the penguin diagrams [51]. However, the amplitudes of penguin transitions comprise hadronic matrix elements, which affect the measurement of the CKM parameters. Nonetheless, the extraction of the UT angle γ and the B_s^0 mixing phase $2\beta_s$ from $B_{(s)}^0 \rightarrow h^+h'^-$ is actually feasible. A possible strategy [52–55] relies on the assumption of U-spin symmetry¹⁹ and on the combination of the time-dependent CP asymmetries in the $B^0 \rightarrow \pi^+\pi^-$ and $B_s^0 \rightarrow K^+K^-$ decays. Any deviation concerning the values of γ and $2\beta_s$, measured with other B meson decays dominated by pure tree amplitudes, would be a sign of new physics.

Section 1.3.1 illustrates the various Feynman diagrams topologies governing the $B_{(s)}^0 \rightarrow h^+h'^-$ processes. Section 1.3.2 specifies the connection between the CP violation asymmetries and the UT parameters for the $B_{(s)}^0 \rightarrow h^+h'^-$ decays.

1.3.1 Topologies contributing to $B_{(s)}^0 \rightarrow h^+h'^-$ decays

The quark transitions $b \rightarrow q_1\bar{q}_2d(s)$, with $q_{1,2} \in \{u, d, c, s\}$, lead the hadronic two-body decays of the B mesons. Figure 1.8 illustrates all the main Feynman diagrams responsible for $B_{(s)}^0 \rightarrow h^+h'^-$ decays [56–58]. Beyond the tree-level diagrams (T), gluon mediated penguins (P) and color-suppressed electroweak penguins P_{EW}^C are present. A common aspect of these diagrams is that a spectator quark d (s) can be identified. Other relevant topologies involve both the initial state quarks: they are the annihilation penguins (PA) and the exchange diagrams (E). The penguin diagrams can be as relevant as tree-level diagrams –or even dominate the decay – even if they correspond to higher-order terms in the perturbation theory. For example, $B^0 \rightarrow K^+\pi^-$ decays include the contribution of a tree-level amplitude proportional to the CKM factor $V_{ub}^*V_{us}$. Penguin amplitudes, instead, are characterized by a loop structure, which introduces the CKM factor $V_{tb}^*V_{ts}$. Since $V_{ub}^*V_{us}/V_{tb}^*V_{ts} \approx 0.02$, QCD penguin amplitudes actually dominate this particular process. Besides, one could expect that EW penguins should be negligible with respect to QCD penguins, because the ratio between of the QED and QCD couplings is $\alpha/\alpha_s = \mathcal{O}(10^{-2})$. Actually, the high mass of the top quark entering the loop enhance the contribution of EW penguins, producing sizeable effects [59].

¹⁷The CP -conjugated modes are implicitly considered.

¹⁸ CP violation measurements in charmless two-body decays of the Λ_b^0 baryon at the LHCb experiment are reported in [50]

¹⁹Namely, the approximate invariance of the strong interaction under the substitution between the d and s quarks.

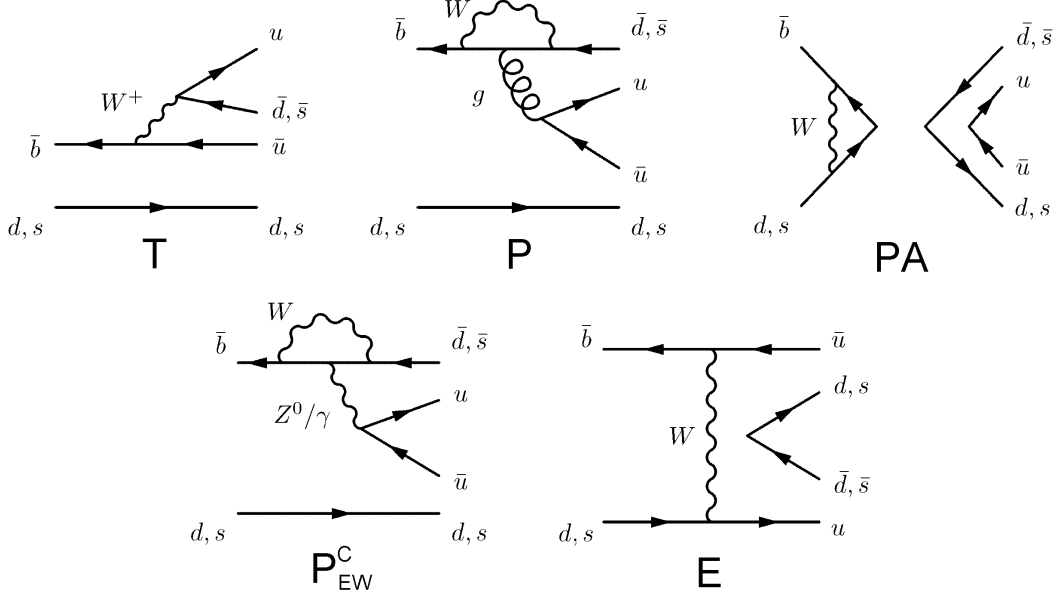


Figure 1.8: Diagrams contributing to the amplitudes of charmless $B_{(s)}^0$ decays to two charged mesons: Tree (T), Penguin (P), Penguin Annihilation (PA), Colour-suppressed Electroweak Penguin (P_{EW}^C) and Exchange (E).

The following outline reports the Feynman diagram topologies involved in each $B_{(s)}^0 \rightarrow h^+ h'^-$ decay:

$$\underbrace{B^0 \rightarrow K^+ K^-}_{PA+E} \quad d \longleftrightarrow s \quad \underbrace{B_s^0 \rightarrow \pi^+ \pi^-}_{PA+E} \quad (1.89)$$

$$\underbrace{B^0 \rightarrow \pi^+ \pi^-}_{T+P+\frac{2}{3}P_{EW}^C+PA+E} \quad d \longleftrightarrow s \quad \underbrace{B_s^0 \rightarrow K^+ K^-}_{T+P+\frac{2}{3}P_{EW}^C+PA+E} \quad (1.90)$$

$$\underbrace{B^0 \rightarrow K^+ K^-}_{PA+E} \quad d \longleftrightarrow s \quad \underbrace{B_s^0 \rightarrow \pi^+ \pi^-}_{PA+E} \quad (1.91)$$

$$\underbrace{B^0 \rightarrow K^+ \pi^-}_{T+P+\frac{2}{3}P_{EW}^C} \quad d \longleftrightarrow s \quad \underbrace{B_s^0 \rightarrow \pi^+ K^-}_{T+P+\frac{2}{3}P_{EW}^C} \quad (1.92)$$

$$\underbrace{B^0 \rightarrow K^+ \pi^-}_{T+P+\frac{2}{3}P_{EW}^C} \quad d \overset{\text{spect.}}{\longleftrightarrow} s \quad \underbrace{B_s^0 \rightarrow K^+ K^-}_{T+P+\frac{2}{3}P_{EW}^C+PA+E} \quad (1.93)$$

$$\underbrace{B^0 \rightarrow \pi^+ \pi^-}_{T+P+\frac{2}{3}P_{EW}^C+PA+E} \quad d \overset{\text{spect.}}{\longleftrightarrow} s \quad \underbrace{B_s^0 \rightarrow \pi^+ K^-}_{T+P+\frac{2}{3}P_{EW}^C} \quad (1.94)$$

The pattern highlights also the links between the various channels due to the U -spin transformation. In the first four cases, the symmetry applies to all the d and s quarks. Instead, the $B^0 \rightarrow \pi^+ \pi^-$ and $B_s^0 \rightarrow \pi^+ K^-$ decays are not properly connected by the U -spin symmetry. Even if they differ just by the interchange of the spectator quark (hence the label “spect.”), the PA and E diagrams contribute to the former decay but

not to the latter. Anyway, such contributions are expected to be small, and their size can be estimated from the measurement of the branching ratios of the $B^0 \rightarrow K^+K^-$ and $B_s^0 \rightarrow \pi^+\pi^-$ decays, where only the PA and E topologies contribute. Similar arguments hold for the $B_s^0 \rightarrow K^+K^-$ and $B^0 \rightarrow K^+\pi^-$ decays. The branching ratios of all these decays are finally reported in Table 1.3.

Branching Ratio	Experimental Value
$\mathcal{B}(B^0 \rightarrow \pi^+\pi^-)$	$(5.12 \pm 0.19) \times 10^{-6}$
$\mathcal{B}(B^0 \rightarrow K^+\pi^-)$	$(1.96 \pm 0.05) \times 10^{-5}$
$\mathcal{B}(B^0 \rightarrow K^+K^-)$	$(7.8 \pm 1.5) \times 10^{-8}$
$\mathcal{B}(B_s^0 \rightarrow \pi^+\pi^-)$	$(7.0 \pm 1.0) \times 10^{-7}$
$\mathcal{B}(B_s^0 \rightarrow \pi^+K^-)$	$(5.8 \pm 0.7) \times 10^{-6}$
$\mathcal{B}(B_s^0 \rightarrow K^+K^-)$	$(2.66 \pm 0.22) \times 10^{-5}$
$\mathcal{B}(\Lambda_b^0 \rightarrow p\pi^-)$	$(4.5 \pm 0.8) \times 10^{-6}$
$\mathcal{B}(\Lambda_b^0 \rightarrow pK^-)$	$(5.4 \pm 1.0) \times 10^{-6}$

Table 1.3: Branching ratios of the charmless charged two-body decays relevant for this thesis [4].

1.3.2 $B_{(s)}^0 \rightarrow h^+h'^-$ and UT parameters

The $B^0 \rightarrow \pi^+\pi^-$ decay receives contributions from all the Feynman diagram topologies illustrated in Figure 1.8. According to Ref.s [52–55] the decay amplitude can be decomposed in the following terms:

$$A_{B^0 \rightarrow \pi^+\pi^-} = \lambda_u^{(d)} (A_{\top}^u + A_P^u) + \lambda_c^{(d)} A_P^c + \lambda_t^{(d)} A_P^t$$

where A_{\top}^u is the partial amplitude due to tree-level processes and A_P^j is amplitudes due to QCD and electroweak penguin topologies. In the latter case, all the up-type quark contribute ($j \in \{u, c, t\}$), thus various CKM couplings are presents ($\lambda_j^{(d)} \equiv V_{jd}V_{jb}^*$). The unitarity of V_{CKM} and the Wolfenstein parametrization allow to rewrite the total amplitude as

$$A_{B^0 \rightarrow \pi^+\pi^-} = \left(1 - \frac{\lambda^2}{2}\right) \mathcal{C} [e^{i\gamma} - de^{i\theta}], \quad (1.95)$$

with

$$\mathcal{C} \equiv \lambda^3 AR_b (A_{\top}^u + A_P^u - A_P^t),$$

$$de^{i\theta} \equiv \frac{1}{(1 - \lambda^2/2) R_b} \left(\frac{A_P^c - A_P^t}{A_{\top}^u + A_P^u - A_P^t} \right),$$

where the already introduced parameters of the UT are used. Besides, the parameter λ_f defined in Eq. (1.34) becomes

$$\lambda_{B^0 \rightarrow \pi^+\pi^-} = -e^{-2i\beta} \left[\frac{e^{i\gamma} - de^{i\theta}}{e^{-i\gamma} - de^{i\theta}} \right].$$

This brings to the following expressions of the CP violation parameters for the decay of a neutral meson into a CP eigenstate:

$$\begin{aligned} C_{\pi^+\pi^-} &= - \left[\frac{2d \sin \theta \sin \gamma}{1 - 2d \cos \theta \cos \gamma + d^2} \right] \\ S_{\pi^+\pi^-} &= - \left[\frac{\sin(2\beta + 2\gamma) - 2d \cos \theta \sin(2\beta + \gamma) + d^2 \sin 2\beta}{1 - 2d \cos \theta \cos \gamma + d^2} \right] \end{aligned} \quad (1.96)$$

The parameter $A_{\pi^+\pi^-}^{\Delta\Gamma}$ cannot be measured because the very small value of $\Delta\Gamma_d$ [4] cancels its contribution to the CP asymmetry (1.49).

In analogy to Equation (1.95), the decay amplitude of the $B_s^0 \rightarrow K^+K^-$ decay can be written as

$$A_{B_s^0 \rightarrow K^+K^-} = \lambda C' \left[e^{i\gamma} + \frac{1}{\varepsilon} d' e^{i\theta'} \right]$$

where $\varepsilon \equiv \lambda^2/(1 - \lambda^2/2)$; C' , d' and θ' are the counterpart of C , d and θ in the case of $B^0 \rightarrow \pi^+\pi^-$. The CP -violation parameters are

$$\begin{aligned} C_{K^+K^-} &= - \left[\frac{2d' \sin \theta' \sin \gamma}{1 - 2d' \cos \theta' \cos \gamma + d'^2} \right], \\ S_{K^+K^-} &= + \left[\frac{\sin(2\beta_s + 2\gamma) - 2d' \cos \theta' \sin(2\beta_s + \gamma) + d'^2 \sin 2\beta_s}{1 - 2d' \cos \theta' \cos \gamma + d'^2} \right], \\ A_{K^+K^-}^{\Delta\Gamma} &= - \left[\frac{d'^2 \sin 2\beta_s + 2\varepsilon d' \cos \theta' \cos(2\beta_s + \gamma) + \varepsilon^2 \cos(2\beta_s + 2\gamma)}{d'^2 + 2\varepsilon d' \cos \theta' \cos \gamma + \varepsilon^2 d'^2} \right], \end{aligned} \quad (1.97)$$

where $A_{K^+K^-}^{\Delta\Gamma} = -\sqrt{1 - (C_{K^+K^-})^2 - (S_{K^+K^-})^2}$. The set of Equations (1.96) and (1.97) form a system with 7 unknowns (d , θ , d' , θ' , β , β_s , and γ) and 4 equations. Using external constraints for β (from $b \rightarrow c\bar{c}$ transitions) the number of unknowns reduces to 6. In addition, U -spin symmetry can be used to constrain the relations between $d \leftrightarrow d'$ and $\theta \leftrightarrow \theta'$, removing two additional unknowns. In this way the system becomes solvable.

At quark level, the $B^0 \rightarrow K^+\pi^-$ decay follows from the transition $b \rightarrow \bar{u}u\bar{s}$. Tree-level, gluon-mediated penguins and electroweak penguins are the Feynman diagram topologies entering the total amplitude, whereas the PA and E topologies cannot. Exploiting the usual formalism and the unitarity of V_{CKM} , the decay amplitude takes the form:

$$A_{B^0 \rightarrow K^+\pi^-} = -P [1 - r e^{i\delta} e^{i\gamma}], \quad (1.98)$$

where the parameter P includes the penguin amplitudes, r is the ratio between tree and penguin amplitudes, δ is the CP conserving hadronic phase and γ is the angle of the UT. This decay is flavour-specific, so there cannot be CP violation in the interference of mixing and decay ($A_{\bar{f}} = \bar{A}_f = 0 \Rightarrow \lambda_f = \bar{\lambda}_{\bar{f}} = 0$). Instead, for the CP violation in the decay, one gets

$$A_{CP}^{K^+\pi^-} = \frac{|A_{\bar{B}^0 \rightarrow \pi^+K^-}|^2 - |A_{B^0 \rightarrow K^+\pi^-}|^2}{|A_{\bar{B}^0 \rightarrow \pi^+K^-}|^2 + |A_{B^0 \rightarrow K^+\pi^-}|^2} = \frac{2r \sin(\delta) \sin(\gamma)}{1 + 2r \cos(\delta) \cos(\gamma) + r^2}. \quad (1.99)$$

The $B_s^0 \rightarrow \pi^+K^-$ is the fully U -spin counterpart of $B^0 \rightarrow K^+\pi^-$, and the ‘‘spectator’’ U -spin counterpart of $B^0 \rightarrow \pi^+\pi^-$. Within the usual formalism and exploiting the CKM matrix unitarity, the decay amplitude of this channel can be written as:

$$A_{B_s^0 \rightarrow \pi^+K^-} = P_s \sqrt{\varepsilon} \left[1 + \frac{1}{\varepsilon} r_s e^{i\delta_s} e^{i\gamma} \right].$$

Since this channel is “flavour specific”, the considerations about the time-evolution, mentioned above for the $B^0 \rightarrow K^+\pi^-$ decay, hold also in this case. Consequently, the direct CP asymmetry are:

$$A_{CP}^{\pi^+K^-} = \frac{2r_s \sin(\delta_s) \sin(\gamma)}{1 + 2r_s \cos(\delta_s) \cos(\gamma) + r_s^2} \quad (1.100)$$

1.4 Semileptonic $B_{(s)}^0$ decays

The side of the Unitary Triangle opposite to the β angle is proportional to $|V_{ub}|/|V_{cb}|$. Hence, the accurate determination of the magnitude of these CKM-matrix elements constitutes a crucial test of the SM consistency and complements the results from the CP asymmetries of B decays. The semileptonic transitions $b \rightarrow c\ell\bar{\nu}_\ell$ and $b \rightarrow u\ell\bar{\nu}_\ell$ (with $\ell = e, \mu$) are usually exploited for this kind of measurements²⁰. In both the cases, two approaches are possible. They alternatively comprise inclusive (*i.e.* the sum of all possible hadronic states) or exclusive final states (decays involving a specific meson, $X = D, D^*, \pi, \rho$ *etc.*). The results of the two methods available in the literature [4] are only marginally consistent:

	$ V_{ub} $	$ V_{cb} $	$ V_{ub} / V_{cb} $
Inclusive	$(4.25 \pm 0.30) \times 10^{-3}$	$(42.2 \pm 0.8) \times 10^{-3}$	0.101 ± 0.007
Exclusive	$(3.70 \pm 0.16) \times 10^{-3}$	$(39.5 \pm 0.9) \times 10^{-3}$	0.094 ± 0.005

and require for further experimental inputs. On the one hand, the semileptonic decays of \overline{B}^0 and B^\pm mesons, involving electrons or muons ($\ell = e, \mu$) are generally well measured and consistent with the SM. They are dominated by tree-level W -boson exchange, and are expected to be essentially free from any effect of physics beyond the SM [4]. On the other hand, the B_s^0 sector is rather unexplored²¹. The Chapter 4 of this thesis reports the first exclusive determination of $|V_{cb}|$ involving the $B_s^0 \rightarrow D_s^{(*)-} \mu^+ \nu_\mu$ decays. This Section presents the general formalism to write the differential decay rates where $|V_{cb}|$ appears. The main complication is due to the necessity to account for the effects of the strong interactions on the dynamics of the underlying weak decay. Most of the theoretical approaches assume that the masses $m_{b,c}$ of the b and c quarks are large compared to the scale which determines the low-energy hadronic physics ($\Lambda_{\text{QCD}} \sim 500 - 700$ MeV). Hence, the basis for precise calculations is the systematic expansions in powers of $\Lambda_{\text{QCD}}/m_{b,c}$. The various methods lead to “form factors” which are Lorentz-invariant functions of q^2 , the squared mass of the virtual W . The parametrisation proposed by Caprini, Lellouch, Neubert (CLN) [60] is used. The formalism outlined below considers the two cases with a pseudoscalar ($D_{(s)}$) or a vector ($D_{(s)}^*$) charmed meson in the final state. For simplicity, both the B^0 and B_s^0 mesons, the D^- and D_s^- mesons, and the D^{*-} and D_s^{*-} mesons, are denoted as B , D , and D^* , respectively, clarifying when distinctions are relevant.

1.4.1 Pseudoscalar final state

For a pseudoscalar final state, the hadronic current can be conventionally decomposed in terms of the vector and scalar form factors $f_+(q^2)$ and $f_0(q^2)$. In the limit of negligible lepton masses the differential rate does not depend on $f_0(q^2)$ and has the form [60]

$$\frac{d\Gamma(B \rightarrow D\mu\nu)}{dw} = \frac{G_F^2 m_D^3}{48\pi^3} (m_B + m_D)^2 (w^2 - 1)^{3/2} \eta_{\text{EW}}^2 |V_{cb}|^2 |\mathcal{G}(w)|^2, \quad (1.101)$$

²⁰Purely leptonic transition, as those provided by the $B_c^- \rightarrow \tau\bar{\nu}$, $B^- \rightarrow \tau\bar{\nu}$, and $B^- \rightarrow \mu\bar{\nu}$ decays, are particularly simple from a theoretical point of view. However, no measurement concerning these channels has reached a competitive precision to date [4].

²¹The branching ratios of the decays $B_s^0 \rightarrow D^{(*)-} \mu^+ \nu_\mu$ were firstly determined as results of the measurements presented in this thesis.

in which the form factor $\mathcal{G}(w)$ can be written as

$$|\mathcal{G}(w)|^2 = \frac{4r}{(1+r)^2} |f_+(w)|^2, \quad (1.102)$$

with $r = m_D/m_B$. In the above equations, w is the recoil variable defined as the product of the four-velocities of the B and D mesons,

$$w = v_B \cdot v_D = \frac{m_B^2 + m_D^2 - q^2}{2m_B m_D}, \quad (1.103)$$

which is related to the square of the four-velocity transfer $(v_B - v_D)^2 = 2(1 - v_B \cdot v_D)$. The minimum value $w = 1$ corresponds to a zero recoil of the D meson in the B rest frame, and $q^2 = q_{\max}^2$. The factor $\eta_{\text{EW}} = 1 + \alpha/\pi \ln M_Z/m_B \simeq 1.0066$ [61] accounts for the leading electroweak correction.

The proper parametrisation of the form factors has been the subject of intense investigations, motivated by the need to extrapolate the information obtained in a restricted q^2 region to the whole q^2 range. Lattice calculations, for instance, are typically limited to the highest q^2 region (close to zero recoil), but very recently they have been extended to the full q^2 spectrum for the $B_s^0 \rightarrow D_s^- \mu^+ \nu_\mu$ decays [62].

The CLN parametrisation is based on dispersion relations and unitarity, but it additionally exploits *Heavy Quark Effective Theory* (HQET) to reinforce the unitarity bounds. This allows establishing approximate relations in terms of a reduced number of free parameters. For instance, the form factor $\mathcal{G}(w)$ can be expressed in terms of two parameters only,

$$\mathcal{G}(z) = \mathcal{G}(0) (1 - 8\rho^2 z + (51\rho^2 - 10)z^2 - (252\rho^2 - 84)z^3), \quad (1.104)$$

where

$$z(w) = \frac{\sqrt{w+1} - \sqrt{2}}{\sqrt{w+1} + \sqrt{2}}. \quad (1.105)$$

In (1.104), the two free parameters are the form factor at zero recoil $\mathcal{G}(0)$ (*i.e.*, $\mathcal{G}(w=1) = 2\sqrt{r}/(1+r)f_+(0)$) and the slope ρ^2 . Decays of this type lead to the experimental measurements of $|V_{cb}|$ and ρ^2 , taking as input the values of $\mathcal{G}(0)$ (from lattice calculations) and η_{EW} .

1.4.2 Vector final state

In this case, the decay amplitude is characterized by four variables, *i.e.* the recoil variable w and three helicity angles, which are: the angle between the direction of the lepton in the virtual W rest frame and the direction of the W in the B rest frame, θ_l ; the angle between the direction of the D in the D^* rest frame and the direction of the D^* in the B rest frame, θ_V ; the angle between the plane formed by the D^* decay and that formed by the W decay, χ .

The decay amplitude can be decomposed in three helicity amplitudes H_+ , H_- , and H_0 , which correspond to the polarization states of the D^* meson, two transverse and one longitudinal. The differential decay rate as a function of w and the helicity angles is then written as

$$\frac{d^4\Gamma(B \rightarrow D^* \mu \nu)}{dw d \cos \theta_l d \cos \theta_V d \chi} = \frac{3m_B^3 m_{D^*}^2 G_F^2}{16(4\pi)^4} \eta_{\text{EW}}^2 |V_{cb}|^2 \sum_i^6 \mathcal{H}_i(w) k_i(\theta_l, \theta_V, \chi), \quad (1.106)$$

with the functions $\mathcal{H}_i(w)$ and $k_i(\theta_l, \theta_V, \chi)$ defined in Tab. 1.4. Note that the $k_i(\theta_l, \theta_V, \chi)$ functions differ for $D^* \rightarrow D\gamma$ and $D^* \rightarrow D\pi$ decays.

In the limit of massless leptons, the helicity amplitudes are expressed by three form-factor functions, $h_{A_1}(w)$, $R_1(w)$, and $R_2(w)$, as

$$H_j(w) = 2 \frac{\sqrt{m_B m_{D^*}}}{m_B + m_{D^*}} (1 - r^2)(w + 1)(w^2 - 1)^{\frac{1}{4}} h_{A_1}(w) \tilde{H}_j(w), \quad \text{with } j = \pm, 0, \quad (1.107)$$

and

$$\tilde{H}_{\mp}(w) = \frac{\sqrt{1 - 2wr + r^2}}{1 - r} \left(1 \pm \sqrt{\frac{w - 1}{w + 1}} R_1(w) \right), \quad (1.108)$$

$$\tilde{H}_0(w) = 1 + \frac{(w - 1)(1 - R_2(w))}{1 - r}, \quad (1.109)$$

with $r = m_{D^*}/m_B$. By integrating on the helicity angle, the differential decay rate as a function of w only can be obtained,

$$\frac{d\Gamma(B \rightarrow D^* \mu \nu)}{dw} = \frac{G_F^2 m_{D^*}^3}{48\pi^3} (m_B - m_{D^*})^2 (w^2 - 1)^{1/2} (w + 1)^2 \eta_{EW}^2 |V_{cb}|^2 \left[1 + \frac{4w}{w + 1} \cdot \frac{m_B^2 + m_{D^*}^2 - 2w m_B m_{D^*}}{(m_B - m_{D^*})^2} \right] |\mathcal{F}(w)|^2, \quad (1.110)$$

where the form factors functions are encoded in $|\mathcal{F}|^2(w)$:

$$|\mathcal{F}|^2(w) = h_{A_1}^2(w) \left(1 + 4 \frac{w}{w + 1} \frac{1 - 2wr + r^2}{(1 - r)^2} \right)^{-1} \left[2 \frac{1 - 2wr + r^2}{(1 - r)^2} \left(1 + R_1^2(w) \frac{w - 1}{w + 1} \right) + \left(1 + (1 - R_2(w)) \frac{w - 1}{1 - r} \right)^2 \right]. \quad (1.111)$$

In the CLN parametrisation, the form-factor functions are

$$h_{A_1}(w) = h_{A_1}(1) (1 - 8\rho^2 z + (53\rho^2 - 15)z^2 - (231\rho^2 - 91)z^3), \quad (1.112)$$

$$R_1(w) = R_1(1) - 0.12(w - 1) + 0.05(w - 1)^2, \quad (1.113)$$

$$R_2(w) = R_2(1) - 0.11(w - 1) - 0.06(w - 1)^2, \quad (1.114)$$

where ρ^2 and $R_{1,2}(1) \equiv R_{1,2}$ are the parameters to be measured experimentally, while $h_{A_1}(1)$, usually also denoted as $\mathcal{F}(1)$, is calculated at zero-recoil ($w = 1$) on the lattice [63]. Thus, the experimental analysis of these decays in the CLN parametrisation yields a measurement of $|V_{cb}|$ along with the form-factor parameters ρ^2 , R_1 and R_2 .

Table 1.4: Functions \mathcal{H}_i and $k_i(\theta_l, \theta_V, \chi)$ of the differential decay rate of $B \rightarrow D^* \mu \nu$ decays.

i	$\mathcal{H}_i(w)$	$k_i(\theta_l, \theta_V, \chi)$	
		$D^* \rightarrow D\gamma$	$D^* \rightarrow D\pi$
1	$ H_+(w) ^2$	$\frac{1}{2}(1 + \cos^2 \theta_V)(1 - \cos \theta_l)^2$	$\sin^2 \theta_V(1 - \cos \theta_l)^2$
2	$ H_-(w) ^2$	$\frac{1}{2}(1 + \cos^2 \theta_V)(1 + \cos \theta_l)^2$	$\sin^2 \theta_V(1 + \cos \theta_l)^2$
3	$ H_0(w) ^2$	$2 \sin^2 \theta_V \sin^2 \theta_l$	$4 \cos^2 \theta_V \sin^2 \theta_l$
4	$ H_+(w) H_-(w) $	$4 \sin^2 \theta_V \sin^2 \theta_l \cos 2\chi$	$-2 \sin 2\theta_V \sin^2 \theta_l \cos 2\chi$
5	$ H_+(w) H_0(w) $	$\sin 2\theta_V \sin \theta_l(1 - \cos \theta_l) \cos \chi$	$-2 \sin 2\theta_V \sin \theta_l(1 - \cos \theta_l) \cos \chi$
6	$ H_-(w) H_0(w) $	$-\sin 2\theta_V \sin \theta_l(1 + \cos \theta_l) \cos \chi$	$2 \sin 2\theta_V \sin \theta_l(1 + \cos \theta_l) \cos \chi$

Chapter 2

The LHCb experiment

Introduction

The LHCb experiment [64, 65] is a single-arm forward spectrometer located at the Large Hadron Collider (LHC) at CERN [66]. Its physics program is oriented to the indirect search for new physics through the study of CP violation in the sector of b and c quarks, the measurements of rare processes and the test of lepton-flavour universality. Moreover, LHCb is active in hadron spectroscopy and in the study of ion collisions [67]. The LHCb design is vindicated by outstanding results like: the first evidence for the very rare decay $B_s^0 \rightarrow \mu^+ \mu^-$ [68, 69], the first observations of CP -violation in the B^+ , B_s^0 , D^0 sectors [70–73], and significant precision improvements on the Unitary Triangle parameters, thanks to world-leading measurements in all the heavy-flavour spectrum. Further prominent results are the first evidence of tetraquark and pentaquark [74–77] and the intriguing anomalies in lepton-flavour universality tests [78–83].

Figure 2.1 depicts the detector geometry and highlights LHCb main apparatuses. The geometrical acceptance of the detector is $[10, 250]$ mrad in the vertical plane¹ and $[10, 300]$ mrad in the horizontal plane, which corresponds to a pseudorapidity² range $\eta \in [1.6, 4.9]$. The choice of this region of interest is driven by the fact that heavy-quark pairs, generated in the high-energy proton-proton collisions of the LHC, are mostly boosted along the beam axis (Figure 2.2). Therefore, the instrumented domain can exploit relatively high cross-sections for both the $b\bar{b}$ and $c\bar{c}$ productions (Table 2.1). The main drawbacks of this configuration are the radiation damage to the detector elements closer to the beam and the event reconstruction, that is complicated by the high occupancy of particles in this forward region and by pile-up, namely the occurrence of multiple pp collision per bunch crossing. In order to mitigate these effects, the instantaneous luminosity at the LHCb interaction point is kept below the maximum deliverable from the LHC: $3 \cdot 10^{32} \text{cm}^{-2} \text{s}^{-1}$ in 2011, $4 \cdot 10^{32} \text{cm}^{-2} \text{s}^{-1}$ in 2012, 2015, 2016, 2017 and about $5 \cdot 10^{32} \text{cm}^{-2} \text{s}^{-1}$ in 2018. Besides, a luminosity levelling technique [87] is used to reduce the systematic effects due to the beam degradation: the beams are progressively brought closer to each other in the transverse plane, such that the rate of collisions remains constant. Figure 2.3 shows the integrated luminosity collected depending on the year of data taking.

¹By convention, a right-handed reference frame is assumed: the origin $(0, 0, 0)$ is the interaction point of the LHC proton bunches, the z axis is parallel to the beam pipe, the x and y axes are the horizontal and vertical axis, respectively. Hence, the vertical (horizontal) plane will be labelled as y - z (x - z) plane.

²By definition: $\eta = -\log[\tan(\theta/2)]$, where θ is the polar angle with respect to the beam axis (z).

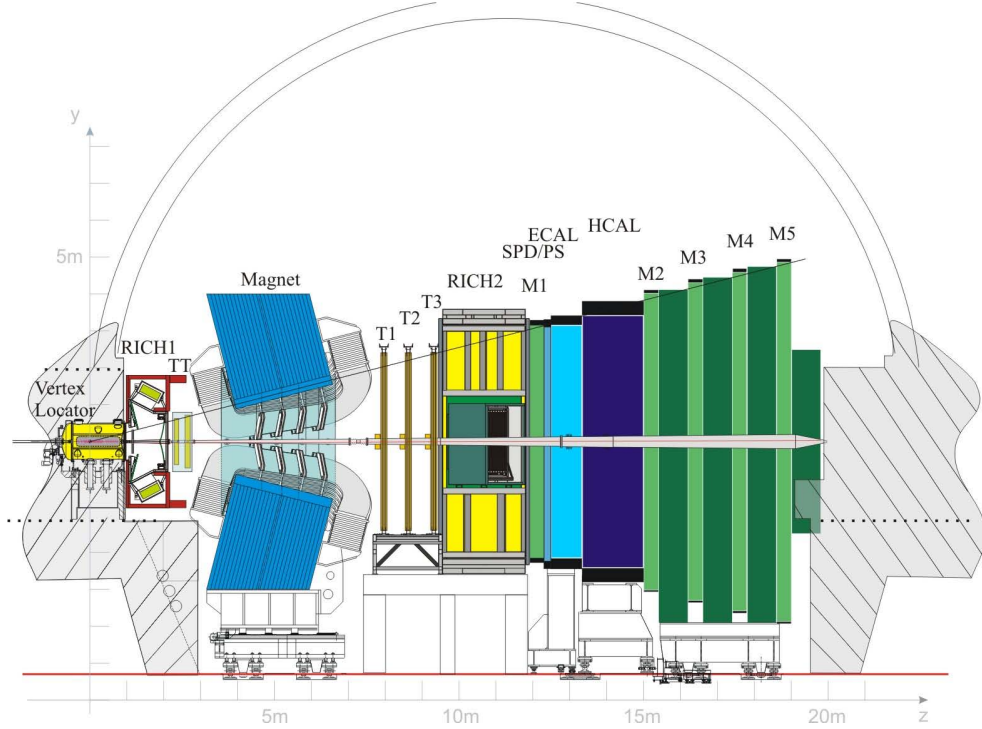


Figure 2.1: The LHCb apparatus. Starting from left, the following subcomponents are visible: Vertex Locator (VELO), ring imaging Cherenkov detector RICH1, Tracker Turicensis (TT), dipole magnet, tracking stations (T1-T3), RICH2, first muon station (M1), electromagnetic calorimeter (ECAL), hadronic calorimeter (HCAL), final muon stations (M2-M5).

Process	Cross-Section [μb]		Ref.
	$\sqrt{s} = 7 \text{ TeV}$	$\sqrt{s} = 13 \text{ TeV}$	
$pp \rightarrow b\bar{b}X$	72.0 ± 6.8	144 ± 21	[84]
$pp \rightarrow c\bar{c}X$	1419 ± 134	2369 ± 192	[85, 86]

Table 2.1: Production cross-sections for b and c quarks in the LHCb acceptance. All values are expressed in μb ; the reported error is the combination of the statistical and systematic uncertainties: further details can be found in the cited references. The two center-of-mass energy options correspond to the conditions provided by LHC in Run1 and Run2, respectively.

In the context of this thesis, it is interesting to note that $\approx 5 \text{ fb}^{-1}$ were collected from the start of the operations to 2016, while the 2017 and 2018 data correspond to $\approx 4 \text{ fb}^{-1}$.

This Chapter reports a brief description of the hadron accelerator system (Section 2.1) and of the various LHCb sub-detectors. The latter ones are grouped as belonging to the Tracking system (Section 2.2) or to the Particle Identification system (Section 2.3). Finally, Section 2.4 explains the peculiarities of the LHCb Trigger system.

The whole experimental structures are currently undertaking an overall upgrade for a progressive increase of the instantaneous luminosity in Run 3 and Run 4 [88–92]. Moreover, plans started for a complete redesign of the detector foreseen for the high luminosity phase of the LHC in Run 5 and Run 6 (HL-LHC) [25, 93, 94]. This exposition refers to the status of the detector at the end of 2018, because this is the relevant one for the measurements of the Chapters 3 and 4.

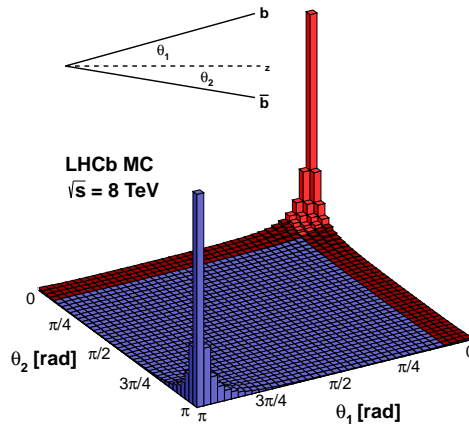


Figure 2.2: Production angles of $b\bar{b}$ pairs with respect to the beam direction according to simulations.

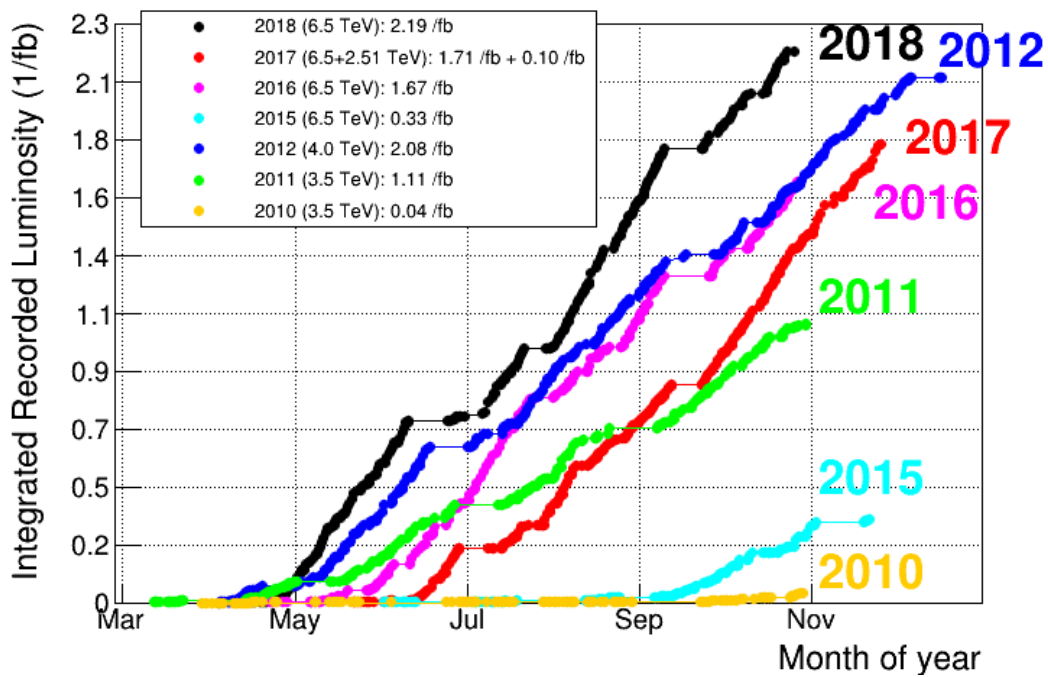


Figure 2.3: Integrated luminosity collected at LHCb, divided by years of data taking.

2.1 The Large Hadron Collider

The LHCb experiment observes the most energetic hadron collisions ever produced at an accelerator machine. This is possible thanks to the Large Hadron Collider (LHC) [66]: a 26.7 km-long synchrotron, installed inside the tunnel formerly used for the Large Electron Positron collider [95] at about 100 m underground across the French and Swiss border, near Geneva. The LHC is able to collide protons up to a centre-of-mass energy of 14 TeV with a luminosity exceeding $10^{34} \text{ cm}^{-2} \text{ s}^{-1}$ and lead ions at 2.76 TeV per nucleon with a luminosity of $10^{27} \text{ cm}^{-2} \text{ s}^{-1}$. The LHC is the last link of the longer accelerator chain illustrated in figure 2.4. The linear accelerator “Linac2” is in charge of bringing the protons from a quasi-rest condition up to 50 MeV and injecting them into the “Proton Synchrotron Booster” (PSB), which, in turn, increases the energy to 1.4 GeV. After that, the hadron beam passes to the “Proton Synchrotron” (PS), that forms bunches of about 10^{11} protons and raises their energy to 25 GeV. Then the “Super Proton Synchrotron” (SPS) provides another acceleration step, reaching 450 GeV and finally injecting the proton bunches into the LHC. Here, the protons circulate in opposite directions inside two accelerating rings, that intersect in four points. The LHCb apparatus and the three other main CERN experiments (ATLAS, CMS and ALICE) are installed in correspondence of these interaction points.

So far, the LHC operations have been divided in two periods. During the Run 1, the centre-of-mass energy of pp collisions was $\sqrt{s} = 7 \text{ TeV}$ in the year 2011 and $\sqrt{s} = 8 \text{ TeV}$ in the 2012. The Run 2, instead, lasted from the 2015 to the 2018 with a collision energy of $\sqrt{s} = 13 \text{ TeV}$.

2.2 Tracking system

The reconstruction of the tracks of the charged particles and the measurement of their momentum are essential tasks for LHCb. Indeed, micro-metric precision on the track position and accurate momentum resolution are critical for the current performance of signal detection and background rejection. A distinctive feature of b -hadrons is that they travel about 1 cm inside the LHCb detector before decay. Therefore, the time-dependent analyses, which rely on the precise measurement of particle decay times, are only feasible thanks to very high spatial resolution on both the primary vertices, where the protons collide, and the secondary vertices, where the long-living particles decay.

The LHCb tracking system is composed by a VERtex LOCator (VELO), dedicated to the accurate reconstruction of primary and secondary vertices, and by tracking stations placed before and after a dipole magnet, to measure the momentum of particles with high precision. Figure 2.5 displays the tracks reconstructed in a typical event.

A dedicated study, reported in Chapter 3, will show that a $\sim 40 \text{ fs}$ resolution on the $B_{(s)}^0$ decay time is achievable. Figure 2.6 illustrates the relative momentum resolution, $\delta p/p$, as a function of the particle total momentum: about 0.5% below 20 GeV/ c and around 0.8% around 100 GeV/ c . Figure 2.6 reports also the transverse impact parameter³ resolution. It varies between $\sim 15 \mu\text{m}$ at high momentum and $\sim 90 \mu\text{m}$ at low momentum.

³The impact parameter (IP) of a track is defined as its distance from the primary vertex at its point of closest approach to the primary vertex. Since the IP is a distance between a point and a line, it is not a Gaussian distributed. However, it is possible to divide the IP in two independent quantities that follow

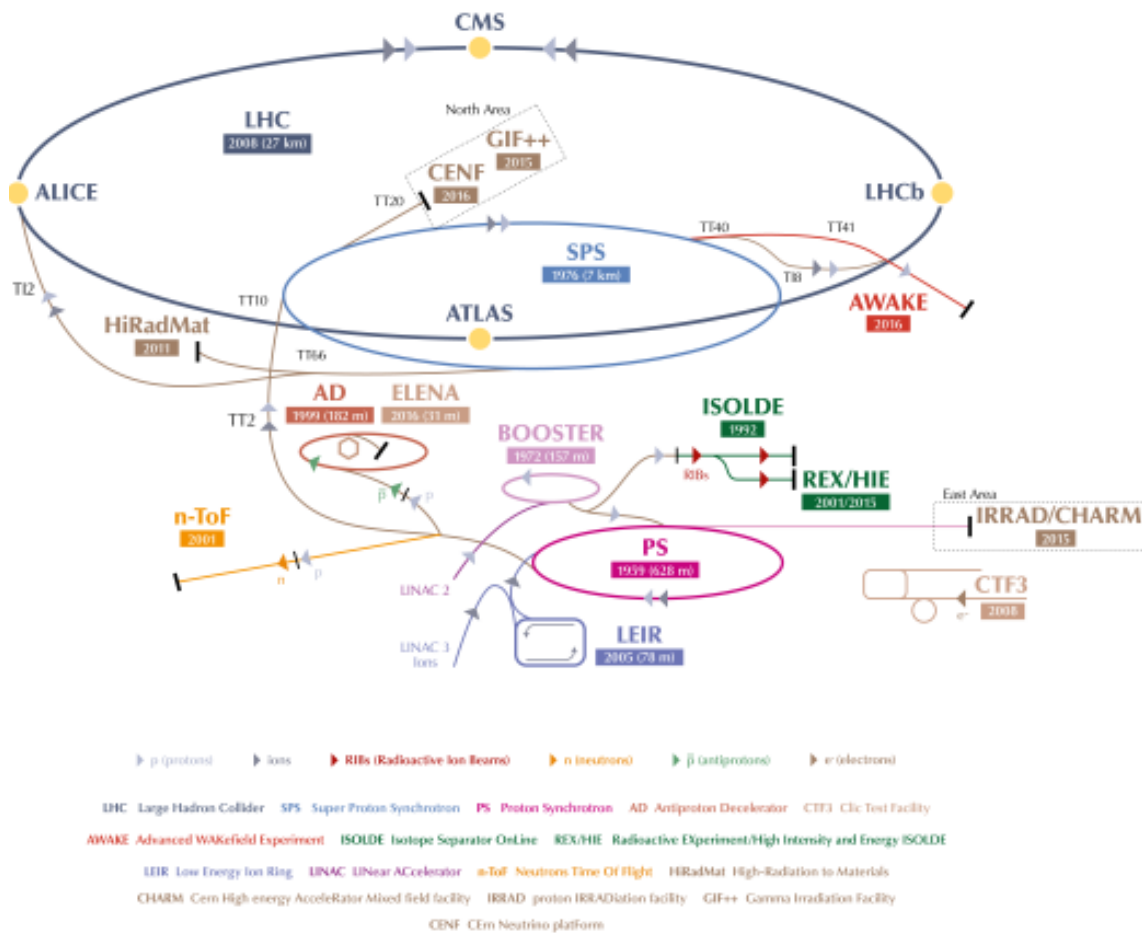


Figure 2.4: Sketch of the CERN accelerator systems [96].

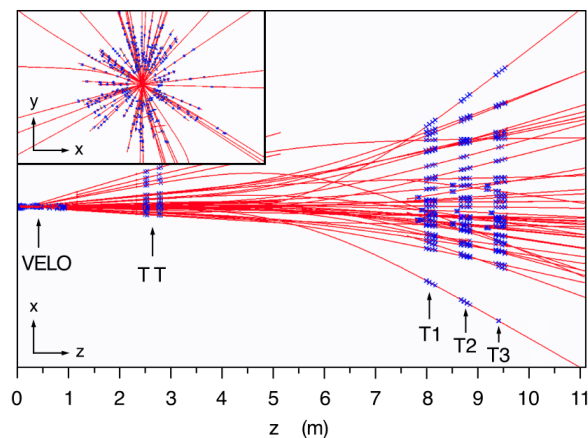


Figure 2.5: Display of the reconstructed tracks and assigned hits in an event in the x - z plane. The insert shows a zoom into the VELO region in the x - y plane [65]. Details in the text.

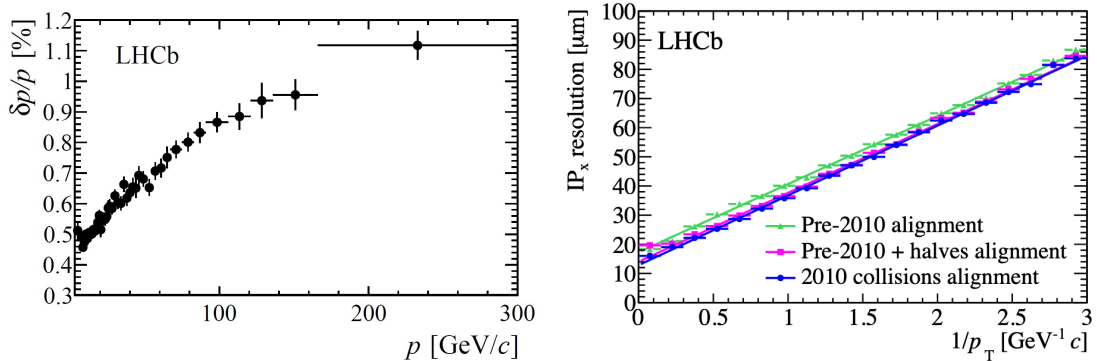


Figure 2.6: Relative momentum resolution (left) and transverse impact parameter resolution (right) versus momentum [65].

2.2.1 VELO

The VELO [97] is the sub-detector located closest to the interaction point. The figures 2.7 and 2.8 illustrate it schematically. A vacuum vessel, separated from the beam vacuum by a 0.5 mm aluminum sheet, contains 23 modules placed orthogonally to the beam. Each module is composed of 300 μm thick silicon-strip sensors with high-radiation tolerance properties. The modules have two different types of sensors: one measures the radial coordinate and one the azimuthal angle of the charged tracks. Besides, they are split in a left and a right part: during the LHC injection they are maintained to a safety distance of 3 cm from the beam, whereas during the data taking the VELO is closed at 7 mm from the beam axis. Two stations, with only radial sensors, are placed upstream of the interaction point, to provide better the pile-up information for the trigger.

The VELO performance depends on various aspects [98]. Some reference values are:

- primary vertex (PV) resolution: 70 μm along the z -axis (beam direction) and 13 μm in the transverse plane when at least 25 tracks are combined;
- impact parameter (IP) resolution: about 12 μm at high transverse momentum (p_T) calculated with respect to the PV;
- decay length resolution: between 220 μm and 370 μm for heavy-flavoured hadrons.

2.2.2 Tracker Turicensis

In order to match the tracks reconstructed in the VELO to the segments in the tracking stations downstream of the magnet, an additional system, called Tracker Turicensis (TT), is present. It is located 2.4 m far from the interaction region: between the RICH1 and the magnet. The TT has four detection layers, 150 cm wide and 130 cm high. They are grouped in two stations, TTa and TTb, 30 cm far from each other. The active material of the layers is composed of silicon micro-strips 500 μm thick. The strips are vertical in the first and in the fourth layer, while in the other layers they are tilted by $+5^\circ$ and -5° , as shown in figure 2.9. The TT achieves about 60 μm resolution on the single hit,

a normal distribution. In LHCb these components are the projections of the IP vector in the transverse plane: IP_x and IP_y [65].

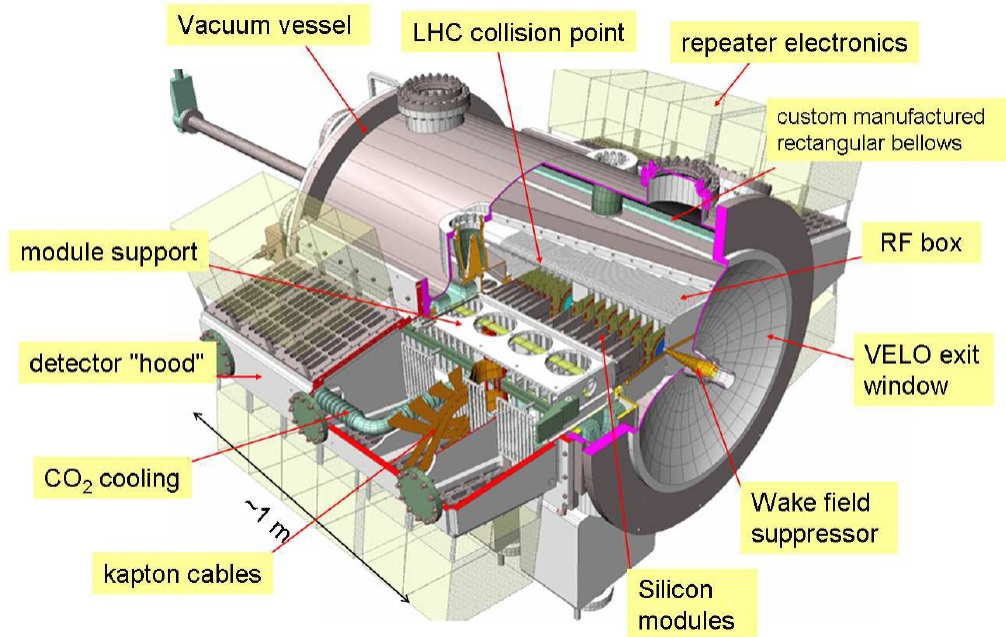


Figure 2.7: the VELO 3D structure

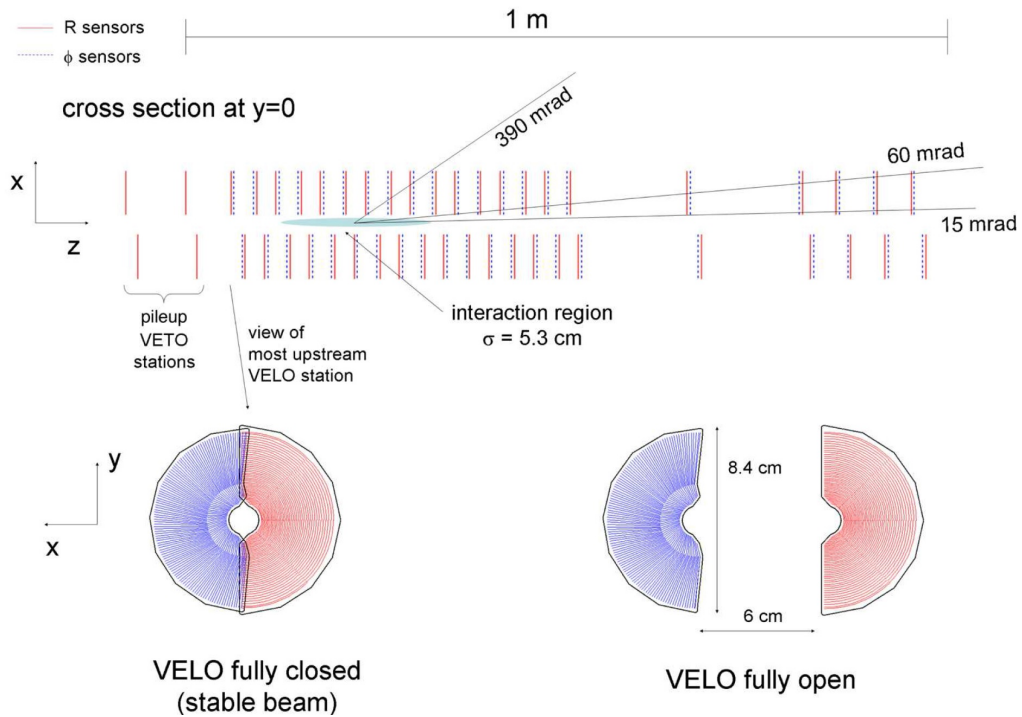


Figure 2.8: Top: sketch of the VELO module arrangement from a top view. Bottom: frontal view sketch of a VELO module in open and closed positions. The radial sensors are represented in red, while the azimuthal sensors are in blue.

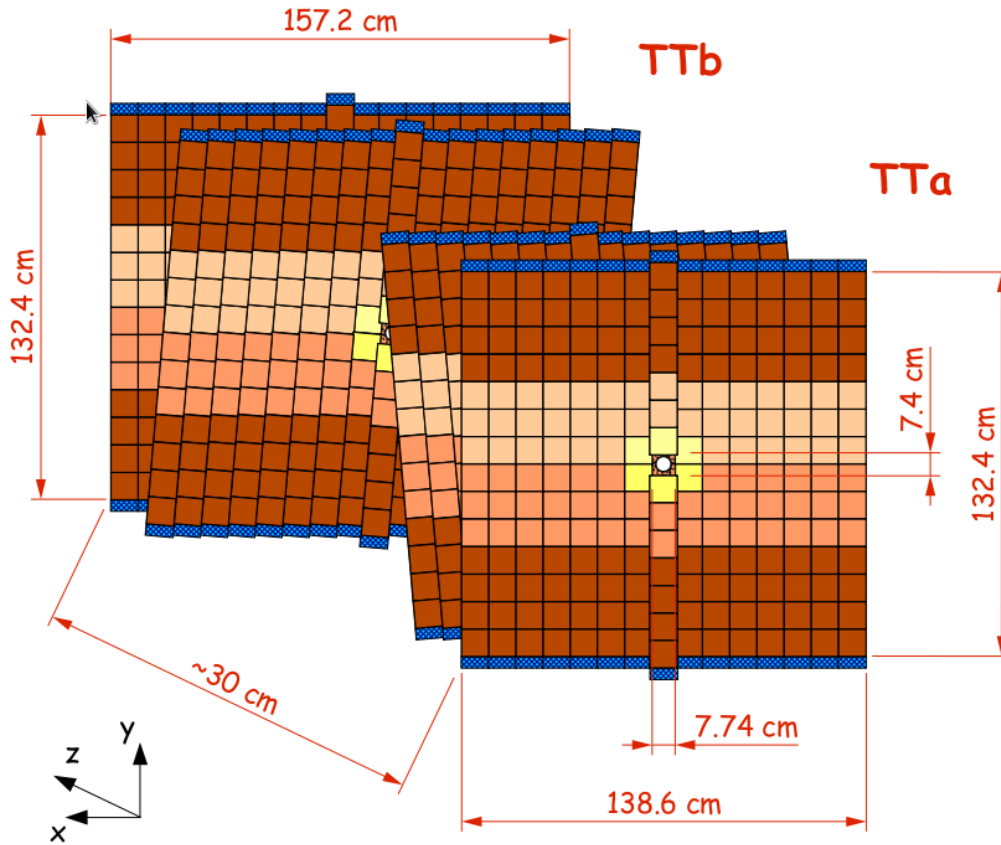


Figure 2.9: Layout of the Tracker Turicensis.

reducing the number of fake tracks (ghost) and improving both the momentum and position resolution.

2.2.3 Magnet

To measure the momentum of the charged particles, it is necessary to bend their trajectory. At LHCb this is done by a warm dipole magnet, located between the TT and the tracking stations. It is formed by two identical saddle-shaped coils, mounted inside an iron yoke (Figure 2.10-left). The weight of the former ones is 54 tons, while the latter is 1500 tons heavy. The maximum circulating current is 6.6 kA for an integrated magnetic field of 4 Tm. The strength of the field changes along the z -axis: from less than 2 mT in the regions occupied by the RICH detectors to about 1 T between the TT and the tracking stations (Figure 2.10-right). The magnetic field has a vertical direction, hence the charged particles are curved in the horizontal plane (x, z). Since positive and negative charged particles are bent to opposite sides, any detection efficiency variation between the left and the right part of the detector could affect CP asymmetry measurements. To minimize this systematic effect, every few weeks of data taking the orientation of the magnetic field is inverted.

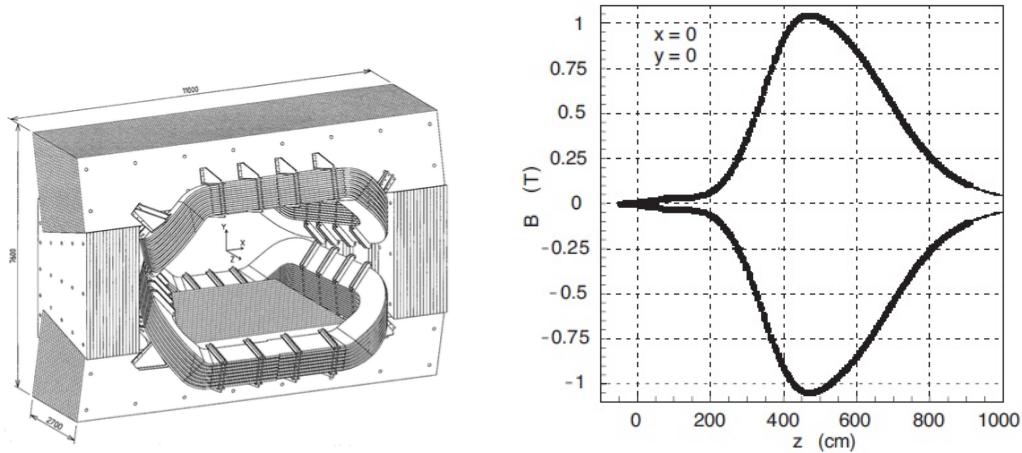


Figure 2.10: Schematic view of the LHCb dipole magnet (left) and magnetic field intensity along the z axis (right).

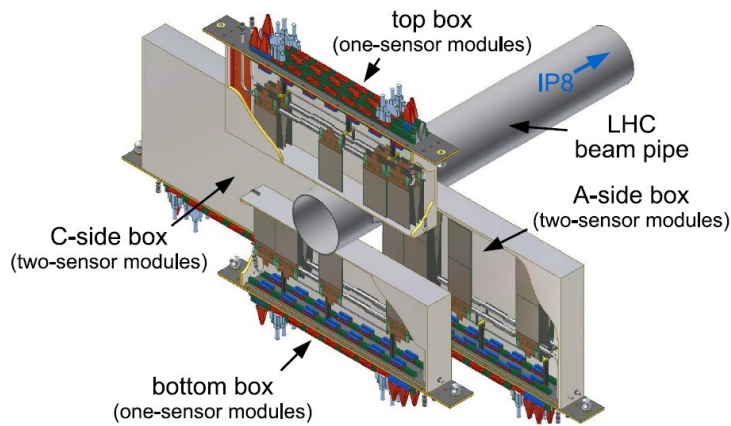


Figure 2.11: The four IT detector boxes around the beam pipe.

2.2.4 Tracking stations

The tracking stations, called T1, T2 and T3, are located downstream of the magnet, after the RICH2 system. They are all divided between two regions –called Inner Tracker (IT) and Outer Tracker (OT)– instrumented with different technologies. The IT [99] consists of silicon micro-strip sensors placed in four individual detector boxes around the beam pipe (Fig. 2.11). Four detection layers lie in each box with an arrangement similar to that of the TT. The single hit resolution is $\sim 50 \mu\text{m}$. The three OT [100] stations are made up of four straw-tubes planes each, with the same geometry as the strips in the TT and in the IT. The straw tubes are arranged in two rows per module composing a honeycomb structure (Fig. 2.12). The diameter of the tubes is 4.9 mm, and they are filled with a mixture of Argon (70%) and CO_2 (30%), which enables a drift time below 50 ns. This brings to a final hit resolution of about $200 \mu\text{m}$.

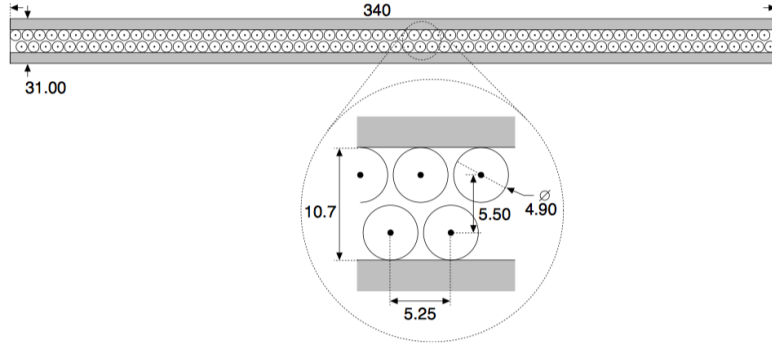


Figure 2.12: Section of an OT plane with a zoom on the straw-tubes. All the dimensions are quoted in mm.

2.3 Particle identification system

The discrimination among the different particle species is a key point for the LHCb success. Various physics mechanisms are exploited to this purpose. Charged particles, travelling in a particular medium with a velocity higher than that of the light, emit Cherenkov photons. The emission follows the rule: $\cos \theta_c = 1/(n\beta)$, where θ_c is the angle with respect to the flight direction (Cherenkov angle), n is the refraction index of the medium and β is the ratio between the velocity of the particle and the speed of light in the vacuum. Therefore, by measuring θ_c and the momentum of a particle it is possible to infer its mass. The LHCb experiment exploits this mechanism to discriminate among charged pions, kaons, and protons. The dedicated sub-detectors are called Ring Imaging Cherenkov (RICH), and are illustrated in Section 2.3.1. A second strategy comes from the energy measurements obtained with the particle absorption. This is particularly important for the photon identification and for the discrimination between electrons and pions. The calorimetric system is devoted to this task (Sections 2.3.2). Last but not the least, the high penetration properties of muons are exploited with a specific apparatus (Section 2.3.3).

At LHCb, the particle identification (PID) information provided by the distinct sub-detectors is combined into two kinds of variables, called “Delta Log. Likelihood” (DLLs) and “Neural Network Probabilities” (ProbNNs). They are the observables finally used in the analyses for particle discrimination. The variables of the former category are presented in the following sections. The latter category, instead, exploits a multivariate approach, that combines DLLs with additional information from the tracking system, the PID detectors, and the particle kinematics. Further details are available in Ref. [101].

2.3.1 Ring Imaging Cherenkov

To cover a broader momentum range, LHCb counts two RICH detectors [102], with different radiator media. The first one is placed between the VELO and the TT, while the second one is located between the last tracking station and the first station of the muon detector. They are both illustrated in figure 2.13. The RICH1 covers the momentum range $[1, 60] \text{ GeV}/c$ and the full LHCb acceptance. Its main⁴ radiator is

⁴During the Run 1 an aerogel layer, mainly related to low-momentum particles, was present, but then removed between Run 1 and Run 2.

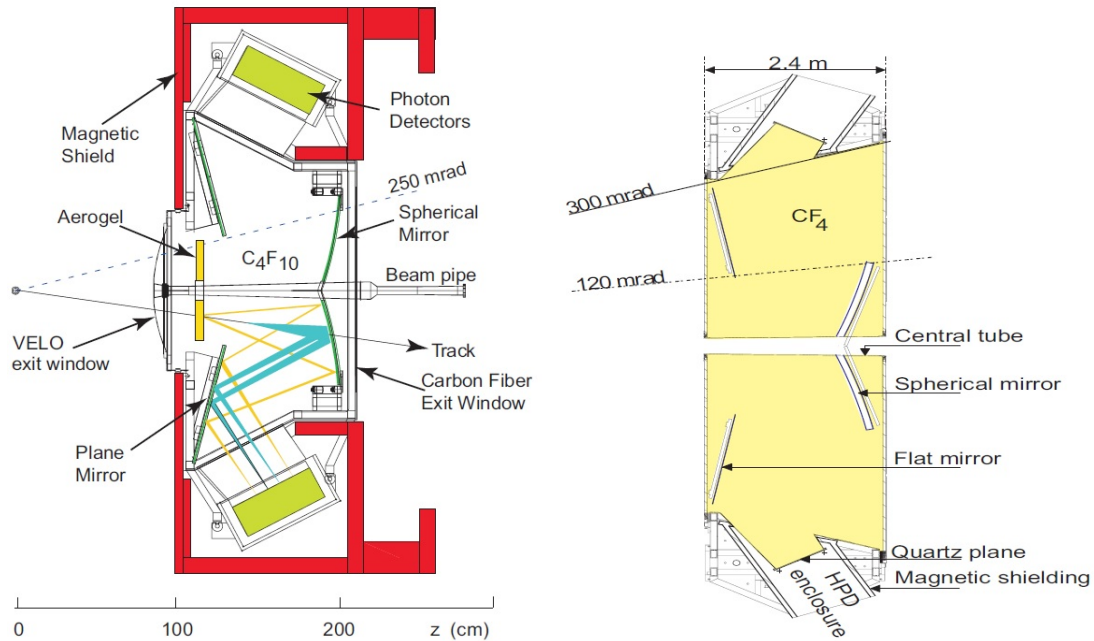


Figure 2.13: Sketches of the RICH1 (left) and RICH2 (right) detectors, sectioned with a vertical and a horizontal plane, respectively.

gaseous fluorobutane (C_4F_{10}). The RICH2, instead, uses tetrafluoromethane (CF_4) as radiator, optimised for the higher momentum range $[15, 100]$ GeV/c. Its acceptance is slightly reduced to $[15, 120]$ mrad in the horizontal plane and up to 100 mrad in the vertical plane.

The light collection system is similar in both the RICHes. Spherical and flat mirrors reflect the Cherenkov light out of the spectrometer acceptance in regions shielded against the residual magnetic field, where lattices of Hybrid Photon Detectors (HPDs) are located. The HPDs are able to detect single incident photons, that hitting the photocathode produce photoelectrons, then accelerated by high voltage (typically 10 to 20 kV) onto a reverse-biased silicon detector. Different Cherenkov angles produce different size rings in the HPD planes. Figure 2.14-left shows the achieved agreement between the Cherenkov angle measured by the RICH1 and the expected, momentum-dependent, distributions for various particle species.

Higher multiplicity and photon contamination from the rest of the event actually complicate the PID process (Figure 2.14-right). As a consequence the following strategy has been adopted for the pattern recognition of the HPD planes. Given the position and the direction of all the particle tracks, the probability to observe a certain pattern on the HPD plane can be calculated. The result of the calculation depends, of course, on the mass hypothesis assigned to each particle. The electron-, muon-, pion-, kaon- and proton-mass hypotheses are considered. Following this approach the problem is solved by the mass association which maximizes the likelihood between the predicted and the observed pattern on the HPD planes. The best set of mass hypotheses is found using an iterative algorithm. First of all, a global likelihood is calculated assuming the pion mass for all the tracks (L_0). After that, for each track, the mass hypothesis is changed, keeping the pion hypothesis for all the other particles. The mass hypothesis which produces the maximal

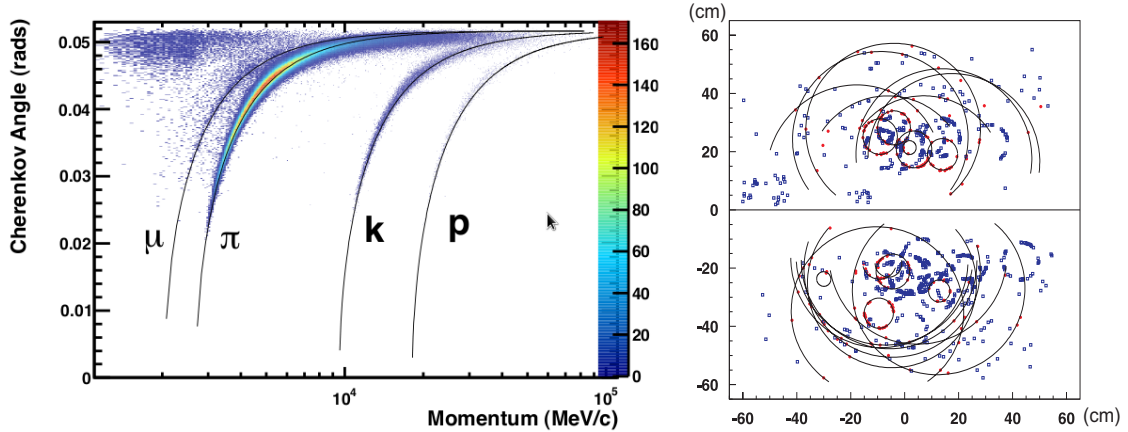


Figure 2.14: Left: Reconstructed Cherenkov angle as a function of particle momentum in RICH1 for isolated μ , π , K and p . The expected curves (solid lines) are superimposed to the experimental results [65]. Right: example of a typical RICH1 event display [64].

increase of the likelihood is associated to the track. The set of mass hypotheses chosen in this way is used to calculate a new global likelihood value (L_i). Then, for each track, the mass hypothesis is changed again, keeping the hypotheses that produced L_i for all the other tracks. Again, the hypothesis generating maximal likelihood increase is chosen and a new global likelihood value (L_{i+1}) is calculated. The procedure is repeated until the global likelihood value converges (L).

To discriminate between different mass hypotheses for a particle (P) the variation after modification of the single P mass hypothesis is used ($L \rightarrow L_h(P)$). The pion hypothesis is usually taken as a reference and the likelihood logarithm is exploited to treat small numbers. Hence:

$$\text{DLL}_{K\pi}(P) \equiv \log L_K(P) - \log L_\pi(P), \quad (2.1)$$

is a measure of the kaon hypothesis reliability: the larger $\text{DLL}_{K\pi}$, the higher is the probability that a particle is a kaon instead of a pion. Typical performances in discriminating between pion, kaons and protons are reported in Figure 2.15.

2.3.2 Calorimeters

The LHCb calorimetric system [104], located between the M1 and M2 stations of the muon system is composed of an electromagnetic calorimeter (ECAL) with Pre-Shower (PS) and Scintillating-Pad Detector (SPD) in front of it, and a hadronic calorimeter (HCAL).

The ECAL is a sampling electromagnetic calorimeter based on shashlik technology. The ECAL cells consist of 66 lead slices 2-mm thick, each one sandwiched between two 4-mm thick polystyrene-based scintillator plates. As shown in Figure 2.16, each layer has a hole pattern to include Wave Length Shifting fibers, which bring the scintillation light to multianode photomultipliers (MAPMTs) located outside the detector and able to generate the readout signal. The cells are 25 radiation lengths (X_0) deep, to fully contain the electromagnetic showers. The lateral size of the cells depends on the distance from the beam axis and is a trade-off between the necessities of high granularity at high occupancy and the cost of the readout channels. Three different granularity regions are present, as depicted in Figure 2.17-left, where cells are arranged in modules of 12 cm side. In total

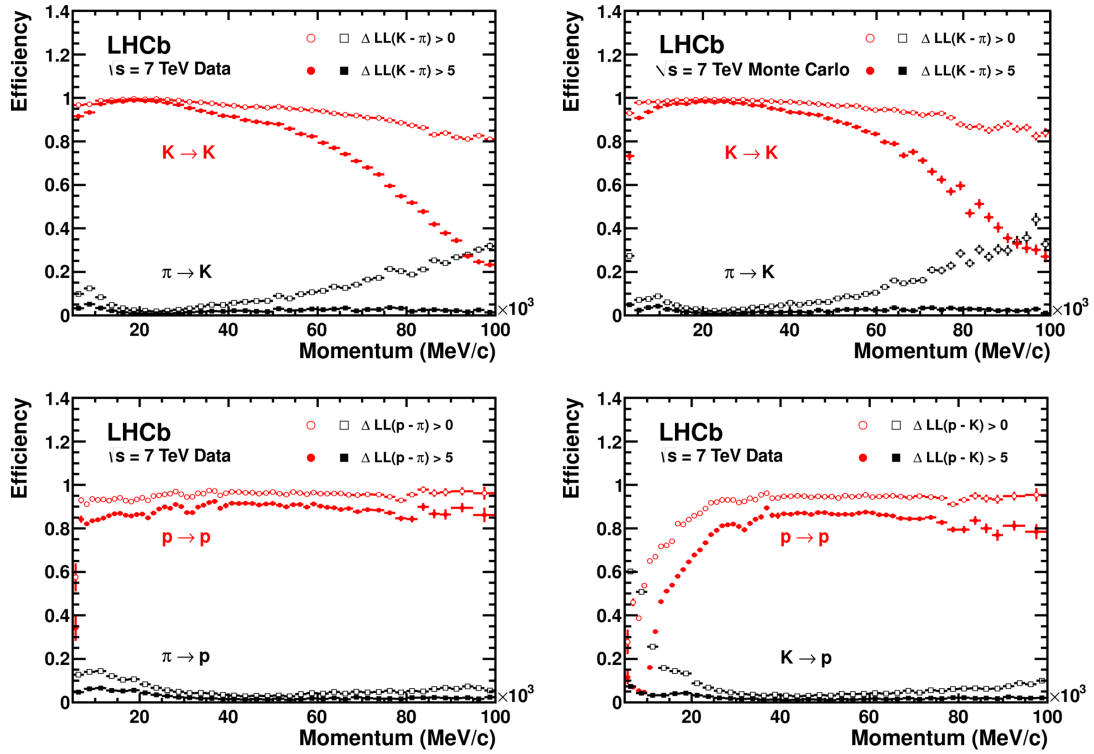


Figure 2.15: Top: Pion mis-identification rate and kaon identification efficiency as a function of the track momentum for (left) data and (right) simulated events. Bottom: proton identification efficiency for (left) pions and (right) kaons from data [103].

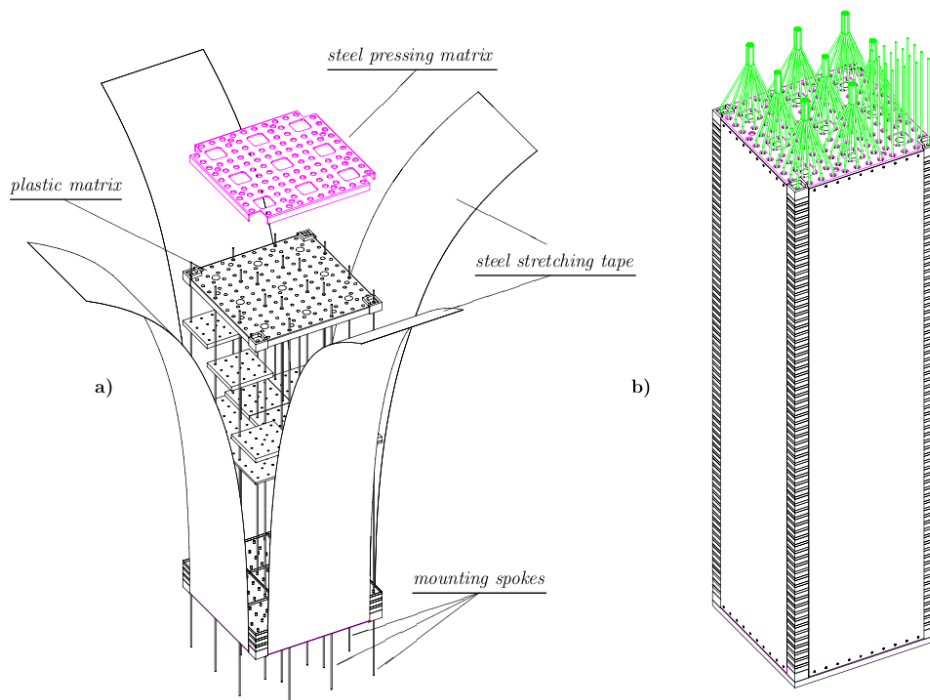


Figure 2.16: Left: Exploded view of one ECAL module. Right: The assembled stack, with the inserted fibers.

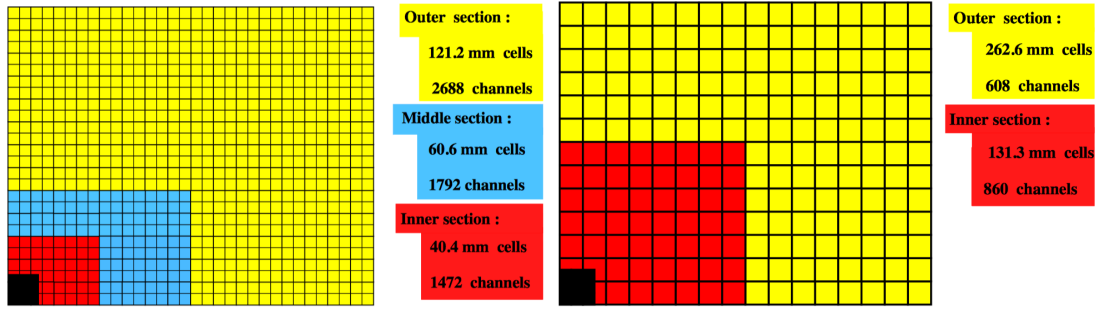


Figure 2.17: Lateral segmentation of one quadrant of (left) ECAL and SPD/PS and (right) HCAL. Cell sizes and number of channels are also reported.

the ECAL is 7.8 m wide and 6.3 m high. The relative energy resolution of the ECAL cells is

$$\frac{\sigma_E}{E} = \frac{9.5\%}{\sqrt{E}} \oplus 1\%, \quad (2.2)$$

with E in GeV. The ECAL is used for electron discrimination against hadrons and is the LHCb subdetector in charge of photon reconstruction. Thus, it is also essential to observe all the decay channels with neutral pions and to correct for the emission of bremsstrahlung photons which affect the electron-momentum reconstruction of electrons.

The PS and the SPD are auxiliary systems placed in front of the ECAL, with the same lateral segmentation. Each cell is made up of a lead plate $2.5X_0$ thick, sandwiched between two identical planes of polystyrene-based scintillating pads with thickness of 15 mm. The set of the front active planes form the SPD, while the planes after the converting lead layer form the PS. The SPD improves the discrimination between charged and neutral particles, since the former produce light in the scintillator material, whereas the latter do not. The PS, instead, is useful to distinguish electrons, which usually begin their shower in the lead layer, and pions, which are more penetrating.

The HCAL consists of 4-mm thick scintillator planes alternated with 16-mm thick iron plates. The tile arrangement is parallel to the beam, as depicted in Figure 2.18. Two different cell granularities are exploited (Figure 2.17-right). The HCAL is 1.2-m thick, corresponding to just 5.6 interaction lengths (λ_{int}). Its energy resolution is

$$\frac{\sigma_E}{E} = \frac{(72.9 \pm 2.9)\%}{\sqrt{E}} \oplus (10.11 \pm 0.45)\%, \quad (2.3)$$

with E expressed in GeV. The HCAL is mainly used to provide trigger information that do not need extremely accurate energy measurements.

Information about the hadron-electron discrimination are provided by all the three apparatuses. Similarly to the RICH case, a DLL variable is defined:

$$\text{DLL}_{eh}^{\text{CALO}} = \text{DLL}_{eh}^{\text{ECAL}} + \text{DLL}_{eh}^{\text{HCAL}} + \text{DLL}_{eh}^{\text{PS}}. \quad (2.4)$$

Figure 2.19 illustrates the performance of this observable. The request $\text{DLL}_{eh}^{\text{CALO}} > 2$ yield a 90% electron efficiency and a 3% mis-identification rate.

2.3.3 Muon Stations

Figure 2.20 illustrates the muon system. It comprises five rectangular stations, called

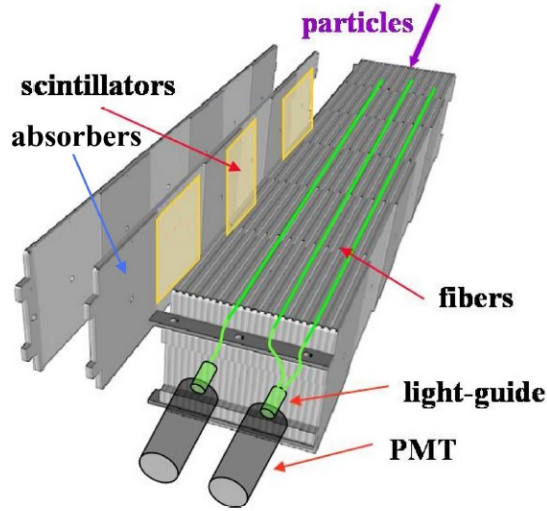


Figure 2.18: Sketch of the HCAL cell structure.

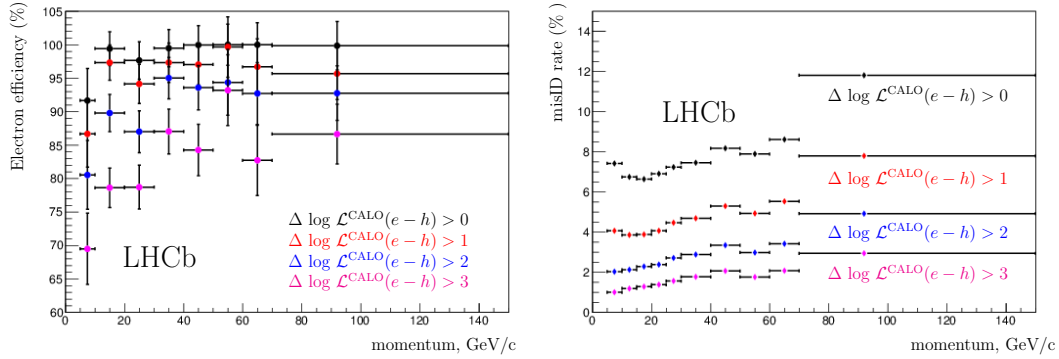


Figure 2.19: Electron identification (left) and mis-identification (right) as a function of momentum and $\text{DLL}_{eh}^{\text{CALO}}$ requirement [65].

M1-M5, covering the angular acceptance ± 300 mrad in the horizontal plane and ± 200 mrad in the vertical plane. Each muon station is separated from the others by an absorber. The calorimetric system is located between the first and the second station, while the other absorber planes are made up of 80 cm thick iron layers. The stations M2-M5 are placed at the end of the LHCb detector. The goal of the muon stations is detecting the position of the muons crossing them, while the absorbers select more penetrating particle at each step. The minimum momentum of a muon able to cross all the stations is 6 GeV/c. In order to cope with the occupancy, each station is divided in four concentric regions (R1-R4), whose linear dimensions and segmentations scale as 1:2:4:8. In total 1368 multi-wire proportional chambers (MWPCs) are used to instrument all the stations except for the innermost region of M1, where 12 chambers composed by two triple Gas Electron Multipliers (GEM) detectors are used. Each MWPC comprises four gas gaps 5 mm thick. Each gas gap hosts in the middle a plane with wires distanced 2 mm one from the other. The gas is a combination of carbon dioxide, tetrafluoromethane and argon. The GEM detectors have three GEM foils sandwiched between cathode and anode planes.

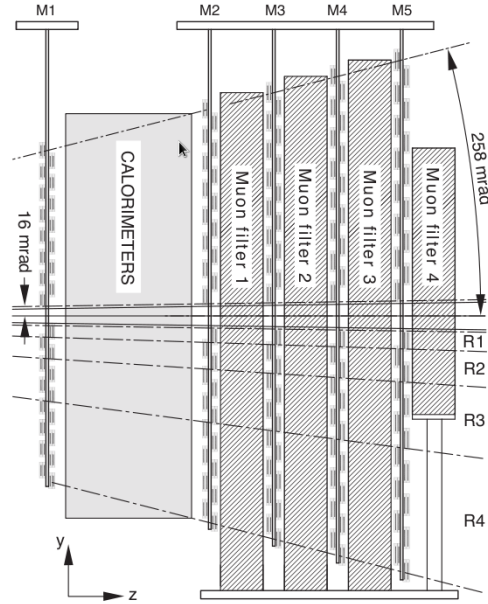


Figure 2.20: Side view of the muon system [64].

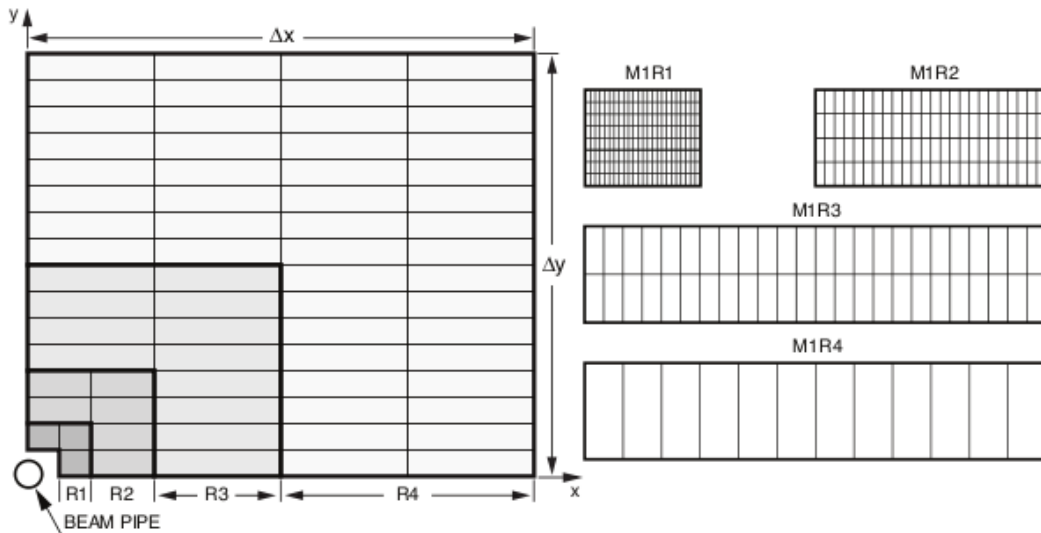


Figure 2.21: (left) Front view of a quadrant of a muon station. Each rectangle represents one chamber. (right) Division into logical pads of four chambers belonging to the M1 station [64].

They are designed to sustain a rate up to 500 kHz/cm^2 of charged particles. Figure 2.21 shows the division of each station in chambers and logical pads that define the spatial resolution along x and y . The first three stations are useful to improve the transverse momentum resolution, thus their spatial resolution along the bending plane is particularly relevant. The last two stations are mostly exploited for trigger purposes, namely the identification of penetrating particles. Three main sets of criteria are used at LHCb for the muon selection [105]:

- A loose binary discrimination based on the number of muon stations traversed by a

muon candidate as a function of its momentum; this information is resumed in the `IsMuon` variable.

- The trajectories of the charged particles reconstructed with high precision by the tracking system can be used to perform an extrapolation to the muon stations. The hit pattern around this extrapolation allow likelihood functions to be calculated for both the muon and non-muon hypotheses. The logarithm of the ratio between these two likelihood functions is the `muDLL` variable.
- A further likelihood depending on the particle hypothesis can be computed including also information from the calorimeter and RICH systems. The logarithm of the ratio between the likelihood in the muon and in the pion hypotheses returns the `DLLμπ` variable.

In addition, rejection power against fake candidate is also provided by the `NShared` variable, namely the number of tracks identified as muons that share a hit with a given muon candidate. As shown in Figure 2.22, above 10 GeV/ c of momentum the LHCb detector can achieve a muon identification efficiency higher than 90%, with a mis-identification rate below 1%.

2.4 Trigger

The LHCb detector produces a huge amount of data which has to be properly skimmed to be manageable. The system committed to this data reduction is called Trigger [106]. Figure 2.23 summarizes the trigger scheme, depending on the year of data taking. As a general feature three levels are present, each one processing the output of the previous one. The first level, called L0, is implemented in the hardware and is synchronous with the bunch crossing rate of the LHC (40 MHz). The other two levels, called High Level Trigger 1 and 2 (HLT1 and HLT2), are implemented using software algorithms and save their output to mass storage. In particular, the HLT software runs on the Event Filter Farm (EFF), which counts about 1700 nodes with 27000 physical cores, and 10 PB of hard disk space. The next paragraphs offer more details on the criteria exploited at each step. In general, the trigger signals are associated with the reconstructed particles. Therefore, selection requirements can be made on the trigger decision itself, depending on the studied channel. When a trigger decision is caused by a signal candidate, the TOS label (Trigger On Signal) is used. Instead, the TIS label (Trigger Independent of Signal) stands for a trigger decision due to other particles produced in the pp collision.

2.4.1 Level-0

The main feature exploited by the L0 is that the decay products of b and c hadrons have larger transverse momentum than the average of the other particles produced in a pp collision. The L0 counts three sub-systems related to different sub-detectors: the L0 `pile-up`, the L0 `calorimeter` and the L0 `muon`. Their information is then sent to a decision unit (DU), which finally decide whether the event is rejected or not. The total L0 latency is 4 μ s, namely the L0 decision must be taken within 4 μ s from the bunch crossing. The L0 `pile-up` is oriented to the luminosity monitoring, getting information from the

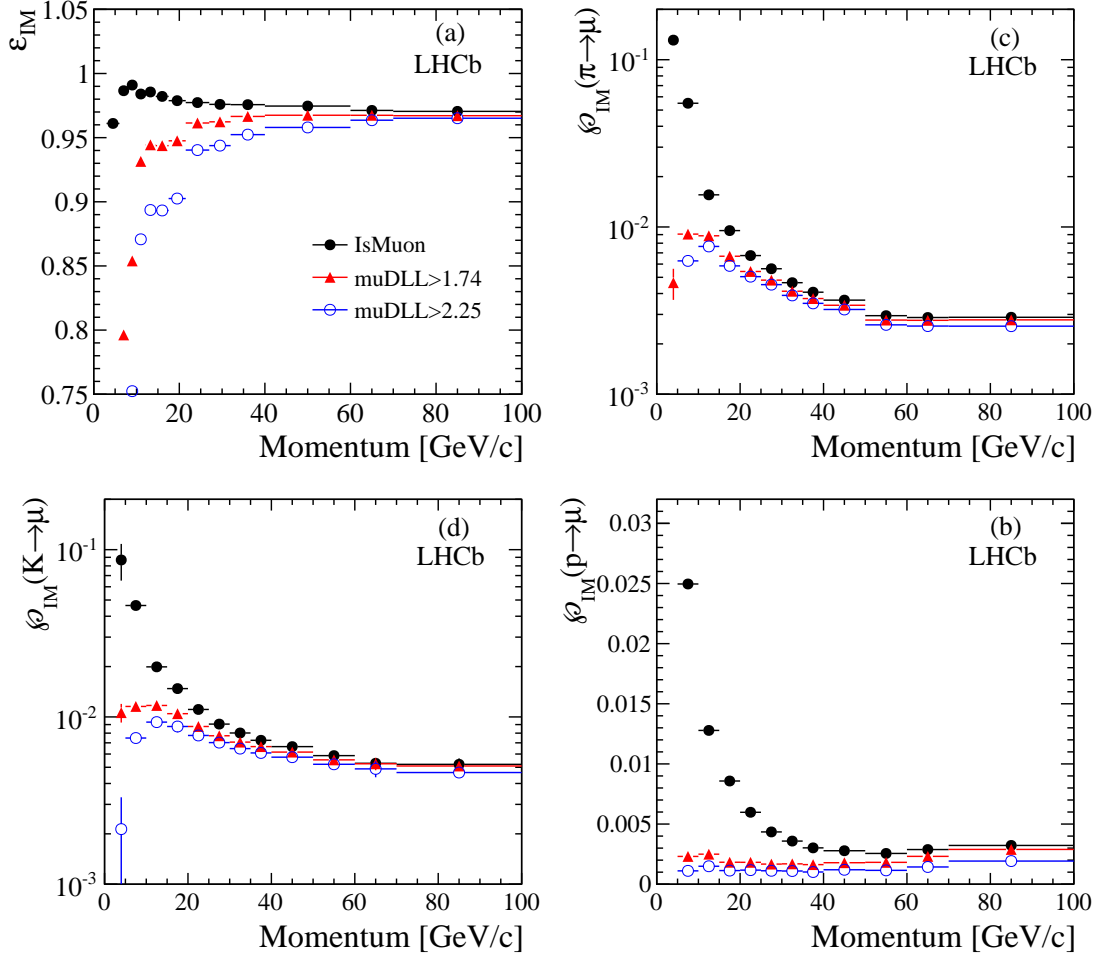


Figure 2.22: Muon identification efficiency and mis-identification probabilities pions (a), kaons (b) and protons as a function of the track momentum.

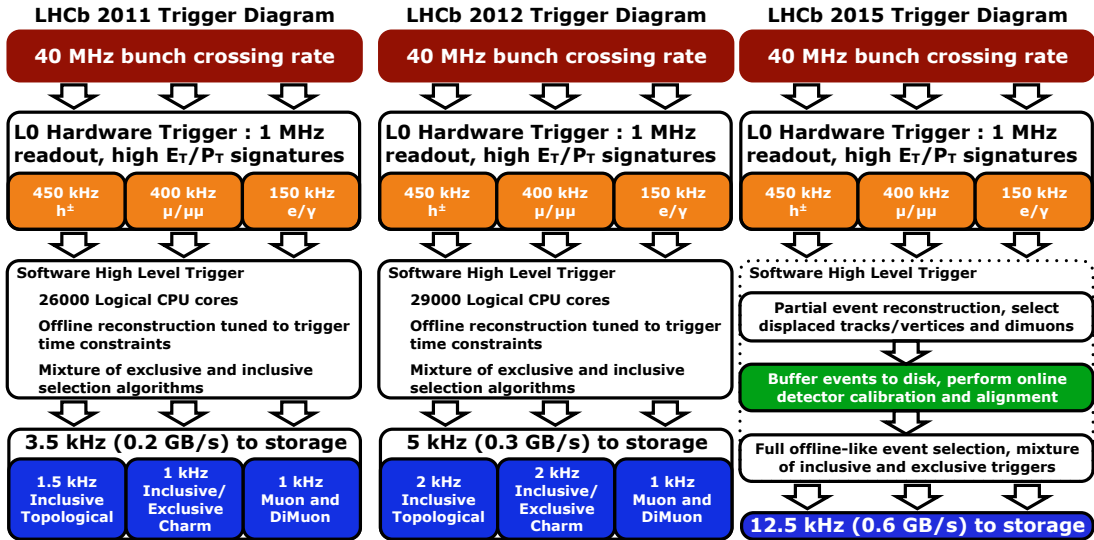


Figure 2.23: Trigger layout during (left) 2011, (centre) 2012 and (right) 2015. The layout used during Run 2 is the same as in 2015.

two pile-up modules of the VELO. The `L0 calorimeter` observe the transverse energy⁵, E_T , released in clusters of 2×2 cells of ECAL or HCAL, according to three criteria:

L0Hadron: selects the maximal E_T among those of the HCAL clusters. If the ECAL cluster with the maximal E_T is aligned, its transverse energy is summed.

L0Photon: selects the maximal E_T among the ECAL clusters, with at most 2 (or 4 in the inner region) PS hits in front of the cluster and no hits in the SPD cells aligned with the PS ones.

L0Electron: has the same requirements of `L0Photon`, but with at least one additional hit in the SPD cell in front of the cluster.

`L0 calorimeter` returns a positive result (*fires* in jargon) when the E_T is higher than 4 GeV for hadrons and 2.7 GeV for electrons and photons. The `L0 Muon` fires when it finds a muon with p_T higher than 1.4 GeV/c. The muon p_T reconstruction starts from a *seed* hit in M3 and then look for other hits in consistent fields of interest (FOI) of M1 and M2. The direction defined by the associated hits provide a 20% accuracy on the p_T estimation.

2.4.2 High Level Trigger 1

The HLT1 operates a preliminary reconstruction using information from the tracking system. At each step of the reconstruction various criteria are applied in order to skim the irrelevant events. A usual reconstruction procedure starts building tracks segments and PVs with the VELO information. The segments are required to have a minimum number of hits and large IP with respect to the closest PV. The VELO tracks are then matched to hits in the TT for a first estimation of their charge and momentum. After that, minimal p and p_T thresholds are applied, and the information from the other tracking is stations added. A Kalman filter [107], which considers multiple scattering and corrects for energy losses due to ionisation is then run, permitting better reconstruction of the tracks, and further requirements on the χ^2 and the IP significance (χ_{IP}^2) of the tracks to be applied. Specific selection criteria are imposed on the reconstructed tracks to select decay topologies. Each algorithm is named *trigger line*. In this thesis, an inclusive HLT1 algorithm is exploited to select events with the presence of at least one track with large p_T or χ_{IP}^2 . The two variables are combined through a multivariate algorithm and requirements are then applied to this quantity [108, 109]. The corresponding trigger lines are named `Hlt1TrackMVA` and `Hlt1TwoTrackMVA`. The former concerns a single track, while the latter considers a pair of tracks and additionally exploits information related to a possible common vertex. Further HLT1 lines relevant for this Thesis are called: `Hlt1TrackAllLO`, `Hlt1TrackMuon`, and `SingleMuonHighPT` [110]. The former generically selects hadron decays which are significantly displaced from a PV. The latter two fire only after an occurrence of `LOMuon`. `Hlt1TrackMuon` accepts events with muon candidates that have significant IP with respect to all PVs, while `SingleMuonHighPT` focuses on muons originating from heavy particles with a negligible lifetime. Table 2.2 resumes their main selection requirements.

⁵The transverse energy, E_T , of a particle is defined as $E_T = E \sin \theta$, where E is its energy and θ is the angle between the beam axis and the particle direction. In this case, the propagation on a straight line intersecting the interaction point is assumed for all candidates.

HLT1 line	Hlt1TrackMuon	SingleMuonHighPT	Hlt1TrackAllLO
Track IP [mm]	> 0.1	–	> 0.1
Track χ^2_{IP}	> 16	–	> 16
Track p_T GeV/ c	> 1	> 4.8	> 1.7
Track p GeV/ c	> 8	> 8	> 10
Track χ^2/ndf	< 2	< 4	< 2.5
No. of VELO hits/tracks	–	–	> 9
No. of missed VELO hits/tracks	–	–	< 3
No. of OT+IT \times 2 hits/tracks	–	–	> 16

Table 2.2: Main requirements applied by the Hlt1TrackMuon, SingleMuonHighPT, and Hlt1TrackAllLO trigger lines [110].

2.4.3 High Level Trigger 2

The HLT2 runs a more refined event reconstruction, similar to the off-line reconstruction, using also information from RICH detectors and calorimeters. The HLT2 includes some hundred trigger lines, which can be grouped in two categories:

Inclusive trigger lines designed to trigger on partially reconstructed b -hadron decays through topological requirements, for example asking at least for two charged tracks coming from a displaced decay vertex fulfilling requirements on track χ^2 , IP and particle identification. Two-body objects are built requiring small distance of closest approach (DOCA) between the two decay particles, and in the same way n -body objects are built combining the $(n - 1)$ -body candidate with another particle [111, 112]. Among the trigger lines belonging to this category, the ones named Hlt2Topo{2,3,4}BodyBBDT are particularly relevant for the analysis described in the Chapter 4 of this Thesis. They are fully described in Ref. [113].

Exclusive trigger lines designed for specific final states, requiring all particles to be reconstructed.

During Run 2, a new data stream was introduced in HLT2, called Turbo stream [114]. For the events selected in this stream only the reconstructed candidates is stored, discarding the information from the rest of the event to save storage space. This stream is advantageous to select decays with high rates.

Chapter 3

Measurements of CP violation with $B_{(s)}^0 \rightarrow h^+ h'^-$ decays

Introduction

As discussed in Chapter 1, the $B_{(s)}^0 \rightarrow h^+ h'^-$ decays are remarkable probes for the indirect search for new physics. This is mainly due to the relevant role played by penguin Feynman-diagram topologies. Physics beyond the SM may provide virtual contributions to their loops and cause deviations of the UT parameter measurements as compared to the values determined from other pure tree-level transitions. However, the penguin-diagram amplitudes contain also additional strong parameters which complicate the extraction of the UT angles from the CP -violation observables. In order to cancel the unknown quantities, the combination of several measurements, exploiting approximate flavour symmetries, is crucial. This Chapter presents the measurement of the following CP -violations parameters:

- the time-integrated CP asymmetries $A_{CP}^{B^0}$ and $A_{CP}^{B_s^0}$, which quantify the CP violation in the decay for the $B^0 \rightarrow K^+ \pi^-$ and $B_s^0 \rightarrow \pi^+ K^-$ modes¹;
- the parameters $C_{\pi^+ \pi^-}$, $S_{\pi^+ \pi^-}$, $C_{K^+ K^-}$, $S_{K^+ K^-}$, $A_{K^+ K^-}^{\Delta\Gamma}$, which determine the time-dependent CP asymmetries in $B^0 \rightarrow \pi^+ \pi^-$ and $B_s^0 \rightarrow K^+ K^-$ decays².

The CDF, BaBar, Belle, and LHCb collaborations extensively studied the $B_{(s)}^0 \rightarrow h^+ h'^-$ decays. Table 3.1 reports the values of the time-integrated asymmetries, as measured by the various experiments. Analogously, Table 3.2 contains the results for the time-dependent CP -violation observables. In particular, the latest LHCb publication [24] provided the first observation of time-dependent CP violation in the B_s^0 sector, along with the most accurate measurements of all the cited quantities to date. These results exploited the pp -collision data collected during the Run1 (years 2011 and 2012) and the first part of the Run2 (2015-2016) of LHCb, corresponding to a total integrated luminosity of about 5 fb^{-1} . Now, 4 more inverse femtobarns are available thanks to the data collected in the years 2017 and 2018 (see Figure 2.3). The purpose of the measurements described in this Chapter is the inclusion of the latest LHCb data samples. The analysis on the 2015

¹Definitions in equations: (1.46), (1.99) and (1.100).

²Definitions in equations: (1.43), (1.96) and (1.97).

Table 3.1: Current knowledge of the time-integrated CP asymmetries of the $B^0 \rightarrow K^+\pi^-$ and $B_s^0 \rightarrow \pi^+K^-$ decays. The first error is statistical, while the second one is systematical. For LHCb only the total uncertainty is given, because the reported result is the combination of two experimental determinations [24, 115]

Experiment	$A_{CP}^{B^0}$	$A_{CP}^{B_s^0}$	Ref.
BaBar	$-0.107 \pm 0.016^{+0.006}_{-0.004}$		[116]
Belle	$-0.069 \pm 0.014 \pm 0.007$		[117]
CDF	$-0.083 \pm 0.013 \pm 0.004$	$0.22 \pm 0.07 \pm 0.02$	[118]
LHCb	-0.0831 ± 0.0034	0.225 ± 0.012	[24]

Table 3.2: Current knowledge of the CP -violation parameters in $B^0 \rightarrow \pi^+\pi^-$ and $B_s^0 \rightarrow K^+K^-$ decays.

Experiment	$C_{\pi^+\pi^-}$	$S_{\pi^+\pi^-}$	Ref.
BaBar	$-0.25 \pm 0.08 \pm 0.02$	$-0.68 \pm 0.10 \pm 0.03$	[116]
Belle	$-0.33 \pm 0.06 \pm 0.03$	$-0.64 \pm 0.08 \pm 0.03$	[119]
LHCb	-0.320 ± 0.038	-0.672 ± 0.034	[24]

Experiment	$C_{K^+K^-}$	$S_{K^+K^-}$	$A_{K^+K^-}^{\Delta\Gamma}$	Ref.
LHCb	0.172 ± 0.031	0.139 ± 0.032	-0.897 ± 0.087	[24]

and 2016 samples is repeated to check the consistency of the analysis strategy. Besides, the 2015 and 2016 data have been reprocessed to remove reconstruction issues discovered in the meantime, although these issues are not expected to influence the published results³.

The considered signal channels count four exclusive final states: $\pi^+\pi^-$, $K^+\pi^-$, π^+K^- and K^+K^- . Section 3.1 presents the data samples, catalogues the possible background sources, and reports the exploited selection criteria. The most insidious background source is the cross contamination among the different final states. In order to better handle this effect, the CP observables are extracted from the data by means of maximum likelihood fits which simultaneously consider all the final states. Two fits are necessary because two sets of selection requirements are developed: one optimized for the measurement of $A_{CP}^{B^0}$, $A_{CP}^{B_s^0}$, $C_{\pi^+\pi^-}$, $S_{\pi^+\pi^-}$ and one optimized for $C_{K^+K^-}$, $S_{K^+K^-}$, $A_{K^+K^-}^{\Delta\Gamma}$. Anyway, the fit strategy (Section 3.7) is essentially the same in both cases.

To properly describe the data components, several experimental effects are considered:

Production Asymmetries. Since LHC is a pp collider the production rates of $B_{(s)}^0$ and $\bar{B}_{(s)}^0$ mesons are not exactly the same. As discussed in Section 3.7, this asymmetry

³The reconstruction issues mainly concerned candidates selected by the L0Muon_TOS trigger line and belonging to the Turbo stream. The contribution of such a set of candidates to the data sample used in the former version of analysis was checked to be negligible after the full selection. Further documentation can be provided upon request.

can be extracted directly from the data, exploiting the information provided by the $B^0 \rightarrow K^+\pi^-$ and $B_s^0 \rightarrow \pi^+K^-$ decays.

Flavour Tagging. As already discussed in section 1.1.1, the flavour identification of the neutral B mesons at their production is a complicated task in a hadron collider environment. Nonetheless, specific methods and algorithms have been developed, that return a flavour prediction along with a per-event mis-tag probability. The raw estimation of this probability has to be calibrated for the specificity of the signal decay modes and then included in the fit model. Details are reported in Section 3.4.

Decay-Time Resolution. The uncertainty on the reconstruction of the decay time of $B_{(s)}^0$ candidates generates a dilution of the time-dependent asymmetries, which has to be estimated in order to disentangle this effect from the actual CP -induced asymmetries. The decay time of $B_{(s)}^0$ -meson candidates is reconstructed by means of the distance between the intersection vertex of the two final state tracks ($\text{ENDV}(B_{(s)}^0)$) and the associated primary pp interaction vertex (PV). Depending on the specificity of each candidate, an error on the decay-time measurement can be estimated, but further studies are necessary to properly calibrate it. Section 3.3 describes this calibration procedure and shows that an average decay-time resolution can be used in the final fit, simplifying the likelihood optimization procedure and introducing negligible systematic effects.

Decay-Time Bias. It is experimentally known that the baseline LHCb reconstruction procedure is possibly affected by misalignment effects. The entity of this issue is estimated in Section 3.3.

Decay-Time Acceptances. The $B_{(s)}^0$ reconstruction efficiency depends on the decay time: the shorter the decay time, the lower the reconstruction efficiency. The exact dependency has to be estimated and considered in the final fit. In particular, it is highly correlated with the extraction of the $A_{K^+K^-}^{\Delta\Gamma}$ observable. Details are reported in Section 3.5.

Final-State Mis-Identification. The association of a wrong mass hypothesis to one or both the final state candidates (mis-ID) generates the cross contamination among the final-state samples (cross-feed background). To determine the contamination due to the mis-identified final states, all the relevant mis-ID probabilities are estimated using calibration samples (see Section 3.2). Such information is exploited in the simultaneous fit to link the signal yield of a given spectrum with the corresponding cross-feed components in the other spectra.

Final-State Detection and Identification Asymmetries. The time-integrated CP asymmetries are determined from the signal counts in the two charge-conjugated final states: $K^+\pi^-$ and π^+K^- . However, the reconstruction efficiency of such states is not experimentally guaranteed to be the same. This is actually due to slightly different performances in the detection and mass hypothesis association (PID) between particles of opposite charge. The raw time-integrated asymmetries obtained by the final fit are then corrected to remove this effect and get the proper $A_{CP}^{B^0}$ and $A_{CP}^{B_s^0}$. This procedure is described in Section 3.6.

To check for eventual discrepancies among various data taking periods, all the experimental effects are independently studied for the 2015-16⁴, 2017, and 2018 samples. As a general rule, when no major deviations are found, only the plots concerning the 2018 samples are reported in the body of the text. Section 3.8 presents the fit results and a set of consistency checks between the results obtained from different data-taking periods.

3.1 Data composition and selection

The analysis employs the data sample of pp collisions collected at a center-of-mass energy of 13 TeV during the entire Run2 of the LHCb experiment, namely the years 2015, 2016, 2017, and 2018. The corresponding global integrated luminosity is about 6 fb^{-1} , as reported in Table 3.3. During each year of data taking the polarity of the LHCb dipole was inverted repeated times, to guarantee the cancellation of eventual left-right asymmetries of the detector. Two sub-samples of almost equal statistics were collected, and labelled as *MagUp* and *MagDown*.

The event reconstruction and selection consist of successive steps: trigger, stripping, and final selection.⁵ The trigger and stripping impose quite loose selection criteria. Their fundamental objective is scaling down total amount of events to be analysed to a manageable quantity. The Sections 3.1.3-3.1.2 describe these steps, summarising all the corresponding requirements. The final offline selection is in charge to optimise the signal significance (Section 3.1.4). As reported in previous studies [24, 115, 120, 121], it has to face three background categories:

Cross-feed background . To achieve an adequate signal significance, the contamination among different final states must be reduced without affecting too much the signal efficiency (Section 3.1.4.1). Besides the signal decays, the only other relevant cross contamination is found to be the additional $\Lambda_b^0 \rightarrow pK^-$ mode.

Combinatorial background. This background category is due to the random association of tracks. Several observables concerning the candidate kinematics and topology

Table 3.3: Integrated luminosity of pp collisions collected during the Run2 of LHCb, depending on the data-taking year.

Year	Integrated luminosity [fb^{-1}]
2015	0.33
2016	1.67
2017	1.71
2018	2.19

⁴This notation stands for the union of the 2015 and 2016 samples. The previous LHCb analysis [120] did not find relevant discrepancies between them, and the statistic collected in 2015 is much lower than the one of the other years. Hence, this arrangement will often be used in the following.

⁵For a definition of the stripping selection the reader can refer to Section 3.1.2.

are helpful to reject it. This analysis exploits a multivariate algorithm based on *Boost Decision Trees* (BDT) [122,123] to combine the relevant quantities into a single variable. This simplifies the final selection optimisation (Section 3.1.4.2).

Partially-Reconstructed background. Decays of B hadron to final states with more than two bodies generate this background category. A large part of this component is out of the signal peak, thanks to the good invariant mass resolution of LHCb.

Figure 3.1-left illustrates the invariant mass distribution of the 2018 sample after the stripping and the trigger steps. The pion mass hypothesis is assumed for all final state tracks. Although the signal peak is visible, the sample is dominated by the combinatorial background. Indeed, the application of the final BDT requirement produces the distribution illustrated in Fig. 3.1-right, where the combinatorial background is strongly suppressed. The various components of the model fitted to data are listed in the legend and fully described in Appendix A.1, which reports the strategy to obtain a background-subtracted sample of generic $B_{(s)}^0 \rightarrow h^+ h'^-$ decays. Subsequently, the PID requirements separate the exclusive final states (Figure 3.2). Section 3.2 describes the quantitative evaluation of the mis-ID induced contamination. Table 3.4 summarises the modes that are finally considered in the fit of each spectrum. The fit observable distributions of all background contributions are deeply studied and documented in the fit model description (Section 3.7).

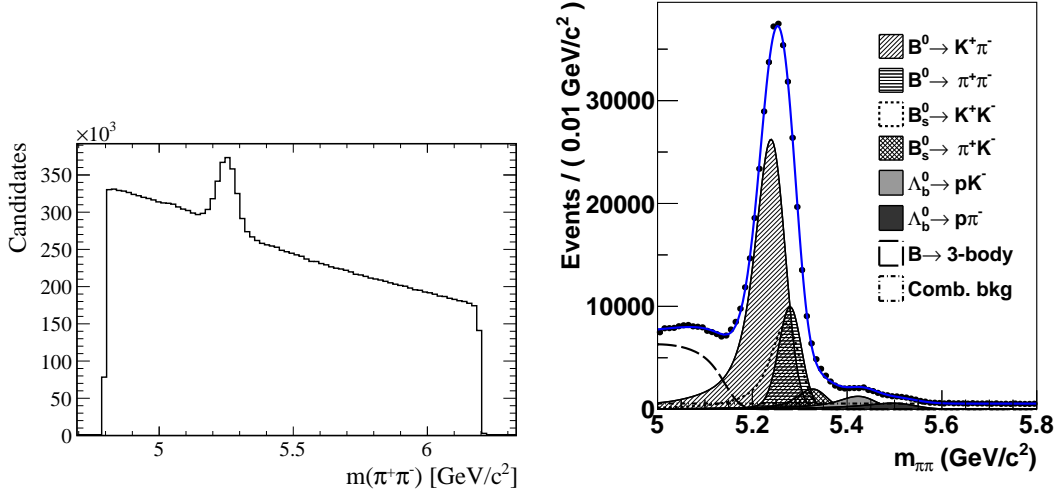


Figure 3.1: Invariant mass distribution for 2018 data. The charged pion hypothesis is assumed for both the final state tracks. *Left*: only trigger and stripping requirements are applied. *Right*: the BDT requirement optimised for the extraction of $A_{CP}^{B^0}$, $A_{CP}^{B_s^0}$, $C_{\pi^+\pi^-}$, $S_{\pi^+\pi^-}$ is added.

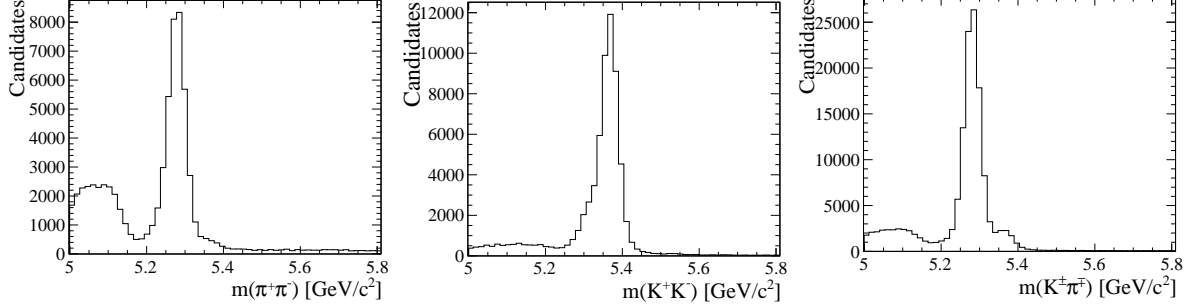


Figure 3.2: Invariant mass distribution for 2018 data after the whole selection optimised for the extraction of $A_{CP}^{B^0}$, $A_{CP}^{B_s^0}$, $C_{\pi^+\pi^-}$, $S_{\pi^+\pi^-}$. *Left*: $\pi^+\pi^-$ spectrum. *Middle*: K^+K^- spectrum. *Right*: $K^\pm\pi^\mp$ spectrum.

Table 3.4: Summary of the signal and mis-ID contributions found to be relevant for the various spectra after the full selection. More details in Section 3.2.

Process	Final State		
	$\pi^+\pi^-$	K^+K^-	$K^\pm\pi^\mp$
$B^0 \rightarrow K^+\pi^-$	✓	✓	✓
$B^0 \rightarrow \pi^+\pi^-$	✓		✓
$B_s^0 \rightarrow K^+K^-$		✓	✓
$B_s^0 \rightarrow \pi^+K^-$			✓
$B_s^0 \rightarrow \pi^+\pi^-$	✓		
$B^0 \rightarrow K^+K^-$		✓	
$\Lambda_b^0 \rightarrow pK^-$		✓	

3.1.1 Simulated samples

Besides the data, simulated samples are employed. Their generation emulates the experimental conditions of the different data-taking periods, with each magnet polarity covering half of the statistics. The trigger, reconstruction, and stripping configurations are specific for each year. The version of the Flavour Tagging algorithms used for the simulated samples is the same as the one used in data. Table 3.5 lists the numbers of simulated events that survive trigger, reconstruction, and stripping. Reconstructed candidates are required to be associated with a true $B_{(s)}^0 \rightarrow h^+ h'^-$ decay.

Table 3.5: Number of simulated events surviving all the steps of trigger, reconstruction and stripping.

Decay	Number of events			
	Year 2015	Year 2016	Year 2017	Year 2018
$B^0 \rightarrow K^+ \pi^-$	276785	1236701	2108351	1841394
$B^0 \rightarrow \pi^+ \pi^-$	288015	1309841	2149094	1872946
$B_s^0 \rightarrow K^+ K^-$	260462	1232328	2112537	1835957
$B_s^0 \rightarrow \pi^+ K^-$	74198	508356	884560	788383
$B_s^0 \rightarrow \pi^+ \pi^-$	86063	520917	999913	788669
$B^0 \rightarrow K^+ K^-$	80665	494913	920816	757608
$\Lambda_b^0 \rightarrow p K^-$	68888	498375	849982	722721

3.1.2 Stripping selection

As explained in Section 2.4, LHCb events need to pass at least one of all the possible trigger lines to be recorded. However, before being ready to be studied, LHCb data undergo a further processing step, which organises the information according to the criteria of several *stripping lines*. Each stripping line comprises a specific reconstruction procedure and a set of selection requirements. This preselection is run centrally, during dedicated *stripping campaigns*. It is particularly useful to save CPU time, increasing the speed of access to data.

In this analysis the following stripping campaigns are adopted:

- Stripping24r1 for 2015 data;
- Stripping28r1 for 2016 data;
- Stripping29r2p2 for 2017 data;
- Stripping34 for 2018 data.

For all samples, the output of the same stripping line is chosen. It is called `StrippingB2HHBDTLine` and combines two oppositely charged tracks into a B candidate, assuming the pion-mass hypothesis for both of them. To reduce the number of combinations the algorithm starts skimming the tracks according to their transverse

Table 3.6: Requirements imposed by `StrippingB2HHBDTLine`. See the text for details.

Variable	Requirement
Track p_T	$> 1 \text{ GeV}/c$
Track χ_{IP}^2	> 16
Track χ^2	< 3
$m_{\pi^+\pi^-}$	$\in [4.5, 6.2] \text{ GeV}/c^2$
$p_T^+ + p_T^-$	$> 4.5 \text{ GeV}/c$
χ_{DOCA}^2	< 9
$p_T(B)$	$> 1.2 \text{ GeV}/c$
$\text{DIRA}(B)$	> 0.99
$\chi_{\text{IP}}^2(B)$	< 9
χ_{FD}^2	> 100

momentum (p_T), minimum impact parameter χ^2 (χ_{IP}^2),⁶ and track quality (χ^2). The invariant mass computed from the quadri-momenta of the available track pairs is required to lie between 4.5 and 6.2 GeV/c^2 . Requirements on the minimum value of the p_T sum and the maximum value of the χ^2 of the distance of closest approach of the two tracks (DOCA) provide additional refinement of the track pairs. The surviving ones are fitted to a common vertex, to generate the B candidates. To be accepted, the B candidates have to satisfy selection criteria regarding their p_T , the cosine of the angle (DIRA) between their momentum and their flight direction from the associated primary vertex (PV), their χ_{IP}^2 concerning the associated PV, and their χ_{FD}^2 concerning the distance between their decay vertex and the associated PV.⁷ Table 3.6 lists the values of all the cited requirements.

Finally, for a better evaluation of the decay time, the PV coordinates are recalculated (*PV refitting*) to check that the charged tracks forming the B candidates are not included in the estimation of the PV positions. This would be expected to cause a bias in the decay time, more often affecting the B candidates with shorter flight distances. Further studies, not reported in this thesis, have shown that the effect of such correction becomes negligible after the final selection application. This is mainly due to the presence of cuts on χ_{IP}^2 of the tracks.

3.1.3 Trigger selection

The B candidates passing the stripping must satisfy the following trigger requirements⁸:

L0 : L0Hadron_TOS OR L0Global_TIS;

Hlt1 : Hlt1TrackMVADecision_TOS OR Hlt1TwoTrackMVADecision_TOS;

Hlt2 : Hlt2B2HHDDecision_TOS.

⁶With χ_{IP}^2 is meant the difference in the vertex-fit χ^2 of a given PV reconstructed with and without the track under consideration

⁷The candidate is associated to the PV with the smallest χ_{IP}^2 .

⁸See Section 2.4 for the definitions of TIS and TOS.

The `H1t2B2HH` trigger line is an exact copy of the stripping line `StrippingB2HHBDTLine`. Therefore, it applies the same selection criteria already summarised by Table 3.6. The only difference is that the HLT2 algorithm is run online, namely during the data taking, whereas the stripping is applied to quantities calculated offline. The two procedures are identical, but slight modifications concerning alignments and calibration parameters could intervene in the reprocessing. Hence, this selection is repeated.

3.1.4 Final selection

The final selection comprises two tasks:

- the choice of the PID criteria to associate a final state hypothesis to each reconstructed candidate and reduce the cross-feed contamination;
- the determination of the kinematic and topological requirements to reject the combinatorial background; this is achieved through training, optimisation, and application of BDT algorithms [122].

The LHCb collaboration deeply investigated the selection optimisation in the previous versions of this analysis. Because of the very similar PID performance between the data-taking years, this part of the selection, optimised in Ref [120] is adopted here as well. Section 3.1.4.1 summarises the procedure that was exploited to deduce these selection criteria. Instead, independent BDT trainings are now performed for the 2015-16, 2017, and 2018 samples. As in the previous analysis, the procedure is replicated after applying two different sets of PID requirements: one to optimise the BDT for the analysis of the $B^0 \rightarrow \pi^+\pi^-$ decay, and the other for the $B_s^0 \rightarrow K^+K^-$ decay. The corresponding BDT variables are labelled as $BDT_{\pi^+\pi^-}$ and $BDT_{K^+K^-}$, respectively. The final BDT requirements result to be independent of the data-taking year (Section 3.1.4.2).

3.1.4.1 Particle identification

Two kinds of PID discriminating variables are available at LHCb. They are called DLL and ProbNN (Section 2.3). Concerning $B_{(s)}^0 \rightarrow h^+h'^-$ decays, the studies reported in Ref. [124] showed similar performances for both of them. Hence, only the DLL variables are used in Ref. [120] for the optimisation of the PID requirement. The primary source of cross-feed background below the $B^0 \rightarrow \pi^+\pi^-$ and $B_s^0 \rightarrow K^+K^-$ invariant-mass peaks comes from $B^0 \rightarrow K^+\pi^-$ decays, where one of the two final state particles is misidentified, hence due to $K \leftrightarrow \pi$ mis-ID. Therefore, the requirement on the $DLL_{K\pi}$ variable is optimised, whereas the cuts on $DLL_{p\pi}$ and DLL_{Kp} variables are fixed in advance to make the contamination from $\Lambda_b^0 \rightarrow p\pi^-$ and $\Lambda_b^0 \rightarrow pK^-$ decays negligible. Table 3.7 reports the corresponding selection criteria. The optimisation procedure considers the potential correlation between the PID and the BDT variables. A two-dimensional scan of requirements is performed:

- $\pi^+\pi^-$ spectrum: $DLL_{K\pi} \in [-9, 0]$, step = 1;
 $BDT_{\pi^+\pi^-} \in [-0.1, 0.1]$, step = 0.02;
- K^+K^- spectrum: $DLL_{K\pi} \in [0, 9]$, step = 1;
 $BDT_{K^+K^-} \in [-0.16, 0.06]$, step = 0.02;

Table 3.7: Final DLL requirements chosen with the aim to identify the three final states according to the $B^0 \rightarrow \pi^+\pi^-$ and $B_s^0 \rightarrow K^+K^-$ optimisations.

	$\pi^+\pi^-$ spectrum	$K^\pm\pi^\mp$ spectrum		K^+K^- spectrum
DLL $_{K\pi}$	$(\pi^\pm) < -2$	$(K^\pm) > 5$	$(\pi^\mp) < -5$	$(K^\pm) > 2$
DLL $_{p\pi}$	$(\pi^\pm) < 3$	-	$(\pi^\mp) < 3$	-
DLL $_{Kp}$	-	$(K^\pm) > -2$	-	$(K^\pm) > -2$

Table 3.8: Comparison of the sensitivity achieved using the chosen requirement configuration (σ) with respect to the one corresponding to the optimal configuration (σ_{best}), as found in the optimisation study [120]. Both the comparison for the $B^0 \rightarrow \pi^+\pi^-$ and $B_s^0 \rightarrow K^+K^-$ optimisations are reported.

	$\pi^+\pi^-$ optimisation		K^+K^- optimisation	
	σ	σ_{best}	σ	σ_{best}
<i>S</i>	0.041	0.039	0.055	0.050
<i>C</i>	0.046	0.044	0.055	0.050

where the BDT output are produced using a preliminary version of the classifier described in Section 3.1.4.2. For each requirement configuration, the amount of the main components contributing to the samples are determined using fits to the invariant mass of selected events. Then ten pseudo experiments are generated and fitted, using a model slightly simplified with respect to the one that is used in this thesis (described in Section 3.7). It is found that the best sensitivities on the CP asymmetries are obtained with loose PID requirements, and that the correlation between PID and BDT requirements is small. Loose DLL $_{K\pi}$ requirements produce the best sensitivity on the CP asymmetries. This means that the amount of cross-feed background has a small impact on the statistical uncertainties, once it is properly described and quantified. However, large contributions from cross-feed backgrounds make difficult to properly describe data and may cause large systematic uncertainties. For these reasons, a working point that is close to the best one indicated by the toys, but with slightly tighter DLL $_{K\pi}$ requirements, is adopted. Table 3.7 lists the cuts of the final PID selections. Table 3.8 underlines the small sensitivity loss between the result of the optimisation procedure (σ_{best}) and the chosen working point (σ).

Concerning the $K^\pm\pi^\mp$ final state, a dedicated optimisation study was performed for the Run1 version of this analysis [121]. The resulting level of the cross-feed contamination is below 10% of the corresponding signal. With this condition, the systematic uncertainties related to the modelling of the cross-feed backgrounds are under control. Therefore, the DLL $_{K\pi}$ requirements for the $K^\pm\pi^\mp$ final state are chosen to achieve the same level of cross-feed background contamination. Table 3.7 lists them.

3.1.4.2 BDT selection

The optimisation of the BDT selection involves four main steps:

- 1) **Training:** samples representative of signal and background candidates are used to combine several variables into a single one, offering better discrimination power.
- 2) **Normalisation:** The signal yields after the application of PID requirements are

determined. They are used in the optimisation procedure of the BDT selection.

- 3) **Optimisation:** definition of the best cut on the new variable;
- 4) **BDT application:** the new variable is calculated for each candidate of the data sample and candidates not satisfying the requirement are rejected.

The next few paragraphs describe the above-cited passages.

The training and optimisation methods exploit subsamples of the analysis data. It is useful to point out here that the BDT application on any candidate, already used to train or optimise the same BDT algorithm, may be a source of bias. To avoid it, the signal and background samples have been randomly separated into three subsamples (**S1**, **S2** and **S3**). Different instances of the BDT algorithm have been trained for each subsample: **BDT1**, **BDT2** and **BDT3** for **S1**, **S2** and **S3**, respectively. In the optimisation phase, requirements are applied to **BDT1** for the events from **S2**, to **BDT2** for events from **S3** and to **BDT3** for events from **S1**. The final analysis is performed cutting on **BDT1** for events from **S3**, on **BDT2** for events from **S1** and on **BDT3** for events from **S2**, respectively.

Training. Separate training procedures are performed for the events surviving the K^+K^- and $\pi^+\pi^-$ PID requirements. For both cases, the default configuration of the BDT algorithms provided within the TMVA package [125] is used, training 850 trees for each BDT and using the **Adaptive Boost** [123]. The combinatorial background is modelled using events taken from the high invariant-mass sideband: $m > 5.6 \text{ GeV}/c^2$ (where m is the invariant mass computed under the K^+K^- or the $\pi^+\pi^-$ hypotheses, according to the considered signal). The signal distributions come from the simulated samples introduced in Section 3.1.1.

The variables used to discriminate between signals and backgrounds are: the p_T of the B candidate ($p_T(B)$), the χ^2 of the distance of flight of the B candidate with respect to the associated primary vertex (χ_{FD}^2), the χ^2 of the impact parameter of the B candidate with respect to the associated primary vertex ($\chi_{\text{IP}}^2(B)$), the maximum and minimum p_T of the two final state tracks, the distance of closest approach (DOCA) between the two tracks, the maximum and minimum χ^2 of the impact parameter of the two tracks evaluated with respect to all the primary vertices ($\chi_{\text{IP}}^2(h^\pm)$), and the quality of the common vertex fit of the two tracks (χ_{vtx}^2). A logarithmic transformation is applied to the distance of flight of the B candidate and the maximum and minimum χ^2 of the impact parameter of the two tracks to avoid feeding the BDT with too-peaked distributions or with distributions with too wide ranges. The variables are summarised in Table 3.9. Their distributions and correlations, are reported in Figures from 3.4 to 3.7 for both background and signal samples. Figure 3.3 shows output distributions of the $BDT_{\pi^+\pi^-}$ and $BDT_{K^+K^-}$ classifiers, distinguishing the samples used to train and test the algorithms. The two distributions are in good agreement, and no evidence of overtraining is found.

Table 3.9: List of variables used to train the BDT algorithms. The meaning of the symbols is explained in the text.

BDT variables	
$\min(p_T^+, p_T^-)$	$\log(\min(\chi_{\text{IP}}^2(h^+), \chi_{\text{IP}}^2(h^-)))$
$\max(p_T^+, p_T^-)$	$\log(\max(\chi_{\text{IP}}^2(h^+), \chi_{\text{IP}}^2(h^-)))$
$p_T(B)$	$\chi_{\text{IP}}^2(B)$
$\log(\chi_{\text{FD}}^2)$	DOCA
χ_{vtx}^2	

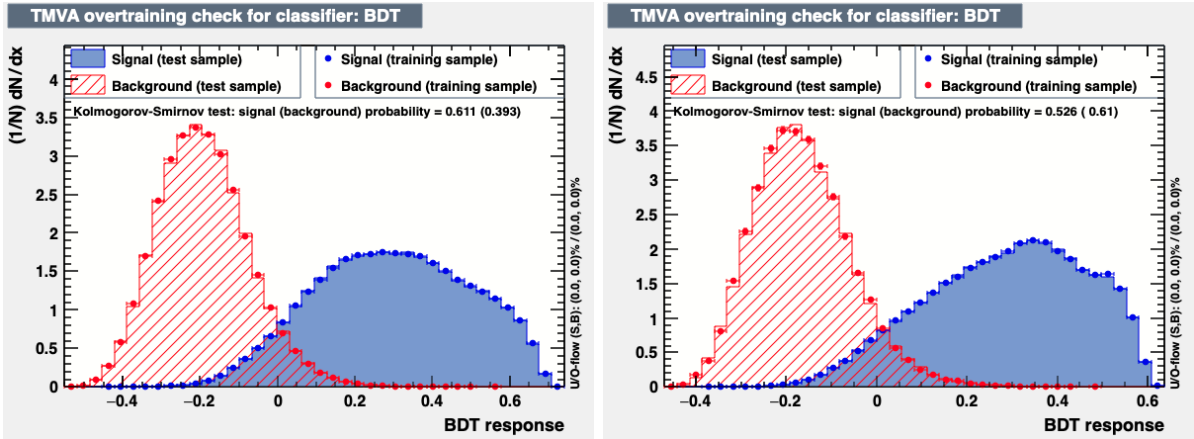


Figure 3.3: Distribution of the BDT output for the (red) background-like and the (blue) signal-like candidates taken from the samples used to (filled histograms) train and (dotted histograms) test the BDT algorithms. Background-like events have been selected applying the PID cut optimised for the (left) K^+K^- final state and for the (right) $\pi^+\pi^-$ final state, on top of the preselection presented in Section 3.1 and the requirement $m_{(K^+K^-, \pi^+\pi^-)} > 5.6 \text{ GeV}/c^2$.

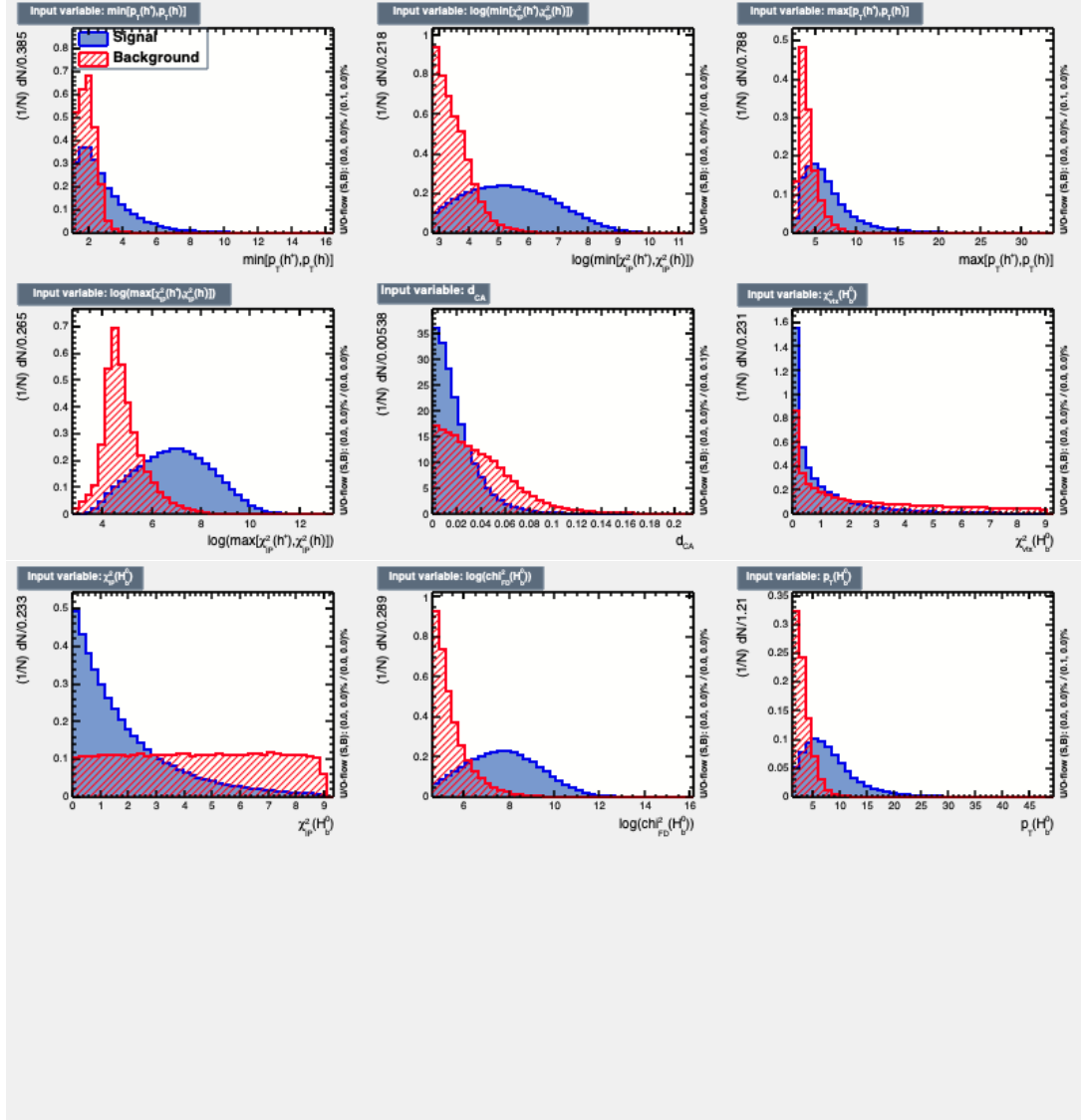


Figure 3.4: Distribution of the variables used in the training of the BDT classifier for (blue) simulated $B^0 \rightarrow \pi^+\pi^-$ decays and (red) candidates in the invariant-mass range $m_{\pi^+\pi^-} > 5.6 \text{ GeV}/c^2$ of the $\pi^+\pi^-$ sample.

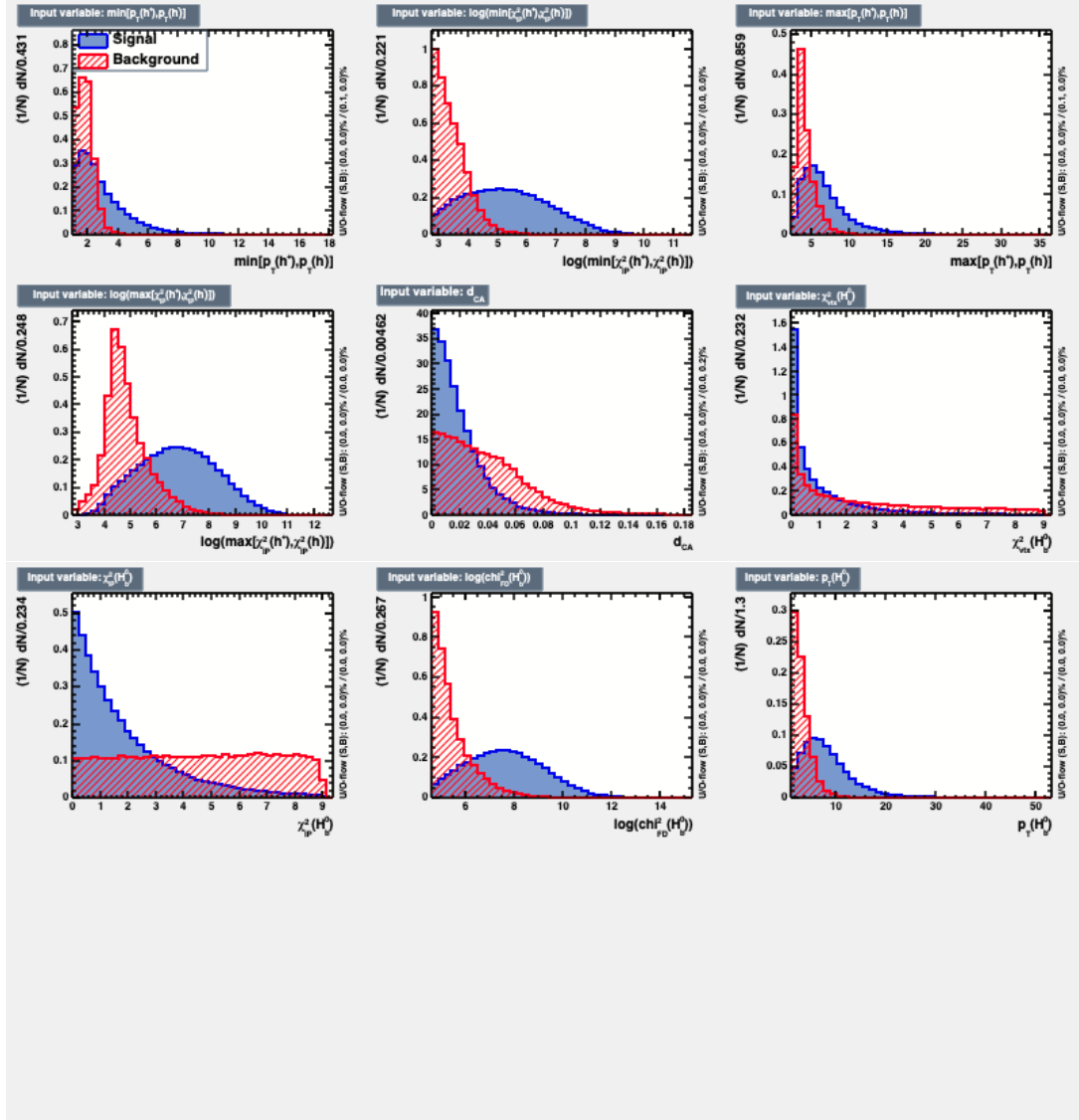


Figure 3.5: Distribution of the variables used in the training of the BDT classifier for (blue) simulated $B_s^0 \rightarrow K^+K^-$ decays and (red) candidates in the invariant-mass range $m_{K^+K^-} > 5.6 \text{ GeV}/c^2$ of the K^+K^- sample.

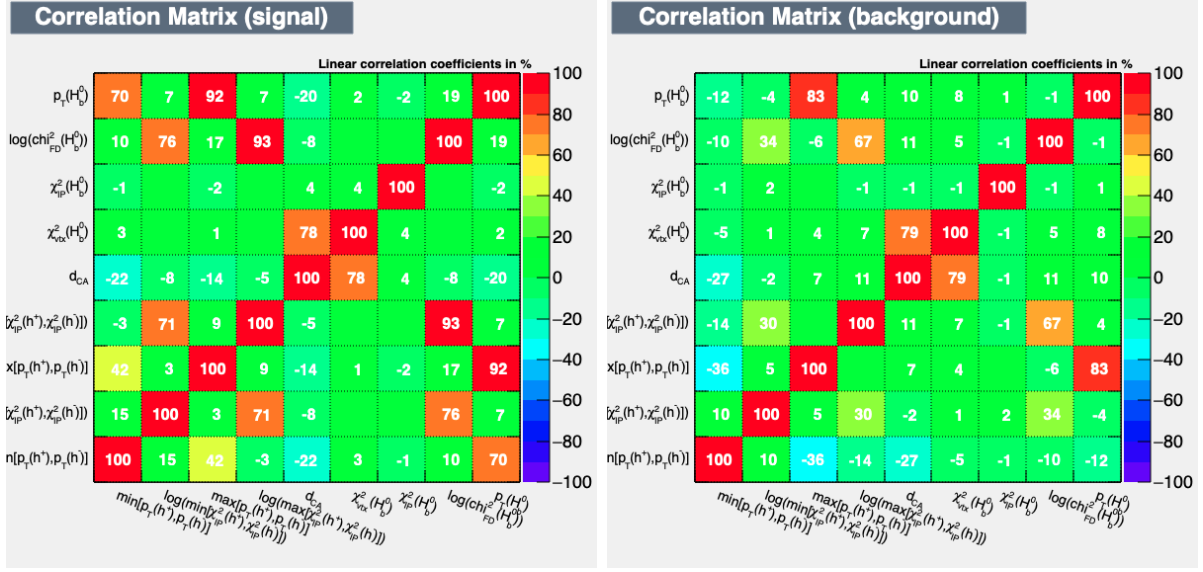


Figure 3.6: Correlation among the variables used to train the BDT algorithm for (left) $B^0 \rightarrow \pi^+\pi^-$ simulated events and (right) candidates in the invariant-mass range $m_{\pi^+\pi^-} > 5.6 \text{ GeV}/c^2$ of the $\pi^+\pi^-$ sample.

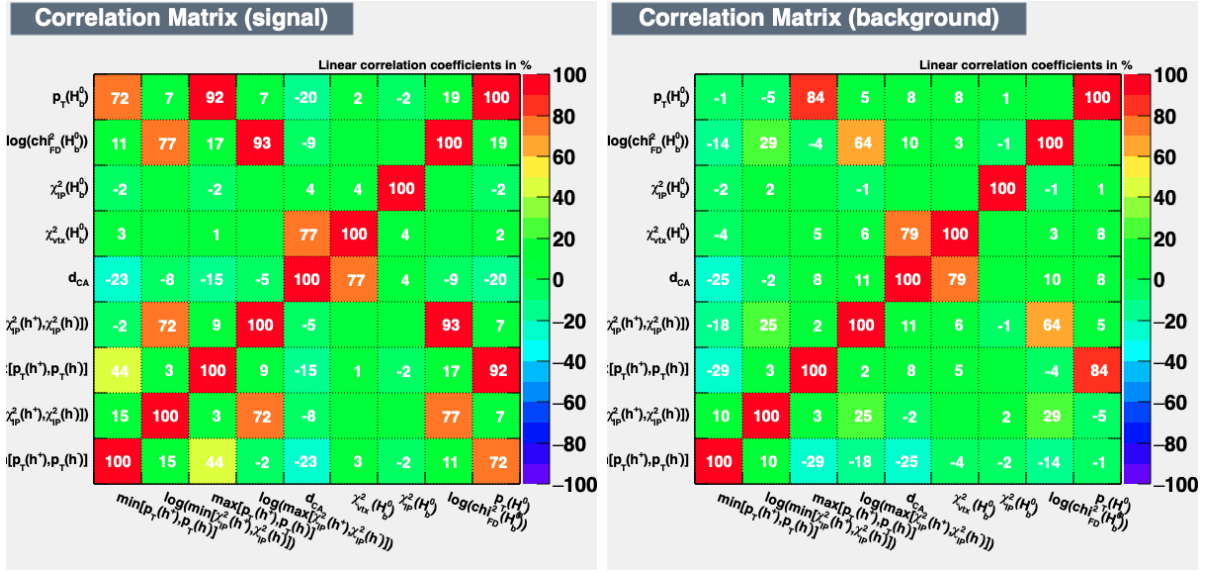


Figure 3.7: Correlation among the variables used to train the BDT algorithm for (left) $B_s^0 \rightarrow K^+K^-$ simulated events and (right) candidates in the invariant-mass range $m_{K^+K^-} > 5.6 \text{ GeV}/c^2$ of the K^+K^- sample.

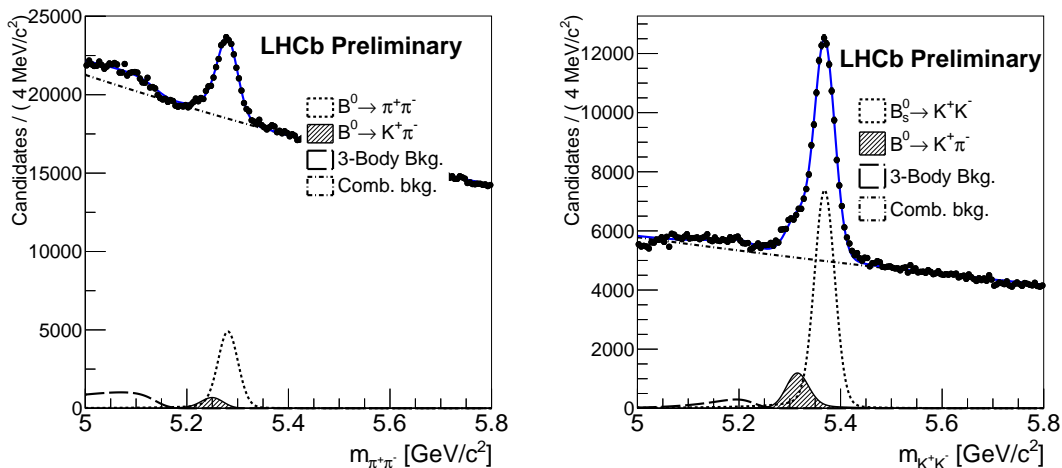


Figure 3.8: Invariant mass fits used for the relative normalisation of signal and background yields in the BDT optimisation: $B^0 \rightarrow \pi^+\pi^-$ (left) and $B_s^0 \rightarrow K^+K^-$ (right).

Table 3.10: Signal yields estimation after trigger, stripping and PID requirements.

Year	$N(B^0 \rightarrow \pi^+\pi^-)$	$N(B_s^0 \rightarrow K^+K^-)$
2015-16	59900 ± 3200	81800 ± 600
2017	48400 ± 6500	69200 ± 500
2018	52500 ± 2000	79900 ± 500

Normalisation. Unbinned maximum likelihood fits to the invariant mass spectra after trigger, stripping, and PID requirements can estimate the signal yields before the application of the requirements on the BDT output. The components described in the fit are:

- the signals, namely the $B_s^0 \rightarrow K^+K^-$ and the $B^0 \rightarrow \pi^+\pi^-$ decays; their distribution is modelled using the sum of a Gaussian function and a Johnson function (see equation (3.48) and Ref. [121] for an extended description);
- the main cross-feed background ($B^0 \rightarrow K^+\pi^-$), whose shape is evaluated applying Kernel Density Estimation methods to simulated events [121, 126];
- the combinatorial background, modelled using an exponential function;
- the partially reconstructed background, modelled using an ARGUS function [127] convolved with a Gaussian resolution, having the same width as the signal model.

Table 3.10 lists the signal yields determined from the fits. Figure 3.8 shows the 2018 data sample with the corresponding fit results superimposed.

Optimisation. The figure of merit used to choose the requirement on the BDT output is $\xi = S/\sqrt{(S+B)}$, where S and B stand for the amount of signal and combinatorial

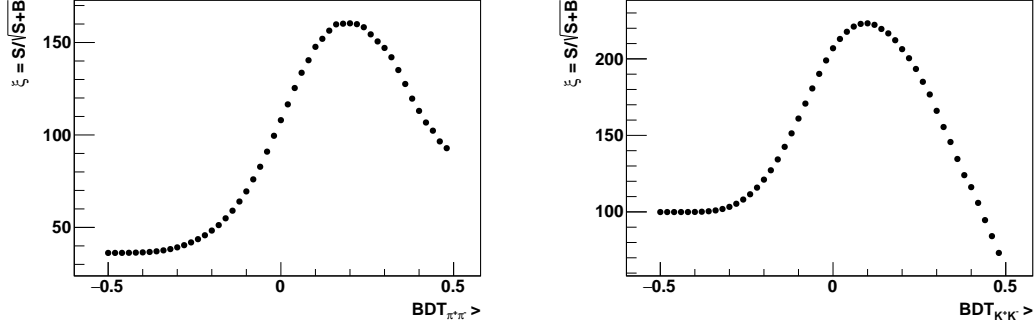


Figure 3.9: Estimated value of $\xi = S/\sqrt{(S+B)}$ as a function on the requirement applied on the BDT output for the $B^0 \rightarrow \pi^+\pi^-$ decays (left) and for the $B_s^0 \rightarrow K^+K^-$ decays (right).

Table 3.11: BDT requirements which optimise $\xi = S/\sqrt{(S+B)}$, depending on the data taking year. The corresponding signal efficiencies (ε_{sig}) and retention rates for the combinatorial background (ε_{bkg}) are also reported.

Year	$BDT_{\pi^+\pi^-}$			$BDT_{K^+K^-}$		
	Best Cut	ε_{sig} [%]	ε_{bkg} [%]	Best Cut	ε_{sig} [%]	ε_{bkg} [%]
2015-16	0.20	67.6 ± 0.2	0.519 ± 0.004	0.10	83.53 ± 0.13	3.64 ± 0.02
2017	0.22	63.5 ± 0.2	0.513 ± 0.005	0.10	83.31 ± 0.14	4.31 ± 0.03
2018	0.20	67.2 ± 0.2	0.642 ± 0.006	0.10	83.61 ± 0.13	4.07 ± 0.03

background candidates within $\pm 60 \text{ MeV}/c^2$ (corresponding to about $\pm 3\sigma$ of the invariant mass resolution) around the B^0 or B_s^0 masses. The number of signal candidates surviving each BDT requirement is estimated from the results of the normalisation fit (described in the previous paragraph) and from the efficiencies of the BDT cuts applied to simulated events. Instead, the amount of combinatorial background is determined using an unbinned maximum likelihood fit of an exponential function to the candidates in the high invariant-mass sideband. The result of each fit permits the extrapolation of the total background yields in the $\pm 60 \text{ MeV}/c^2$ invariant mass window around the signal peak. Figure 3.9 shows ξ calculated as a function of the requirements on $BDT_{\pi^+\pi^-}$ or $BDT_{K^+K^-}$ for the 2018 sample. Analogous plots are obtained for the other samples, as well. Table 3.11 reports the BDT cuts maximising ξ , with the corresponding signal efficiencies and background retention rates. In conclusion, the cuts $BDT_{\pi^+\pi^-} > 0.2$ and $BDT_{K^+K^-} > 0.1$ are chosen for the selections optimised for $B^0 \rightarrow \pi^+\pi^-$ and $B_s^0 \rightarrow K^+K^-$ decays, respectively. In small fraction of events, corresponding to about 0.4 %, multiple candidates are present. In these cases, only one candidate per event is randomly retained.

3.2 PID calibration

The PID calibration is the evaluation of the identification and misidentification probabilities for each $B_{(s)}^0 \rightarrow h^+h'^-$ mode to contribute to the different final states after the final selection. It is advantageous to divide this task into two steps. First of all, the identification and misidentification rates are estimated for single particles, exploiting calibration samples. The kinematic features of calibration decays permit the identification of their final-state particles even without information from the PID system. Furthermore, they have the advantages of high statistics and high purity. In these conditions, the identification and misidentification probabilities correspond to the rates of events passing given PID selection criteria. The rates are measured as a function of the particle momentum (p), pseudorapidity (η), and the number of hits registered by the SPD system (n_{SPD}). This is necessary because:

- the values of the DLL variables depend on p through its relation with the emission angle of Cherenkov photons;
- since the two RICHs detectors have different angular acceptances and are optimised for distinct momentum regions, the DLL values may depend on η ;
- PID performances depend on the event occupancy, whose quantification is efficaciously provided by n_{SPD} .

The distributions of p , η , and n_{SPD} are consequences of the peculiarities of the various decay processes and are related to the kinematic and topological parts of the selection.

The second step implies the correction of the probabilities extracted from the calibration samples for the specificities of each mode actually involved in this analysis. The final PID-calibration results are the average of the efficiencies over the distributions of p , η , and n_{SPD} for each of the various $B_{(s)}^0 \rightarrow h^+h'^-$ decays.

3.2.1 Maps of PID efficiency

The decay processes exploited for the PID calibration are:

- $D^{*+} \rightarrow D^0 (\rightarrow K^-\pi^+) \pi_s^+$ for charged **pions** and **kaons**;
- $\Lambda \rightarrow p\pi^-$ and $\Lambda_c^+ \rightarrow pK^-\pi^+$ for **protons**.

These decays are reconstructed and selected by specific HLT2 lines that apply kinematic requirements to guarantee samples with high purity. The residual background contamination is removed utilising the *sPlot* technique [128], and already *sWeight-ed* samples are provided as part of the `PIDCalibTool` package [129]. All the details about the composition of these samples can be found in Ref. [130].

The maps of PID efficiencies are determined using the following binning scheme [124]:

Track momentum :

- 2 bins for $p \in [0, 10]$ GeV/ c ;
- 45 bins for $p \in [10, 100]$ GeV/ c ;
- 20 bins for $p \in [100, 150]$ GeV/ c ;
- 4 bins for $p \in [150, 500]$ GeV/ c .

Track pseudorapidity : 10 bins for $\eta \in [1, 6]$.

Event occupancy : 3 bins for $n_{SPD} \in [0, 450]$;
 3 bins for $n_{SPD} \in [450, 1000]$.

The center of each bin is indicated by $(p_i, \eta_j, n_{SPD,k})$, where i, j , and k are the bin indices. The requirements of Table 3.7 are now singularly considered. The PID efficiency of a particular cut, in a particular bin, is given by the number of calibration candidates belonging to the bin and passing the cut, divided by number of calibration candidates belonging to the bin:

$$\varepsilon_{h \rightarrow h'}(p_i, \eta_j, n_{SPD,k}) = \frac{N_{h \rightarrow h'}^{\text{pass}}(p_i, \eta_j, n_{SPD,k})}{N_{h \rightarrow h'}^{\text{pass}}(p_i, \eta_j, n_{SPD,k}) + N_{h \rightarrow h'}^{\text{fail}}(p_i, \eta_j, n_{SPD,k})}, \quad (3.1)$$

where h is the identity of the final-state hadron from the calibration sample used in the efficiency calculation, and h' is the final-state hypothesis corresponding to the tested PID cut⁹.

3.2.2 PID efficiencies for $B_{(s)}^0 \rightarrow h^+ h'^-$ decays

The event occupancy and the kinematic of any singular candidate are independent features. Hence, the dependency of the PID efficiency on n_{SPD} can be integrated out, before considering the $B_{(s)}^0 \rightarrow h^+ h'^-$ kinematics. If the analytical expression of any PID efficiency were known ($\varepsilon(p, \eta, n_{SPD})$), its expectation value for any fixed p and η would be:

$$\bar{\varepsilon}_{h \rightarrow h'}(p, \eta) = \int \varepsilon_{h \rightarrow h'}(p, \eta, n_{SPD}) f(n_{SPD}) dn_{SPD}, \quad (3.2)$$

where $f(n_{SPD})$ is an adequate probability density function. As shown by Figure 3.10, its shape slightly changes between the calibration samples (red or green lines) and $B_{(s)}^0 \rightarrow h^+ h'^-$ decays (blue dots). Therefore, for each bin p_i, η_j the PID efficiencies can be estimated according to:

$$\bar{\varepsilon}(p_i, \eta_j) = \frac{1}{N} \sum_{k=1}^N \varepsilon_{h \rightarrow h'}(p_i, \eta_j, n_{SPD,k}), \quad (3.3)$$

where $n_{SPD,k}$ is randomly extracted from the just cited $B_{(s)}^0 \rightarrow h^+ h'^-$ distribution plotted in Figure 3.10. The sharp step of the distribution at $n_{SPD} = 450$ is due to the application of L0Hadron trigger requirements. The number of extractions, N , was set to 200000: several trials proved this number to be large enough to avoid statistical fluctuation in the average without consuming too much computing power. This procedure brings to two-dimension PID efficiency maps in the occupancy regime of $B_{(s)}^0 \rightarrow h^+ h'^-$ decays. Figure 3.11 shows some examples concerning the PID requirement $\text{DLL}_{K\pi} > 2$ AND $\text{DLL}_{Kp} > -2$ for the 2018 data.

The identification (or misidentification) efficiency of a charged track is assumed to be independent of the identification of another track in the same event when their kinematics are fixed. Therefore, the expected PID efficiency for a given $B_{(s)}^0 \rightarrow h^+ h'^-$ candidate is:

$$\bar{\varepsilon}_{h+h'}(p_i^+, \eta_j^+, p_l^-, \eta_m^-) = \bar{\varepsilon}_{h^+}(p_i^+, \eta_j^+) \cdot \bar{\varepsilon}_{h'^-}(p_l^-, \eta_m^-). \quad (3.4)$$

⁹In other words, $h = h'$ marks an identification efficiency, whereas $h \neq h'$ labels a misidentification efficiency.

To estimate the PID efficiency the joint distribution of p^+ , η^+ , p^- , η^- has to be taken into account. This is done, exploiting the background-subtracted samples described in appendix A.1 and performing the calculation:

$$\hat{\varepsilon}_{h^+h'^-} = \frac{1}{N} \sum_{k=1}^N \bar{\varepsilon}_{h^+}(p_k^+, \eta_k^+) \cdot \bar{\varepsilon}_{h'^-}(p_k^-, \eta_k^-), \quad (3.5)$$

where p_k^+ , η_k^+ , p_k^- , η_k^- evidently indicate the bins occupied by the final-state hadrons of the k -th candidate in the background subtracted sample, while N is the total number of candidates in the sample. This procedure is conclusive because the p - η distributions of the calibration samples completely overlap the p - η distributions of the $B_{(s)}^0 \rightarrow h^+h'^-$ decays (Figure 3.12). The final PID calibration results are listed in the Table 3.12.

3.2.3 Uncertainties on the PID efficiencies

Two sources of uncertainties are studied. The first one is related to statistics available for the calibration and the $B_{(s)}^0 \rightarrow h^+h'^-$ samples. It is estimated by propagating the statistical errors of the amount of signal and the efficiency maps in each bin used to split the phase space. The second source is related to the binning scheme used to map the phase space. The corresponding uncertainty is determined by changing the number and range of the various bins. The nominal binning scheme involves 71 bins in momentum, 10 bins in pseudorapidity and 8 bins in azimuthal angle. A set of 27 different bin configurations are taken into account doubling and halving the number of bins of all three variables in turn. The average and the root-mean-square of the results are used as mean value and uncertainty. The uncertainty due to the binning scheme is dominant as compared to that due to the statistics.

Table 3.12: Identification and mis-identification efficiencies for the $B_{(s)}^0 \rightarrow h^+ h'^-$ decay modes. The top table considers the BDT selection optimised for the extraction of $C_{\pi^+\pi^-}$, $S_{\pi^+\pi^-}$, $A_{CP}^{B^0}$, and $A_{CP}^{B_s^0}$, while in the bottom table the BDT selection optimised for the extraction of $C_{K^+K^-}$, $S_{K^+K^-}$, $A_{K^+K^-}^{\Delta\Gamma}$, is concerned. For each reported decay, the subscript, $_{[h^+,h'^-]}$, represents the final state reconstruction hypothesis. The efficiency values are divided by data taking year. These quantities are fixed in the final fits.

Selection $\pi^+\pi^-$			
Parameter	Year		
	2015-16	2017	2018
$\varepsilon_{\text{PID}}(B^0 \rightarrow K^+\pi^-_{[K^+K^-]})$ [%]	3.62 ± 0.06	3.60 ± 0.06	3.66 ± 0.06
$\varepsilon_{\text{PID}}(B^0 \rightarrow K^+\pi^-_{[K^+\pi^-]})$ [%]	46.66 ± 0.49	46.07 ± 0.52	44.64 ± 0.47
$\varepsilon_{\text{PID}}(B^0 \rightarrow K^+\pi^-_{[\pi^+\pi^-]})$ [%]	2.10 ± 0.07	1.86 ± 0.07	1.81 ± 0.07
$\varepsilon_{\text{PID}}(B^0 \rightarrow \pi^+K^-_{[K^+K^-]})$ [%]	3.60 ± 0.06	3.58 ± 0.06	3.68 ± 0.06
$\varepsilon_{\text{PID}}(B^0 \rightarrow \pi^+K^-_{[K^+\pi^-]})$ [%]	46.75 ± 0.50	46.17 ± 0.51	44.64 ± 0.47
$\varepsilon_{\text{PID}}(B^0 \rightarrow \pi^+K^-_{[\pi^+\pi^-]})$ [%]	2.01 ± 0.07	1.81 ± 0.07	1.80 ± 0.07
$\varepsilon_{\text{PID}}(B^0 \rightarrow \pi^+\pi^-_{[K^+\pi^-]})$ [%]	1.06 ± 0.04	0.99 ± 0.04	1.01 ± 0.04
$\varepsilon_{\text{PID}}(B^0 \rightarrow \pi^+\pi^-_{[\pi^+K^-]})$ [%]	1.09 ± 0.04	1.01 ± 0.04	1.00 ± 0.04
$\varepsilon_{\text{PID}}(B^0 \rightarrow \pi^+\pi^-_{[\pi^+\pi^-]})$ [%]	55.47 ± 0.78	54.39 ± 0.81	52.85 ± 0.77
$\varepsilon_{\text{PID}}(B_s^0 \rightarrow K^+K^-_{[K^+K^-]})$ [%]	59.88 ± 0.71	59.83 ± 0.70	58.67 ± 0.68
$\varepsilon_{\text{PID}}(B_s^0 \rightarrow K^+K^-_{[K^+\pi^-]})$ [%]	0.50 ± 0.02	0.44 ± 0.02	0.43 ± 0.02
$\varepsilon_{\text{PID}}(B_s^0 \rightarrow K^+K^-_{[\pi^+K^-]})$ [%]	0.57 ± 0.02	0.47 ± 0.02	0.43 ± 0.02

Selection K^+K^-			
Parameter	Year		
	2015-16	2017	2018
$\varepsilon_{\text{PID}}(B^0 \rightarrow K^+\pi^-_{[K^+K^-]})$ [%]	3.52 ± 0.06	3.52 ± 0.06	3.58 ± 0.06
$\varepsilon_{\text{PID}}(B^0 \rightarrow K^+\pi^-_{[K^+\pi^-]})$ [%]	49.26 ± 0.50	48.77 ± 0.51	47.46 ± 0.49
$\varepsilon_{\text{PID}}(B^0 \rightarrow K^+\pi^-_{[\pi^+\pi^-]})$ [%]	2.04 ± 0.07	1.81 ± 0.07	1.75 ± 0.07
$\varepsilon_{\text{PID}}(B^0 \rightarrow \pi^+K^-_{[K^+K^-]})$ [%]	3.50 ± 0.06	3.51 ± 0.06	3.60 ± 0.06
$\varepsilon_{\text{PID}}(B^0 \rightarrow \pi^+K^-_{[K^+\pi^-]})$ [%]	49.35 ± 0.51	48.86 ± 0.53	47.44 ± 0.49
$\varepsilon_{\text{PID}}(B^0 \rightarrow \pi^+K^-_{[\pi^+\pi^-]})$ [%]	1.94 ± 0.07	1.75 ± 0.07	1.73 ± 0.07
$\varepsilon_{\text{PID}}(B^0 \rightarrow \pi^+\pi^-_{[K^+\pi^-]})$ [%]	1.05 ± 0.04	0.99 ± 0.04	1.01 ± 0.04
$\varepsilon_{\text{PID}}(B^0 \rightarrow \pi^+\pi^-_{[\pi^+K^-]})$ [%]	1.08 ± 0.04	1.01 ± 0.04	1.01 ± 0.04
$\varepsilon_{\text{PID}}(B^0 \rightarrow \pi^+\pi^-_{[\pi^+\pi^-]})$ [%]	57.73 ± 0.81	56.80 ± 0.82	55.33 ± 0.80
$\varepsilon_{\text{PID}}(B_s^0 \rightarrow K^+K^-_{[K^+K^-]})$ [%]	62.09 ± 0.68	62.21 ± 0.70	61.16 ± 0.66
$\varepsilon_{\text{PID}}(B_s^0 \rightarrow K^+K^-_{[K^+\pi^-]})$ [%]	0.49 ± 0.02	0.43 ± 0.02	0.42 ± 0.02
$\varepsilon_{\text{PID}}(B_s^0 \rightarrow K^+K^-_{[\pi^+K^-]})$ [%]	0.58 ± 0.02	0.47 ± 0.02	0.43 ± 0.02

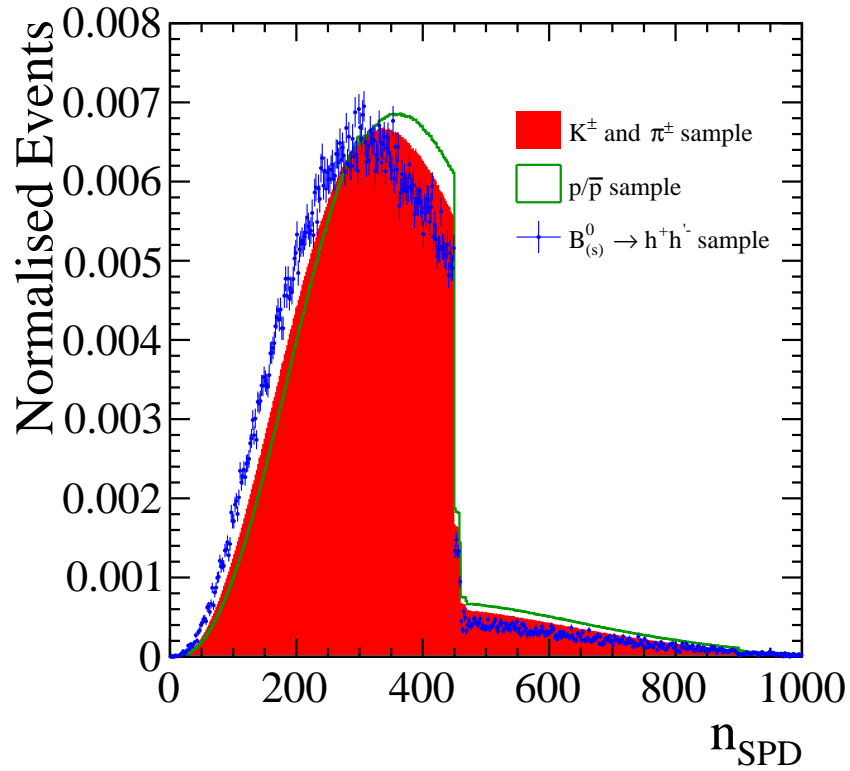


Figure 3.10: Background subtracted distributions of the number hits in the SPD system (n_{SPD}) for: $B_{(s)}^0 \rightarrow h^+ h'^-$ decays (blue dots), $D^{*+} \rightarrow D^0 (\rightarrow K^- \pi^+) \pi_s^+$ decays contained in the PID calibration sample (red filled histogram), and $\Lambda \rightarrow p \pi^-$ decays contained in the PID calibration sample (green histogram). The *sPlot* technique has been used to subtract the background components, as explained in Appendix A.1. This plot concerns the 2018 sample.

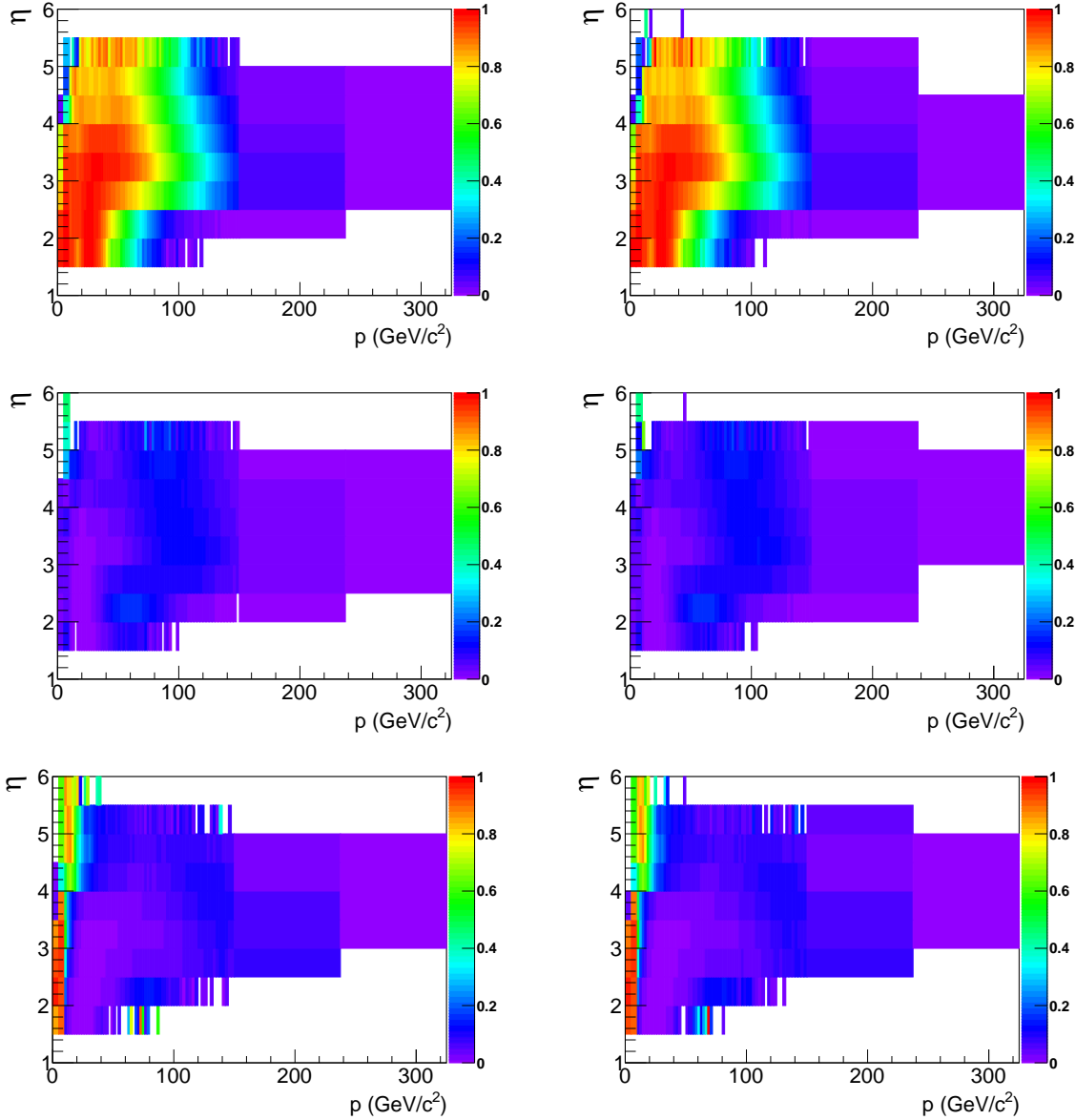


Figure 3.11: Estimated probability, in bins of particle momentum (p) and pseudorapidity (η), for different particles species to survive the PID requirement $DLL_{K\pi} > 2$ AND $DLL_{Kp} > -2$. From top to bottom: estimated probabilities for kaon, pions, and protons, respectively. On the left the estimated probabilities for positively charged particles are shown, while on the right estimated probabilities for negatively charged particles are reported. These plot concern the 2018 samples.

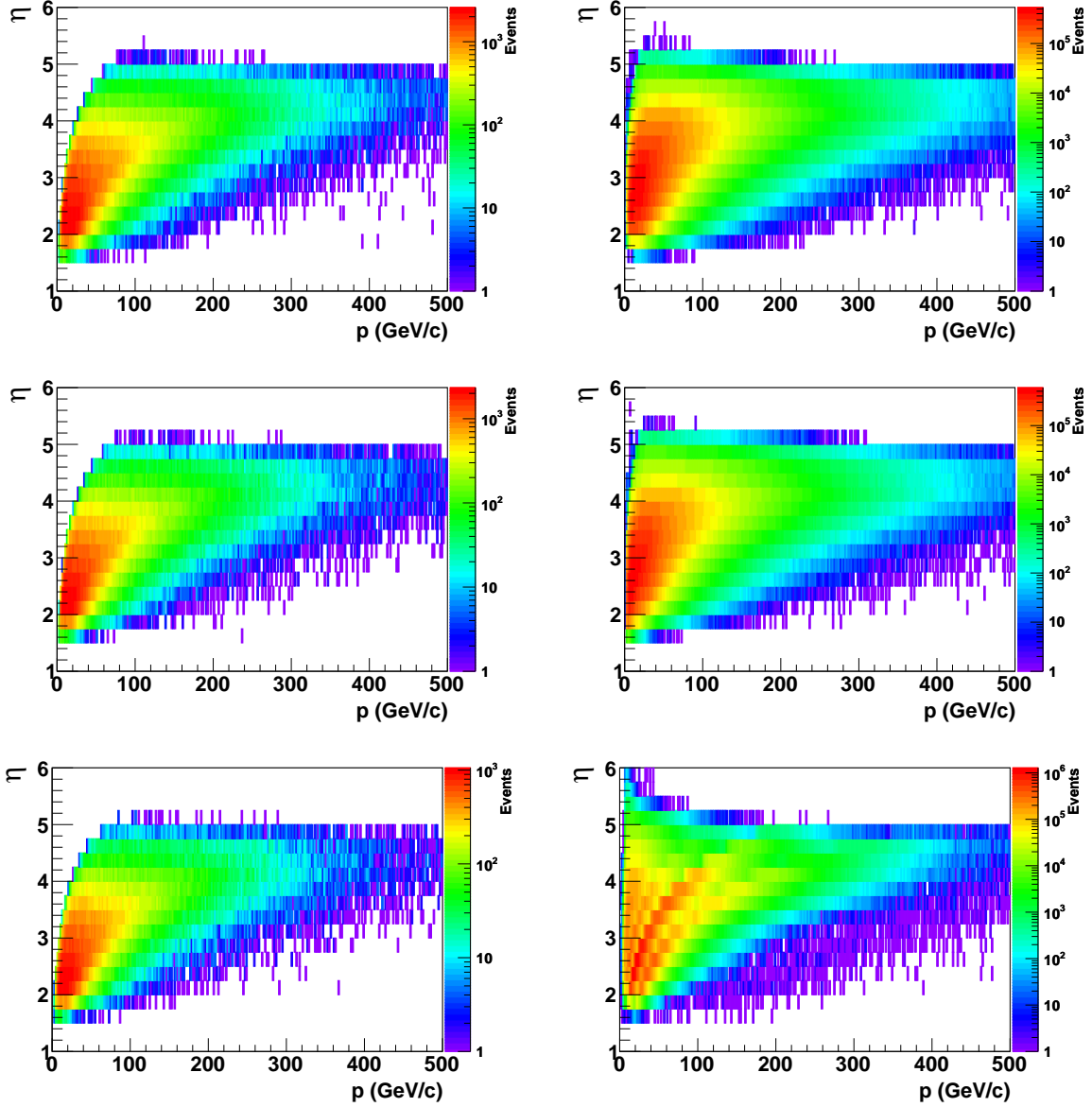


Figure 3.12: Distributions of kaons, pions and protons coming from $B_{(s)}^0 \rightarrow h^+ h'^-$ decays (left) and PID calibration sample (right), in the plane of particle momentum (p) and pseudorapidity (η). Distribution of particles from $B_{(s)}^0 \rightarrow h^+ h'^-$ decays are taken from fully simulated MC events, while the distributions of particles from the PID calibration samples are obtained from background subtracted events (as explained in the text). These plots concern the 2018 samples.

3.3 Decay-Time Resolution

The decay-time resolution of the LHCb experiment is expected to produce an appreciable dilution of the time-dependent asymmetry for $B_s^0 \rightarrow K^+ K^-$ decays. Such phenomenon can be explained assuming that the observed decay-time distributions originate from convolutions between the expressions reported in the equations (1.41)-(1.42) and a Gaussian, with null mean and standard deviation σ_t . Once the effects of the convolutions are propagated to the time-dependent asymmetry (1.49), its amplitude changes by a factor [131, 132]

$$D_{\sigma_t} = e^{-(\Delta m^2 \cdot \sigma_t^2)/2}. \quad (3.6)$$

As a consequence, the observed value of the CP violation parameter $C_f^{\text{obs.}}$ ($S_f^{\text{obs.}}$) is affected by the same rescaling: $C_f^{\text{obs.}} = D_{\sigma_t} \cdot C_f$ ($S_f^{\text{obs.}} = D_{\sigma_t} \cdot S_f$). Previous studies [120] showed that the decay-time resolution of LHCb is approximately $\sigma_t \approx 40$ fs. The current world averages of the B_s^0 and B^0 mass differences are [4]

$$\Delta m_s = (17.741 \pm 0.020) \times 10^{12} \text{ } \hbar\text{s}^{-1}, \quad \Delta m_d = (50.65 \pm 0.19) \times 10^{10} \text{ } \hbar\text{s}^{-1}, \quad (3.7)$$

Such values cause the dilution factors

$$D_{\sigma_t}(B^0) \approx 0.9998, \quad D_{\sigma_t}(B_s^0) \approx 0.7774, \quad (3.8)$$

which justify the expectation of a sizeable (negligible) modification of the CP parameters for $B_s^0 \rightarrow K^+ K^-$ ($B^0 \rightarrow \pi^+ \pi^-$) decays.

A bias in determining the decay time is also very dangerous for the measurements of the CP asymmetries in $B_s^0 \rightarrow K^+ K^-$ decays. Assuming the simplistic formula of the time-dependent CP asymmetry, $A_{CP} = -C \cos(\Delta m_s t) + S \sin(\Delta m_s t)$, a bias, B , in the decay time would have the effect of the transformation $t' = t + B$. As a consequence the observed time-dependent CP asymmetry is

$$A_{CP}^{\text{obs}}(t') = A_{CP}(t) = -C_{K^+K^-} \cos[\Delta m_s(t' - B)] + S_{K^+K^-} \sin[\Delta m_s(t' - B)]. \quad (3.9)$$

The subtraction formulae of sine and cosine provide

$$\begin{aligned} A_{CP}^{\text{obs}}(t') = & - [C_{K^+K^-} \cos(\Delta m_s B) + S_{K^+K^-} \sin(\Delta m_s B)] \cos(\Delta m_s t') \\ & + [S_{K^+K^-} \cos(\Delta m_s B) - C_{K^+K^-} \sin(\Delta m_s B)] \sin(\Delta m_s t'), \end{aligned} \quad (3.10)$$

where t' is the measured decay time and the terms between squared brackets are the observed values of $C_{K^+K^-}$ and $S_{K^+K^-}$, respectively:

$$C_{K^+K^-}^{\text{obs}} = C_{K^+K^-} \cos(\Delta m_s B) + S_{K^+K^-} \sin(\Delta m_s B); \quad (3.11)$$

$$S_{K^+K^-}^{\text{obs}} = S_{K^+K^-} \cos(\Delta m_s B) - C_{K^+K^-} \sin(\Delta m_s B). \quad (3.12)$$

By substituting the values of $C_{K^+K^-}$ and $S_{K^+K^-}$ from Ref. [24], Δm_s from [4] and assuming a bias $B \approx -5$ fs (see Section 3.3.2), one obtains

$$C_{K^+K^-}^{\text{obs}} - C_{K^+K^-} \approx -1.3\%, \quad S_{K^+K^-}^{\text{obs}} - S_{K^+K^-} \approx 1.5\%, \quad (3.13)$$

that would be a bias corresponding to about 50% of the statistical uncertainties quoted in Ref. [24] and about the same size of the statistical uncertainties expected in this analysis.

Table 3.13: Summary of the selection criteria of the `PromptJPsi2MuMuControlLine` stripping line. See text for details.

Variable	Cut
$\min(\chi_{\text{IP}}^2(\mu))$	< 9
$\chi^2(\mu)/\text{ndf}$	< 3
Ghost Prob.	< 0.2
ProbNN_μ	> 0.65
$p_{\text{T}}(\mu)$	$> 300 \text{ MeV}$
χ_{vtx}^2	< 2.5
$\chi_{\text{FD}}^2(J/\psi)$	< 9
$\chi_{\text{IP}}^2(J/\psi)$	< 9

The decay-time resolution is evaluated for each data-taking year using the calibration of the event-dependent estimation of the decay-time error δ_t .¹⁰ The calibration samples involve prompt- $J/\psi \rightarrow \mu^+\mu^-$ decays. They are described in Section 3.3.1. Since these decays are produced directly in the PV, any structure in their decay time is due to the resolution of the detector. Besides, simulated samples are exploited to correct and consider the differences between the calibration and signal decays. The functional formulation of the calibration relation is preliminarily studied with a binned calibration method. (Section 3.3.2). Subsequently, the actual calibration parameters are extracted by an unbinned calibration strategy (Section 3.3.3). The final fit utilises an average decay-time resolution. Section 3.3.4 explains the motivations of such choice.

3.3.1 Prompt- $J/\psi \rightarrow \mu^+\mu^-$ calibration samples

The $J/\psi \rightarrow \mu^+\mu^-$ calibration samples are selected imposing requirements on the following features of the final state tracks: the minimum χ^2 of the impact parameter with respect to the any PV in the event ($\min(\chi_{\text{IP}}^2(\mu))$), the ghost probability, the χ^2 of the track fit ($\chi^2(\mu)$), the muon PID (ProbNN_μ), the transverse momentum ($p_{\text{T}}(\mu)$). The fit for the combination vertex of the two muon candidates need a small χ^2 (χ_{vtx}^2). Besides, the reconstructed J/ψ candidates have to satisfy requirements on the χ^2 of their flight distance ($\chi_{\text{FD}}^2(J/\psi)$) and of their impact parameter with respect to the closest primary vertex ($\chi_{\text{IP}}^2(J/\psi)$). Table 3.13 lists the values of all the above cited selection criteria.

The offline selection involves loose cuts on the invariant mass ($m(\mu^+\mu^-) \in [2.99, 3.20] \text{ GeV}/c^2$), the decay time ($t \in [-1, 1] \text{ ps}$), and the decay-time error ($\delta_t \in [0.01, 0.1] \text{ ps}$). Simulated candidates are required to be associated with a true $J/\psi \rightarrow \mu^+\mu^-$ decay originating in the PV. These selection criteria reduce the contamination from non-prompt J/ψ , *i.e.* due to J/ψ produced in the decays of B hadrons, to a negligible level. This is evident in Figure 3.17, where no tail at high decay time is observed. The whole statistic available is more than enough for the calibration purposes of this analysis. This is the reason why the total samples are reduced selecting only a random fraction of the events. Their size is reported, depending on the data-taking year,

¹⁰The quantity δ_t is provided by the global fit of the decay chain performed by the standard LHCb reconstruction algorithms.

Table 3.14: Number of reconstructed candidates and stripping campaign label for the prompt- $J/\psi \rightarrow \mu^+\mu^-$ samples used for the decay-time resolution calibration. For each year, almost equal statistics comes from *MagUp* and *MagDown* configurations. Top: data samples, bottom: simulated samples.

Data		
Year	Sample Size	Stripping Ver.
2016	641623	28r2
2017	788379	29r2
2018	704987	34
Simulation		
Year	Sample Size	Stripping Ver.
2016	2502610	28r2
2017	2545490	29r2
2018	2545170	34

in Table 3.14¹¹. For internal reference, the labels of the stripping campaigns are listed in the same tables.

Figure 3.13 illustrates a fit to the invariant mass spectrum of the 2018 simulated sample. The model for the J/ψ peak comprises a Gaussian and two Crystal-Ball functions [133]. All the distributions have common mean and independent standard deviations (σ_G , σ_{CB1} , σ_{CB2}). The two Crystal-Ball components share the parameters ruling the power-law function describing the low mass tail. All parameters are free in the fit to the simulation sample. The same model is used to fit the J/ψ peak of the 2018 data sample. In this case, the peak mean and the standard deviation of the Gaussian, σ_G , are free. The results of the fit to the simulated samples are used fix the ratios σ_{CB1}/σ_G , σ_{CB2}/σ_G , and all the other parameters of the J/ψ peak model. The small combinatorial background is empirically modelled with a second order Chebychev polynomial [134] with free parameters. The fit result is superimposed to the 2018 data in Figure 3.14. The resulting sample purity is approximately 85%. The *sPlot* technique [128] is applied to calculate the *sWeights* and obtain a background-subtracted calibration sample.

3.3.2 Preliminary binned calibration

The relation between the decay-time resolution, σ_t , and the decay-time error, δ_t , estimated by the decay-time fit in the reconstruction, is studied by dividing the prompt- $J/\psi \rightarrow \mu^+\mu^-$ calibration samples into bins of δ_t . For each bin, the Root Mean Squared (RMS) of the reconstructed decay time, t , is calculated, as an estimator of σ_t . The bin scheme involves 26 bins of equal width in the range $\delta_t \in [0.01, 0.1]$ ps. The same procedure is applied to the $B_s^0 \rightarrow K^+K^-$ simulated samples¹² with the obvious exception that the difference between the reconstructed decay time, t , and the true decay time, t_{true} , is used in the RMS calculations. Figure 3.15 shows that a linear function is appropriate to describe the

¹¹For simplicity the 2015 sample is not included in this study: its statistics is low, and the previous analysis did not find relevant deviations between the 2015 and the 2016 decay-time resolutions.

¹²The whole selection, concerning the K^+K^- final state, is applied to this sample.

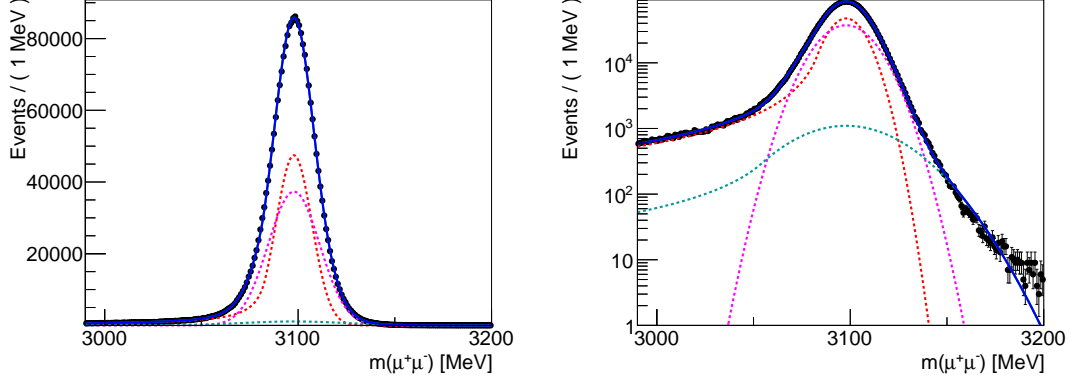


Figure 3.13: Fit to the 2018 prompt- $J/\psi \rightarrow \mu^+\mu^-$ simulated sample (black dots). The solid blue line shows the total fit model after the fit. The dashed lines are the three model components described in the text. *Left*: linear scale. *Right*: logarithmic scale.

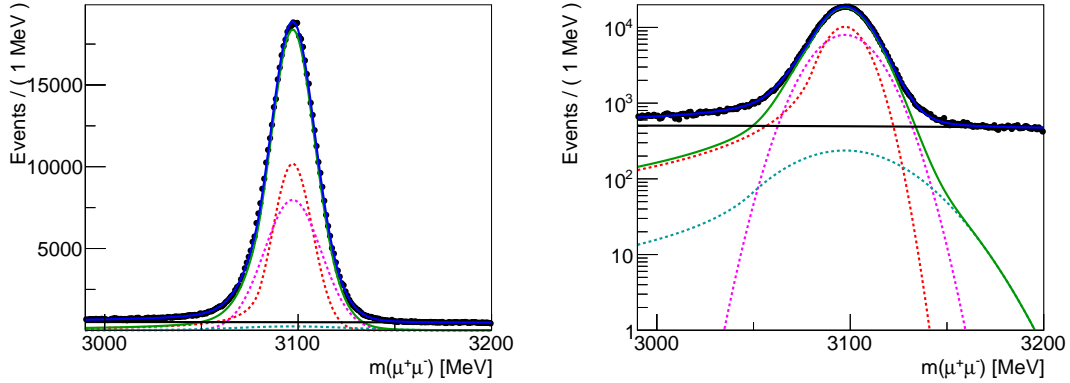


Figure 3.14: Fit to the 2018 prompt- $J/\psi \rightarrow \mu^+\mu^-$ data sample (black dots). The solid blue line shows the total fit model after the fit. The solid green and black lines are the signal and background components respectively. The signal model is the sum of the three distributions illustrated by the dashed lines and described in the text. *Left*: linear scale. *Right*: logarithmic scale.

relation between δ_t and $\text{RMS}(t)$ ($\text{RMS}(t - t_{\text{true}})$) for all cases. A slight deviation from this behaviour is actually present. However, it happens at high δ_t , affecting a negligible statistics.

The eventual presence of a decay-time bias is studied with the same binned approach, which has just been presented. Figure 3.16 illustrates the mean of t ($t - t_{\text{true}}$ for the $B_s^0 \rightarrow K^+K^-$ simulation) as a function of δ_t . In the simulation samples the bias is essentially negligible: $|\text{mean}(t)| \approx 0.3$ fs, with no dependence on δ_t . Instead, the prompt- $J/\psi \rightarrow \mu^+\mu^-$ data sample reveals a dependence of the bias on δ_t . A parabolic function is empirically chosen to describe such a behaviour. The bias is maximal ($\text{mean}(t) \approx -5$ fs) close to the average of decay-time error ($\delta_t \sim 40$ fs).

3.3.3 Unbinned calibration

The final parameters of decay-time error calibration are extracted using unbinned maximum-likelihood fits. The fit observables are δ_t and t . As before, the former is

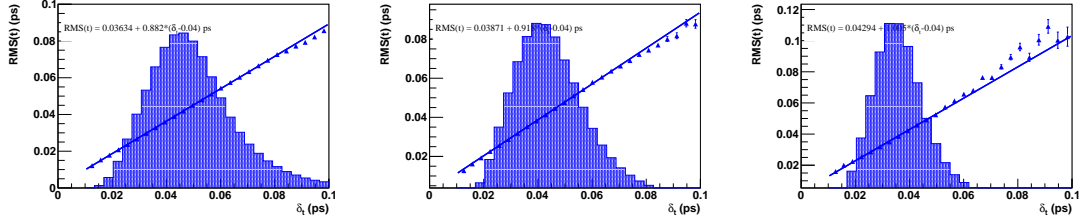


Figure 3.15: Preliminary binned calibration for the 2018 samples. *Left*: prompt- $J/\psi \rightarrow \mu^+\mu^-$ simulation; *middle*: prompt- $J/\psi \rightarrow \mu^+\mu^-$ data; *right*: $B_s^0 \rightarrow K^+K^-$ simulation. The distributions of the decay-time error δ_t is also shown with arbitrary normalization. The equations of the straight lines fitting the calibration points are also reported, as a reference.

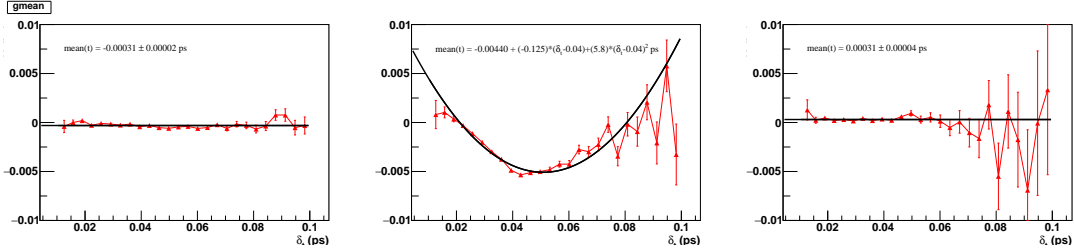


Figure 3.16: Decay-time bias as a function of the decay time error for the 2018 samples. *Left*: prompt- $J/\psi \rightarrow \mu^+\mu^-$ simulation; *middle*: prompt- $J/\psi \rightarrow \mu^+\mu^-$ data; *right*: $B_s^0 \rightarrow K^+K^-$ simulation. A constant and a parabolic function are used to fit the points in the simulation and real data cases, respectively. The function found by the fits are reported on each plot as a reference.

the decay-time error, while the latter stands for the difference between the reconstructed decay time and the true decay time, which is null for the prompt- $J/\psi \rightarrow \mu^+\mu^-$ samples. The fit model is

$$f(t, \delta_t) = g(t; \mu(\delta_t), \sigma_t(\delta_t) | \delta_t) \cdot h(\delta_t), \quad (3.14)$$

where:

- $h(\delta_t)$ is a histogram describing the distribution of the decay-time error δ_t .
- $g(t; \mu(\delta_t), \sigma_t(\delta_t) | \delta_t)$ is the probability density function of t conditioned to δ_t . The parameters μ and σ_t represent the decay-time bias and the decay-time resolution, respectively. In general, they are written as functions of δ_t . The parametrisation of g is slightly different between the various samples:

$J/\psi \rightarrow \mu^+\mu^-$ simulation : g is a Gaussian with mean μ and standard deviation σ_t ; μ does not depend on δ_t and is freely adjusted by the fit.

$J/\psi \rightarrow \mu^+\mu^-$ data : g is a Gaussian with mean μ and standard deviation σ_t ; μ has a parabolic dependence on δ_t :

$$\mu(\delta_t) = q_0 + q_1(\delta_t - 0.04) + q_2(\delta_t - 0.04)^2,$$

where q_0 , q_1 , and q_2 are free parameters.

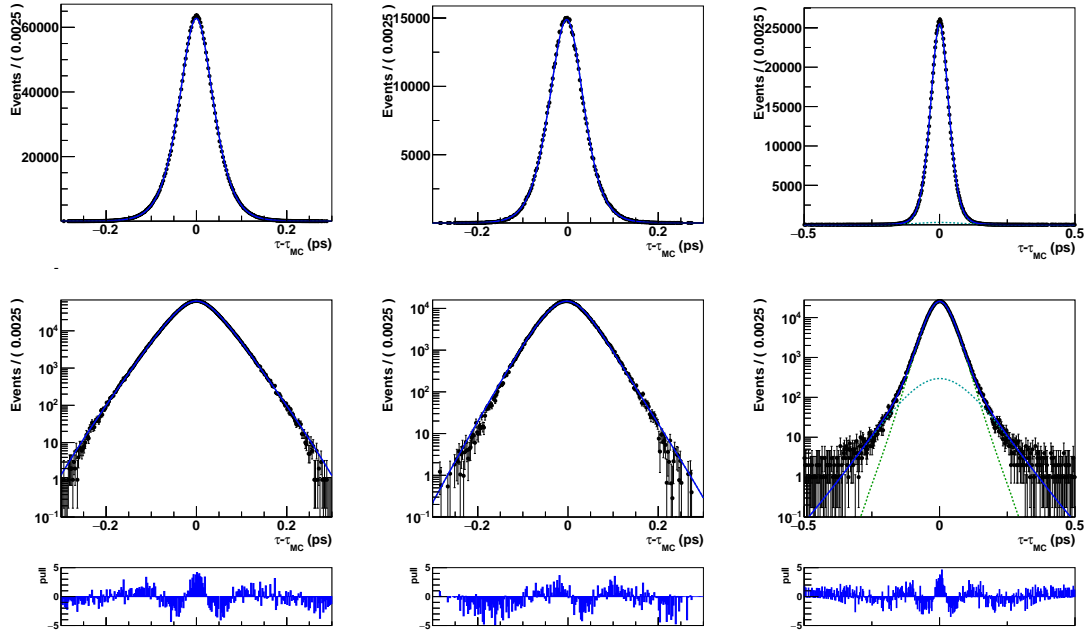


Figure 3.17: Fit for the unbinned decay-time resolution calibration of the 2018 samples. *Left*: prompt- $J/\psi \rightarrow \mu^+\mu^-$ simulation; *middle*: prompt- $J/\psi \rightarrow \mu^+\mu^-$ real data; *right*: $B_s^0 \rightarrow K^+K^-$ simulation.

Table 3.15: Parameters governing the decay-time resolution model described in the text for the $J/\psi \rightarrow \mu^+\mu^-$ simulated samples.

year	2016	2017	2018
μ [fs]	-0.30 ± 0.02	-0.31 ± 0.02	-0.31 ± 0.02
p_0 [fs]	36.377 ± 0.017	36.290 ± 0.017	36.329 ± 0.017
p_1	0.8851 ± 0.0013	0.8830 ± 0.0013	0.8829 ± 0.0013

$B_s^0 \rightarrow K^+K^-$ **simulation** : g is the sum of two Gaussians:

$$g(t|\delta_t) = fG(t; \mu, \sigma_t(\delta_t)|\delta_t) + (1 - f)G(t; \mu, C \cdot \sigma_t(\delta_t)|\delta_t),$$

where f is their relative fraction, C is the ratio between their standard deviations, and the common mean μ does not depend on δ_t ; all of them are freely adjusted by the fit.

In all the cases, σ_t linearly depends on δ_t according to

$$\sigma_t(\delta_t) = p_0 + p_1(\delta_t - 0.04), \quad (3.15)$$

where p_0 and p_1 are always free parameters.

Figure 3.17 illustrates the distributions of t with the results of the best fits superimposed. The values of the parameters obtained by the fits are reported in the Tables 3.15, 3.16, and 3.17. The information extracted from each fit leads to a different calibration of the

Table 3.16: Parameters governing the decay-time resolution model described in the text for the $J/\psi \rightarrow \mu^+\mu^-$ sample.

year	2016	2017	2018
q_0 [fs]	-4.40 ± 0.07	-5.39 ± 0.07	-4.42 ± 0.07
q_1	-0.107 ± 0.005	-0.121 ± 0.004	-0.125 ± 0.005
q_2 [ps $^{-1}$]	5.7 ± 0.2	6.1 ± 0.2	5.9 ± 0.3
p_0 [fs]	38.83 ± 0.05	38.87 ± 0.04	38.71 ± 0.04
p_1	0.904 ± 0.004	0.929 ± 0.003	0.919 ± 0.003

Table 3.17: Parameters governing the decay-time resolution model described in the text for $B_s^0 \rightarrow K^+K^-$ simulated samples.

year	2016	2017	2018
f	0.9760 ± 0.0009	0.9733 ± 0.0007	0.9715 ± 0.0009
C	2.60 ± 0.03	2.57 ± 0.02	2.51 ± 0.02
μ [fs]	0.17 ± 0.05	0.22 ± 0.04	0.33 ± 0.04
p_0 [fs]	40.23 ± 0.06	40.15 ± 0.04	40.08 ± 0.05
p_1	0.946 ± 0.004	0.951 ± 0.003	0.943 ± 0.003

functional relation between σ_t , μ and δ_t . The final calibration function of the individual decay-time error for the B_s^0 data combines all of them through the expression

$$\sigma_{t,i}(\delta_{t,i}, B_s^0 \text{ data}) = \sigma_{t,i}(\delta_{t,i}; J/\psi \rightarrow \mu^+\mu^- \text{ data}) \cdot \frac{\tilde{\sigma}_{t,i}(\delta_{t,i}; B_s^0 \rightarrow K^+K^- \text{ sim.})}{\sigma_{t,i}(\delta_{t,i}; J/\psi \rightarrow \mu^+\mu^- \text{ sim.})}, \quad (3.16)$$

where the result of the calibration obtained with the prompt- $J/\psi \rightarrow \mu^+\mu^-$ data is rescaled by the ratio between the calibrations for the $B_s^0 \rightarrow K^+K^-$ and prompt- $J/\psi \rightarrow \mu^+\mu^-$ simulated samples, to correct for their different kinematics. In equation (3.16), the subscript i , that runs over the events of each sample, is added for later convenience. It stresses the fact that this calibration formula operates on a per-event basis. Since the fits to the prompt- $J/\psi \rightarrow \mu^+\mu^-$ samples involve a single Gaussian, their calibration functions follow the equation (3.15) with respective values of the parameters p_0 and p_1 . The fit to the $B_s^0 \rightarrow K^+K^-$ simulated samples involves two Gaussians, hence the function $\tilde{\sigma}_{t,i}(\delta_{t,i}; B_s^0 \rightarrow K^+K^- \text{ sim.})$ depends also on the parameters f and C . It is computed first by averaging the dilution factors of the two Gaussian functions

$$D_{\sigma_{t,i}}(\delta_{t,i}; B_s^0 \rightarrow K^+K^- \text{ sim.}) = f \exp \left[\frac{-\Delta m_s^2 \sigma_{t,i}^2(\delta_{t,i})}{2} \right] + (1 - f) \exp \left[\frac{-\Delta m_s^2 C^2 \sigma_{t,i}^2(\delta_{t,i})}{2} \right], \quad (3.17)$$

where the function $\sigma_{t,i}(\delta_{t,i})$ follows the expression (3.15) with adequate values of the parameters p_0 and p_1 . Then, the average dilution factor is converted, exploiting Eq. (3.6), into the effective resolution width

$$\tilde{\sigma}_{t,i}(\delta_{t,i}; B_s^0 \rightarrow K^+K^- \text{ sim.}) = \frac{\sqrt{-2 \ln [D_{\sigma_{t,i}}(\delta_{t,i}; B_s^0 \rightarrow K^+K^- \text{ sim.})]}}{\Delta m_s} \quad (3.18)$$

Table 3.18: Final estimation of the average of the decay-time resolution and decay time bias for the $B_s^0 \rightarrow K^+K^-$ decay modes.

Year	$\hat{\sigma}_t(B_s^0 \text{ data})$ [fs]	$\hat{b}_t(B_s^0 \text{ data})$ [fs]
2015-16	43.2 ± 0.2	-3.6
2017	41.1 ± 0.2	-4.1
2018	40.7 ± 0.2	-3.1

3.3.4 Average decay-time resolution

Equation (3.16) permits the decay-time error to be calibrated on a per-event basis. The Run1 version of this analysis [115] used this kind of information in the final fit to measure the time-dependent CP asymmetries. Instead, the subsequent publication [24] showed that a resolution averaged on the whole sample, generates only an increase of 1% of the relative uncertainties on $C_{K^+K^-}$ and $S_{K^+K^-}$ with negligible effects on the other measured quantities. Moreover, this approach brings the advantage of a considerable simplification of the fit model. For these reasons, in this analysis an averaged decay-time resolution is used. The averaged value of the decay-time resolution is evaluated in two steps. First the averaged dilution factor for $B_s^0 \rightarrow K^+K^-$ decays is computed

$$\langle D \rangle = \sum_{i=1}^N \exp \left[-\frac{(\Delta m_s \cdot \sigma_{t,i}(\delta_{t,i}, B_s^0 \text{ data}))^2}{2} \right], \quad (3.19)$$

where $\sigma_{t,i}(\delta_{t,i}, B_s^0 \text{ data})$ is given by the relation (3.16), and the index i runs over the N events of the K^+K^- sample with invariant mass belonging to the range $[5.30, 5.43] \text{ GeV}/c^2$. The requirements on the mass range is such that the contribution from combinatorial background and $B^0 \rightarrow K^+\pi^-$ cross-feed background can be neglected. After that, the averaged dilution factor, $\langle D \rangle$ is converted into an effective resolution width, inverting Eq. (3.6). For the averaged decay-time bias a simple average over the same sample is performed. Table 3.18 summarises the averaged decay-time resolution widths and biases, that are used in the final fit to data.

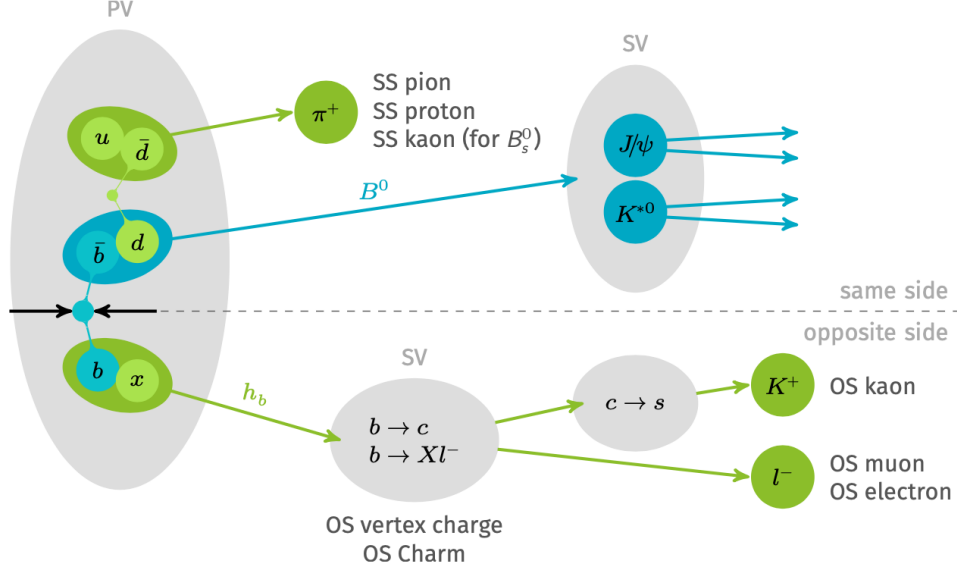


Figure 3.18: Schematic representation of the FT algorithms available at LHCb [135].

3.4 Flavour tagging

At LHCb the flavour of the neutral B mesons at the instants of their production is determined by specific algorithms, called *taggers* [135]. They are based on multivariate classifiers, exploiting geometrical and kinematic variables as input information. Each tagger looks for a specific kind of particle generated in the pp collision, whose electric charge is highly correlated with the flavour of the signal $B_{(s)}^0$ meson. Two main categories of tagging algorithms have been developed: the *Opposite Side* (OS) taggers and the *Same Side* (SS) taggers. The inputs of the latter are related to the remnants of the fragmentation of the signal b quark. Instead, the targets of the former are particles coming from the decay of the other B in the event. That is the reason why all OS taggers are suitable for both B^0 and B_s^0 tagging, whereas different SS taggers are devoted to different mesons. A schematic representation of the various algorithms is illustrated by Figure 3.18. The OS taggers seek the correlation between the signal $B_{(s)}^0$ flavour and the charge of: a kaon (OS $_K$) produced by the $b \rightarrow c \rightarrow s$ decay chain, a muon (OS $_\mu$) or an electron (OS $_e$) coming from a semileptonic b decay, a reconstructed secondary charm hadron (SS $_c$), and the inclusive secondary vertex reconstructed from the opposite b -hadron decay products (OS $_{\text{Vtx}}$) [29, 30]. The SS taggers exploit the information coming from a pion (SS $_\pi$) or a proton (SS $_p$) in case of a B^0 signal hypothesis [32], and from a kaon (SS $_K$) in the case of a B_s^0 signal hypothesis [31], within a certain kinematic region around the signal candidate. All taggers return two output variables: the decision, ξ_{tag} , and the predicted mistag probability, η_{tag} . The variable ξ_{tag} can take alternatively one of the discrete values $+1$, -1 , and 0 . The first two options correspond to the $B_{(s)}^0$ and $\bar{B}_{(s)}^0$ flavour decision, respectively. The outcome 0 means that the algorithm was not able to assign an hypothesis (*untagged* candidate). Consequently, the tagging efficiency is defined as:

$$\varepsilon_{\text{tag}} = \frac{N_R + N_W}{N_R + N_W + N_U}, \quad (3.20)$$

where N_R , N_W , N_U are the yields of candidates rightly tagged, wrongly tagged, and untagged respectively.

The variable η_{tag} is a continuous observable, belonging to the range $\eta_{\text{tag}} \in [0, 0.5]$. It can be studied through the decays of charged B mesons, where it is possible to compare the flavour of the reconstructed candidate with the tagging decision. In this condition, the mistag probability can be directly calculated as:

$$\eta_{\text{tag}} = \frac{N_W}{N_W + N_R}. \quad (3.21)$$

For the neutral B mesons, the estimation of the mistag probability is complicated by the flavour oscillations. In this case, the value of η_{tag} returned by the taggers can be calibrated for the specificities of each analysis, exploiting flavour-specific decays. The calibration parameters can be extracted by a fit to the B^0 flavour oscillations as a function of the proper decay-time, as it will be shown in the following. The result of the calibration is defined mistag rate, $\omega_{\text{tag}} = \omega_{\text{tag}}(\eta_{\text{tag}})$.

The occurrence of wrong tagging decisions generates a damping of the measured time-dependent CP asymmetries:

$$\begin{aligned} A_{CP}^{\text{meas}}(t) &= \frac{[\bar{N}_R(t) + N_W(t)] - [N_R(t) + \bar{N}_W(t)]}{[\bar{N}_R(t) + N_W(t)] + [N_R(t) + \bar{N}_W(t)]} \\ &= \frac{\bar{N}(t)(1 - \omega_{\text{tag}}) + N(t)\omega_{\text{tag}} - N(1 - \omega_{\text{tag}}) - \bar{N}(t)\omega_{\text{tag}}}{\bar{N}(t)(1 - \omega_{\text{tag}}) + N(t)\omega_{\text{tag}} + N(t)(1 - \omega_{\text{tag}}) + \bar{N}(t)\omega_{\text{tag}}} \\ &= (1 - 2\omega_{\text{tag}}) \frac{\bar{N}(t) - N(t)}{\bar{N}(t) + N(t)} = (1 - 2\omega_{\text{tag}})A_{CP}(t), \end{aligned} \quad (3.22)$$

where $N(t) \equiv N_R(t) + N_W(t)$ ($\bar{N}(t) \equiv \bar{N}_R(t) + \bar{N}_W(t)$) is the actual time-dependent yield of tagged $B_{(s)}^0$ ($\bar{B}_{(s)}^0$). Hence, the CP asymmetries and their statistical uncertainties are related to ω_{tag} according to

$$A_{CP}(t) = \frac{A_{CP}^{\text{meas}}(t)}{1 - 2\omega_{\text{tag}}}; \quad \sigma_{A_{CP}(t)} \propto \frac{1}{\sqrt{N_{\text{TOT}}\varepsilon_{\text{tag}}(1 - 2\omega_{\text{tag}})}}, \quad (3.23)$$

where N_{TOT} is the total number of signal candidates (tagged + untagged). The quantity

$$\varepsilon_{\text{eff}} \equiv \varepsilon_{\text{tag}}(1 - 2\omega_{\text{tag}})^2 \quad (3.24)$$

is called effective tagging power and represents the fraction of signal that effectively provide useful information for the determination of the time-dependent CP violation parameters.

This analysis utilises the information from the taggers on a per-event basis. The Sections 3.4.1 and 3.4.2 discuss the calibration of the individual OS and SS taggers, respectively. Background subtracted samples of $B^0 \rightarrow D^+\pi^-$ decays are used for this purpose. After the calibration the OS taggers are combined into a unique OS tagger that is used in the final fit. The combination assumes no correlation among the various OS taggers. Due to this hypothesis, the combined OS tagger is recalibrated on-the-fly during the final fit thanks to information from $B^0 \rightarrow K^+\pi^-$ decays. The same approach holds for the combined SS tagger, which is an input to the fit optimised for the extraction of $C_{\pi^+\pi^-}$ and $S_{\pi^+\pi^-}$. Instead, the SS_K tagger is singularly calibrated with $B_s^0 \rightarrow D_s\pi^-$ decays, and individually used in the fit optimised for $C_{K^+K^-}$, $S_{K^+K^-}$, and $A_{K^+K^-}^{\Delta\Gamma}$. The natural calibration channel would be the $B_s^0 \rightarrow \pi^+K^-$ decay, but its available statistics is too low to perform also this calibration during the final fit.

Table 3.19: Final values for the calibration parameters for the various OS taggers along with their statistical uncertainties. The 2018 data-taking period is concerned.

Tagger	p_0	p_1	$\langle\eta_{\text{tag}}\rangle$
OS _e	0.373 ± 0.006	1.25 ± 0.08	0.359
OS _{μ}	0.307 ± 0.004	1.29 ± 0.06	0.331
OS _K	0.396 ± 0.003	1.38 ± 0.06	0.408
OS _{Vtx}	0.380 ± 0.003	1.08 ± 0.04	0.385
SS _c	0.354 ± 0.005	0.86 ± 0.11	0.365

Table 3.20: Tagging performance for the various OS tagging algorithms. The 2018 data-taking period is concerned.

Tagger	ε_{tag} [%]	ε_{eff} [%]
OS _e	3.92 ± 0.04	0.44 ± 0.03
OS _{μ}	10.92 ± 0.05	1.92 ± 0.07
OS _K	20.56 ± 0.07	1.21 ± 0.05
OS _{Vtx}	21.62 ± 0.07	1.69 ± 0.07
SS _c	5.7 ± 0.04	0.52 ± 0.04

3.4.1 Calibration of OS taggers

The combinatorial background component is subtracted from the $B^0 \rightarrow D^+\pi^-$ calibration samples with the *sPlot* technique [128]. It involves an unbinned maximum likelihood fit to the invariant mass as discriminant variable (more details in Ref. [136]). A dependence of the mis-tag rate on the transverse momentum (p_T) of the B is observed. Hence the kinematic of the calibration samples are reweighted to match the $B_{(s)}^0 \rightarrow h^+h'^-$ samples.

After that, the parameters governing the relation between η_{tag} and ω_{tag} are determined on a per-event basis by means of a binomial regression performed by the Espresso Performance Monitor tool [137], specifically developed within LHCb. The calibration functions are shown in Figure 3.19 along with the corresponding η_{tag} distributions. The points correspond to the average observed mistag rate in bins of the predicted mistag probability. The linear relation

$$\omega_{\text{tag}}(\eta_{\text{tag}}) = p_0 + p_1(\eta_{\text{tag}} - \langle\eta_{\text{tag}}\rangle) \quad (3.25)$$

is observed to be suitable for all the cases. Table 3.19 reports the final calibration parameters concerning the 2018 case, while Table 3.20 lists the OS tagging performances for the same period of data taking. No significant difference is observed for the analogous quantities for the other data-taking periods.

3.4.2 Calibration of SS taggers

The individual calibrations of the SS algorithms follow the same strategy already explained for the OS taggers. The SS _{π} , and SS_p taggers are calibrated with the same background

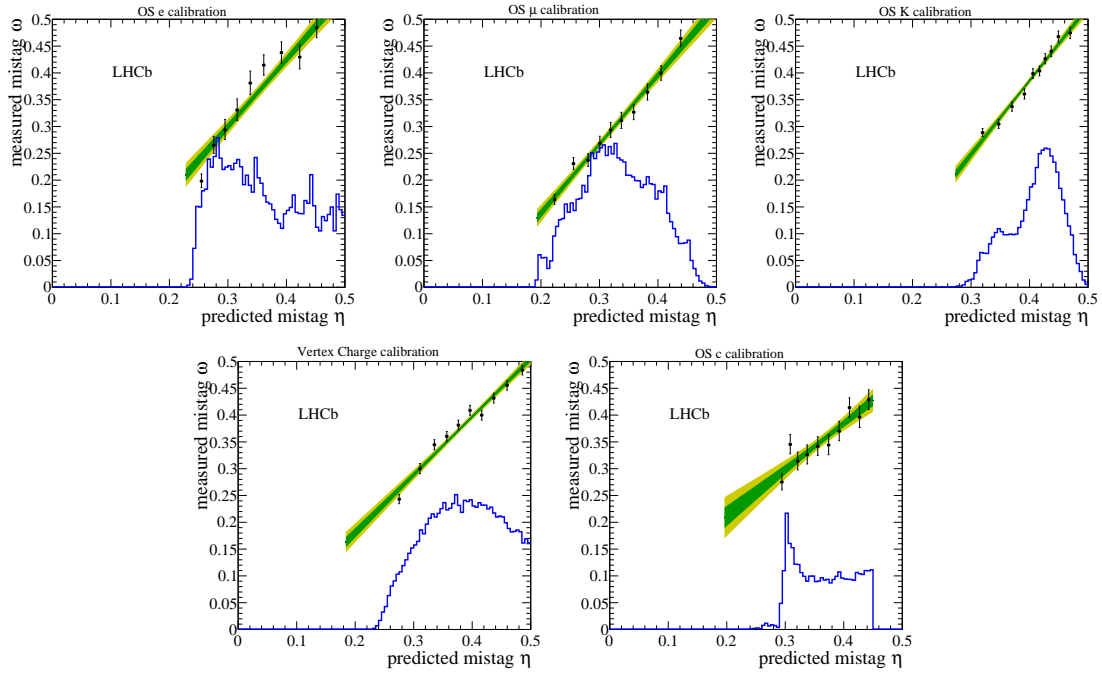


Figure 3.19: Calibration functions for the various OS taggers concerning the 2018 sample. From left to right OS_e , OS_μ , OS_K , OS_{Vtx} and SS_c . The data points correspond to the average observed mistag rate (ω_{tag}) obtained in bins of the predicted mistag (η_{tag}). The η_{tag} distribution is also shown.

Table 3.21: Calibration parameters for the various SS taggers with their statistical uncertainties. The 2018 data-taking period is concerned.

Tagger	p_0	p_1	$\langle \eta \rangle$
SS_π	0.4602 ± 0.0018	0.86 ± 0.04	0.462
SS_p	0.4580 ± 0.0026	0.10 ± 0.06	0.460
SS_K	0.437 ± 0.007	0.78 ± 0.07	0.426

subtracted sample of $B^0 \rightarrow D^+\pi^-$ decays. Instead, the SS_K tagger exploits $B_s^0 \rightarrow D_s\pi^-$ decays. The calibration parameters are determined by the EPM tool with the mistag on a per-event basis. Figure 3.20 shows the calibration plots. The data points indicate the average observed mistag rate for each bin of the predicted mistag probability. The results of the calibrations concerning the 2018 are reported in Table 3.21. Table 3.22 lists the performances of the SS taggers on the 2018 samples. No significant difference is observed between the different data-taking periods.

3.4.3 Tagger combination

Once the calibration parameters for the mistag rate are determined, the various taggers are combined on a per-event basis with the following method. For each tagger, the probability

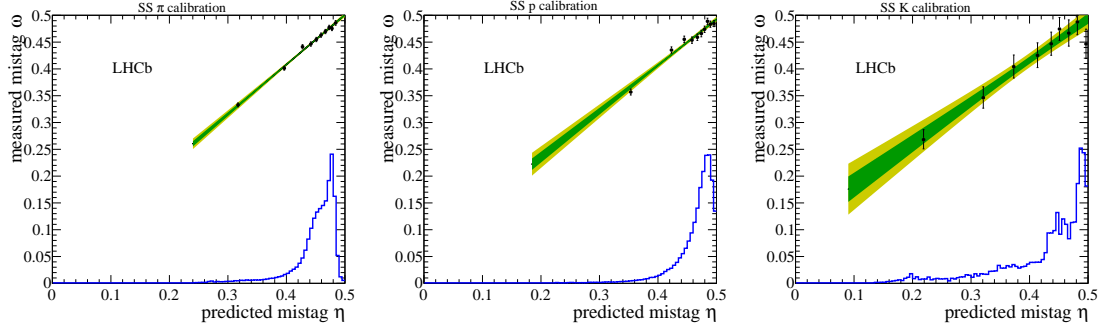


Figure 3.20: Calibration functions for the various SS taggers concerning the 2018 sample: from left to right SS_π , SS_p and SS_K . The calibrations of the SS_π and SS_p taggers have been evaluated on a sample of $B^0 \rightarrow D^0 \pi^-$ decays, while for the SS_K algorithm the $B_s^0 \rightarrow D_s \pi^-$ is exploited. The data points represent the average observed mistag rate (ω_{tag}) obtained in different bins of the predicted mistag (η_{tag}). The η_{tag} distribution is also shown.

Table 3.22: Tagging performance for the various SS tagging algorithms. The 2018 data-taking period is concerned. The performance of the SS_π and SS_p have been evaluated on a sample of $B^0 \rightarrow D^0 \pi^-$ while the $B_s^0 \rightarrow D_s \pi^-$ decays is used for the SS_K taggers. The different phase space of the $B^0 \rightarrow D^0 \pi^-$ and $B_s^0 \rightarrow D_s \pi^-$ with respect to the $B \rightarrow h^+ h'^-$ decays is taken into account performing a simultaneous reweighting on p_T of the B meson and the $nSPD$ hits distribution.

Tagger	ε_{tag} [%]	ε_{eff} [%]
SS_π	80.18 ± 0.07	1.15 ± 0.04
SS_p	41.05 ± 0.09	0.44 ± 0.03
SS_K	70.2 ± 0.3	2.2 ± 0.3

associated to a $B_{(s)}^0$ occurrence, given the tagging decision ξ_i and the mistag rate ω_i , is:

$$p_i(B_{(s)}^0 | \xi_i, \omega_i) = (1 - \omega_i) \delta_{\xi_i, 1} + \omega_i \delta_{\xi_i, -1} + 0.5 \delta_{d_i, 0}$$

where $\delta_{j,k}$ is the Kronecker delta symbol and the subscript i is used to indicate the i -th tagger, among the n to be combined ($i \in \{1, \dots, n\}$). Assuming independence among the tagger outputs, the total probability becomes:

$$p(B_{(s)}^0 | \vec{\xi}, \vec{\omega}) = \frac{\prod_{i=1}^n p_i(B_{(s)}^0 | \xi_i, \omega_i)}{\prod_{i=1}^n p_i(B_{(s)}^0 | \xi_i, \omega_i) + \prod_{i=1}^n [1 - p_i(B_{(s)}^0 | \xi_i, \omega_i)]}$$

where $\vec{\xi}$ and $\vec{\omega}$ are the set of tagging decisions and mistag rates to be combined for a given event. Finally, the combined decision, $\tilde{\xi}$, and mistag rate, $\tilde{\omega}$, are:

$$\begin{aligned} \tilde{\xi} = +1, \quad \tilde{\omega} = 1 - p(B_{(s)}^0 | \vec{\xi}, \vec{\omega}) & \quad \text{when } p(B_{(s)}^0 | \vec{\xi}, \vec{\omega}) > 0.5; \\ \tilde{\xi} = -1, \quad \tilde{\omega} = p(B_{(s)}^0 | \vec{\xi}, \vec{\omega}) & \quad \text{when } p(B_{(s)}^0 | \vec{\xi}, \vec{\omega}) < 0.5; \\ \tilde{\xi} = 0, \quad \tilde{\omega} = 0.5 & \quad \text{when } p(B_{(s)}^0 | \vec{\xi}, \vec{\omega}) = 0.5. \end{aligned}$$

3.5 Decay-time efficiency

Some requirements of the final selection affect the reconstruction efficiency of signal candidates as a function of the decay time. This efficiency is an input for the time-dependent fit models of the $B_{(s)}^0 \rightarrow h^+h'^-$ decays. The decay-time efficiencies are mainly determined from a background-subtracted data sample of $B^0 \rightarrow K^+\pi^-$ decays. This channel has high statistics and its decay-time distribution, before any selection requirement, is a pure exponential with well known lifetime: $\Gamma_d = 0.6579 \pm 0.0017 \text{ ps}^{-1}$ [23]. To include the slight differences between the various $B_{(s)}^0 \rightarrow h^+h'^-$ acceptances, the time-dependent efficiency determined from the $B^0 \rightarrow K^+\pi^-$ data sample is corrected by the ratios between the acceptances estimated from the simulation of other modes, and the simulation of the $B^0 \rightarrow K^+\pi^-$ decays itself. The discrepancies, that are indeed very small, are mainly due to slightly different kinematics induced by the different PID requirements. The effects of the PID requirements on the simulation are introduced with a data-driven technique. The following two paragraphs provide the details about the preparation of the data and simulation samples, respectively. After that, the fits for the extractions of the decay time-acceptances are described.

Background subtraction for $B^0 \rightarrow K^+\pi^-$ data. Only $B^0 \rightarrow K^+\pi^-$ candidates within a narrow window around its mass peak ($m \in [5.23, 5.32] \text{ GeV}/c^2$) are considered. After this selection, the only relevant background category in this range is the combinatorial one¹³. This contamination is subtracted, injecting combinatorial-background candidates from the right-hand mass sideband ($m \in [5.6, 6.2] \text{ GeV}/c^2$) with negative weights. The weight w_i associated to the i -th candidate is the ratio between the probabilities to observe a combinatorial background candidate with the decay time t_i in the two mass windows,

$$w_i = - \frac{\int_{5.23 \text{ GeV}/c^2}^{5.32 \text{ GeV}/c^2} e^{-\alpha(t_i)m} dm}{\int_{5.6 \text{ GeV}/c^2}^{6.2 \text{ GeV}/c^2} e^{-\alpha(t_i)m} dm}, \quad (3.26)$$

where the integrand function is the invariant mass probability density function (*pdf*) for the combinatorial background, conditioned by the decay-time value. The whole expression of the function $\alpha(t)$ is reported in Eq. (3.86) in Section 3.7.4 where its origin will be explained. With this weighting, the dependency of the decay-time shape of combinatorial-background on the invariant mass is properly taken into account in the subtraction.

Simulation reweightings. The trigger, stripping, and BDT requirements described in Sections 3.1.2 and 3.1.4 are directly applied to all simulated samples. Instead, the effects of the PID requirements are included assigning a proper weight to each simulated candidate:

$$w_i = \varepsilon_{h^+}(p_i^+, \eta_i^+) \varepsilon_{h'^-}(p_i^-, \eta_i^-) \quad (3.27)$$

where p^\pm and η^\pm are the momentum and the pseudorapidity of the two final-state particles of the i -th candidate. The symbols ε_{h^\pm} indicate their respective PID-efficiency maps presented in Section 3.2. Besides, the residual discrepancies between the B meson

¹³A very small contribution from the $B^0 \rightarrow \pi^+\pi^-$ and $B_s^0 \rightarrow K^+K^-$ decays, misidentified under the $K^+\pi^-$ hypothesis, and $B_s^0 \rightarrow \pi^+K^-$ decays is present, but it is estimated to be around 1.5% of the $B^0 \rightarrow K^+\pi^-$ contribution, hence negligible.

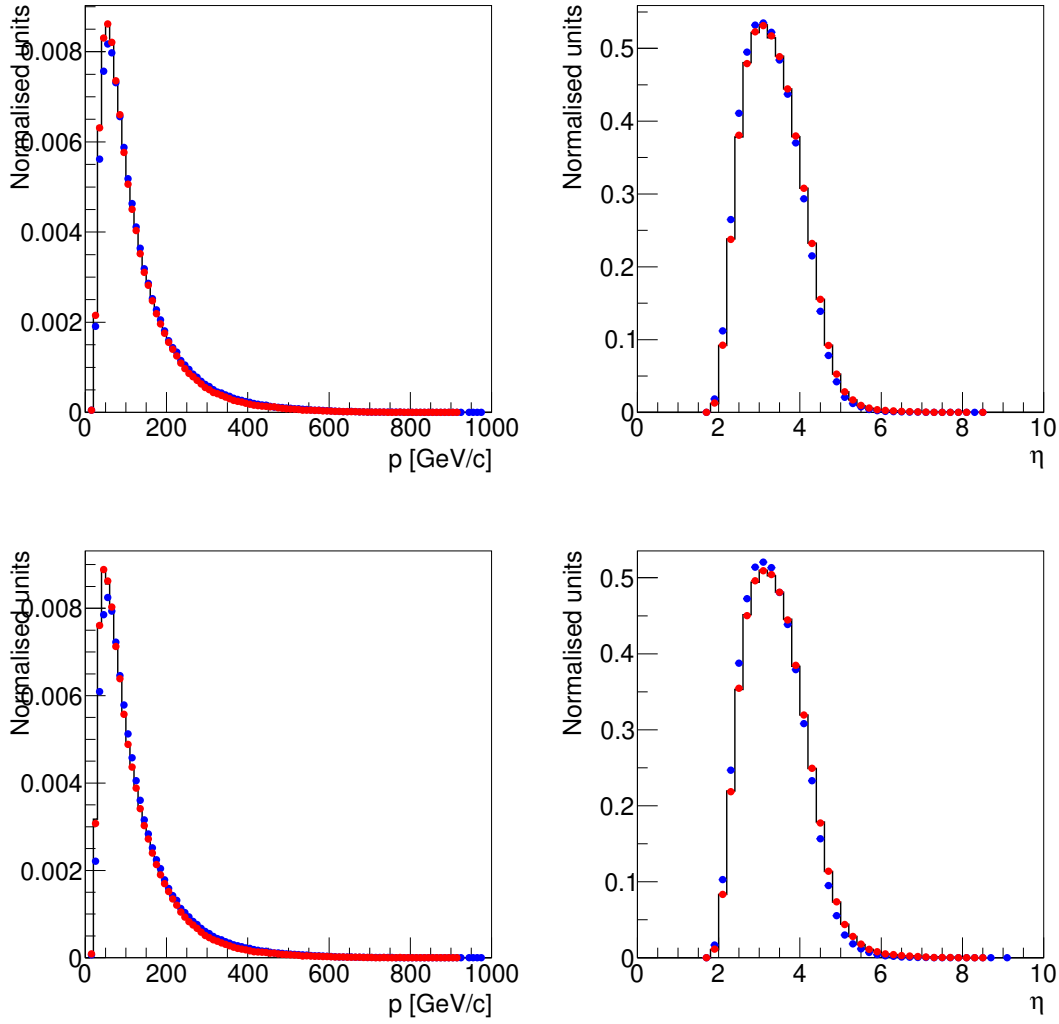


Figure 3.21: Distribution of the (left) B momentum and (right) pseudorapidity for $H_b \rightarrow h^+h'^-$ decays from (black histogram) background-subtracted data, (blue dots) fully simulated $B^0 \rightarrow K^+\pi^-$ decays, and (red dots) $B^0 \rightarrow K^+\pi^-$ decays after the weighting procedure described in the text. Distributions are shown for events surviving (top) the selection optimised for the $B^0 \rightarrow \pi^+\pi^-$ decay and (bottom) the selection optimised for the $B_s^0 \rightarrow K^+K^-$ decay.

kinematics observed in data and simulation are corrected with an additional weight, concerning the two-dimensional distribution of momentum, p , and pseudorapidity, η . The target pdf is provided by the background subtraction described in Section A.1. Figure 3.21 shows, as an example, the comparison between the p and η distribution of data and simulated $B^0 \rightarrow K^+\pi^-$ decays, together with the distributions obtained after the reweighting.

Acceptance determination. The decay-time pdf for the $B^0 \rightarrow K^+\pi^-$ decay is

$$P(t) = K e^{-\Gamma t} \varepsilon(t), \quad (3.28)$$

where K is a normalisation constant, $\Gamma_d = 0.6579 \pm 0.0017 \text{ ps}^{-1}$ is the decay width of the B^0 meson [138] and $\varepsilon(t)$ is the decay-time acceptance. In general, the other $B_{(s)}^0 \rightarrow h^+ h'^-$ modes have different distributions:

$$P_{B^0}(t) = K e^{-\Gamma_d t} \varepsilon(t), \quad (3.29)$$

$$P_{\Lambda_b^0}(t) = K e^{-\Gamma_{\Lambda_b^0} t} \varepsilon(t), \quad (3.30)$$

$$P_{B_s^0, \text{FS}}(t) = K [e^{-\Gamma_H t} + e^{-\Gamma_L t}] \varepsilon(t), \quad (3.31)$$

$$P_{B_s^0, \text{CP}}(t) = K [(1 - A_f^{\Delta\Gamma})e^{-\Gamma_H t} + (1 + A_f^{\Delta\Gamma})e^{-\Gamma_L t}] \varepsilon(t), \quad (3.32)$$

where the subscripts B^0 , Λ_b^0 , B_s^0, FS and B_s^0, CP refer to B^0 meson, Λ_b^0 baryon, B_s^0 meson decaying to flavour specific final states, and B_s^0 meson decaying to CP eigenstates, respectively. The same expression holds for all B^0 decays because of the negligible difference between the decay widths of its mass eigenstates ($\Delta\Gamma_d \approx 0$) [4]. The parameters Γ_L and Γ_H are the decay widths of the mass eigenstates of the B_s^0 system; $A_f^{\Delta\Gamma}$ is the value of the CP violation parameter defined in equation (1.43); $\Gamma_{\Lambda_b^0}$ is the decay-time width of the Λ_b^0 baryon.

The background-subtracted and simulated samples are fitted according to the distributions in Equations (3.28) to (3.32), where the decay-time efficiency is described using the effective function

$$\varepsilon(t) \propto 1 + b_1 \tanh(b_2(t - b_0)) + d_1 \tanh[d_2(t - d_0) + d_3(t - d_0)^2 + d_4(t - d_0)^3], \quad (3.33)$$

that is observed to provide a good description of the acceptance for all cases. All the physics parameters are fixed to the values used in the simulation and only the parameters of the decay-time acceptances ($\{b_j\}$ with $j = 0, 1, 2$ and $\{d_k\}$ with $k = 0, 1, 2, 3, 4$) are free to vary in the fits.

Besides, the decay-time acceptance is observed to depend on the ability of the SS-tagger to take a decision. Hence, the fits are repeated once for the total samples (irrespectively of the SS-tagging) and once for the subsamples containing only SS-tagged candidates, determining distinct acceptances for the two cases. The results of the best fits are reported in Figure 3.22, overlaid on the background-subtracted $B^0 \rightarrow K^+ \pi^-$ candidates corresponding to the 2018 data-taking period. No significant difference is observed between different data-taking periods.

As an example, Figure 3.23 illustrates the ratios between the decay-time acceptances determined from the simulations of $B_s^0 \rightarrow K^+ K^-$ and $B^0 \rightarrow K^+ \pi^-$ decays, with and without applying the PID weighting. These ratios are finally exploited to multiply the acceptance estimated from the $B^0 \rightarrow K^+ \pi^-$ data and get the final acceptances for all the other decays.

Because of technical reasons, the final fit exploits cubic spline functions to implement the acceptances. For each component, the acceptance is calculated in the following decay-time values: $\{0.2, 0.27, 0.4, 0.6, 0.8, 1, 1.25, 1.75, 2, 2.3, 3, 4, 5, 6, 7, 8, 9\}$. Then the points are interpolated by a cubic spline function. Several checks showed no relevant deviation between this implementation and the original functions [120].

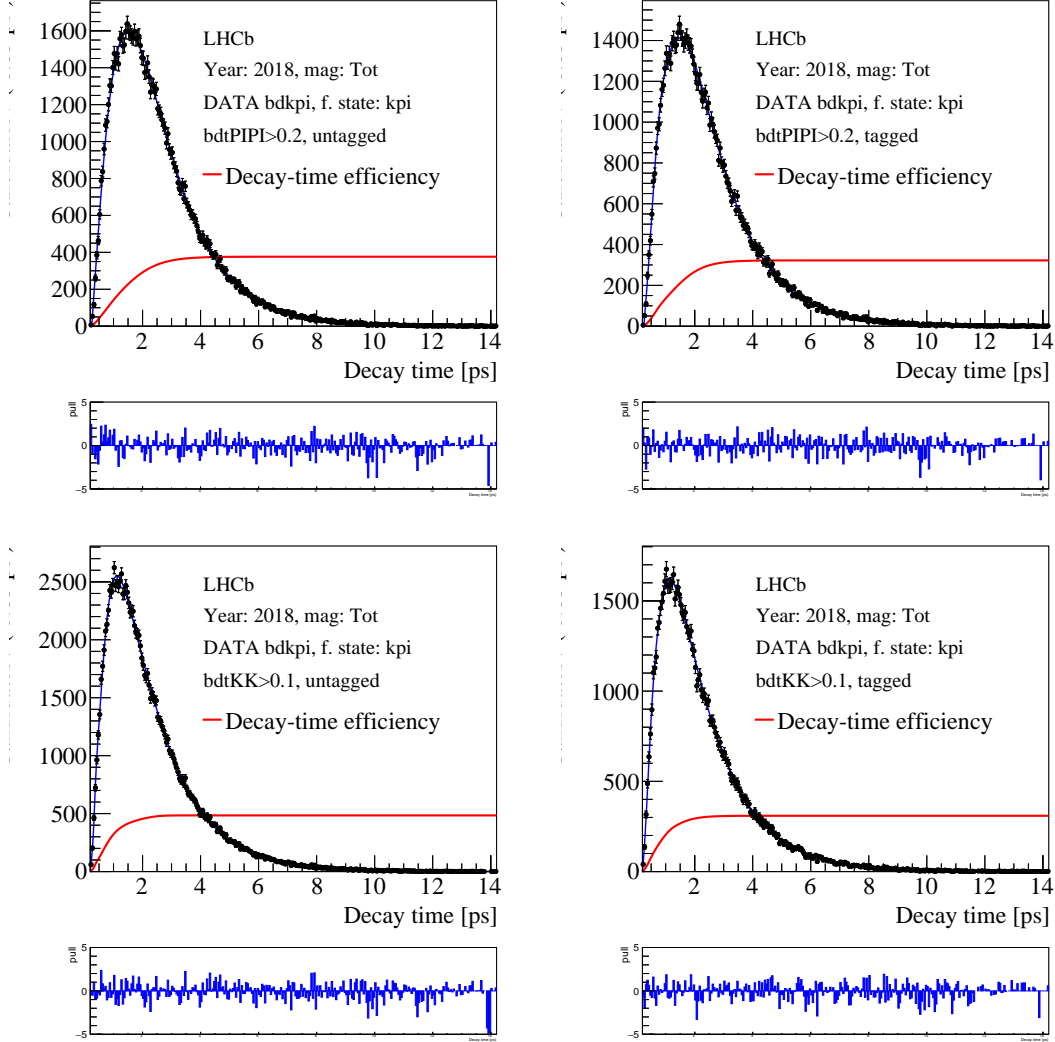


Figure 3.22: Distribution of background-subtracted candidates in the mass window $5.23 < m < 5.32 \text{ GeV}/c^2$ of the $K^+\pi^-$ sample. The result of the best fit, using the PDF defined in Eq. (3.28), are overlaid with a blue line. The shape of the decay-time acceptance determined from the fit is also represented by a red line. Candidates are those from the 2018 data-taking period surviving the selection optimised for the (top) $B^0 \rightarrow \pi^+\pi^-$ and (bottom) $B_s^0 \rightarrow K^+K^-$ decays. On the left the entire selected candidates are used, while on the right only the candidates for which the (top) SS tagger and (bottom) SS_K tagger have been able to take a decision.

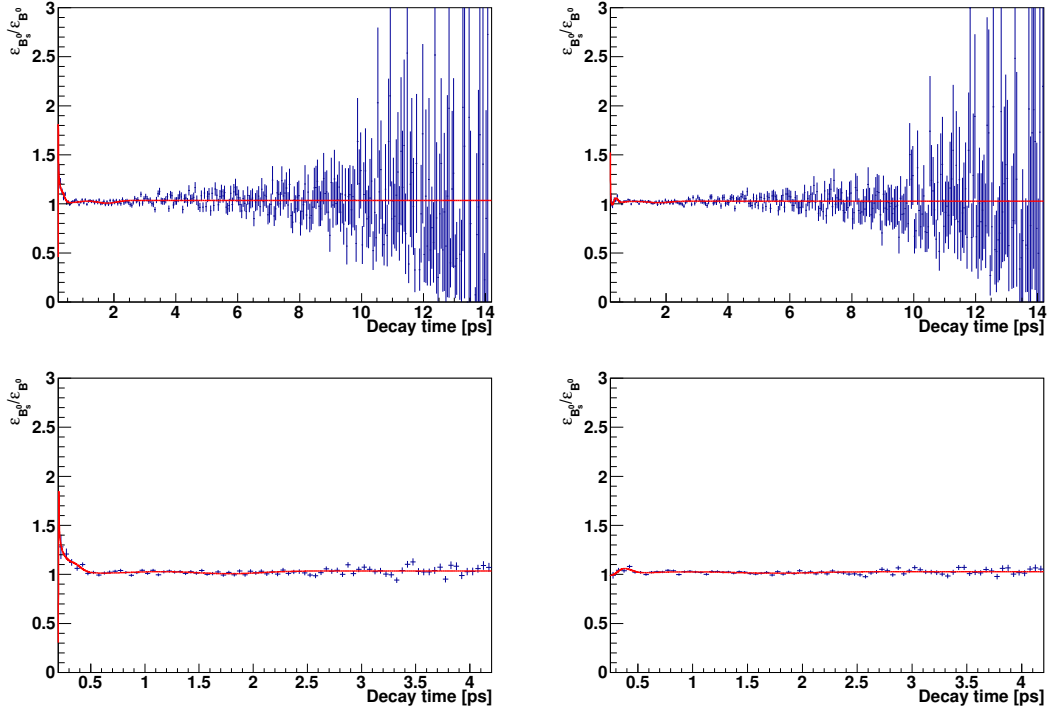


Figure 3.23: Ratio between the decay-time acceptances for $B_s^0 \rightarrow K^+K^-$ and $B^0 \rightarrow K^+\pi^-$ decays, surviving the selection optimised for $C_{K^+K^-}$, $S_{K^+K^-}$ and $A_{K^+K^-}^{\Delta\Gamma}$. The points represent the ratio obtained from simulated data, while the overlaid red curves are obtained computing the ratio of the acceptances obtained from fitting the simulated samples as described in the text. On the left, the plot is obtained considering the PID weights, while on the right the same plot is produced but neglecting the PID weights. The two bottom plots are the zoomed version of the two top plots.

3.6 Final state asymmetries

The time-integrated CP asymmetries ($A_{CP}^{B(s)}$) deviates from the raw asymmetries of the yields of the charge conjugated flavour-specific decays ($A_{\text{raw}}^{B(s)}$), because of two experimental effects: the production asymmetry (A_P) and the final state asymmetry (A_f). The definitions of these quantities are:

$$A_{CP}^{B(s)} = \frac{\mathcal{B}(\bar{B}_{(s)}^0 \rightarrow \bar{f}) - \mathcal{B}(B_{(s)}^0 \rightarrow f)}{\mathcal{B}(\bar{B}_{(s)}^0 \rightarrow \bar{f}) + \mathcal{B}(B_{(s)}^0 \rightarrow f)} \quad (3.34)$$

$$A_{\text{raw}}^{B(s)} = \frac{N(\bar{B}_{(s)}^0 \rightarrow \bar{f}) - N(B_{(s)}^0 \rightarrow f)}{N(\bar{B}_{(s)}^0 \rightarrow \bar{f}) + N(B_{(s)}^0 \rightarrow f)} \quad (3.35)$$

$$A_P = \frac{\mathcal{R}(\bar{B}_{(s)}^0) - \mathcal{R}(B_{(s)}^0)}{\mathcal{R}(\bar{B}_{(s)}^0) + \mathcal{R}(B_{(s)}^0)} \quad (3.36)$$

$$A_f = \frac{\varepsilon_{\text{tot}}(\bar{f}) - \varepsilon_{\text{tot}}(f)}{\varepsilon_{\text{tot}}(\bar{f}) + \varepsilon_{\text{tot}}(f)} \quad (3.37)$$

where \mathcal{B} stands for the branching fraction, N is the experimental yield, \mathcal{R} is the production rate of the $B_{(s)}^0$ or $\bar{B}_{(s)}^0$ mesons, and ε_{tot} is the total efficiency in the reconstruction and selection of the flavour-specific final states f and \bar{f} ($f = K^+\pi^-$ for B^0 mesons, whereas $f = K^-\pi^+$ when B_s^0 mesons are concerned). The raw and the production asymmetries can be extracted by the final fit (Section 3.7). On the contrary, calibration samples are needed to estimate the final state asymmetries. They are actually due to the sum of two contributions:

$$A_f = A_D^{K\pi} + A_{\text{PID}}^{K\pi}, \quad (3.38)$$

namely the detection asymmetry between the $K^+\pi^-$ and π^+K^- final states, $A_D^{K\pi}$, and the asymmetry between the efficiencies of the PID requirements applied in the selection of the candidates in the $K^\pm\pi^\mp$ final states, $A_{\text{PID}}^{K\pi}$. These asymmetries are defined by

$$\begin{aligned} A_D^{K\pi} &= \frac{\varepsilon_D(\pi^+K^-) - \varepsilon_D(K^+\pi^-)}{\varepsilon_D(\pi^+K^-) + \varepsilon_D(K^+\pi^-)} \\ A_{\text{PID}}^{K\pi} &= \frac{\varepsilon_{\text{PID}}(\pi^+K^-) - \varepsilon_{\text{PID}}(K^+\pi^-)}{\varepsilon_{\text{PID}}(\pi^+K^-) + \varepsilon_{\text{PID}}(K^+\pi^-)} \end{aligned} \quad (3.39)$$

where ε_D and ε_{PID} are the detection and PID efficiencies, respectively. Since $A_{CP}^{B_s^0}$ is defined with the opposite order with respect to $A_{CP}^{B^0}$, the CP asymmetries for $B^0 \rightarrow K^+\pi^-$ and $B_s^0 \rightarrow \pi^+K^-$ decays are defined in the following as

$$A_{CP} = A_{\text{raw}} + \zeta A_f, \quad (3.40)$$

where ζ will be equal to -1 for the B^0 mode and +1 for the B_s^0 mode, respectively.

Table 3.23: Results for the final-state detection asymmetries.

Year	$A_D^{K\pi}$ [%]
2015	-0.965 ± 0.314
2016	-1.052 ± 0.129
2017	-0.936 ± 0.132
2018	-0.948 ± 0.123

3.6.1 Asymmetry of detection

The strategy adopted to determine the final state detection asymmetries was validated in previous measurements performed by the LHCb collaboration, and the earlier versions of this analysis have already benefitted from it. The method involves the measurement and the combination of the raw asymmetries of two calibration modes: $D^+ \rightarrow K^- \pi^+ \pi^+$ and $D^+ \rightarrow \bar{K}^0 \pi^+$. In these cases, the raw asymmetries definitions are

$$A_{\text{raw}}^{K\pi\pi} = A_P^{D^+} + A_D^{K\pi} + A_D^\pi, \quad (3.41)$$

$$A_{\text{raw}}^{K^0\pi} = A_P^{D^+} + A_D^\pi - A_D^{K^0}. \quad (3.42)$$

where $A_P^{D^+}$ is the production asymmetry of the D^+ meson, the A_D asymmetries are the final-state detection asymmetries for the various particles, and null CP asymmetry is expected in these modes. The difference between the relations (3.41)-(3.42) provides:

$$A_D^{K\pi} = A_{\text{raw}}^{K\pi\pi} - A_{\text{raw}}^{K^0\pi} - A_D^{K^0}. \quad (3.43)$$

Since the interaction cross-sections of the K^+ and K^- mesons with the detector material depend on the kaon momentum, $A_D^{K\pi}$ has been measured in different momentum ranges in an LHCb internal note [139]. Kinematic reweight was applied simultaneously on the momentum and the transverse momentum of the D^+ and π^+ mesons to guarantee a perfect cancellation of $A_P^{D^+}$ and A_D^π between the two decay modes. The final-state detection asymmetry for the K^0 meson was taken as an external input from a previous LHCb measurement [140]. It is equal to $A_D^{K^0} = (0.054 \pm 0.014)\%$, and includes both the CP violation of the $K^0 \rightarrow \pi^+ \pi^-$ decay and the different interaction rates of the K^0 and \bar{K}^0 mesons with the LHCb detector. Effects due to left-right asymmetries of the detector are removed averaging the measurements performed with opposite polarities of the magnet.

The final detection asymmetry is the result of the convolution between the values of $A_D^{K\pi}$ and the kaon momentum distributions coming from the $B^0 \rightarrow K^+ \pi^-$ and $B_s^0 \rightarrow \pi^+ K^-$ samples, obtained by applying stringent invariant mass requirements around the two signal peaks. The residual contamination due to the combinatorial background is found to be negligible. The integrated definitive values of the final-state detection asymmetries are reported in Table 3.23. Since no significant difference is found for the two signals, a unique value of $A_D^{K\pi}$ is quoted.

3.6.2 Asymmetry of the PID efficiencies

The correction for the CP asymmetries due to the PID requirements utilises the PID efficiency maps created in Section 3.2 From the maps, PID asymmetries as a function of

Table 3.24: Final results for $A_{\text{PID}}^{K\pi}$.

Year	$A_{\text{PID}}^{K\pi}$ [%]
2015	-1.2 ± 0.7
2016	0.5 ± 0.3
2017	0.8 ± 0.4
2018	0.7 ± 0.3

the final-state particle kinematic are produced. Then, the PID asymmetry for the $K\pi$ final state as a function of the two-track kinematic is

$$A_{\text{PID}}^{K\pi}(p_K, \eta_K, \phi_K, p_\pi, \eta_\pi, \phi_\pi) = \frac{A_{\text{PID}}^K(p_K, \eta_K, \phi_K) - A_{\text{PID}}^\pi(p_\pi, \eta_\pi, \phi_\pi)}{1 - A_{\text{PID}}^K(p_K, \eta_K, \phi_K)A_{\text{PID}}^\pi(p_\pi, \eta_\pi, \phi_\pi)}, \quad (3.44)$$

where $A_{\text{PID}}^K(p_K, \eta_K, \phi_K)$ and $A_{\text{PID}}^\pi(p_\pi, \eta_\pi, \phi_\pi)$ represent the PID asymmetries of kaons and pions as function of their kinematic. The final integrated value of the PID asymmetry $A_{\text{PID}}^{K\pi}$ is obtained by a convolution with the phase space of the $B_{(s)}^0 \rightarrow h^+h'^-$ decays. Such results are listed in Table 3.24, where the uncertainties are obtained similarly to those of the PID efficiencies (Section 3.2).

3.7 Fit strategy

This Section describes the model that is adapted to the data to determine the CP violation parameters. The model describes the distributions of the following observables:

- the invariant mass, m ;
- the decay-time, t ;
- the tagging decisions, ξ_{tag} , and the mistag probabilities, η_{tag} , for both the OS and the SS taggers (tag = OS, SS);
- the associated final state, namely the satisfaction of the PID criteria related to the various exclusive final states. This is encoded by the observable $\psi \in \{-1, 0, 1, 2\}$, whose values are associated to the π^+K^- , $\pi^+\pi^-$, $K^+\pi^-$, and K^+K^- final states, respectively. When $B_{(s)}^0 \rightarrow h^+h'^-$ decays are concerned, the cases $\psi = \pm 1$ correspond to flavour-specific decays: they will often be resumed as “FS” final states. Instead, when $\psi \in \{0, 2\}$, the final states are CP eigenstates: they will be labelled with “CP”.

The whole set of observables will be indicated by the vector $\vec{x} = (m, t, \vec{\xi}_{\text{tag}}, \vec{\eta}_{\text{tag}}, \psi)$, where in turn: $\vec{\xi}_{\text{tag}} = (\xi_{\text{OS}}, \xi_{\text{SS}})$ and $\vec{\eta}_{\text{tag}} = (\eta_{\text{OS}}, \eta_{\text{SS}})$.

Four different components are found to be significant. Each one involves various contributions, which are similarly treated. They are:

- **signals:** $B_{(s)}^0 \rightarrow h^+h'^-$ decays, where the final state particles have been correctly identified;
- **cross-feed backgrounds:** $B_{(s)}^0 \rightarrow h^+h'^-$ decays where at least one of the final state particles has been misidentified;
- **partially reconstructed (or 3-body) backgrounds:** $B_{(s)}^0 \rightarrow h^+h'^-X$ decays, where only two out of the three daughters are reconstructed and used to form the $B_{(s)}^0$ candidate;
- **combinatorial backgrounds:** candidates composed by random pairs of oppositely charged particles coming from different decay chains.

Their probability density functions (*pdf*) are deduced from: physical expectations¹⁴, expectation from simulated samples, and templates from adequate data samples. They are fully described in the rest of this Section. Most of these considerations are supported by the previous analyses [120, 121]. In particular, the fit model is complicated by the correlations among the observables that are schematically summarised in Figure 3.24.

3.7.1 Signal model

The signal modes are:

- $B^0 \rightarrow K^+\pi^-$ and $B_s^0 \rightarrow \pi^+K^-$, when the $K^\pm\pi^\mp$ final states are concerned;

¹⁴In particular for decay-time distributions of the signal and cross-feed components.

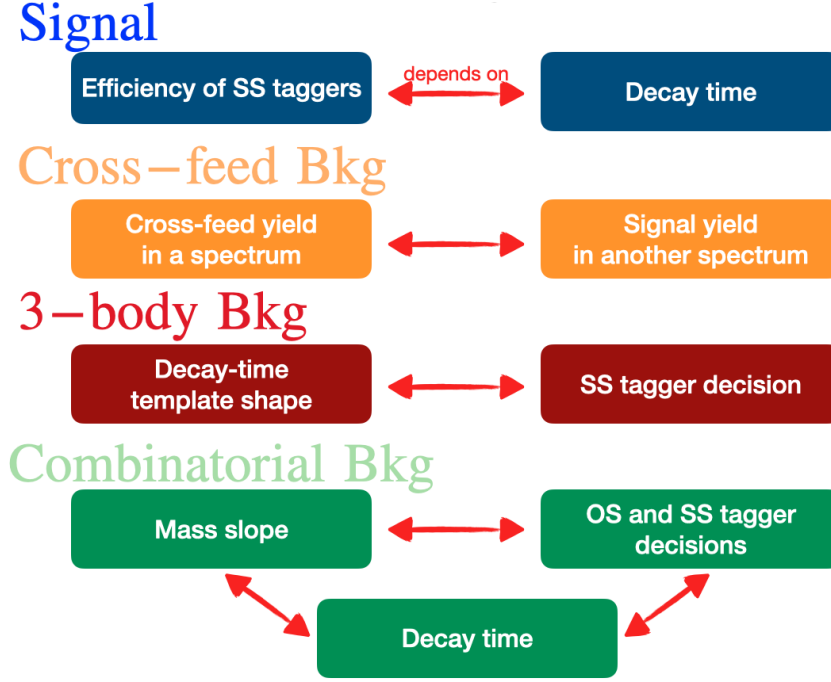


Figure 3.24: Schematic summary of the dependencies among the various aspects of the fit model.

- $B^0 \rightarrow \pi^+\pi^-$ and $B_s^0 \rightarrow \pi^+\pi^-$, when the $\pi^+\pi^-$ final state is concerned;
- $B_s^0 \rightarrow K^+K^-$ and $B^0 \rightarrow K^+K^-$, when the K^+K^- final state is concerned;

Their invariant mass distributions are found to be independent of the other fit observables. Hence, the generic signal *pdf* can be factorised:

$$p_{\text{sig}}(\vec{x}) = p_{\text{sig}}(m) \cdot p_{\text{sig}_\psi}(t, \vec{\xi}_{\text{tag}}, \vec{\eta}_{\text{tag}}). \quad (3.45)$$

The $p_{\text{sig}}(m)$ function is analogous for final states, whereas $p_{\text{sig}_\psi}(t, \xi_{\text{tag}}, \eta_{\text{tag}})$ changes between the FS and the CP cases because of the different expected decay-time distributions¹⁵. The flavour-tagging information can be treated similarly for all cases:

$$p_{\text{sig}_\psi}(t, \xi_{\text{tag}}, \eta_{\text{tag}}) = p_{\text{sig}_\psi}(t, \Omega^{\text{sig}}(t, \vec{\xi}_{\text{tag}}, \vec{\eta}_{\text{tag}}), \bar{\Omega}^{\text{sig}}(t, \vec{\xi}_{\text{tag}}, \vec{\eta}_{\text{tag}})), \quad (3.46)$$

where $\Omega^{\text{sig}}(t, \vec{\xi}_{\text{tag}}, \vec{\eta}_{\text{tag}})$ ($\bar{\Omega}^{\text{sig}}(t, \vec{\xi}_{\text{tag}}, \vec{\eta}_{\text{tag}})$) is the probability associated to the $B_{(s)}^0$ ($\bar{B}_{(s)}^0$) tagging decision. They depend on t because of the correlation between the SS-tagger decision and the decay-time acceptance. For these reasons, the signal model is introduced in three steps: first of all the invariant mass *pdf* is described, secondly the distributions (3.46) are explained (they contain the target *CP* observables and the parametrizations of the experimental effects), finally the Ω functions are presented.

Invariant mass model for signals. Studies on fully simulated events showed that the following *pdf* provides a good description of the invariant mass shape for the signals:

$$p_{\text{sig}}(m) = (1 - f_{\text{tail}})[f_g \cdot G_1(m, \mu + \delta, \sigma_1) + (1 - f_g) \cdot G_2(m, \mu + \delta, \sigma_2)] + f_{\text{tail}} \cdot J(m, \mu, \delta, \sigma_1, \alpha_1, \alpha_2) \quad (3.47)$$

¹⁵See the equations from (1.35) to (1.38).

Table 3.25: Tail parameters of the invariant mass model for the signal candidates, as determined from fits to fully simulated samples. These values are fixed in the final fit.

Decay	Selection $\pi^+\pi^-$		Selection K^+K^-	
	α_1	α_2	α_1	α_2
$B^0 \rightarrow K^+\pi^-$	0.650 ± 0.013	0.574 ± 0.007	0.664 ± 0.013	0.565 ± 0.007
$B^0 \rightarrow \pi^+\pi^-$	0.694 ± 0.013	0.578 ± 0.007	0.721 ± 0.012	0.561 ± 0.006
$B^0 \rightarrow K^+K^-$	0.565 ± 0.037	0.604 ± 0.023	0.549 ± 0.033	0.600 ± 0.021
$B_s^0 \rightarrow K^+K^-$	0.598 ± 0.012	0.560 ± 0.007	0.610 ± 0.011	0.547 ± 0.006
$B_s^0 \rightarrow \pi^+K^-$	0.660 ± 0.048	0.606 ± 0.022	0.704 ± 0.046	0.586 ± 0.020
$B_s^0 \rightarrow \pi^+\pi^-$	0.676 ± 0.050	0.579 ± 0.019	0.696 ± 0.047	0.559 ± 0.018

where $G(m, \mu + \delta, \sigma_1)$ and $G(m, \mu + \delta, \sigma_2)$ are two Gaussian functions with the same mean $\mu + \delta$, widths σ_1 and σ_2 , respectively, and with relative fraction f_g . The variable μ is fixed to the B^0 or B_s^0 masses [4]. The parameter f_{tail} is the relative fraction between the sum of the two Gaussian functions and the Johnson function, $J(m, \mu, \delta, \sigma_1, \alpha_1, \alpha_2)$, used to describe the asymmetric tails, is

$$J(m, \mu, \delta, \sigma_1, \alpha_1, \alpha_2) = \frac{\alpha_2}{\sigma_1 \sqrt{2\pi(1+z^2)}} \exp \left[-\frac{1}{2}(\alpha_1 + \alpha_2 \sinh^{-1} z)^2 \right], \quad (3.48)$$

where the parameter σ_1 is shared with the first Gaussian and z is defined as

$$z \equiv \left[\frac{m - (\mu + \delta)}{\sigma_1} \right]. \quad (3.49)$$

In the final fit all the parameters are left free to vary except for the parameters describing the tails ($\alpha_1, \alpha_2, f_{tails}$), which are fixed to the values determined from a fit to the invariant mass distribution of fully simulated samples. Such samples underwent the same selection as the data, with PID requirements applied by means of the same reweighting already introduced for the determinations of the decay-time acceptances (Section 3.5). Table 3.25 lists the final values of these fixed parameters.

Decay-time models for FS signals. For a flavour-specific decay like the $B^0 \rightarrow K^+\pi^-$ and the $B_s^0 \rightarrow \pi^+K^-$, the distinction between the two charge-conjugate final states ($K^\pm\pi^\mp$), for which the observable ψ assumes the value +1 and -1, is mandatory. The rates as a function of the decay-time are expressed by

$$p_{\text{sig}_{\text{FS}}}(t, \Omega^{\text{sig}}(t, \vec{\xi}_{\text{tag}}, \vec{\eta}_{\text{tag}}), \bar{\Omega}^{\text{sig}}(t, \vec{\xi}_{\text{tag}}, \vec{\eta}_{\text{tag}})) = K^{-1}(1 - \psi A_{CP})(1 - \psi A_f) \cdot \left\{ \left[(1 - A_P)\Omega^{\text{sig}} + (1 + A_P)\bar{\Omega}^{\text{sig}} \right] H_+(t) + \psi \left[(1 - A_P)\Omega^{\text{sig}} - (1 + A_P)\bar{\Omega}^{\text{sig}} \right] H_-(t) \right\}, \quad (3.50)$$

where K is a normalization constant, A_{CP} is the direct CP asymmetry, A_P is the production asymmetry, A_f is asymmetry of the final-state reconstruction and selection.¹⁶ It is

¹⁶Such asymmetries are defined by the equations (3.34), (3.36), and (3.37), respectively.

advantageous noting that, when terms of the second order are neglected, the product $(1 - \psi A_{CP})(1 - \psi A_f)$ can be written as $A_{CP} + A_f$ up to a very good approximation. Hence, in the fit A_f will be fixed to zero. The fit will determine the quantity $A_{\text{raw}} = A_{CP} + A_f$, that will be corrected *a-posteriori* using the values of A_f determined in Section 3.6.

The functions $H_+(t)$ and $H_-(t)$ are

$$\begin{aligned} H_+(t) &= \left[\exp(-\Gamma t') \cosh\left(\frac{\Delta\Gamma}{2} t'\right) \right] \otimes R(t - t'), \\ H_-(t) &= [\exp(-\Gamma t') \cos(\Delta m t')] \otimes R(t - t'), \end{aligned} \quad (3.51)$$

where Γ is the average width of the B meson decay, $\Delta\Gamma$ and Δm are the decay-width difference and mass difference between the mass eigenstates. The function R is the decay-time resolution model, namely a Gaussian, whose mean and standard deviation were determined in Section 3.3.

Decay-time model for CP signals. For the decays to CP -eigenstates, the final states f and \bar{f} are the same, hence the observable ψ is not necessary. The time-dependent decay rates are described by

$$\begin{aligned} p_{\text{sig}_{CP}}(t, \Omega^{\text{sig}}(t, \vec{\xi}_{\text{tag}}, \vec{\eta}_{\text{tag}}), \bar{\Omega}^{\text{sig}}(t, \vec{\xi}_{\text{tag}}, \vec{\eta}_{\text{tag}})) = \\ K^{-1} \left\{ \left[(1 - A_P) \Omega^{\text{sig}} + (1 + A_P) \bar{\Omega}^{\text{sig}} \right] I_+(t) + \right. \\ \left. \left[(1 - A_P) \Omega^{\text{sig}} - (1 + A_P) \bar{\Omega}^{\text{sig}} \right] I_-(t) \right\}, \end{aligned} \quad (3.52)$$

where K is a normalisation constant. The functions $I_+(t)$ and $I_-(t)$ are

$$I_+(t) = \left\{ e^{-\Gamma t'} \left[\cosh\left(\frac{\Delta\Gamma}{2} t'\right) - A_f^{\Delta\Gamma} \sinh\left(\frac{\Delta\Gamma}{2} t'\right) \right] \right\} \otimes R(t - t'), \quad (3.53)$$

$$I_-(t) = \left\{ e^{-\Gamma t'} [C_f \cos(\Delta m t') - S_f \sin(\Delta m t')] \right\} \otimes R(t - t'). \quad (3.54)$$

The parameter $A_f^{\Delta\Gamma}$ could be parametrised as

$$A_f^{\Delta\Gamma} = \pm \sqrt{1 - C_f^2 - S_f^2}, \quad (3.55)$$

where the ambiguity in the sign of this relation reflects the invariance of the decay rates under the exchange $(\Delta\Gamma, A_f^{\Delta\Gamma}) \rightarrow (-\Delta\Gamma, -A_f^{\Delta\Gamma})$. In the case of the $B^0 \rightarrow \pi^+ \pi^-$ decay, where $\Delta\Gamma$ can be assumed negligible, the ambiguity is not relevant, in contrast to the case of the $B_s^0 \rightarrow K^+ K^-$ decay. Alternatively, $A_f^{\Delta\Gamma}$ can also be left free to vary in the fit, as it is done in this analysis.

Signal tagging probabilities. The functions Ω^{sig} and $\bar{\Omega}^{\text{sig}}$ are the probability functions for the flavour tagging observables $(\xi_{OS}, \xi_{SS}, \eta_{OS}, \eta_{SS})$ and t . The decay-time acceptance is different for SS-tagged and SS-untagged candidates, whereas no difference depending on the OS-tagger decision is observed. This means that the Ω functions can be factorised:

$$\Omega^{\text{sig}}(t, \xi_{OS}, \xi_{SS}, \eta_{OS}, \eta_{SS}) = \Omega_{OS}^{\text{sig}}(\xi_{OS}, \eta_{OS}) \Omega_{SS}^{\text{sig}}(t, \xi_{SS}, \eta_{SS}), \quad (3.56)$$

$$\bar{\Omega}^{\text{sig}}(t, \xi_{OS}, \xi_{SS}, \eta_{OS}, \eta_{SS}) = \bar{\Omega}_{OS}^{\text{sig}}(\xi_{OS}, \eta_{OS}) \bar{\Omega}_{SS}^{\text{sig}}(t, \xi_{SS}, \eta_{SS}), \quad (3.57)$$

where $\Omega_{\text{OS}}^{\text{sig}}$ and $\bar{\Omega}_{\text{OS}}^{\text{sig}}$ are:

$$\Omega_{\text{OS}}^{\text{sig}}(\xi_{\text{OS}}, \eta_{\text{OS}}) = \left\{ \delta_{\xi_{\text{OS}}, 1} \varepsilon_{\text{OS}}^{\text{sig}} \left[1 - \omega_{\text{OS}}^{\text{sig}}(\eta_{\text{OS}}) \right] + \delta_{\xi_{\text{OS}}, -1} \varepsilon_{\text{OS}}^{\text{sig}} \omega_{\text{OS}}^{\text{sig}}(\eta_{\text{OS}}) \right\} h_{\text{OS}}^{\text{sig}}(\eta_{\text{OS}}) + \delta_{\xi_{\text{OS}}, 0} (1 - \varepsilon_{\text{OS}}^{\text{sig}}) U(\eta_{\text{OS}}), \quad (3.58)$$

$$\bar{\Omega}_{\text{OS}}^{\text{sig}}(\xi_{\text{OS}}, \eta_{\text{OS}}) = \left\{ \delta_{\xi_{\text{OS}}, -1} \bar{\varepsilon}_{\text{OS}}^{\text{sig}} \left[1 - \bar{\omega}_{\text{OS}}^{\text{sig}}(\eta_{\text{OS}}) \right] + \delta_{\xi_{\text{OS}}, 1} \bar{\varepsilon}_{\text{OS}}^{\text{sig}} \bar{\omega}_{\text{OS}}^{\text{sig}}(\eta_{\text{OS}}) \right\} h_{\text{OS}}^{\text{sig}}(\eta_{\text{OS}}) + \delta_{\xi_{\text{OS}}, 0} (1 - \bar{\varepsilon}_{\text{OS}}^{\text{sig}}) U(\eta_{\text{OS}}), \quad (3.59)$$

while $\Omega_{\text{SS}}^{\text{sig}}$ and $\bar{\Omega}_{\text{SS}}^{\text{sig}}$ are

$$\Omega_{\text{SS}}^{\text{sig}}(t, \xi_{\text{SS}}, \eta_{\text{SS}}) = \left\{ \delta_{\xi_{\text{SS}}, 1} \varepsilon_{\text{SS}}^{\text{sig}}(t) \left[1 - \omega_{\text{SS}}^{\text{sig}}(\eta_{\text{SS}}) \right] + \delta_{\xi_{\text{SS}}, -1} \varepsilon_{\text{SS}}^{\text{sig}}(t) \omega_{\text{SS}}^{\text{sig}}(\eta_{\text{SS}}) \right\} h_{\text{SS}}^{\text{sig}}(\eta_{\text{SS}}) + \delta_{\xi_{\text{SS}}, 0} \left[\varepsilon(t) - \varepsilon_{\text{SS}}^{\text{sig}}(t) \right] U(\eta_{\text{SS}}), \quad (3.60)$$

$$\bar{\Omega}_{\text{SS}}^{\text{sig}}(\xi_{\text{SS}}, \eta_{\text{SS}}) = \left\{ \delta_{\xi_{\text{SS}}, -1} \bar{\varepsilon}_{\text{SS}}^{\text{sig}}(t) \left[1 - \bar{\omega}_{\text{SS}}^{\text{sig}}(\eta_{\text{SS}}) \right] + \delta_{\xi_{\text{SS}}, 1} \bar{\varepsilon}_{\text{SS}}^{\text{sig}}(t) \bar{\omega}_{\text{SS}}^{\text{sig}}(\eta_{\text{SS}}) \right\} h_{\text{SS}}^{\text{sig}}(\eta_{\text{SS}}) + \delta_{\xi_{\text{SS}}, 0} \left[\varepsilon(t) - \bar{\varepsilon}_{\text{SS}}^{\text{sig}}(t) \right] U(\eta_{\text{SS}}). \quad (3.61)$$

In these equations $\varepsilon_{\text{tag}}^{\text{sig}}$ ($\bar{\varepsilon}_{\text{tag}}^{\text{sig}}$) ($\text{tag} = \text{OS}, \text{SS}$) is the efficiency for B (\bar{B}) meson to be tagged, which depends on the decay time SS-tagger case, $\varepsilon(t)$ is the decay-time acceptance independent of the decision of the SS-tagger, such that $\varepsilon(t) - \varepsilon_{\text{SS}}^{\text{sig}}(t)$ is the decay-time acceptance for candidates that are untagged according to the SS-tagger, $\omega_{\text{tag}}^{\text{sig}}(\eta_{\text{tag}})$ ($\bar{\omega}_{\text{tag}}^{\text{sig}}(\eta_{\text{tag}})$) is the mistag probability for the B (\bar{B}) meson as a function of the predicted mistag η_{tag} , $h_{\text{tag}}^{\text{sig}}(\eta_{\text{tag}})$ is the *pdf* describing the distribution of η_{tag} up to $\eta_{\text{tag}} = 0.5$ that is the limit above which the candidate is considered untagged, $U(\eta_{\text{tag}})$ is a uniform distribution of η_{tag} in the range $0 \leq \eta_{\text{tag}} \leq 0.5$. The functional dependency between η_{tag} and ω_{tag} is given by the relations

$$\omega_{\text{tag}}^{\text{sig}}(\eta_{\text{tag}}) = p_0^{\text{tag}} + p_1^{\text{tag}} (\eta_{\text{tag}} - \hat{\eta}_{\text{tag}}), \quad (3.62)$$

$$\bar{\omega}_{\text{tag}}^{\text{sig}}(\eta_{\text{tag}}) = \bar{p}_0^{\text{tag}} + \bar{p}_1^{\text{tag}} (\eta_{\text{tag}} - \hat{\eta}_{\text{tag}}), \quad (3.63)$$

where $\hat{\eta}_{\text{tag}}$ is the average value of η_{tag} over $h_{\text{tag}}^{\text{sig}}(\eta_{\text{tag}})$. In order to reduce the correlation among $\varepsilon_{\text{tag}}^{\text{sig}}$ and $\bar{\varepsilon}_{\text{tag}}^{\text{sig}}$, and p_0^{tag} , \bar{p}_0^{tag} , p_1^{tag} , and \bar{p}_1^{tag} , these variables have been parameterised in the following way:

$$\varepsilon_{\text{tag}}^{\text{sig}} = \hat{\varepsilon}_{\text{tag}}^{\text{sig}} (1 + \Delta \varepsilon_{\text{tag}}^{\text{sig}}), \quad (3.64)$$

$$\bar{\varepsilon}_{\text{tag}}^{\text{sig}} = \hat{\varepsilon}_{\text{tag}}^{\text{sig}} (1 - \Delta \varepsilon_{\text{tag}}^{\text{sig}}), \quad (3.65)$$

$$p_0^{\text{tag}} = \hat{p}_0^{\text{tag}} (1 + \Delta p_0^{\text{tag}}), \quad (3.66)$$

$$\bar{p}_0^{\text{tag}} = \hat{p}_0^{\text{tag}} (1 - \Delta p_0^{\text{tag}}), \quad (3.67)$$

$$p_1^{\text{tag}} = \hat{p}_1^{\text{tag}} (1 + \Delta p_1^{\text{tag}}), \quad (3.68)$$

$$\bar{p}_1^{\text{tag}} = \hat{p}_1^{\text{tag}} (1 - \Delta p_1^{\text{tag}}), \quad (3.69)$$

where $\hat{p}_{0,1}^{\text{tag}}$ and $\Delta p_{0,1}^{\text{tag}}$ are the average and the asymmetry between $p_{0,1}^{\text{tag}}$ and $\bar{p}_{0,1}^{\text{tag}}$, respectively, and $\hat{\varepsilon}_{\text{tag}}^{\text{sig}}$ and $\Delta \varepsilon_{\text{tag}}^{\text{sig}}$ are the average and the asymmetry between $\varepsilon_{\text{tag}}^{\text{sig}}$ and $\bar{\varepsilon}_{\text{tag}}^{\text{sig}}$, respectively. The dependency from the decay-time is considered only for the averaged efficiency $\hat{\varepsilon}_{\text{SS}}^{\text{sig}}$

and not also for the asymmetry $\Delta\varepsilon_{\text{tag}}^{\text{sig}}$. The strategy used to determine the decay-time acceptances $\varepsilon(t)$ and $\hat{\varepsilon}_{\text{SS}}^{\text{sig}}(t)$ was reported in Section 3.5.

It is important to note that all the parameters in Equations (3.64) to (3.69) are free to vary in the final fit and are determined thanks to the information from the $B^0 \rightarrow K^+\pi^-$ decay. The only exception are the asymmetry parameters of the SS_K tagger for the B_s^0 meson, that are fixed to the values obtained by fitting the $B_s^0 \rightarrow D_s\pi^-$ calibration sample with the model defined in Equation (3.50)

3.7.2 Cross-feed background model

Now the following cases are considered:

- $B^0 \rightarrow \pi^+\pi^-$ and $B_s^0 \rightarrow K^+K^-$ decays misidentified as $K^\pm\pi^\mp$ final states (CP \rightarrow FS);
- $B^0 \rightarrow K^+\pi^-$ decays misidentified as $\pi^+\pi^-$ and K^+K^- final states (FS \rightarrow CP);
- $A_b^0 \rightarrow \text{p}K^-$ decays misidentified as K^+K^- final states ($A_b^0 \rightarrow$ CP).

Further contributions, due to double misidentification, are found to be negligible.

The models for the cross-feed backgrounds are similar to those for the signals. Nonetheless, some modifications are necessary to include the effects of the wrong PID selection. The following paragraphs account for these models.

The main issue about the cross-feed backgrounds is that their invariant mass peaks are very close to the signal peaks and overwhelmed by the latter. Hence, the estimation of the cross-feed yields is highly non-trivial. The crucial point is that, a cross-feed mode for a certain final state is at the same time a signal mode for another one¹⁷. The approach of this analysis is to simultaneously analyse all the final states connecting the yields of the cross-feed background to those of the corresponding signals with the relation:

$$N_{\hat{h}^+\hat{h}'^-}(B_{(s)}^0 \rightarrow h^+h'^-) = N(B_{(s)}^0 \rightarrow h^+h'^-) \cdot \frac{\varepsilon_{\hat{h}^+\hat{h}'^-}(B_{(s)}^0 \rightarrow h^+h'^-)}{\varepsilon_{h^+h'^-}(B_{(s)}^0 \rightarrow h^+h'^-)}, \quad (3.70)$$

where: $N_{\hat{h}^+\hat{h}'^-}(B_{(s)}^0 \rightarrow h^+h'^-)$ is the number of $B_{(s)}^0 \rightarrow h^+h'^-$ candidates under the $\hat{h}^+\hat{h}'^-$ hypothesis, $N(B_{(s)}^0 \rightarrow h^+h'^-)$ represents the number of $B_{(s)}^0 \rightarrow h^+h'^-$ events correctly identified by the PID requirements; the parameters $\varepsilon_{\hat{h}^+\hat{h}'^-}(B_{(s)}^0 \rightarrow h^+h'^-)$ and $\varepsilon_{h^+h'^-}(B_{(s)}^0 \rightarrow h^+h'^-)$ are the probabilities to assign the $\hat{h}^+\hat{h}'^-$ and the correct mass hypothesis to the $B_{(s)}^0 \rightarrow h^+h'^-$ decay, respectively. In the fit, these PID efficiencies are fixed to the values determined in Section 3.2.

Invariant mass models for cross-feed backgrounds. The determination of these models involves a Kernel Density Estimation method (KDE) [126] applied to fully simulated samples. They are selected by the same criteria imposed to the real data (Section 3.1.4). To properly describe the effects of the PID requirements, weights are assigned to the simulated candidates using the PID efficiencies. The method is analogous to the one used to study the signal decay-time acceptances (Ed. (3.27)), but the misidentification

¹⁷Except for the $A_b^0 \rightarrow \text{p}K^-$ channel, whose expected contribution is small: below 0.5% of the $B^0 \rightarrow K^+\pi^-$ yield.

efficiency maps are exploited now. Subsequently, the KDE method is applied to these weighted samples to determine non-parametric *pdfs*. In the final fit, they are convolved with the same resolution used for the invariant mass of the signal.

Decay-time models for cross-feed backgrounds. The definition of these models assumes that the decay time calculated under the wrong mass hypothesis is not very different from the correct one. This hypothesis is verified by fitting the model to the decay-time distribution of simulated decays reconstructed with the wrong mass hypothesis.

The final states of $B^0 \rightarrow \pi^+\pi^-$ and $B_s^0 \rightarrow K^+K^-$ decays are self-conjugate. Hence, the decay rates of these modes, misidentified in the $K^\pm\pi^\mp$ final state, do not depend explicitly on ψ . Their time-dependent *pdf* is:

$$p_{\text{CP}\rightarrow\text{FS}}(t, \Omega^{\text{sig}}(t, \vec{\xi}_{\text{tag}}, \vec{\eta}_{\text{tag}}), \bar{\Omega}^{\text{sig}}(t, \vec{\xi}_{\text{tag}}, \vec{\eta}_{\text{tag}})) = K^{-1} \left\{ \left[(1 - A_{\text{P}}) \Omega^{\text{sig}} + (1 + A_{\text{P}}) \bar{\Omega}^{\text{sig}} \right] I_+(t) + \left[(1 - A_{\text{P}}) \Omega^{\text{sig}} - (1 + A_{\text{P}}) \bar{\Omega}^{\text{sig}} \right] I_-(t) \right\}, \quad (3.71)$$

where K is a normalisation factor and the dependence on ψ is implicit as $B^0 \rightarrow \pi^+\pi^-$ and $B_s^0 \rightarrow K^+K^-$ can be misidentified as both $K^+\pi^-$ and $K^-\pi^+$ final states.

In the case of the $B^0 \rightarrow K^+\pi^-$ decays misidentified in the $\pi^+\pi^-$ or K^+K^- final state, the information provided by the observation of the two charge-conjugated final states ($K^+\pi^-$ and $K^-\pi^+$) is lost. This produces the marginalisation of ψ from the signal *pdf* (3.50). As a result:

$$p_{\text{FS}\rightarrow\text{CP}}(t, \Omega^{\text{sig}}(t, \vec{\xi}_{\text{tag}}, \vec{\eta}_{\text{tag}}), \bar{\Omega}^{\text{sig}}(t, \vec{\xi}_{\text{tag}}, \vec{\eta}_{\text{tag}})) = K^{-1} \left\{ (1 + A_{\text{CP}}A_{\text{f}}) \left[(1 - A_{\text{P}}) \Omega^{\text{sig}} + (1 + A_{\text{P}}) \bar{\Omega}^{\text{sig}} \right] H_+(t) - (A_{\text{CP}} + A_{\text{f}}) \left[(1 - A_{\text{P}}) \Omega^{\text{sig}} - (1 + A_{\text{P}}) \bar{\Omega}^{\text{sig}} \right] H_-(t) \right\}, \quad (3.72)$$

where K is a normalisation constant.

Also in the case of the $\Lambda_b^0 \rightarrow pK^-$ decay misidentified in the K^+K^- spectrum, the information concerning the flavour-specific final state is lost. In addition, the time-dependent decay rate of the Λ_b^0 baryon is a pure exponential. Therefore, the tagged time-dependent *pdf* of the Λ_b^0 cross-feed is:

$$p_{\Lambda_b^0\rightarrow\text{CP}}(t, \Omega^{\text{sig}}(t, \vec{\xi}_{\text{tag}}, \vec{\eta}_{\text{tag}}), \bar{\Omega}^{\text{sig}}(t, \vec{\xi}_{\text{tag}}, \vec{\eta}_{\text{tag}})) = K^{-1} \left[(1 - A_{\text{P}}) (1 - A_{\text{f}}) (1 - A_{\text{CP}}) \Omega^{\text{sig}} + (1 + A_{\text{P}}) (1 + A_{\text{f}}) (1 + A_{\text{CP}}) \bar{\Omega}^{\text{sig}} \right] T(t) \quad (3.73)$$

where:

$$T(t) = e^{-\Gamma t'} \otimes R(t - t'), \quad (3.74)$$

K is a normalisation constant, Γ is the decay width of the Λ_b^0 baryon, A_{P} is the production asymmetry of the Λ_b^0 baryon, A_{f} is the detection asymmetry of the pK^- and $\bar{p}K^+$ final states and A_{CP} is the CP asymmetry of the $\Lambda_b^0 \rightarrow pK^-$ decay. The functions $\Omega^{\text{sig}}(t, \vec{\xi}_{\text{tag}}, \vec{\eta}_{\text{tag}})$ and $\bar{\Omega}^{\text{sig}}(t, \vec{\xi}_{\text{tag}}, \vec{\eta}_{\text{tag}})$ provide the probability of a Λ_b^0 baryon to be tagged

as a B meson or a \bar{B} meson, respectively. As for the other $B_{(s)}^0 \rightarrow h^+h'^-$ modes, they include the decay-time acceptance. Considering the very small contribution of this decay to the K^+K^- final state, the difference between Ω^{sig} and $\bar{\Omega}^{\text{sig}}$ is neglected and hence the total *pdf* is finally rewritten as: $K^{-1}T(t)\Omega^{\text{sig}}(t, \vec{\xi}_{\text{tag}}, \vec{\eta}_{\text{tag}})$

3.7.3 Partially-reconstructed background model

The partially-reconstructed background is studied from the left-hand sidebands of the invariant mass spectra. ($m \in [5.0, 5.2] \text{ GeV}/c^2$), that is dominated by the combinatorial and partially-reconstructed background components. The contribution of the former can be subtracted by injecting candidates taken from the right-hand sideband with negative weights. The strategy is analogous to that developed to subtract the combinatorial background from the data sample used to determine the signal decay-time acceptances (Section 3.5). In this case, the weights are:

$$w_i = - \frac{\int_{5.0 \text{ GeV}/c^2}^{5.2 \text{ GeV}/c^2} e^{-\alpha(t_i)m} dm}{\int_{5.6 \text{ GeV}/c^2}^{6.2 \text{ GeV}/c^2} e^{-\alpha(t_i)m} dm}. \quad (3.75)$$

The integration range at the numerator is changed, as compared to Eq. (3.26), to match the left-hand sideband limits.

The invariant mass distribution of the partially-reconstructed background is found to be independent of the other observables. Instead, the SS-tagger decision modifies the decay-time distribution, requiring to have distinct decays models for SS-tagged or SS-untagged candidates. In addition, the probability of an asymmetry in the tagging between $K^+\pi^-$ and π^+K^- final states is taken into account, as suggested by data. Finally, the tagging asymmetry between the $K^+\pi^-$ and $K^-\pi^+$ final states needs a parametrisation. The total *pdf* for the partially reconstructed background is given by the product:

$$p_{3\text{-body}_\psi}(m, t, \vec{\xi}_{\text{tag}}, \vec{\eta}_{\text{tag}}) = p_{3\text{-body}}(m) \cdot p_{3\text{-body}}(t|\xi_{\text{SS}}) \cdot p_{3\text{-body}}(\psi|\xi_{\text{OS}}, \xi_{\text{SS}}) \cdot \Omega_{\text{tag}}^{3\text{-body}}(\vec{\xi}_{\text{tag}}, \vec{\eta}_{\text{tag}}). \quad (3.76)$$

The following paragraphs describe the various factors.

Invariant mass model for 3-body backgrounds. The invariant mass shape comprises an ARGUS function [127], convolved with a double-gaussian resolution:

$$p_{3\text{-body}}(m) = A \cdot \left[m' \sqrt{1 - \frac{m'^2}{m_0^2}} \Theta(m_0 - m') e^{c \frac{m'}{m_0}} \right] \otimes G(m - m'; \delta_m, \sigma_1, \sigma_2, f_g), \quad (3.77)$$

where A is a normalization constant, c is a parameter governing the shape of the ARGUS function, G is a double Gaussian resolution model and \otimes stands for the convolution product. The parameters δ (common mean of the two Gaussian functions), σ_1 and σ_2 (width of the two Gaussian functions), and f_g (relative fraction between the two Gaussian functions) are shared with the resolution model used for the signal (Eq. (3.47)). The ARGUS function can parametrise both the partially reconstructed B^0 and B_s^0 decays. In the first case, the end point of the ARGUS (m_0) is set to $m_{B^0} - m_{\pi^0}$, whereas the value $m_{B_s^0} - m_{\pi^0}$ is used in the second case. The quantities m_{B^0} , $m_{B_s^0}$, and m_{π^0} are the world averages for the masses of the B^0 , B_s^0 , π^0 mesons, respectively [4]. The left-hand sideband

of the $\pi^+\pi^-$ sample is well described by a single ARGUS function, modelling the mass shape of partially-reconstructed B^0 -meson decays. Similarly, only partially-reconstructed B_s^0 -meson decays need to be modelled, in the K^+K^- sample. In the $K^\pm\pi^\mp$ spectrum, instead, both the components are necessary.

Decay-time model for 3-body backgrounds. These decay-time distributions are described with a non-parametric *pdf* determined by the application of the KDE method to the background-subtracted left-hand sideband. The SS-tagged and SS-untagged events present different shapes. Hence, the decay-time distribution of the partially-reconstructed background is a conditional *pdf*:

$$p_{3\text{-body}}(t|\xi_{\text{SS}}) = \delta_{|\xi_{\text{SS}}|,1} \frac{T_1(t)}{N_1} + \delta_{|\xi_{\text{SS}}|,0} \frac{T_0(t)}{N_0}, \quad (3.78)$$

where the $T_i(t)$ are the templates obtained from the application of the KDE method and the N_i are the corresponding normalisation constants.

Tagging probabilities. The *pdf* for the flavour-tagging observables are:

$$\Omega^{3\text{-body}}(\xi_{\text{OS}}, \xi_{\text{SS}}, \eta_{\text{OS}}, \eta_{\text{SS}}) = \Omega_{\text{OS}}^{3\text{-body}}(\xi_{\text{OS}}, \eta_{\text{OS}}) \cdot \Omega_{\text{SS}}^{3\text{-body}}(\xi_{\text{SS}}, \eta_{\text{SS}}), \quad (3.79)$$

where the parametrisations of the OS and SS probabilities are similar ($\text{tag} = \{\text{OS}, \text{SS}\}$)

$$\begin{aligned} \Omega_{\text{tag}}^{3\text{-body}}(\xi_{\text{tag}}, \eta_{\text{tag}}) = & \delta_{\xi_{\text{tag}},1} \varepsilon_{\text{tag}}^{3\text{-body}} h_{\text{tag}}^{3\text{-body}}(\eta_{\text{tag}}) + \delta_{\xi_{\text{tag}},-1} \bar{\varepsilon}_{\text{tag}}^{3\text{-body}} h_{\text{tag}}^{3\text{-body}}(\eta_{\text{tag}}) + \\ & \delta_{\xi_{\text{tag}},0} (1 - \varepsilon_{\text{tag}}^{3\text{-body}} - \bar{\varepsilon}_{\text{tag}}^{3\text{-body}}) U(\eta_{\text{tag}}). \end{aligned} \quad (3.80)$$

The parameters $\varepsilon_{\text{tag}}^{3\text{-body}}$ and $\bar{\varepsilon}_{\text{tag}}^{3\text{-body}}$ are the probabilities to tag a partially-reconstructed background candidate as B or \bar{B} , respectively; $h_{\text{tag}}^{3\text{-body}}(\eta_{\text{tag}})$ is the normalised distribution of η_{tag} for the partially-reconstructed background events. In the fit, the tagging probabilities are parametrised as a function of their average ($\hat{\varepsilon}_{\text{tag}}^{3\text{-body}}$) and their asymmetry ($\Delta\varepsilon_{\text{tag}}^{3\text{-body}}$):

$$\varepsilon_{\text{tag}}^{3\text{-body}} = \frac{\hat{\varepsilon}_{\text{tag}}^{3\text{-body}}}{2} (1 + \Delta\varepsilon_{\text{tag}}^{3\text{-body}}), \quad (3.81)$$

$$\bar{\varepsilon}_{\text{tag}}^{3\text{-body}} = \frac{\hat{\varepsilon}_{\text{tag}}^{3\text{-body}}}{2} (1 - \Delta\varepsilon_{\text{tag}}^{3\text{-body}}). \quad (3.82)$$

The templates used to parameterise $h_{\text{tag}}^{3\text{-body}}(\eta_{\text{tag}})$ are built from histograms filled with the background-subtracted candidates from the left-hand sideband.

Distinction between the $K^+\pi^-$ and $K^-\pi^+$ final states. For the $K^\pm\pi^\mp$ sample, the distinction between the cases $\psi = 1$ and $\psi = -1$ can not be neglected. To parametrise a global asymmetry, the variable $A_{\text{raw}}^{3\text{-body}}$ is introduced. Besides, the asymmetry between the flavour tagging efficiencies $\Delta\varepsilon_{\text{tag}}^{3\text{-body}}$ may depend on the final state. To include this possible effect, for both OS and SS taggers, two additional asymmetries have been introduced: $A_{\text{OS}}^{3\text{-body}}$ and $A_{\text{SS}}^{3\text{-body}}$. In this way, $\Delta\varepsilon_{\text{tag}}^{3\text{-body}}$ is the tagging-efficiency asymmetry averaged over the two different final states, while $A_{\text{OS}}^{3\text{-body}}$ and $A_{\text{SS}}^{3\text{-body}}$ differentiate the tagging-efficiency

asymmetry for $K^+\pi^-$ and $K^-\pi^+$ final states, respectively. These considerations lead to the function:

$$p_{3\text{-body}}(\psi|\xi_{\text{OS}}, \xi_{\text{SS}}) = \frac{(1 - \psi A_{\text{raw}}^{3\text{-body}})(1 - \psi \xi_{\text{OS}} A_{\text{OS}}^{3\text{-body}})(1 - \psi \xi_{\text{SS}} A_{\text{SS}}^{3\text{-body}})}{\sum_{\psi=-1,1} (1 - \psi A_{\text{raw}}^{3\text{-body}})(1 - \psi \xi_{\text{OS}} A_{\text{OS}}^{3\text{-body}})(1 - \psi \xi_{\text{SS}} A_{\text{SS}}^{3\text{-body}})}, \quad (3.83)$$

that is a probability function conditional to the tagging decisions $\vec{\xi}_{\text{tag}}$.

The final states of the $\pi^+\pi^-$ and K^+K^- samples are CP -conjugated of themselves, hence this probability function is unnecessary ($p_{3\text{-body}}(\psi|\xi_{\text{OS}}, \xi_{\text{OS}}) = 1$ when $\psi \in \{0, 2\}$).

3.7.4 Combinatorial background model

The determination of the model for the combinatorial background benefits from the right-hand sideband of the invariant mass distribution ($m \in [5.6, 6.2] \text{ GeV}/c^2$), where only this component is expected. In a very first approximation the invariant mass shape is an exponential function with a negative slope. However, further studies show that such slope depends on the decay time. In turn, this fact implies that the decay-time distribution can not be directly determined from the right-hand sideband. In addition, the invariant mass slope and the decay time distribution are correlated with the decisions of both the OS and SS taggers. Furthermore, the efficiency of the OS tagger depend on whether the SS tagger was able or not to take a decision. Last but not the least, the tagging efficiency may change between the $K^+\pi^-$ and the $K^-\pi^+$ samples. To consider all these effects, the combinatorial background *pdf* is written as:

$$p_{\text{comb}}(\vec{x}) = p_{\text{comb}}(m|t, \vec{\xi}_{\text{tag}}) \cdot p_{\text{comb}}(t|\vec{\xi}_{\text{tag}}) \cdot p_{\text{comb}}(\psi|\vec{\xi}_{\text{tag}}) \cdot \Omega^{\text{comb}}(\vec{\xi}_{\text{tag}}, \vec{\eta}_{\text{tag}}). \quad (3.84)$$

The following paragraphs explain the various terms.

Invariant mass model for the combinatorial backgrounds. The invariant mass shape is described using an exponential function of the kind

$$f(m) = N \exp(-\alpha m), \quad (3.85)$$

where m is the invariant mass, N is the normalisation constant and α is the slope of the exponential function. Figure 3.25 illustrates the dependency of the slope on the decay-time. The plot considers the sample surviving the selection optimised for $C_{\pi^+\pi^-}$ and $S_{\pi^+\pi^-}$. It is obtained by splitting the right-hand sideband of the $\pi^+\pi^-$ spectrum into bins of decay time with about 1000 entries each. Then an exponential function is fitted to the invariant mass distribution of each bin. The black dots report the slope value extracted by each fit, as a function of the averaged decay time inside the bin. Finally, the red curve is the result of the best fit to the data points with the empirical function:

$$\alpha(t) = p_0 \{1 + \tanh [p_1 (t - p_2)]\}, \quad (3.86)$$

where t is the decay time and the $\{p_i\}$ ($i = 0, 1, 2$) are parameters free to be adjusted by the fit. To remove any dependence on the binning scheme, the final values of the p_i parameters, fixed in the fit model,¹⁸ are actually extracted by unbinned maximum

¹⁸And in all the occurrences of the slope function $\alpha(t)$.

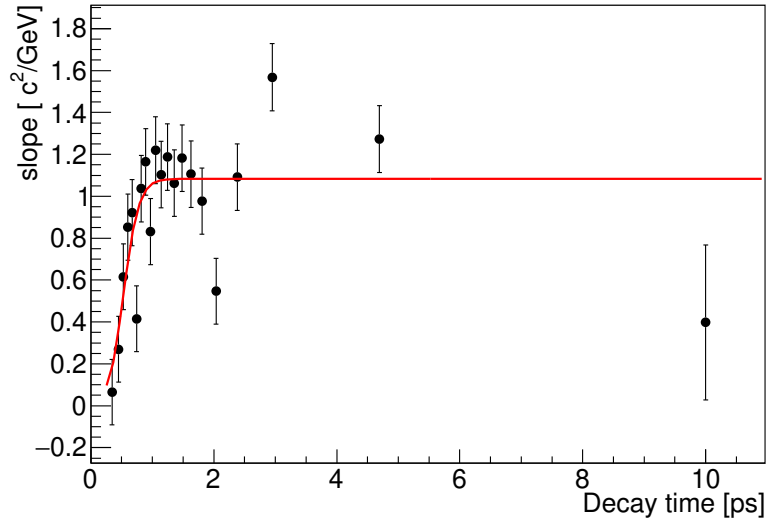


Figure 3.25: Values of the slope of the invariant mass model of Eq. 3.85, determined by fitting the events in the right-hand sideband of the $\pi^+\pi^-$ sample in bins of decay time. The red line is the result of the best fit to the points of the function in Eq. (3.86).

likelihood fits in mass and decay time. These fits consider the data of the right-hand sideband, separated according to the ability of the OS and SS taggers to take a decision, therefore, four slope functions are necessary to describe the mass distribution for each final state. The parameters p_i determined here are fixed in the final fit to the data. The total pdf describing the mass distribution of the combinatorial background is:

$$p_{\text{comb}}(m|t, \vec{\xi}_{\text{tag}}) = \sum_{j=0,1} \sum_{k=0,1} \delta_{|\xi_{\text{OS}}|,j} \delta_{|\xi_{\text{SS}}|,k} \frac{e^{-\alpha_{jk}(t)m}}{\int e^{-\alpha_{jk}(t)m'} dm'}, \quad (3.87)$$

The function $\alpha_{i,j}(t)$ returns the value of the mass slope, as a function of t , for the corresponding (j, k) -th tagging category ($(j, k) \in \{(0, 0), (0, 1), (1, 0), (1, 1)\}$).

Decay-time model for the combinatorial backgrounds. The dependency of the slope from the decay time means that the decay-time distribution of the combinatorial-background candidates observed in the right-hand sideband does not correspond to the decay-time distribution of the background candidates over the entire mass window. To study a model able to describe the shape of the decay-time distribution, the candidates in the right-hand sideband are weighted. The weight w_i associated to the i -th candidate is

$$w_i = \frac{\int_{5.0 \text{ GeV}/c^2}^{6.2 \text{ GeV}/c^2} e^{-\alpha(t_i)m} dm}{\int_{5.6 \text{ GeV}/c^2}^{6.2 \text{ GeV}/c^2} e^{-\alpha(t_i)m} dm}, \quad (3.88)$$

where $\alpha(t_i)$ is computed according to Eq. (3.86) and t_i is the decay time of the i -th candidate. Subsequently, the weighted sample is used as input for a KDE method [126], which provides a non-parametric shape. Both the invariant mass slope and the decay time depend on the ability of the OS and SS tagger to take a decision. Therefore, also

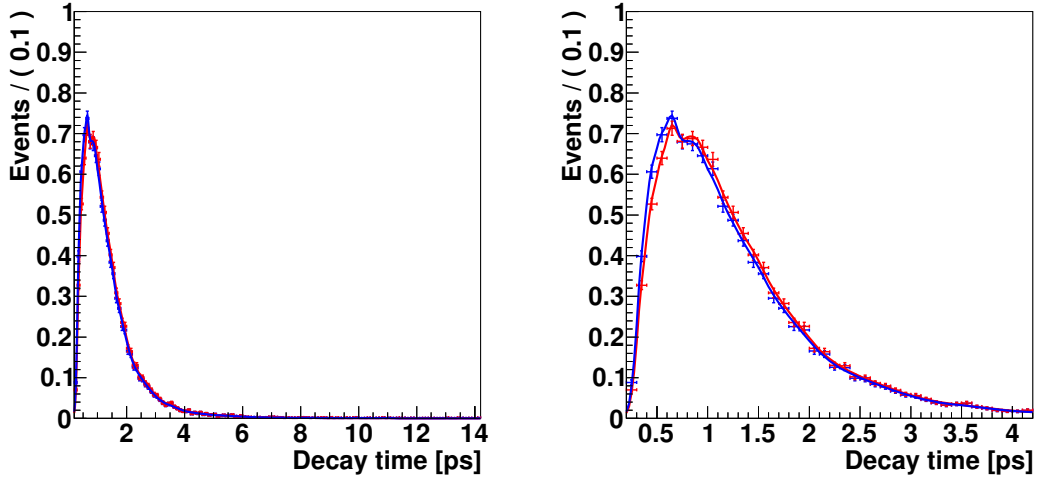


Figure 3.26: Decay-time distribution of candidates in the right-hand sideband ($5.6 < m < 6.2 \text{ GeV}/c^2$) of the $\pi^+\pi^-$ sample surviving the selection optimised for the measurement of $C_{\pi^+\pi^-}$ and $S_{\pi^+\pi^-}$. The red points correspond to the candidates weighted according to Eq. (3.86), while the blue points are obtained without considering the weights. The red and blue curve are the PDF obtained applying the KDE method to the two histograms. Histograms are normalised to the same area. On the right the plot is a zoomed version of the left plot.

the KDE method is applied on four exclusive subsamples for each spectrum. The *pdf* of decay time for the combinatorial background is formally written as:

$$p_{\text{comb}}(t|\vec{\xi}_{\text{tag}}) = \sum_{j=0,1} \sum_{k=0,1} \delta_{|\xi_{\text{OS}}|,j} \delta_{|\xi_{\text{SS}}|,k} \frac{T_{jk}(t)}{N_{jk}}, \quad (3.89)$$

where $T_{i,j}(t)$ is the template obtained by the KDE method and corresponding to the (j, k) -th tagging category; N_{ij} is its normalisation constant.

To visualise the effect of the weighting procedure, the decay-time distribution from the right-hand sideband of the $\pi^+\pi^-$ sample surviving the selection optimised for the $C_{\pi^+\pi^-}$ and $S_{\pi^+\pi^-}$ is reported in Figure 3.26, with and without the weights applied.

To show how much the shape of decay-time for combinatorial-background event changes depending on the invariant mass, Figure 3.27 shows the *pdf* of Eq. (3.84) projected on the decay time integrating over different ranges of invariant mass¹⁹.

Tagging probabilities. The *pdf* for the flavour tagging observables is:

$$\Omega^{\text{comb}}(\vec{\xi}_{\text{tag}}, \vec{\eta}_{\text{tag}}) = [\delta_{\xi_{\text{SS}},1} \varepsilon_{\text{SS}}^{\text{comb}} + \delta_{\xi_{\text{SS}},-1} \bar{\varepsilon}_{\text{SS}}^{\text{comb}}] h_{\text{SS}}^{\text{comb}}(\eta_{\text{SS}}) \Omega_{\text{OS},1}^{\text{comb}}(\xi_{\text{OS}}, \eta_{\text{OS}}) + \delta_{\xi_{\text{SS}},0} (1 - \varepsilon_{\text{SS}}^{\text{comb}} - \bar{\varepsilon}_{\text{SS}}^{\text{comb}}) U(\eta_{\text{SS}}) \Omega_{\text{OS},0}^{\text{comb}}(\xi_{\text{OS}}, \eta_{\text{OS}}), \quad (3.90)$$

¹⁹The double bump structure is an effect of the size of the kernel used in the KDE method that was tuned to follow the steep increase of the shape at low decay time and followed the dip in the data. That does not affect the fit to the CP asymmetries as it is compatible with a statistical fluctuation in data.

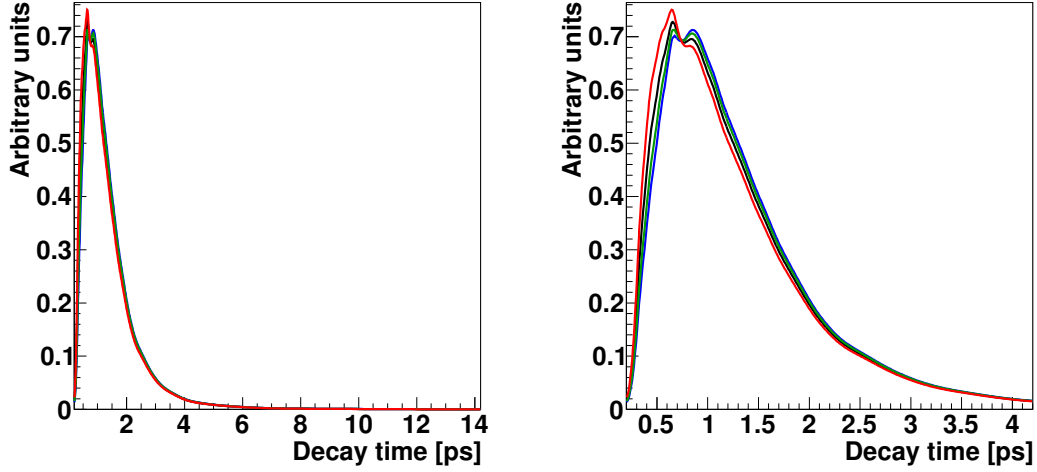


Figure 3.27: Projection on the decay-time of the PDF of combinatorial-background candidates described in Eq. (3.84). Each curve is obtained integrating over different ranges of invariant mass m : (red) $5.6 < m < 6.2 \text{ GeV}/c^2$, (green) $5.23 < m < 5.33 \text{ GeV}/c^2$, (blue) $m < 5.2 \text{ GeV}/c^2$ and (black) $5.0 < m < 6.2 \text{ GeV}/c^2$. The plot on the right is the zoomed version of the plot on the left.

where the functions $\Omega_{\text{OS},j}^{\text{comb}}(\xi_{\text{OS}}, \eta_{\text{OS}})$ ($j = 0, 1$) are the probability functions for the OS taggers and are defined as

$$\Omega_{\text{OS},j}^{\text{comb}}(\xi_{\text{OS}}, \eta_{\text{OS}}) = [\delta_{\xi_{\text{OS}},1} \varepsilon_{\text{OS},j}^{\text{comb}} + \delta_{\xi_{\text{OS}},-1} \bar{\varepsilon}_{\text{OS},j}^{\text{comb}}] h^{\text{comb}}(\eta_{\text{OS}}) + \delta_{\xi_{\text{OS}},0} (1 - \varepsilon_{\text{OS},j}^{\text{comb}} - \bar{\varepsilon}_{\text{OS},j}^{\text{comb}}) U(\eta_{\text{OS}}), \quad (3.91)$$

where: $h_{\text{tag}}^{\text{comb}}(\eta_{\text{tag}})$ is the distributions of η_{tag} described using histograms taken from the right-hand sideband (tag = OS, SS); U is a uniform distribution; $\varepsilon_{\text{tag}}^{\text{comb}}$ and $\bar{\varepsilon}_{\text{tag}}^{\text{comb}}$ are the efficiencies to tag a combinatorial background candidate as B or \bar{B} , respectively, by the corresponding tagger. For numerical reasons they are implemented as

$$\varepsilon_{\text{tag}}^{\text{comb}} = \frac{\hat{\varepsilon}_{\text{tag}}^{\text{comb}}}{2} (1 + \Delta\varepsilon_{\text{tag}}^{\text{comb}}), \quad (3.92)$$

$$\bar{\varepsilon}_{\text{tag}}^{\text{comb}} = \frac{\hat{\varepsilon}_{\text{tag}}^{\text{comb}}}{2} (1 - \Delta\varepsilon_{\text{tag}}^{\text{comb}}), \quad (3.93)$$

such that the fit to data determines the average efficiency to tag a combinatorial background as B or \bar{B} ($\hat{\varepsilon}_{\text{tag}}^{\text{comb}}$), and the asymmetry between the two efficiencies ($\Delta\varepsilon_{\text{tag}}^{\text{comb}}$). For the OS tagger, the distinction labelled by the index $j = 0, 1$ is used to differentiate the OS-tagging efficiency between cases that have $\xi_{\text{SS}} = 0$ ($i = 0$) and $\xi_{\text{SS}} \neq 0$ ($i = 1$). In this way, for example, $\hat{\varepsilon}_{\text{OS},0}^{\text{comb}}$ is the efficiency for the OS tagger to tag a combinatorial-background event in case the SS tagger has not been able to take a tagging decision, while $\hat{\varepsilon}_{\text{OS},1}^{\text{comb}}$ is the efficiency for the OS tagger to tag a combinatorial-background event in case the SS tagger has taken a tagging decision.

Distinction between the $K^+\pi^-$ and $K^-\pi^+$ final states. Concerning the distinction between the cases $\psi = \pm 1$, the same considerations already reported for the partially-

reconstructed background hold. Therefore, with an analogous notation:

$$p_{\text{comb}}(\psi|\xi_{\text{OS}}, \xi_{\text{SS}}) = \frac{(1 - \psi A_{\text{raw}}^{\text{comb}})(1 - \psi \xi_{\text{OS}} A_{\text{OS}}^{\text{comb}})(1 - \psi \xi_{\text{SS}} A_{\text{SS}}^{\text{comb}})}{\sum_{\psi=-1,1} (1 - \psi A_{\text{raw}}^{\text{comb}})(1 - \psi \xi_{\text{OS}} A_{\text{OS}}^{\text{comb}})(1 - \psi \xi_{\text{SS}} A_{\text{SS}}^{\text{comb}})}. \quad (3.94)$$

On the contrary: $p_{\text{comb}}(\psi|\xi_{\text{OS}}, \xi_{\text{SS}}) = 1$ when $\psi \in \{0, 2\}$.

3.7.5 Summary of the fixed parameters

The following parameters are fixed in the final fits to data:

- the parameters α_1 and α_2 appearing in Eq. (3.48) and governing the tail of the invariant mass signal model. Their values are listed in Table 3.25; besides, tail fraction f_{tail} and the fraction between the two resolution functions f_g (Eq.s (3.47)-(3.77)) are fixed to value determined from full simulation: 0.15 and 0.77, respectively;
- the end point of the ARGUS functions governing the partially reconstructed B decays, namely m_0 in Eq. (3.77); when the model describes B^0 partially reconstructed decays the end point is fixed to 5.1446 GeV/ c^2 , while when the model describes the B_s^0 partially reconstructed background the end point is fixed to 5.2318 GeV/ c^2 ;
- the shapes of the decay-time acceptances for the $B_{(s)}^0 \rightarrow h^+ h'^-$ decays are fixed according to the strategy described in Section 3.5;
- the values of Δm_d , Δm_s , $\Delta \Gamma_d$, Γ_s and $\Delta \Gamma_s$ for the B^0 and B_s^0 decays, entering Eqs. (3.51) and (3.51), are taken from HFLAV [138]. They are listed in Table 3.26. Instead, the value of Γ_d is left free to be adjusted by the fit as a further cross-check of the robustness of the procedure used to describe the decay-time acceptance;
- the mean and width of the Gaussian function accommodating the decay-time resolution, $R(t - t')$ in Eqs. (3.53) and (3.51), are fixed to the value reported in Table 3.18;
- the PID efficiencies $\varepsilon_{h^+ h'^-}$, governing the relative yields between the correctly identified and misidentified $B_{(s)}^0 \rightarrow h^+ h'^-$ decays (Eq. (3.70)), are obtained in Section 3.2;
- in the case of the measurement of $C_{K^+ K^-}$, $S_{K^+ K^-}$ and $A_{K^+ K^-}^{\Delta \Gamma}$, the parameters governing the calibration of the SS_K tagger for the B_s^0 mesons are fixed to those reported in Table 3.21;
- the parameters governing the dependency of the mass slope from the decay-time for the combinatorial background, namely p_0 , p_1 and p_2 in Eq. (3.86), are fixed by the fit to the right-hand sideband described in Section 3.7.4.

Table 3.26: Values of the parameters Δm_d , Δm_s , $\Delta\Gamma_d$, Γ_s and $\Delta\Gamma_s$ that are fixed in the fit to data. Used values corresponds to averages computed by the HFLAV collaboration [138]. In the case of Γ_s and $\Delta\Gamma_s$ the values are those reported in Ref. [141], *i.e.* the combination of the LHCb measurement of these quantities using $B_s^0 \rightarrow J/\psi K^+ K^-$ and $B_s^0 \rightarrow J/\psi \pi^+ \pi^-$ decays. Since these values will be used to determine a systematic uncertainty, we report also their errors. For the Γ_s and $\Delta\Gamma_s$ parameters we also report the correlation factor between these two quantities.

Parameter	Value
Δm_d	$0.5065 \pm 0.0019 \text{ ps}^{-1}$
$\Delta\Gamma_d$	0 ps^{-1}
$\rho(\Gamma_d, \Delta\Gamma_d)$	0
Δm_s	$17.757 \pm 0.021 \text{ ps}^{-1}$
Γ_s	$0.6562 \pm 0.0021 \text{ ps}^{-1}$
$\Delta\Gamma_s$	$0.082 \pm 0.005 \text{ ps}^{-1}$
$\rho(\Gamma_s, \Delta\Gamma_s)$	-0.170

3.8 Fit results

The fit model described in the previous Section is adapted to data with an unbinned maximum-likelihood fit, simultaneous to all the final-state samples. The most relevant physics results are reported in the following.

The yields of the various components are reported in Table 3.27. The parameters of the flavour tagging calibration for the OS and SS tagger (Equations (3.62) to (3.69)) are extracted directly from the fit, thanks to the flavour-specific $B^0 \rightarrow K^+ \pi^-$ decay²⁰. Their final values are listed in Table 3.28. The results for the production asymmetries of the B^0 and B_s^0 mesons are reported in Table 3.29. They are all consistent between the various years. The decay width of the B^0 meson obtained from the fits (Table 3.30) is in agreement with the world average.

The Figures 3.28 and 3.29 illustrate the raw time-dependent asymmetry of the $K^\pm \pi^\mp$ spectrum obtained from the invariant-mass region dominated by the $B^0 \rightarrow K^+ \pi^-$ decays ($m \in [5.20, 5.32] \text{ GeV}/c^2$) and by the $B_s^0 \rightarrow \pi^+ K^-$ decays ($m \in [5.32, 5.45] \text{ GeV}/c^2$), respectively. The quality of the fits is in general very good as shown by the Figures from 3.32 to 3.49. The statistical correlations among the CP -violation parameters are reported in the Table 3.31. The correlations between $C_{\pi^+\pi^-}$, $S_{\pi^+\pi^-}$, $A_{\text{raw}}^{B^0}$ and $A_{\text{raw}}^{B_s^0}$ are taken from the fits to the samples surviving the selection optimised for the $B^0 \rightarrow \pi^+ \pi^-$ decays. The correlations between $C_{K^+K^-}$, $S_{K^+K^-}$ and $A_{K^+K^-}^{\Delta\Gamma}$ are taken from the fit to the samples passing the selection optimised for the $B_s^0 \rightarrow K^+ K^-$ decays. For the remaining cases, the largest value between those observed by the two fits is assumed. The biggest correlation is that between $C_{\pi^+\pi^-}$ and $S_{\pi^+\pi^-}$ ($\approx 40\%$), whereas the other correlations are well below the 10%. For completeness, the Tables 3.32 and 3.33 document the correlation matrices relative to the two fit separately.

The CP -violation parameters obtained by this analysis, utilising the 2015-16 sample, are in agreement with the ones reported in the latest LHCb publication, and concerning the

²⁰And to much minor extent to the $B_s^0 \rightarrow \pi^+ K^-$ decay.

same data-taking period²¹:

Parameter	Ref. [24]	this thesis
	sample 2015-16	sample 2015-16
$C_{\pi^+\pi^-}$	-0.311 ± 0.045	-0.314 ± 0.047
$S_{\pi^+\pi^-}$	-0.706 ± 0.042	-0.708 ± 0.043
$A_{\text{raw}}^{B^0}$	-0.0903 ± 0.0033	-0.0905 ± 0.0034
$A_{\text{raw}}^{B_s^0}$	$+0.238 \pm 0.013$	$+0.238 \pm 0.013$
$C_{K^+K^-}$	$+0.164 \pm 0.034$	$+0.159 \pm 0.036$
$S_{K^+K^-}$	$+0.123 \pm 0.034$	$+0.137 \pm 0.036$
$A_{K^+K^-}^{\Delta\Gamma}$	-0.833 ± 0.054	-0.850 ± 0.056

where the $C_{\pi^+\pi^-}$, $S_{\pi^+\pi^-}$, $A_{\text{raw}}^{B^0}$ and $A_{\text{raw}}^{B_s^0}$ are taken from the fit to the events surviving the selection optimised for the $B^0 \rightarrow \pi^+\pi^-$ and using the OS and SS tagging information, while $C_{K^+K^-}$, $S_{K^+K^-}$ and $A_{K^+K^-}^{\Delta\Gamma}$ are obtained from the fit to the events surviving the selection optimised for the $B_s^0 \rightarrow K^+K^-$ and using the OS and SS_K tagging information. The CP violation parameters measured with 2017 and 2018 data samples are:

Parameter	this thesis	this thesis
	sample 2017	sample 2018
$C_{\pi^+\pi^-}$	-0.303 ± 0.050	-0.314 ± 0.047
$S_{\pi^+\pi^-}$	-0.738 ± 0.047	-0.727 ± 0.044
$A_{\text{raw}}^{B^0}$	-0.0901 ± 0.0038	-0.0856 ± 0.0035
$A_{\text{raw}}^{B_s^0}$	$+0.262 \pm 0.014$	$+0.246 \pm 0.013$
$C_{K^+K^-}$	-0.032 ± 0.037	$+0.011 \pm 0.032$
$S_{K^+K^-}$	$+0.133 \pm 0.037$	$+0.204 \pm 0.032$
$A_{K^+K^-}^{\Delta\Gamma}$	-1.008 ± 0.057	-0.952 ± 0.053

The raw asymmetries, $A_{\text{raw}}^{B^0}$ and $A_{\text{raw}}^{B_s^0}$, are consistent between the various years and, once they are corrected for the detection asymmetries reported in Tables 3.23 and 3.24, they lead to

Parameter	this thesis	this thesis
	sample 2017	sample 2018
$A_{CP}^{B^0}$	$-0.0887 \pm 0.0038 \pm 0.0042$	$-0.0831 \pm 0.0035 \pm 0.0042$
$A_{CP}^{B_s^0}$	$+0.261 \pm 0.014 \pm 0.004$	$+0.244 \pm 0.013 \pm 0.004$

where the first uncertainty is statistical, and the second comes from the uncertainties due to the detection-asymmetry corrections. These quantities are very compatible between all the data-taking periods. The CP -violation parameters of the $B^0 \rightarrow \pi^+\pi^-$ decay, $C_{\pi^+\pi^-}$ and $S_{\pi^+\pi^-}$, as well as the parameter $A_{K^+K^-}^{\Delta\Gamma}$ for the $B_s^0 \rightarrow K^+K^-$ decay are also consistent between all the data-taking periods. Instead, the values of $C_{K^+K^-}$ and $S_{K^+K^-}$ show a discrepancy exceeding the 3 standard deviations between the 2015-16 and the

²¹The slight increase of the statistical uncertainties is due to minor modifications in the setup of the BDT training, which reduced the signal and background yields. This effect was checked performing the analysis after the application of the old BDT. Since the overall change of the uncertainties is very small and the new BDT relies on a more recent version of the TMVA package, it was kept anyway as the baseline solution.

Table 3.27: Yields of all the components contributing to the final-state samples as determined from the fits to data.

Parameter	Selection $\pi^+\pi^-$		
	2015-16	2017	2018
$N(B^0 \rightarrow K^+\pi^-)$	111760 ± 360	92080 ± 320	104650 ± 350
$N(B^0 \rightarrow \pi^+\pi^-)$	36460 ± 210	29620 ± 190	34070 ± 200
$N(B_s^0 \rightarrow K^+K^-)$	47560 ± 250	40230 ± 230	46240 ± 240
$N(B_s^0 \rightarrow \pi^+K^-)$	8410 ± 120	6970 ± 110	7940 ± 120
$N(B_s^0 \rightarrow \pi^+\pi^-)$	1262 ± 59	1070 ± 52	1004 ± 53
$N(B^0 \rightarrow K^+K^-)_k$	760 ± 90	551 ± 81	712 ± 83
$N(\Lambda_b^0 \rightarrow pK^-)$	190 ± 48	165 ± 66	171 ± 55
$N(3 - \text{body}_{K^+K^-})$	5160 ± 100	4693 ± 97	4920 ± 110
$N(3 - \text{body}_{K^\pm\pi^\mp,1})$	19750 ± 290	15980 ± 250	17900 ± 260
$N(3 - \text{body}_{K^\pm\pi^\mp,2})$	4800 ± 310	3720 ± 270	4290 ± 280
$N(3 - \text{body}_{\pi^+\pi^-})$	23000 ± 170	17890 ± 150	20180 ± 150
$N(\text{COMB}_{K^+K^-})$	6480 ± 140	5090 ± 130	6000 ± 140
$N(\text{COMB}_{K^\pm\pi^\mp})$	9560 ± 140	7100 ± 120	7330 ± 120
$N(\text{COMB}_{\pi^+\pi^-})$	14390 ± 150	10830 ± 130	11580 ± 140

Parameter	Selection K^+K^-		
	2015-16	2017	2018
$N(B^0 \rightarrow K^+\pi^-)$	147140 ± 430	121540 ± 380	140330 ± 410
$N(B^0 \rightarrow \pi^+\pi^-)$	47290 ± 270	38620 ± 240	44420 ± 260
$N(B_s^0 \rightarrow K^+K^-)$	62810 ± 290	52950 ± 270	61440 ± 280
$N(B_s^0 \rightarrow \pi^+K^-)$	11170 ± 150	9290 ± 130	10600 ± 140
$N(B_s^0 \rightarrow \pi^+\pi^-)$	1590 ± 110	1406 ± 89	1287 ± 91
$N(B^0 \rightarrow K^+K^-)$	1111.737 ± 110	780 ± 95	1000 ± 100
$N(\Lambda_b^0 \rightarrow pK^-)$	150.744 ± 94	250 ± 100	140 ± 70
$N(3 - \text{body}_{K^+K^-})$	8420 ± 140	6530 ± 120	7750 ± 130
$N(3 - \text{body}_{K^\pm\pi^\mp,1})$	27250 ± 390	21940 ± 330	25420 ± 350
$N(3 - \text{body}_{K^\pm\pi^\mp,2})$	7300 ± 440	5950 ± 360	6260 ± 380
$N(3 - \text{body}_{\pi^+\pi^-})$	31520 ± 220	24650 ± 190	28360 ± 200
$N(\text{COMB}_{K^+K^-})$	24080 ± 220	19760 ± 200	20930 ± 200
$N(\text{COMB}_{K^\pm\pi^\mp})$	57670 ± 310	42070 ± 260	44160 ± 270
$N(\text{COMB}_{\pi^+\pi^-})$	84430 ± 360	61780 ± 300	65280 ± 310

other data-taking periods. This issue motivates the studies documented in the following Section 3.8.1. They have lead to the exclusion of several eventual sources of systematic error, however the cause of the discrepancy has not been found yet. At the time of writing this Thesis, the effect on the decay-time bias due to the VELO misalignment reported in Ref. [142] is under investigation thorough simulation studies.

Table 3.28: Values for the calibration parameters of the flavour tagging obtained from the fits. The value of $\hat{\eta}_{OS}$ and $\hat{\eta}_{SS}$ are fixed in the fit. The calibration parameters of SS are not determined for the Selection optimised for the $B_s^0 \rightarrow K^+K^-$, since the SS_K is used instead in that case. The values of the effective tagging powers (ε_{eff}) calculated from the fit results are also reported, distinguishing and combining SS and OS taggers.

Parameter	Selection $\pi^+\pi^-$		
	Year		
	2015-16	2017	2018
$\hat{\varepsilon}_{OS}^{sig}$	0.3694 ± 0.0015	0.3710 ± 0.0017	0.3714 ± 0.0016
$\Delta\varepsilon_{OS}^{sig}$	-0.0169 ± 0.0061	-0.0001 ± 0.0066	-0.0048 ± 0.0062
\hat{p}_0^{OS}	0.4041 ± 0.0038	0.3974 ± 0.0041	0.3966 ± 0.0038
Δp_0^{OS}	0.0102 ± 0.0050	0.0026 ± 0.0057	0.0188 ± 0.0053
\hat{p}_1^{OS}	0.834 ± 0.033	0.774 ± 0.036	0.835 ± 0.034
Δp_1^{OS}	0.020 ± 0.022	-0.024 ± 0.025	-0.031 ± 0.022
$\hat{\eta}_{OS}$ (fixed)	0.37	0.37	0.37
$\hat{\varepsilon}_{SS}^{sig}$	0.8580 ± 0.0011	0.8594 ± 0.0012	0.8609 ± 0.0010
$\Delta\varepsilon_{SS}^{sig}$	0.0009 ± 0.0018	0.0004 ± 0.0019	-0.0011 ± 0.0016
\hat{p}_0^{SS}	0.4364 ± 0.0025	0.4391 ± 0.0027	0.439 ± 0.0025
Δp_0^{SS}	0.0056 ± 0.0035	0.0103 ± 0.0038	0.0105 ± 0.0035
\hat{p}_1^{SS}	0.980 ± 0.051	1.007 ± 0.056	0.895 ± 0.053
Δp_1^{SS}	0.014 ± 0.033	-0.068 ± 0.034	-0.018 ± 0.037
$\hat{\eta}_{SS}$ (fixed)	0.44	0.44	0.44
$\varepsilon_{eff}(OS)$ [%]	3.0 ± 0.2	3.2 ± 0.2	3.3 ± 0.2
$\varepsilon_{eff}(SS)$ [%]	1.6 ± 0.2	1.6 ± 0.2	1.5 ± 0.2
$\varepsilon_{eff}(Tot)$ [%]	4.5 ± 0.2	4.7 ± 0.2	4.7 ± 0.2

Parameter	Selection K^+K^-		
	Year		
	2015-16	2017	2018
$\hat{\varepsilon}_{OS}^{sig}$	0.3699 ± 0.0013	0.3706 ± 0.0015	0.3713 ± 0.0014
$\Delta\varepsilon_{OS}^{sig}$	-0.0079 ± 0.0051	0.0059 ± 0.0056	-0.0042 ± 0.0051
\hat{p}_0^{OS}	0.4029 ± 0.0033	0.3990 ± 0.0036	0.3950 ± 0.0033
Δp_0^{OS}	0.0136 ± 0.0046	0.0019 ± 0.0051	0.0185 ± 0.0047
\hat{p}_1^{OS}	0.848 ± 0.029	0.817 ± 0.032	0.834 ± 0.029
Δp_1^{OS}	0.025 ± 0.020	0.004 ± 0.022	-0.006 ± 0.020
$\hat{\eta}_{OS}$ (fixed)	0.37	0.37	0.37
$\varepsilon_{eff}(OS)$ [%]	3.9 ± 0.2	4.0 ± 0.2	4.0 ± 0.2
$\varepsilon_{eff}(SS_K)$ [%]	1.4 ± 0.2	1.3 ± 0.2	1.7 ± 0.2
$\varepsilon_{eff}(Tot)$ [%]	5.1 ± 0.2	5.2 ± 0.2	5.4 ± 0.2

Table 3.29: Final fit results for the production asymmetries of B^0 and B_s^0 mesons.

Parameter	Selection $\pi^+\pi^-$		
	Year		
	2015-16	2017	2018
$A_P(B^0)$ [%]	-0.15 ± 0.53	-0.49 ± 0.57	-0.51 ± 0.53
$A_P(B_s^0)$ [%]	-0.6 ± 1.9	-0.1 ± 2.0	-2.0 ± 1.8

Parameter	Selection K^+K^-		
	Year		
	2015-16	2017	2018
$A_P(B^0)$ [%]	-0.54 ± 0.48	-0.63 ± 0.52	-0.67 ± 0.49
$A_P(B_s^0)$ [%]	-0.9 ± 1.5	-1.1 ± 1.6	-2.9 ± 1.4

Table 3.30: Final fit results for the effective decay rate of B^0 .

Parameter	Selection $\pi^+\pi^-$		
	Year		
	2015-16	2017	2018
Γ_d [ps^{-1}]	0.6561 ± 0.0019	0.6566 ± 0.0021	0.6598 ± 0.0020

Parameter	Selection K^+K^-		
	Year		
	2015-16	2017	2018
Γ_d [ps^{-1}]	0.6562 ± 0.0018	0.6563 ± 0.0019	0.6580 ± 0.0018

Table 3.31: Statistical correlation among CP violation parameters.

Year 2015-16							
	$C_{\pi^+\pi^-}$	$S_{\pi^+\pi^-}$	$A_{\text{raw}}^{B^0}$	$A_{\text{raw}}^{B_s^0}$	$C_{K^+K^-}$	$S_{K^+K^-}$	$A_{K^+K^-}^{\Delta\Gamma}$
$C_{\pi^+\pi^-}$	1.000						
$S_{\pi^+\pi^-}$	0.379	1.000					
$A_{\text{raw}}^{B^0}$	-0.022	0.017	1.000				
$A_{\text{raw}}^{B_s^0}$	0.000	0.000	0.055	1.000			
$C_{K^+K^-}$	-0.009	-0.038	0.003	0.000	1.000		
$S_{K^+K^-}$	-0.008	0.008	-0.006	0.002	-0.067	1.000	
$A_{K^+K^-}^{\Delta\Gamma}$	0.000	0.000	0.002	0.000	0.025	0.019	1.000
Year 2017							
	$C_{\pi^+\pi^-}$	$S_{\pi^+\pi^-}$	$A_{\text{raw}}^{B^0}$	$A_{\text{raw}}^{B_s^0}$	$C_{K^+K^-}$	$S_{K^+K^-}$	$A_{K^+K^-}^{\Delta\Gamma}$
$C_{\pi^+\pi^-}$	1.000						
$S_{\pi^+\pi^-}$	0.377	1.000					
$A_{\text{raw}}^{B^0}$	-0.005	0.018	1.000				
$A_{\text{raw}}^{B_s^0}$	0.000	0.000	0.053	1.000			
$C_{K^+K^-}$	0.002	-0.002	0.001	0.000	1.000		
$S_{K^+K^-}$	-0.008	-0.031	-0.001	0.000	-0.003	1.000	
$A_{K^+K^-}^{\Delta\Gamma}$	0.000	0.000	0.001	0.000	-0.006	0.025	1.000
Year 2018							
	$C_{\pi^+\pi^-}$	$S_{\pi^+\pi^-}$	$A_{\text{raw}}^{B^0}$	$A_{\text{raw}}^{B_s^0}$	$C_{K^+K^-}$	$S_{K^+K^-}$	$A_{K^+K^-}^{\Delta\Gamma}$
$C_{\pi^+\pi^-}$	1.000						
$S_{\pi^+\pi^-}$	0.374	1.000					
$A_{\text{raw}}^{B^0}$	-0.005	0.012	1.000				
$A_{\text{raw}}^{B_s^0}$	0.000	0.000	0.053	1.000			
$C_{K^+K^-}$	0.002	-0.013	0.003	0.000	1.000		
$S_{K^+K^-}$	-0.017	-0.022	-0.003	0.000	-0.002	1.000	
$A_{K^+K^-}^{\Delta\Gamma}$	0.000	0.000	0.002	0.000	-0.005	0.030	1.000

Table 3.32: Statistical correlation among CP violation parameters obtained from the fit to the sample surviving the selection optimised for the $B^0 \rightarrow \pi^+\pi^-$ decay. From top to bottom: 2015-16, 2017, and 2018 sample.

Year 2015-16							
	$C_{\pi^+\pi^-}$	$S_{\pi^+\pi^-}$	$A_{\text{raw}}^{B^0}$	$A_{\text{raw}}^{B_s^0}$	$C_{K^+K^-}$	$S_{K^+K^-}$	$A_{K^+K^-}^{\Delta\Gamma}$
$C_{\pi^+\pi^-}$	1.000						
$S_{\pi^+\pi^-}$	0.379	1.000					
$A_{\text{raw}}^{B^0}$	-0.022	0.017	1.000				
$A_{\text{raw}}^{B_s^0}$	0.000	0.000	0.055	1.000			
$C_{K^+K^-}$	-0.009	-0.038	0.003	0.000	1.000		
$S_{K^+K^-}$	-0.008	0.008	-0.006	0.002	-0.067	1.000	
$A_{K^+K^-}^{\Delta\Gamma}$	0.000	0.000	0.001	0.000	0.025	0.019	1.000
Year 2017							
	$C_{\pi^+\pi^-}$	$S_{\pi^+\pi^-}$	$A_{\text{raw}}^{B^0}$	$A_{\text{raw}}^{B_s^0}$	$C_{K^+K^-}$	$S_{K^+K^-}$	$A_{K^+K^-}^{\Delta\Gamma}$
$C_{\pi^+\pi^-}$	1.000						
$S_{\pi^+\pi^-}$	0.377	1.000					
$A_{\text{raw}}^{B^0}$	-0.005	0.018	1.000				
$A_{\text{raw}}^{B_s^0}$	0.000	0.000	0.053	1.000			
$C_{K^+K^-}$	0.002	0.000	0.000	0.000	1.000		
$S_{K^+K^-}$	-0.008	-0.031	0.000	0.000	0.000	1.000	
$A_{K^+K^-}^{\Delta\Gamma}$	0.000	0.000	0.001	0.000	-0.011	0.030	1.000
Year 2018							
	$C_{\pi^+\pi^-}$	$S_{\pi^+\pi^-}$	$A_{\text{raw}}^{B^0}$	$A_{\text{raw}}^{B_s^0}$	$C_{K^+K^-}$	$S_{K^+K^-}$	$A_{K^+K^-}^{\Delta\Gamma}$
$C_{\pi^+\pi^-}$	1.000						
$S_{\pi^+\pi^-}$	0.374	1.000					
$A_{\text{raw}}^{B^0}$	-0.005	0.012	1.000				
$A_{\text{raw}}^{B_s^0}$	0.000	0.000	0.053	1.000			
$C_{K^+K^-}$	0.002	-0.011	0.003	0.000	1.000		
$S_{K^+K^-}$	-0.017	-0.022	-0.003	0.000	-0.022	1.000	
$A_{K^+K^-}^{\Delta\Gamma}$	0.000	0.000	0.001	0.000	0.000	0.031	1.000

Table 3.33: Statistical correlation among CP violation parameters obtained from the fit to the sample surviving the selection optimised for the $B_s^0 \rightarrow K^+K^-$ decay. From top to bottom: 2015-16, 2017, and 2018 sample.

Year 2015-16							
	$C_{\pi^+\pi^-}$	$S_{\pi^+\pi^-}$	$A_{\text{raw}}^{B^0}$	$A_{\text{raw}}^{B_s^0}$	$C_{K^+K^-}$	$S_{K^+K^-}$	$A_{K^+K^-}^{\Delta\Gamma}$
$C_{\pi^+\pi^-}$	1.000						
$S_{\pi^+\pi^-}$	0.399	1.000					
$A_{\text{raw}}^{B^0}$	-0.038	0.011	1.000				
$A_{\text{raw}}^{B_s^0}$	0.000	0.000	0.048	1.000			
$C_{K^+K^-}$	-0.008	-0.027	0.002	0.000	1.000		
$S_{K^+K^-}$	-0.008	-0.001	-0.003	0.000	-0.016	1.000	
$A_{K^+K^-}^{\Delta\Gamma}$	0.000	0.000	0.002	0.000	0.028	0.026	1.000
Year 2017							
	$C_{\pi^+\pi^-}$	$S_{\pi^+\pi^-}$	$A_{\text{raw}}^{B^0}$	$A_{\text{raw}}^{B_s^0}$	$C_{K^+K^-}$	$S_{K^+K^-}$	$A_{K^+K^-}^{\Delta\Gamma}$
$C_{\pi^+\pi^-}$	1.000						
$S_{\pi^+\pi^-}$	0.415	1.000					
$A_{\text{raw}}^{B^0}$	0.011	0.028	1.000				
$A_{\text{raw}}^{B_s^0}$	0.000	0.000	0.044	1.000			
$C_{K^+K^-}$	0.002	-0.002	0.001	0.000	1.000		
$S_{K^+K^-}$	-0.008	-0.014	-0.001	0.000	-0.003	1.000	
$A_{K^+K^-}^{\Delta\Gamma}$	0.000	0.000	0.001	0.000	-0.006	0.025	1.000
Year 2018							
	$C_{\pi^+\pi^-}$	$S_{\pi^+\pi^-}$	$A_{\text{raw}}^{B^0}$	$A_{\text{raw}}^{B_s^0}$	$C_{K^+K^-}$	$S_{K^+K^-}$	$A_{K^+K^-}^{\Delta\Gamma}$
$C_{\pi^+\pi^-}$	1.000						
$S_{\pi^+\pi^-}$	0.389	1.000					
$A_{\text{raw}}^{B^0}$	-0.016	0.017	1.000				
$A_{\text{raw}}^{B_s^0}$	0.000	0.000	0.045	1.000			
$C_{K^+K^-}$	0.000	-0.013	0.002	0.000	1.000		
$S_{K^+K^-}$	-0.007	-0.009	-0.003	0.000	-0.002	1.000	
$A_{K^+K^-}^{\Delta\Gamma}$	0.000	0.000	0.002	0.000	-0.005	0.030	1.000

Plots of time-dependent asymmetries for $B^0 \rightarrow K^+\pi^-$ decays

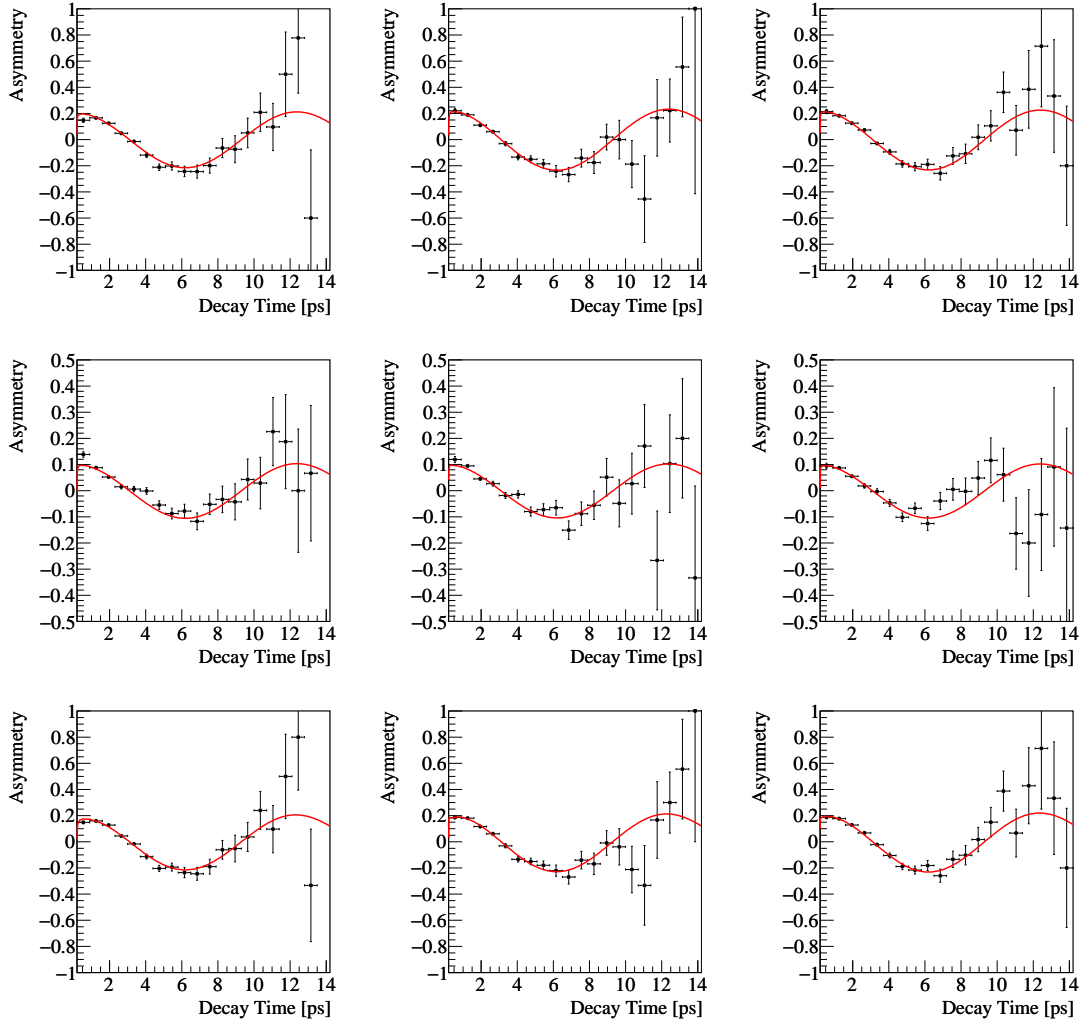


Figure 3.28: Raw time-dependent asymmetry for the $K^\pm\pi^\mp$ spectrum in the invariant mass region dominated by the $B^0 \rightarrow K^+\pi^-$ decay, $m_{K^\pm\pi^\mp} \in [5.20, 5.32] \text{ GeV}/c^2$. The asymmetries observed using the OS-tagger decision and SS-tagger decision for events surviving the selection optimised for the $B^0 \rightarrow \pi^+\pi^-$ decay are shown in the top and middle rows, respectively. The bottom row displays the asymmetry observed using the OS-tagger decision, for events surviving the selection optimised for the $B_s^0 \rightarrow K^+K^-$ decay. The left, middle and right columns correspond to the 2015-15, 2017, and 2018 data-taking period, respectively. The red line is the projection of the best fit to data for the total *pdfs*.

Plots of time-dependent asymmetries for $B_s^0 \rightarrow \pi^+ K^-$ decays

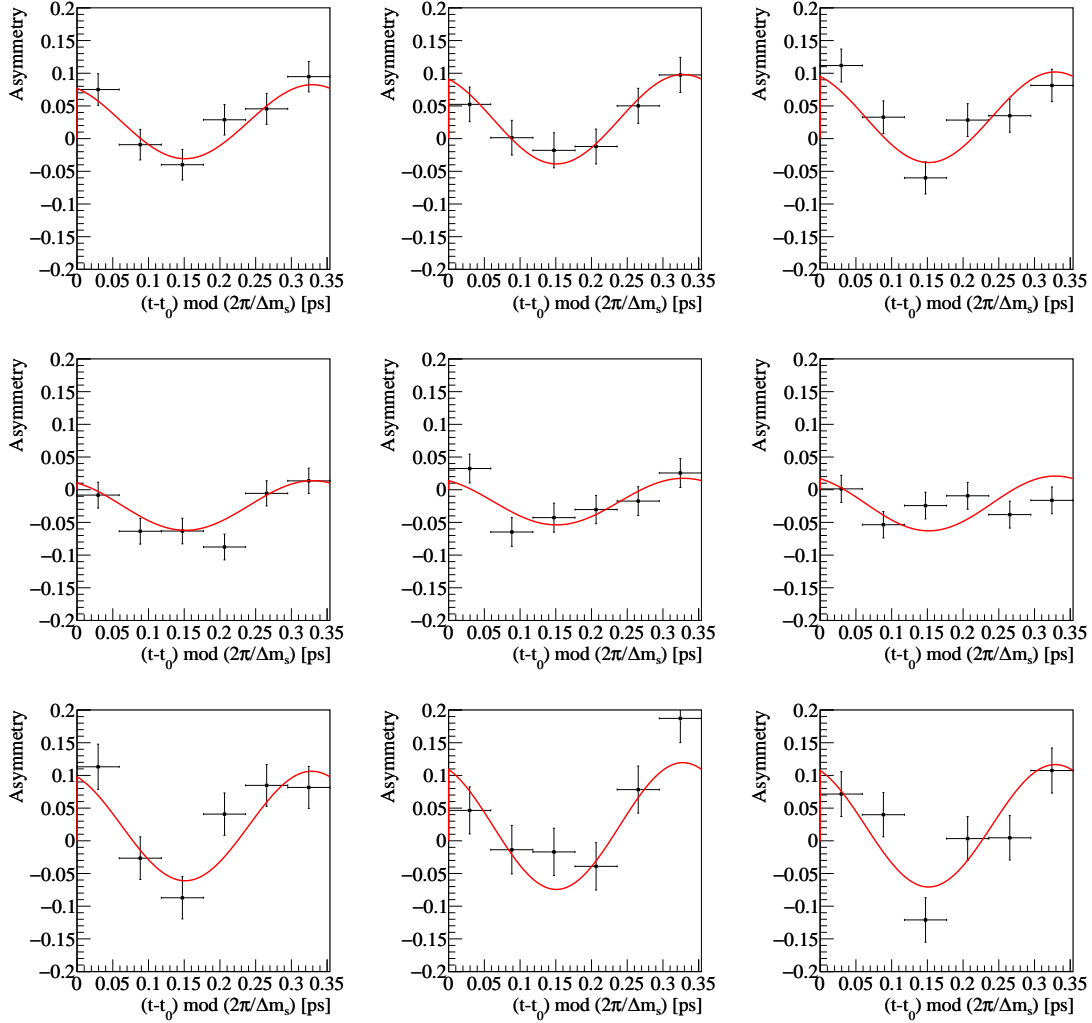


Figure 3.29: Raw time-dependent asymmetry for the $K^\pm \pi^\mp$ spectrum for the invariant mass region where most of the $B_s^0 \rightarrow \pi^+ K^-$ decays are lying ($m_{K^\pm \pi^\mp} \in [5.32, 5.45] \text{ GeV}/c^2$). The asymmetries observed using the OS-tagger decision and SS_K -tagger decision for events surviving the selection optimised for the $B_s^0 \rightarrow K^+ K^-$ decay are shown in the top and middle rows, respectively. The bottom row displays the asymmetry observed using the OS-tagger decision, for events surviving the selection optimised for the $B^0 \rightarrow \pi^+ \pi^-$ decay. The left, middle and right columns correspond to the 2015-15, 2017, and 2018 data-taking period, respectively. The red line is the projection of the best fit to data for the total $pdfs$.

Plots of time-dependent asymmetries for $B^0 \rightarrow \pi^+\pi^-$ decays

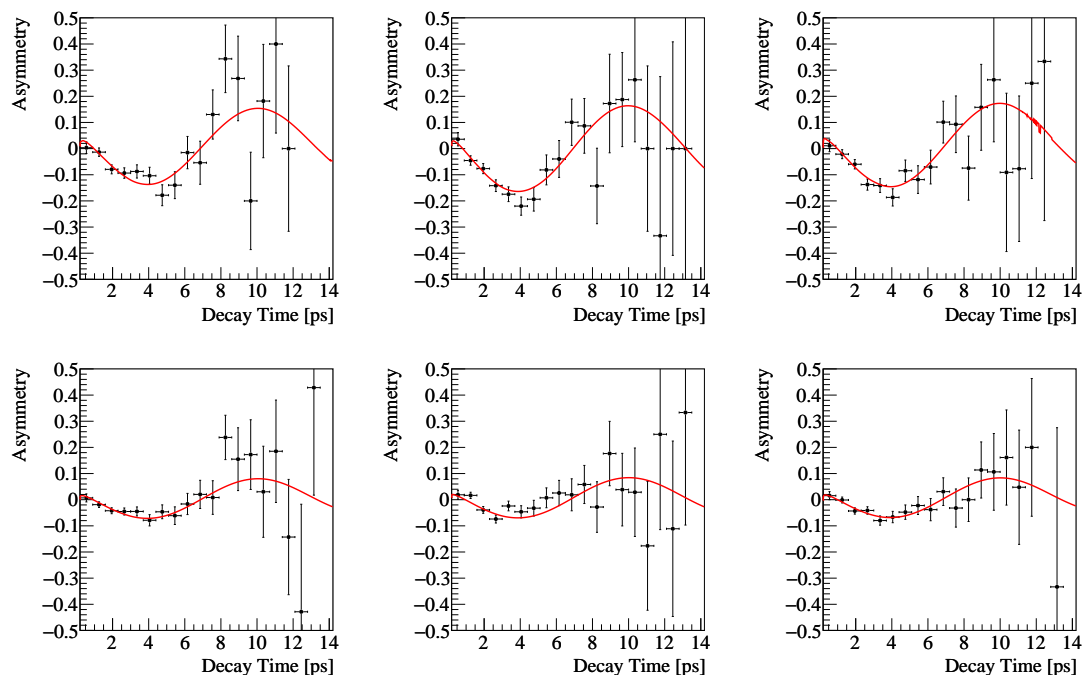


Figure 3.30: Time-dependent asymmetry for the $\pi^+\pi^-$ sample surviving the selection optimised for $C_{\pi^+\pi^-}$ and $S_{\pi^+\pi^-}$. Only the candidates in the mass regions dominated by the signals ($m_{\pi^+\pi^-} \in [5.20, 5.35] \text{ GeV}/c^2$) are used. The OS-tagger (SS-tagger) decision is used in the first (second) row. The columns correspond to the 2015-16, 2017, and 2018 data taking periods, respectively. The red lines are the projections of the best fits to data for the total $pdfs$.

Plots of time-dependent asymmetries for $B_s^0 \rightarrow K^+K^-$ decays

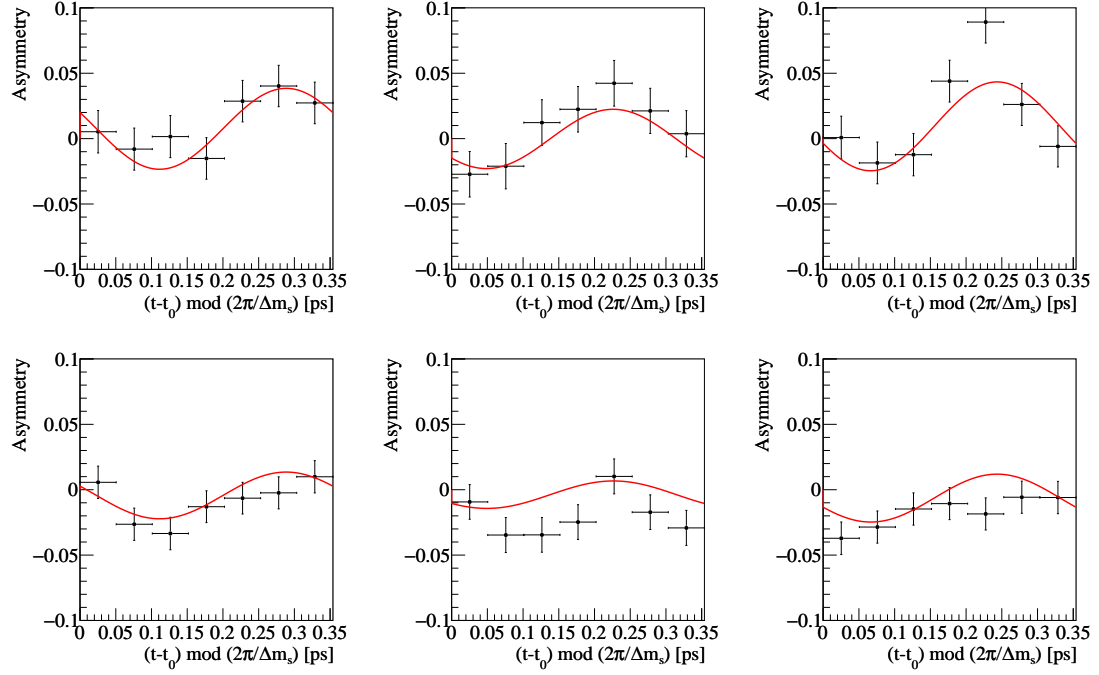


Figure 3.31: Time-dependent asymmetry for the K^+K^- sample surviving the selection optimised for $C_{K^+K^-}$, $S_{K^+K^-}$ and $A_{K^+K^-}^{\Delta\Gamma}$. Only the candidates in the mass regions dominated by the signals ($m_{K^+K^-} \in [5.30, 5.44] \text{ GeV}/c^2$) are used. The OS-tagger (SS $_K$ -tagger) decision is used in the first (second) row. The columns correspond to the 2015-16, 2017, and 2018 data taking periods, respectively. The red lines are the projections of the best fits to data for the total $pdfs$.

Fit projections, 2015-16 data samples

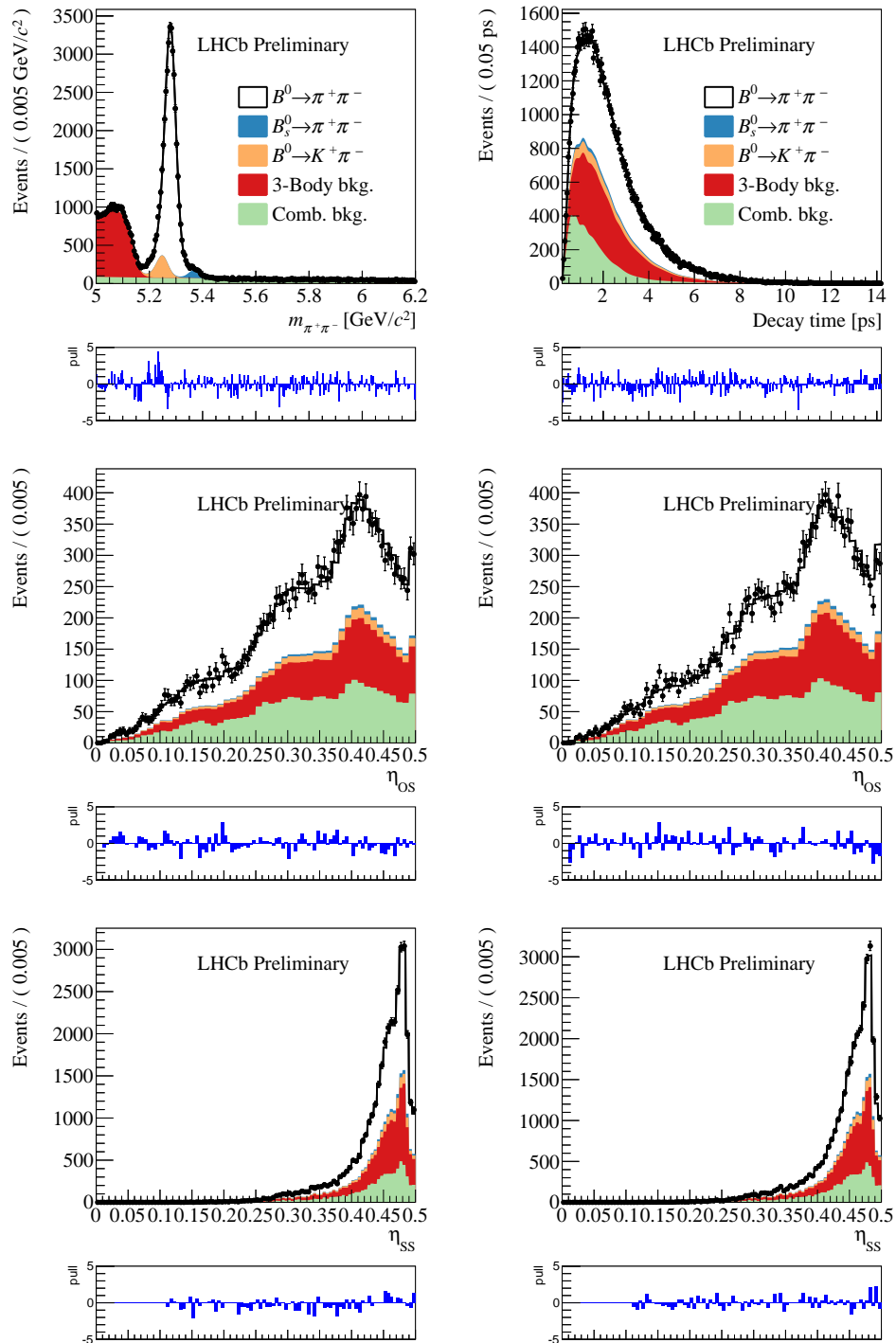


Figure 3.32: Distribution of events in the $\pi^+ \pi^-$ sample surviving the requirements optimised for the determination of $C_{\pi^+ \pi^-}$ and $S_{\pi^+ \pi^-}$. The distribution of (top left) mass, (top right) decay time, η_{OS} for events tagged as (middle left) B and (middle right) \bar{B} , η_{SSc} for events tagged as (bottom left) B and (bottom right) \bar{B} , are shown with the projection of the result of the best fit superimposed. Year of data-taking: 2015-16.

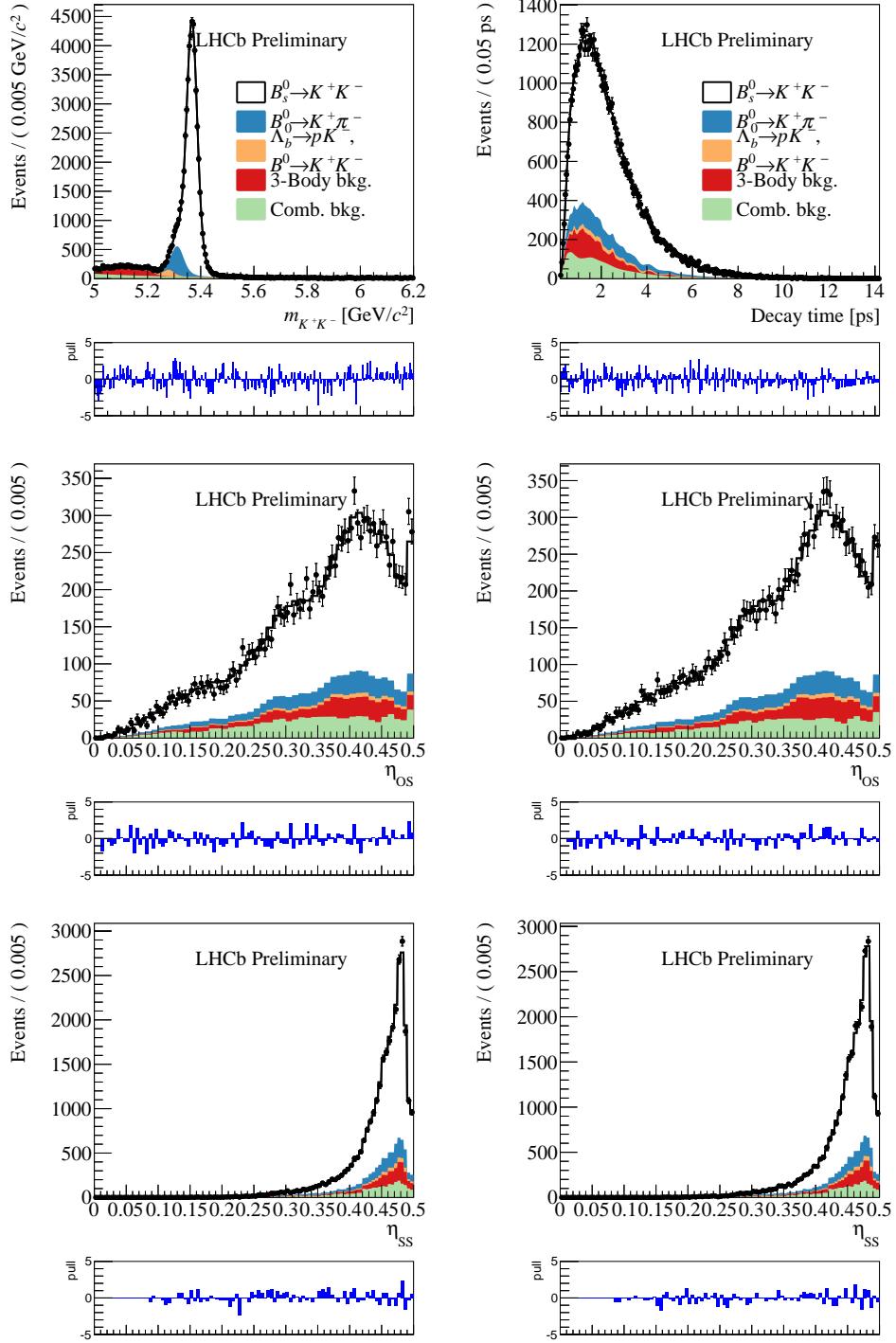


Figure 3.33: Distribution of events in the K^+K^- sample surviving the requirements optimised for the determination of $C_{\pi^+\pi^-}$ and $S_{\pi^+\pi^-}$. The distribution of (top left) mass, (top right) decay time, η_{OS} for events tagged as (middle left) B and (middle right) \bar{B} , η_{SSc} for events tagged as (bottom left) B and (bottom right) \bar{B} , are shown with the projection of the result of the best fit superimposed. Year of data-taking: 2015-16.

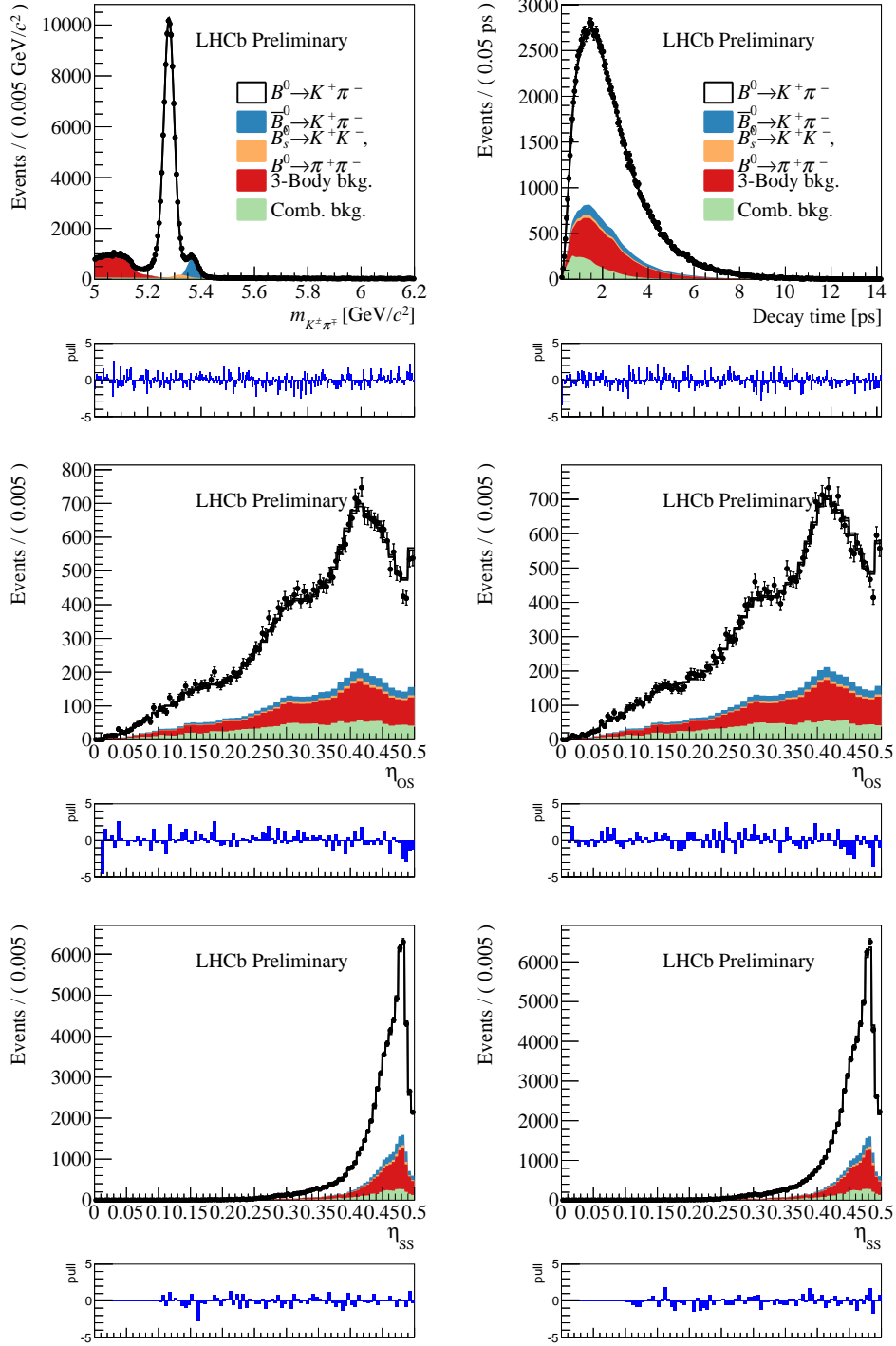


Figure 3.34: Distribution of events in the $K^+\pi^-$ sample surviving the requirements optimised for the determination of $C_{\pi^+\pi^-}$ and $S_{\pi^+\pi^-}$. The distribution of (top left) mass, (top right) decay time, η_{OS} for events tagged as (middle left) B and (middle right) \bar{B} , η_{SSc} for events tagged as (bottom left) B and (bottom right) \bar{B} , are shown with the projection of the result of the best fit superimposed. Year of data-taking: 2015-16.

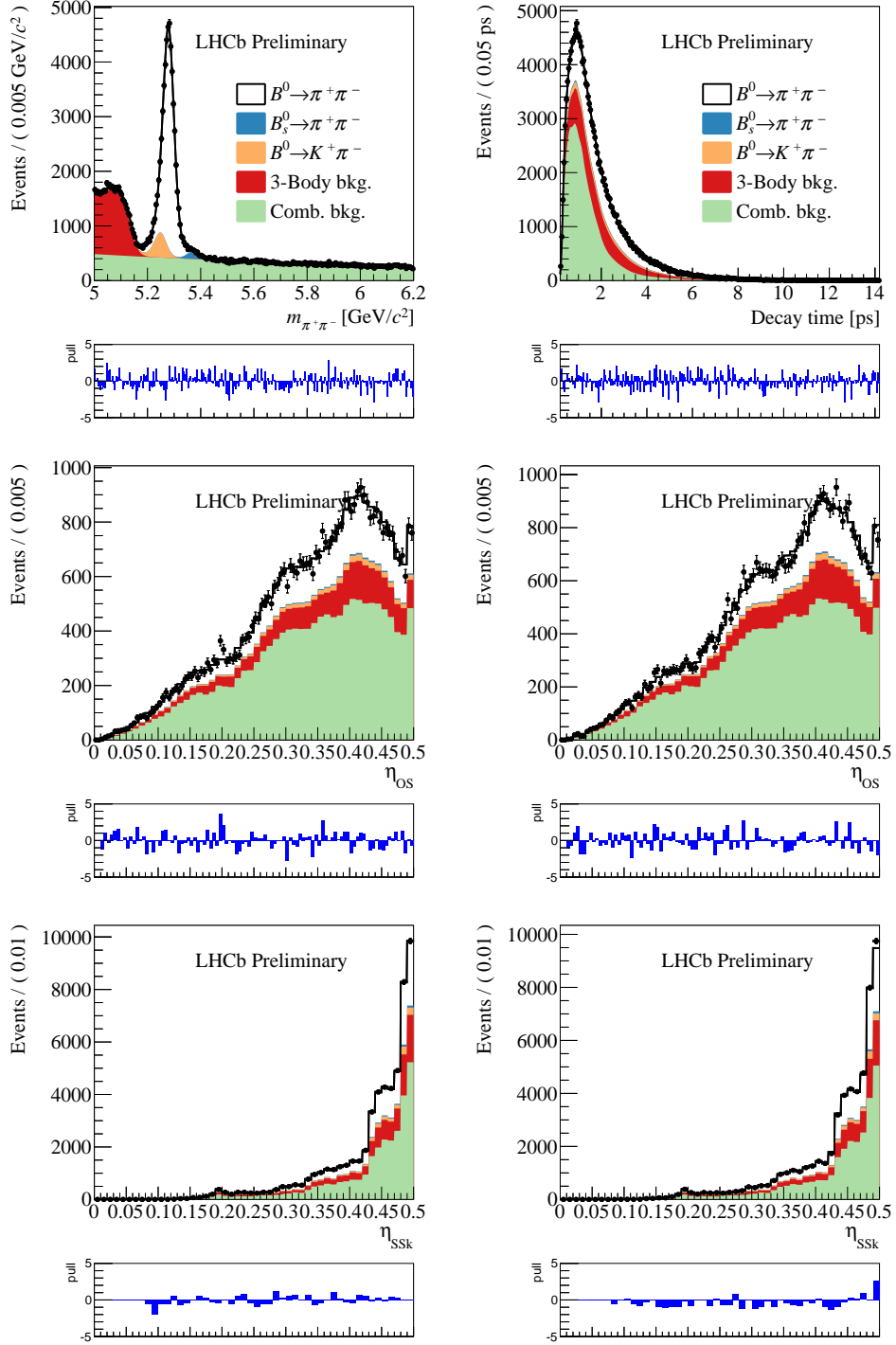


Figure 3.35: Distribution of events in the $\pi^+ \pi^-$ sample surviving the requirements optimised for the determination of $C_{K^+ K^-}$, $S_{K^+ K^-}$ and $A_{K^+ K^-}^{\Delta\Gamma}$. The distribution of (top left) mass, (top right) decay time, η_{OS} for events tagged as (middle left) B and (middle right) \bar{B} , η_{SSK} for events tagged as (bottom left) B and (bottom right) \bar{B} , are shown with the projection of the result of the best fit superimposed. Year of data-taking: 2015-16.

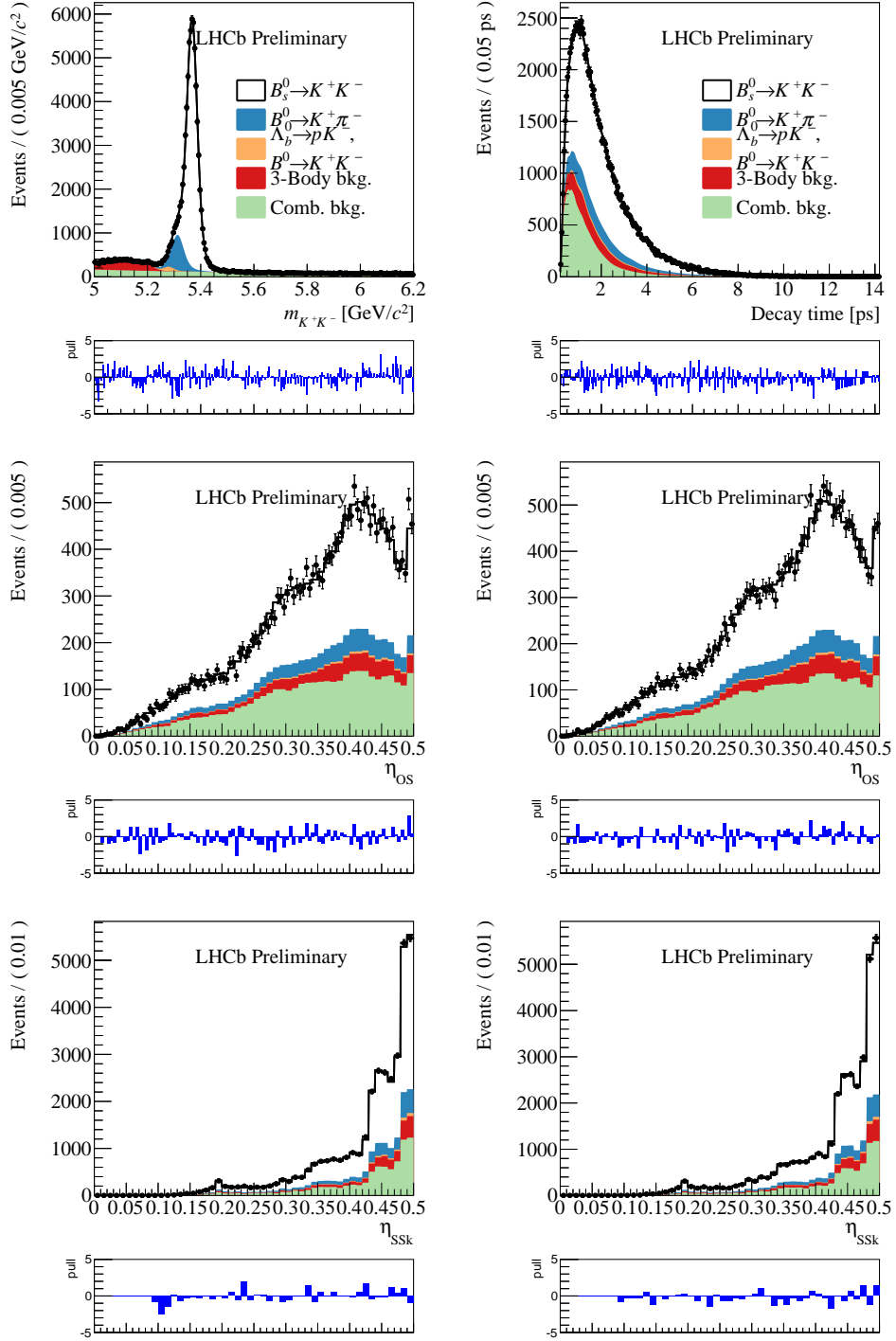


Figure 3.36: Distribution of events in the K^+K^- sample surviving the requirements optimised for the determination of $C_{K^+K^-}$, $S_{K^+K^-}$ and $A_{K^+K^-}^{\Delta\Gamma}$. The distribution of (top left) mass, (top right) decay time, η_{OS} for events tagged as (middle left) B and (middle right) \bar{B} , η_{SSK} for events tagged as (bottom left) B and (bottom right) \bar{B} , are shown with the projection of the result of the best fit superimposed. Year of data-taking: 2015-16.

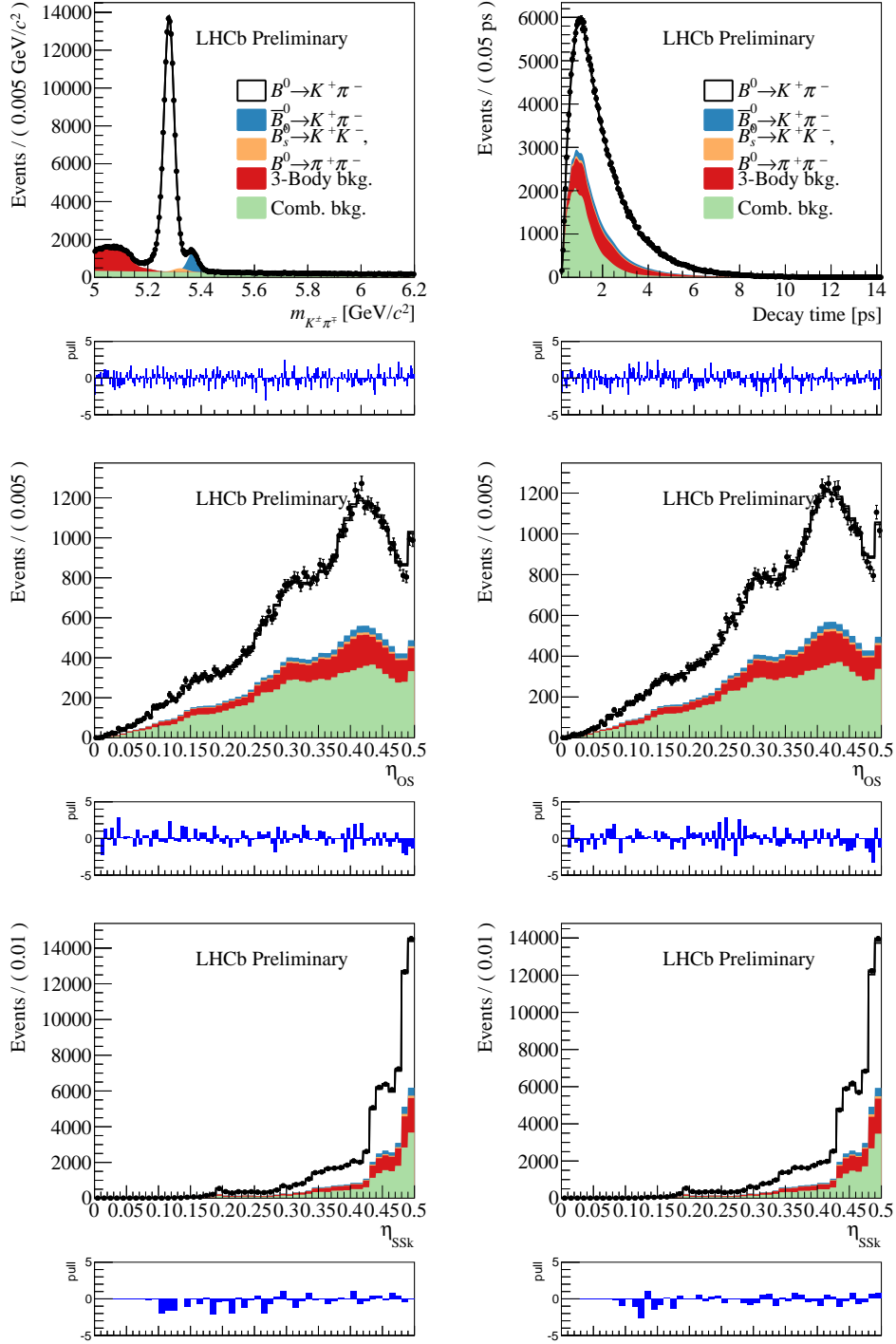


Figure 3.37: Distribution of events in the $K^+\pi^-$ sample surviving the requirements optimised for the determination of $C_{K^+K^-}$, $S_{K^+K^-}$ and $A_{K^+K^-}^{\Delta\Gamma}$. The distribution of (top left) mass, (top right) decay time, η_{OS} for events tagged as (middle left) B and (middle right) \bar{B} , η_{SSK} for events tagged as (bottom left) B and (bottom right) \bar{B} , are shown with the projection of the result of the best fit superimposed. Year of data-taking: 2015-16.

Fit projections, 2017 data samples

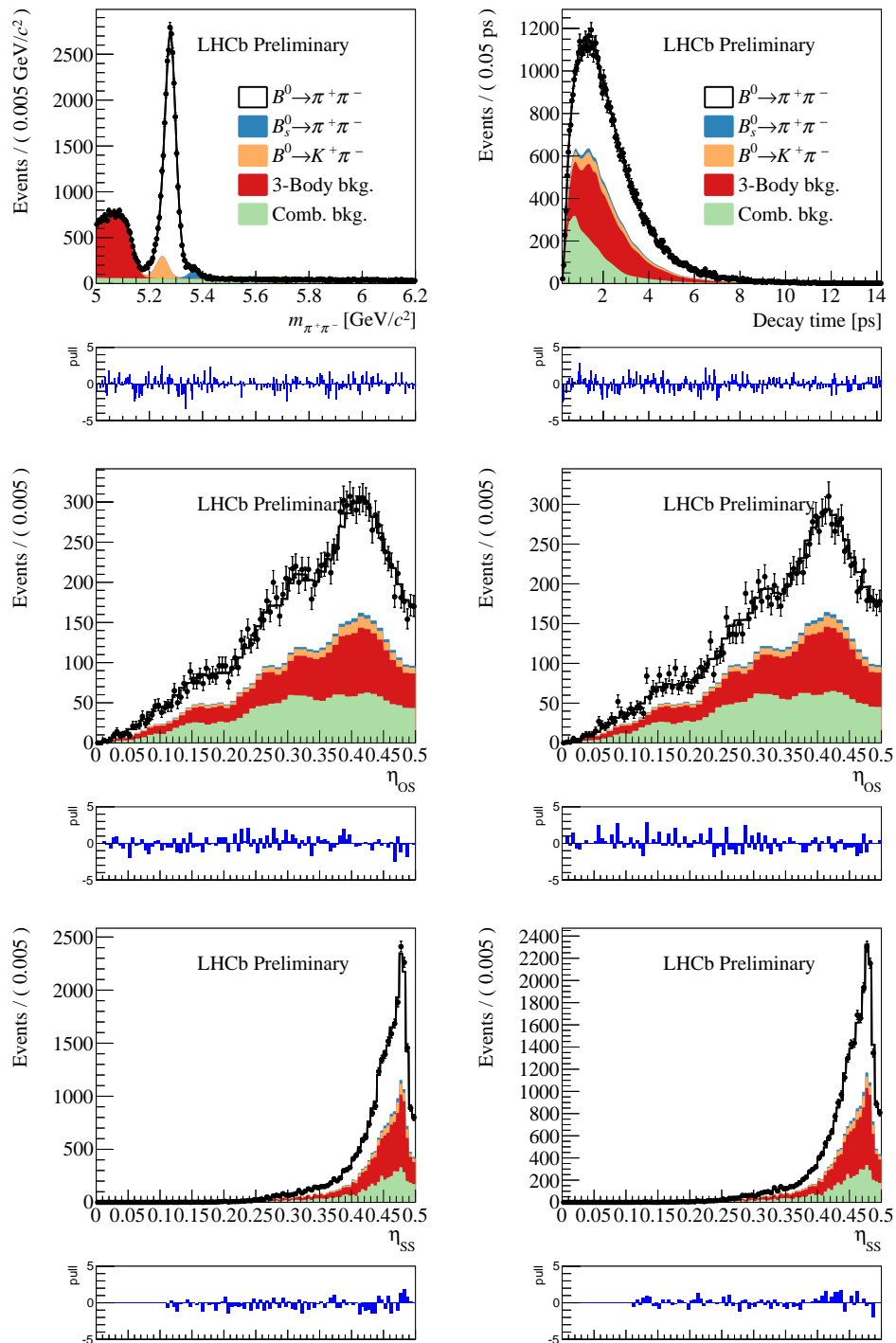


Figure 3.38: Distribution of events in the $\pi^+ \pi^-$ sample surviving the requirements optimised for the determination of $C_{\pi^+ \pi^-}$ and $S_{\pi^+ \pi^-}$. The distribution of (top left) mass, (top right) decay time, η_{OS} for events tagged as (middle left) B and (middle right) \bar{B} , η_{SSc} for events tagged as (bottom left) B and (bottom right) \bar{B} , are shown with the projection of the result of the best fit superimposed. Year of data-taking: 2017.

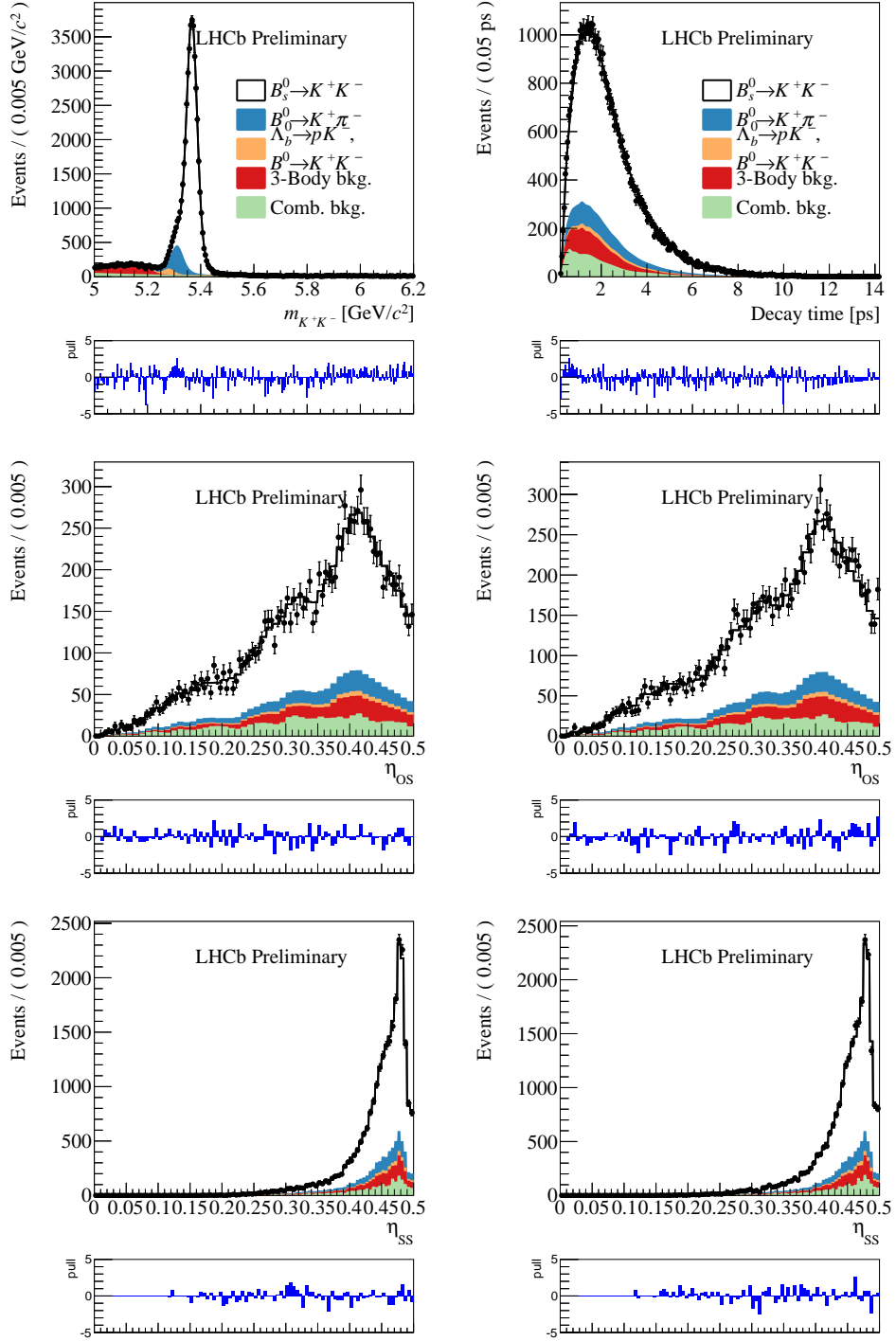


Figure 3.39: Distribution of events in the K^+K^- sample surviving the requirements optimised for the determination of $C_{\pi^+\pi^-}$ and $S_{\pi^+\pi^-}$. The distribution of (top left) mass, (top right) decay time, η_{OS} for events tagged as (middle left) B and (middle right) \bar{B} , η_{SSc} for events tagged as (bottom left) B and (bottom right) \bar{B} , are shown with the projection of the result of the best fit superimposed. Year of data-taking: 2017.

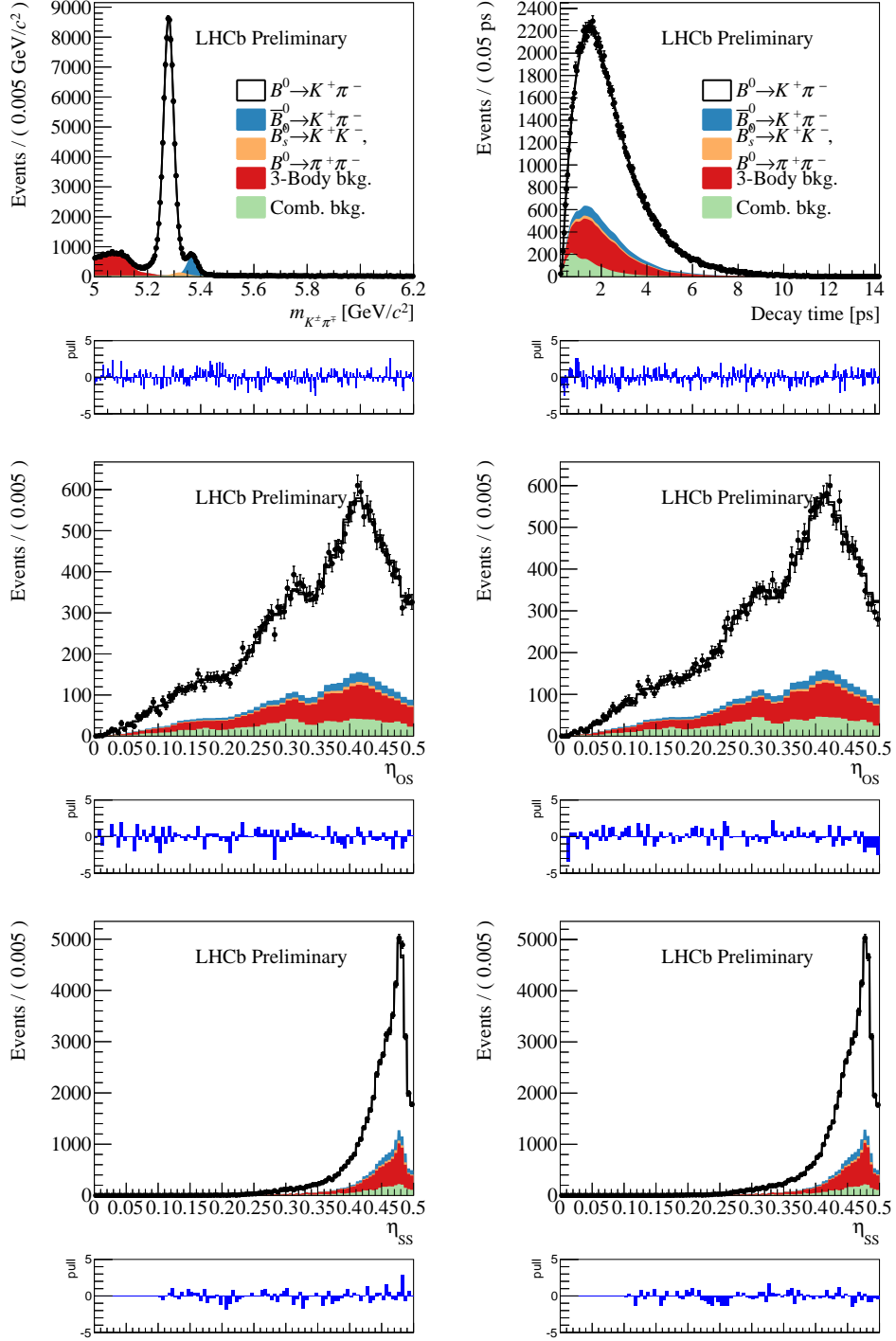


Figure 3.40: Distribution of events in the $K^+\pi^-$ sample surviving the requirements optimised for the determination of $C_{\pi^+\pi^-}$ and $S_{\pi^+\pi^-}$. The distribution of (top left) mass, (top right) decay time, η_{OS} for events tagged as (middle left) B and (middle right) \bar{B} , η_{SSc} for events tagged as (bottom left) B and (bottom right) \bar{B} , are shown with the projection of the result of the best fit superimposed. Year of data-taking: 2017.

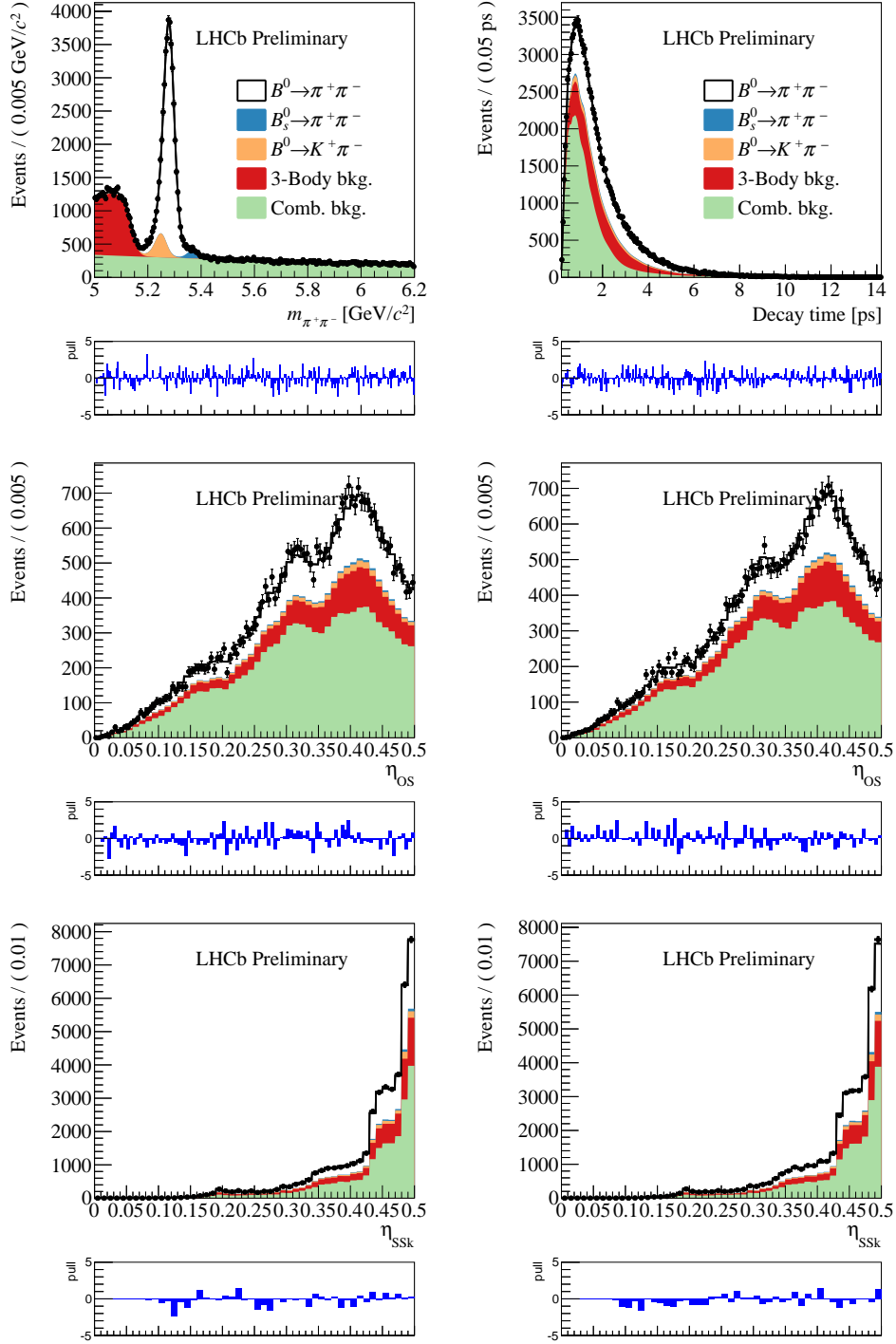


Figure 3.41: Distribution of events in the $\pi^+\pi^-$ sample surviving the requirements optimised for the determination of $C_{K^+K^-}$, $S_{K^+K^-}$ and $A_{K^+K^-}^{\Delta\Gamma}$. The distribution of (top left) mass, (top right) decay time, η_{OS} for events tagged as (middle left) B and (middle right) \bar{B} , η_{SSK} for events tagged as (bottom left) B and (bottom right) \bar{B} , are shown with the projection of the result of the best fit superimposed. Year of data-taking: 2017.

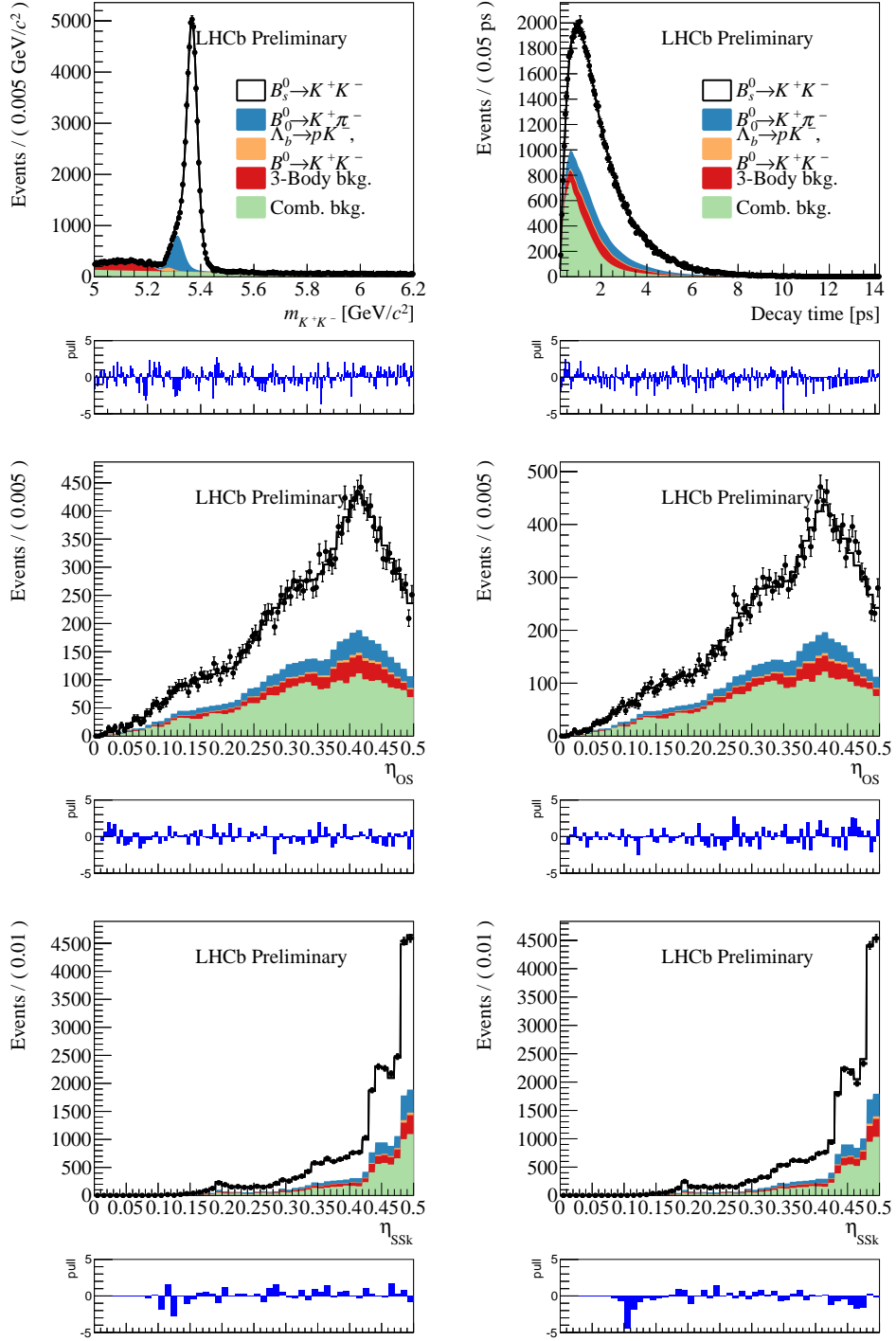


Figure 3.42: Distribution of events in the K^+K^- sample surviving the requirements optimised for the determination of $C_{K^+K^-}$, $S_{K^+K^-}$ and $A_{K^+K^-}^{\Delta\Gamma}$. The distribution of (top left) mass, (top right) decay time, η_{OS} for events tagged as (middle left) B and (middle right) \bar{B} , η_{SS_K} for events tagged as (bottom left) B and (bottom right) \bar{B} , are shown with the projection of the result of the best fit superimposed. Year of data-taking: 2017.

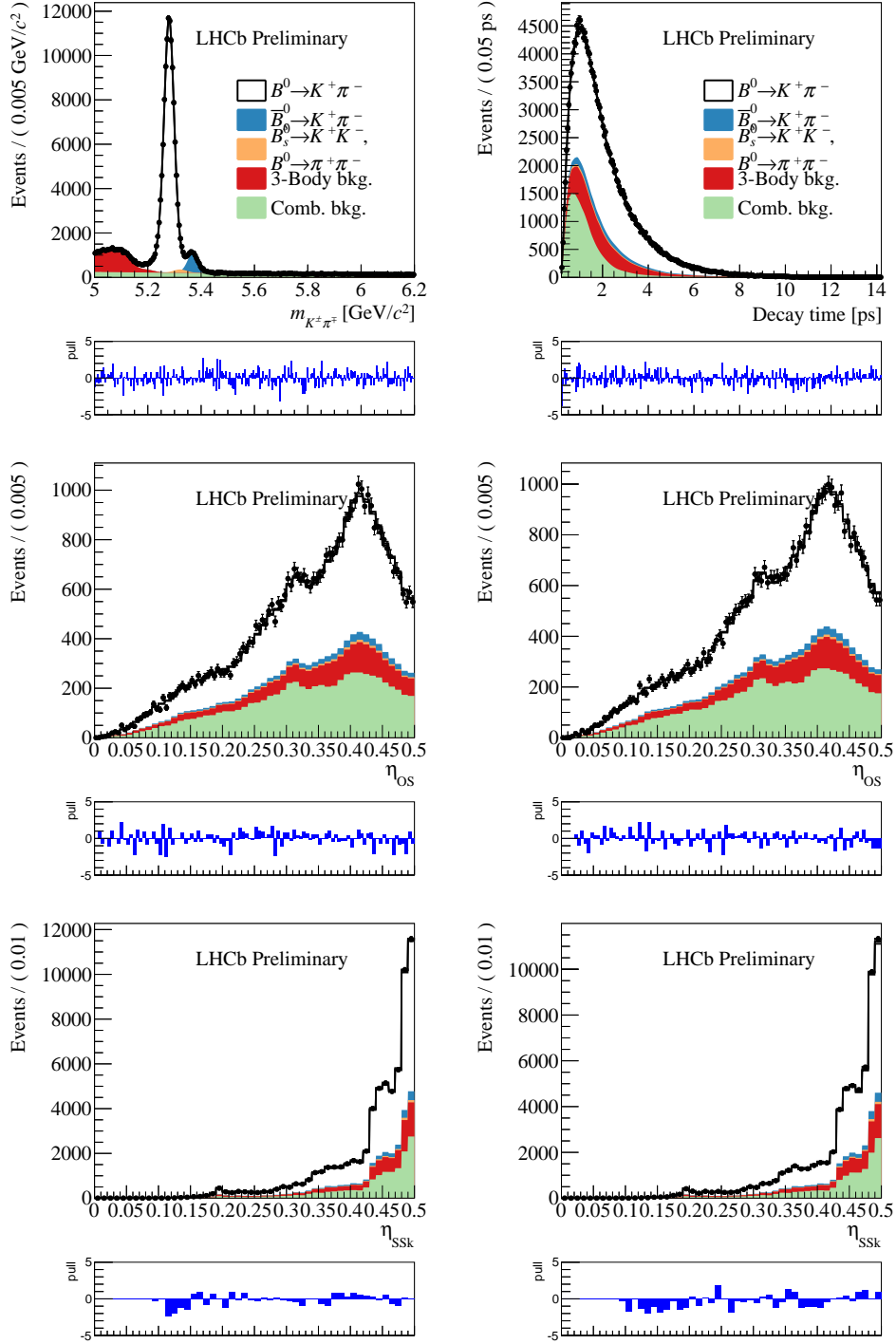


Figure 3.43: Distribution of events in the $K^+\pi^-$ sample surviving the requirements optimised for the determination of $C_{K^+K^-}$, $S_{K^+K^-}$ and $A_{K^+K^-}^{\Delta\Gamma}$. The distribution of (top left) mass, (top right) decay time, η_{OS} for events tagged as (middle left) B and (middle right) \bar{B} , η_{SSK} for events tagged as (bottom left) B and (bottom right) \bar{B} , are shown with the projection of the result of the best fit superimposed. Year of data-taking: 2017.

Fit projections, 2018 data samples

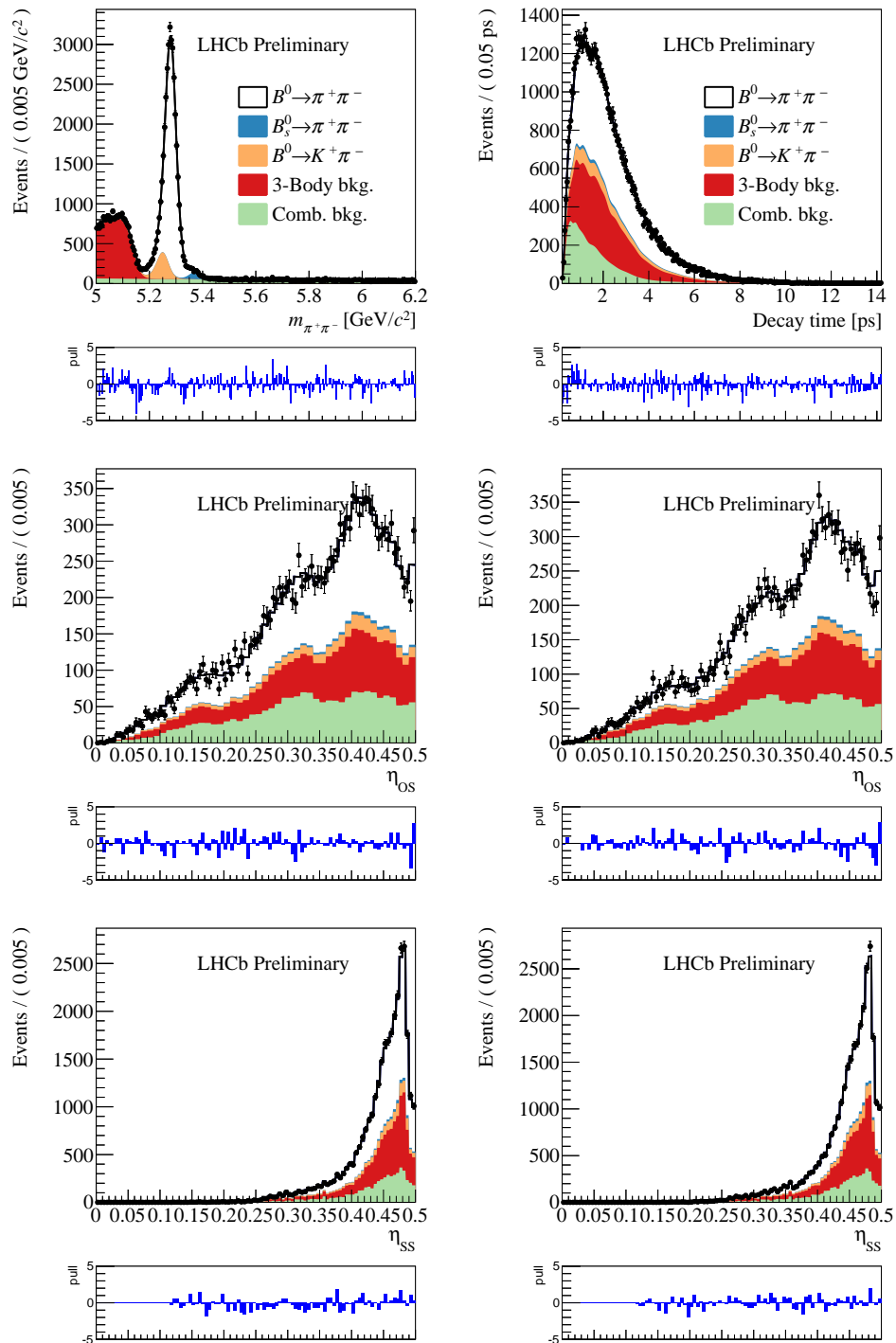


Figure 3.44: Distribution of events in the $\pi^+\pi^-$ sample surviving the requirements optimised for the determination of $C_{\pi^+\pi^-}$ and $S_{\pi^+\pi^-}$. The distribution of (top left) mass, (top right) decay time, η_{OS} for events tagged as (middle left) B and (middle right) \bar{B} , η_{SSc} for events tagged as (bottom left) B and (bottom right) \bar{B} , are shown with the projection of the result of the best fit superimposed. Year of data-taking: 2018.

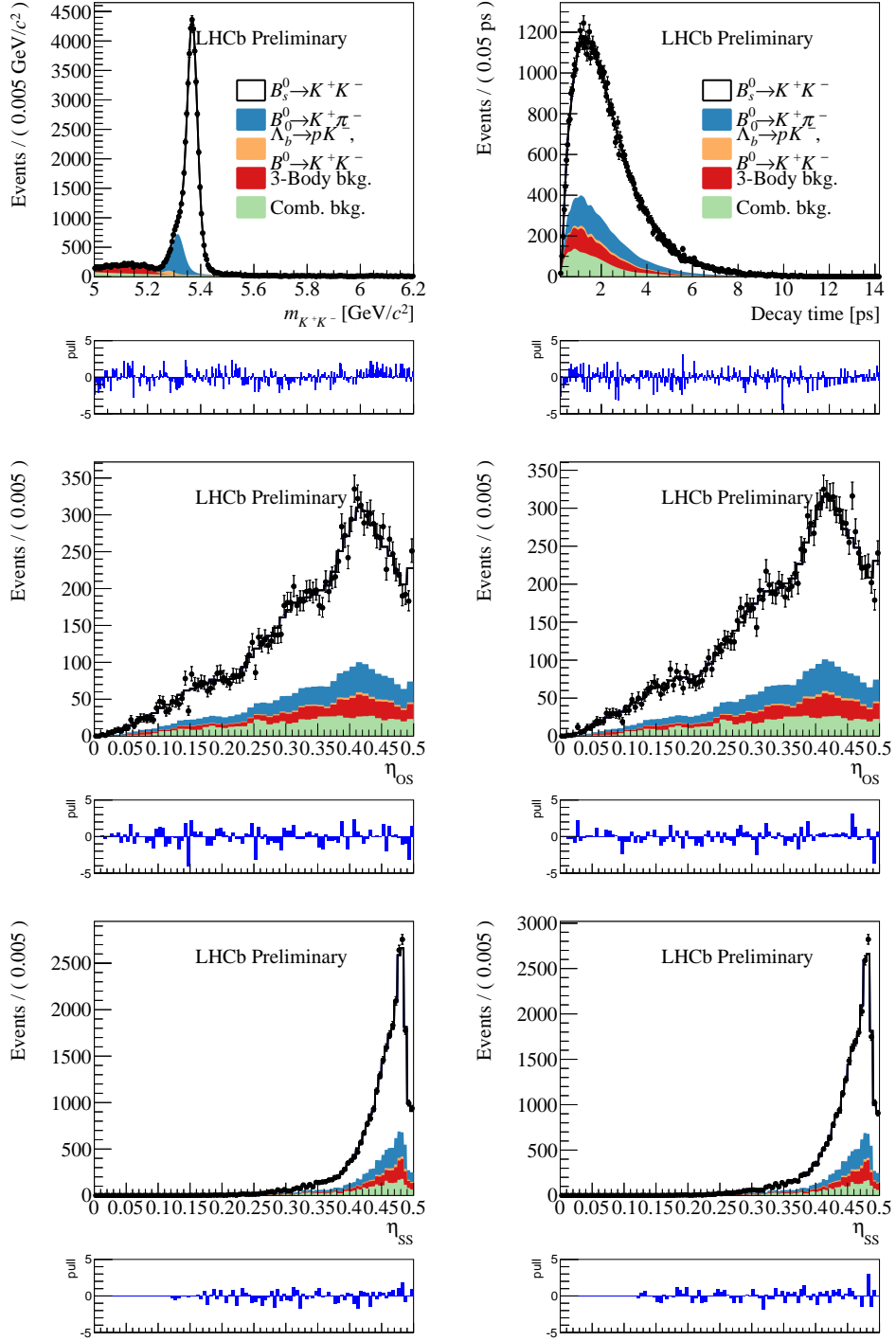


Figure 3.45: Distribution of events in the K^+K^- sample surviving the requirements optimised for the determination of $C_{\pi^+\pi^-}$ and $S_{\pi^+\pi^-}$. The distribution of (top left) mass, (top right) decay time, η_{OS} for events tagged as (middle left) B and (middle right) \bar{B} , η_{SS} for events tagged as (bottom left) B and (bottom right) \bar{B} , are shown with the projection of the result of the best fit superimposed. Year of data-taking: 2018.

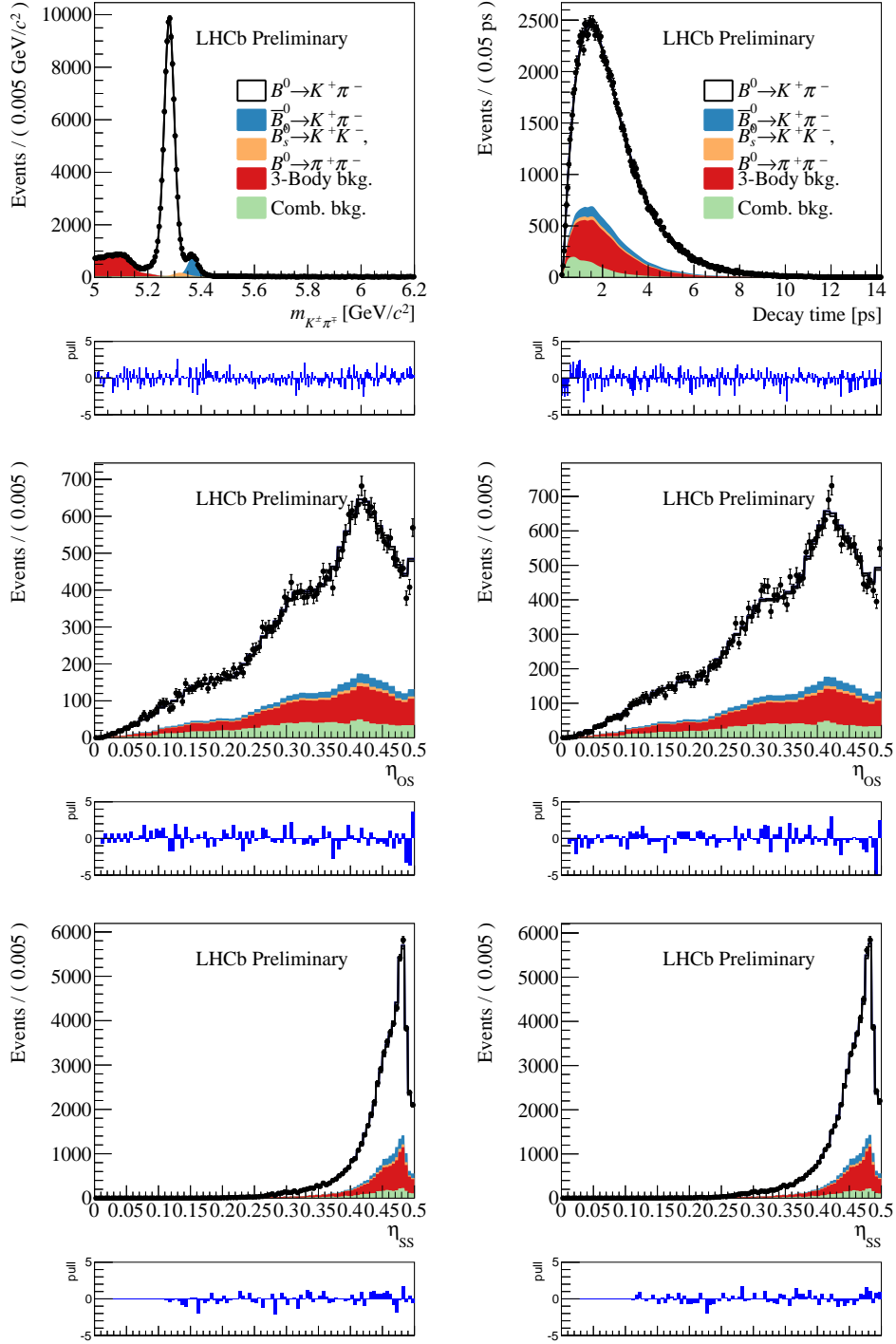


Figure 3.46: Distribution of events in the $K^+\pi^-$ sample surviving the requirements optimised for the determination of $C_{\pi^+\pi^-}$ and $S_{\pi^+\pi^-}$. The distribution of (top left) mass, (top right) decay time, η_{OS} for events tagged as (middle left) B and (middle right) \bar{B} , η_{SSc} for events tagged as (bottom left) B and (bottom right) \bar{B} , are shown with the projection of the result of the best fit superimposed. Year of data-taking: 2018.

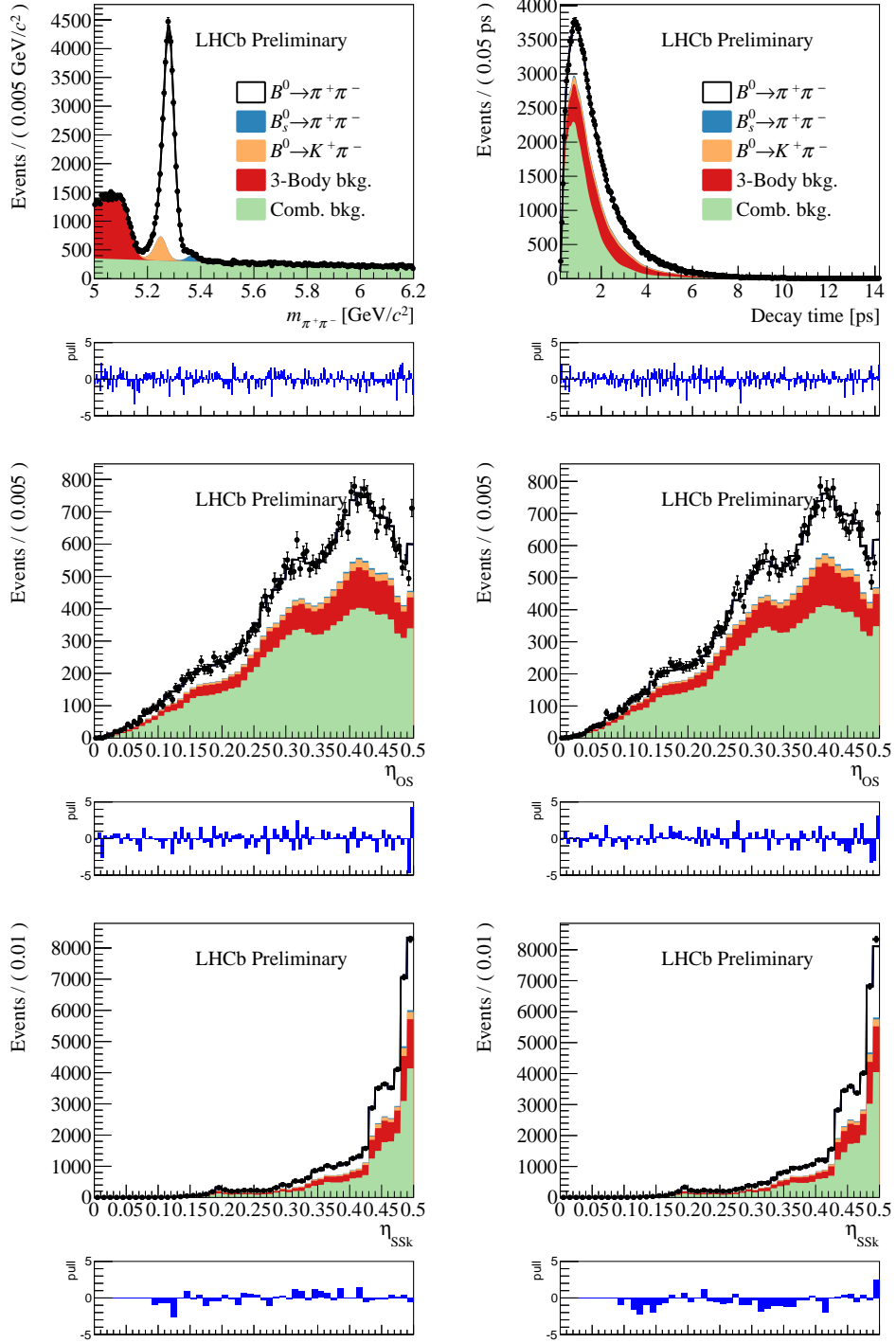


Figure 3.47: Distribution of events in the $\pi^+\pi^-$ sample surviving the requirements optimised for the determination of $C_{K^+K^-}$, $S_{K^+K^-}$ and $A_{K^+K^-}^{\Delta\Gamma}$. The distribution of (top left) mass, (top right) decay time, η_{OS} for events tagged as (middle left) B and (middle right) \bar{B} , η_{SSK} for events tagged as (bottom left) B and (bottom right) \bar{B} , are shown with the projection of the result of the best fit superimposed. Year of data-taking: 2018.

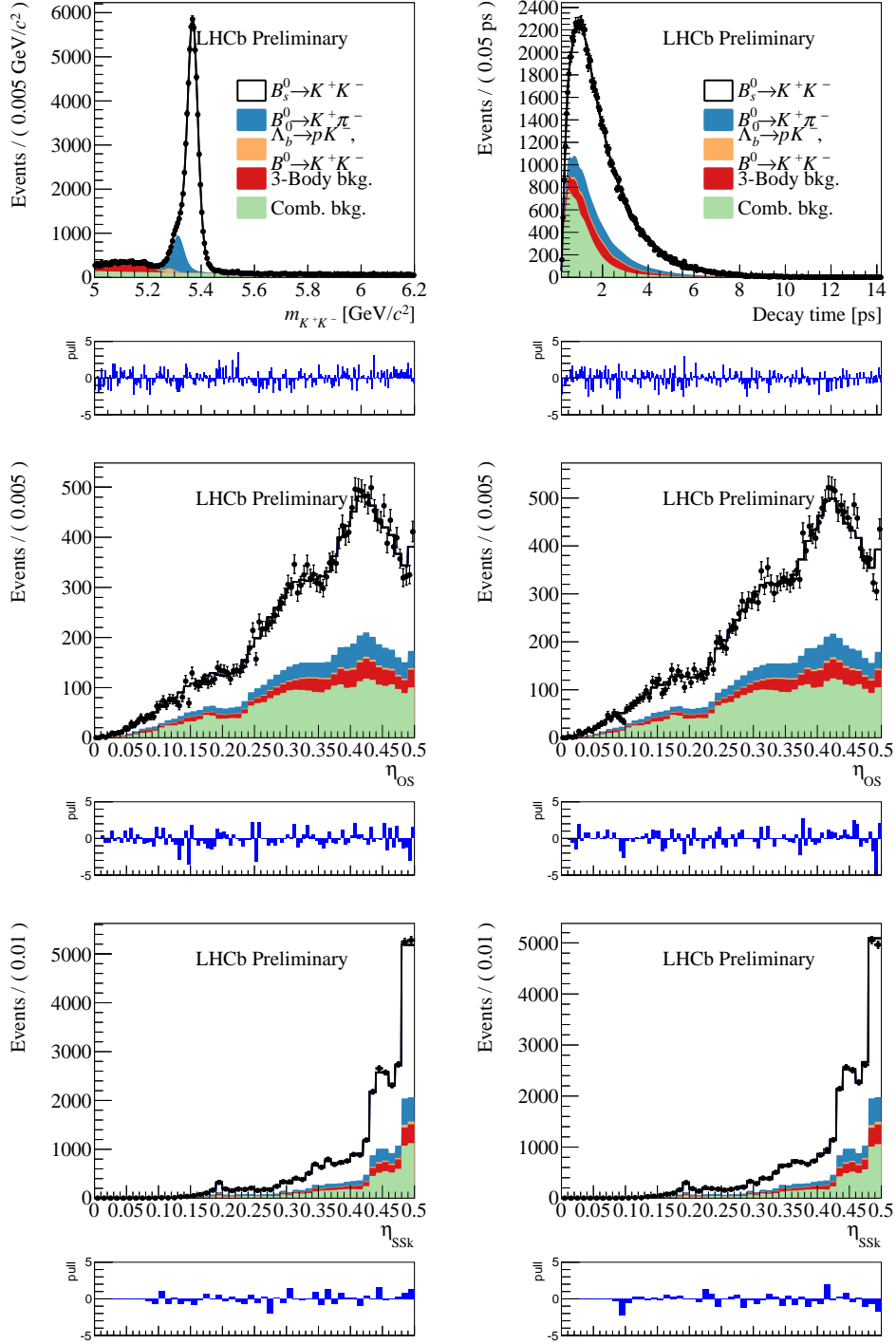


Figure 3.48: Distribution of events in the K^+K^- sample surviving the requirements optimised for the determination of $C_{K^+K^-}$, $S_{K^+K^-}$ and $A_{K^+K^-}^{\Delta\Gamma}$. The distribution of (top left) mass, (top right) decay time, η_{OS} for events tagged as (middle left) B and (middle right) \bar{B} , η_{SSK} for events tagged as (bottom left) B and (bottom right) \bar{B} , are shown with the projection of the result of the best fit superimposed. Year of data-taking: 2018.

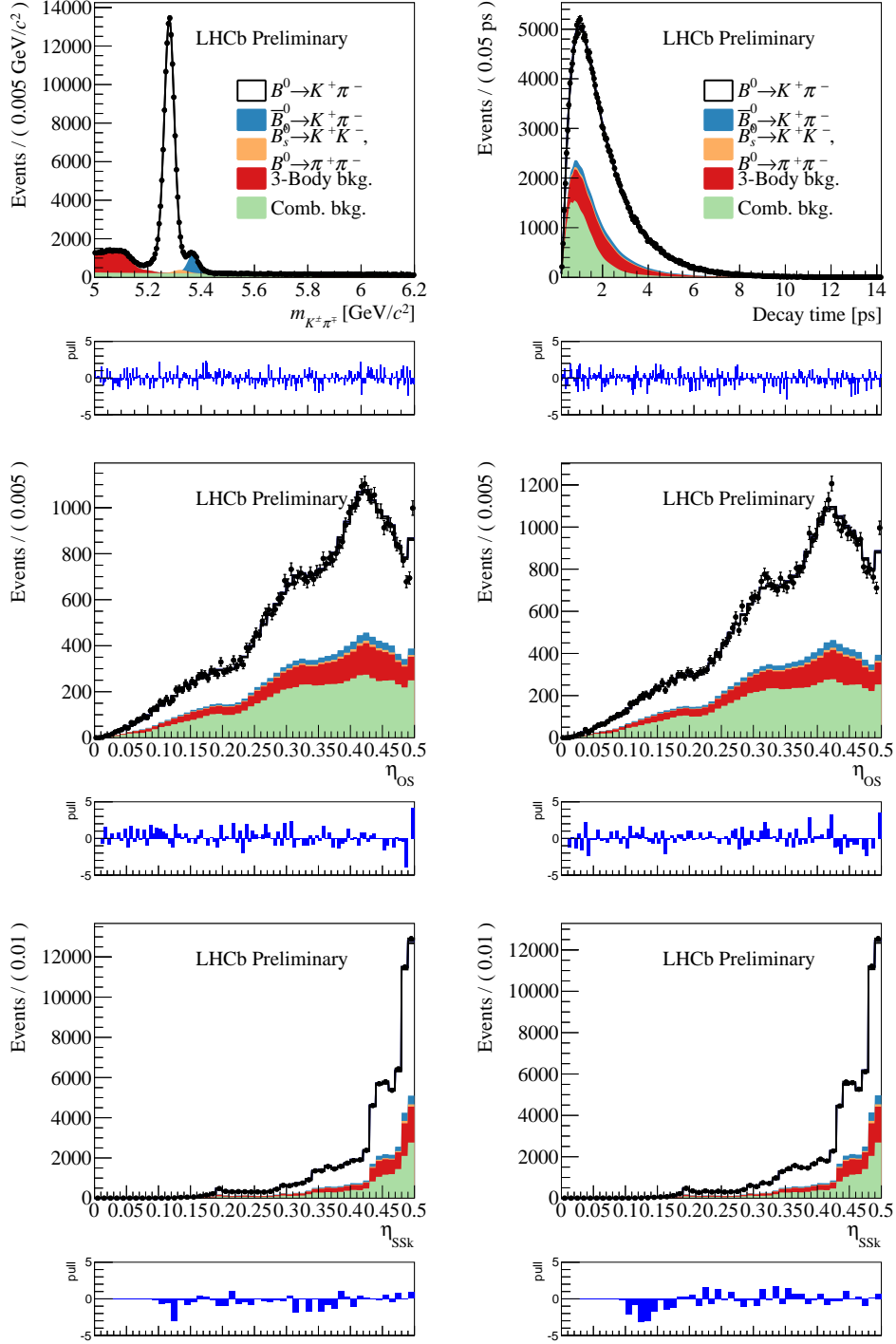


Figure 3.49: Distribution of events in the $K^+\pi^-$ sample surviving the requirements optimised for the determination of $C_{K^+K^-}$, $S_{K^+K^-}$ and $A_{K^+K^-}^{\Delta\Gamma}$. The distribution of (top left) mass, (top right) decay time, η_{OS} for events tagged as (middle left) B and (middle right) \bar{B} , η_{SSK} for events tagged as (bottom left) B and (bottom right) \bar{B} , are shown with the projection of the result of the best fit superimposed. Year of data-taking: 2018.

3.8.1 Fit Cross-Checks

To study the discrepancies in the CP violation parameters extracted from different data-taking periods, the following list of tests is executed. The Table 3.34 resumes the values of $C_{K^+K^-}$ and $S_{K^+K^-}$ extracted from all the trials²². No relevant modifications of the baseline results are found.

MagUp and MagDown The analysis is run independently for the *MagUp* and the *MagDown* samples. In particular, the PID calibration, the decay-time efficiencies, and all the templates used in the final fit are recalculated, exploiting the samples with the corresponding experimental conditions.

No SS_K The final fit is run neglecting the information from the SS_K-tagger, to test for the presence of any eventual issue in its calibration.

Tight PID To check for the presence of any systematic effect due to the cross-feed backgrounds, harder PID cuts are imposed for the selection of the K^+K^- final state:

$$\text{DLL}_{K\pi} > 5 \quad \text{AND} \quad \text{DLL}_{Kp} > -2.$$

This leads to the modification of the PID calibration parameters, the decay-time efficiencies, and all the templates used in the final fit.

1 PV Only the events with a single reconstructed primary vertex are accepted in the final data sample to avoid any kind of issue related to the PV association requirements. The decay-time templates are recalculated.

Free Δm_s The baseline analysis configuration is assumed, but the value of Δm_s is left free to be adjusted by the final fit, to look for eventual issues affecting of the oscillation period of the B_s^0 mesons. The final values of Δm_s observed in the fits are compatible one with the other and with the world average.

MyTime The decay time was recalculated by hand, starting from the measured momenta and the reconstructed flight distance of the B candidates. This was done to exclude any issue related to the implementation of the `DecayTreeFitter` [143], namely the algorithm that performs a refitting of the whole decay chain, assuming the mass hypotheses corresponding to the reconstructed identity of each particle. The decay-time efficiencies and all the templates related to the decay time are recalculated²³.

$t > 1.2$ ps and $t > 1.5$ ps The candidates with decay time smaller than 1.2 or 1.5 ps are removed from the fitted samples to reduce eventual mismodelling effects related to the combinatorial background and the decay-time efficiencies. Indeed, the combinatorial background description is the most complex part of the fit model, and the average decay-time of this component is smaller than that of the signal. Besides, the

²²In all the cases, only the selection optimised for the extraction of $C_{K^+K^-}$, $S_{K^+K^-}$, and $A_{K^+K^-}^{\Delta\Gamma}$ is considered

²³This test was replicated even without the *PV refitting*, namely the correction for the eventual presence of the final state hadrons among the set of tracks exploited to determine the position of the PV associated to the signal candidate (see Section 3.1.2). However, no modifications concerning $C_{K^+K^-}$ and $S_{K^+K^-}$ are observed.

determination of the decay-time efficiency is insidious at small decay times due to the shape of the acceptance functions (see Figure 3.22).

For numerical reasons, the practical implementations to the decay-time acceptances and templates are recalculated imposing this additional requirement.

Angle($\mathbf{h}^+\mathbf{h}'^-$) > 5° The smaller the angle between the final state tracks, the higher the uncertainty on the reconstructed position of the B -meson decay vertex. Therefore, all the candidates with an angle smaller than 5 degree are removed from the fitted samples. The decay time acceptance, and all the templates used in the final fit are recalculated, as a consequence.

Run Number Split In Ref [142], a 5-fs bias affecting the decay time reconstruction of B_s^0 mesons was observed. The cause of the bias was ascribed to the known misalignment of the VELO system. In this regard, a new set of alignment parameters was assumed during the 2018, to partially correct the effect. Therefore, this analysis is replicated splitting the 2018 sample before and after the application of the new VELO calibration²⁴. However, no relevant modifications of C_{K+K^-} and S_{K+K^-} are found:

Parameter	runNumber < 210300	runNumber > 210300
C_{K+K^-}	-0.07 ± 0.06	0.05 ± 0.04
S_{K+K^-}	0.20 ± 0.06	0.20 ± 0.04

As evidenced from the summary reported in Table 3.34, none of the above tests give conclusive indications about the source of the discrepancy. However, some indications can be extracted from the tests. The flavour tagging is unlikely to be the source of the discrepancy, since the parameters of the $B^0 \rightarrow \pi^+\pi^-$ decay are very compatible between the data-taking years. The only source of discrepancy may arise from the SS_K tagging, that is not calibrated during the fit and is not used for the $B^0 \rightarrow \pi^+\pi^-$ decay, but the fits performed using only OS-tagging information do not indicate any deviation with respect to the baseline results. A not-perfect modelling of the decay-time efficiency is excluded from the fits to the samples with $t > 1.2$ ps and $t > 1.5$ ps, as well as a not-perfect modelisation of the combinatorial background, that accumulates at low decay time. A systematic incorrect association with the PV is excluded from the test restricting the sample to the events with a single PV. At the time of writing this Thesis the best explanation for the discrepancy is a not-perfect calibration of the decay-time bias that may differ between the years. Further studies and cross-checks are ongoing.

²⁴Namely the runNumber = 210300 [142]

Table 3.34: Summary of the values of $C_{K^+K^-}$ and $S_{K^+K^-}$ obtained from the various alternative fits described in the text.

Test	$C_{K^+K^-}$				$S_{K^+K^-}$			
	Year 2015-16	Year 2017	Year 2018	Year 2015-16	Year 2017	Year 2018	Year 2018	
Baseline	0.16 ± 0.04	-0.03 ± 0.04	0.01 ± 0.03	0.14 ± 0.04	0.13 ± 0.04	0.20 ± 0.03		
<i>MagUp</i>	0.18 ± 0.05	-0.07 ± 0.05	0.08 ± 0.05	0.10 ± 0.05	0.06 ± 0.05	0.24 ± 0.05		
<i>MagDown</i>	0.13 ± 0.05	0.01 ± 0.05	-0.06 ± 0.05	0.17 ± 0.05	0.21 ± 0.05	0.17 ± 0.05		
No SS_K	0.14 ± 0.04	-0.04 ± 0.04	-0.03 ± 0.04	0.15 ± 0.04	0.13 ± 0.04	0.23 ± 0.04		
Tight PID	0.15 ± 0.04	-0.03 ± 0.04	0.01 ± 0.04	0.15 ± 0.04	0.13 ± 0.04	0.21 ± 0.04		
1 PV	0.11 ± 0.05	-0.04 ± 0.05	0.03 ± 0.04	0.11 ± 0.05	0.17 ± 0.05	0.22 ± 0.04		
Free Δm_s	0.15 ± 0.04	-0.02 ± 0.04	-0.03 ± 0.04	0.15 ± 0.04	0.13 ± 0.03	0.20 ± 0.03		
MyTime	0.15 ± 0.04	-0.03 ± 0.04	0.02 ± 0.03	0.15 ± 0.04	0.12 ± 0.04	0.20 ± 0.03		
$t > 1.2$ ps	0.15 ± 0.04	-0.03 ± 0.04	0.03 ± 0.04	0.12 ± 0.04	0.12 ± 0.04	0.22 ± 0.04		
$t > 1.5$ ps	0.17 ± 0.04	0.00 ± 0.05	0.05 ± 0.04	0.12 ± 0.04	0.11 ± 0.05	0.20 ± 0.04		
Angle($h^+ h'^-$) $> 5^\circ$	0.17 ± 0.04	-0.05 ± 0.04	0.00 ± 0.03	0.14 ± 0.04	0.12 ± 0.04	0.19 ± 0.03		

Chapter 4

First measurement of $|V_{cb}|$ with $B_s^0 \rightarrow D_s^{(*)-} \mu^+ \nu$ decays

Introduction

The magnitude of the V_{cb} element of the CKM matrix is an important constraint of the UT. Moreover, the discrepancy between the *inclusive* and *exclusive* determinations of this quantity is a long standing puzzle in the sector of flavour physics [144, 145]. To elucidate such intriguing results, it is essential to expand the experimental programme to other dynamical systems, which are potentially subject to different sources of systematic uncertainties. In particular, semileptonic B_s^0 decays are copiously produced at the LHC and have not yet been fully exploited.

Semileptonic B_s^0 decays are also more advantageous from the theoretical point of view, since the absence of light valence quarks implies that lattice-QCD results have smaller statistical uncertainties and are less computationally expensive, thus possibly allowing for more stringent tests of the Standard Model [146–149].

In this chapter the $B_s^0 \rightarrow D_s^- \mu^+ \nu_\mu$ and $B_s^0 \rightarrow D_s^{*-} \mu^+ \nu_\mu$ decays are exploited to measure the matrix element $|V_{cb}|$ and also to determine their exclusive branching fractions. This is the first measurement of $|V_{cb}|$ from B_s^0 decays or using exclusive decays at a hadron-collider experiment, and the first measurement of these exclusive branching fractions. The form factors are modelled with the parametrisation derived Caprini, Lellouch and Neubert (CLN) [60], whose formalism is described in Section 1.4.

The exclusive $B_s^0 \rightarrow D_s^- \mu^+ \nu_\mu$ and $B_s^0 \rightarrow D_s^{*-} \mu^+ \nu_\mu$ are partially reconstructed in the analysis. The neutrino cannot be detected and in the $D_s^{*-} \rightarrow D_s^- X$ decay only the D_s^- meson is reconstructed using the $[K^+ K^-]_\phi \pi^-$ final state, with kaon pairs having an invariant mass in the vicinity of the $\phi(1020)$ resonance. The B_s^0 branching fractions are determined using as reference channels the exclusive decays $B^0 \rightarrow D^- \mu^+ \nu_\mu$ and $B^0 \rightarrow D^{*-} \mu^+ \nu_\mu$, selecting D^- in the Cabibbo-suppressed $[K^+ K^-]_\phi \pi^-$ mode. Since signal and reference mode have identical final states and similar kinematics, in the ratios of

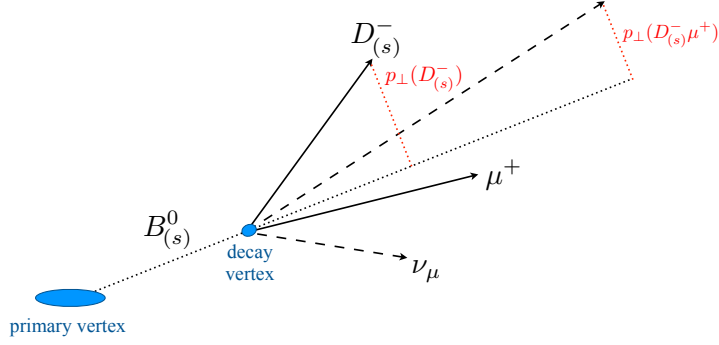


Figure 4.1: Sketch illustrating the topology of a semileptonic $B_{(s)}^0$ decay.

branching fractions

$$\mathcal{R} \equiv \frac{\mathcal{B}(B_s^0 \rightarrow D_s^- \mu^+ \nu_\mu)}{\mathcal{B}(B^0 \rightarrow D^- \mu^+ \nu_\mu)}, \quad (4.1)$$

$$\mathcal{R}^* \equiv \frac{\mathcal{B}(B_s^0 \rightarrow D_s^{*-} \mu^+ \nu_\mu)}{\mathcal{B}(B^0 \rightarrow D^{*-} \mu^+ \nu_\mu)}, \quad (4.2)$$

systematic uncertainties, that would otherwise affect the calculation of the efficiencies, are suppressed. The value of the ratio of the B_s^0 and B^0 fragmentation fractions f_s/f_d is taken as an external input to determine \mathcal{R} and \mathcal{R}^* from measured decay yields and efficiencies. By using the known values of the reference branching fractions, the B_s^0 branching fractions can be parametrized in terms of the decay form factors and $|V_{cb}|$.

The value of $|V_{cb}|$, the form factors parameters and the branching fractions of the exclusive B_s^0 decays are determined from a binned fit to the two-dimensional distribution of the corrected mass, m_{corr} , and of the D_s^- momentum transverse to the B_s^0 flight direction, p_\perp (see Fig. 4.1), accounting for efficiency and resolution effects. The corrected mass is determined from the visible mass, $m(D_s^- \mu^+)$, and from the momentum of the $D_s^- \mu^+$ system transverse to the B_s^0 flight direction, $p_\perp(D_s^- \mu^+)$, as

$$m_{\text{corr}} = \sqrt{m^2(D_s^- \mu^+) + p_\perp^2(D_s^- \mu^+) + p_\perp(D_s^- \mu^+)}. \quad (4.3)$$

The p_\perp and m_{corr} variables provide powerful means for the determination of the sample composition, because the distributions of signal and background decays accumulate in well-separated regions of the two-dimensional p_\perp vs m_{corr} space. In addition, p_\perp preserves information on the decay form factors because it is highly correlated with the squared dilepton mass q^2 and, to a minor extent, also to the helicity angles of the $B_s^0 \rightarrow D_s^{*-} \mu^+ \nu_\mu$ decay. With respect to methods that rely on the estimate of the unreconstructed neutrino momentum to compute these variables, p_\perp has the advantage of being fully reconstructible from the tracks originating from the D_s decay. This results in a narrower, unbiased resolution in q^2 and in no loss of signal candidates.

Templates used in the two-dimensional fit, as well as the efficiencies for the reconstruction and selection of the signal and normalization modes, are determined using simulated samples, corrected for known data-simulation discrepancies. The entire analysis procedure is validated on a control sample of $B^0 \rightarrow D^- (\rightarrow K^+ \pi^- \pi^-) \mu^+ \nu_\mu X$ decays, normalised

again to $B^0 \rightarrow D^-(\rightarrow K^+K^-\pi^-)\mu^+\nu_\mu X$ decays, to measure ratios of branching fractions compatible with unity and values of decay form factors in agreement with world averages.

The analysis uses a data sample corresponding to an integrated luminosity of 3 fb^{-1} collected by LHCb during Run 1. The analysis was not extended to Run 2 data due to several reasons. Firstly, the uncertainty on $|V_{cb}|$ is expected to be largely dominated by the uncertainty on the external inputs. The relative statistical uncertainty on $|V_{cb}|$ based on Run 1 data is 1.5%, while the uncertainty from the external inputs is more than twice as large, dominated by that on f_s/f_d . The determination of f_s/f_d from the independent Run 2 sample of semileptonic B_s^0 decays [150], taking into account the dependence of f_s/f_d on the proton-proton collision energy described in Ref. [151], yields a relative uncertainty on $|V_{cb}|$ of about 2.7%. An additional consideration about restricting the analysis to Run 1 data is that the amount of Run 2 simulated events was limited due to technical issues in the generation of the samples [152]. Hence, performing the analysis on Run 2 data would have lead to a dominant statistical uncertainty from this source. Delaying the result of this analysis to wait for the production of additional simulated samples was not justified.

This Chapter is structured as follows. Data and simulation samples are presented in Sections 4.1 and 4.2, respectively. Section 4.2 also describes the estimation of the efficiency ratios and the expected sample composition. Section 4.3 presents the details of the two-dimensional fit to the $(m_{\text{corr}}, p_\perp)$ distribution that determines the parameters of interest. Section 4.4 describes the validation of the analysis with a control sample of B^0 data and with pseudo-experiments. Systematic uncertainties are discussed in Section 4.5 and finally results are presented in Section 4.6, before concluding.

4.1 Data samples

The analysis uses the entire data set collected by LHCb during Run 1, which consists of approximately 3 fb^{-1} of integrated luminosity.

Candidate $B_s^0 \rightarrow D_s^-(\rightarrow K^+K^-\pi^-)\mu^+\nu_\mu X$ and $B^0 \rightarrow D^-(\rightarrow K^+K^-\pi^-)\mu^+\nu_\mu X$ decays are reconstructed from the `b2DsPhiPiMuXB2DMuNuX` stripping line, while $B^0 \rightarrow D^-(\rightarrow K^+\pi^-\pi^-)\mu^+\nu_\mu X$ candidates are reconstructed from the `b2DpMuXB2DMuNuX` stripping line. The stripping selections are outlined in Table 4.1. Each line also reconstructs candidates where the muon and the charmed meson candidates have the same charge. Such *same sign* (SS) events are used to model the combinatorial background formed by a real $D_{(s)}$ meson associated with a random muon. The SS sample has been proven to be a good proxy for the combinatorial background in Refs. [153, 154], from which most of the offline selection requirements are inherited.

Stripping candidates are first filtered according to how they were selected at trigger level (Section 2.4): candidates are required to be `L0Muon TOS` on the muon; at `Hlt1`, the muon is required to be `TOS` on `Hlt1TrackAllL0` or `Hlt1TrackMuon` or `Hlt1SingleMuonHighPT`; at `Hlt2`, the B candidate is required to be `TOS` on one of the topological lines `Hlt2Topo{2,3,4}BodyBBDT`. The resulting candidates are then required to satisfy the offline selection summarized in Table 4.2, which aims at suppressing background under the $D_{(s)}$ peak and combinatorial background from $D_{(s)}^-\mu^+$ pairs that do not originate from a semileptonic $B^0_{(s)}$ decay.

Known sources of background from decays to misidentified final states are suppressed through mass vetoes. Candidate $B_s^0 \rightarrow \psi(\rightarrow \mu^+\mu^-)\phi(\rightarrow K^+K^-)$ decays, where ψ indicates

either the $1S$ or the $2S$ charmonium state, and where one of the muons from the ψ is misidentified as a pion, are removed by vetoing the corresponding regions in dimuon mass computed after assigning the muon mass to the charged particle originally identified as a pion. Candidate $\bar{A}_b^0 \rightarrow \bar{A}_c^- (\rightarrow \bar{p}K^+\pi^-)\mu^+\nu X$ decays, where the proton is misidentified as a kaon (for $K^+K^-\pi^-$) or a pion (for $K^+\pi^-\pi^-$) are also removed by a veto on the $pK\pi$ mass computed with the proper mass assignments. Background from fully-reconstructed $B_{(s)}^0 \rightarrow D_{(s)}^-\pi^+$ (from decays in-flight of the π^+) and combinatorial background are removed by requiring the visible B mass to be smaller than $5.2 \text{ GeV}/c^2$.

Requirements on (transverse) momenta and on particle identification of the $D_{(s)}$ daughters are used to further reduce the non- $D_{(s)}$ background. Most of these requirements are more stringent variants of the stripping criteria. In addition, requirements are tightened on quantities that can increase the signal-to-background ratio while maintaining a sufficient sample size, like particle-identification criteria $\text{ProbNNpi}(\pi)$. Requirements are also imposed on momenta, transverse momenta, and pseudorapidity of kaons, pions and muon, and on the impact parameter of the muon, to restrict the sample into fiducial regions for the corrections of the simulation described in Sect. 4.2.1 (such requirements are applied to both data and simulation).

Background from decays of a b hadron into final states with a pair of charmed hadrons, of which one peaks at the $D_{(s)}$ mass and the other decays semileptonically, contributes at lower corrected B masses. Similarly, background from B decays to semimuonic final state with a nonresonant $D_{(s)}K$ or $D\pi$ state can pollute this region. Such backgrounds, described in detail in Sec. 4.2.3, are suppressed by the requirement $p_\perp [\text{GeV}/c] < 1.5 + 1.1 \times (m_{\text{corr}} [\text{GeV}/c^2] - 4.5)$, detailed in Sec. 4.3. Semitaupic decays and cross-feed decays from B mesons are also suppressed by this requirement.

Figures 4.2 and 4.3 show the $K^+K^-\pi^-$ and $K^+\pi^-\pi^-$ invariant mass distributions and the $B_{(s)}^0$ corrected mass distributions, respectively, for candidates after selection requirements. A total of 2.72×10^5 $B_s^0 \rightarrow D_s^- (\rightarrow K^+K^-\pi^-)\mu^+\nu_\mu X$ signal candidates meet the final selection criteria; 0.82×10^5 B^0 candidates meet the $K^+K^-\pi^-$ and 1.89×10^6 the $K^+\pi^-\pi^-$ selection criteria.

4.2 Simulated samples and their corrections

Simulation is used to (i) have a detailed overview of all sources of b -hadron decays that contribute to the sample, (ii) model the relevant distributions used in the analysis and (iii) evaluate the efficiency of reconstructing and selecting signal and reference decays. The simulated decays, before being processed in the analysis, are corrected for known data-simulation mismodelings (see Section 4.2.1) and truth-matched to the generated quantities. Simulated data undergo the same processing of reconstruction and selection as the experimental data. The track-smearing tool is used to obtain more reliable resolutions. Table 4.3 lists all simulated samples, together with the number of truth-matched candidates passing the final selection.

4.2.1 Corrections to the simulation

The simulated samples are corrected for known mismodeling in the tracking and trigger (L0 and HLT1) efficiencies, in the response of particle-identification (PID) algorithms, and

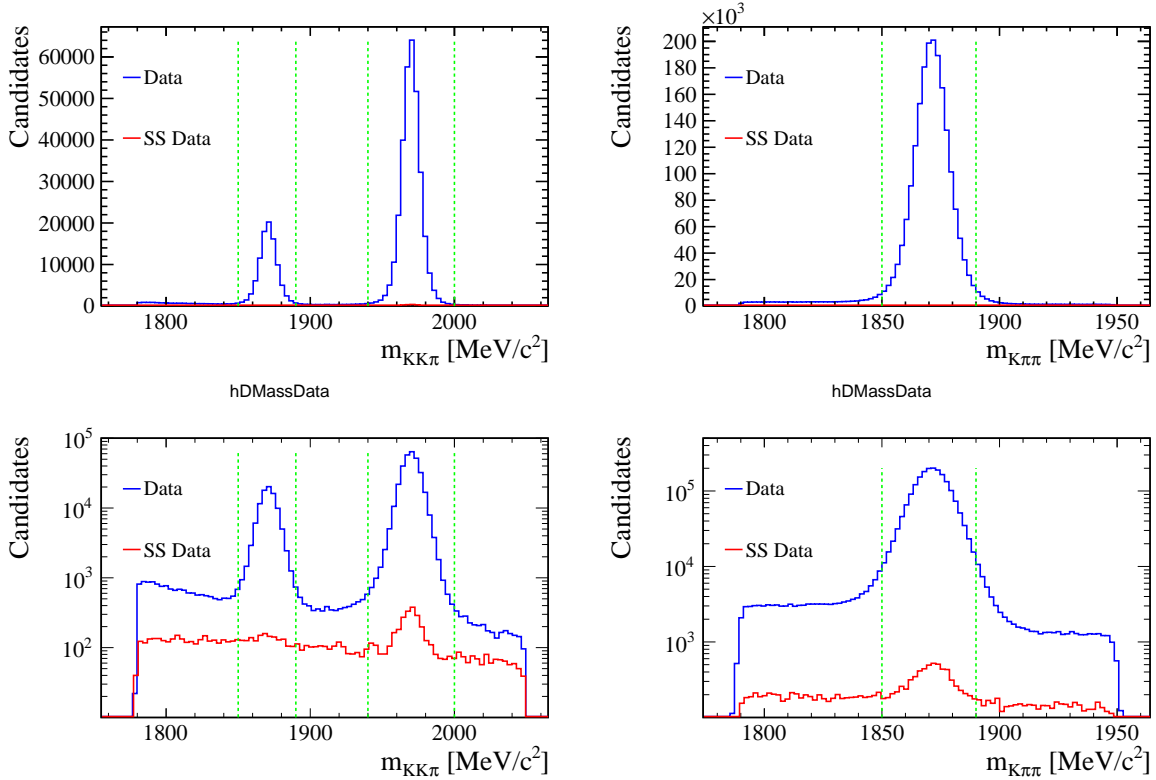


Figure 4.2: Distributions of (top left) $K^+K^-\pi^-$ and (top right) $K^+\pi^-\pi^-$ invariant masses for the candidates passing the final selection, except for the $D_{(s)}$ mass requirements (indicated by the vertical lines). The corresponding plots in logarithmic scale are shown in the bottom part of the figure.

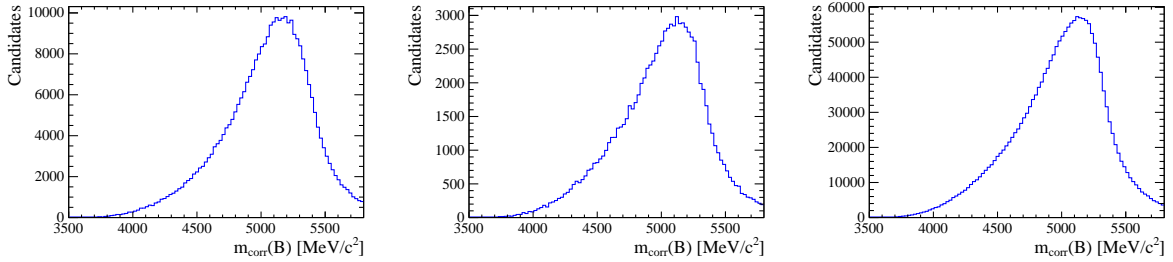


Figure 4.3: Distributions of corrected mass for (left) $B_s^0 \rightarrow D_s^-(\rightarrow K^+K^-\pi^-)\mu^+\nu_\mu X$, (center) $B^0 \rightarrow D^-(\rightarrow K^+K^-\pi^-)\mu^+\nu_\mu X$ and (right) $B^0 \rightarrow D^-(\rightarrow K^+\pi^-\pi^-)\mu^+\nu_\mu X$ candidates passing the final selection.

in the generated (parent) b -meson kinematics. The corrections rely on either standard LHCb tools and/or on large samples of control decays. In particular, data and simulated $B^- \rightarrow J/\psi K^-$ and $B_s^0 \rightarrow J/\psi \phi$ decays are used, where $J/\psi \rightarrow \mu^+\mu^-$ and $\phi \rightarrow K^+K^-$. The corresponding samples are inherited from Ref. [155]. The selection described in Table 4.4 is applied to obtain the mass distributions shown in Fig. 4.4. The distributions feature clean signal peaks on top of a smooth combinatorial background. Other physics backgrounds are either neglected or cut away by the mass requirement applied to select

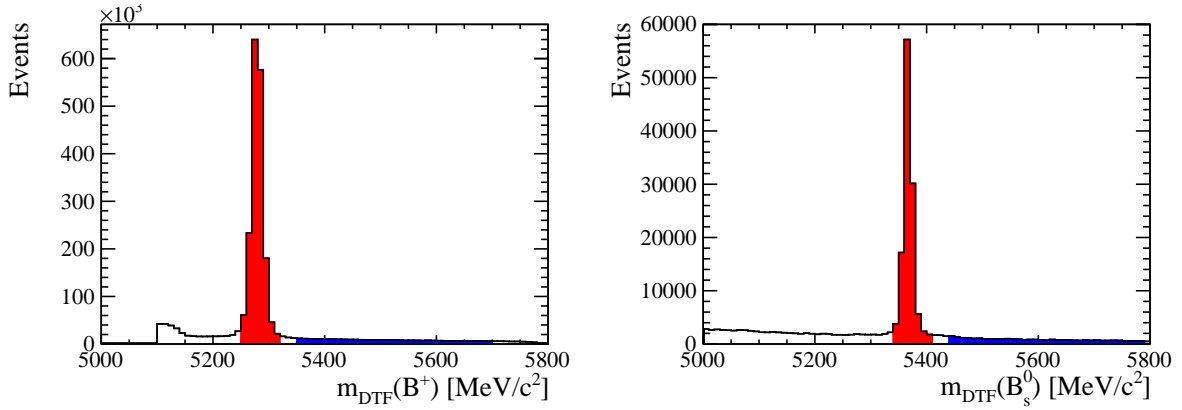


Figure 4.4: Distributions of the B mass for the selected (left) $B^- \rightarrow J/\psi K^-$ and (right) $B_s^0 \rightarrow J/\psi \phi$ candidates. The red (blue) area gives the signal region (sideband considered for the background subtraction).

the signal peaks (red regions in Fig. 4.4). Sideband candidates (blue regions in Fig. 4.4) are used to subtract the combinatorial background under the signal peak. The simulated samples are selected using the same criteria applied to data as well as truth-matching information.

The agreement between data and the corrected simulation is shown in App. B.2 for the control sample of $B^0 \rightarrow D^-(\rightarrow K^+\pi^-\pi^-)\mu^+\nu_\mu X$ decays. Residual small differences will be accounted for in the systematic uncertainties.

4.2.1.1 Tracking efficiency

The track reconstruction efficiency determined using data [156] differs from that measured in simulation. The *Tracking & Alignment* group provides tables of weights that can be applied to simulation to correct for such mismodeling. The map shown in Fig. 4.5 (taken from Ref. [157]) is used to correct all simulation samples. The different stripping version has no impact on the evaluation of these corrections.

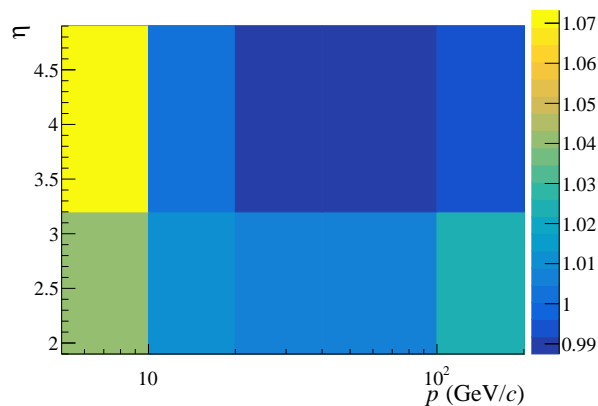


Figure 4.5: Data-to-simulation ratio as a function of the track momentum and pseudorapidity used to correct the tracking efficiency in simulation. The map is provided by the *Tracking & Alignment* group.

4.2.1.2 L0 and HLT1 efficiency

The correction to the efficiency of the L0 and HLT1 triggers is obtained from the control sample of $B^- \rightarrow J/\psi K^-$ decays with a *tag-and-probe* method. No explicit selection is applied to the *tag* muon, while the probe is tested with respect to the L0 and HLT1 requirements reported in Sec. 4.1, *i.e.*, L0Muon_TOS AND (Hlt1TrackAllL0_TOS OR Hlt1TrackMuon_TOS OR Hlt1SingleMuonHighPT_TOS). The efficiency is evaluated as a function of $p_T(\mu)$, $\eta(\mu)$ and $IP(\mu)$. The resulting data-based three-dimensional efficiency map is compared to that obtained from simulated $B^- \rightarrow J/\psi K^-$ decays. Tracking-efficiency corrections are applied to the simulated $B^- \rightarrow J/\psi K^-$ candidates as discussed in 4.2.1.1. The ratio between data- and simulation-based efficiencies is used to compute per-candidate weights that correct the simulated samples. The one-dimensional projections of the three-dimensional ratio between data- and simulation-based efficiency maps are shown in Fig. 4.6.

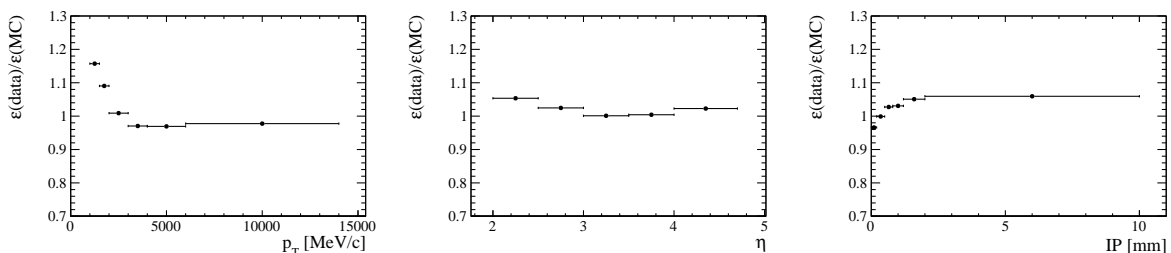


Figure 4.6: Data-to-simulation ratio of trigger (L0 and HLT1) efficiency maps projected as a function of (left) transverse momentum, (middle) pseudorapidity and (right) impact parameter of the muon.

4.2.1.3 PID response

The simulated response of the PID algorithms is corrected using the methods described in Ref. [158]. The simulated response for hadrons is corrected with the PIDCorr method that accounts for the correlation between the response of the different PID algorithms used in the analysis (*e.g.*, those based on likelihood ratios and those based on artificial neural networks). For muons, since only likelihood-ratio PID variables are used in the analysis, the PIDGen method is used instead. The PIDGen method is based on a resampling approach. Let $p_{\text{exp}}(x|p, \eta, N_{\text{tr}})$ be the *p.d.f.* of a generic PID variable x , depending on the momentum, p , and the pseudorapidity, η , of a given simulated candidate, and on the number of charged tracks, N_{tr} , in the same event. The inversion of the corresponding cumulative distribution,

$$P_{\text{exp}}(x|p, \eta, N_{\text{tr}}) = \int_{-\infty}^x p_{\text{exp}}(y|p, \eta, N_{\text{tr}}) dy,$$

provides the way to generate a random number x_{corr} distributed according to p_{exp} and representing the corrected PID variable. In particular: $x_{\text{corr}} = P_{\text{exp}}^{-1}(\xi|p, \eta, N_{\text{tr}})$, where ξ is uniformly distributed between 0 and 1. This method discards the value x_{MC} of the PID variable obtained by the simulation. The PIDCorr method, instead, calculates ξ as:

$$\xi' = P_{\text{MC}}(x_{\text{MC}}|p, \eta, N_{\text{tr}}) = \int_{-\infty}^{x_{\text{MC}}} p_{\text{MC}}(y|p, \eta, N_{\text{tr}}) dy,$$

where p_{MC} is the *p.d.f.* of x_{MC} . This modification is necessary to adequately preserve the correlation between multiple PID variables associated to the same final-state candidate. The functions p_{exp} and p_{MC} are obtained using a KDE method [159]. In the case of p_{exp} , it is applied on the calibration samples provided with the PIDCalib tool (see Sect. 3.2.1 and Ref.s [129,130]), whereas the samples simulated for this analysis are used for p_{MC} .

4.2.1.4 $B^0_{(s)}$ meson kinematics

The kinematic distributions of the parent b meson are corrected for, on a candidate-by-candidate basis, using weights derived from $B^- \rightarrow J/\psi K^-$ decays (for the B^0 and B^+ samples) and $B_s^0 \rightarrow J/\psi \phi$ decays (for the B_s^0 samples). $B^- \rightarrow J/\psi K^-$ and $B_s^0 \rightarrow J/\psi \phi$ decays from data and simulation are used to build ratios of two-dimensional (p_T, η) distributions. The simulation samples are corrected for tracking, trigger and PID as discussed before. The data-to-simulation ratio of the two-dimensional (p_T, η) distribution is shown in Fig. 4.7. A different binning scheme is employed for $B^- \rightarrow J/\psi K^-$ and $B_s^0 \rightarrow J/\psi \phi$ decays due to the different sample size. Finally, semileptonic candidates from the simulation samples are weighted using these maps and the candidates' true p_T and η .

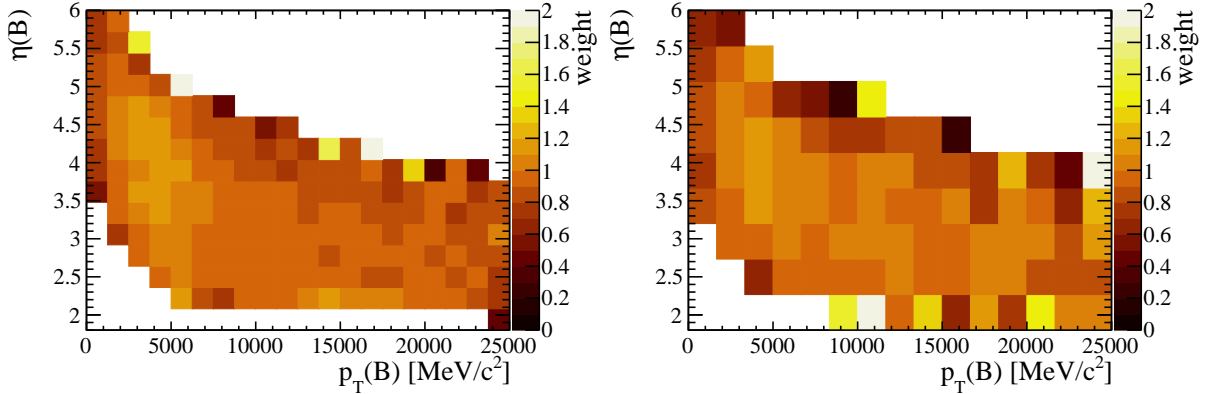


Figure 4.7: Data-to-simulation ratio for (left) $B^- \rightarrow J/\psi K^-$ and (right) $B_s^0 \rightarrow J/\psi \phi$ candidates as a function of the B transverse momentum and pseudorapidity.

4.2.2 Simulation of signal and reference decays

The $B^0 \rightarrow D^- \mu^+ \nu_\mu$ decays are simulated with the EVTGEN decay model HQET2 1.18 1.074, which uses the CLN parametrisation (see Section 1.4) of the decay form factors and where the first number gives the values of the parameter ρ^2 and the second the normalisation $\mathcal{G}(0)$. The $B^0 \rightarrow D^{*-} \mu^+ \nu_\mu$ decay is generated with the EVTGEN decay model HQET 1.20 1.426 0.818 0.908, which uses the CLN parametrisation and where the numbers correspond to the parameters ρ^2 , R_1 , R_2 , $\mathcal{F}(1)$, respectively, with Eq. (1.112) truncated at the second order in z . This configuration is changed to HQET2 1.122 0.921 1.270 0.852, with a change in the ordering of the numbers, which now represent ρ^2 , $\mathcal{F}(1)$, R_1 and R_2 , respectively. The change is made with a reweighting procedure, which is also used in the fit described in Sec. 4.3. Such a reweighting updates the model to the full expression of Eq. (1.111) and the parameters to the most recent known values from the 2019 HFLAV average (for consistency also the $B^0 \rightarrow D^- \mu^+ \nu_\mu$ parameters have been

updated using $\rho^2(D) = 1.131$). The D^{*-} is forced to decay to a D^- with either a π^0 (with $\sim 95\%$ probability) or a γ (with $\sim 5\%$ probability). The D^- is forced to decay to either the $K^+K^-\pi^-$ or $K^+\pi^-\pi^-$ final state; in both cases, the full Dalitz structure is simulated.

The $B_s^0 \rightarrow D_s^- \mu^+ \nu_\mu$ decay is generated with the EVTGEN decay model HQET2 1.17 1.074, while the $B_s^0 \rightarrow D_s^{*-} \mu^+ \nu_\mu$ decay with HQET2 1.16 1.37 0.845 0.921. The latter is changed to HQET2 1.122 0.921 1.270 0.852 to mirror the $B^0 \rightarrow D^{*-} \mu^+ \nu_\mu$ update, while the value of $\rho^2(D_s)$ is updated to 1.229 following the study on lattice data presented in Appendix B.1. The D_s^{*-} meson is simulated to decay to a D_s^- with either a π^0 (with $\sim 6\%$ probability) or a γ (with $\sim 94\%$ probability). The D_s^- meson is forced to decay to the $K^+K^-\pi^-$ final state and the full Dalitz structure is simulated. Table 4.5 resumes the setup of the Form Factor parameters after the corrections to the simulation described in this Section.

4.2.2.1 Efficiency ratios

The simulated candidates are used to calculate the efficiency of reconstructing and selecting signal and reference decays that are input to the fit described in Section 4.3 used to determine $|V_{cb}|$, \mathcal{R} , and \mathcal{R}^* . The efficiencies are computed separately for 2011 and 2012 data-taking conditions, and then averaged with weights representing the relative amount of data for each period.

Table 4.6 reports the efficiencies for signal and reference decays from which the following ratios are derived:

$$\xi \equiv \frac{\epsilon(B_s^0 \rightarrow D_s^- \mu^+ \nu_\mu)}{\epsilon(B^0 \rightarrow D^- (\rightarrow K^+ K^- \pi^-) \mu^+ \nu_\mu)} = 1.5679 \pm 0.0083, \quad (4.4)$$

$$\xi^* \equiv \frac{\epsilon(B_s^0 \rightarrow D_s^{*-} \mu^+ \nu_\mu)}{\epsilon(B^0 \rightarrow D^{*-} [\rightarrow D^- (\rightarrow K^+ K^- \pi^-) X] \mu^+ \nu_\mu)} = 1.4635 \pm 0.0073, \quad (4.5)$$

$$\xi_d \equiv \frac{\epsilon(B^0 \rightarrow D^- (\rightarrow K^+ \pi^- \pi^-) \mu^+ \nu_\mu)}{\epsilon(B^0 \rightarrow D^- (\rightarrow K^+ K^- \pi^-) \mu^+ \nu_\mu)} = 2.3718 \pm 0.0093, \quad (4.6)$$

$$\xi_d^* \equiv \frac{\epsilon(B^0 \rightarrow D^{*-} [\rightarrow D^- (\rightarrow K^+ \pi^- \pi^-) X] \mu^+ \nu_\mu)}{\epsilon(B^0 \rightarrow D^{*-} [\rightarrow D^- (\rightarrow K^+ K^- \pi^-) X] \mu^+ \nu_\mu)} = 2.3539 \pm 0.0110. \quad (4.7)$$

The departure from unity of the efficiency ratios between signal and normalisation decays is mainly due to the requirement on $m(K^+K^-)$ to be around the ϕ mass, which is applied in the stripping, and makes the kinematics of signal and normalisation decays more similar to each other. The efficiency of this requirement relies on an accurate description in the simulation of the $D_{(s)}^- \rightarrow K^+K^-\pi^-$ amplitude model; a systematic uncertainty is assigned to cover a possible mismodeling in Section 4.5.2. It is worth noticing that the efficiency ratios between the B^0 control and normalisation decays, ξ_d and ξ_d^* , deviate from unity more than for the B_s^0 efficiency ratios, ξ and ξ^* , because the control mode uses a different D^+ final state. This provides a nice validation of the measurements of \mathcal{R} and \mathcal{R}^* (and thus $|V_{cb}|$) based on corrections 40% larger than those needed for the B_s^0 decays, as discussed in Section 4.4.2.

Given the above efficiency ratios and assuming unit values for \mathcal{R} and \mathcal{R}^* , the $B_s^0 \rightarrow D_s^- \mu^+ \nu_\mu$ and $B_s^0 \rightarrow D_s^{*-} \mu^+ \nu_\mu$ exclusive decays are expected to constitute about 30% and 60% of the inclusive B_s^0 sample, respectively. The $B^0 \rightarrow D^- \mu^+ \nu_\mu$ and $B^0 \rightarrow D^{*-} \mu^+ \nu_\mu$ exclusive decays are expected to constitute about 50% and 30% of the inclusive B^0 sam-

ple, respectively (the branching fraction of $D^{*-} \rightarrow D^- X$ decays, about 30%, must be considered for the $B^0 \rightarrow D^{*-} \mu^+ \nu_\mu$ decay).

4.2.3 Physics backgrounds

Simulation is also used to compute the efficiency of the background decays that are expected to contribute to the B_s^0 and B^0 samples, such that an estimate of their fraction with respect to the signals can be made from known (or guessed) branching fractions. The background efficiencies are reported in Table 4.7 grouped by categories as detailed in the following sections.

4.2.3.1 Feed-down from semimuonic $B_{(s)}^0$ decays

Table 4.8 reports the full list of feed-down backgrounds from $B_{(s)}^0$ semimuonic decays to excited $D_{(s)}^-$ states other than $D_{(s)}^{*-}$, indicated inclusively as $D_{(s)}^{**}$ in the following, or with a non-resonant combination of a $D_{(s)}^{(*)-}$ with pions that are considered in the analysis.

In the B^0 case, such backgrounds are expected to contribute about 9% of the inclusive sample. Their composition reflects what considered in several other LHCb analyses (*e.g.*, Ref. [160]) when modelling the inclusive sample of semileptonic B^0 decays, and it is mostly based on experimental measurements as discussed in Ref. [161]. As for the signal modes, the D^{*-} is forced to decay to a D^- with either a π^0 (about 95% of the times) or a γ (for the remaining 5%) and the D^- is forced to decay to either the $K^+ K^- \pi^-$ or $K^+ \pi^- \pi^-$ final state with the full Dalitz structure for both cases.

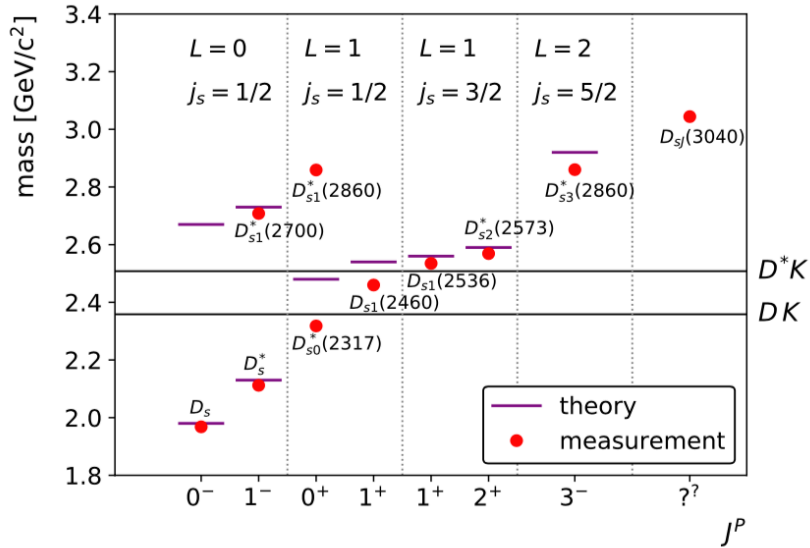


Figure 4.8: Mass spectrum of D_s^- meson states, reproduced from Ref. [162]. The y axis shows the mass, the x axis the total angular momentum (J) and parity (P). Reported between the vertical dotted lines are the orbital angular momentum (L) and total angular momentum of the s quark (j_s). Also shown are the DK and DK^* thresholds.

Less experimental information is available for B_s^0 decays of the same type that contribute to the B_s^0 sample. An overview of the observed and predicted D_s^{*-} states is shown

in Fig. 4.8. The thresholds above which D_s^{*-} states decay strongly to DK or D^*K final states are also reported. The backgrounds considered in the analysis are limited to the semimuonic decays of the B_s^0 meson to the two lightest states, D_{s0}^{*-} (2317) and D_{s1}^- (2460), and to the D_{s1}^- (2536) state, which, despite being above the DK^* threshold, has been observed to decay to $D_s^- \pi^+ \pi^-$ and $D_s^- \gamma$ [4]. The D_{s0}^{*-} (2317) is required to decay to $D_s^- \pi^0$; the D_{s1}^- (2460) to $D_s^- \gamma$ (branching fraction 0.0337), $D_s^{*-} \pi^0$ (0.097), $D_s^- \pi^+ \pi^-$ (0.0077), $D_s^- \pi^0 \pi^0$ (0.0038), $D_s^- \gamma \gamma$ (0.008), and $D_s^{*-} \gamma$ (0.008).

The D_s^{*-} is required to decay to a D_s^- with either a π^0 (with $\sim 6\%$ probability) or a γ (with $\sim 94\%$ probability) and the D_s^- is forced to decay to the $K^+ K^- \pi^-$ final state with the full Dalitz structure. Branching fractions of these semimuonic B_s^0 decays are not known, but based on what observed in Ref. [154], this background should be a few percent of the signal. The requirement on the plane ($m_{\text{corr}}, p_{\perp}$) is effective in suppressing this background, and tighter and looser variation of this requirement will be considered to estimate a systematic uncertainty due to the residual contamination (Section 4.5).

4.2.3.2 Feed-down from semitauonic $B^0_{(s)}$ decays

Semitauonic $B^0_{(s)}$ decays, where the τ decays into the $\mu\nu\nu$ final state, are also considered, as reported in Table 4.9. Also, these decays are part of the nominal model of the inclusive sample of semileptonic B^0 decays discussed in Ref. [161]. These decays are estimated to contribute less than 1% for both the B_s^0 and B^0 samples.

4.2.3.3 Semileptonic B^+ decays

In the B^0 sample, a contribution of about 9% from semileptonic B^+ decays is expected (*e.g.*, see Section 3.2 of Ref. [154]). The composition of this background is detailed in Table 4.10 and includes both semimuonic and semitauonic modes, with $\tau \rightarrow \mu\nu\nu$. The composition is estimated following Ref. [161], as for several other LHCb analyses (*e.g.*, Ref. [160]).

4.2.3.4 Decays of b hadrons to doubly charmed final states

Background can originate from B , B_s^0 or A_b^0 decaying into a pair of charm hadrons, where one hadron is the fully reconstructed $D_{(s)}^-$ candidate and the other decays semileptonically. While such background is expected to be negligible in the B^0 sample, it is estimated to contribute up to about 2% of the B_s^0 sample following Ref. [154] and is considered in the analysis using the simulated decays listed in Table 4.3.

4.2.3.5 Cross-feed from semileptonic b -hadron decays

While semileptonic B_s^0 decays are expected to give a negligible contribution to the inclusive B^0 or B^+ samples, semileptonic B^0 and B^+ decays to final states with a D_s^- and an unreconstructed kaon, such as $B \rightarrow D_0^*(2400)(\rightarrow D_s^{(*)-} K) \mu^+ \nu$, can contribute to the inclusive B_s^0 sample. Following Ref. [154], this contamination, which is estimated to be at most 2% of the B_s^0 sample, is therefore considered in the analysis.

4.3 Determination of the parameters of interest

The value of $|V_{cb}|$ and the ratios of the branching fractions, \mathcal{R} and \mathcal{R}^* as defined in Eqs. (4.1)-(4.2), are derived from the signal and reference yields measured in the inclusive $B_s^0 \rightarrow D_s^- (\rightarrow K^+ K^- \pi^-) \mu^+ \nu_\mu X$ and $B^0 \rightarrow D^- (\rightarrow K^+ K^- \pi^-) \mu^+ \nu_\mu X$ samples, respectively. The signal and reference yields, $N_s^{(*)}$ and $N_{\text{ref}}^{(*)}$, can be precisely measured through a fit to the corrected mass distribution of the inclusive samples [153, 154]. However, this variable doesn't provide information on the decay form factors. These can be studied by measuring the variation of the signal yields as a function of w or q^2 , but these variables are not directly accessible in semileptonic decay because of the undetected neutrino. The method adopted here is described in the following.

4.3.1 The p_\perp variable

The per-candidate q^2 can be approximately inferred from the reconstructed quantities, using kinematic constraints and assuming that only the neutrino is undetected, through a second-order equation in the component of the neutrino momentum parallel to the flight direction of the $B^0_{(s)}$ candidate. Generally, this introduces a two-fold ambiguity that can be resolved, *e.g.*, by using multivariate regression algorithms [163]. This approach suffers from $\mathcal{O}(25\%)$ inefficiencies because, due to resolution effects, the second order equation does not always have real solutions. It also results in a broad resolution and, for the $B_s^0 \rightarrow D_s^{*-} \mu^+ \nu_\mu$ decay, there is a further bias if only the D_s^- is reconstructed in D_s^{*-} decays. The inability to use candidates for which no real solutions are found also restricts the allowed values of m_{corr} to those that are smaller than the nominal $B^0_{(s)}$ mass, hence reducing the discrimination power between the different sample components.

To overcome such problems, an alternative approach is adopted in which the momentum of the $D_{(s)}$ meson transverse to the $B^0_{(s)}$ flight direction, p_\perp , is used as a proxy variable for q^2 . In $B_s^0 \rightarrow D_s^- \mu^+ \nu_\mu$ decays, the p_\perp vector is opposite and equal in magnitude to the W momentum vector transverse to the B_s^0 direction. This is invariant with respect to the B_s^0 boost. In $B_s^0 \rightarrow D_s^{*-} \mu^+ \nu_\mu$ decays, the unreconstructed γ or π^0 from the D_s^{*+} decay only leads to a small dilution. The p_\perp variable has the advantage of being fully reconstructable from the tracks of the D_s decay products. As shown in Fig. 4.9, p_\perp is highly correlated with q^2 , and its distribution depends on the form factors. This is shown by the variation of the distribution as a function of the parameter ρ^2 for a sample of simulated $B_s^0 \rightarrow D_s^- \mu^+ \nu_\mu$ and $B_s^0 \rightarrow D_s^{*-} \mu^+ \nu_\mu$ decay. In the case of $B_s^0 \rightarrow D_s^{*-} \mu^+ \nu_\mu$ decays, the p_\perp variable also presents correlations with the helicity angle θ_V , and very little with angle θ_l (none with χ). This is shown in Fig. 4.10. Such correlations turn out to be important to gain sensitivity on the $R_1(w)$ and $R_2(w)$ form factors, which are not accessible if studying the q^2 distribution only. The variation of the efficiency (in arbitrary units) as a function of p_\perp^{true} , *i.e.*, the value of p_\perp calculated from true-level momenta, is shown in Figure 4.11.

The p_\perp distribution is correlated with the m_{corr} variable, meaning that the latter is also influenced by the assumed form-factor values. The m_{corr} and p_\perp variables provide a powerful discrimination in the determination of the sample composition, as the distribution of the two signal decays, as well as those of the background decays accumulate in well-separated regions in the two-dimensional space of p_\perp and m_{corr} . This is shown in Fig. 4.12 for all decays contributing to the B_s^0 sample. The two-dimensional distribution is plotted

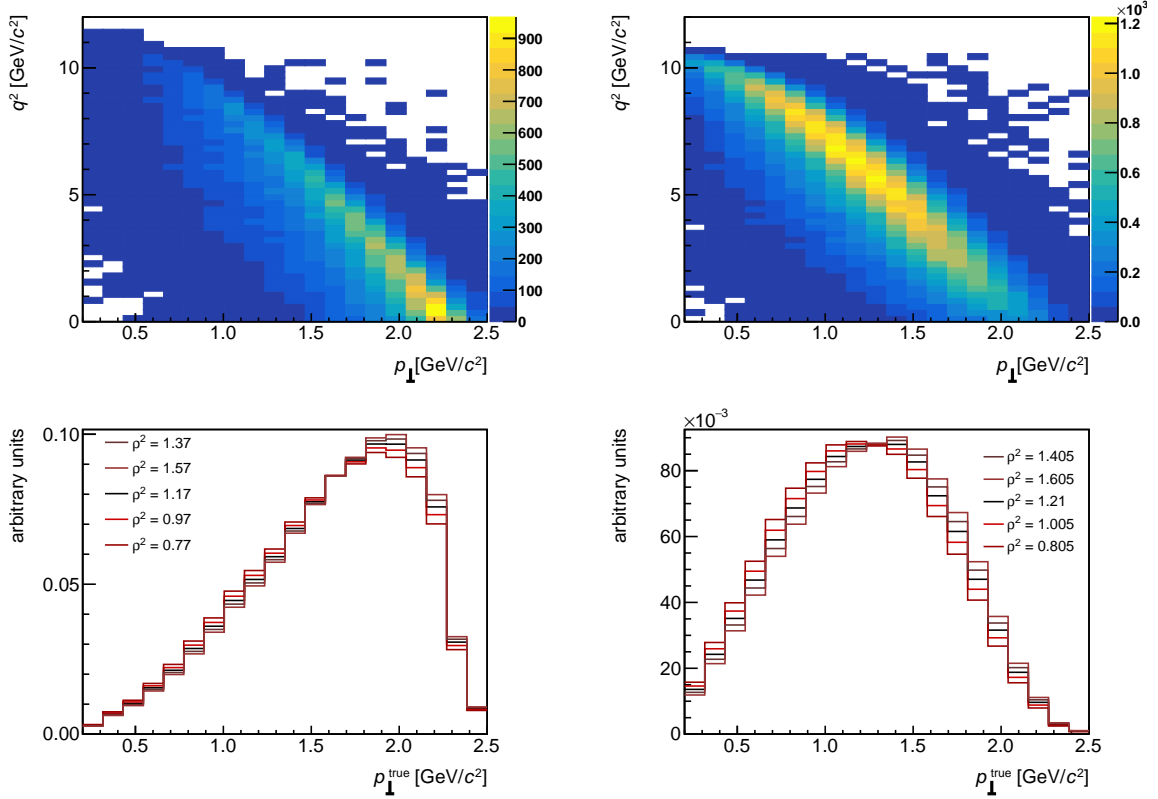


Figure 4.9: For (left column) $B_s^0 \rightarrow D_s^- \mu^+ \nu_{\mu}$ and (right column) $B_s^0 \rightarrow D_s^{*-} \mu^+ \nu_{\mu}$ simulated candidates, (top) reconstructed p_{\perp} distribution versus true q^2 after the full selection; (bottom) distribution of p_{\perp}^{true} for different values of ρ^2 .

without the requirement $p_{\perp} [\text{GeV}/c] < 1.5 + 1.1 \times (m_{\text{corr}} [\text{GeV}/c^2] - 4.5)$, which is drawn as a black line, to show how such a requirement suppresses background decays. The red line shows a tighter cut applied on top of the baseline requirement to further suppress the background and thus assess a systematic uncertainty on the residual background contamination (see Sec. 4.5.3).

4.3.2 χ^2 fit function

A binned least-squares fit to the two-dimensional distribution of the m_{corr} and p_{\perp} variables is used to determine the sample composition and the parameters of interest. The inclusive samples of B_s^0 and B^0 decays are described by several components, as explained in the following sections. Each component is modelled in the two-dimensional $(m_{\text{corr}}, p_{\perp})$ plane by a two-dimensional histogram template. The templates describing the physics decays, signal and background, are derived from simulated candidates, with 2011 and 2012 conditions, summed with the same proportions as in data. The template describing the combinatorial background is modelled using SS data.

The fit minimizes the following χ^2 -like variable, which also accounts for the limited size of the simulated samples:

$$\chi^2 = \sum_i^{\text{bins}} \frac{[n_i - p_i]^2}{\sigma_{n_i}^2 + \sigma_{p_i}^2}, \quad (4.8)$$

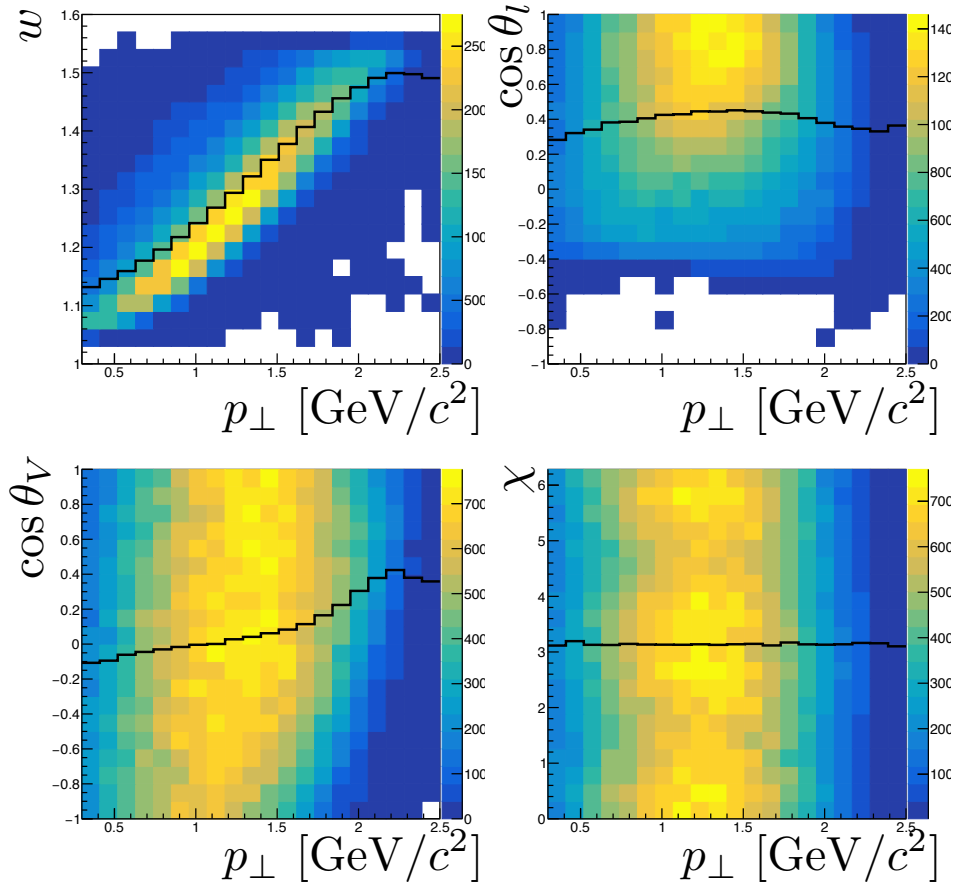


Figure 4.10: Simulated $B_s^0 \rightarrow D_s^{*-} \mu^+ \nu_\mu$ candidates after the full selection: distribution of p_\perp versus (top-left) true w , (top-right) $\cos \theta_l$, (bottom-left) $\cos \theta_V$, and (bottom-right) χ .

where n_i (p_i) is the number of observed (predicted) data candidates in bin i of the $(m_{\text{corr}}, p_\perp)$ plane, and σ_{n_i} (σ_{p_i}) is its statistical uncertainty. The number of predicted candidates is

$$p_i = \sum_j N_j h_{ji},$$

where N_j is the total yield for component j with template h_j , which contributes h_{ji} fractional candidates to bin i of the $(m_{\text{corr}}, p_\perp)$ plane. The templates are normalized to unity in the fit range. The uncertainty on the prediction is computed by propagating the statistical uncertainty on the template bin content $\sigma_{h_{ji}}$. The yields of the fit components are floating parameters of the fit. In the case of the fit to the B_s^0 sample, the yield of the two signal decays can be expressed as a function of $|V_{cb}|$, or \mathcal{R} and \mathcal{R}^* , as presented in Sects. 4.3.5 and 4.3.6.

The signal templates are functions of the form factors. This dependence is made explicit in the fit through a reweighting procedure. The fit function of Eq. (4.8) is minimized numerically with the MINUIT package; during the minimization, at each MINUIT call of the χ^2 function, the $(m_{\text{corr}}, p_\perp)$ -histogram templates are refilled using the simulated candidates for the given component, and each candidate is weighted with a weight that depend on the form factors. Such a weight is calculated with the one-dimensional decay

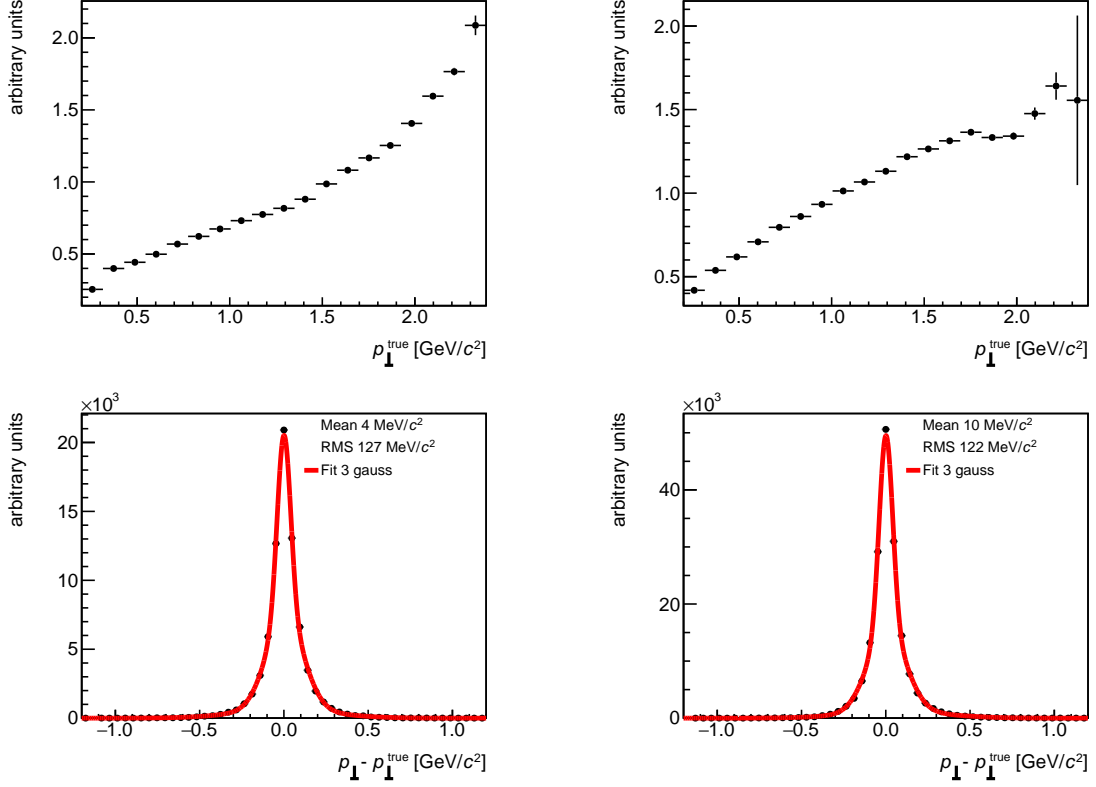


Figure 4.11: For (left column) $B_s^0 \rightarrow D_s^- \mu^+ \nu_\mu$ and (right column) $B_s^0 \rightarrow D_s^{*-} \mu^+ \nu_\mu$ simulated candidates, (top) efficiency as a function of p_\perp^{true} ; (bottom) distribution of $p_\perp - p_\perp^{\text{true}}$, fit with a sum of three Gaussian functions.

rate of Eq. (1.101) for the $B_s^0 \rightarrow D_s^- \mu^+ \nu_\mu$ candidates, and with the four-dimensional decay rate of Eq. (1.106) for the $B_s^0 \rightarrow D_s^{*-} \mu^+ \nu_\mu$ candidates. The weights are

$$\omega_D(\vec{q}_{\text{true}}) = \left[\frac{d\Gamma(B \rightarrow D\mu\nu)}{dw}(\vec{q}_{\text{true}}|\vec{x}) \right] \Bigg/ \left[\frac{d\Gamma(B \rightarrow D\mu\nu)}{dw}(\vec{q}_{\text{true}}|\vec{x}_{\text{sim}}) \right], \text{ and} \quad (4.9)$$

$$\omega_{D^*}(\vec{q}_{\text{true}}) = \left[\frac{d^4\Gamma(B \rightarrow D^*\mu\nu)}{dwd \cos \theta_V d \cos \theta_l d\chi}(\vec{q}_{\text{true}}|\vec{x}) \right] \Bigg/ \left[\frac{d^4\Gamma(B \rightarrow D^*\mu\nu)}{dwd \cos \theta_V d \cos \theta_l d\chi}(\vec{q}_{\text{true}}|\vec{x}_{\text{sim}}) \right] \quad (4.10)$$

for $B_s^0 \rightarrow D_s^- \mu^+ \nu_\mu$ and $B_s^0 \rightarrow D_s^{*-} \mu^+ \nu_\mu$ decays, respectively. Here, \vec{q}_{true} are true-level particles quadrivectors used to compute w and the helicity angles, \vec{x} is the vector of the decay form-factor parameters being minimized, and \vec{x}_{sim} are the parameters fixed at the values used in the generation of the simulated candidates. For instance, in the CLN parametrization, for the decay $B_s^0 \rightarrow D_s^- \mu^+ \nu_\mu$, $d\Gamma/dw$ is given by Eq. (1.101) with the parametrization of Eq. (1.104), $\vec{x} \equiv \{\rho^2\}$, and $\vec{x}_{\text{sim}} \equiv \{\rho^2 = 1.229\}$; for the decay $B_s^0 \rightarrow D_s^{*-} \mu^+ \nu_\mu$, $d^4\Gamma/dwd \cos \theta_V d \cos \theta_l d\chi$ is given by Eq. (1.106) with the parametrization of Eqs. (1.112)–(1.114), $\vec{x} \equiv \{\rho^2, R_1, R_2\}$, and $\vec{x}_{\text{sim}} \equiv \{\rho^2 = 1.122, R_1 = 1.270, R_2 = 0.852\}$. This procedure allows minimizing the χ^2 function by continuously scanning the parameter space, while accounting for any variation of the efficiency and resolution as a function of $(m_{\text{corr}}, p_\perp)$. With this method, both efficiency and resolution do not depend on the value of the parameters used in the generation of the simulated samples.

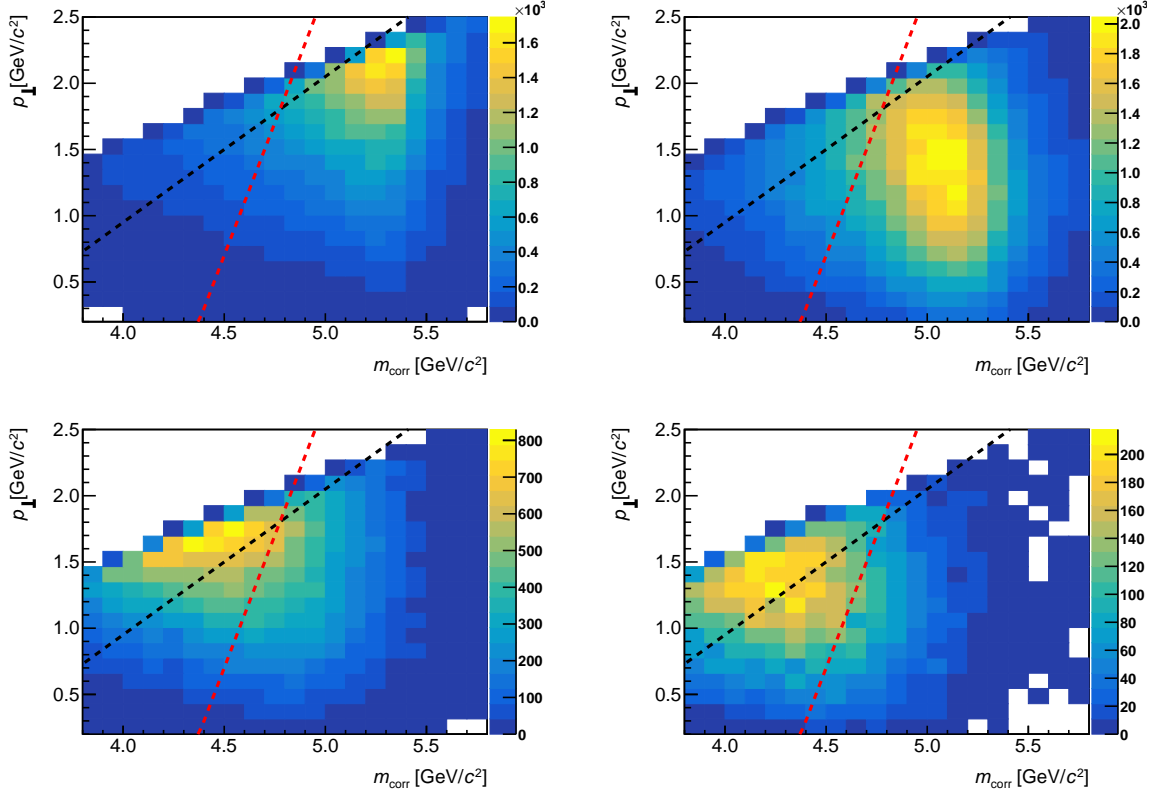


Figure 4.12: Two-dimensional distribution in the m_{corr} and p_{\perp} variables for simulated (top-left) $B_s^0 \rightarrow D_s^- \mu^+ \nu_{\mu}$ decays; (top-right) $B_s^0 \rightarrow D_s^{*-} \mu^+ \nu_{\mu}$ decays; (bottom-left) background decays from B_s^0 feed-down and b hadron decays to a doubly-charmed final state; (bottom-right) background decays from B cross-feed and semitauonic B_s^0 decays. The background are grouped together according to their shapes in the $(m_{\text{corr}}, p_{\perp})$ plane. The requirement $p_{\perp} [\text{GeV}/c] < 1.5 + 1.1 \times (m_{\text{corr}} [\text{GeV}/c^2] - 4.5)$ is drawn as a black line, while the red line is a tighter cut applied to assess a systematic uncertainty on the residual background contamination.

A comment on the weight ω_{D^*} for the $B_s^0 \rightarrow D_s^{*-} \mu^+ \nu_{\mu}$ decays. As shown in Tab. 1.4, the angular functions differs for D_s^{*-} decays to final states with a photon or a pion. The D_s^{*-} decays are not reconstructed in the analysis, so the weight ω_{D^*} is calculated as an average of the differential decay rate for a photon final state and that for a pion final state, weighted by their branching fractions (95% for $D_s^{*-} \rightarrow D_s^- \gamma$ and 5% for $D_s^{*-} \rightarrow D_s^- \pi^0$). The same applies to the B^0 case (but swapping the numbers for the branching fractions of the decays to a photon or a pion).

4.3.3 Determination of the reference yields

The yields of the $B^0 \rightarrow D^- \mu^+ \nu_{\mu}$ and $B^0 \rightarrow D^{*-} \mu^+ \nu_{\mu}$ control decays are determined by a fit to the $(m_{\text{corr}}, p_{\perp})$ data distribution with the following components:

1. $B^0 \rightarrow D^- \mu^+ \nu_{\mu}$ decays;
2. $B^0 \rightarrow D^{*-} \mu^+ \nu_{\mu}$ decays;

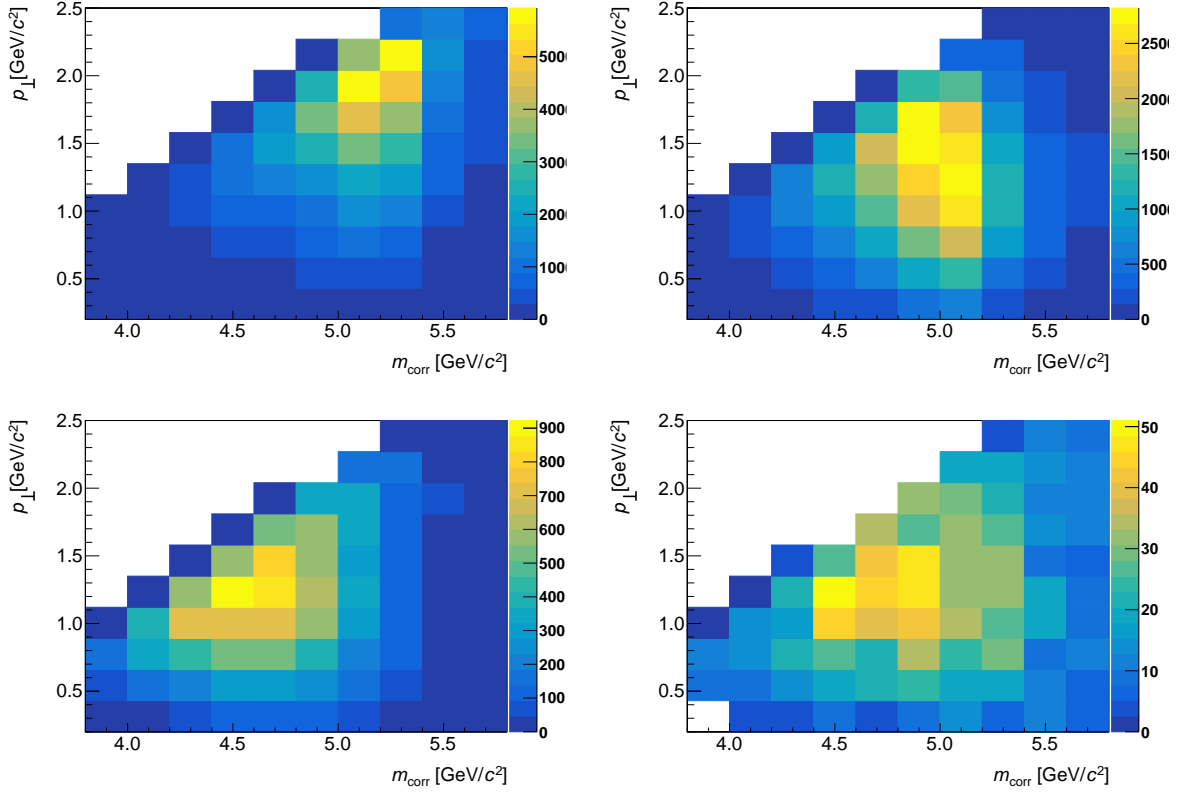


Figure 4.13: Two-dimensional distribution in the m_{corr} and p_{\perp} variables used as template in the fit to the reference sample (top-left) $B^0 \rightarrow D^- \mu^+ \nu_{\mu}$ decays; (top-right) $B^0 \rightarrow D^{*-} \mu^+ \nu_{\mu}$ decays; (bottom-left) background decays from B^0 feed-down and B^+ decays; (bottom-right) combinatorial background.

3. the sum of the B^0 and B^+ background decays described in Secs. 4.2.3.1 and 4.2.3.3, which are considered as a single component;
4. combinatorial background.

The B^0 and B^+ background components are lumped together in a single template because their $(m_{\text{corr}}, p_{\perp})$ distributions are indistinguishable, providing no discrimination handles in the fit. The templates are merged to increase the histograms statistics and minimise fluctuations, by considering an equal proportion between the two backgrounds as per Table 4.7. Background from semitauonic decays (Sec. 4.2.3.2) is neglected because it is found to be compatible with zero in an alternate fit in which it is included, and no significant change of the reference yields are observed. The templates describing each component are shown in Fig. 4.13. The fit parameters are the reference yields, N_{ref} and N_{ref}^* , the yields of the background components, N_{bkg} and N_{comb} , and the form-factor parameters of the CLN parametrisation, $\rho^2(D)$, $\rho^2(D^*)$, R_1 and R_2 .

The one-dimensional projections are shown in Fig. 4.14. One-dimensional projections in m_{corr} for different bins of p_{\perp} (and viceversa) are shown in App. B.3. The fit describes the data reasonably well, with a χ^2/ndf at the minimum of 76/70 (probability of 29%),

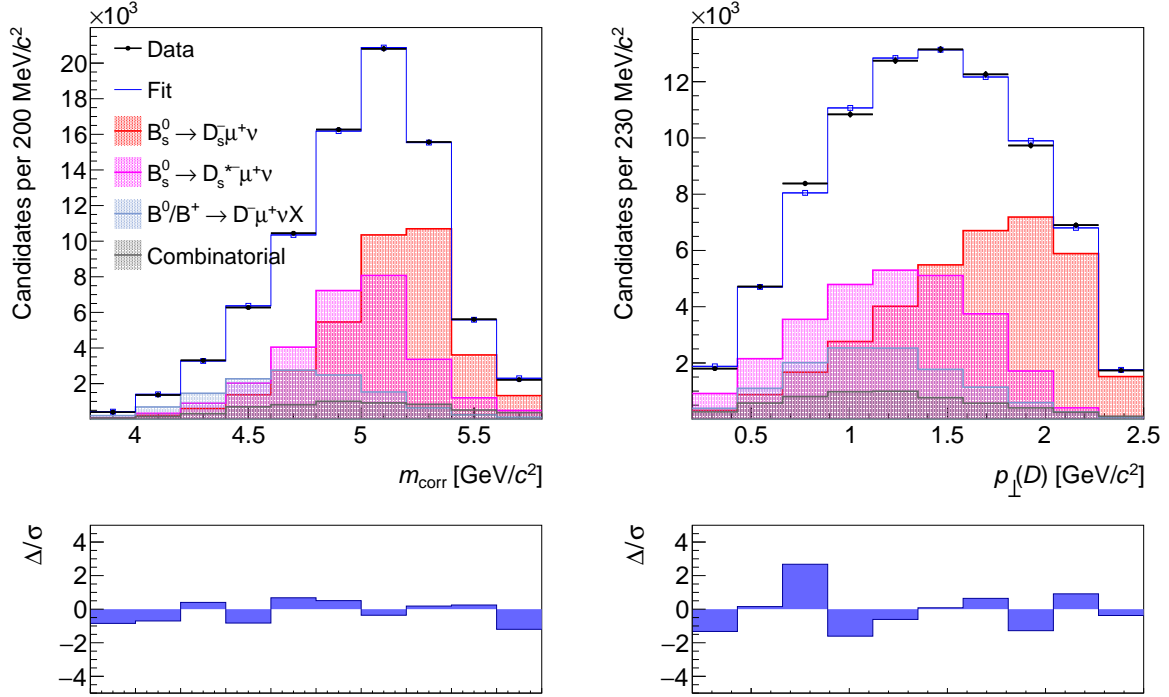


Figure 4.14: Normalisation sample: distribution of (left) m_{corr} and (right) p_{\perp} variables with fit projections overlaid.

and measures

$$N_{\text{ref}} = 36432 \pm 1602, \quad (4.11)$$

$$N_{\text{ref}}^* = 27757 \pm 1155, \quad (4.12)$$

with a correlation of -0.703 . The value of all fit parameters are reported in Tab. 4.11. Form factors parameters are measured to be in agreement with world averages.

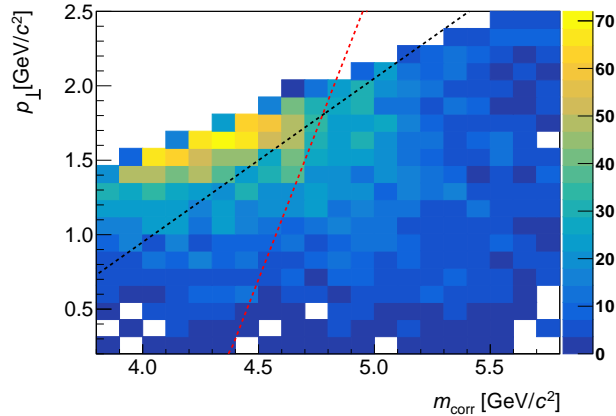


Figure 4.15: The two-dimensional distribution of m_{corr} and p_{\perp} variables for SS data used as fit template describing the combinatorial background to the B_s^0 sample.

4.3.4 Components of the fit to the B_s^0 sample

The fit to the B_s^0 sample features the following components:

1. $B_s^0 \rightarrow D_s^- \mu^+ \nu_{\mu}$ signal decays;
2. $B_s^0 \rightarrow D_s^{*-} \mu^+ \nu_{\mu}$ signal decays;
3. the sum of background sources from feed-down semimuonic B_s^0 decays described in Sec. 4.2.3.1 and b hadron decays to a doubly charmed final state described in Sec. 4.2.3.4, which are considered as a single component, named “background 1”;
4. the sum of background sources from cross-feed semileptonic B decays described in Sec. 4.2.3.5 and B_s^0 semitauonic decays described in Sec. 4.2.3.2, considered as a single component, named “background 2”;
5. combinatorial background.

The background sources lumped together in the two categories “background 1” and “background 2” have very similar shapes in the $(m_{\text{corr}}, p_{\perp})$ plane and cannot be discriminated by the fit when separated. They are therefore merged according to the expected approximate fractions presented in Table 4.7. The templates for components one to four of the above list are those displayed in Fig. 4.12, with the nominal requirement applied ($p_{\perp} [\text{GeV}/c] < 1.5 + 1.1 \times (m_{\text{corr}} [\text{GeV}/c^2] - 4.5)$, corresponding to the black line). The template for the combinatorial background is modelled with SS data, and it is shown in Fig. 4.15. The background yields are left free to float. The signal yields are parametrised differently in the case of the fit to determine $|V_{cb}|$ or \mathcal{R} and \mathcal{R}^* , as explained in the following sections.

Table 4.1: Summary of stripping selections. (*) The requirement on $m(K^+K^-)$ is applied only to the `b2DsPhiPiMuXB2DMuNuX` line, all other requirements are applied also to the `b2DpMuXB2DMuNuX` line.

Quantity	Requirement
<code>ProbNNghost(μ, π, K)</code>	< 0.5
Minimum IP $\chi^2(\mu)$	> 9.0
Minimum IP $\chi^2(\pi, K)$	> 4.0
$p_T(\mu)$	$> 1.0 \text{ GeV}/c$
$p(\mu)$	$> 6.0 \text{ GeV}/c$
<code>PIDmu(μ)</code>	> 0.0
<code>IsMuon(μ)</code>	True
Track χ^2/ndf	< 4.0
$p_T(K), p_T(\pi)$	$> 250 \text{ MeV}/c$
$p(K), p(\pi)$	$> 2.0 \text{ GeV}/c$
<code>PIDK(K)</code>	> -5.0
<code>PIDK(π)</code>	< 20.0
D daughters' $\sum p_T$	$> 1.8 \text{ GeV}/c$
D vertex χ^2/ndf	< 6.0
D χ^2/ndf separation from PV	> 25
D DIRA	> 0.99
$m(D_{(s)}^-)$	$\in [1789.650, 2048.340] \text{ MeV}/c^2$
$m(K^+K^-)$	$\in [979.455, 1059.455] \text{ MeV}/c^2$ (*)
B vertex χ^2/ndf	< 6.0
B DIRA	> 0.999
$m(D_{(s)}\mu)$	$\in [0, 9999] \text{ GeV}/c^2$
$v_z(D) - v_z(B)$	$> -0.1 \text{ mm}$
<code>nLongTracks</code>	< 250

Table 4.2: Summary of offline selection criteria for the (left) $K^+K^-\pi^-$ and (right) $K^+\pi^-\pi^-$ samples. See text for motivations for the various mass vetoes.

Quantity	Requirement	
	$K^+K^-\pi^-$	$K^+\pi^-\pi^-$
PIDK(π)	< 20	< 10
PIDK(K)	> 0	> 4
ProbNNpi(π)	> 0.2	> 0.5
ProbNNk(K)		> 0.2
PIDmu(μ)		> 0
$p(K)$		$[5.0, 100.0]$ GeV/ c
$p(\pi)$		$[5.0, 100.0]$ GeV/ c
$p(\mu)$		$[5.0, 200.0]$ GeV/ c
$p_T(K), p_T(\pi)$	> 0.3 GeV/ c	> 0.5 GeV/ c
$p_T(\mu)$		$[1.0, 14.0]$ GeV/ c
$\eta(\pi), \eta(K), \eta(\mu)$		$[2.0, 4.7]$
$\chi_{\text{IP}}^2(\mu)$		> 25
IP(μ)		< 10 mm
$m(K^+K^-)$	$\in [1.008, 1.032]$ GeV/ c^2	–
$m(Kp\pi)$		$\notin [2.260, 2.310]$ GeV/ c^2
$m(\mu^+\mu^-)$		$\notin [3.040, 3.160]$ GeV/ c^2 $\notin [3.635, 3.735]$ GeV/ c^2
$m(D_{(s)}^-)$	$\in [1.85, 1.89]$ GeV/ c^2 for B^0 $\in [1.945, 1.995]$ GeV/ c^2 for B_s^0	$\in [1.85, 1.89]$ GeV/ c^2
$D_{(s)}^-$ vertex χ^2/ndf		< 6
$\chi_{\text{IP}}^2(D_{(s)}^-)$		< 9
$z_{\text{vtx}}(D) - z_{\text{vtx}}(B)$		> 0
$t(D_{(s)}^-)$		> 0.1 ps
$p_{\perp}(D_{(s)}^-)$		$\in [0.2, 2.5]$ GeV/ c
$p_{\perp}(D_{(s)}^-)[\text{GeV}/c]$		$< 1.5 + 1.1 \times (m_{\text{corr}}[\text{GeV}/c^2] - 4.5)$
$m(D_{(s)}^-\mu^+)$		$\in [3.1, 5.2]$ GeV/ c^2
m_{corr}		$\in [3.5, 5.8]$ GeV/ c^2

Table 4.3: Samples of simulated data used in the analysis.

Sample	Event type	Candidates	
		Generated	Selected
$B_s^0 \rightarrow D_s^- (\rightarrow K^+ K^- \pi^-) \mu^+ \nu_\mu X$	13774206	710 458 278	276 130
$B^0 \rightarrow D^- (\rightarrow K^+ K^- \pi^-) \mu^+ \nu_\mu X$	11874025	593 437 520	145 487
$B^0 \rightarrow D^- (\rightarrow K^+ \pi^- \pi^-) \mu^+ \nu_\mu X$	11874044	1 195 632 500	695 452
$B^+ \rightarrow D^- (\rightarrow K^+ K^- \pi^-) \pi^+ \mu^+ \nu_\mu X$	12875043	1 949 011	10 977
$B^+ \rightarrow D^- (\rightarrow K^+ \pi^- \pi^-) \pi^+ \mu^+ \nu_\mu X$	12875033	91 006 096	29 898
$B^+ \rightarrow D^{(*)0} D_s^{(*)+}$	12875613	15 370 705	941
$B^0 \rightarrow D^{(*)-} D_s^{(*)+}$	11876203	15 356 601	755
$B_s^0 \rightarrow D_s^{(*)-} D_s^{(*)+}$	13574612	15 369 532	1 502
$\Lambda_b^0 \rightarrow \Lambda_c^+ D_s^{(*)-} (\pi^0)$	15674313	31 407 407	1 705
$B^- \rightarrow D_0^{*0} (2400) (\rightarrow D_s^{(*)+} K^+) \mu^- \nu_\mu X$	12775003	28 968 714	3 736
$\bar{B}^0 \rightarrow D_0^{*-} (2400) (\rightarrow D_s^{(*)+} K_S^0) \mu^- \nu_\mu X$	11774003	29 815 146	3 604

 Table 4.4: Selection requirements of the $B^- \rightarrow J/\psi K^-$ and $B_s^0 \rightarrow J/\psi \phi$ control samples.

Requirement	$B^- \rightarrow J/\psi K^-$	$B_s^0 \rightarrow J/\psi \phi$
$p(\mu, K)$	[5, 200] GeV/c	
$p_T(\mu)$	[1.0, 14.0] GeV/c	
$\eta(\mu)$	[2.0, 4.7]	
$\eta(K)$	[2.0, 4.8]	
$\chi_{\text{IP}}^2(B)$	< 25	
$\chi_{\text{IP}}^2(\mu)$	> 25	
m_{KK}	-	[1.000, 1.040] GeV/c ²
$m_{\mu\mu}$	[3.050, 3.150] GeV/c ²	
PIDK(K)	> 0	
$m_{\text{DTF}}(B)$	[5.250, 5.320] GeV/c ²	[5.340, 5.410] GeV/c ²

Decay	Model	ρ^2	$\mathcal{G}(0)$	$\mathcal{F}(1)$	R_1	R_2
$B^0 \rightarrow D^- \mu^+ \nu_\mu$	HQET2	1.131	1.074	-	-	-
$B^0 \rightarrow D^{*-} \mu^+ \nu_\mu$	HQET2	1.122	-	0.921	1.270	0.852
$B_s^0 \rightarrow D_s^- \mu^+ \nu_\mu$	HQET2	1.229	1.074	-	-	-
$B_s^0 \rightarrow D_s^{*-} \mu^+ \nu_\mu$	HQET2	1.122	-	0.921	1.270	0.852

Table 4.5: Values of the Form Factors parameters assumed in the simulation after the corrections described in Sect. 4.2.2.

Table 4.6: Efficiencies of reconstructing and selecting signal, reference, and control decays.

Decay	Efficiency [10^{-3}]		
	2011	2012	Total
$B_s^0 \rightarrow D_s^- \mu^+ \nu_\mu$	0.454 ± 0.002	0.495 ± 0.003	0.481 ± 0.002
$B_s^0 \rightarrow D_s^{*-} \mu^+ \nu_\mu$	0.402 ± 0.001	0.442 ± 0.002	0.429 ± 0.001
$B^0 \rightarrow D^-(\rightarrow K^+ K^- \pi^-) \mu^+ \nu_\mu$	0.285 ± 0.002	0.318 ± 0.001	0.307 ± 0.001
$B^0 \rightarrow D^{*-}[\rightarrow D^-(\rightarrow K^+ K^- \pi^-)X] \mu^+ \nu_\mu$	0.269 ± 0.002	0.305 ± 0.002	0.293 ± 0.001
$B^0 \rightarrow D^-(\rightarrow K^+ \pi^- \pi^-) \mu^+ \nu_\mu$	0.683 ± 0.002	0.751 ± 0.001	0.728 ± 0.001
$B^0 \rightarrow D^{*-}[\rightarrow D^-(\rightarrow K^+ \pi^- \pi^-)X] \mu^+ \nu_\mu$	0.642 ± 0.002	0.713 ± 0.002	0.690 ± 0.001

Table 4.7: Expected approximate composition of the inclusive $B_s^0 \rightarrow D_s^-(\rightarrow K^+ K^- \pi^-) \mu^+ \nu_\mu X$ and $B^0 \rightarrow D^-(\rightarrow K^+ K^- \pi^-) \mu^+ \nu_\mu X$ samples in terms of the two signal modes and of the dominant background components. Together with the expected fraction, the total selection efficiency of each component is also reported.

Sample components	Efficiency [10^{-3}]	Fraction [%]
$B_s^0 \rightarrow D_s^-(\rightarrow K^+ K^- \pi^-) \mu^+ \nu_\mu X$		
$B_s^0 \rightarrow D_s^- \mu^+ \nu_\mu$ signal	0.481 ± 0.002	30
$B_s^0 \rightarrow D_s^{*-} \mu^+ \nu_\mu$ signal	0.429 ± 0.001	60
B_s^0 feed-down	0.282 ± 0.002	$\mathcal{O}(5)$
B_s^0 semitauonic decays	0.070 ± 0.002	< 1
doubly charmed final states	0.067 ± 0.001	2
B cross-feed	0.130 ± 0.001	2
$B^0 \rightarrow D^-(\rightarrow K^+ K^- \pi^-) \mu^+ \nu_\mu X$		
$B^0 \rightarrow D^- \mu^+ \nu_\mu$ signal	0.307 ± 0.001	50
$B^0 \rightarrow D^{*-} \mu^+ \nu_\mu$ signal	0.293 ± 0.001	30
B^0 feed-down	0.104 ± 0.001	9
B^0 semitauonic decays	0.030 ± 0.001	< 1
B^+ decays	0.054 ± 0.001	9

Table 4.8: Background decays contributing to the simulated samples of inclusive (top) $B^0 \rightarrow D^- \mu^+ \nu_\mu X$ and (bottom) $B_s^0 \rightarrow D_s^- \mu^- \nu_\mu X$ decays. Branching fractions and decay models used in the generation are also reported.

Process	\mathcal{B} [%]	EVTGEN model
$B^0 \rightarrow D_0^{*-} (\rightarrow D^{(*)-} X) \mu^+ \nu_\mu$	0.14355	ISGW2
$B^0 \rightarrow D_1^{\prime-} (\rightarrow D^{(*)-} X) \mu^+ \nu_\mu$	0.06156	ISGW2
$B^0 \rightarrow D_1^- (\rightarrow D_{(0)}^* X) \mu^+ \nu_\mu$	0.18477	ISGW2
$B^0 \rightarrow D_2^{*-} (\rightarrow D_{(0)}^{(*)} X) \mu^+ \nu_\mu$	0.16516	ISGW2
$B^0 \rightarrow D^- \pi^0 \mu^+ \nu_\mu$	0.01980	GOITY_ROBERTS
$B^0 \rightarrow D^- \pi^0 \pi^0 \mu^+ \nu_\mu$	0.02940	PHSP
$B^0 \rightarrow D^- \pi^+ \pi^- \mu^+ \nu_\mu$	0.11970	PHSP
$B^0 \rightarrow D^{*-} (\rightarrow D^- X) \pi^0 \mu^+ \nu_\mu$	0.01492	GOITY_ROBERTS
$B^0 \rightarrow D^{*-} (\rightarrow D^- X) \pi^0 \pi^0 \mu^+ \nu_\mu$	0.02374	PHSP
$B^0 \rightarrow D^{*-} (\rightarrow D^- X) \pi^+ \pi^- \mu^+ \nu_\mu$	0.09021	PHSP
$B_s^0 \rightarrow D_{s0}^{*-} (\rightarrow D_s^{(*)-} X) \mu^+ \nu_\mu$	0.7000	ISGW2
$B_s^0 \rightarrow D_{s1}^- (\rightarrow D_s^{(*)-} X) \mu^+ \nu_\mu$	0.4000	ISGW2
$B_s^0 \rightarrow D_{s1}^{\prime-} (\rightarrow D_s^{(*)-} X) \mu^+ \nu_\mu$	0.4000	ISGW2

Table 4.9: Semitaauonic background decays contributing to the simulated samples of inclusive (top) $B^0 \rightarrow D^- \mu^+ \nu_\mu X$ and (bottom) $B_s^0 \rightarrow D_s^- \mu^- \nu_\mu X$ decays. Branching fractions and decay models used in the generation are also reported.

Process	\mathcal{B} [%]	EVTGEN model
$B^0 \rightarrow D^- \tau^+ \nu_\tau$	0.19096	ISGW2
$B^0 \rightarrow D^{*-} (\rightarrow D^- X) \tau^+ \nu_\tau$	0.08411	ISGW2
$B^0 \rightarrow D_1^- (\rightarrow D_{(0)}^* X) \tau^+ \nu_\tau$	0.00867	ISGW2
$B^0 \rightarrow D_0^{*-} (\rightarrow D^{(*)-} X) \tau^+ \nu_\tau$	0.00689	ISGW2
$B^0 \rightarrow D_1^{\prime-} (\rightarrow D^{(*)-} X) \tau^+ \nu_\tau$	0.00534	ISGW2
$B^0 \rightarrow D_2^{*-} (\rightarrow D_{(0)}^{(*)} X) \tau^+ \nu_\tau$	0.01103	ISGW2
$B_s^0 \rightarrow D_s^- \tau^+ \nu_\tau$	0.138	ISGW2
$B_s^0 \rightarrow D_s^{*-} (\rightarrow D_s^{(*)-} X) \tau^+ \nu_\tau$	0.2770	ISGW2
$B_s^0 \rightarrow D_{s0}^{*-} (\rightarrow D_s^{(*)-} X) \tau^+ \nu_\tau$	0.038	ISGW2
$B_s^0 \rightarrow D_{s1}^- (\rightarrow D_s^{(*)-} X) \tau^+ \nu_\tau$	0.022	ISGW2
$B_s^0 \rightarrow D_{s1}^{\prime-} (\rightarrow D_s^{(*)-} X) \tau^+ \nu_\tau$	0.022	ISGW2

Table 4.10: Processes contributing to the simulated samples of inclusive $B^+ \rightarrow D^- \mu^+ \nu X$ decays. Branching fractions and decay models used in generation are also specified.

Process	\mathcal{B} [%]	EVTGEN model
$B^+ \rightarrow D_0^{*0}(\rightarrow D^{(*)-} X) \mu^+ \nu$	0.2628	ISGW2
$B^+ \rightarrow D_2^{*0}(\rightarrow D_{(0)}^{(*)} X) \mu^+ \nu$	0.2304	ISGW2
$B^+ \rightarrow D_1^0(\rightarrow D_{(0)}^{(*)} X) \mu^+ \nu$	0.2082	ISGW2
$B^+ \rightarrow D^- \pi^+ \mu^+ \nu$	0.0895	GOITY_ROBERTS
$B^+ \rightarrow D^{*-}(\rightarrow D^- X) \pi^+ \mu^+ \nu$	0.0706	GOITY_ROBERTS
$B^+ \rightarrow D_1^{\prime 0}(\rightarrow D^{(*)-} X) \mu^+ \nu$	0.0690	ISGW2
$B^+ \rightarrow D_2^{*0}(\rightarrow D_{(0)}^{(*)} X) \tau^+(\rightarrow \mu^+ \nu \nu) \nu$	0.0154	ISGW2
$B^+ \rightarrow D_0^{*0}(\rightarrow D^{(*)-} X) \tau^+(\rightarrow \mu^+ \nu \nu) \nu$	0.0126	ISGW2
$B^+ \rightarrow D_1^0(\rightarrow D_{(0)}^{(*)} X) \tau^+(\rightarrow \mu^+ \nu \nu) \nu$	0.0098	ISGW2
$B^+ \rightarrow D_1^{\prime 0}(\rightarrow D^{(*)-} X) \tau^+(\rightarrow \mu^+ \nu \nu) \nu$	0.0060	ISGW2

Table 4.11: Result of the fit to the B^0 normalisation sample.

Parameter	value
N_{ref}	36432 ± 1602
N_{ref}^*	27757 ± 1155
N_{phys}	12391 ± 838
N_{comb}	5715 ± 1553
$\rho^2(D)$	0.87 ± 0.18
$\rho^2(D^*)$	0.93 ± 0.53
R_1	1.70 ± 0.86
R_2	1.08 ± 0.44

4.3.5 Fit for $|V_{cb}|$ in the CLN parametrisation

The yields of the $B_s^0 \rightarrow D_s^{(*)-} \mu^+ \nu$ signal decays can be written as

$$N_s^{(*)} = \frac{\mathcal{B}(B_s^0 \rightarrow D_s^{(*)-} \mu^+ \nu)}{\mathcal{B}(B^0 \rightarrow D^{(*)-} \mu^+ \nu)} \mathcal{N}^{(*)}, \quad (4.13)$$

where

$$\mathcal{N} \equiv \xi N_{\text{ref}} \frac{f_s}{f_d} \frac{\mathcal{B}(D_s^- \rightarrow K^+ K^- \pi^-)}{\mathcal{B}(D^- \rightarrow K^+ K^- \pi^-)}, \quad (4.14)$$

$$\mathcal{N}^* \equiv \xi^* N_{\text{ref}}^* \frac{f_s}{f_d} \frac{\mathcal{B}(D_s^- \rightarrow K^+ K^- \pi^-)}{\mathcal{B}(D^{*-} \rightarrow D^- X) \mathcal{B}(D^- \rightarrow K^+ K^- \pi^-)}. \quad (4.15)$$

Here, $N_{\text{ref}}^{(*)}$ are the measured yields of the reference $B^0 \rightarrow D^{(*)-} \mu^+ \nu$ decays of Eqs. (4.11)–(4.12), and $\xi^{(*)}$ is the ratio of efficiencies computed in Sec. 4.2.2.1.

The B_s^0 branching fractions can be written in terms of the differential decay rates of Eqs. (1.101) and (1.110) and the B_s^0 lifetime $\tau(B_s^0)$, such as

$$\mathcal{B}(B_s^0 \rightarrow D_s^{(*)-} \mu^+ \nu) = |V_{cb}|^2 \eta_{\text{EW}}^2 \mathcal{X}^2 \tau(B_s^0) \int_1^{w_{\text{max}}^{(*)}} \frac{d\Gamma(B_s^0 \rightarrow D_s^{(*)-} \mu^+ \nu)}{dw} dw \quad (4.16)$$

with $w_{\text{max}}^{(*)}$ being the endpoint of the recoil variable, $\mathcal{X} = \mathcal{G}(0)$ for $B_s^0 \rightarrow D_s^- \mu^+ \nu$ decays and $\mathcal{X} = \mathcal{F}(1)$ for $B_s^0 \rightarrow D_s^{*-} \mu^+ \nu$ decays. The dependence on $|V_{cb}|^2 \eta_{\text{EW}}^2 \mathcal{X}$ is made explicit in Eq. 4.16 by taking this term out of the integral of the differential decay rates of Eqs. (1.101)–(1.110). By taking as input the value of $\mathcal{G}(0)$, $\mathcal{F}(1)$ and η_{EW} , the signal yields of both decays are expressed solely in terms of $|V_{cb}|$ and the form factors parameters, according to the chosen parametrisation, used also in the templates reweighting (Eqs. (4.9) and (4.10)).

Firstly, the data are fit to determine $|V_{cb}|$ using the CLN parametrisation. The form-factor functions are given by the CLN equations, Eq. (1.104) for the $B_s^0 \rightarrow D_s^- \mu^+ \nu_\mu$ decay, and Eqs. (1.112)–(1.114) for the $B_s^0 \rightarrow D_s^{*-} \mu^+ \nu_\mu$ decay. The full list of fit parameters is reported in Table 4.12. Those marked as *gauss* are Gaussian-constrained in the χ^2 fit function, using the reported values and uncertainties. Correlations are taken into account where necessary for Gaussian-constrained parameters. The value of the f_s/f_d constraint is obtained from the independent Run 2 sample of semileptonic B_s^0 decays [150], taking into account the measured dependence of f_s/f_d on the proton-proton collision energy [151]: the values of f_s/f_d at 7 and 8 TeV are determined (considering the correlation between the energy-dependent scale factors) and averaged according to the size of the datasets collected at the two centre-of-mass energies. All branching fractions and the particle masses are constrained to their PDG 2019 averages [164]. The only exception is the branching ratio of the decay $D_s^- \rightarrow K^+ K^- \pi^-$, which is fixed in the fit (to the PDG 2019 value), because the uncertainty on this input cancels with that of f_s/f_d , in which the same input is used. Because of this cancellation, the contribution of the branching ratio of $D_s^- \rightarrow K^+ K^- \pi^-$ decays has been also subtracted from the uncertainty of f_s/f_d . The same applies to the B_s^0 lifetime, which is also fixed in the fit. The value of η_{EW} is constrained to $\eta_{\text{EW}} = 1.0066 \pm 0.0050$ following Ref. [61]. The parameters $\mathcal{G}(0)$ and $\mathcal{F}(1)$ are constrained to the most recent lattice calculations: $\mathcal{G}(0) = 1.072 \pm 0.036$ is derived in Appendix B.1 and $\mathcal{F}(1) = 0.9020 \pm 0.013$ from Ref. [165].

Following the study described in Appendix B.1, the value of $\rho^2(D_s)$ is constrained, taking into account its correlation with $\mathcal{G}(0)$, to gain additional precision in the measurement of $|V_{cb}|$. The fit is performed without and with this additional Gaussian constraint, and the results are compared in Table 4.12: the second-to-last column (titled “w/o LQCD(q^2)”) reports the values in the fit where $\rho^2(D_s)$ is not Gaussian-constrained from lattice data, but only $\mathcal{G}(0)$ is constrained; the last column reports the values in the fit with the constraint on $\rho^2(D_s)$ (titled “w/ LQCD(q^2)”). The naming “LQCD(q^2)” is used to highlight the fact that the lattice inputs originate from a calculation in the full q^2 , and not only at maximum q^2 (or $w = 1$), which is also the case for the fit “w/o LQCD(q^2)” where only $\mathcal{G}(0)$ and $\mathcal{F}(1)$ are given as input. In the fit w/o LQCD(q^2), the value of $\rho^2(D_s)$ agrees with that derived from lattice (reported in the third column). The uncertainty on $|V_{cb}|$ present a 10% improvement on the precision when fitting w/ LQCD(q^2).

The $|V_{cb}|$ results from the two fits are in agreement, and they also agree with determination from B decays. That w/ LQCD(q^2) is considered as the nominal result. The correlation matrix is reported in Tab. 4.13 for the nominal CLN fit. One-dimensional projections of the fit on m_{corr} and p_{\perp} are displayed in Fig. 4.16, and those in m_{corr} for different bins of p_{\perp} (and viceversa) are shown in App. B.4. Only distributions for the fit w/ LQCD(q^2) are shown since there is no visible difference in the fit projections between the fit w/ or w/o LQCD(q^2).

For each configuration, w/o and w/ LQCD(q^2), the fit is performed twice: firstly, all Gaussian-constrained parameters are left floating; secondly, they are fixed at the values obtained at the χ^2 minimum of the previous fit. By construction, the second fit converges to the same minimum of the first fit, but the parameter uncertainties do not include the uncertainties on the external constraints. The fit thus returns only the statistical uncertainty of the fit parameters, while the uncertainties from the constraints are considered as systematic uncertainties in Sec. 4.5.1. In the second fit, the values of the normalisation yields and of the efficiencies ratios are not fixed, as they are considered as part of the statistical uncertainties of the measurements. Also, the uncertainties due to the size of the simulated and SS samples used for the templates fit are included in the statistical uncertainties. In the fit w/ LQCD(q^2), the parameters $\rho^2(D_s)$ and $\mathcal{G}(0)$, although Gaussian constrained in the first fit, are not fixed in the second fit, since $\rho^2(D_s)$ is determined by both the data and the input from the lattice calculation, and $\mathcal{G}(0)$ cannot be disentangled because of its large correlation with $\rho^2(D_s)$. Hence, the uncertainties of the fit w/ LQCD(q^2) includes both the statistical contribution of the data sample (and templates) and the contribution from the uncertainty of the lattice data of the $B_s^0 \rightarrow D_s^- \mu^+ \nu_{\mu}$ decay.

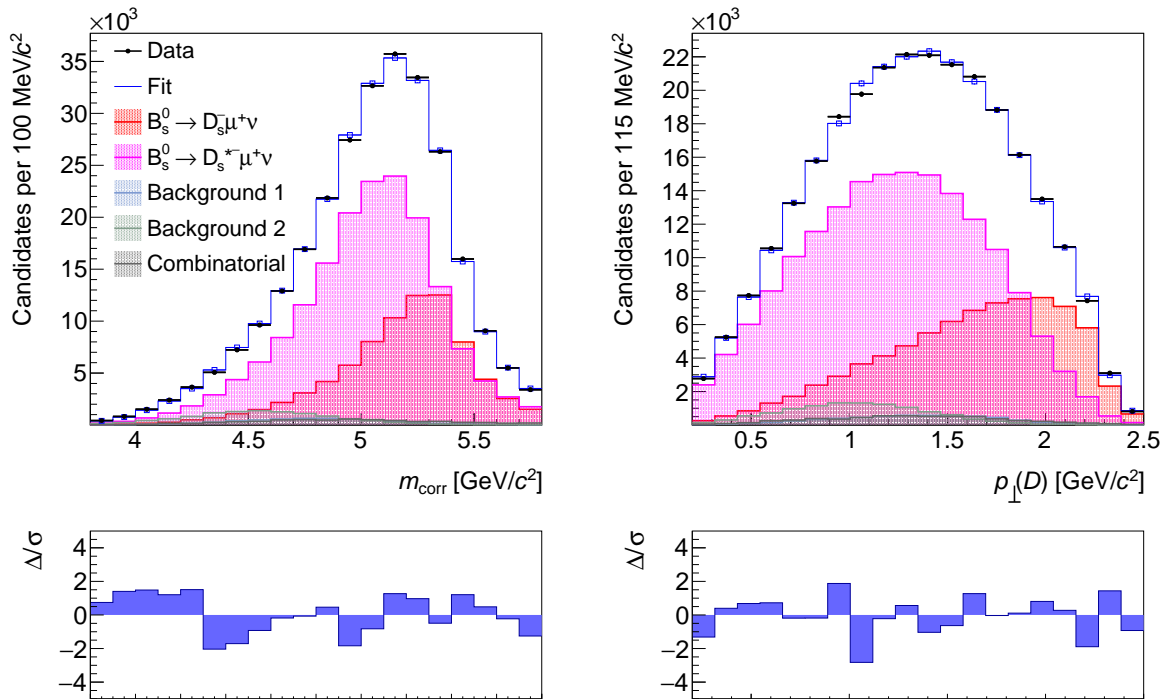


Figure 4.16: Signal sample fit in the CLN parametrisation w/ LQCD(q^2): (left) distribution of m_{corr} and (right) p_{\perp} variables with fit projections overlaid.

Table 4.12: Parameters of the fit to the signal sample of $B_s^0 \rightarrow D_s^- (\rightarrow K^+ K^- \pi^-) \mu^+ \nu_\mu X$ decays to determine $|V_{cb}|$ with the CLN parametrisation. The fit results are reported in the last two columns, with the second-to-last column showing the case “w/o LQCD(q^2)” (no constraint on $\rho^2(D_s)$) and the last column showing the case “w/ LQCD(q^2)” (constraint on both $\rho^2(D_s)$ and $\mathcal{G}(0)$, with their correlation). The second column indicates whether the parameter is Gaussian-constrained in the fit (gauss) or not (free); in the former case, the value used in the constraint is reported in the third column (note that $\rho^2(D_s)$ is Gaussian-constrained only for the configuration “w/ LQCD(q^2)”). The free parameters are reported in the upper pane of the table; the Gaussian-constrained parameters on the lower pane.

Parameter	Comment	Constraint value	CLN w/o LQCD(q^2)	CLN w/ LQCD(q^2)
$ V_{cb} [10^{-3}]$	free	–	$41.76 \pm 1.49(0.79)$	$41.36 \pm 1.30(0.57)$
$\rho^2(D_s)$	free/gauss	$-(1.229 \pm 0.051)$	$1.302 \pm 0.075(0.059)$	$1.268 \pm 0.047(0.047)$
$\rho^2(D_s^*)$	free	–	$1.25 \pm 0.17(0.16)$	$1.23 \pm 0.17(0.17)$
R_1	free	–	$1.33 \pm 0.25(0.25)$	$1.34 \pm 0.25(0.25)$
R_2	free	–	$0.82 \pm 0.16(0.16)$	$0.83 \pm 0.16(0.16)$
$N_{\text{bkg-1}}$	free	–	$5538 \pm 2250(2250)$	$5550 \pm 2250(2248)$
$N_{\text{bkg-2}}$	free	–	$10993 \pm 1053(1053)$	$11010 \pm 1050(1048)$
N_{comb}	free	–	$5903 \pm 2347(2346)$	$5940 \pm 2344(2339)$
$\mathcal{G}(0)$	gauss	1.073 ± 0.036	1.100 ± 0.034	1.102 ± 0.034
$\mathcal{F}(1)$	gauss	0.902 ± 0.013	0.898 ± 0.013	0.899 ± 0.013
η_{EW}	gauss	1.0066 ± 0.0055	1.0066 ± 0.0055	1.0066 ± 0.0055
N_{ref}	gauss	36430 ± 1602	37876 ± 1428	37723 ± 1193
N_{ref}^*	gauss	27757 ± 1155	26710 ± 1068	26822 ± 866
f_s/f_d	gauss	0.2324 ± 0.0092	0.2324 ± 0.0092	0.2324 ± 0.0092
ξ	gauss	1.5684 ± 0.0083	1.5684 ± 0.0083	1.5684 ± 0.0083
ξ^*	gauss	1.46306 ± 0.0073	1.46306 ± 0.0073	1.46306 ± 0.0073
$\mathcal{B}(D_s^- \rightarrow K^+ K^- \pi^-)$	fixed	0.0545	–	–
$\mathcal{B}(D^- \rightarrow K^+ K^- \pi^-)$	gauss	0.00993 ± 0.00024	0.00993 ± 0.00024	0.00993 ± 0.00024
$\mathcal{B}(D^{*-} \rightarrow D^- X)$	gauss	0.323 ± 0.006	0.323 ± 0.006	0.323 ± 0.006
$\mathcal{B}(B^0 \rightarrow D^- \mu^+ \nu_\mu)$	gauss	0.0231 ± 0.0010	0.0225 ± 0.0010	0.0228 ± 0.0009
$\mathcal{B}(B^0 \rightarrow D^{*-} \mu^+ \nu_\mu)$	gauss	0.0505 ± 0.0014	0.0510 ± 0.0014	0.0507 ± 0.0013
$\tau(B_s^0)$ [ps]	fixed	1.510	–	–
B_s^0 mass [GeV/ c^2]	gauss	5.36688 ± 0.00017	5.36688 ± 0.00017	5.36688 ± 0.00017
D_s^- mass [GeV/ c^2]	gauss	1.96834 ± 0.00007	1.96834 ± 0.00007	1.96834 ± 0.00007
D_s^{*-} mass [GeV/ c^2]	gauss	2.1122 ± 0.0004	2.1122 ± 0.0004	2.1122 ± 0.0004
χ^2/dof			279/284	279/285
Probability			0.56	0.58

Table 4.13: Correlation matrix of the uncertainties of the physics parameters (including external inputs) in the nominal CLN fit for Vcb.

	$\mathcal{B}(D^- \rightarrow K^+ K^- \pi^-)$	$\mathcal{B}(D^{*-} \rightarrow D^- X)$	$\mathcal{B}(B^0 \rightarrow D^- \mu^+ \nu_\mu)$	$\mathcal{B}(B^0 \rightarrow D^{*-} \mu^+ \nu_\mu)$	R_1	R_2	$\rho^2(D_s)$	$\mathcal{G}(0)$	$\rho^2(D_s^*)$	$\mathcal{F}(1)$	η_{EW}	V_{cb}
f_s/f_d	0.002											
$\mathcal{B}(D^- \rightarrow K^+ K^- \pi^-)$		0.001										
$\mathcal{B}(D^{*-} \rightarrow D^- X)$			-0.001									
$\mathcal{B}(D^0 \rightarrow D^- X)$			0.079									
$\mathcal{B}(B^0 \rightarrow D^- \mu^+ \nu_\mu)$				0.112								
$\mathcal{B}(B^0 \rightarrow D^{*-} \mu^+ \nu_\mu)$					0.034							
R_1						-0.001						
R_2						0.000						
$\rho^2(D_s)$						-0.000						
$\mathcal{G}(0)$						0.024						
$\rho^2(D_s^*)$						-0.018						
$\mathcal{F}(1)$						0.042						
η_{EW}						-0.025						
						0.011						
						-0.025						
						0.004						
						-0.168						
						0.838						
							0.004					
							0.891					
							-0.966					
							0.159					
								0.027				
								-0.011				
								0.042				
									0.151			
										-0.028		
											-0.000	
												-0.000
												-0.260
												-0.156

4.3.6 Fit for \mathcal{R} and \mathcal{R}^*

When fitting for \mathcal{R} and \mathcal{R}^* , the signal yields are expressed by Eq. (4.13), which is simply rewritten as

$$N_s^{(*)} = \mathcal{R}^{(*)} \mathcal{N}^{(*)}, \quad (4.17)$$

where \mathcal{R} and \mathcal{R}^* are free parameters in the fit. Results are given in Table 4.14. The correlation matrix is given in Tab. 4.15.

Table 4.14: Results for \mathcal{R} and \mathcal{R}^* . The uncertainty corresponds to the fit using the Gaussian constraints for the input parameters. The number reported between parentheses is the uncertainty obtained when fixing all Gaussian-constrained parameters to their values at the global minimum, *i.e.* the uncertainty including only the statistical components due to the limited data and simulation samples sizes and due to lattice data.

CLN	
\mathcal{R}	$1.093 \pm 0.074(0.054)$
\mathcal{R}^*	$1.059 \pm 0.071(0.047)$
χ^2/dof	278/284
Probability	0.59

Table 4.15: Correlation matrix of the uncertainties of the physics parameters (including external inputs) in the nominal fit for \mathcal{R} and \mathcal{R}^* .

	$\mathcal{B}(D^- \rightarrow K^+ K^- \pi^-)$	$\mathcal{B}(D^{*-} \rightarrow D^- X)$	\mathcal{R}	\mathcal{R}^*
f_s/f_d	0.001	0.001	-0.581	-0.588
$\mathcal{B}(D^- \rightarrow K^+ K^- \pi^-)$		-0.000	0.355	0.360
$\mathcal{B}(D^{*-} \rightarrow D^- X)$			-0.000	0.295
\mathcal{R}				0.140

4.4 Analysis validation

The full analysis is validated by means of pseudoexperiments and with the large $B^0 \rightarrow D^-(\rightarrow K^+ \pi^- \pi^-) \mu^+ \nu_\mu$ control sample, as described in the following.

4.4.1 Pseudoexperiments

Pseudoexperiments are generated by resampling with repetitions (bootstrapping) the samples of fully-simulated signal and background decays that pass the selection requirements. The combinatorial background is obtained bootstrapping the same-sign data sample. For each pseudoexperiment, 280k candidates in total are bootstrapped to make the $B_s^0 \rightarrow D_s^-(\rightarrow K^+ K^- \pi^-) \mu^+ \nu_\mu X$ sample. The relative proportions of signals and backgrounds found in the nominal fit to data are reproduced in the toys. Since the number of generated events in each toy is different from that present in data, the efficiency ratios ξ_d

and ξ_d^* are rescaled to take into account this difference. Moreover, the mean values and uncertainties of the Gaussian constraints on N_{ref} and N_{ref}^* are modified such that \mathcal{R} and \mathcal{R}^* yield unit value; $\mathcal{G}(0)$ and $\mathcal{F}(1)$ are also rescaled to have $|V_{cb}|$ equal to 40×10^{-3} . All these scale factors are very close to unity.

Three sets of pseudoexperiments are studied. In the first set, the generated samples are fit without considering the uncertainty due to the finite size of the simulated samples used to create the fit templates ($\sigma_{p_i}^2$ term in Eq. (4.8)) to prove that the fit estimates are unbiased with a correct assessment of the fit uncertainty, which corresponds to normal pull distributions (Gaussian with mean zero and unit width) for each parameter. The fits are performed by floating also the Gaussian-constrained parameters, where the central values of the constraint are resampled from Gaussian distributions for each pseudoexperiment (accounting for correlations when present). The results of the fits are reported in Table 4.16; no biases are observed, or are considered negligible with respect to the statistical uncertainty, in both the configuration w/ and w/o LQCD(q^2). The pull distributions for the nominal CLN fit are shown in Figure 4.17.

Table 4.16: Summary of the results obtained from the toy studies of the CLN parameterisation, where fit templates uncertainties are neglected. The second column report the case w/ LQCD(q^2), the third column the case w/o LQCD(q^2). For each parameter, the first row is the mean of the pull distribution with its uncertainty, the second row is the width of the pull distribution with its uncertainty and (if present) the third row is the mean of the residuals' distribution with its uncertainty (to assess the potential bias on the parameter). For each configuration 2000 pseudoexperiments were generated and fitted.

	w/ LQCD	w/o LQCD
$ V_{cb} $	0.04 ± 0.02	0.06 ± 0.02
	0.99 ± 0.02	0.96 ± 0.02
	$(-4 \pm 4) \cdot 10^{-5}$	
$\mathcal{G}(0)$	-0.03 ± 0.02	-0.05 ± 0.02
	1.01 ± 0.02	1.01 ± 0.02
	$(-7 \pm 7) \cdot 10^{-4}$	
$\mathcal{F}(1)$	0.06 ± 0.02	0.04 ± 0.02
	1.00 ± 0.02	0.99 ± 0.02
	$(7 \pm 3) \cdot 10^{-4}$	
$\rho^2(D_s)$	-0.05 ± 0.02	-0.08 ± 0.02
	1.02 ± 0.02	1.02 ± 0.02
	$(-1 \pm 1) \cdot 10^{-3}$	
$\rho^2(D_s^*)$	-0.06 ± 0.02	-0.08 ± 0.02
	1.05 ± 0.02	1.04 ± 0.02
	$(-3 \pm 3) \cdot 10^{-3}$	
R_1	-0.03 ± 0.02	-0.05 ± 0.02
	1.06 ± 0.02	1.03 ± 0.02
	$(-10 \pm 4) \cdot 10^{-3}$	
R_2	0.00 ± 0.02	0.02 ± 0.02
	1.05 ± 0.02	1.03 ± 0.02
	$(-1 \pm 2) \cdot 10^{-3}$	

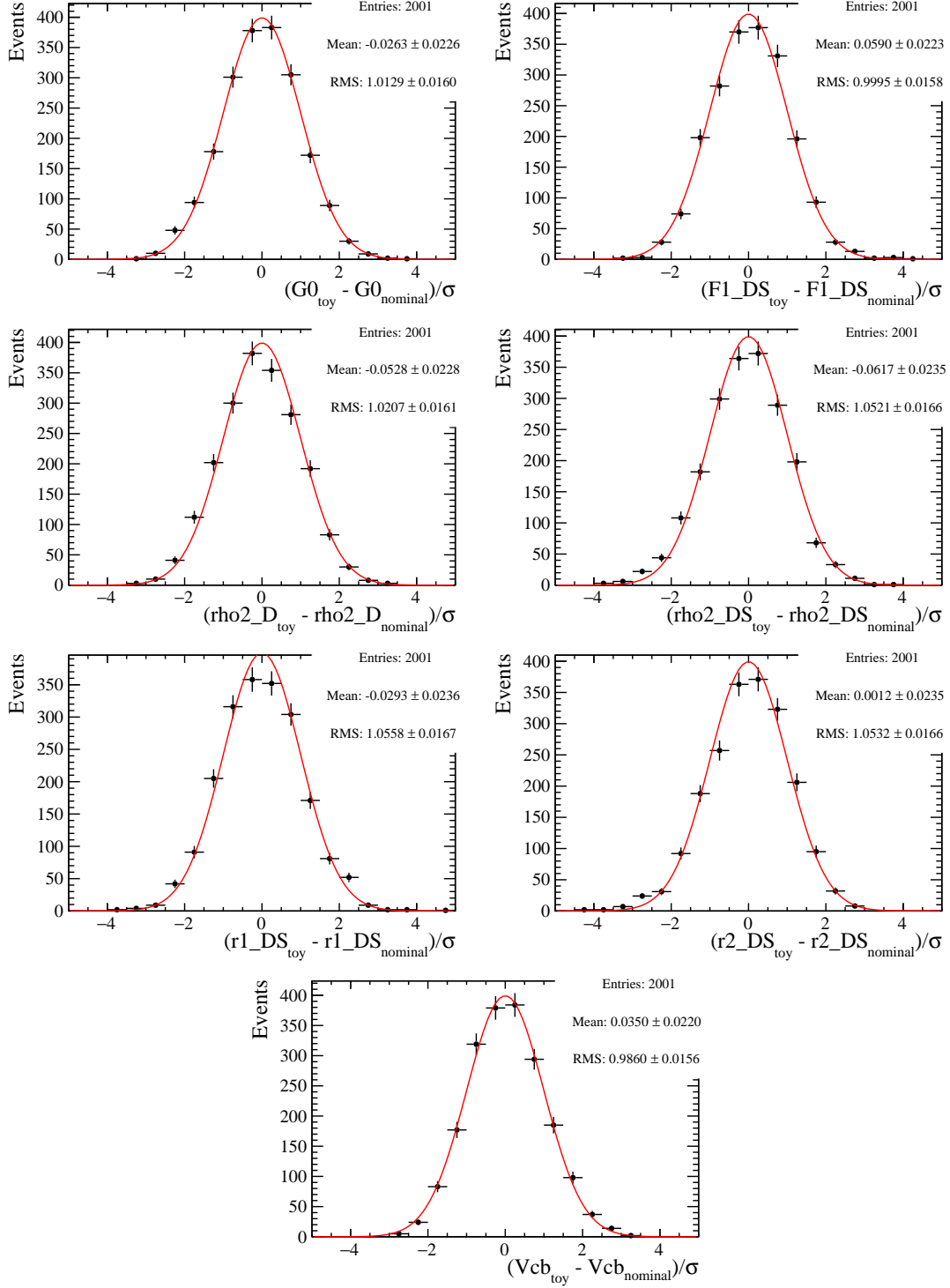


Figure 4.17: Pull distributions for the nominal configuration for (top-left) $\mathcal{G}(0)$, (top-right) $\mathcal{F}(1)$, (mid-top-left) $\rho^2(D_s)$, (mid-top-right) $\rho^2(D_s^*)$, (mid-bottom-left) R_1 , (mid-bottom-right) R_2 and (bottom) $|V_{cb}|$. A Normal distribution is shown as reference.

In the second set of toys, the generated samples are fit with the nominal χ^2 function, *i.e.* considering also the $\sigma_{p_i}^2$ uncertainty in the χ^2 . This set of toys is only run for the nominal configuration. The statistical fluctuations of the fit templates are not simulated. The pull distributions are thus expected to have a width smaller than 1, with the deviation of the

Table 4.17: Width of the pull distribution obtained from the toy studies including the uncertainty on the templates. Results of the nominal fit are shown. For each parameter, the first row is the width of the pull distribution with its uncertainty when the fit templates are not randomised, and the second row is the width of the pull distribution with its uncertainty when the fit templates are randomised. A total of 2000 pseudoexperiments were generated and fitted. Only parameters which are not Gaussian constrained are reported.

	CLN w/ LQCD
$ V_{cb} $	0.86 ± 0.01
	1.02 ± 0.02
$\rho^2(D_s^*)$	0.79 ± 0.01
	1.06 ± 0.02
R_1	0.80 ± 0.01
	1.08 ± 0.02
R_2	0.79 ± 0.01
	1.07 ± 0.02

width from 1 quantifying the contribution of the uncertainties on the fit templates. The results are reported in Table 4.17 for the parameters that are not Gaussian-constrained (Gaussian constrained parameters are fixed, such that only the statistical contribution to the uncertainties is considered). The uncertainties on the templates increase the estimated statistical uncertainty on $|V_{cb}|$ by about 10-15%, and on the form-factor parameters by about 20%.

In the third set of toys the statistical fluctuations of the fit templates are also simulated by bootstrapping the samples used to create the templates. The results are shown in Table 4.17, where the width of the resulting pull distributions is reported in the second row for each parameter; the width is found to be compatible with unity for $|V_{cb}|$, as expected, while it is found to be a few percent larger than unity for the form-factor parameters (suggesting a small underestimation of the fit uncertainty).

4.4.2 Control sample analysis

The $B^0 \rightarrow D^-(\rightarrow K^+\pi^-\pi^-)\mu^+\nu_\mu$ control sample is analysed to measure values of \mathcal{R} and \mathcal{R}^* compatible with unity. Eq. (4.13) is thus modified to account for the $B^0 \rightarrow D^-(\rightarrow K^+\pi^-\pi^-)\mu^+\nu_\mu$ and $B^0 \rightarrow D^{*-}[\rightarrow D^-(\rightarrow K^+\pi^-\pi^-)X]\mu^+\nu_\mu$ decays at the numerator, keeping as reference the $B^0 \rightarrow D^-(\rightarrow K^+K^-\pi^-)\mu^+\nu_\mu$ and $B^0 \rightarrow D^{*-}[\rightarrow D^-(\rightarrow K^+K^-\pi^-)X]\mu^+\nu_\mu$ decays; the value of f_s/f_d is fixed to unity, $\xi^{(*)}$ and $\mathcal{B}(D_s^- \rightarrow K^+K^-\pi^-)$ are replaced with $\xi_d^{(*)}$ and $\mathcal{B}(D^- \rightarrow K^+\pi^-\pi^-)$, respectively, while the factor $\mathcal{B}(D^{*-} \rightarrow D^-X)$ is removed being in common to both numerator and denominator. The branching fractions for $\mathcal{B}(D^- \rightarrow K^+\pi^-\pi^-)$ and $\mathcal{B}(D^- \rightarrow K^+K^-\pi^-)$ are taken from Ref. [166] and the 55% correlation between their uncertainties is included in the fit.

The components of the sample are the same as those of the reference sample described in Section 4.3.3:

1. $B^0 \rightarrow D^-\mu^+\nu_\mu$ decays;
2. $B^0 \rightarrow D^{*-}\mu^+\nu_\mu$ decays;
3. sum of the B^0 and B^+ background components of Section 4.2.3.1 and Section 4.2.3.3, which are fit as a single component, because they are indistinguishable in the $(m_{\text{corr}}, p_\perp)$ plane;
4. combinatorial background.

Again, the background from semitaunoic B^0 decays is neglected, as it is found to be compatible with zero when included, with no significant change to the other parameters. The templates for each component are shown in Figure 4.18. The fit parameters are reported in Table 4.18. One-dimensional projections of the fit to the m_{corr} and p_\perp variables are displayed in Figure 4.19, and those in m_{corr} for different bins in p_\perp (and viceversa) are shown in App. B.5.

The value of \mathcal{R} is found to be compatible with unity within 1.6σ ; the value of \mathcal{R}^* was found to be compatible with unity within 1.1σ . We consider this level of agreement satisfactory.

The form-factor parameters are compared with the latest HFLAV averages, $\rho^2(D) = 1.131 \pm 0.024 \pm 0.023$, $\rho^2(D^*) = 1.122 \pm 0.015 \pm 0.019$, $R_1 = 1.270 \pm 0.026$, and $R_2 = 0.852 \pm 0.018$; the values of $\rho^2(D)$, $\rho^2(D^*)$ and R_1 are in agreement with the HFLAV averages, while the parameter R_2 shows some tension.¹ Again we consider the level of agreement satisfactory for our purposes.

¹It should be noted that the uncertainties on HFLAV values of R_1 and R_2 have been criticized by part of the theory community [167].

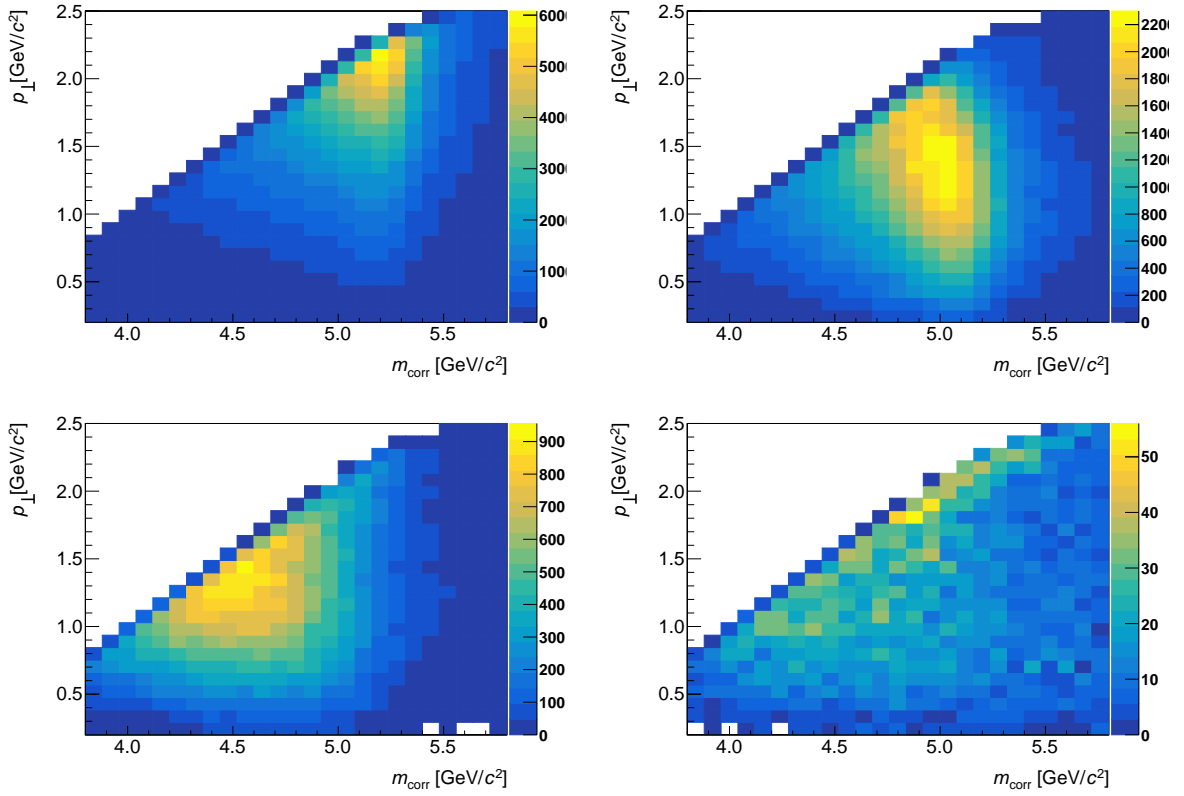


Figure 4.18: Two-dimensional distribution in the m_{corr} and p_{\perp} variables for (top-left) simulated $B^0 \rightarrow D^- \mu^+ \nu_{\mu}$ decays; (top-right) $B^0 \rightarrow D^{*-} \mu^+ \nu_{\mu}$ decays; (bottom left) background decays from B^0 feed-down and B^+ decays; (bottom right) same-sign data used to model the combinatorial background. The background components are grouped together according to their shapes in the $(m_{\text{corr}}, p_{\perp})$ plane.

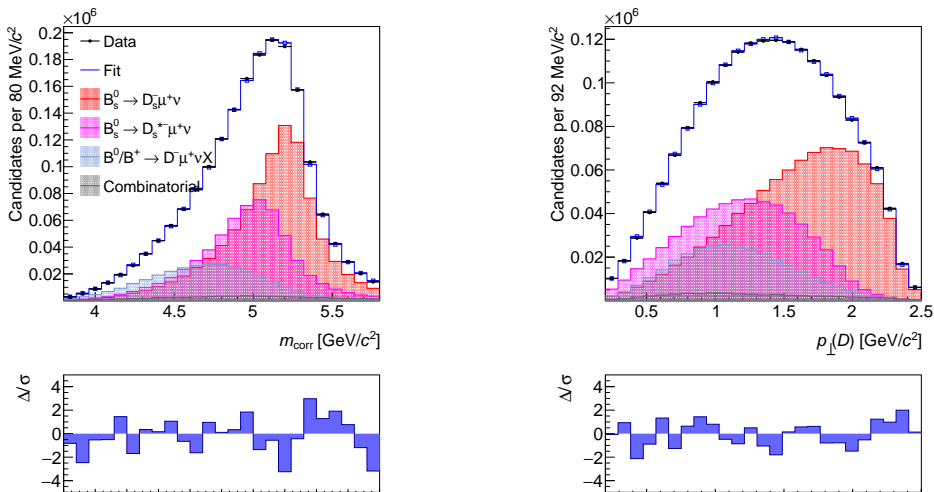


Figure 4.19: Distribution of (left) m_{corr} and (right) p_{\perp} with fit projections for the control sample

Table 4.18: Parameters of the fit to the control sample of $B^0 \rightarrow D^-(\rightarrow K^+\pi^-\pi^-)\mu^+\nu_\mu X$ decays. The second column indicates whether the parameter is Gaussian-constrained in the fit (gauss) or not (free); in the former case, the value used in the constraint is reported in the third column.

Parameter	Comment	Constraint value	CLN fit
\mathcal{R}	free	–	1.096 ± 0.057
\mathcal{R}^*	free	–	0.948 ± 0.049
$\rho^2(D)$	free	–	1.159 ± 0.029
$\rho^2(D^*)$	free	–	0.84 ± 0.22
R_1	free	–	0.98 ± 0.31
R_2	free	–	1.24 ± 0.15
N_{phys}	free	–	30597 ± 7099
N_{comb}	free	–	55141 ± 6922
N_{ref}	gauss	36430 ± 1602	36430 ± 1595
N_{ref}^*	gauss	27757 ± 1155	27757 ± 1154
ξ_d	gauss	2.3718 ± 0.0093	2.3718 ± 0.0093
ξ_d^*	gauss	2.3539 ± 0.0110	2.3539 ± 0.0110
$\mathcal{B}(D^- \rightarrow K^+\pi^-\pi^-)$	gauss	0.0914 ± 0.0020	0.0914 ± 0.0020
$\mathcal{B}(D^- \rightarrow K^+K^-\pi^-)$	gauss	0.00935 ± 0.00029	0.00935 ± 0.00029
χ^2/dof			516/443
Probability			0.9%

4.4.3 Allowing different $|V_{cb}|$ parameters for $B_s^0 \rightarrow D_s^- \mu^+ \nu_\mu$ and $B_s^0 \rightarrow D_s^{*-} \mu^+ \nu_\mu$

The consistency of the $|V_{cb}|$ results as determined by the two signal decays is checked. A new parameter, S , is introduced and the signal yield of the $B_s^0 \rightarrow D_s^- \mu^+ \nu_\mu$ decays reparametrised in terms of $|V_{cb}|$, while that of the $B_s^0 \rightarrow D_s^{*-} \mu^+ \nu_\mu$ decays in terms of $S|V_{cb}|$. We obtain:

$$|V_{cb}| = (42.3 \pm 1.8) \times 10^{-3}, \quad (4.18)$$

$$S = 0.96 \pm 0.05. \quad (4.19)$$

4.5 Systematic uncertainties

Systematic uncertainties for the relevant parameters are split into two main categories: those due to external inputs, indicated with (ext); and those due to the experimental methods, indicated with (syst). They are all discussed in the following. A summary list is presented in Table 4.19 for both $|V_{cb}|$ and $\mathcal{R}^{(*)}$.

Table 4.19: Summary of the uncertainties affecting the measurements of $|V_{cb}|$ and $\mathcal{R}^{(*)}$. The upper pane reports the systematic uncertainties due to the external inputs; the middle pane those due to the experimental methods; and the lower pane the comparison with the statistical uncertainties and the total uncertainty, given by the sum in quadrature of the uncertainties named (stat), (syst), and (ext).

Source	Uncertainty							
	$ V_{cb} $ [10^{-3}]	$\rho^2(D_s)$	$\mathcal{G}(0)$	$\rho^2(D_s^*)$	R_1	R_2	\mathcal{R}	\mathcal{R}^*
$f_s/f_d \times \mathcal{B}(D_s^- \rightarrow K^+ K^- \pi^-) (\times \tau)$	0.80	0.000	0.000	0.00	0.00	0.00	0.043	0.042
$\mathcal{B}(D^- \rightarrow K^+ K^- \pi^-)$	0.49	0.000	0.000	0.00	0.00	0.00	0.026	0.026
$\mathcal{B}(D^{*-} \rightarrow D^- X)$	0.19	0.000	0.001	0.00	0.01	0.00	0.000	0.019
$\mathcal{B}(B^0 \rightarrow D^- \mu^+ \nu)$	0.35	0.001	0.003	0.01	0.02	0.01	0.000	0.000
$\mathcal{B}(B^0 \rightarrow D^{*-} \mu^+ \nu)$	0.30	0.001	0.002	0.01	0.01	0.01	0.000	0.000
$m(B_s^0), m(D_s^{(*)})$	0.00	0.000	0.000	0.00	0.00	0.00	0.000	0.000
$\mathcal{F}(1)$	0.32	0.001	0.002	0.01	0.01	0.01	0.000	0.000
η_{EW}	0.20	0.000	0.000	0.00	0.00	0.00	0.000	0.000
All external input (ext)	1.17	0.001	0.004	0.01	0.02	0.01	0.051	0.053
$D_{(s)}^- \rightarrow K^+ K^- \pi^-$ decay model	0.84	0.000	0.000	0.00	0.00	0.00	0.045	0.042
Background	0.39	0.032	0.022	0.05	0.09	0.07	0.039	0.061
Tracking efficiency	0.00	0.000	0.001	0.00	0.00	0.00	0.000	0.000
Trigger efficiency	0.01	0.001	0.003	0.00	0.00	0.00	0.000	0.000
B_s^0 kinematics	0.01	0.001	0.004	0.00	0.01	0.00	0.001	0.001
form factor parametrisation	–	–	–	–	–	–	0.004	0.007
All experimental (syst)	0.93	0.032	0.022	0.05	0.09	0.07	0.060	0.074
Statistical (stat)	0.58	0.047	0.034	0.17	0.25	0.16	0.054	0.047
Total (stat) \oplus (syst) \oplus (ext)	1.58	0.057	0.041	0.17	0.26	0.18	0.095	0.100

4.5.1 External inputs

The external inputs are included in the fit through Gaussian constraints. To determine the purely statistical uncertainty resulting solely from our data these parameters are fixed in the fit (note that in the nominal fits of the configuration w/ LQCD(q^2) the form-factor parameters of the $B_s^0 \rightarrow D_s^- \mu^+ \nu_\mu$ decays are not considered as “pure” external inputs and are not fixed in this fit). They are then released one by one, using the constraint, to calculate the contribution of each individual input to the parameter uncertainty. This contribution, which is assigned as systematic uncertainty, is calculated as the difference in quadrature of the parameter uncertainty obtained in the fit with the Gaussian constraint and that from the baseline fit.

The uncertainty on $f_s/f_d \times \mathcal{B}(D_s^- \rightarrow K^+ K^- \pi^-)(\times \tau)$ comprises also that due to a difference in the distribution of the transverse momentum of the $D\mu$ system with respect to Ref. [150], which results in a relative 1% change of the value of f_s/f_d . The branching fractions of the B^0 decays taken in input are obtained from averages that assume isospin symmetry in decays of the $\Upsilon(4S)$ meson [168]. This symmetry is observed to hold with a precision of 1-2%, and no uncertainty is assigned therefore. However, it is noted that considering the correction suggested in Ref. [169] increases the value of $|V_{cb}|$ by 0.2×10^{-3} .

The results are reported in the upper pane of Tables 4.19; the sum in quadrature of all these contributions gives the uncertainty referred to as “(ext)”, *i.e.* the line “All external inputs” in these Tables. The largest contribution to $|V_{cb}|$ is given by the uncertainty on f_s/f_d , followed by that on the $D^- \rightarrow K^+ K^- \pi^-$ branching fraction, and on the branching fractions of the normalisation B^0 mode. In the measurement of \mathcal{R} and \mathcal{R}^* , the dominant contribution is again given by the uncertainty on f_s/f_d .

4.5.2 $D_{(s)}^- \rightarrow K^+ K^- \pi^-$ decay model

A requirement on $m(K^+ K^-)$ to be around the ϕ mass is applied in the analysis to suppress the background under the $D_{(s)}^-$ peaks and make the kinematics of signal and normalisation decays more similar to each other. The efficiency of such requirement is evaluated using simulation and is included in the ratios of Eqs. (4.4) and (4.5). The simulated model of the intermediate amplitudes contributing to the $D_{(s)}^- \rightarrow K^+ K^- \pi^-$ decays may, however, be inaccurate. A systematic uncertainty is thus estimated by comparing the efficiency of the $m(K^+ K^-)$ requirement derived from simulation with that derived from data. Since the $m(K^+ K^-)$ requirement is already applied in the stripping, Run 2 data and simulation samples are used instead. Figure 4.20 shows that some level of disagreement is observed between the $m(K^+ K^-)$ distributions obtained from background-subtracted data and from simulation. The ξ and ξ^* ratios change by a relative -4% when substituting the simulation-based efficiency of the $m(K^+ K^-)$ requirement with that determined from data. This variation corresponds to systematic uncertainties of 0.84, 0.045 and 0.042 on $|V_{cb}|$, \mathcal{R} and \mathcal{R}^* , respectively. Affecting only the normalisation scale, negligible variations are observed for form-factor parameters, hence negligible systematic uncertainties are assigned on these parameters. The correlation of this uncertainty between \mathcal{R} and \mathcal{R}^* is assumed to be 100%, while it is zero for all other parameters.

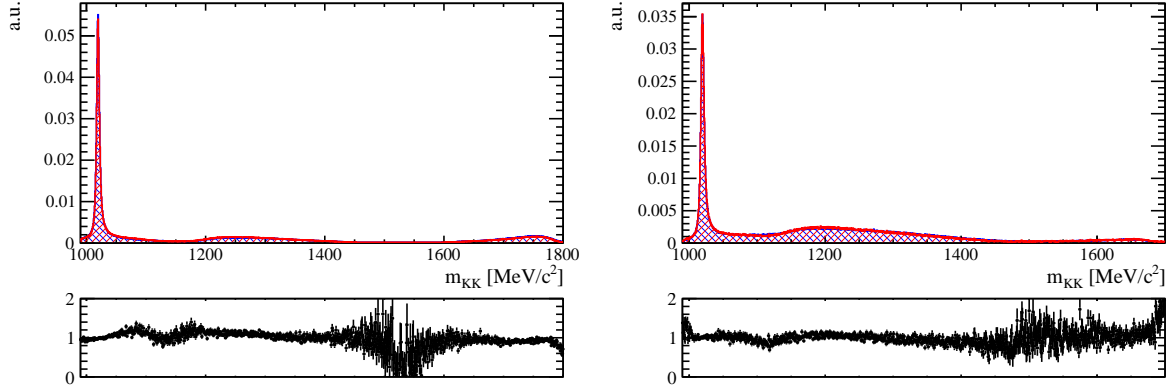


Figure 4.20: Normalized distributions of $m(K^+K^-)$ for (left) $D_s^- \rightarrow K^+K^-\pi^-$ and (right) $D^- \rightarrow K^+K^-\pi^-$ candidates from (red) background-subtracted data and (blue) simulated Run 2 samples of $B_{(s)}^0 \rightarrow D_{(s)}^-\mu^+X$ decays. The bottom panels show the ratio between the two distributions.

Table 4.20: Efficiencies of the various background sources for the variations of the baseline cut in the $(m_{\text{corr}}, p_{\perp})$ plane described in the text. The second column gives the efficiencies with no requirement; the third column is the baseline configuration; the last column gives the efficiencies with the tighter requirement. For comparison, also the efficiencies of the two signal decays are reported.

Background	Efficiency [10^{-3}]		
	No requirement	Baseline	Tighter requirement
B_s^0 feed-down	0.379 ± 0.002	0.281 ± 0.002	0.198 ± 0.001
B_s^0 semitauonic decays	0.101 ± 0.002	0.070 ± 0.002	0.033 ± 0.001
doubly charmed final states	0.160 ± 0.001	0.067 ± 0.001	0.041 ± 0.001
B cross-feed	0.209 ± 0.002	0.130 ± 0.001	0.056 ± 0.001
$B_s^0 \rightarrow D_s^- \mu^+ \nu_{\mu}$ signal	0.540 ± 0.002	0.481 ± 0.002	0.448 ± 0.002
$B_s^0 \rightarrow D_s^{*-} \mu^+ \nu_{\mu}$ signal	0.478 ± 0.001	0.429 ± 0.001	0.389 ± 0.001

4.5.3 Background contamination

The knowledge on the physics background composition of the B_s^0 sample is very limited due to the lack of experimental measurements. However, the selection requirement $p_{\perp} [\text{GeV}/c] < 1.5 + 1.1 \times (m_{\text{corr}} [\text{GeV}/c^2] - 4.5)$ is expected to greatly suppress this background and hence reduce its influence on the results. Assuming the composition reported in Sec. 4.2.3.1, the fraction of background candidates determined by the fit is just a few percent of the $B_s^0 \rightarrow D_s^- (\rightarrow K^+K^-\pi^-) \mu^+ \nu_{\mu} X$ sample. To understand by how much such contamination (or a mis-modelling of its composition) can affect the determination of the parameters of interest, the fit is repeated using two alternative requirements in the $(m_{\text{corr}}, p_{\perp})$ plane. The resulting variation of the background efficiencies is reported in Table 4.20.

In the first variation, the more restrictive requirement $p_{\perp} [\text{GeV}/c] < 0.7 + 4.0 \times (m_{\text{corr}} [\text{GeV}/c^2] - 4.5)$ is added on top of the baseline selection. Such a requirement is shown as a red line in Figs. 4.12 and 4.15: it eliminates most of the background while still

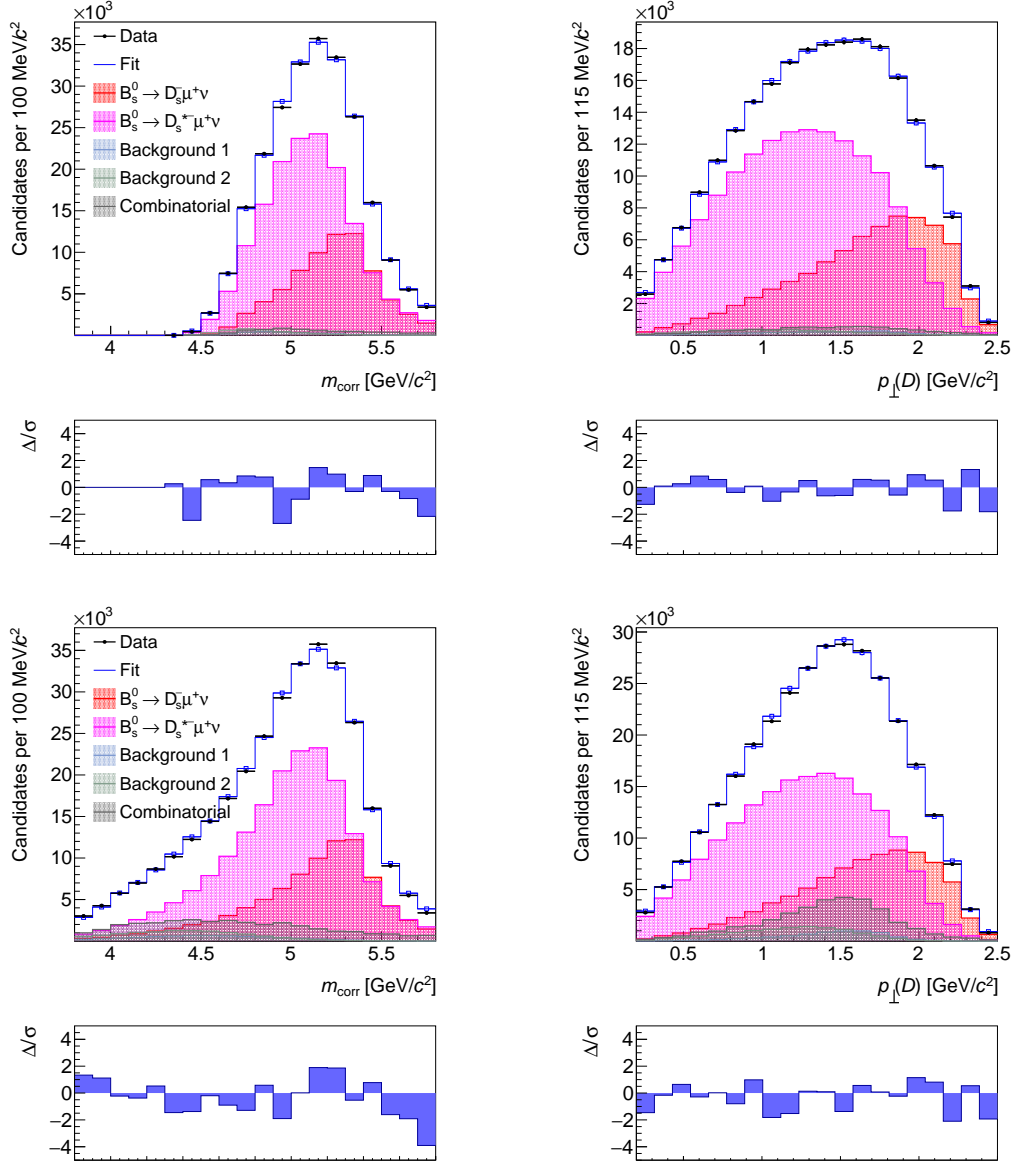


Figure 4.21: Distributions for the signal sample of the (left) m_{corr} and (right) p_{\perp} variables with fit projecti. In the top (bottom) row, the fit with the tighter (no) requirement is applied.

preserving a good signal efficiency (see Table 4.20). The resulting sample is fit accounting for the changes in the fit templates and in the efficiency ratios. The fit gives a χ^2/dof of 197/221 (probability of 87%) for $|V_{cb}|$, and a χ^2/dof of 197/220 (probability of 87%) in the fit to \mathcal{R} and \mathcal{R}^* . The fit projections in the m_{corr} and p_{\perp} variables are shown in Fig. 4.21 (top).

In the second variation, the baseline requirement $p_{\perp}[\text{GeV}/c] < 1.5 + 1.1 \times (m_{\text{corr}}[\text{GeV}/c^2] - 4.5)$ (black line in Figs. 4.12 and 4.15) is removed to allow maximum background contamination. The fit to the resulting sample gives a χ^2/dof of 323/319 (probability of 43%) for $|V_{cb}|$, and a χ^2/dof of 320/318 (probability of 44%) in the fit for \mathcal{R} and \mathcal{R}^* . The fit projections in the m_{corr} and p_{\perp} variables are shown in Fig. 4.21 (bottom).

The residuals for each parameter are computed as the difference between the values

Table 4.21: Residuals between the alternate and baseline CLN fits resulting from the variations of the requirement in the $(m_{\text{corr}}, p_{\perp})$ plane aimed at suppressing the contamination of the physics backgrounds. The last row reports the RMS of the two variations that is assigned as systematic uncertainty.

Variation	Uncertainty							
	$ V_{cb} $ [10^{-3}]	$\rho^2(D_s)$	$\mathcal{G}(0)$	$\rho^2(D_s^*)$	R_1	R_2	\mathcal{R}	\mathcal{R}^*
Tighter requirement	0.44	-0.030	-0.025	-0.07	-0.13	0.07	-0.052	0.062
No requirement	-0.33	-0.034	-0.019	0.01	-0.03	0.08	-0.018	-0.061
RMS	0.39	0.032	0.022	0.05	0.09	0.07	0.039	0.061

obtained in the alternate and baseline fits (see Table 4.21). The RMS calculated from the residuals resulting from the two variations is taken as systematic uncertainty. The correlations between the residuals are also provided in Table 4.22 for the $|V_{cb}|$ fits. The correlation between \mathcal{R} and \mathcal{R}^* is -0.441 .

Table 4.22: Correlation matrix of the systematic uncertainties from the physics background in the CLN fit for $|V_{cb}|$.

	R_2	$\rho^2(D_s)$	$\mathcal{G}(0)$	$\rho^2(D_s^*)$	$ V_{cb} $
R_1	-0.820	0.820	0.919	0.920	-0.632
R_2		-1.000	-0.979	-0.531	0.074
$\rho^2(D_s)$			0.979	0.530	-0.073
$\mathcal{G}(0)$				0.692	-0.274
$\rho^2(D_s^*)$					-0.884

4.5.4 Corrections to the simulation

The simulation is corrected for known data-simulation differences as explained in Sec. 4.2.1 through per-candidate weights computed as a function of the candidate kinematics using corrections maps derived from control samples of data. First, the impact of the corrections on the results is quantified by repeating the analysis without applying any correction to the simulation. The efficiency ratios ξ and ξ^* change from 1.5679 ± 0.0083 and 1.4635 ± 0.0073 to 1.5674 ± 0.0081 and 1.4639 ± 0.0071 , respectively. The results are reported in Tables 4.23 and compared with the baseline analysis. The differences between the two sets of values are only a fraction of the statistical uncertainty.

The correction maps, and hence the weights, have an uncertainty due to the limited statistics of the samples from which they are derived and due to systematic uncertainties assigned in the determination of the maps. To quantify the impact of these uncertainties, the weights are randomized by sampling from a Gaussian distribution centered at the nominal correction value and with a width given by the associated uncertainty. The fit templates and efficiency ratios are changed accordingly, and a new fit to the data is performed. The procedure is repeated 100 times: the RMS of the distributions of the fit

Table 4.23: Comparison between the baseline analysis and that where no corrections to the simulation are considered: Δ is the absolute value of the differences between the two sets of results.

Variation	Uncertainty							
	$ V_{cb} $ [10^{-3}]	$\rho^2(D_s)$	$\mathcal{G}(0)$	$\rho^2(D_s^*)$	R_1	R_2	\mathcal{R}	\mathcal{R}^*
Δ	-0.14	0.001	0.001	-0.02	-0.08	-0.01	-0.008	-0.001

parameters are then taken as systematic uncertainties. The results are reported in the middle pane of Table 4.21.

These systematic uncertainties are significantly smaller than all other quoted uncertainties. We then assume their correlations to be negligible and compute the correlation matrix for the sum of the ‘‘All experimental’’ systematics named (syst)– see Table 4.19 – by considering only the contributions due to the $D_{(s)}^- \rightarrow K^+ K^- \pi^-$ decay model and the backgrounds. The resulting correlation matrix is reported in Table 4.24 for the measurement of $|V_{cb}|$. The correlation of the total experimental systematic uncertainty between \mathcal{R} and \mathcal{R}^* is 0.189.

4.5.5 Total uncertainties and correlations

The total uncertainties of the parameters are reported in the last row of Table 4.19, and they are the sum in quadrature of the independent contributions, the statistical (stat), the external input (ext), and the experimental systematics (syst). The correlation matrices of the total uncertainties are reported in Tables 4.25, for the measurement of $|V_{cb}|$, and in Table 4.26 for the measurement of \mathcal{R} and \mathcal{R}^* .

Table 4.24: Correlation matrix of the systematic uncertainties named ‘‘Experimental’’ in Table 4.19 for the $|V_{cb}|$ fit.

	R_2	$\rho^2(D_s)$	$\mathcal{G}(0)$	$\rho^2(D_s^*)$	$ V_{cb} $
R_1	-0.820	0.820	0.919	0.920	-0.268
R_2		-1.000	-0.979	-0.531	0.033
$\rho^2(D_s)$			0.979	0.530	-0.032
$\mathcal{G}(0)$				0.692	-0.117
$\rho^2(D_s^*)$					-0.375

4.6 Final results and conclusions

A study of the $B_s^0 \rightarrow D_s^- \mu^+ \nu_\mu$ and $B_s^0 \rightarrow D_s^{*-} \mu^+ \nu_\mu$ decays is presented, which is based on a sample of proton-proton collisions collected with the LHCb detector at centre-of-mass energies of 7 and 8 TeV, and corresponding to an integrated luminosity of 3 fb^{-1} . A novel analysis method is used to identify the two exclusive decay modes from the

Table 4.25: Correlation matrix of the total uncertainties of the $|V_{cb}|$ measurement.

	$\mathcal{B}(D^- \rightarrow K^+ K^- \pi^-)$	$\mathcal{B}(D^{*-} \rightarrow D^- X)$	$\mathcal{B}(B^0 \rightarrow D^- \mu^+ \nu_\mu)$	$\mathcal{B}(B^0 \rightarrow D^{*-} \mu^+ \nu_\mu)$	R_1	R_2	$\rho^2(D_s)$	$\mathcal{G}(0)$	$\rho^2(D_s^*)$	$\mathcal{F}(1)$	η_{EW}	$ V_{cb} $
f_s/f_d	0.002											
$\mathcal{B}(D^- \rightarrow K^+ K^- \pi^-)$		0.001										
$\mathcal{B}(D^{*-} \rightarrow D^- X)$			-0.001									
$\mathcal{B}(D^0 \rightarrow D^- \mu^+ \nu_\mu)$				0.001								
$\mathcal{B}(B^0 \rightarrow D^- \mu^+ \nu_\mu)$			0.079	-0.047	0.000	-0.000	0.000	0.000	0.000	0.001	0.001	0.480
$\mathcal{B}(B^0 \rightarrow D^{*-} \mu^+ \nu_\mu)$				0.112	0.022	-0.016	0.006	-0.024	0.018	0.050	0.000	0.134
R_1					-0.052	0.038	-0.015	0.059	-0.043	-0.118	0.000	0.262
R_2					0.031	-0.023	0.009	-0.034	0.026	0.071	0.000	0.190
$\rho^2(D_s)$						-0.872	0.175	0.187	0.894	-0.033	-0.000	-0.004
$\mathcal{G}(0)$							-0.383	-0.341	-0.911	0.024	0.000	-0.073
$\rho^2(D_s^*)$								0.873	0.236	-0.009	-0.000	0.170
$\mathcal{F}(1)$									0.246	0.037	-0.000	0.020
η_{EW}										-0.027	-0.000	-0.029
											-0.000	-0.201
												-0.121

Table 4.26: Correlation matrix of the total uncertainties of the measurement of \mathcal{R} and \mathcal{R}^* .

	$\mathcal{B}(D^- \rightarrow K^+ K^- \pi^-)$	$\mathcal{B}(D^{*-} \rightarrow D^- X)$	\mathcal{R}	\mathcal{R}^*
f_s/f_d	0.001	0.001	-0.453	-0.362
$\mathcal{B}(D^- \rightarrow K^+ K^- \pi^-)$		-0.000	0.277	0.222
$\mathcal{B}(D^{*-} \rightarrow D^- X)$			-0.000	0.182
\mathcal{R}				0.313

inclusive samples of partially reconstructed $B_s^0 \rightarrow D_s^-(\rightarrow K^+ K^- \pi^-) \mu^+ \nu_\mu X$ candidates, and measure the CKM matrix element V_{cb} using analogous B^0 decays as normalisation. The measurement of V_{cb} is performed using the CLN parametrisation of the form factor and also using the recent lattice calculations for $B_s^0 \rightarrow D_s^- \mu^+ \nu_\mu$ decays reported in Ref. [62].

The result is

$$|V_{cb}| = (41.4 \pm 0.6 \text{ (stat)} \pm 0.9 \text{ (syst)} \pm 1.2 \text{ (ext)}) \times 10^{-3},$$

where the first uncertainty is statistical, the second is systematic, and the third is due to the limited knowledge of the external inputs. These is the first determination of $|V_{cb}|$ from exclusive decays at a hadron collider and the first using B_s^0 decays. The result is in agreement with measurements based on B^0 and B^+ decays, and is compared with previous measurements and world averaged in Fig. 4.22.

In addition, the form-factor parameters are found to be

$$\begin{aligned} \rho^2(D_s) &= 1.268 \pm 0.047 \text{ (stat)} \pm 0.032 \text{ (syst)} \pm 0.001 \text{ (ext)}, \\ \mathcal{G}(0) &= 1.102 \pm 0.034 \text{ (stat)} \pm 0.022 \text{ (syst)} \pm 0.004 \text{ (ext)}, \\ \rho^2(D_s^*) &= 1.23 \pm 0.17 \text{ (stat)} \pm 0.05 \text{ (syst)} \pm 0.01 \text{ (ext)}, \\ R_1 &= 1.34 \pm 0.25 \text{ (stat)} \pm 0.09 \text{ (syst)} \pm 0.02 \text{ (ext)}, \\ R_2 &= 0.83 \pm 0.16 \text{ (stat)} \pm 0.07 \text{ (syst)} \pm 0.01 \text{ (ext)}, \end{aligned}$$

Correlation matrix is provided for the sum of the statistical and external-input uncertainties in Table 4.13 and for the systematic uncertainties in Table 4.24.

The ratio of the branching fractions of the B_s^0 decays relative to those of B^0 decays are also measured. These ratios are found to be

$$\begin{aligned} \frac{\mathcal{B}(B_s^0 \rightarrow D_s^- \mu^+ \nu_\mu)}{\mathcal{B}(B^0 \rightarrow D^- \mu^+ \nu_\mu)} &= 1.093 \pm 0.054 \text{ (stat)} \pm 0.060 \text{ (syst)} \pm 0.051 \text{ (ext)}, \\ \frac{\mathcal{B}(B_s^0 \rightarrow D_s^{*-} \mu^+ \nu_\mu)}{\mathcal{B}(B^0 \rightarrow D^{*-} \mu^+ \nu_\mu)} &= 1.059 \pm 0.047 \text{ (stat)} \pm 0.074 \text{ (syst)} \pm 0.053 \text{ (ext)}, \end{aligned}$$

By taking the measured branching fractions of the $B^0 \rightarrow D^- \mu^+ \nu_\mu$ and $B^0 \rightarrow D^{*-} \mu^+ \nu_\mu$ decays as additional inputs, the exclusive semileptonic B_s^0 branching fraction are also determined for the first time

$$\begin{aligned} \mathcal{B}(B_s^0 \rightarrow D_s^- \mu^+ \nu_\mu) &= (2.49 \pm 0.12 \text{ (stat)} \pm 0.14 \text{ (syst)} \pm 0.16 \text{ (ext)}) \times 10^{-2}, \\ \mathcal{B}(B_s^0 \rightarrow D_s^{*-} \mu^+ \nu_\mu) &= (5.38 \pm 0.25 \text{ (stat)} \pm 0.46 \text{ (syst)} \pm 0.30 \text{ (ext)}) \times 10^{-2}, \end{aligned}$$

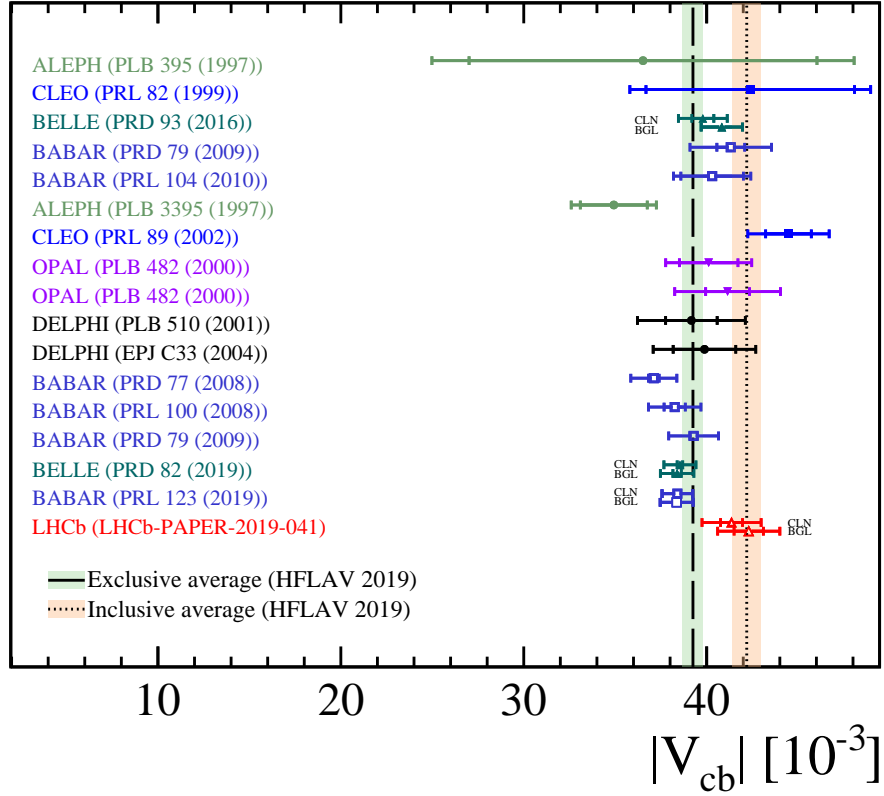


Figure 4.22: Summary of all the measurements of V_{cb} performed with exclusive decays. The larger error bar represents the total uncertainty, whereas the shorter (when present) show the statistical uncertainty. The measurement from this analysis is reported in red as LHCb-PAPER-2019-041.

where the third uncertainty also includes that due to the normalisation branching fractions. Finally, the ratio of $B_s^0 \rightarrow D_s^- \mu^+ \nu_\mu$ to $B_s^0 \rightarrow D_s^{*-} \mu^+ \nu_\mu$ branching fractions is determined to be

$$\frac{\mathcal{B}(B_s^0 \rightarrow D_s^- \mu^+ \nu_\mu)}{\mathcal{B}(B_s^0 \rightarrow D_s^{*-} \mu^+ \nu_\mu)} = 0.464 \pm 0.013 \text{ (stat)} \pm 0.043 \text{ (syst)}.$$

The relative uncertainty on the $|V_{cb}|$ measurement described in this Thesis is larger than the uncertainty obtained by the BaBar and Belle experiments (Table 4.27). However, the analysis strategy presented here is promising from many points of view. First of all, it demonstrated the feasibility of the $|V_{cb}|$ measurement at a hadron collider. Besides, the systematic effects which dominate its sensitivity are essentially led by the knowledge of the $D_{(s)}^- \rightarrow K^+ K^- \pi^+$ process. On the one hand, the knowledge of its decay model constitutes the higher systematic for this analysis. On the other hand, its branching ratio provides the main contribution to the systematics of the f_s/f_d measurement. In this respect, progress is expected from the physics programmes of both the LHCb and Belle II experiments. The latter, whose operation conditions facilitate the precise knowledge of the instantaneous luminosity, may be particularly valuable for the update of all the absolute branching fractions, affecting this analysis as external inputs [170].

Further developments of this study will probably focus on the extraction of $|V_{cb}|$ using

$B^0 \rightarrow D^{*+} \mu^- \bar{\nu}_\mu$ decays and inclusive semimuonic decays of B mesons, $B^{0,+} \rightarrow X_c \mu \nu X$, as signal and normalization channels, respectively. From preliminary tests, the same analysis approach presented here seems suitable for this purpose, which remarkably benefits from the no-need of the f_s/f_d correction.

Experiment	V_{cb}	Result	Relative Uncert.	Ref.
Belle		$(39.0 \pm 0.9) \times 10^{-3}$	2.3%	[171]
BaBar		$(39.4 \pm 0.9) \times 10^{-3}$	2.3%	[172]
LHCb		$(41.4 \pm 1.6) \times 10^{-3}$	3.9%	this thesis, [173]

Table 4.27: Comparison of the latest $|V_{cb}|$ determinations. The combination of the statistical and systematic uncertainties is reported. All the results involve the CLN parametrisation of the form factors.

Chapter 5

Simulation and characterization of the LHCb Upgrade II ECAL

Introduction

The essential purpose of this work is identifying the basic parameters of an electromagnetic calorimeter (ECAL), which may manage the extreme demanding environment, foreseen for the Upgrade II of the LHCb experiment. As explained in Ref. [174,175], an instantaneous luminosity of up to $1.5 \times 10^{34} \text{ cm}^{-2} \text{ s}^{-1}$ may be provided at the LHCb interaction point (IP8) during the Run 5 of the LHC. On the one hand, this might permit to collect a data sample at least a factor six higher than that at the end of Run 4 and a factor thirteen higher than that at the end of Run 3. According to Ref. [25]: “...*the impact of Upgrade II in flavor physics will be comparable to that for on-shell new particle searches of increasing the LHC collision energy from 14 TeV to 27 TeV*”. On the other hand, this would mean a factor ten increase in instantaneous luminosity, with respect to the expected conditions in the upcoming Run 3, and a factor fifty increase with respect to the conditions in which LHCb has operated in the Run 1 and Run 2 of the LHC. These extreme conditions pose several experimental challenges, both in terms of radiation tolerance and pile-up managing. The latter is particularly challenging for the ECAL, whose performance are tightly related to occupancy. Equipping the ECAL with the capability to precisely measure the time of arrival of particles on its surface is fundamental to properly associate particles to the corresponding p - p collision in the event. Therefore, it is necessary to simulate the ECAL response to the expected running conditions, evaluating its performance. Main parameters to be considered are:

- intrinsic energy resolution of the cells;
- size and placement of the cells, determining the segmentation of the surface of the ECAL;
- resolution in determining the time of arrival of particles on the ECAL surface;
- the gain in performance having a further segmentation of the cells along the z direction.

The aim of the study is to determine the above-mentioned parameters that allow the LHCb Upgrade II ECAL to reach the same signal yields and background levels per fb^{-1}

of integrated luminosity achieved by the LHCb ECAL in Run 2.

This Chapter is organised as follow. Section 5.1 summarises the aspects of the R&D project which drive the study. In Section 5.2 the simulation of particles produced in the p - p collisions, their transport to the ECAL surface, and their interaction with the ECAL material is described. Section 5.3 presents the algorithms used to reconstruct photons, neutral pions and electrons. Section 5.4 reports the studies conducted to compare the performance of the LHCb ECAL in its Run 2 and Upgrade II configurations with respect to two important decay channels for the LHCb physics programme: the $B^0 \rightarrow \pi^+\pi^-\pi^0$ and the $B^0 \rightarrow K^{*0}e^+e^-$.

5.1 Technologies and description of LHCb Upgrade II ECAL

The LHCb ECAL used in Run 1 and Run 2, that will operate also in Run 3 and Run 4, is based on Shashlik modules and is described in Section 2.3.2. That ECAL configuration is assumed also in this Chapter when performance for Run 2 conditions are evaluated. Considering the luminosity increase expected for the Run 5 and beyond, a redesign of the detector has been proposed in Ref. [94] and is summarised in this Section. The critical parameters that lead the redesign are the resistance of the detector to the radiation dose and the degradation of the performance due to the increased occupancy. In Figure 5.1, the expected accumulated dose corresponding to an integrated luminosity of 300 fb^{-1} (foreseen by the end of Run 6), is reported [94]. In the region close to the beampipe, the ECAL modules must sustain a total integrated dose of 1 MGy ($\leq 6 \times 10^{15} \text{ 1 MeV } n_{\text{eq}}/\text{cm}^2$), that is much higher than the limit of 40 kGy of the Shashlik module [176,177]. Finer cell granularity with respect to the current limit of $4 \times 4 \text{ cm}^2$ of the Shashlik modules will be fundamental to deal with the much increased occupancy. A corresponding decrease of the Molière radius in order to reduce the lateral size of the showers, allowing the amount of distinct clusters to remain at the same level of Run 2, is also necessary in the

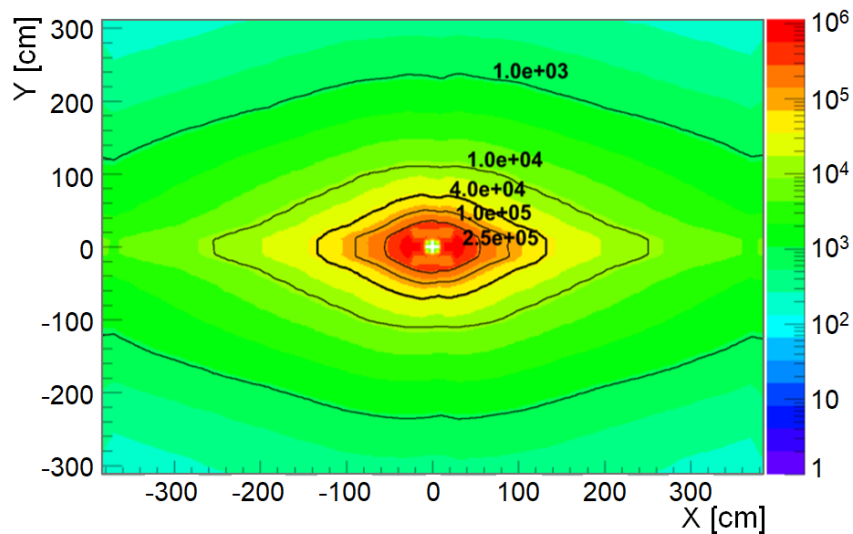


Figure 5.1: Expected radiation dose (in Gy) accumulated on the ECAL surface after an integrated luminosity of 300 fb^{-1} .

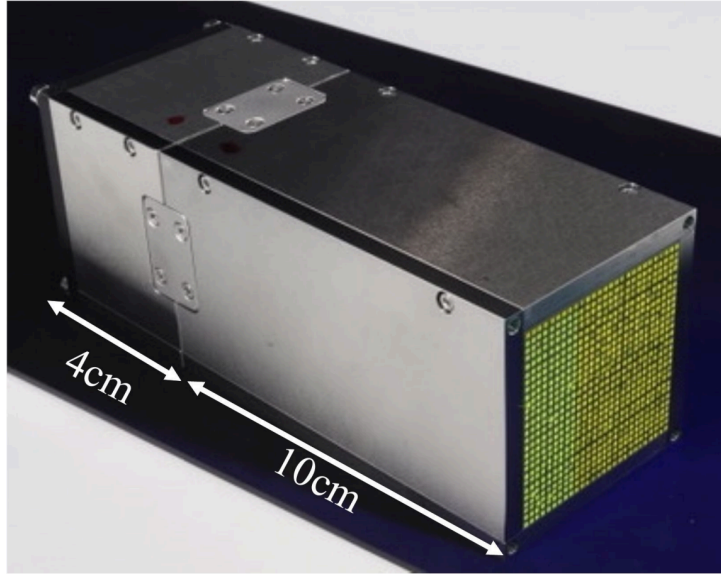


Figure 5.2: Picture of a SpaCal prototype developed by LHCb in 2019. Crystal fibres (yellow-green) are visible from the open section on the right side and are encapsulated in a tungsten absorber. The longitudinal segmentation of the module is visible as well.

central regions. The technological solution currently proposed to equip the regions of the ECAL where the integrated dose exceeds the limit of the Shashlik modules is the so-called Spaghetti Calorimeter (SpaCal) [178, 179]. SpaCal modules consist of a matrix of scintillating fibres longitudinally arranged along the beam line and encapsulated in the absorber material, as shown in Figure 5.2. To bring the light to the photodetectors, this solution does not require wavelength-shifting fibres, that are the main driver of ageing effects for the Shashlik technology. In addition, SpaCal technology permits great flexibility in defining the cell size, allowing it to be tuned by simply changing the area over which the fibres are read out. Crystal fibres are found to meet the radiation-hardness requirement of the hottest region close to the beampipe where the integrated dose will be ≥ 200 kGy. Studies conducted to find the best crystals identified GAGG garnet as the most promising choice for the active material, owing to its large light yields (between 27900 and 49500 photons/MeV) and fast rising and decay characteristic times of about 70 ps and 50 ns, respectively [180]. Using 1×1 mm² crystal fibres with 1.67 mm pitch inside an absorber made of tungsten, a Molière radius of approximately 15 mm is achieved. In the intermediate region, with integrated dose ranging between 40 kGy and 200 kGy and less severe occupancy, SpaCal modules with polystyrene plastic fibres and lead absorber are found to be adequate. Modern polystyrene fibres shows high light yield of 10000 photons/MeV and a very fast scintillating decay time of 2.8 ns. Also in this case 1×1 mm² fibres are used with a pitch of 1.67 mm, leading to a Molière radius of approximately 30 mm. In the outer regions, where radiation-hardness requirements are less severe, Shashlik technology fits the requirements. An additional leverage to deal with the high occupancy is provided by the possibility, for both SpaCal and Shashlik technologies, to longitudinally split the ECAL modules in two sections at around the shower maximum. Using the information provided from the separate readout of the front and back sections improved performance in clustering, reconstruction and particle identification are achievable. For example, the fact that electromagnetic showers are less

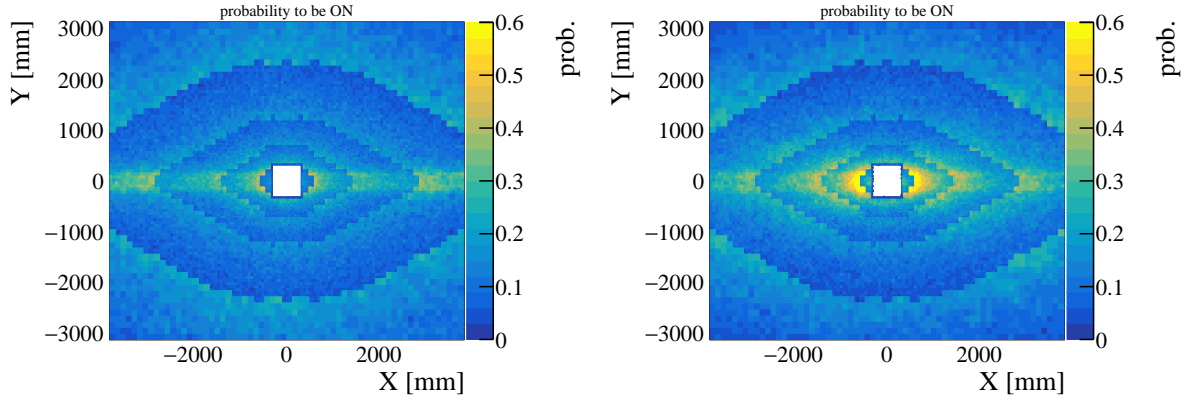


Figure 5.3: Occupancies of front (left) and back section (right) of LHCb ECAL cells determined using simulated p - p collision events with instantaneous luminosity $L = 1.5 \times 10^{34} \text{ cm}^{-2} \text{ s}^{-1}$. Occupancy for each cell is defined as the fraction of events where the cell registered a transverse energy $E_T > 25 \text{ MeV}$.

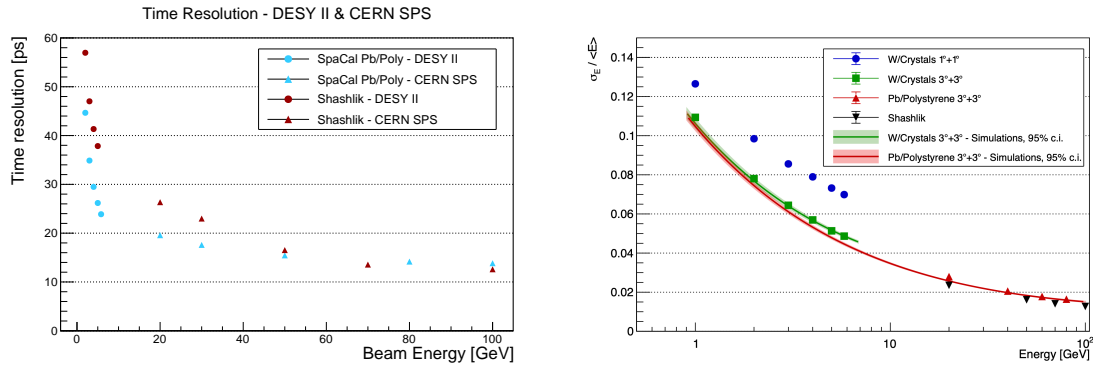


Figure 5.4: Time resolution (left) and relative energy resolution (right) for SpaCal and Shashlik modules, as determined in test beam [94].

developed in their initial stages means that in the front section pile-up effects are mitigated (see Figure 5.3). The development of pattern-recognition algorithms dedicated to exploit this feature is currently ongoing as the natural continuation of the work presented in this thesis, but is not discussed here. Performances for time and energy resolution obtained from beam test with high-energy electrons of SpaCal and Shashlik prototypes are reported in Figure 5.4.

Despite beam tests demonstrates that SpaCal and Shashlik technologies are able to achieve time resolutions in the ballpark of few tens of picoseconds already for electrons of 5 GeV [94], in order to achieve the ultimate precision, the implementation of a dedicated timing layer, inserted between the front and back sections of the modules, is being investigated. Among the proposed solutions there is also that based on the idea, dating back to 1990's [181], of using Micro-Channel Plate (MCP) detectors to sample the charged component of electromagnetic showers. Photodetectors based on MCP (MCP-PMTs) have excellent spatial and time resolutions, but are known to suffer from limitations regarding their lifetime, dead-time and cost. An intense programme of feasibility studies has been conducted in the last two years to investigate the possibility to use the Large-Area Picosecond PhotoDetecotr (LAPPD) [182, 183] for the timing layer of the LHCb

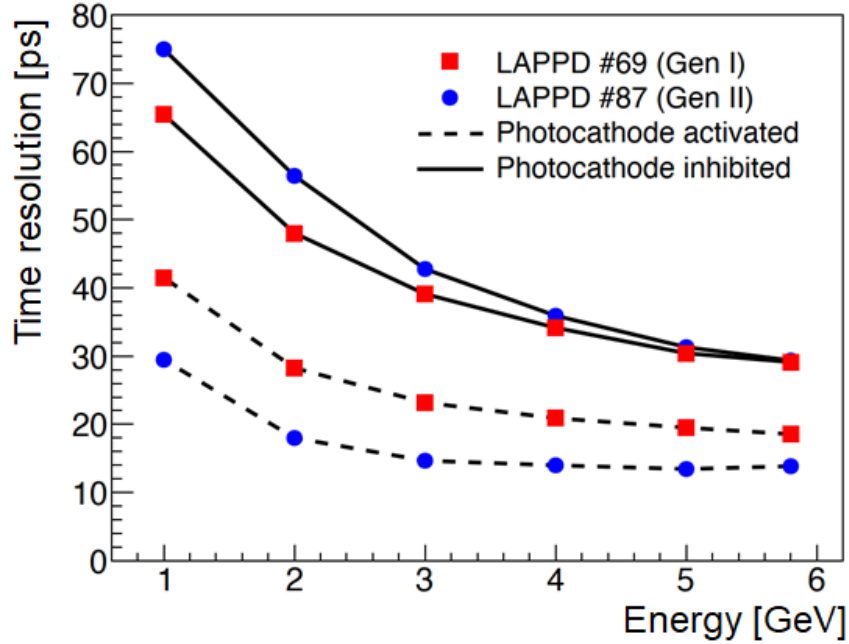


Figure 5.5: Time resolutions for the MCP-PMT timing layer as measured in test beam in different configurations [94].

Upgrade II ECAL. The LAPPD is currently the largest MCP-PMT available on the market ($20 \times 20 \text{ cm}^2$) and is built with inexpensive material. In particular, the MCP wafers are made adding thin layers of resistive and emissive materials, using atomic-layer deposition (ALD), on a substrate of commercial borosilicate glass. Lifetime issues of MCP-PMTs are related to the ageing of the photocathode, that shows important performance degradation for integrated anodic charge above 30 C/cm^2 [184–186], that is insufficient for the LHCb Upgrade II requirements. However, this inconvenience can be overcome by operating these devices without the photocathode, detecting the ionisation directly produced in the MCPs by the particles of the electromagnetic shower, as proposed in Refs. [187, 188]. Two LAPPD devices have been tested with high-energy electrons at the DESY beamtest facility, placing them between the two sections of a GAGG/W SpaCal module. Results in terms of time resolution are shown in Figure 5.5 [94]. Time resolutions of 15 ps and 30 ps are achieved for electrons of 5 GeV when the LAPPD is operated with the photocathode enabled and inhibited, respectively. These time resolutions are promising, considering that the employed LAPPDs were off-shelf devices and would benefit from an LHCb-optimised design. However, discussing potential improvements is beyond the scope of this thesis and is not treated here.

A schematic view of the SpaCal modules of the LHCb Upgrade II ECAL is reported in Figure 5.6. The scheme, showing the SpaCal modules longitudinally segmented with the timing layer inserted between them, is valid also for Shashlik modules and corresponds to the baseline design that is tested in the simulations reported in this thesis. The optimisation of the final geometry of the Upgrade II ECAL, based also on the studies reported in this thesis, is still being evaluated, but a baseline configuration is already defined in Ref. [94]. It is shown in Figure 5.6 and the main features of the modules used in each region are summarised in Table 5.1. The borders and the shape of these regions in the $x - y$ plane are defined according to the total radiation dose expected after the

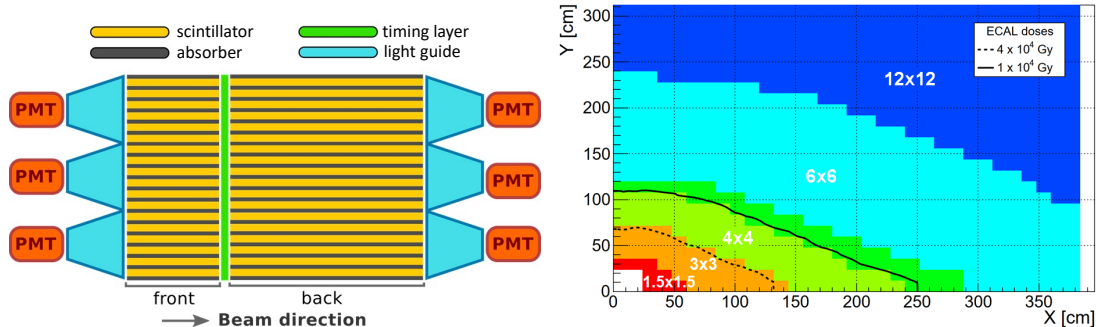


Figure 5.6: On the left: schematic view of the SpaCal modules of the LHCb Upgrade II ECAL. The same longitudinal split with the presence of the timing layer can be applied also to Shashlik modules. On the right: baseline configuration of ECAL regions and cell sizes as defined in Ref. [94] and summarised in Table 5.1. From the inner to the outer regions: (white) beampipe hole, (red) Region 0, (orange) Region 1, (green) Region 2, (slightly darker green) Region 3, (cyan) Region 4 and (blue) Region 5. No material or segmentation difference between Region 2 and Region 3 will be considered in this thesis. Such distinction was initially utilised by the R&D team because of studies on the integrated radiation dose absorbed by the ECAL modules. For this reason, it is still implemented in this simulation even if it does not really differentiate the ECAL properties.

Table 5.1: Summary of technologies used to equip each region of the LHCb Upgrade II ECAL in the studies conducted in this thesis. Main parameters of the different technologies are also reported.

Region	Module type	Cell size [mm ²]	Segmentation [mm] / [X_0]	R_M [mm]	$\sigma_E/E = A/\sqrt{E} \oplus B$ A/B [%]
0	SpaCal W/GAGG	15×15	$45 + 105 / 7 + 18$	14.5	9.1 / 1.4
1	SpaCal Pb/Poly	30×30	$80 + 210 / 7 + 18$	29.5	10.4 / 0.6
2	Shashlik	40×40	$120 + 300 / 7 + 18$	35.0	10.0 / 1.0
3	Shashlik	40×40	$120 + 300 / 7 + 18$	35.0	10.0 / 1.0
4	Shashlik	60×60	$120 + 300 / 7 + 18$	35.0	10.0 / 1.0
5	Shashlik	120×120	$120 + 300 / 7 + 18$	35.0	10.0 / 1.0

collection of 300 fb^{-1} of integrated luminosity at the end of the Run 6 of the LHC. All the regions are defined such that they are composed by an integer number of modules with a dimension of $120 \times 120 \text{ mm}^2$. In such a way, each region can be simulated using any of the possible cell sizes: $15 \times 15 \text{ mm}^2$, $30 \times 30 \text{ mm}^2$, $40 \times 40 \text{ mm}^2$, $60 \times 60 \text{ mm}^2$ and $120 \times 120 \text{ mm}^2$.

For completeness, in Ref. [94], also other technological solutions are proposed for the LHCb Upgrade II ECAL. One is to build a completely different electromagnetic calorimeter with silicon detector layers interleaved with tungsten absorber. Another proposed solution is to use, instead of the MCP-based timing layer, a timing layer built with three layers of silicon detectors interleaved with tungsten absorber. These technological solutions are not studied in this thesis.

5.2 Simulation

The simulation used in this study consists of three steps. In the first one, described in Section 5.2.1, the primary p - p collisions (also referred to as primary vertex or PV) are generated, and the produced particles are propagated to the surface of the ECAL. In the second step (Section 5.2.2), the p - p collisions are grouped in events to reproduce the pile-up at the luminosity expected during the Run 5 of LHCb. In the third step (Section 5.2.3), the interaction of particles with the ECAL is simulated, producing the information to be passed to the reconstruction algorithms described in Section 5.3.

For calibration and cross-check purposes the simulation of events containing only one particle will be often exploited. This configuration will be referred to as “particle-gun” simulation.

5.2.1 Generation of p - p collisions

The standard LHCb package GAUSS [189] is employed to generate the primary p - p collisions using PYTHIA [190] with a configuration specifically developed for LHCb [191]. The decays of unstable particles are described using EVTGEN [192], where the emission of soft-photons in the final state is generated using PHOTOS [193]. Table 5.2 summarises the beam parameters assumed to generate the p - p collisions¹. The version of the LHCb standard simulation used in this study is able to determine the spatial distribution of the PVs, but not their time of production. Since the time information is a fundamental ingredient to resolve the high pile-up expected in Run 5 a simple model is used to assign to each PV a corresponding time of production. Since the total crossing angle between the beams is small (see Table 5.2) the bunches are assumed to hit each other head-on. The transversal dimension of the bunches is also neglected in the model, because it is

Table 5.2: Beam parameters. ν is the mean number of PVs per bunch-crossing (the mean number of visible PV is $\mu = 0.699\nu$); \sqrt{s} is the total energy in the center of mass of the beams; β^* is the normalized beta function; ϵ^* is the normalized emittance; $\sigma_{x,y}$ is the transverse RMS of the bunch; σ_z is the longitudinal RMS of the bunch.

Beam Parameter	Run 2	Run 5
Circulating bunches	2300	2400
Revolution frequency [kHz]	11.2	11.2
\sqrt{s} [TeV]	13	14
Crossing angle (x - z plane) [μ rad]	-395	135
Crossing angle (y - z plane) [μ rad]	0	120
β^* [m]	3	2.8
ϵ^* [μ m]	2.5	3.8
$\sigma_{x,y}$ [μ m]	33	33
σ_z [cm]	9	9

¹The nominal beam parameters are reported in Ref.s [174, 175]. Slightly different values are used in this simulation because of private communications with the LHCb management.

much smaller than the longitudinal dimension. Under these assumptions, the bunches are described as Gaussian distributions, with standard deviation σ_z , and means moving along the z axis at the speed of light, c , in opposite directions

$$G_{\pm}(z \pm ct, \sigma_z) = C \cdot \exp \left[\frac{(z \pm ct)^2}{2\sigma_z^2} \right], \quad (5.1)$$

where C is a normalization constant. The corresponding PV distribution in z and t is the product of the two Gaussian functions

$$G_{\text{PV}} = G_+(z + ct, \sigma_z) \cdot G_-(z - ct, \sigma_z) \propto \exp \left[\frac{2z^2 + 2(ct)^2}{2\sigma_z^2} \right], \quad (5.2)$$

which can be rewritten as

$$G_{\text{PV}} \propto \exp \left[\frac{z^2}{2(\sigma_z/\sqrt{2})^2} \right] \cdot \exp \left[\frac{t^2}{2(\sigma_z/(c\sqrt{2}))^2} \right]. \quad (5.3)$$

From this basic argument, it is possible to see that the distributions of the PVs in space and time are uncorrelated, and have standard deviations $\sigma_z(PV) = \sigma_z/\sqrt{2}$ and $\sigma_t(PV) = \sigma_z/(c\sqrt{2})$, respectively. Using the values of the Table 5.2, they become $\sigma_z(PV) = 63$ mm and $\sigma_t(PV) = 212$ ps.

The propagation of the produced particles and their interaction with the detector material is simulated using the GEANT4 toolkit [194], integrated inside the GAUSS package. The material budget upstream of the ECAL is important for this study, since it is responsible for the production of secondary particles, increasing the rate of incident particles per unit of ECAL surface. Since the LHCb detector to be used in Run 5 is not yet defined, a detailed description of its subdetectors is not possible, hence the model of the LHCb Upgrade I detector is used in this study [88]. Even though this is not a perfect representation of the future Upgrade II LHCb detector, it constitutes the best estimation for its material budget, to date. In Figure 5.7 the coordinates in the $x - z$ plane of the origin vertex of all the simulated particles hitting the ECAL surface from few hundreds of $p-p$ collisions is reported, clearly showing where the main contributors to the creation of secondary particles are.

This part of the simulation procedure is very CPU consuming, hence it is performed only once. About 2.2 millions of $p-p$ collisions are simulated to be used in the following steps. They constitute the ‘‘Minimum-bias’’ sample. In addition, samples of $p-p$ collisions, where the presence of specific B -meson decays is forced, are also generated in order to study the performance of the ECAL in reconstructing and selecting those signals. All the samples of $p-p$ collisions are summarised in Table 5.3, with the corresponding number of generated events.

5.2.2 Simulation of luminosity conditions in Run 5

According to Refs. [174, 175], different scenarios are available for the luminosity conditions expected in Run 5 at the LHCb interaction point (IP8). The most important difference with respect to the previous runs is that the instantaneous luminosity will not be levelled anymore. During Run 1 and Run 2, as well as it is expected in Run 3 and Run 4, this was possible using a relative displacement of the beams one with respect to the other. During

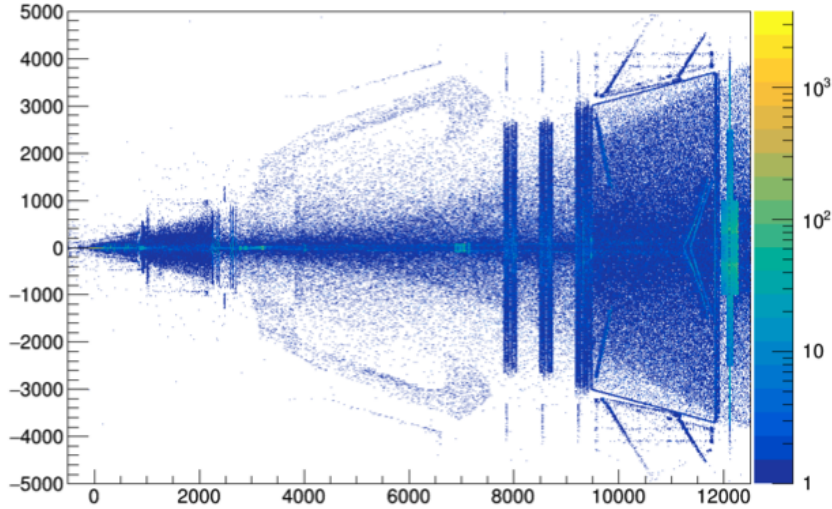


Figure 5.7: Position in the $x - z$ plane of the origin vertex of all the particles hitting the ECAL surface from few hundreds of simulated $p-p$ collision events. The spatial coordinates are expressed in mm.

Table 5.3: Number of generated events for each simulated sample.

Mode	Generated Events
Minimum Bias	2.2×10^6
$B^0 \rightarrow \pi^+ \pi^- \pi^0$	8.0×10^4
$B^0 \rightarrow K^{*0} e^+ e^-$	4.0×10^4
$B^0 \rightarrow K^{*0} \pi^+ \pi^-$	4.0×10^4

Run 5 the levelling of the instantaneous luminosity will be possible only for a limited time along the duration of the LHC fill. In Figure 5.8, taken from Refs. [174, 175], the different scenarios are shown, in terms of instantaneous luminosity along the fill duration and expected integrated luminosity per year. In this work the beam conditions maximising the total integrated luminosity of Run 5 will be investigated. Such a condition consists of a peak luminosity of $1.5 \times 10^{34} \text{ cm}^{-2} \text{ s}^{-1}$ that will be maintained constant for about 2 hours. After the 2 hours the instantaneous luminosity will drop according to an exponential function with half life of 4 hours. The total fill duration will be 10 hours long. Assuming the normal duty cycle of the LHC (corresponding to 10^7 s per year with an efficiency of 50%), LHCb expects to collect slightly less than 50 fb^{-1} of integrated luminosity each year.

Given the evolution of the luminosity over the fill duration, the mean number of $p-p$ collisions present in one event (ν) will vary as well, according to the equation

$$\nu = \frac{L \sigma_{\text{mb}}}{f N}, \quad (5.4)$$

where L is the instantaneous luminosity, σ_{mb} is the total cross-section, f is the revolution frequency of the bunches inside the LHC, and N is the total number of bunches inside the LHC. According to the parameters reported in Table 5.2, a luminosity of $1.5 \times 10^{34} \text{ cm}^{-2} \text{ s}^{-1}$

corresponds to $\nu = 57$.² This information is used to decide how many PVs must be combined in order to form an event. First a random number is generated uniformly between 0 and the fill duration, and the corresponding instantaneous luminosity is computed. The equivalent value of ν is computed using Eq. (5.4), and the number of PVs to be combined is randomly extracted according to a Poisson distribution with mean equal to ν . Finally, each event is accepted or rejected according to the probability that at least one of its PVs produced a $b\bar{b}$ pair. This probability can be written as

$$P(n_{b\bar{b}} \geq 1 | N_{\text{PV}}) = 1 - (1 - p_{b\bar{b}})^{N_{\text{PV}}}, \quad (5.5)$$

where N_{PV} is the number of PVs in the event, $n_{b\bar{b}}$ is the number of PVs producing $b\bar{b}$ pairs and $p_{b\bar{b}}$ is the probability that a given PV produces a $b\bar{b}$ pair within the LHCb acceptance. The probability $p_{b\bar{b}}$ correspond to the ratio between the $b\bar{b}$ -pair cross section within the LHCb acceptance $\sigma_{b\bar{b}} = 144 \pm 1 \pm 21 \mu\text{b}$ [84] and the total cross section $\sigma_{\text{mb}} = 100 \text{ mb}$ [4]. For each event, a random number is uniformly generated between 0 and 1 and the event is accepted only if the random number is lower than the probability in Eq. (5.5). The final sample is composed repeating the procedure many times, each time ensuring the presence in each event of one PV where the signal decay under study is produced. In Figure 5.9 the distribution of the number of PVs in each event is shown, both as a function of the time after the start of the LHC fill and integrated over the fill duration. The same procedure is used to produce samples with Run 2 pile-up conditions, corresponding to a constant levelled luminosities of $4 \times 10^{32} \text{ cm}^{-2} \text{ s}^{-1}$ ($\nu = 1.6$).

5.2.3 Simulation of ECAL detector

The simulation of the interaction of particles with the ECAL is based on a standalone package, specifically developed for this work, using the GEANT4 toolkit. A full simulation

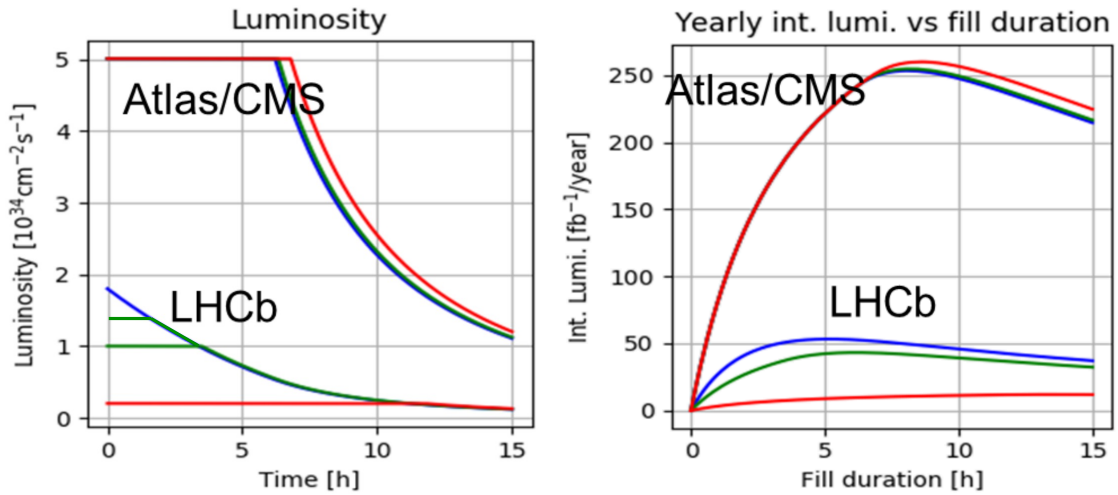


Figure 5.8: Fill luminosity scenarios expected for the LHC experiment during Run 5. The scenario for LHCb used in this work is described in the text and correspond to the green line starting with a luminosity levelling of 2 hours at $L = 1.5 \times 10^{34} \text{ cm}^{-2} \text{ s}^{-1}$.

²According to LHCb studies the mean number of visible collisions, *i.e.* mean number of collisions producing any detectable signal inside the LHCb detector, is $\mu = 0.699\nu$.

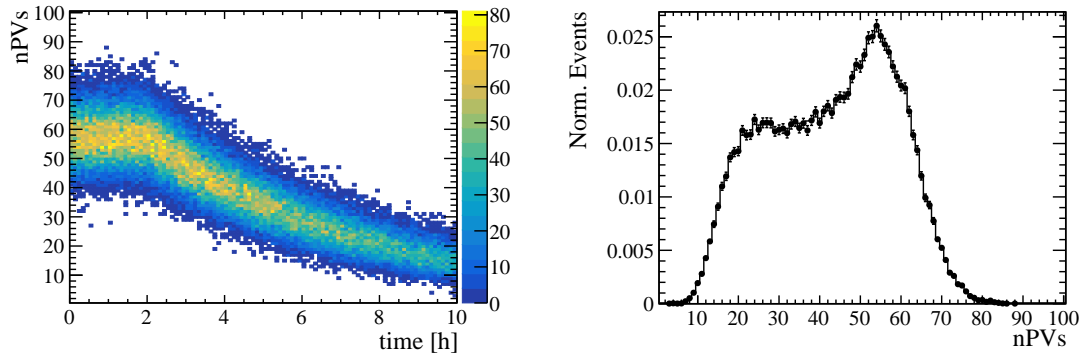


Figure 5.9: Distribution of the number of PVs (left) as a function of the elapsed time after the start of an LHC fill and (right) integrated over the entire duration of an LHC fill.

of all the components of the ECAL, as described in Section 5.1, would be very CPU consuming, in particular when all the geometrical details of the modules are considered. A less detailed, but much faster and more flexible simulation is developed.

The first simplification consists in substituting the detailed geometry of the SpaCal and Shashlik cells with homogeneous materials. The compositions of these materials are computed starting from the main volumes and materials of the three technologies. In the innermost region, the SpaCal cells are composed for 48% of their volume by tungsten absorber, for 36% of their volume by crystal scintillating fibres and for 16% of their volume by air filling the gaps between fibres and absorber. The same volume fractions apply to the SpaCal cells located in the second innermost region, where lead is used as absorber and polystyrene fibres are used as active material. Finally, for the Shashlik cells, the lead absorber corresponds to about one third of the total volume of the cells, while the polystyrene scintillating tiles occupy the rest of the volume. A summary of the “averaged” materials, with their corresponding properties, is illustrated in Figure 5.10.

Once homogeneous materials are assumed for ECAL cells, the definition of surfaces, dividing cells made of the same material, becomes redundant³. Hence, a second simplification consists in merging the ECAL cells into homogeneous blocks, corresponding to the regions defined in Figure 5.6, and split only along the z axis to separate the front and back section of the calorimeter. After the simulation of the particle transport, the association of energy deposits and ECAL cells can be done using their x and y coordinates. To check the goodness of the simplifications, some key quantities are studied and compared to the results of the detailed simulation of the SpaCal modules developed in Ref. [195]. Few of these tests are illustrated in the Figures 5.11 and 5.12.

To reproduce the effect on energy resolution due to the fraction of active material present in the SpaCal and Shashlik technologies, the energy deposits simulated by the GEANT4 toolkit are accepted or rejected according to a random number extracted uniformly between 0 and 1. The threshold on the random number is tuned to obtain a sampling term of about 10% in the energy resolution, as expected from the detailed simulation of

³When the GEANT4 toolkit simulates the passage of a particle through a complex object, it keeps information not only about the energy deposits but also about the crossings of the surfaces separating the various parts which define the object. On the one hand, this is useful to know the time of the passages from the front to the back section of the ECAL. On the other hand, when cells made of the same material are considered, the details about the transports across their lateral surfaces are superfluous.

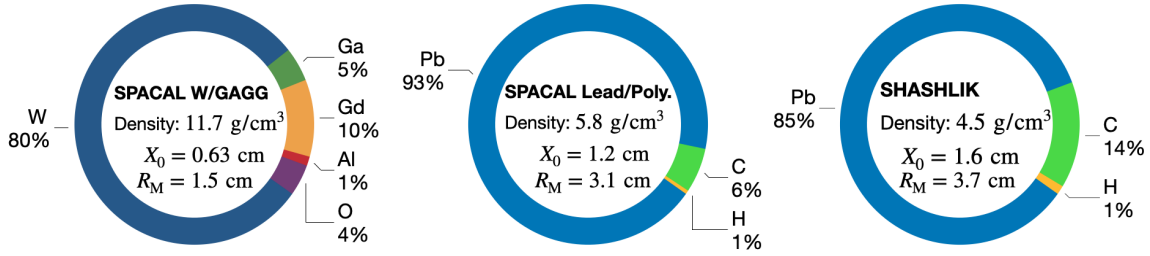


Figure 5.10: Mixture compositions of the homogeneous materials assumed to simulate the apparatuses of the various ECAL technologies. Besides the mass fractions of the various elements, the overall densities, radiation lengths (X_0), and Molière radii are reported.

both the technologies. The calibration of this sort of “sampling fraction” is performed using four datasets of simulated photons, originating from the LHCb interaction point in particle-gun configuration. All the datasets contain 1.5×10^3 photons, whose energy is uniformly distributed within a corresponding energy range. The limits of such ranges are: 10 MeV, 1 GeV, 5 GeV, 10 GeV, and 100 GeV.

Figure 5.13 shows the sampled energy versus the total deposited energy for the various regions of the ECAL. A fit with a straight line is performed, and the result is used to convert the sampled energy into the “reconstructed” value of the energy used by the reconstruction algorithms, when analysing simulated events. In Figure 5.14 the relative energy resolution as a function of the reconstructed energy is shown, separately for the different regions of the ECAL. This strategy is used to determine the reconstructed energy for all the particles hitting the ECAL, hadrons included.

In the ECAL configuration presented in Section 5.1, the time information of particles arriving to the ECAL is provided by a timing layer placed between the front and back section of the ECAL. The signals of the timing layer are due to the detection of electrons and positrons of the electromagnetic showers crossing the timing layer. Hence, the time information for each cell of the ECAL is determined as the average of the times at which the charged particles traverse the surface between the front and back section of the cells. In this way, the intrinsic effect on the time resolution due to the fluctuations in the propagation of the electromagnetic shower is taken into account. The effect is evidenced in Figure 5.15, which reports the expected number of crossings for 5 GeV simulated electrons as a function of the time elapsed from the first crossing due to the same shower. The distribution has a very long tail, but the vast majority of the particles is contained within few picoseconds. Besides this intrinsic effect, the resolution of the apparatus performing the time measurement has to be comprehended. To test how the performance of the ECAL are affected by this parameter, three time resolutions options, 15, 30, and 50 ps, are probed in this thesis. This is done by adding to the time information a random number, generated according to a Gaussian function with width equal to the corresponding resolution. This simulation approach has the advantage that the average crossing time considers the finite propagation velocity and the multiplicity of the showers. Therefore, the time measurement is straightforwardly simulated also when different showers of the same event overlap in the same ECAL cell. Further considerations concerning the timing are reported in Section 5.3.6, where the information from the individual ECAL cells are combined with the energy and direction of the reconstructed particles.

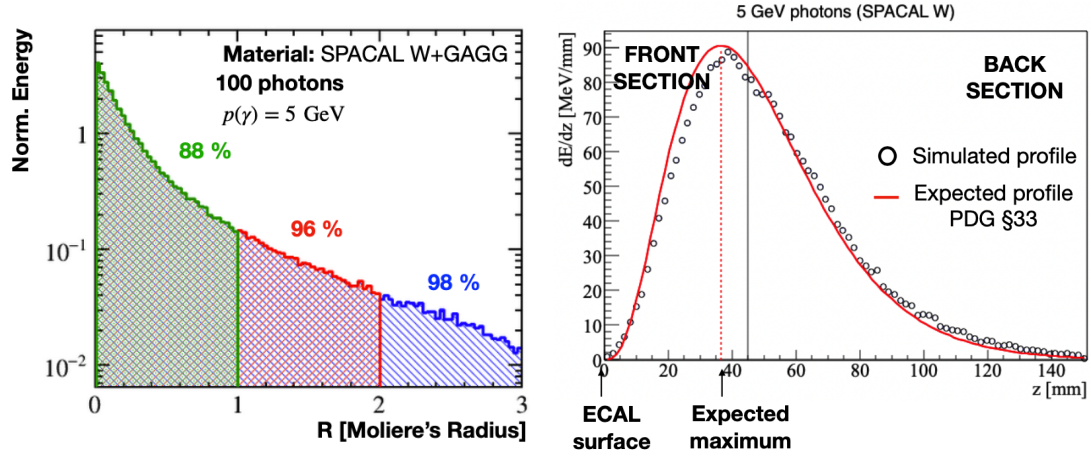


Figure 5.11: The plot on the left shows the radial profile of the energy deposited by 5 GeV simulated photons, perpendicularly hitting the SpaCal W/GAGG material, in particle-gun configuration. The percentages in green, red, and blue report the fraction of the total energy deposited within 1, 2, and 3 Molière’s radii. They are consistent with the expectations. The plot on the right depicts the longitudinal shower profile of the same photons into the homogeneous SpaCal W/GAGG material simulated in this thesis. The red line shows the expected distribution according to Ref. [4].

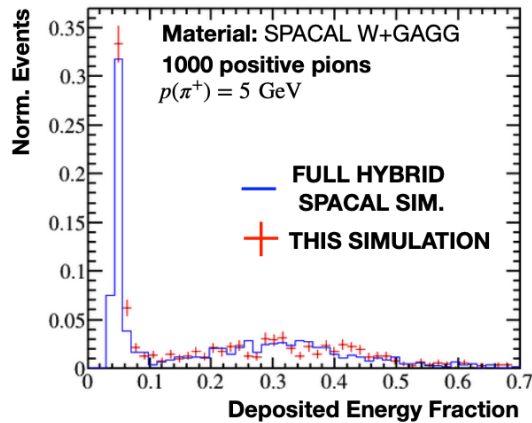


Figure 5.12: Distribution of the fraction between the energy deposited in the SpaCal W/GAGG material and the total energy for simulated pions with a 5 GeV momentum in particle-gun configuration. The blue line shows the prediction by the detailed SpaCal simulation [195], while the red crosses illustrate the consistent distribution, obtained by this work of thesis.

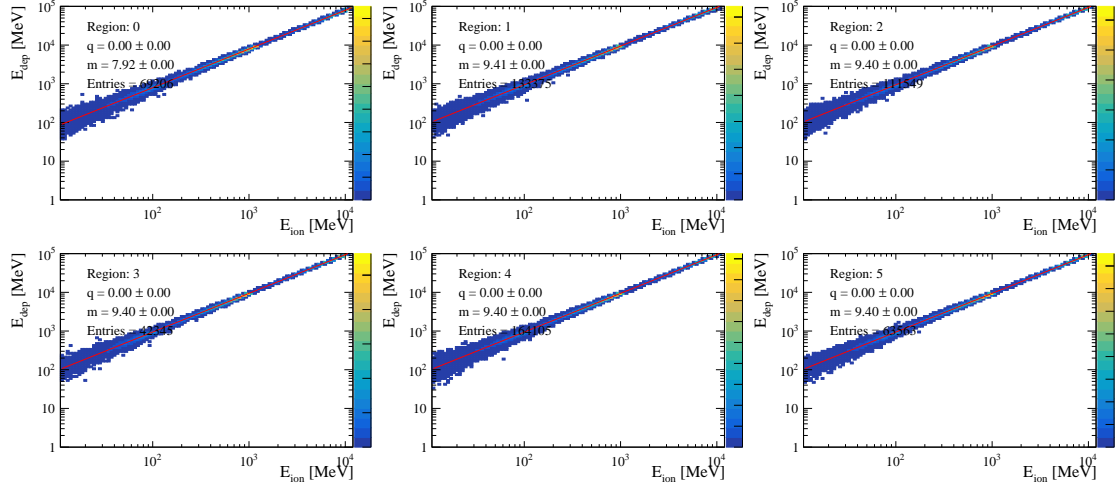


Figure 5.13: Sampled energy deposit (E_{ion}) versus total energy deposit (E_{dep}) for the various regions of the LHCb ECAL in its baseline Upgrade II configuration. Different calibrations are performed for the different regions and simulated technologies summarised in Table 5.1. . The red straight line, used for the fit, is parametrised as $E_{\text{dep}} = q + mE_{\text{ion}}$.

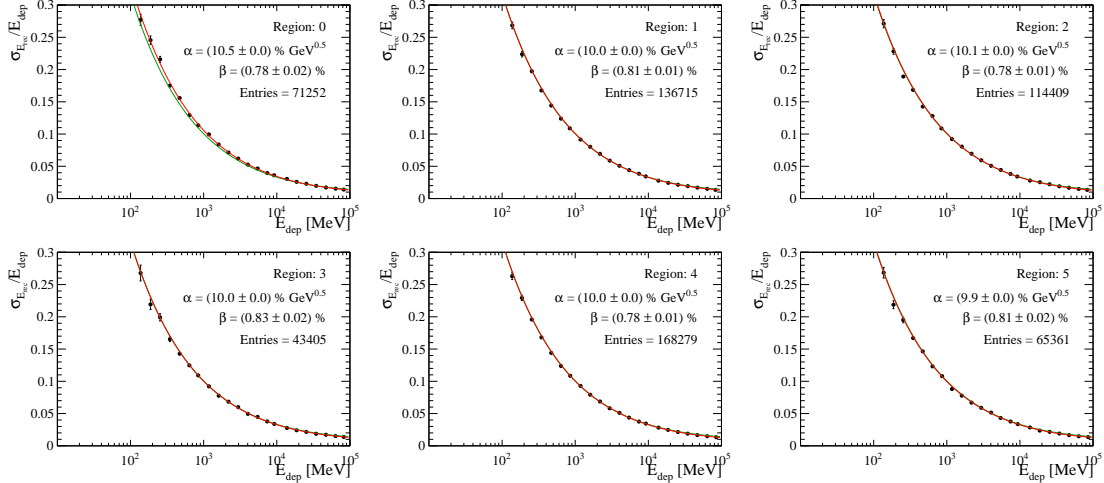


Figure 5.14: Relative energy resolution as a function of deposited energy obtained applying the calibrations of Figure 5.13 to sampled energy deposits. The red curve is the result of the fit to points with the function $\sigma_{E_{\text{dep}}}/E_{\text{dep}} = \sqrt{\alpha^2/E_{\text{dep}} + \beta^2}$. The green curves show the same function with the parameter fixed to target values: $\alpha = 10\% \text{ GeV}^{0.5}$ and $\beta = 1\%$.

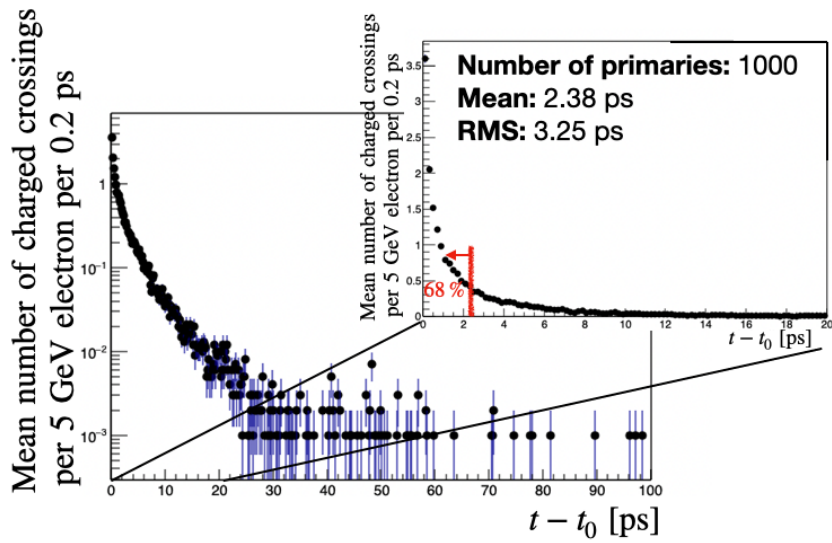


Figure 5.15: Time spread of the crossings between the front and the back section of a SpaCal W/GAGG module for the charged particles of the electromagnetic showers generated by 5 GeV simulated electrons. The variable t represent the time of the crossing of each charged particle, while t_0 is the time of the first crossing in the same shower. The distribution is obtained by counting the occurrences of $t - t_0$ falling in bins 0.2-ps wide, and then dividing by the number of primary electrons. The plot on the top-right is just a zoom of the other one. The 68% of the crossing happens within 2.38 ps, whereas the whole distribution is contained within 100 ps.

5.3 Reconstruction algorithms

This section describes the pattern-recognition algorithms used to interpret the information simulated in Section 5.2. The algorithms are implemented according to Ref. [196], which documents the current pattern recognition of the LHCb calorimeter. The following sections report the functioning of the reconstruction methods with emphasis on the differences from Ref. [196], implemented to deal with the simplified simulation used in this work.

5.3.1 Seed finding and cluster reconstruction

The energy deposited by the electromagnetic shower generated by a particle hitting the ECAL usually activates more than one ECAL cell, hence a clusterisation procedure based on a Cellular Automaton algorithm is used [197]. The clusterisation starts finding the so-called seeds, *i.e.* cells that are the centre of a cluster. Two types of seeds are used in the reconstruction:

Primary seed: cells presenting a local maximum of registered energy with respect to their neighbouring cells,⁴ with a minimal registered transverse energy of $E_T > 50$ MeV.⁵

Secondary seed: cell with the largest registered energy among the neighbouring cells of a primary seed.

Clusters are defined by a seed cell and its neighbours. While primary seeds, once they are identified, always generate a cluster, secondary seeds are used to reconstruct so-called merged π^0 and can be turned-off as it is explained in the Sections 5.3.2 and 5.3.4.2.

Since the usual situation includes squared-shaped cells, with equal dimensions, clusters are qualified as 9 cells arranged in a group “ 3×3 ”. Nonetheless, different configurations are possible, *e.g.* when the cluster includes cells on the border between ECAL regions with different cell sizes. A reconstructed particle is then associated to each identified cluster. A raw expectation of the reconstructed particle energy is given by the sum of the energy values measured by all the cells composing the cluster:

$$E_{RAW} = \sum_j E_j. \quad (5.6)$$

A raw expectation of the point where the particle hits the ECAL surface, is given by the cluster barycentre:

$$x_{RAW} = \frac{1}{E_{RAW}} \sum_j E_j x_j; \quad y_{RAW} = \frac{1}{E_{RAW}} \sum_j E_j y_j; \quad (5.7)$$

where (x_j, y_j) are the coordinates of the centre of the j -th cell included in the cluster. Then, these “raw” quantities must be calibrated to reproduce as good as possible the quantities of the particles that actually generated the cluster. The following sections describe these corrections. The same samples of particle-gun photons, already introduced in Section 5.2.3, are exploited as calibration samples.

⁴The neighbours of a given cell is the set of cells that touch the first one, at least in one point.

⁵The transverse energy of a cell is defined as $E_T = E \sin \theta$, where θ is the angle between the z axis and the straight line between the point $(0, 0, 0)$ and the centre of the cell.

5.3.1.1 Energy-leak correction

Considering the Molière radii and cell sizes of the various ECAL technologies, electromagnetic showers are not fully confined in the cluster they activate. This causes a negative bias in the difference between the actual energy of the particle originating the shower (E_{TRUE}) and E_{RAW} . For each photon of the calibration sample the E_{RAW} of the corresponding cluster is computed. Then E_{RAW} is compared with the total true energy of the photon and the distribution of the quantity $(E_{RAW} - E_{TRUE})/E_{TRUE}$ for the total calibration sample is studied. In the reconstruction procedure the mean (μ_E) of the distribution of $(E_{RAW} - E_{TRUE})/E_{TRUE}$ for the calibration sample is used to correct the raw energy of the clusters using the formula

$$E_{\text{calib}} = \frac{E_{RAW}}{1 + \mu_E}. \quad (5.8)$$

Different μ_E corrections are determined for the different technologies and regions used in the ECAL. Figures 5.16 and 5.17 shows the distributions of $(E_{RAW} - E_{TRUE})/E_{TRUE}$ used to determine μ_E in the different regions of the ECAL for the Run 2 and the Upgrade II configurations, respectively.

5.3.1.2 Corrections to cluster position

The momentum direction of photons is reconstructed assuming they come from the origin $(0, 0, 0)$ and point to the three-dimensional barycentre of the electromagnetic shower (x_c, y_c, z_c) . Two effects must be taken into account in order to properly determine the coordinates of the shower barycentre: the dependency from the photon energy of the longitudinal penetration of the electromagnetic shower, and the finite size of the cells and their Molière radii. The first effect is corrected (“L”-correction) by calibrating the parameter α_L in the equation:

$$z_c = z_{ECAL} + \alpha_L \ln(E_{\text{calib}}), \quad (5.9)$$

where z_{ECAL} is the z position of the ECAL surface. Since the ECAL material and the incidence angle of the particles changes with the radial distance from the beampipe, the parameter α_L must be calibrated separately for the different regions of the ECAL. In Figure 5.18 and 5.19, the dependency from the photon energy of $z_c - z_{ECAL}$ is shown for the different regions of ECAL in its Run 2 and Upgrade II configurations.

As an example, the effect due to the discrete size of the cells and their Molière radii is illustrated in Figure 5.20 for the Outer region of the Run 2 ECAL. In the plot, using the photons from the calibration sample, the coordinates of the cluster barycentres (x_{RAW} and y_{RAW}) are compared with the true coordinates of the shower barycentre (x_c and y_c), all with respect to the centres of the seed cells (x_{seed} and y_{seed}). An S-shaped dependency between the two sets of coordinates is well visible. In Ref. [196] an analytic formula is used to describe this dependency, while in this work, the calibration sample is used to build profile histograms that are subsequently employed to determine the correction to be applied to the raw coordinates of the cluster barycentres. It is important to note that also for the “S”-correction there is a dependency on the incidence angle of photons, requiring to perform separate calibrations for the different regions of the ECAL. Moreover, the correction must be done separately for the left and right side of the ECAL (as it is well visible from Figure 5.20) and for the top and bottom section. Figure 5.20 shows the effect

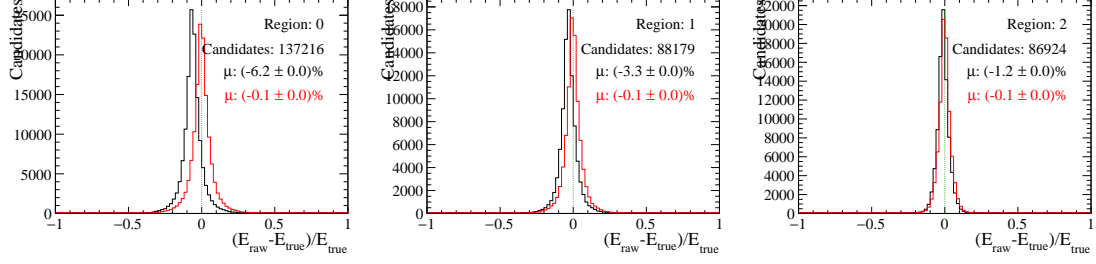


Figure 5.16: Distributions of $(E_{RAW} - E_{TRUE})/E_{TRUE}$ (black) and $(E_{calib} - E_{TRUE})/E_{TRUE}$ (red) for the sample of calibration photons described in the text. Photons are separated by the region where they hit the ECAL surface in Run 2 configuration: (left) Inner, (centre) Middle and (right) Outer. The means of the histograms are also reported with corresponding colors.

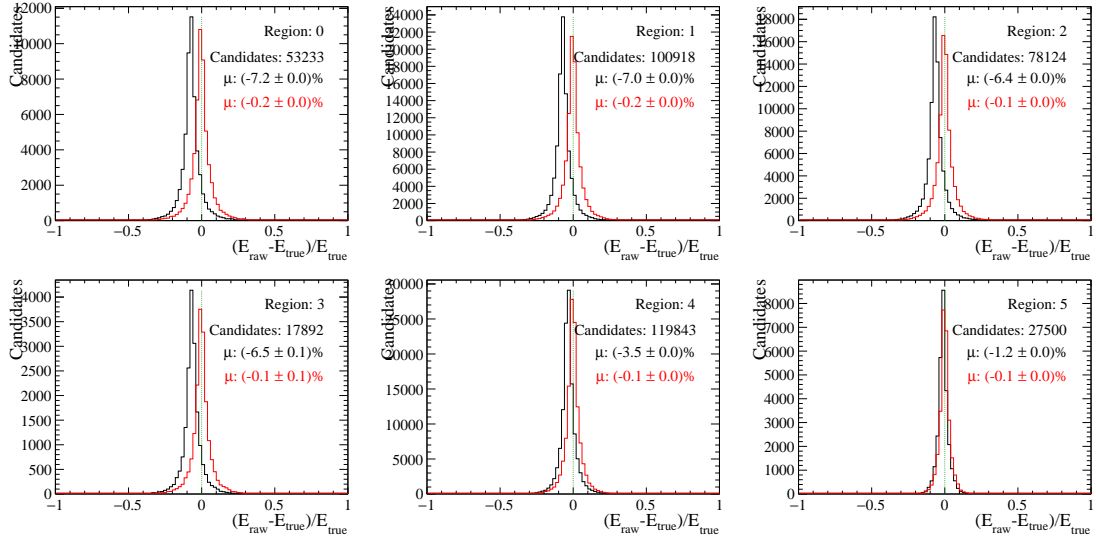


Figure 5.17: Distributions of $(E_{RAW} - E_{TRUE})/E_{TRUE}$ (black) and $(E_{calib} - E_{TRUE})/E_{TRUE}$ (red) for the sample of calibration photons described in the text. Photons are separated by the region where they hit the ECAL surface in the Upgrade II configuration. The means of the histograms are also reported with corresponding colors.

of the ‘‘S’’-calibration on different regions of the ECAL in the Run 2 conditions. It is important to note that from the reconstructed position of the shower barycentre it is possible to determine the coordinates where the particle generating the cluster hit the ECAL surface, that are:

$$(x_{ECAL}, y_{ECAL}) = (x_c, y_c) \times \frac{z_{ECAL}}{z_c}. \quad (5.10)$$

5.3.2 Energy redistribution and event reconstruction

The reconstruction algorithms, presented until now, considered each clusters as if it is the only one in an event. However, with the large number of particles produced in p - p collision events, in particular at higher instantaneous luminosities, it may happen that some cells belong to more than one cluster. Given the definitions of seeds and clusters in Section 5.3.1,

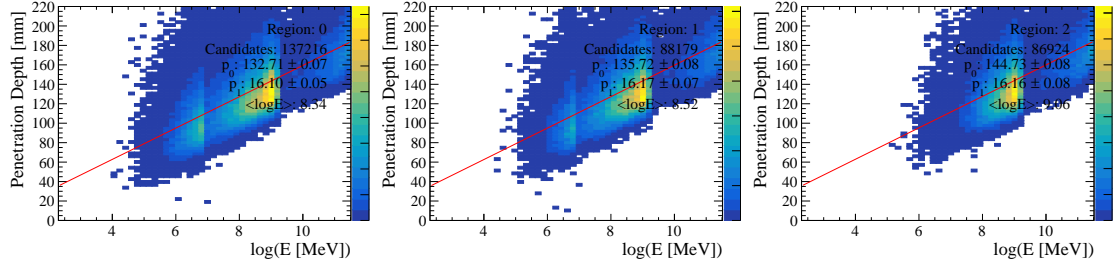


Figure 5.18: Dependency of $z_c - z_{ECAL}$ as a function of the logarithm of E_{calib} , determined from the calibration sample of photons described in the text. The fit with a straight line is overlaid on the points and the determined parameter α_L is reported. The calibration is performed for the three regions of the Run 2 ECAL configuration: (left) Inner, (centre) Middle and (right) Outer.

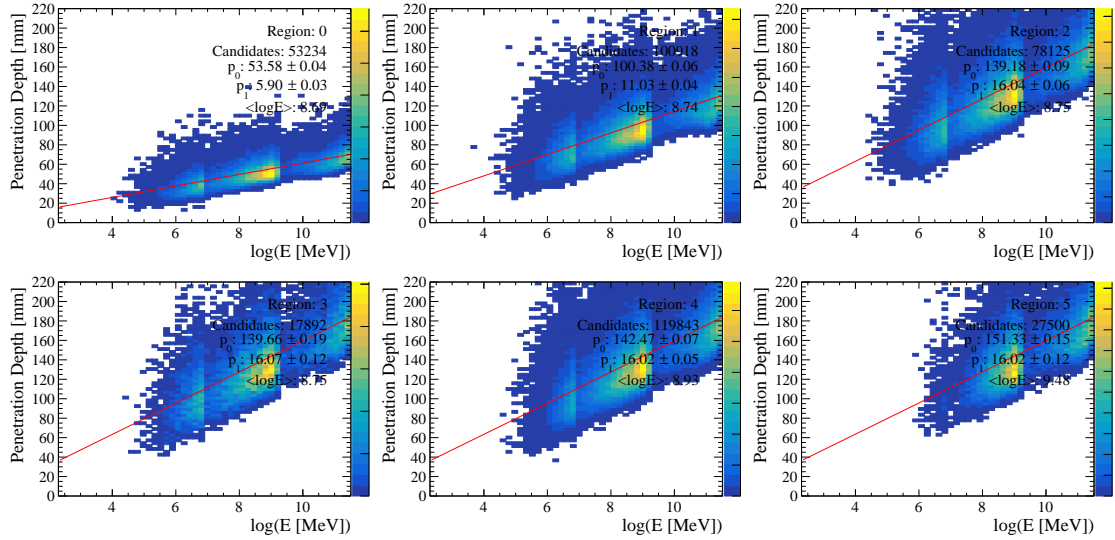


Figure 5.19: Dependency of $z_c - z_{ECAL}$ as a function of the logarithm of E_{calib} , determined from the calibration sample of photons described in the text. The fit with a straight line is overlaid on the points and the determined parameter α_L is reported. The calibration is performed for the three regions of the Upgrade II ECAL configuration: (top left) Innermost, (top centre) Inner, (top right) Middle, (bottom left) Outer and (bottom right) Outermost.

this happens when either a secondary seed is activated or some of the neighbours of a primary seed are also neighbours of another primary seed, as depicted in Figure 5.22. The energy of these cells must be distributed among the corresponding clusters to avoid biases in the reconstruction of energy and position of the clusters themselves. First of all the calibration sample of photons used in the previous section is used to determine the fraction of shower energy that a cell contains as a function of the radial distance of its centre from the shower barycentre. The corresponding profile is shown in Figure 5.23 for different regions of the ECAL and where the radial distance is normalised to the cell sizes. Then an iterative procedure starts assuming that two clusters with shared cells have their barycentres in the centre of the corresponding seeds. With this assumption, a fraction of the energy of the shared cells is assigned to each cluster according to the radial energy profile of Figure 5.23. Then the new coordinates of the cluster barycentres are computed according to Eq. (5.7), and the corresponding “L” and “S” corrections are

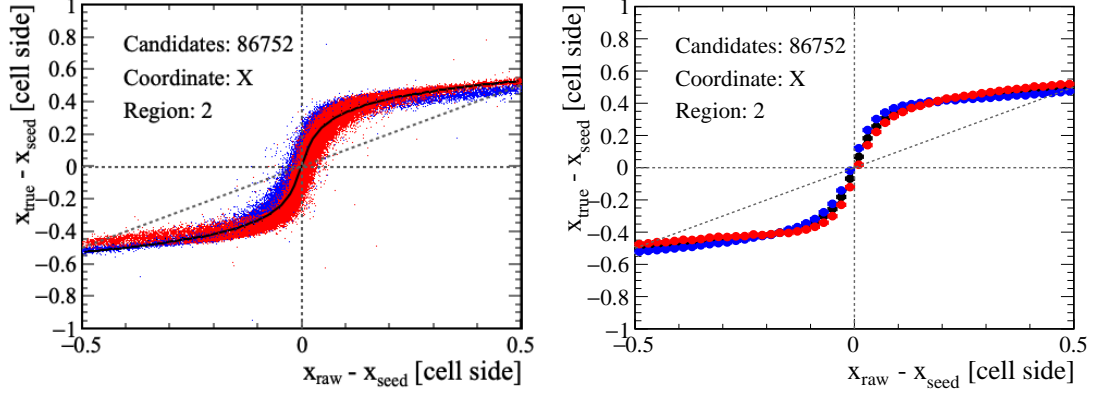


Figure 5.20: The plot on the left shows the comparison between the raw coordinates of the cluster barycentres (x_{RAW} , y_{RAW}) and the coordinates of the shower barycentres (x_c , y_c) \equiv (x_{true} , y_{true}), relatively to the coordinates of the seed cells (x_{seed} , y_{seed}), for the photons of the calibration sample described in the text hitting the ECAL in the Outer region of its Run 2 configuration. The blue point refers to cases with $x < 0$ while the red point stand for cases with $x > 0$. The black curve is the result of the fit to the all point with the function employed in Ref. [196]. The plot on the right report the profiles of the distribution just cited. Such profiles are used to perform the “S”-calibration within this simulation.

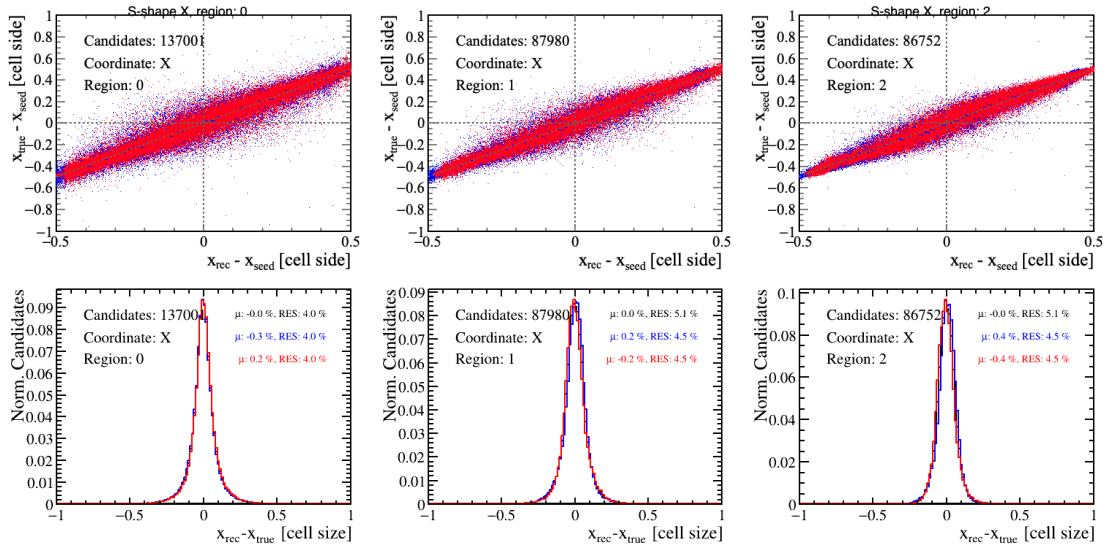


Figure 5.21: S-calibrations results for the x variable, for inner region (left), middle (center), outer (right), regions of the ECAL Run 2 configuration. The plots on the top are analogous to the one in Figure 5.20-left, but here the S-calibration is applied ($x_{raw} \rightarrow x_{rec}$). The plots on the bottom show the distributions of difference between the reconstructed (x_{rec}) and the true positions (x_{true}) of the showers. The values of the mean (μ) and root mean squared (RES) of the distributions are also reported. The blue (red) color refers to clusters with $x < 0$ ($x > 0$), the black color considers all the clusters.

applied. The procedure is repeated using each time the new coordinates of the cluster barycentres to distribute the energy of the shared cells among clusters. The iterative procedure ends when the coordinates of the cluster barycentres converge, that is found to happen within 5 iterations. Once the convergence of the barycentre positions is reached,

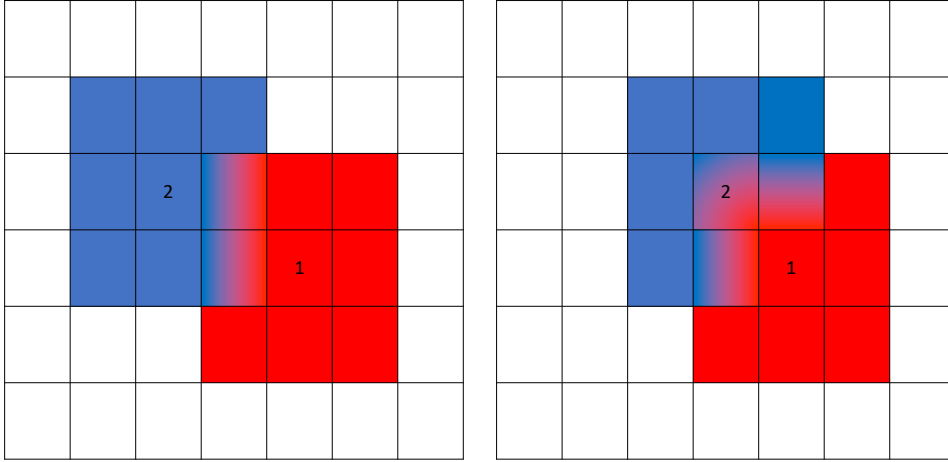


Figure 5.22: Examples of situations where clusters overlap in certain cells. On the left: two clusters with primary seeds (1 and 2) share two cells. On the right: two clusters on with primary seed (1) and the other with secondary seed (2) share three four cells (including their seeds).

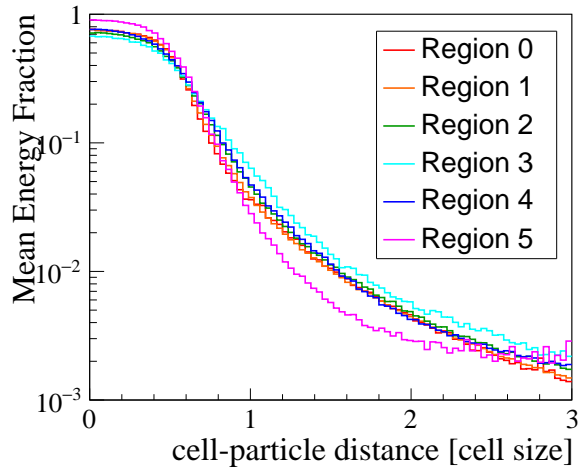


Figure 5.23: Fraction of energy deposited in a cell as a function of the radial distance between the cell centre and the shower barycentre for the various regions of the Upgrade II ECAL.

the raw energies of the clusters are corrected for the energy leak according to Eq. (5.8). At this stage the secondary seeds in the event are re-evaluated and turned off if they do not pass the requirements defined for them to be compatible with merged π^0 as defined in Sec. 5.3.4.2. Finally, the iterative energy distribution is performed one last time.

5.3.2.1 MonteCarlo association of clusters

In order to determine the performance of the reconstruction algorithms it is fundamental to associate the simulated particles hitting the ECAL with the corresponding cluster, the so-called MonteCarlo association. The best criterium found to perform this task is to associate to a cluster the particle that hits the ECAL closest to its reconstructed position. The full MonteCarlo story of the associated particles is also kept in order to

perform an *a-posteriori* association of the clusters with relevant particles. These are the cases, for example, of photons coming from $\pi^0 \rightarrow \gamma\gamma$ decays, or photons generating an e^+e^- pair when interacting with the detector material. In the latter case, when the pair generation happens after the magnetic field the e^- and e^+ are produced very collinear with the photon direction and usually hit the ECAL in the same cell generating a cluster very similar to the one that would have been generated by the original photon, and is treated accordingly. Another relevant case where the full MonteCarlo history of a particle is fundamental to evaluate the performance of the reconstruction algorithm is the case of bremsstrahlung photons that must be associated with the e^\pm that generated them. Their treatment is discussed in Sec. 5.3.5.

5.3.3 Identification of neutral and charged clusters

A fundamental ingredient of the pattern recognition of the ECAL is the identification of so-called neutral and charged clusters. A cluster is defined as charged when it is found to be compatible to be generated by the energy released in the ECAL by a charged particle, while clusters incompatible with charged particles are defined as neutral. In the current LHCb reconstruction, charged particles are reconstructed thanks to the tracking detectors. In this study the tracking algorithms of LHCb are not used for two reasons. The first reason is that no tracking algorithm is available yet for the tracking detectors expected to be installed in the LHCb Upgrade II. Second reason is that, as explained in Section 5, the aim of the LHCb Upgrade II detector is to obtain performance per fb^{-1} of integrated luminosity similar to those as in Run 2. Hence, in this work we assume that the effects of tracking performance factorise and simplify in the relative comparison between Run 2 and Upgrade II ECAL performance. For this reason perfect tracking is assumed, *i.e.* that charged particles are reconstructed with no error in the determination of their trajectory and momentum. The only requirement that is applied is that charged particles generated in the p - p collisions are considered reconstructed only if they generate hits in the Upstream Tracker (UT) and in the Scintillator Fibre Tracker (Sci-Fi) [91]. The condition is assumed to be realised if the particle trajectory, as determined from the MonteCarlo truth, is found in the acceptance of the two detectors. The requirements on the x and y coordinates of the trajectory at the entrance and exit of the UT ($z = 2330, 2660$ mm) and the Sci-Fi ($z = 7800, 9600$ mm) are summarised in Table 5.4. Only electrons, muons, pions, kaons and protons are considered as charged particles that can be tracked. The momentum assigned to each tracked particle is their true momentum, with the only exception of electrons and positrons. In this case the momentum assigned to the particle is the one it has before entering the magnetic field, *i.e.* at the exit of the UT detector. The reason for this choice is due to the energy loss of e^\pm caused by bremsstrahlung effects and is further analysed in Section 5.3.5.

According to Ref. [196] the match between a track and a cluster is performed on the basis of a two-dimensional χ^2 between the cluster barycentre, projected on the ECAL surface, and the point the track hits the ECAL, according to its trajectory extrapolation. If the minimum χ^2 of a cluster with respect to all the tracks is above a certain threshold then the cluster is considered neutral, and the photon hypothesis is assigned to the cluster. Otherwise, the cluster is considered charged and associated to the track with the minimum χ^2 . In this work the match between clusters and tracks is performed on the basis of the minimum distance of the cluster with respect to all the hits of charged

Table 5.4: Conditions on x and y coordinates of charged-particle trajectory at the entrance and exit of UT and Sci-Fi, in order to consider the particle to be reconstructed. The z coordinates of the entry and exit point for UT and Sci-Fi are also reported.

Detector	z [mm]	Beam-plug [mm]	Tracker Plane [mm]
UT entry	2330	$ x > 20$ or $ y > 20$	$ x < 800$ and $ y < 800$
UT exit	2660	$ x > 20$ or $ y > 20$	$ x < 900$ and $ y < 800$
Sci-Fi entry	7800	$ x > 100$ or $ y > 100$	$ x < 2800$ and $ y < 2200$
Sci-Fi exit	9600	$ x > 100$ or $ y > 100$	$ x < 3000$ and $ y < 2000$

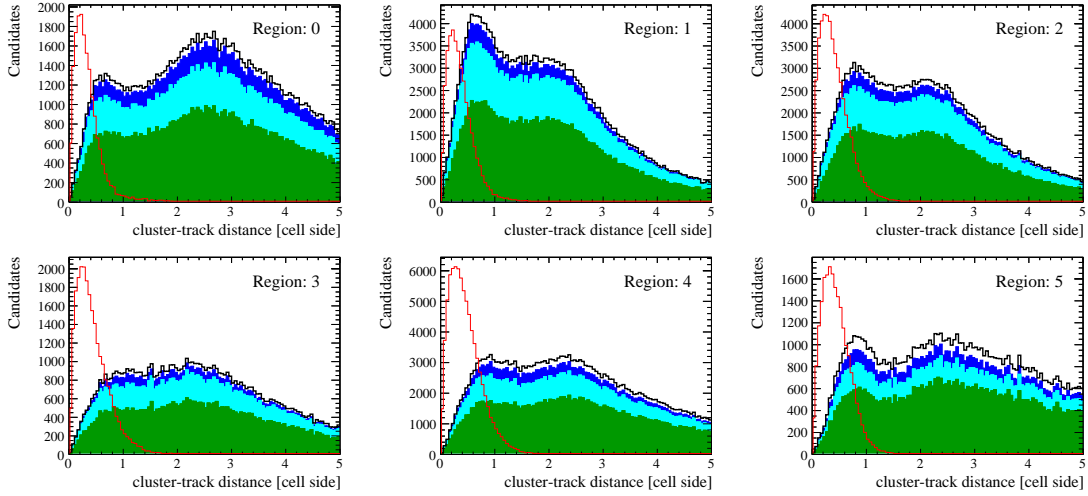


Figure 5.24: Distribution of the distance from the cluster positions and the closest extrapolation of a charged track on the ECAL surface in Upgrade II conditions. The red histograms involve cases where the clusters are associated with the track according to the criterion defined in Section 5.3.2.1 (truly charged clusters). The black histogram considers all the other cases. The contributions from photons, and not-“trackable” electron, pion or other kind of particles are also evidenced with green, azure, blue, and white stacked histograms, respectively. The minimal energy of the clusters included is $E_T > 200 \text{ MeV}/c$.

tracks on the ECAL (d_T). The threshold to be applied on d_T to assign the neutral and charged hypothesis to a cluster is studied using a large sample of p - p collision events with Upgrade II instantaneous luminosity. Reconstructed clusters are associated with simulated particles according to the criterion defined in Section 5.3.2.1 and the distributions of d_T is studied for clusters truly associated with charged tracked particle and clusters truly associated with other particles. The latter are mainly photons, but also electrons or pions out of the tracking-system acceptance (*e.g.* those originated because of interactions with the detector material) are presents. The distributions of d_T for the three cases are shown in Figure 5.24. The threshold used to distinguish between neutral and charged particles is defined to correspond to the end of the d_T distribution for clusters truly associated with any charged tracked particle. Performances in discriminating between truly neutral and truly charged clusters are reported in Table 5.5.

Table 5.5: Performances in separating between neutral and charged cluster in Upgrade II conditions using the requirement on d_T described in the text in Upgrade II conditions. Categories in the rows correspond to the MonteCarlo association assigned according to the criteria defined in Sec. 5.3.2.1, while categories in the columns correspond to the hypothesis associated according to the value of $d_T > 1$ cell size. The minimal energy of the clusters included is $E_T > 200$ MeV/ c .

Fraction	Charged hypothesis	Neutral hypothesis
True charged	17%	1%
True neutral	15%	67%

5.3.4 Reconstruction of π^0

Depending on their momentum, neutral pions can be reconstructed either as “resolved” π^0 or as “merged” π^0 . Low momentum π^0 ’s are mostly reconstructed as pairs of well separated, or “resolved”, photons, *i.e.* as a pair of clusters both defined around a primary seed. For high-momentum π^0 , the relativistic boost of the two photons of the $\pi^0 \rightarrow \gamma\gamma$ decay is such that the angle between the photon trajectory is small. Hence, a large fraction of the photon pairs generate two clusters that largely overlap one with each other, hence the name “merged”.

5.3.4.1 Resolved π^0

The first step to reconstruct resolved π^0 ’s is to select all clusters with assigned neutral hypothesis according to the requirement described in Sec. 5.3.3, and consider them as reconstructed photons. Then all the combinations of photon pairs in the event is analysed and their invariant mass is computed. The only additional requirement applied on the clusters, in order to reduce the combinatorial background, is for them to have a transverse momentum (p_T) larger than 200 MeV/ c . Figure 5.25 shows the invariant mass distribution of reconstructed π^0 ’s in p - p collision events with luminosity conditions and ECAL configurations corresponding to Run 2 and Upgrade II. The invariant mass distribution of the candidates associated with true π^0 ’s is emphasised, evidencing the very large contribution of combinatorial background due to pairs of random photons already in Run 2 conditions. An even much larger amount of combinatorial background is present in Upgrade II conditions. It is due to the higher instantaneous luminosity and the finer ECAL granularity. Both the plots involve all the resolved- π^0 ’s candidates identified by the Run 2 version of the LHCb reconstruction algorithm. Further selection requirements may improve the situation, but the drastic increase of the combinatorial background already suggests that dedicated a R&D task is necessary to continue profiting from the resolved π^0 ’s also in Upgrade II. This will be the main subject of Sect. 5.4.1. It reports a simulation study, where the time information of the ECAL cells is used to improve the reconstruction of $B^0 \rightarrow \pi^+\pi^-\pi^0$ decays.

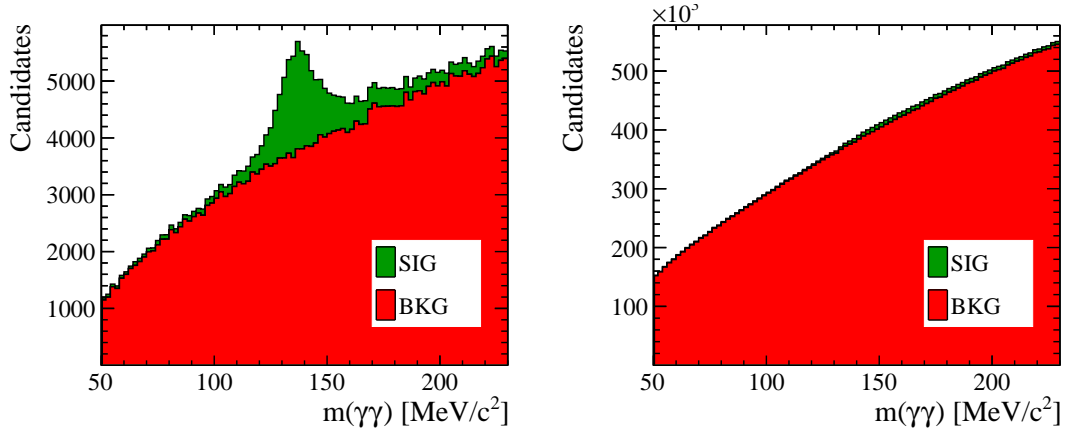


Figure 5.25: Invariant mass distribution of resolved π^0 reconstructed in Run 2 and Upgrade II conditions. The contribution of true π^0 is also shown.

5.3.4.2 Merged π^0

The so-called “merged” π^0 are reconstructed starting from two neutral clusters with adjacent seed cells, one being a primary seed and the other being a secondary seed. As already described in Section 5.3.2 the two clusters are considered as separate entities with the energy of the shared cells distributed among the two. In order to clean the sample from false merged π^0 's, the following additional requirements are applied to the candidates:

- The two clusters are required to have a minimum distance between the points they hit the ECAL surface. According to relativistic kinematic the minimal distance between the two hits of the photons on the ECAL surface is $d_{\gamma\gamma} \approx 2z_{ECAL}m_{\pi^0}/E_{\pi^0}$ and the requirement is applied on this quantity.
- The invariant mass of the merged π^0 is required to be within a certain range.

In Figure 5.26 the distributions of $d_{\gamma\gamma}$ and invariant mass of merged π^0 reconstructed in Run 2 conditions are shown, separately for true and false merged π^0 's, according to the MonteCarlo association defined in Sec. 5.3.2.1.

5.3.5 Recovery of bremsstrahlung photons

A fundamental rôle of the ECAL is to reconstruct bremsstrahlung photons produced by electrons and positrons when interacting with the detector material. Bremsstrahlung photons may be emitted also as synchrotron radiation when e^\pm are bent by the magnetic field of LHCb, but this component is negligible. Figure 5.27 shows the origin points in the $x - z$ plane of bremsstrahlung photons and also the projection along the z axis of the same figure. It is clear that the vast majority of bremsstrahlung photons comes from the interaction of e^\pm with detector material. Particularly dangerous are the bremsstrahlung photons produced before the e^\pm enter the magnetic field. In fact, the momentum measured by the tracking system of LHCb is the one that charged particles have when they enter the magnetic field. Without recovering the energy loss due to bremsstrahlung photons emitted before the magnetic field, the measured momentum of e^\pm would suffer from non-optimal

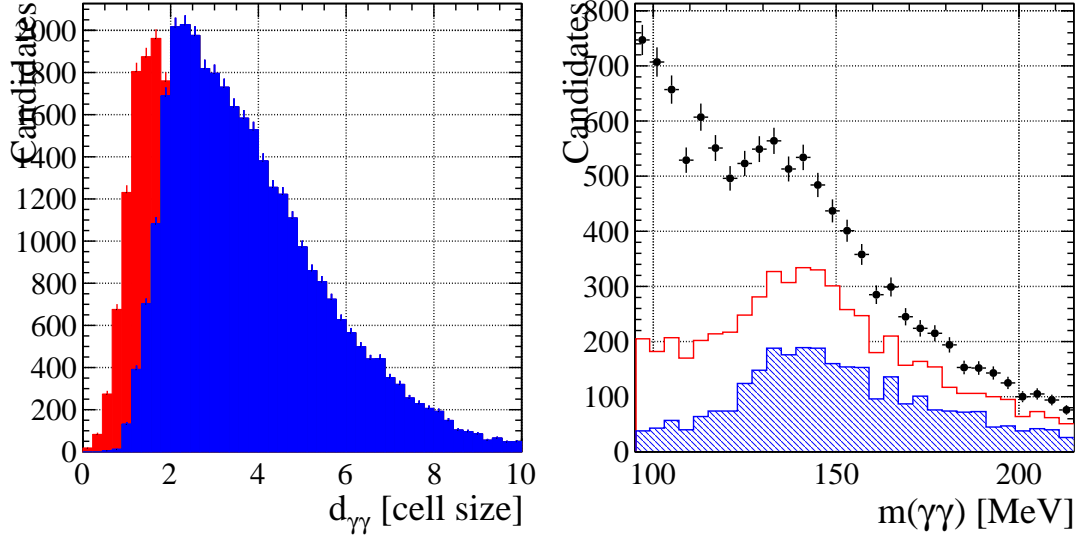


Figure 5.26: Left: distributions of $d_{\gamma\gamma}$ for π^0 reconstructed as merged (red) or resolved (blue). Right: invariant mass for merged π^0 in the $B^0 \rightarrow \pi^+\pi^-\pi^0$ sample. Candidates associated with true π^0 are indicated by the red histogram. The blue histogram shows the contribution from true signal candidates.

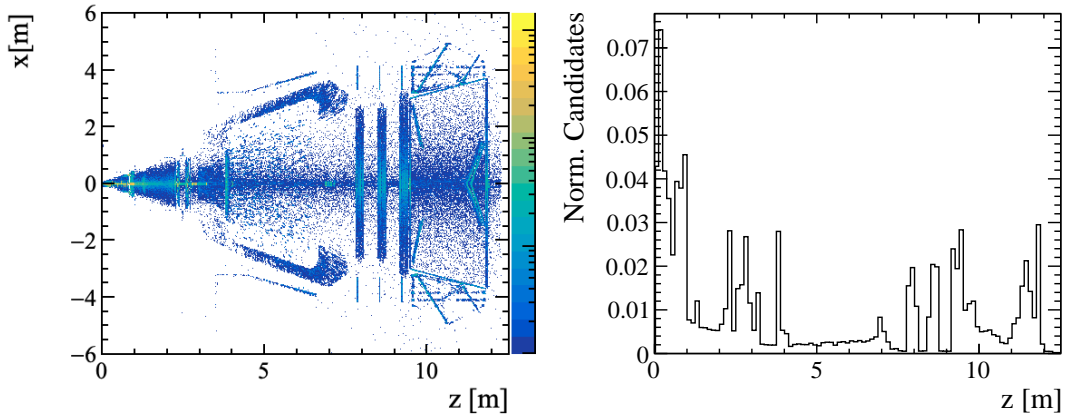


Figure 5.27: On the left: origin point in the $x - z$ plane of bremsstrahlung photons. On the right: projection along the z axis of the plot on the left.

resolution. As a consequence the invariant mass reconstructed for decays containing e^\pm in the final state, like $B^0 \rightarrow K^{*0}e^+e^-$, is distorted, leading to a poor separation of signal and background. A description of the algorithm used to search for bremsstrahlung photons and associate them to their original e^\pm can be found in Ref. [198] and is summarised in the following. Photons are matched with a corresponding electron or positron if their cluster on the ECAL are found within the region illustrated in Figure 5.28. The electron (or positron) track (in this work the true electron that pass the acceptance requirement defined in Sec 5.3.3) is linearly extrapolated to the ECAL surface from two points: its origin vertex and the point where it exits from the UT detector ($z = 2660$ mm). All the photon clusters with barycentre around the line connecting the two extrapolated points are matched to the electron under consideration and their quadri-momentum is added to

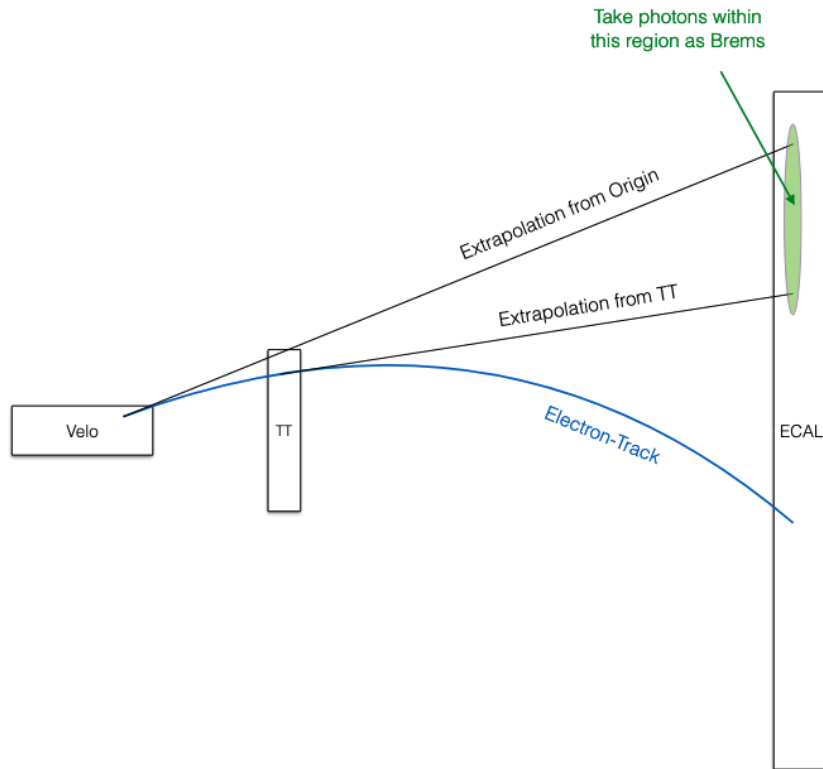


Figure 5.28: Schematic illustration from Ref. [198] showing the method used to identify the region within searching for bremsstrahlung photons.

the one of the matched electron. In Ref. [198] the width of the search area corresponds to the 2σ interval of the combined error of the track extrapolation and the reconstructed position of a given photon on the ECAL. In this work, since we do not have access to the errors of the track extrapolation, the search area corresponds to the union of two boxes of the same size of the cells in that region and centred around the two extrapolated points, as sketched in Figure 5.29. Figure 5.30 shows the energy resolution for electron and positrons before and after recovering the energy loss due to bremsstrahlung applying the search algorithm just described to events simulated in Run 2 conditions.

5.3.6 Correction to time measurements of the cells

No time information is used in the reconstruction algorithms described there in Refs. [196, 198]. However, this is a fundamental infofeature available in the LHCb Upgrade II ECAL. The way the time information is obtained from the timing layer is described in Sec. 5.2.3, *i.e.* by averaging the time of incidence on the timing layer of all the charged particles traversing the ECAL, and then applying a Gaussian smearing. The correspondence between the time registered by the timing layer, t , and the time the original particles hit the ECAL surface, t_0 , must be calibrated. Calibrations are studied by means of samples of single-photon events with energy of 0.5, 1, 2, 5, 10, 15, and 20 GeV and impinging point on the ECAL uniformly distributed over the entire surface. The main correction to be applied is due to the incidence angle of primary particles on the ECAL, as shown by the scheme reported in Figure 5.31. Depending on the incidence angle, the distance travelled by the electromagnetic shower before reaching the timing layer changes. In

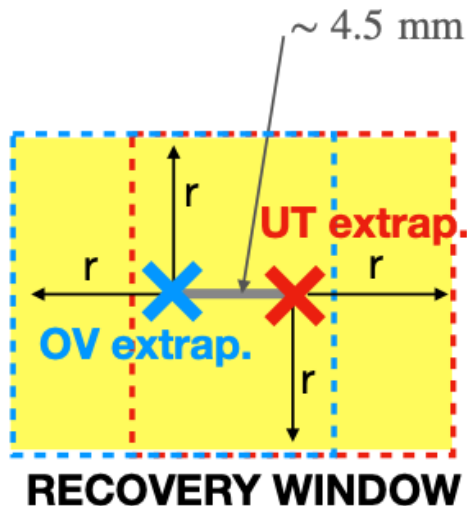


Figure 5.29: Schematic illustration of the search window for bremsstrahlung photons around the two extrapolation points defined in the text: one (OV) determined extrapolating the particle trajectory from its origin point and the other (UTV) determined extrapolating the particle trajectory from the point it exits the UT detector.

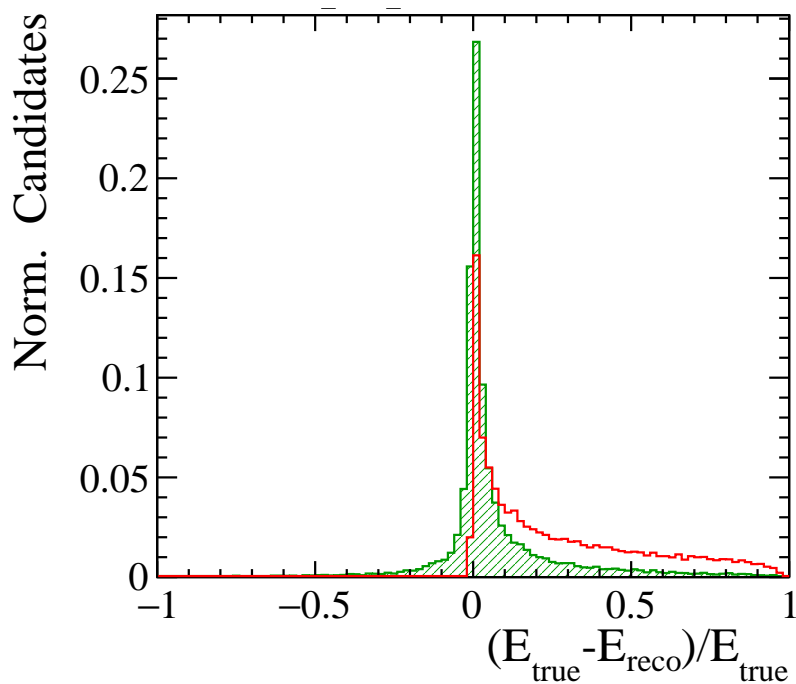


Figure 5.30: Energy resolution for electrons and positrons before (red) and after (green) recovering the energy loss due to bremsstrahlung in Run 2 conditions. Bremsstrahlung photons are associated to the corresponding charged particle using the algorithm described in the text.

addition, considering the radial spread of the shower, also the spread of the arrival time of particles on the timing layer increase with increased incidence angles. The global effect of it is visualised in Figure 5.32, where the distribution of $t - t_0$ is shown for different regions of the Upgrade II ECAL. The time the original particles hit the ECAL surface, t_0 , is subtracted in order to correct for the different paths they travelled before arriving at

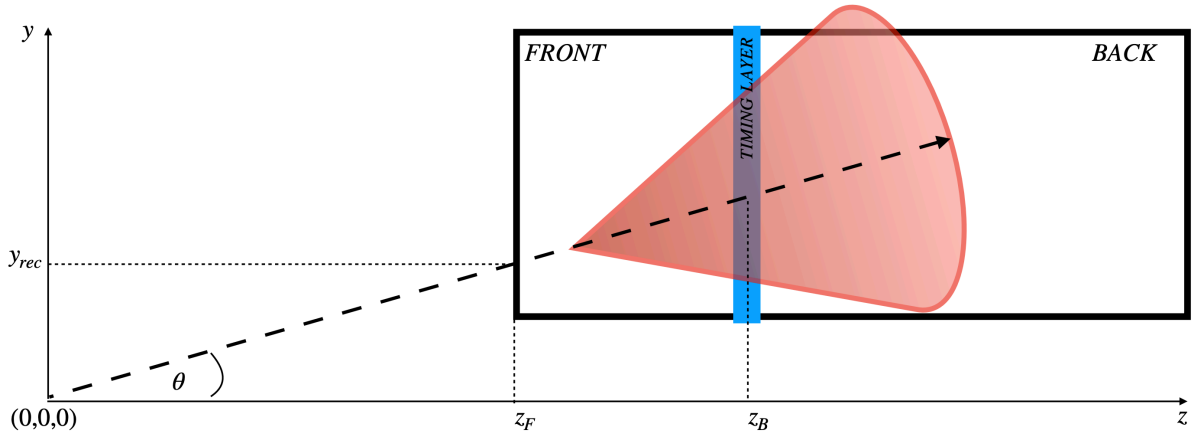


Figure 5.31: Schematic view of how time information propagates from the ECAL surface to the timing layer.

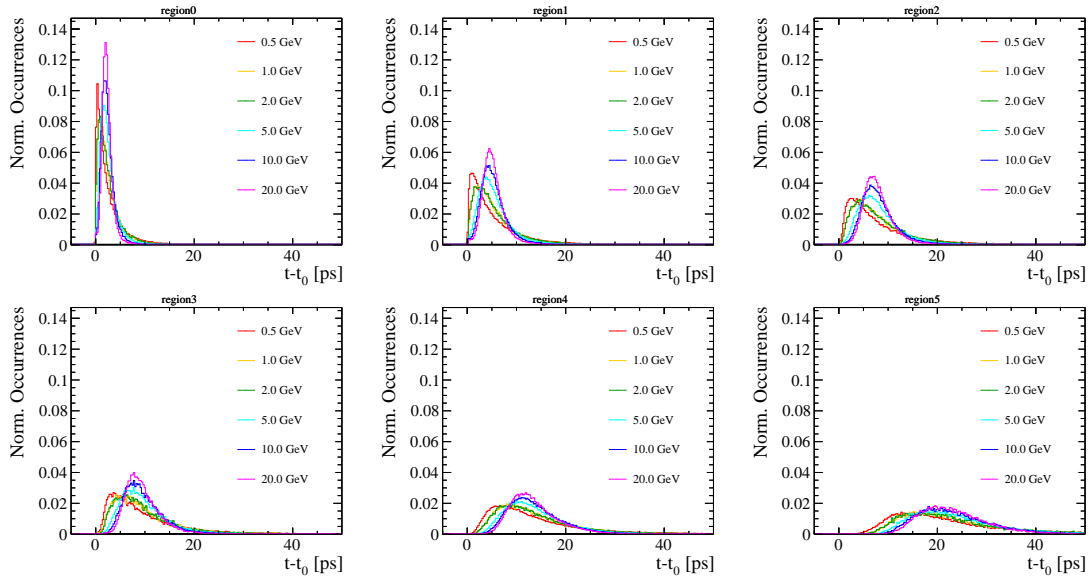


Figure 5.32: Average time on the timing layer (\hat{t}) of charged particles in electromagnetic showers with respect to the time the primary particle hit the ECAL surface (t_0). Distributions are shown for primary particles with energies of 0.5, 1, 2, 5, 10, and 20 GeV.

the ECAL. Even after this subtraction it is well visible that the distributions of $t - t_0$ for the outer regions are more biased toward higher times with respect to the distributions for inner regions. In addition, the spread of the distributions increase moving from inner regions to outer regions, that means from small incidence angles to large incidence angles. Geometrical considerations are used to correct for the incidence angle using the equation

$$t_0 = t - \frac{z_B - z_F}{c \cos \theta}, \quad (5.11)$$

where z_F and z_B are the z positions of the ECAL surface and the timing layer, respectively, c is the speed of light, and θ is the incidence angle that is computed assuming the primary particles to come from the origin $(0, 0, 0)$. The effect of this correction is shown in the Figures 5.33 and 5.34, for the innermost and outermost region of the Upgrade II ECAL

configuration, respectively.

Despite the improvement, the distributions of $t - t_0$ still show a bias, in particular at higher energies. Several effects are responsible for this bias, the most important being the increase of shower multiplicity with the energy of the primary particle. The higher the multiplicity, the higher the amount in the shower of slower particles and particles that travelled longer because of multiple scattering. A correction based on general considerations and taking into account all of this is hard to formalise. However, it is found empirically that the relation between the mode of $t - t_0$ and the energy of the primary particle can be described by the logarithmic function

$$t_{\max} = p_0 + p_1 \log E, \quad (5.12)$$

where t_{\max} is the mode of the mean time, p_0 and p_1 are parameters to be calibrated, and E is the energy of the primary particle. Figure 5.35 shows the relation between t_{\max} and E for different regions of the Upgrade II ECAL configuration.

The final thing to consider is how to assign a time to the reconstructed clusters. Given the radial spread of electromagnetic showers is very limited before they reach their maximum at about 5-6 X_0 , the majority of charged particles in the shower traverse the timing layer in correspondence of the seed cell of the cluster. This consideration is supported by the simulation used in this work. Hence, it is decided to assign to a given cluster the time registered by its seed cell and corrected for the effects discussed above. Trying to use the energy-averaged time registered by all the cells of the cluster is found to give negligible improvement.

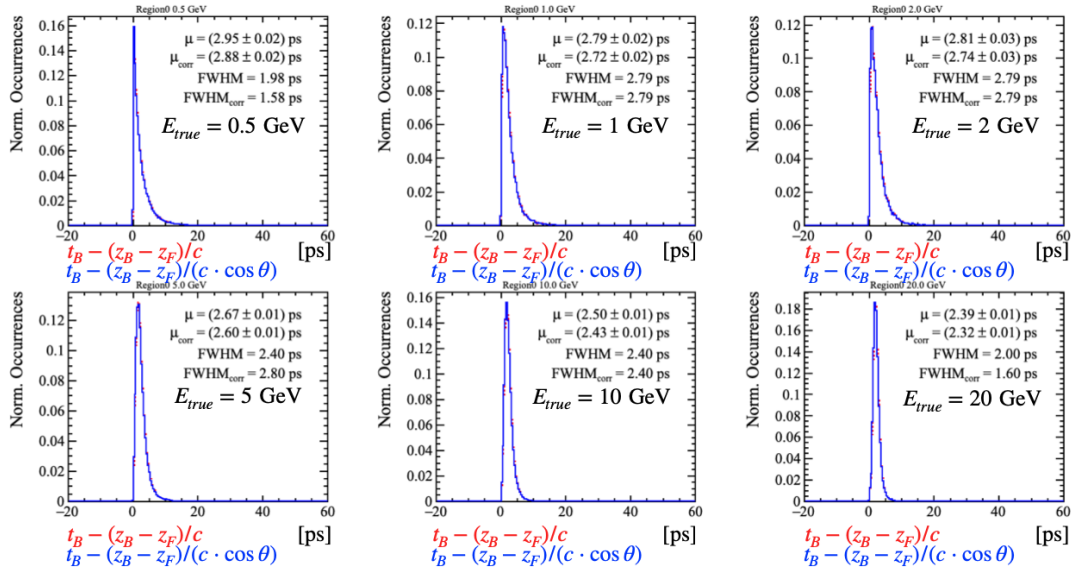


Figure 5.33: Difference between the mean time on the timing layer (\hat{t}) of charged particles in electromagnetic showers and the time the primary particle hit the ECAL surface (t_0), (blue) before and (red) after the correction for the incidence angle. Distributions are shown for the innermost region of the Upgrade II ECAL configuration and for primary photons of 0.5, 1, 2, 5, 10, and 20 GeV.

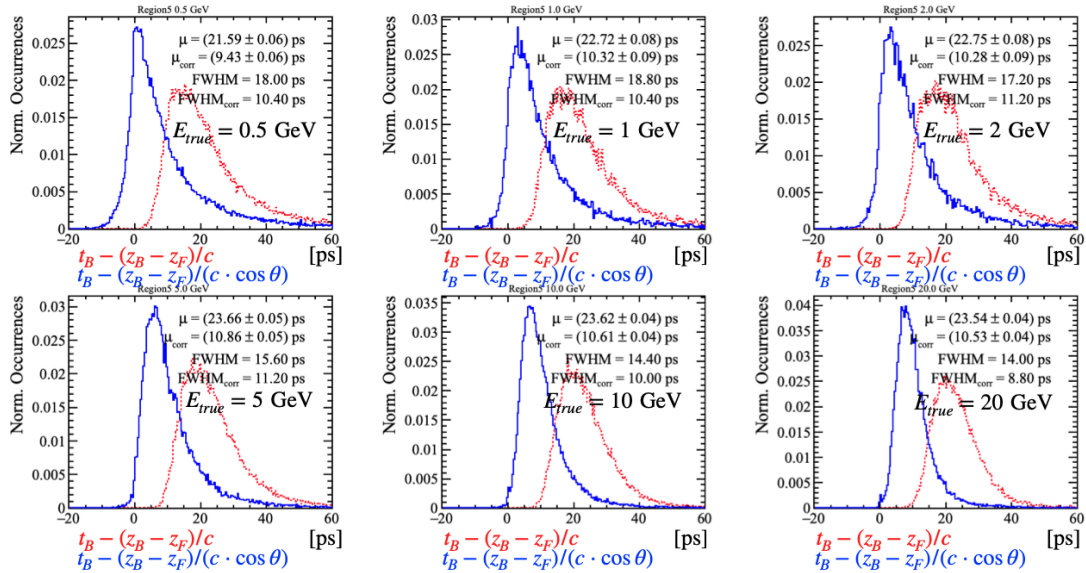


Figure 5.34: Difference between the mean time on the timing layer (\hat{t}) of charged particles in electromagnetic showers and the time the primary particle hit the ECAL surface (t_0), (blue) before and (red) after the correction for the incidence angle. Distributions are shown for the outermost region of the Upgrade II ECAL configuration and for primary photons of 0.5, 1, 2, 5, 10, and 20 GeV.

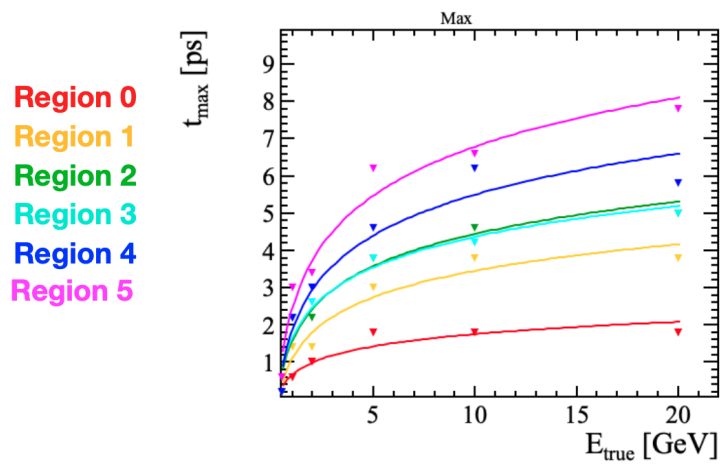


Figure 5.35: Mode of the difference between the mean time on the timing layer (\hat{t}) of charged particles in electromagnetic showers and the time the primary particle hit the ECAL surface (t_0), versus the energy of the primary particle E . Different colours are used for the different regions of the Upgrade II ECAL configuration.

5.4 Physics performance studies

In this Section, the performance achievable in Run 5 conditions are studied and compared to the ones in Run 2 conditions. Two important decays for the LHCb physics programme are considered: the $B^0 \rightarrow \pi^+\pi^-\pi^0$ and the $B^0 \rightarrow K^{*0}e^+e^-$. The former is strictly related to the π^0 reconstruction, while the latter relies on the recovery of bremsstrahlung photons and on the $e - \pi$ discrimination.

In the following, the **Run2** and **Run5** labels indicate the occupancy conditions experienced and expected at LHCb in the corresponding runs (Section 5.2.3). In **Run2** conditions the current ECAL setup is always considered. In **Run5** conditions, besides the ECAL arrangement already summarised in Table 5.1, two higher granularity options are investigated in the following, maintaining the same geometry of the ECAL regions. Table 5.6 summarises the cell sizes of the tested configurations with their respective Molière radii.

Region		Run2	
name	index	Cell side [mm]	R_M [mm]
Inner	0	40	35
Middle	1	60	35
Outer	2	120	35

Region		Run5-opt.1		Run5-opt.2		Run5-opt.3	
name	index	Cell side [mm]	R_M [mm]	Cell side [mm]	R_M [mm]	Cell side [mm]	R_M [mm]
Innermost	0	15	15	15	15	15	15
Inner	1	30	30	30	30	15	15
Middle	2	40	35	40	35	40	35
Outer	4	60	35	40	35	40	35
Outermost	5	120	35	60	35	60	35

Table 5.6: Summary of the ECAL configurations simulated in this Section. Squared cells are always assumed. The tables report the size of their side and the Molière radius (R_M) of their material. The top table resumes the ECAL configuration in Run 2 simulations, while the bottom table resumes the configurations tested for the LHCb Upgrade II.

Merged π^0	Resolved π^0
γ -track distance > 1 cell side	
$p_T(\gamma) > 200$ MeV/ c	
$p_T(\pi^0) > 2.5$ GeV/ c	$p_T(\pi^0) > 1.5$ GeV/ c
$m(\pi^0) \in [75, 195]$ GeV/ c^2	$m(\pi^0) \in [110, 170]$ GeV/ c^2
$p_T(B^0) > 3$ GeV/ c	$p_T(B^0) > 2.5$ GeV/ c
$m(B^0) \in [5.1, 5.5]$ GeV/ c^2	

Table 5.7: Selection applied to the $B^0 \rightarrow \pi^+\pi^-\pi^0$ decays in all the simulated conditions. It corresponds to the main criteria of the stripping selection assumed for the analysis of LHCb data in Ref. [199].

5.4.1 Study of $B^0 \rightarrow \pi^+\pi^-\pi^0$ decays

The analysis of the ECAL performance with $B^0 \rightarrow \pi^+\pi^-\pi^0$ decays is presented in three steps. Section 5.4.1.1 specifies the algorithms and the criteria utilised to reconstruct and select the simulated events. Section 5.4.1.2 introduces the way the time information is exploited to reject the combinatorial background due to the random association of ECAL clusters. Section 5.4.1.3 resumes and discuss the performance in the various occupancy conditions and ECAL configurations.

5.4.1.1 Reconstruction and kinematic selection

The reconstruction directly starts from the signal charged pions of each event. The combinatorial background due to random association of tracks and the uncertainty on the momentum determination are neglected. Indeed, such effects do not depend on the ECAL response. Moreover, background levels and B^0 momentum resolutions are dominated by the contributions coming from the π^0 reconstruction. The only selection requirement on the charged pions is applied in generation phase, imposing that their initial direction is inside the LHCb geometrical acceptance. Further requirements related to the acceptance of the tracking system and the decay vertex positions were tested, but they did not modify the conclusions on the ECAL performance. Hence, they were removed from the selection to exploit the entire statistic generated. In other words, the charged pion reconstruction efficiency is considered as common scale factor, which do not alter the comparisons of the ECAL performance between Run2 and Run5 .

The signal charged pions are combined with π^0 candidates built according to the algorithms presented in Section 5.3.4. Only π^0 candidates with transverse momentum higher than 900 MeV/ c and B^0 candidates with invariant mass belonging to the range $m(B^0) \in [4.98, 5.88]$ GeV/ c^2 are accepted. A minimal set of selection requirements, listed in Table 5.7, is then applied to mimic the trigger and the stripping selections adopted in Ref. [199] for the analysis of $B^0 \rightarrow \pi^+\pi^-\pi^0$ decays with LHCb data. They comprise minimal requirements on the transverse momentum and isolation from charged tracks for the photons associated to the ECAL clusters. Besides, the neutral pions, resulting from the combination of such photons, have to satisfy transverse momentum thresholds and invariant mass ranges specific for each π^0 category (resolved or merged). Transverse momentum thresholds are applied also to the B^0 candidates. The final invariant-mass

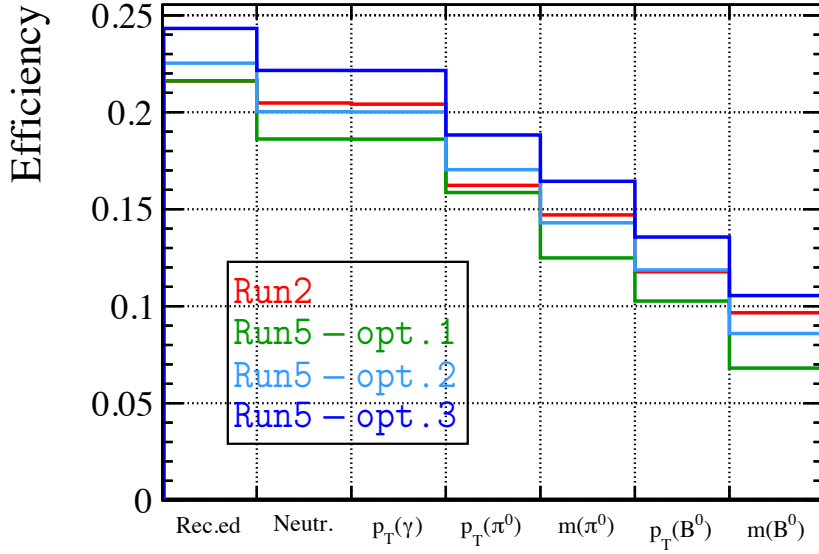


Figure 5.36: Signal efficiency for $B^0 \rightarrow \pi^+ \pi^- \pi^0$ decays after the various step of the selection defined in Table 5.7. The efficiency denominator is the number of generated signal events ($S_{\text{gen.}} = 80000$, as reported in Table 5.3). The first bin (Rec.ed) concerns the signal $B^0 \rightarrow \pi^+ \pi^- \pi^0$ reconstructed candidates, before the application of the requirements of Table 5.7. Besides the criteria imposed by the π^0 reconstruction algorithm described in the text, the following loose cuts are imposed at this step: $p_T(\pi^0) > 900 \text{ MeV}/c$, $m(B^0) \in [4.98, 5.88] \text{ GeV}/c^2$. The second bin (Neutr.) concern the requirement γ -track distance > 1 cell side for the rejection of the clusters related to charged particles. The other bins imply different threshold for candidates with merged or resolved π^0 . The last bin concern candidates the invariant mass range $m(B^0) \in [5.1, 5.5] \text{ GeV}/c^2$. The time information is not considered in any configuration.

range for the B^0 candidates defines the region of interest for the evaluation of the ECAL performance. It is chosen to be approximately plus or minus twice the full-width-half-maximum (FWHM) of the distribution around the B^0 nominal mass. Figure 5.36 compares the efficiencies of the selection requirements for the simulated occupancies and ECAL configurations. From the breakdown of the efficiencies in Figure 5.36, it is possible to understand that there are two main sources that cause the drop in signal efficiency between Run2 and Run5. The first one is the identification of neutral clusters, that is mainly related to the granularity of the ECAL. In fact, with the higher granularity of Run5-opt.1 this effect is more than compensated. The second source of inefficiency comes from the requirements applied to the invariant mass of the π^0 and B^0 mesons. The reason for this difference is due to the much higher occupancy in the Run5 conditions, where the energy of other particles for which a seed is not found leaks inside the cluster of the signal photons. The effect is very clear also in Figures 5.38 and 5.39, where a more pronounced high-mass tail is present in the distributions for Run5 conditions with respect to Run2 conditions. The higher granularity of Run5-opt.1 benefits also the efficiency in identifying the seeds, leading to higher reconstruction efficiency as evidenced by the first bin of the plot in Figure 5.36.

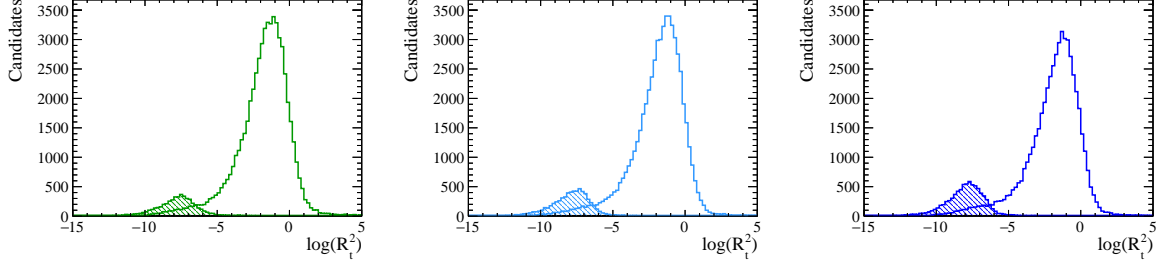


Figure 5.37: Distributions of the R_t^2 variable for signal (filled histograms) and background (empty histograms) $B^0 \rightarrow \pi^+\pi^-\pi^0$ candidates after the entire selection reported in Table 5.7. The logarithmic transformation is used to enlarge the region with small R_t^2 values and compact the long right tail due to the background. The left, middle, and right plots concern the Run5-opt.1, Run5-opt.2, and Run5-opt.3 configurations, respectively. The simulated timing resolution of the ECAL cells is set to $\delta t = 15$ ps, and R_t is expressed in ns.

5.4.1.2 Background rejection with time information

The variable which is used to test the impact of the time information for the $B^0 \rightarrow \pi^+\pi^-\pi^0$ selection in Run5 conditions is defined as follows:

$$R_t^2 = (t_1^{ECAL} - t_1^{\text{expect.}})^2 + (t_2^{ECAL} - t_2^{\text{expect.}})^2. \quad (5.13)$$

The quantities t_i^{ECAL} ($i = 1, 2$) are the times of the ECAL clusters, whose information are combined to build a given π^0 candidate. The $t_i^{\text{expect.}}$ variables are the corresponding expected times. They are calculated assuming linear propagation at the speed of light from the decay vertex of the B^0 candidate, $(x_B^{\text{end}}, y_B^{\text{end}}, z_B^{\text{end}})$, to the hits on the ECAL surface, as reconstructed by the just-mentioned clusters, $(x_i^{ECAL}, y_i^{ECAL}, z_i^{ECAL})$:

$$t_{1,2}^{\text{expect.}} = \sqrt{(x_i^{ECAL} - x_B^{\text{end}})^2 + (y_i^{ECAL} - y_B^{\text{end}})^2 + (z_i^{ECAL} - z_B^{\text{end}})^2} + t_B^{\text{end}}, \quad (5.14)$$

where t_B^{end} is the time associated to the end vertex of the B^0 candidate by another LHCb subdetector. Since both the spatial and the time resolution of the VELO detector in Upgrade II configurations are expected to be smaller than those of the ECAL, the true information on the end vertex of the signal B^0 is exploited in this simulation.

The procedure exploited to optimise the R_t requirements is presented in the next section. When a 15-ps resolution is simulated the cut $R_t < 50$ ps is found to be optimal for all ECAL configurations in Run5 conditions. Figure 5.37 shows the distribution of R_t distinguishing candidates associated to the signal or to the background according to the prescriptions of Section 5.3.2.1. The Figures 5.38 and 5.39 illustrate the effect of the best R_t cut on the π^0 and B^0 invariant mass spectra, respectively. The corresponding spectra in Run2 conditions are plotted in Figure 5.40. The comparison of such plots clearly manifest the advantage due to the exploitation of the time information in Upgrade conditions.

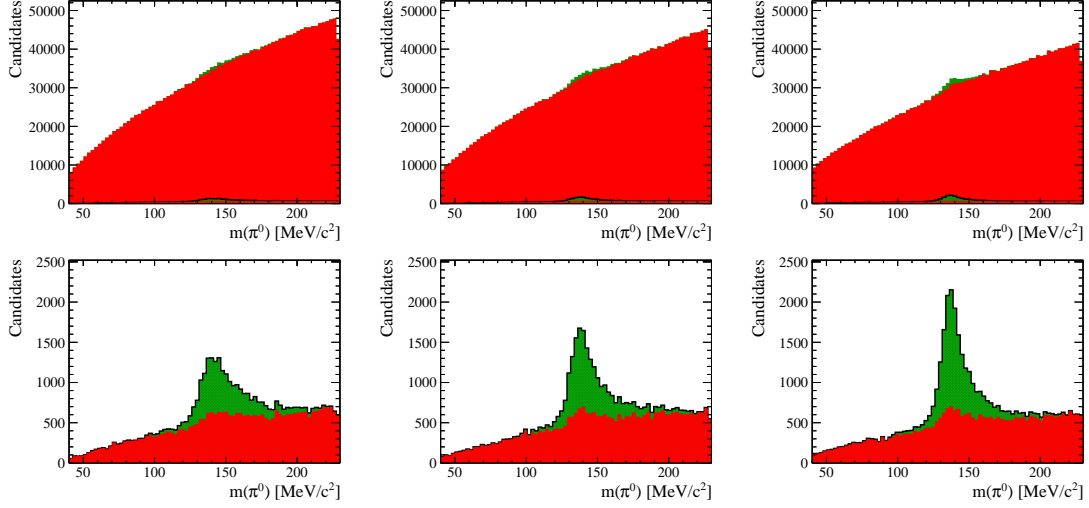


Figure 5.38: Invariant mass for the reconstructed π^0 candidates after the selection in Table 5.7, except for the requirements on the $m(\pi^0)$, $p_T(B^0)$. The range $m(B^0) \in [4.98, 5.88] \text{ GeV}/c^2$ is considered. The signal and background contributions are illustrated with green and red stacked histograms, respectively. In the top row, the cases before (filled histogram) and after (textured histogram with black contour) the application of the best timing cut ($R_t < 50 \text{ ps}$) are superimposed. In the bottom row only the case after the timing cut is depicted. The left, middle, and right plots concern the Run5-opt.1, Run5-opt.2, and Run5-opt.3 configurations, respectively.

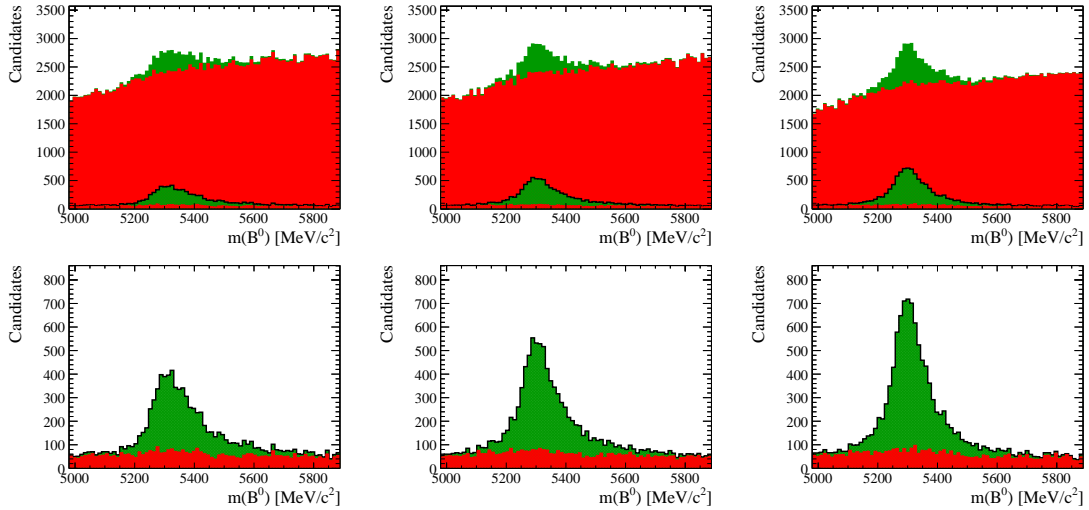


Figure 5.39: Invariant mass for the reconstructed B^0 candidates after the selection in Table 5.7. The signal and background contributions are illustrated with green and red stacked histograms, respectively. In the top row, the cases before (filled histogram) and after (textured histogram with black contour) the application of the best timing cut ($R_t < 50 \text{ ps}$) are superimposed. In the bottom row only the case after the timing cut is depicted. The left, middle, and right plots concern the Run5-opt.1, Run5-opt.2, and Run5-opt.3 configurations, respectively.

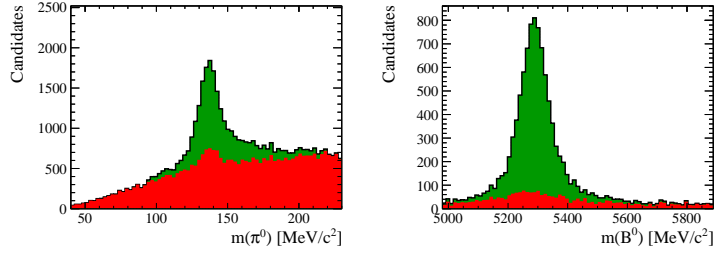


Figure 5.40: Invariant mass for the reconstructed π^0 (left) and B^0 (right) candidates in Run2 conditions. The plots are analogous to the corresponding ones illustrated in the Figures 5.38 5.39, but time information is never used here.

5.4.1.3 Performance comparison

Two figures of merit are chosen to compare the total performance of selection and reconstruction of $B^0 \rightarrow \pi^+\pi^-\pi^0$ decays. The first one is the efficiency,

$$\varepsilon = \frac{S}{S_{\text{gen.}}}, \quad (5.15)$$

namely the number of candidates associated to the signal and passing the whole selection, S , divided by the total number of generated signal events ($S_{\text{gen.}} = 80000$, as reported in Table 5.3). The second one is the significance, which is defined as

$$\xi = \frac{S}{\sqrt{S+B}}, \quad (5.16)$$

where B is the number of candidates associated to the background, passing the whole selection. Figure 5.41 resumes and compare the performance of the various configurations. The plot clearly manifests the decisive advantage provided by the time information: a remarkable significance gain is obtained with a relatively small efficiency loss. In Run5 conditions, this is essential to get performance per inverse femtobarn as close as possible to the ones of Run2. Besides, the values of maximal efficiency observed in Run5 show that the effect of the higher occupancy regime is not compensated by the higher granularity of the baseline option for the LHCb Upgrade II (Run5-opt.1). Only the very demanding configuration named Run5-opt.3 presents overall ECAL performance comparable with Run2.

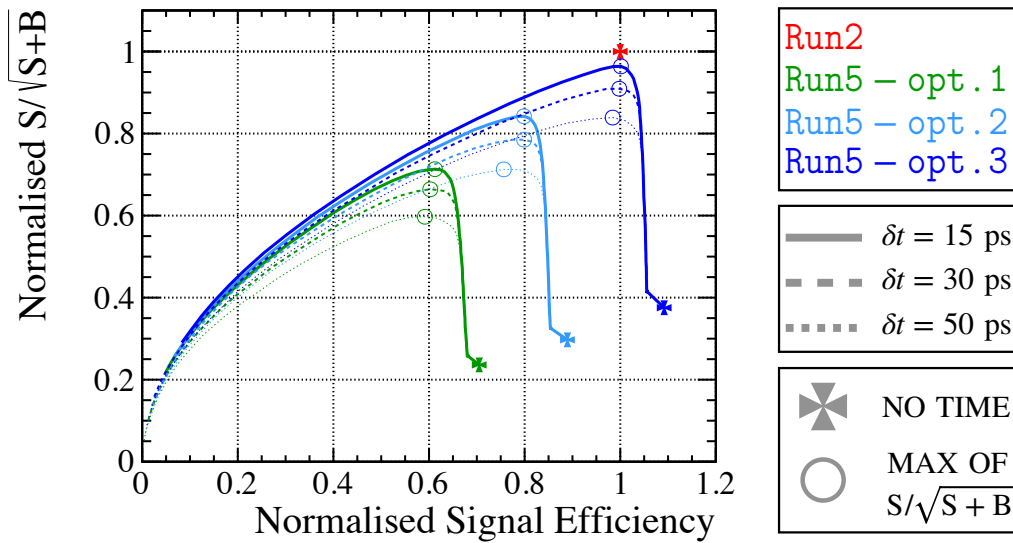


Figure 5.41: The definitions of signal efficiency and significance ($S/\sqrt{S+B}$) are given in the text. Here, they are divided by the corresponding figures of merit in Run2 conditions. Each point of the curves represents the performance of a particular R_t cut for a certain configuration. As indicated in the legend, different line styles stand for different timing resolution, while the various line colours distinguish the various combinations of occupancy and ECAL arrangement. The circles evidence the cases with the best significances. The crosses mark the cases where no time information is used. The small steps close to the crosses are due to the cases, where no charged particle crossing the front-back interface of the seed cell is found in one of the two clusters at least.

5.4.2 Study of $B^0 \rightarrow K^{*0}e^+e^-$ decays

The ECAL contribution is crucial for both the reconstruction and the identification of the electrons of the $B^0 \rightarrow K^{*0}e^+e^-$ channel. The first task involves the correction of the momentum measured by the tracking system, to include the effect of the emission of bremsstrahlung photons before the magnet. The second task comprises the distinction between the electron and the pion mass hypotheses, which is fundamental to abate the mis-ID background.

To study these topics, samples containing 40000 $B^0 \rightarrow K^{*0}e^+e^-$ and $B^0 \rightarrow K^{*0}\pi^+\pi^-$ decays are simulated for all the above-mentioned occupancy conditions and ECAL configurations (Table 5.3). All the reconstructed candidates are associated to the corresponding signal processes. The cases with signal electrons, or pions, whose trajectories do not intersect all the subdetectors of the tracking system, are rejected, as not reconstructible. No background due to the random selection of the final states is considered.

5.4.2.1 Bremsstrahlung recovery

The baseline algorithm for the identification of the bremsstrahlung photons is outlined in Section 5.3.5. Here, the invariant mass distribution is used to compare the ECAL performance between the **Run2** and **Run5** conditions. At this stage, all the background sources are neglected, except for the consequences of a wrong bremsstrahlung recovery, namely not reconstructed bremsstrahlung photons or additional random clusters included in the recovery window. The following paragraph assumes the baseline algorithm and compares the bremsstrahlung-recovery performance between the different occupancy and ECAL configurations. Then, a first attempt to include the timing information in the bremsstrahlung-recovery methods is presented.

The recent LHCb internal note in Ref. [200] studied the bremsstrahlung recovery with the nominal LHCb full simulation, to compare the ECAL performance in **Run2** conditions with those expected for the upcoming Run 3 of the LHC ($\nu = 7.6$ and same ECAL configuration as in the Run 2.). Figure 5.42 reports the invariant-mass spectrum of the reconstructed $B^0 \rightarrow K^{*0}e^+e^-$ decays. An analogous test is carried out with the simulation developed in this thesis and the corresponding invariant-mass distributions are shown in Figure 5.43. The occupancy conditions of **Run3** are reproduced using the same technique described in Section 5.2.1, while the ECAL configuration is the same of **Run2**. The invariant mass calculation assumes the MonteCarlo truth for the momentum of the K^{*0} meson. The momenta of the final-state electron and positron are taken just upstream of the magnet, to consider the effect of the bremsstrahlung emission on the momentum measurement by the tracking system. The bremsstrahlung photons, reconstructed by the ECAL, are included in the calculation as additional final states. Despite small differences introduced by the perfect tracking used in this thesis, the invariant-mass distributions are in a satisfactory agreement with those obtained with the nominal LHCb full simulation in Figure 5.42. The main discrepancy is observed for the **Run3** configuration with no bremsstrahlung recovery. This is ascribed to a bug in the neutral cluster identification used in Ref. [200].⁶ The same test is conducted in **Run5** conditions and the corresponding invariant-mass distributions are reported in Figure 5.44. In spite of the different granularity options, the

⁶This information is obtained from private communication with the authors of Ref. [200]. At the time of writing this thesis an updated version of the internal document is not yet available.

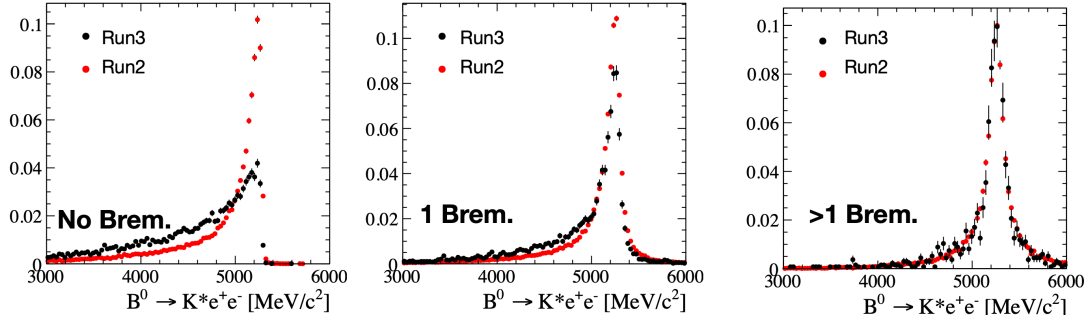


Figure 5.42: Invariant mass distribution as reconstructed by the nominal LHCb full simulation in Run 2 (red) and Run 3 (black) experimental conditions for $B^0 \rightarrow K^{*0} e^+ e^-$ decays. From left to right, the plots show the spectrum for the cases with zero, one, and more than one recovered bremsstrahlung photons, respectively. These images are taken from Ref. [200].

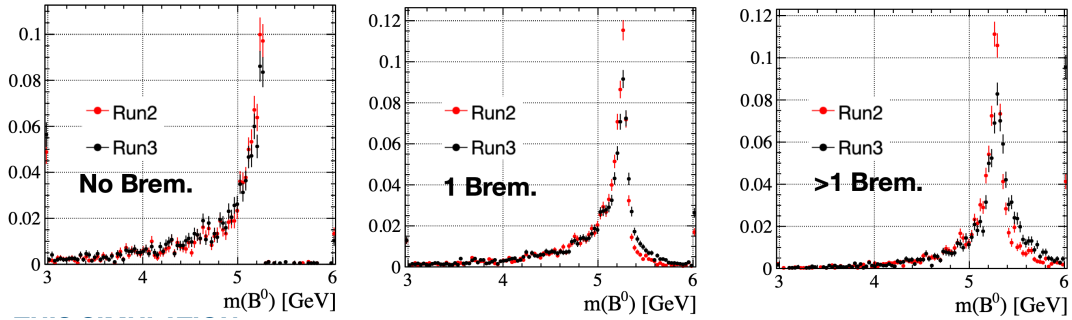


Figure 5.43: Invariant mass distribution for $B^0 \rightarrow K^{*0} e^+ e^-$ decays as simulated and reconstructed by the simulation developed in this thesis in Run2 and Run3 conditions. From left to right, the plots show the spectrum for the cases with zero, one, and more than one recovered bremsstrahlung photons, respectively.

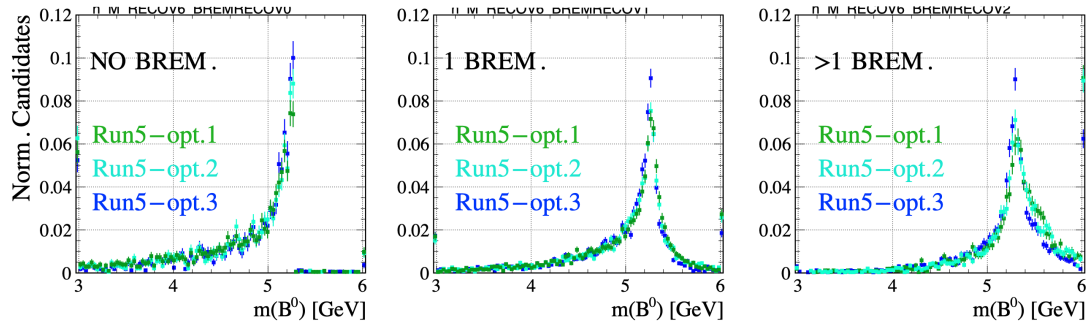


Figure 5.44: Invariant mass distribution for $B^0 \rightarrow K^{*0} e^+ e^-$ decays as simulated and reconstructed by the simulation developed in this thesis for Run5 conditions. From left to right, the plots show the spectrum for the cases with zero, one, and more than one recovered bremsstrahlung photons, respectively.

	0 brem.	1 brem.	> 1 brem.
without timing information			
Run2	19%	48%	33%
Run3	21%	49%	30%
Run5-opt.1	22%	49%	29%
Run5-opt.2	20%	48%	32%
Run5-opt.3	17%	48%	35%
with timing information			
Run5-opt.1	31%	50%	19%
Run5-opt.2	29%	50%	21%
Run5-opt.3	26%	50%	24%

Table 5.8: Fraction of $B^0 \rightarrow K^{*0}e^+e^-$ candidates with zero, one, or more than one recovered bremsstrahlung photons. The top part of the Table does not consider the timing information, while the bottom part does.

Configuration	$\varepsilon_{[5.0,5.4]}$	
	without time	with time
Run2	61%	
Run3	54%	
Run5-opt.1	49%	50%
Run5-opt.2	50%	51%
Run5-opt.3	55%	55%

Table 5.9: Fraction of reconstructed $B^0 \rightarrow K^{*0}e^+e^-$ signal decays with invariant mass belonging to the range $m(B^0) \in [5.0, 5.4] \text{ GeV}/c^2$. In Run5 conditions, the same quantities are reported also for the bremsstrahlung recovery method including the timing information.

fraction of candidates with zero, one, or more than one bremsstrahlung photon are similar between the various configurations, as summarised in Table 5.8. However, the issues related to the degraded bremsstrahlung-recovery performance affect the invariant-mass distributions. In particular, the enhanced right tails of the Run5 spectra of Figure 5.44 manifest the presence of extra-energy, included in the recovery region, but due to other particles in the event. Such occupancy effect is only partially compensated by the higher granularity of the Run5-opt.3 configuration. The overall bremsstrahlung-recovery performance are summarised in Table 5.9 and Figure 5.45. For each configuration, the Table reports the fraction of candidates whose reconstructed invariant mass falls in the range $m(B^0) \in [5.0, 5.4] \text{ GeV}/c^2$. The Figure shows the corresponding invariant-mass distributions without discriminations on the number of recovered bremsstrahlung photons. No particular improvement is observed due to the increased granularity.

In principle, the timing information could be relevant to increase the bremsstrahlung-recovery performance. The time registered by the seed cell of a cluster (t_{clust}) associated to a bremsstrahlung photon can be compared to the corresponding expected time,

$$t_{\text{expect.}} = t_B^{\text{END}} + \frac{1}{c} \sqrt{(x_{\text{clust}} - x_B^{\text{END}})^2 + (y_{\text{clust}} - y_B^{\text{END}})^2 + (z_{\text{clust}} - z_B^{\text{END}})^2}, \quad (5.17)$$

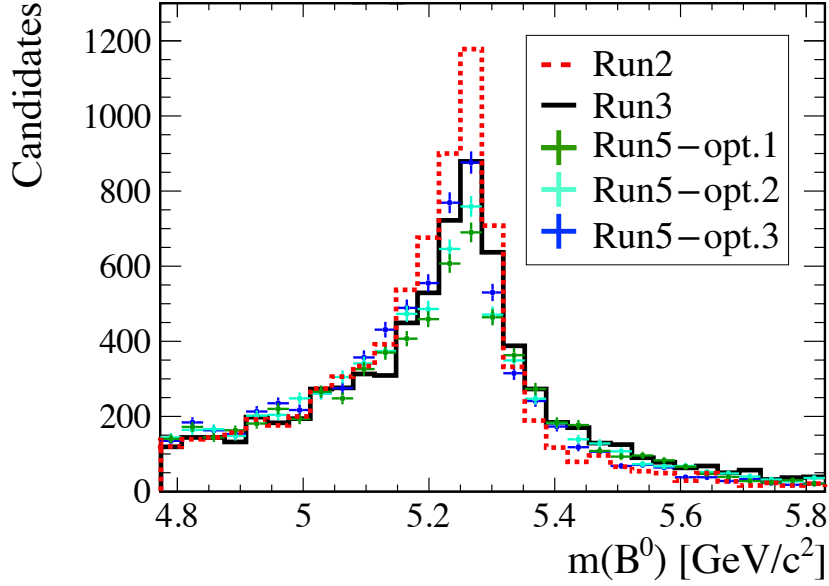


Figure 5.45: Invariant mass spectrum for the reconstructed $B^0 \rightarrow K^{*0} e^+ e^-$ signal decays. The distributions obtained by the various simulation configurations are distinguished by the styles reported in the legend. The histograms are not normalised to unit area, but the total number of generated events is equal for all the cases.

which is calculated assuming a linear propagation at the speed of light from the decay vertex of the signal B^0 meson, $(x_B^{\text{END}}, y_B^{\text{END}}, z_B^{\text{END}})$, to the reconstructed position of the cluster on the ECAL surface, $(x_{\text{clust}}, y_{\text{clust}}, z_{\text{clust}})$. Figure 5.46 illustrates how the distribution of $t_{\text{clust}} - t_{\text{expect.}}$ is related to the distance, $R_{\text{brem}}^{\text{REC}}$, between the center of the bremsstrahlung-recovery window and the cluster position. The clusters associated to photons coming from the signal decay chain present small values of both these quantities, whereas the background cases, namely the clusters to be rejected, have high values. Only the intrinsic time resolution is simulated in this study, to consider the best timing performance as possible. The selection requirement $|t_{\text{clust}} - t_{\text{expect.}}| < 50$ ps is chosen as a reference working point and added to the requirements defining the baseline bremsstrahlung-recovery window. Figure 5.47 illustrates the effect of the inclusion of the timing information on the $B^0 \rightarrow K^{*0} e^+ e^-$ invariant mass spectrum in Run5-opt.1 configuration. The right tail of the distribution is slightly reduced, but no remarkable performance improvement is observed. The same kind of test, conducted on the Run5-opt.2 and Run5-opt.3 configurations, brings to similar results. This is manifested by Table 5.9 and Figure 5.48. The former reports the fraction of reconstructed candidates belonging to the usual invariant-mass range, the latter graphically compares the invariant-mass distributions of the various Run5 configurations. No significant increase in the fraction of events in the mass range $[5.0, 5.4]$ GeV/c^2 is observed when including time information. In conclusion, the bremsstrahlung recovery performance are led by the ECAL granularity and not critical advantage is observed as a result of the timing information inclusion.

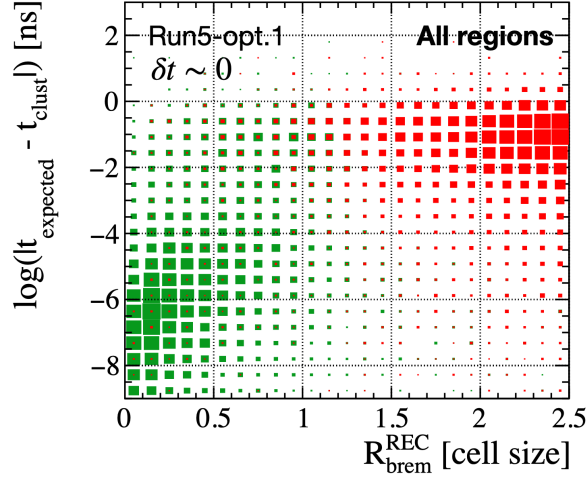


Figure 5.46: Two-dimensional distribution of the spatial and temporal distance between the clusters in the bremsstrahlung-recovery window and the corresponding expected quantities. The precise definitions of $R_{\text{brem}}^{\text{rec}}$, t_{clust} , and $t_{\text{expect.}}$ are reported in the text. The logarithmic transformation of the y component is applied to enhance the region with small temporal distance. The contributions from all the ECAL region in Run5-opt.1 configuration are considered. Only the intrinsic time resolution is simulated to look for the best timing performance as possible. The green squares are indicates clusters associate to the signal bremsstrahlung photons, while the red in used for the background cases.

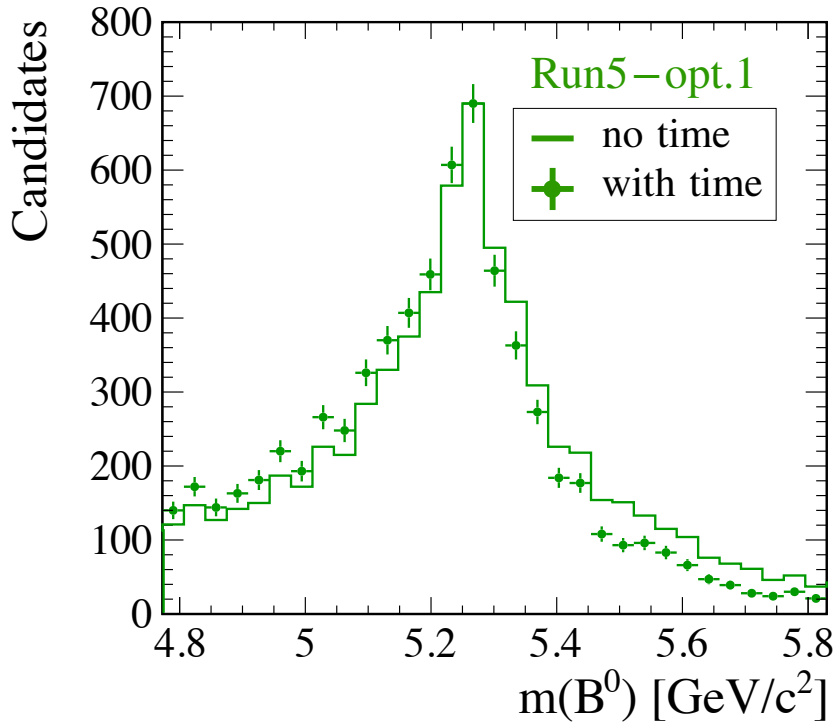


Figure 5.47: Invariant mass spectrum for the reconstructed $B^0 \rightarrow K^{*0}e^+e^-$ signal decays in Run5-opt.1 configuration. The line indicates the distribution obtained with the baseline bremsstrahlung recovery method, while the dots illustrates the results of the procedure including the timing information. The histograms are not normalised to unit area, but the total number of generated events is equal for both the cases.

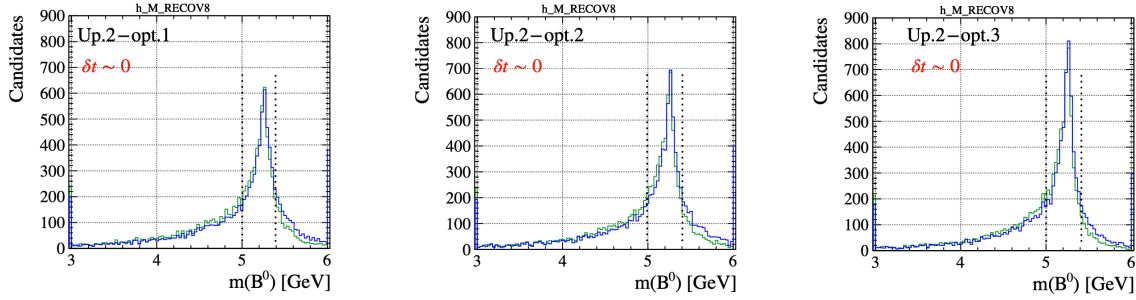


Figure 5.48: Invariant mass spectrum for the reconstructed $B^0 \rightarrow K^{*0}e^+e^-$ signal decays. The left, middle, and right plots are related to the Run5-opt.1, Run5-opt.2, and Run5-opt.3 simulated configurations, respectively. The histograms are not normalised to unit area but the same number of events (40000) is simulated for all the cases. The blue histograms are obtained with the baseline bremsstrahlung-recovery algorithm, while the green histograms concern the method including the timing information.

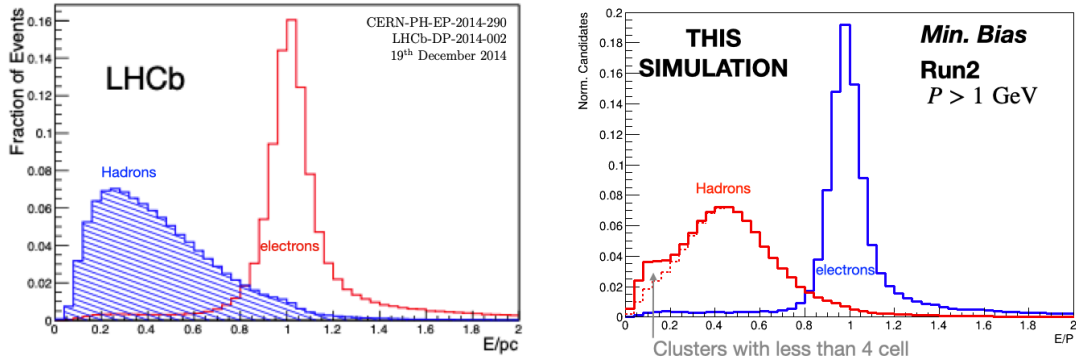


Figure 5.49: Distribution of E/P (definition in the text) as obtained from LHCb data (left) and from this simulation in Run2 conditions (right). Both the electrons and the hadrons (mainly pions) are taken from the Minimum Bias simulated sample, applying a 1-GeV/ c threshold on their momentum. Histograms are normalised to unit area. The left plot is taken from Ref. [65].

5.4.2.2 Performance of $e-\pi$ discrimination

The $B^0 \rightarrow K^{*0}\pi^+\pi^-$ decay is an insidious background source for preminent LHCb analyses [201, 202], concerning rare decays of B mesons to final states with electrons. Indeed, the double $\pi \rightarrow e$ misidentification of the final state pions could generate a background component, peaking under the core of the signal invariant-mass distribution. The current performance of the LHCb detector can reduce this effect to negligible levels. However, it is still unknown whether the same will be feasible also in the high occupancy regimes foreseen for the Run 5.

The main observable, now exploited for the $e-\pi$ discrimination, is “ E/P ”, namely the energy measured by the ECAL cluster associated to the candidate electron divided by the momentum measured by the tracking system, without considering the bremsstrahlung recovery. Figure 5.49 compares the distribution of this observable as obtained from this simulation and from real LHCb data.

The longitudinal segmentation of the ECAL in Upgrade II configuration may be relevant to improve the $e-\pi$ discrimination, since pions develop showers at the end of

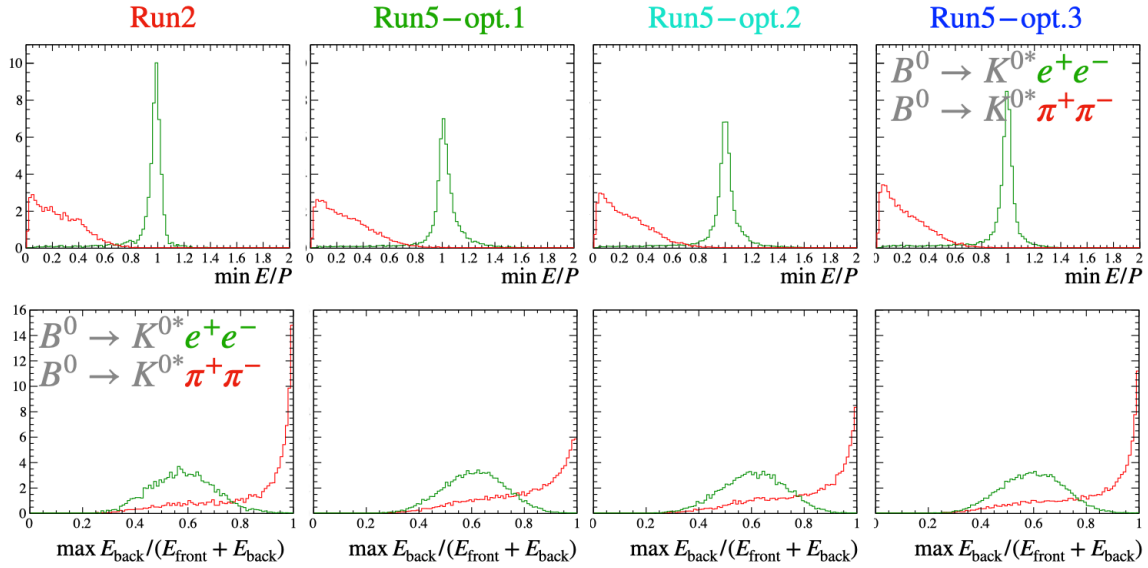


Figure 5.50: Distributions of the $\min[E/P]$ (top) and $\max[E_{\text{back}}/E]$ (bottom) simulated observables (definitions in the text). From left to right the quantities concerning the Run2, Run5-opt.1, Run5-opt.2, Run5-opt.3 configuration are shown, respectively. All the histograms are normalised to unit area. The green ones are obtained with $B^0 \rightarrow K^{*0}e^+e^-$ simulated decays, while the red ones concern $B^0 \rightarrow K^{*0}\pi^+\pi^-$ simulated decays.

electromagnetic calorimeters. Hence, the distribution of the quantity E_{back}/E , where E_{back} is the energy measured by the back section of the cells of the cluster, is expected to be different between pions and electrons. Figure 5.50 illustrates the distribution of $\min[E/P]$ and $\max[E_{\text{back}}/E]$ obtained from the $B^0 \rightarrow K^{*0}e^+e^-$ and $B^0 \rightarrow K^{*0}\pi^+\pi^-$ simulated samples⁷. Both quantities offer discrimination power between the two different mass hypotheses, but the higher occupancy of the Run5 conditions is still a concern. The e - π discrimination performance is summarised by two figures of merit:

the signal efficiency, defined as the ratio between the number of $B^0 \rightarrow K^{*0}e^+e^-$ candidates passing a specific discrimination requirement and the total number of reconstructed $B^0 \rightarrow K^{*0}e^+e^-$ candidates;

the background rejection, defined as the number of $B^0 \rightarrow K^{*0}\pi^+\pi^-$ candidates rejected by a specific discrimination requirement divided by the total number of reconstructed $B^0 \rightarrow K^{*0}\pi^+\pi^-$ candidates.

Figure 5.51 relates these two quantities: each point of the curves plots the values of the two figures of merit obtained by the same $\min[E/P]$ requirement. As expected, the performance in Run5 conditions improves with the increasing of the ECAL granularity. However, it is always poorer than the one in Run2 configuration.

The eventual advantage arising because of the longitudinal segmentation of the ECAL is estimated as follows. A two-dimensional scan of $\min[E/P]$ and $\max[E_{\text{back}}/E]$ is performed applying the corresponding pair of requirements and calculating the ECAL performance. The method is clarified by Figure 5.52, which shows the two-dimensional distribution of $\min[E/P]$ and $\max[E_{\text{back}}/E]$, illustrating some examples of the rectangular cuts that

⁷The minimum and maximum operations concern the two signal final-states electrons or pions.

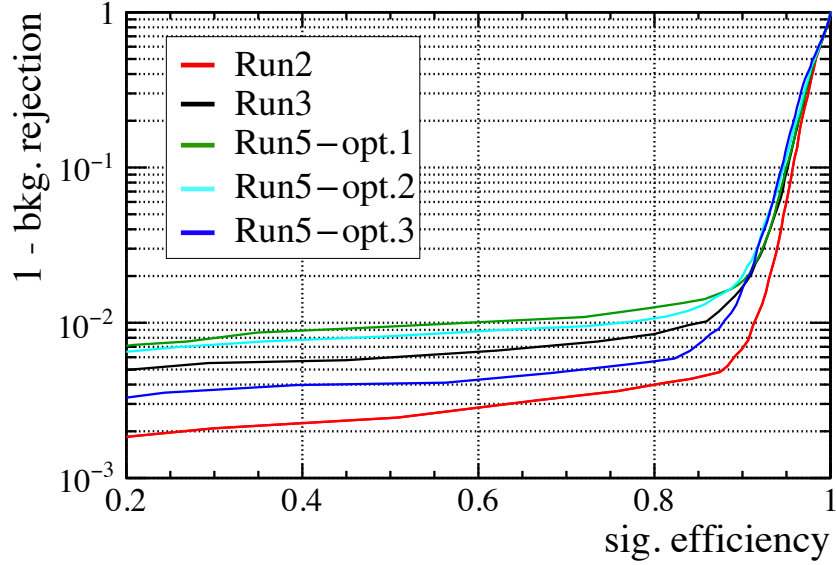


Figure 5.51: Electron identification rate (sig. efficiency) versus pion to electron misidentification rate (1-bkg. rejection). Each point of the curves correspond to the performance of an E/P requirement on the $B^0 \rightarrow K^{*0}e^+e^-$ and $B^0 \rightarrow K^{*0}\pi^+\pi^-$ samples (details in the text). The areas above the curves provide direct comparisons of the $e-\pi$ discrimination performance obtained with the various simulated configurations.

results from the two-dimensional scan. Figure 5.53 finally compare the performance. To not overload the plot, only the curves concerning the Run5-opt.1 and Run5-opt.3 configurations are reported⁸. The comparison of the cases, involving or not the E_{back}/E variable, shows that the longitudinal ECAL segmentation provides relevant information for the $e-\pi$ discrimination task. As a reference, the point corresponding to a 80% signal efficiency is marked for the Run2 configuration. In Run5 conditions, this target is reached only by the higher granularity option (Run5-opt.3) with information from the longitudinal segmentation.

⁸The two-dimensional scan described in the text does not actually produce a curve but a grid of performance point, namely cases with similar signal efficiency, but very different background rejection, and *viceversa*. The curves plotted in Figure 5.53 are those with the best background rejection for a given signal efficiency.

Run5 – opt.1

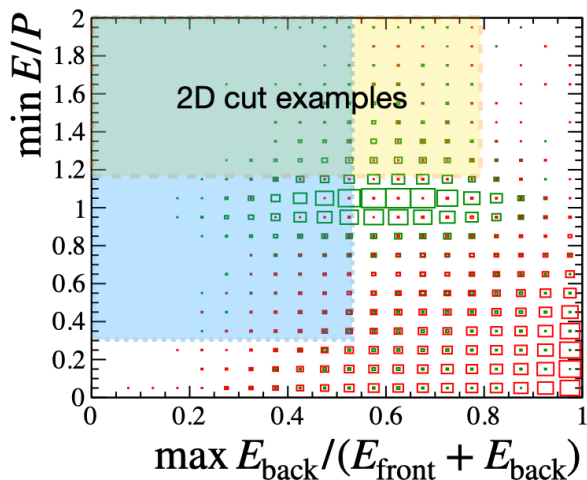


Figure 5.52: Two-dimensional distribution of $\min[E/P]$ and $\max[E_{\text{back}}/E]$ configuration. The green and the red boxes are related to the electrons of the $B^0 \rightarrow K^{*0}e^+e^-$ samples and to the pions of the $B^0 \rightarrow K^{*0}\pi^+\pi^-$ samples, respectively. The yellow- and azure-shaded areas illustrates two examples of the rectangular cuts mentioned in the text. The top left corner of the boxes is fixed, while the bottom right corner changes according to the two-dimensional scan. For each case, the candidates falling inside the resulting rectangle are accepted, the other ones are rejected.

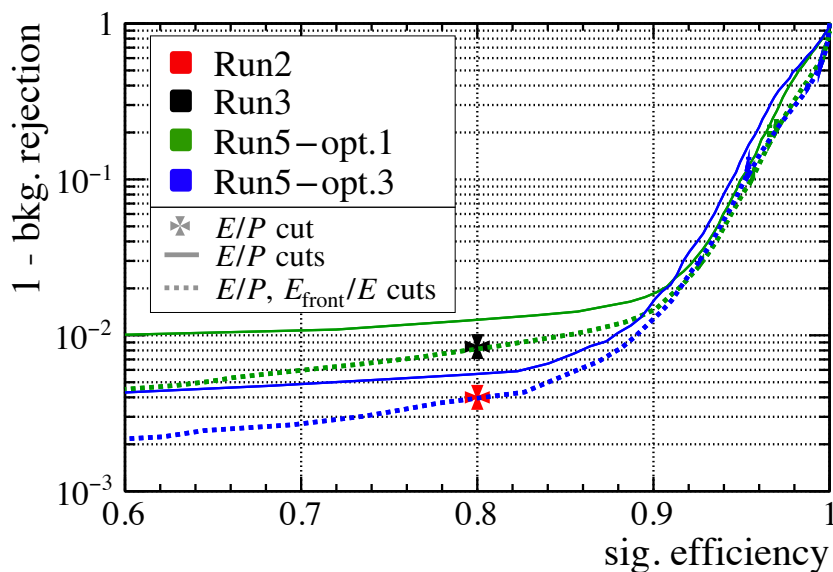


Figure 5.53: Electron identification rate (sig. efficiency) versus pion to electron misidentification rate (1-bkg. rejection). Each point of the curves correspond to the performance of the same discrimination requirement on the $B^0 \rightarrow K^{*0}e^+e^-$ and $B^0 \rightarrow K^{*0}\pi^+\pi^-$ simulated samples. The solid lines involve only requirements on the E/P variables, while the dashed lines include also the information coming from the longitudinal segmentation of the ECAL (detail in the text). Different color stand for different occupancy and ECAL configurations, as reported in the legend. In the Run2 case, only the point corresponding to an 80% signal efficiency is marked to not overload the plot.

5.5 Summary and conclusions

The simulation study reported in this Chapter concerns the development of a fast and flexible simulation framework, to evaluate the ECAL response in the high occupancy regime foreseen for the Run 5 of the LHCb detector, and understand which characteristics may provide performance per inverse femtobarn comparable with the current ones.

Various simplifications are employed and investigated, observing that they provide an adequate level of approximation for this study. The generation phase takes a decisive advantage from the “bootstrapping” technique presented in Section 5.2.2. On the one hand, the simulation of the particle interactions with ECAL cells is accelerated by the assumption of homogeneous materials. On the other hand, the detailed simulation of the electromagnetic and hadronic showers is borrowed from the GEANT4 toolkit, keeping all and only the necessary information. Thus, the simulation can take into account the longitudinal segmentation of the ECAL and the angles of the incoming particles. The timing information collected by the ECAL cells is simulated in a simplified but accurate way. The specific reproduction of the signal generated by timing layers located between the front and the back section of the cells is omitted. However, the intrinsic time-resolution effects can be studied and corrected. Besides, the overall time resolution is introduced in an agile way: the machinery performing the time smearing can be run on top of all the other simulation and reconstruction steps. This feature permits different time-resolutions instances to be quickly tested without the computational cost related to the expensive repetition of identical operations.

The studied physics cases involve tasks driving the ECAL performance: the π^0 reconstruction, the bremsstrahlung recovery, and the e - π discrimination. The first topic is faced simulating and analysing $B^0 \rightarrow \pi^+\pi^-\pi^0$ decays, that are meaningful for measurements of the UT angle α [203–205] and are equipped with a wide π^0 -momentum range. The reconstruction efficiency is observed to be strongly dependent on the segmentation of the ECAL surface. In high occupancy conditions, the electromagnetic showers due to the signal often overlap those due to the rest of the event (minimum bias background). This phenomenon causes reconstruction artefacts, like the enhancement of the right tail of the π^0 and B^0 invariant-mass spectrum due to additional energy contributions, or even the loss of the signal candidates when the energy of the background overwhelms the one from the signal. Both the effects are observed to be relevant with baseline configuration for the Upgrade II of the LHCb ECAL (Run-opt.1). Smaller cell sizes and Molière radii can compensate for these effects. However, they lead the rapid increment of the costs related to the experimental apparatuses. Restrictions to higher momentum regimes for the π^0 mitigate the situation, but they are not always neutral from the LHCb physics programme point of view. For instance, the large part of the $B^0 \rightarrow \pi^+\pi^-\pi^0$ decays generates low-momentum resolved π^0 s. In this context, the exploitation of the timing information is observed to be extremely effective in rejecting the combinatorial background without important loss of signal (see Figure 5.41). The result of this performance study is a demanding target for the detector R&D: a timing resolution ranging from 10 to 20 ps. The developing projects are now close to this goal (Figures 5.4 and 5.5).

The degradation of the ECAL response concerning the bremsstrahlung recovery and the e - π discrimination in Run 5 conditions is quantified with the simulation of $B^0 \rightarrow K^{*0}e^+e^-$ and $B^0 \rightarrow K^{*0}\pi^+\pi^-$ decays. The ECAL granularity is observed as an essential factor for both tasks. Nevertheless, the current algorithms, applied in Run 5 conditions, do

not match the Run 2 performance, even when the highest granularity configuration (`Run5-opt.3`) is tested (Figures 5.45 and 5.51). Two methods are investigated to face the problem: the inclusion of the time information in the bremsstrahlung-recovery algorithm, and the exploitation of the longitudinal segmentation of the ECAL cells. The preliminary results do not demonstrate relevant benefits from the first method, even with an almost perfect time resolution. Two reasons justify this observation. On the one hand, the assumption of perfect tracking, along with the small cell sizes tested in Run 5 conditions, permits the spatial dimension of the bremsstrahlung recovery window to be relatively small. This restriction effectively reduced the contamination due to ECAL clusters dominated by energy contributions of the minimum-bias background. On the other hand, minimum-bias background remarkably affects the time information. Thus, the timing lead to the rejection of cases with relevant background contamination, which mainly concern the right tail of the invariant-mass spectrum (Figure 5.47). However, when the bremsstrahlung-recovery window is small, the number of selected clusters is typically low. Hence, very often, the information coming from the signal bremsstrahlung photons, being included in the same cluster, was rejected, as well. The longitudinal segmentation of the ECAL was utilised to improve the e - π discrimination. Including the information about the energy deposited in the front and back sections of the ECAL cells, the `Run5-opt.3` configuration achieved the same performance as the `Run2` (Figure 5.53). Relevant improvements are observed also with lower granularity, manifesting the importance of the longitudinal segmentation in the Upgrade II ECAL of LHCb.

The considerations reported in this thesis are driven by the unexplored path they had to undergo. This condition led to the choice to operate only minimal modifications to the current LHCb reconstruction algorithms. The corroboration of the hypotheses about the advantages arising from proposed new ECAL features is the main result of this study, and –together with several consistent results from the rest of the LHCb collaboration– has already oriented the R&D project for the LHCb Upgrade II. Now, additional simulation analyses are necessary to optimise the combination of this new information. The *seed finding* is expected to be a strategic task to improve the efficiency and the resolution of ECAL reconstruction. In particular, the different occupancy regimes foreseen for the front and back sections of the Upgrade II ECAL (Figure 5.3) are probably meaningful in this regard. After that, further optimisations of the methods for the redistribution of the energy between overlapping clusters will be presumably necessary. These optimisations may improve all the observables directly related to the ECAL clusters, and not only the performance for merged π^0 . For the reasons discussed above, they may also enhance the positive contribution of the timing information to the recovery of the bremsstrahlung photons. Another essential step will be the integration of the ECAL simulation with the simulations of other LHCb sub-detector in Upgrade II configuration. Above all, the simulation of the tracking system is necessary for a more accurate estimation of the ECAL performance and to finally fix its granularity. More in general, a promising direction to exploit the full potentialities of the Upgrade II ECAL involves multivariate-analysis methods to optimise the combination of the energy, space and time measurements. The simulation framework developed in this thesis is ready to be updated for these efforts.

Conclusions

This thesis contains original contributions to the measurements of relevant flavour-physics observables with the data collected by the LHCb experiment. It also contains original simulation studies that contribute to the design and development of the future electromagnetic calorimeter of the LHCb Upgrade II detector.

The sample of p - p collisions collected with the LHCb detector during the entire Run 2 is analysed in Chapter 3 to determine the CP violation parameters $C_{\pi^+\pi^-}$, $S_{\pi^+\pi^-}$, $C_{K^+K^-}$, $S_{K^+K^-}$, and $A_{K^+K^-}^{\Delta\Gamma}$. These parameters quantify CP violation in the decay and in the interference between mixing and decay of the $B^0 \rightarrow \pi^+\pi^-$ and $B_s^0 \rightarrow K^+K^-$ decays. The direct CP asymmetries of the $B^0 \rightarrow K^+\pi^-$ and $B_s^0 \rightarrow \pi^+K^-$ decays, $A_{CP}(B^0 \rightarrow K^+\pi^-)$ and $A_{CP}(B_s^0 \rightarrow \pi^+K^-)$, are measured as well. The most recent LHCb determination of these parameters involved a sample corresponding to 5 fb^{-1} of integrated luminosity and included the first observation of time-dependent CP violation in the decays of the B_s^0 meson, along with world leading measurements of all the parameters. The new analysis, included in this Thesis, involves additional 4 fb^{-1} of integrated luminosity, corresponding to the data collected in 2017 and 2018. Besides, 2 fb^{-1} of already analysed data are reprocessed and included as well, to serve as a cross-check. This test is fully positive. However, the results for $C_{K^+K^-}$ and $S_{K^+K^-}$ with the 2017 and 2018 datasets manifest a discrepancy with the previous determination exceeding 3 standard deviations. A long list of cross-check is performed to find the cause of this inconsistency and is documented in this Thesis. At the time of writing, further tests are ongoing.

The Chapter 4 illustrates the measurement of the magnitude of the Cabibbo-Kobayashi-Maskawa matrix element named V_{cb} with the semileptonic $B_s^0 \rightarrow D_s^- \mu^+ \nu_\mu$ and $B_s^0 \rightarrow D_s^{*-} \mu^+ \nu_\mu$ decays. The result is

$$|V_{cb}| = (41.4 \pm 0.6 \text{ (stat)} \pm 0.9 \text{ (syst)} \pm 1.2 \text{ (ext)}) \times 10^{-3},$$

where the uncertainties are statistical, systematic, and due to external inputs, respectively. This determination is consistent with the world average. It is the first measurement of $|V_{cb}|$ at a hadron collider and the absolute first with B_s^0 mesons. Besides, the branching ratios and form factors parameters of the $B_s^0 \rightarrow D_s^{(*)-} \mu^+ \nu_\mu$ decays are measured for the

first time:

$$\begin{aligned}
\mathcal{B}(B_s^0 \rightarrow D_s^- \mu^+ \nu_\mu) &= (2.49 \pm 0.12 \text{ (stat)} \pm 0.14 \text{ (syst)} \pm 0.16 \text{ (ext)}) \times 10^{-2} \\
\mathcal{B}(B_s^0 \rightarrow D_s^{*-} \mu^+ \nu_\mu) &= (5.38 \pm 0.25 \text{ (stat)} \pm 0.46 \text{ (syst)} \pm 0.30 \text{ (ext)}) \times 10^{-2} \\
\rho^2(D_s) &= 1.268 \pm 0.047 \text{ (stat)} \pm 0.032 \text{ (syst)} \pm 0.001 \text{ (ext)}, \\
\mathcal{G}(0) &= 1.102 \pm 0.034 \text{ (stat)} \pm 0.022 \text{ (syst)} \pm 0.004 \text{ (ext)}, \\
\rho^2(D_s^*) &= 1.23 \pm 0.17 \text{ (stat)} \pm 0.05 \text{ (syst)} \pm 0.01 \text{ (ext)}, \\
R_1 &= 1.34 \pm 0.25 \text{ (stat)} \pm 0.09 \text{ (syst)} \pm 0.02 \text{ (ext)}, \\
R_2 &= 0.83 \pm 0.16 \text{ (stat)} \pm 0.07 \text{ (syst)} \pm 0.01 \text{ (ext)}.
\end{aligned}$$

The simulation framework described in Chapter 5 is found to be adequate to estimate the response of an electromagnetic calorimeter (ECAL) to be used in the high luminosity conditions expected in the Run 5 of the LHCb experiment. The performance studies show a general degradation of the ECAL performance, the main limiting factor being its granularity. To overcome this problem the impact of new features, proposed by the LHCb Upgrade II ECAL R&D group, is estimated for the first time in the LHCb context. In particular it is shown that measuring the time-of-arrival of particles on the ECAL with resolutions between 10 and 20 ps is necessary to reject the combinatorial background contaminating the samples of decays with π^0 in their final states. The identification and reconstruction of the bremsstrahlung photons, instead, manifests no relevant benefits from the inclusion of the time information. More studies, including a complete simulation of the tracking system, that is not yet available, are considered necessary to confirm this conclusion. A longitudinal segmentation of the ECAL is observed to be effective to improve electron-pion discrimination. These studies are included in the Framework Technical Design Report of the LHCb Upgrade II detector. They already set targets for the hardware R&D, and will serve as basis for the improvement and optimisation of the reconstruction algorithms.

Appendix A

CP violation measurements in the decay of $B_{(s)}^0$ mesons to two charged pions and kaons

A.1 Background subtraction for $B_{(s)}^0 \rightarrow h^+h'^-$ decays

The background subtraction of the $B_{(s)}^0 \rightarrow h^+h'^-$ events is performed fitting the invariant mass computed assuming both final state particles to be pions ($m_{\pi\pi}$) and applying the *sPlot* technique [128]. The event selection comprises all the criteria described in Section 3.1.4, except for the PID requirements. The shapes of signal contributions is parameterised with a Kernel Estimation Method [126] to the distribution of $m_{\pi^+\pi^-}$ for fully simulated events, where $m_{\pi^+\pi^-}$ has been computed assuming perfect invariant mass resolution. The obtained non-parametric distributions are convolved with a Gaussian resolution model with free mean and width. The relative fractions between the various $B_{(s)}^0 \rightarrow h^+h'^-$ decays are fixed to the values measured by LHCb in Reference [206]. For the Λ_b^0 decays the world averages of the absolute branching ratios computed by the Heavy Flavour Averaging Group (HFLAV) and reported in Reference [138] are used. The assumed value of the hadronization fraction of the Λ_b^0 baryons is taken from the LHCb measurement of $f_{\Lambda_b^0}/(f_d + f_u)$, published in Reference [207], assuming also $f_d \approx f_u$. The measurement is dominated by the external input of the \mathcal{B} ($\Lambda_c^+ \rightarrow pK^-\pi^+$), and the central value is with a good approximation inversely proportional to this branching ratio. Hence, we rescaled the value of $f_{\Lambda_b^0}/(f_d + f_u)$ by the ratio between the input used in the LHCb paper, and the updated value published by Belle in Reference [208]. The contribution due to combinatorial background is parameterised with an exponential function, while the component coming from partially reconstructed 3-body B decays has been described using an ARGUS function [127] convolved with the same Gaussian resolution model of the signal shapes and described in Section 3.7.3. Figure A.1 illustrates the $m_{\pi\pi}$ distribution and the fit result.

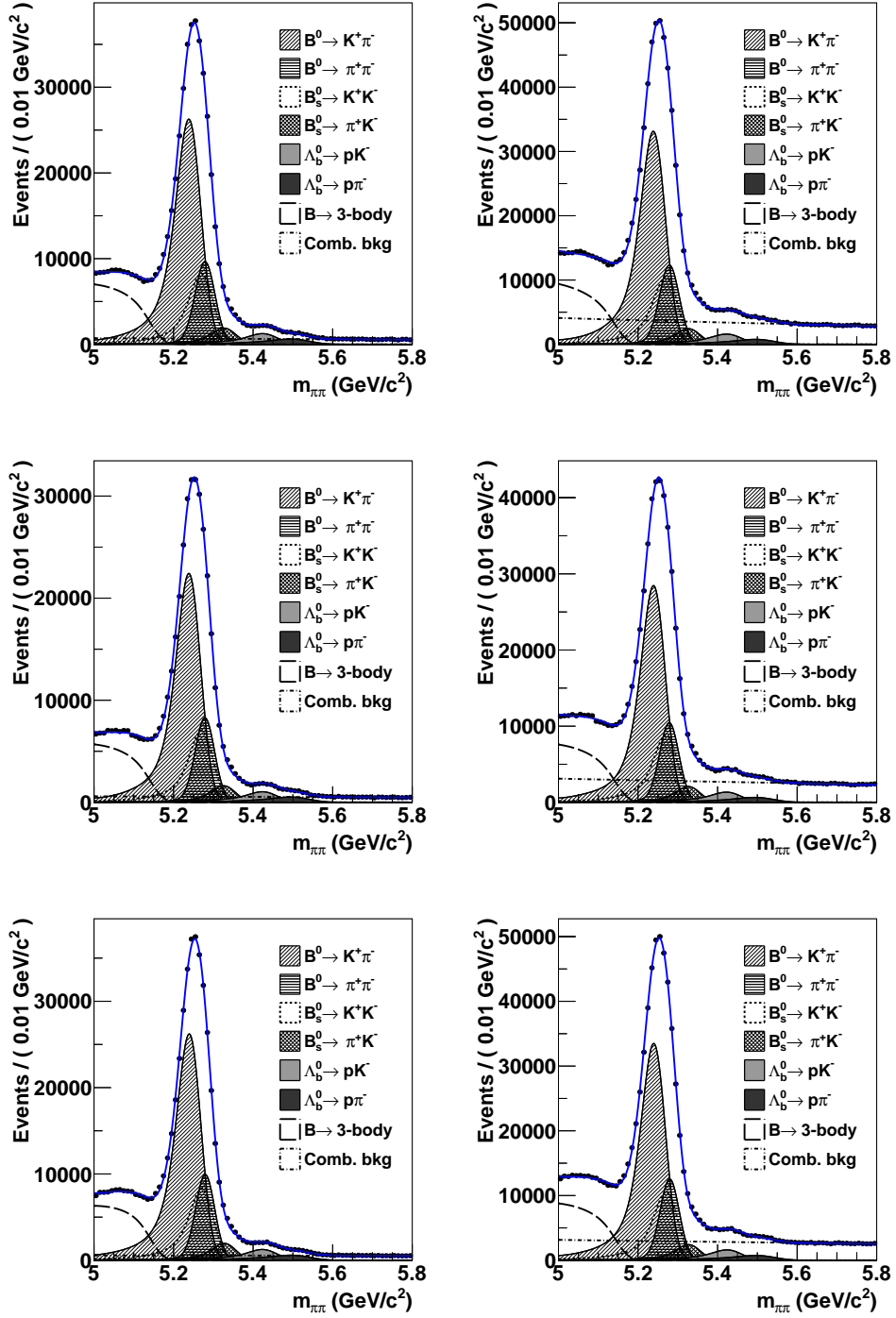


Figure A.1: Distribution of invariant mass under the $\pi^+\pi^-$ final state hypothesis for the events surviving the BDT requirements corresponding to (left) $BDT_{\pi^+\pi^-}$ and (right) $BDT_{K^+K^-}$. From top to bottom: 2015-16, 2017, 2018 sample. The result of the best fit used to extract the $B_{(s)}^0 \rightarrow h^+h^-$ weights using the *sPlot* technique is overlaid on the data points. The fitting model and the choice of relative fractions for the various $B_{(s)}^0 \rightarrow h^+h^-$ decays is explained in the text.

Appendix B

First measurement of $|V_{cb}|$ with $B_s^0 \rightarrow D_s^{(*)-} \mu^+ \nu$ decays

B.1 Lattice data for $B_s^0 \rightarrow D_s^- \mu^+ \nu_\mu$ decays

The HPQCD collaboration presented first calculations of the form-factor function $f_+(q^2)$ (see Eq. (1.102)) in the full q^2 spectrum in Ref. [62]. The function, shown in Fig. B.1, is given in terms of a slightly different parametrisation than that used in this Thesis (see the paper for more details), providing the set of parameters and their covariance.

The HPQCD results are reproduced by generating 1000 $f_+(q^2)$ functions by sampling the parameters reported in Ref. [62], taking into account their covariance. For each function, a histogram of 10M entries is generated and fit with the CLN parametrisations presented in Sect. 1.4. From these fits, the values of $\rho^2(D_s)$ and $\mathcal{G}(0)$ are determined. The mean and width of the distribution of the fit parameters are taken as central value and uncertainty of each parameter, respectively. The distributions are shown in Fig. B.2.

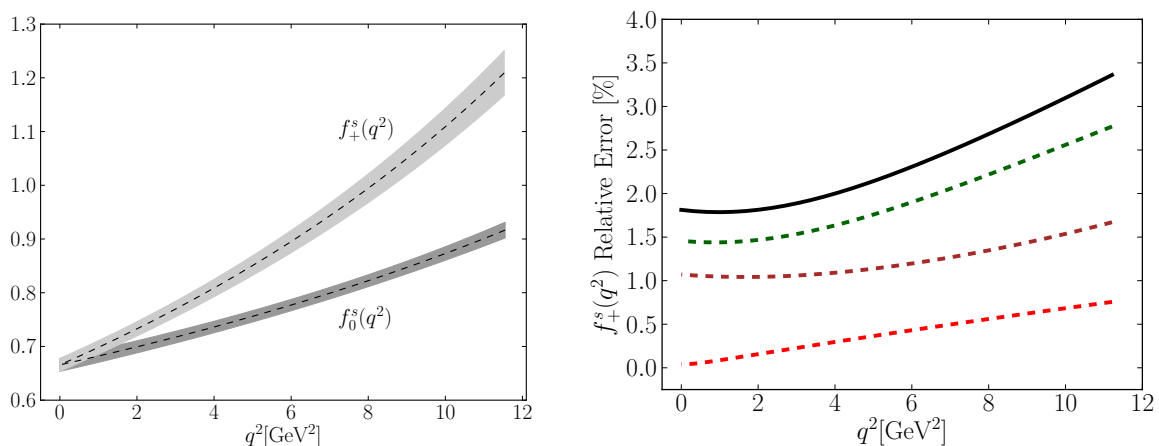


Figure B.1: (Left) The function $f_+(q^2)$ as determined in Ref. [62] (the function $f_0(q^2)$ is the scalar form factors when the muon mass is not neglected). (Right) Error budget for $f_+(q^2)$ as determined in Ref. [62].

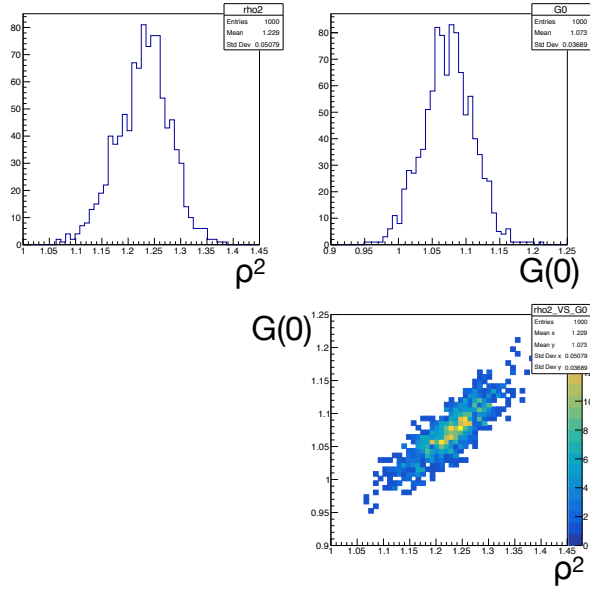


Figure B.2: Distributions of the parameters determined in the CLN parametrisations.

The numerical results are

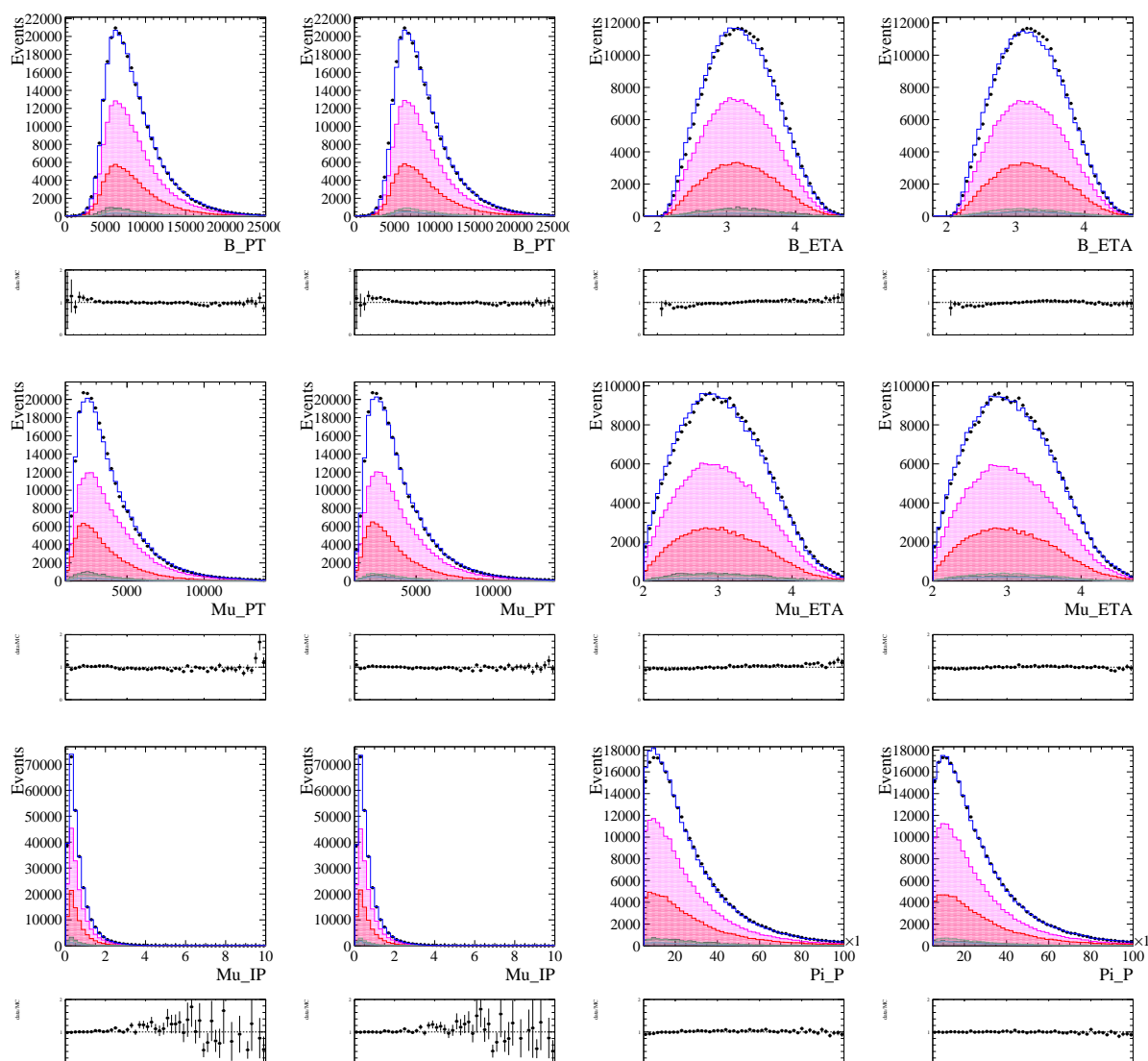
$$\rho^2(D_s) = 1.229 \pm 0.051, \quad (\text{B.1})$$

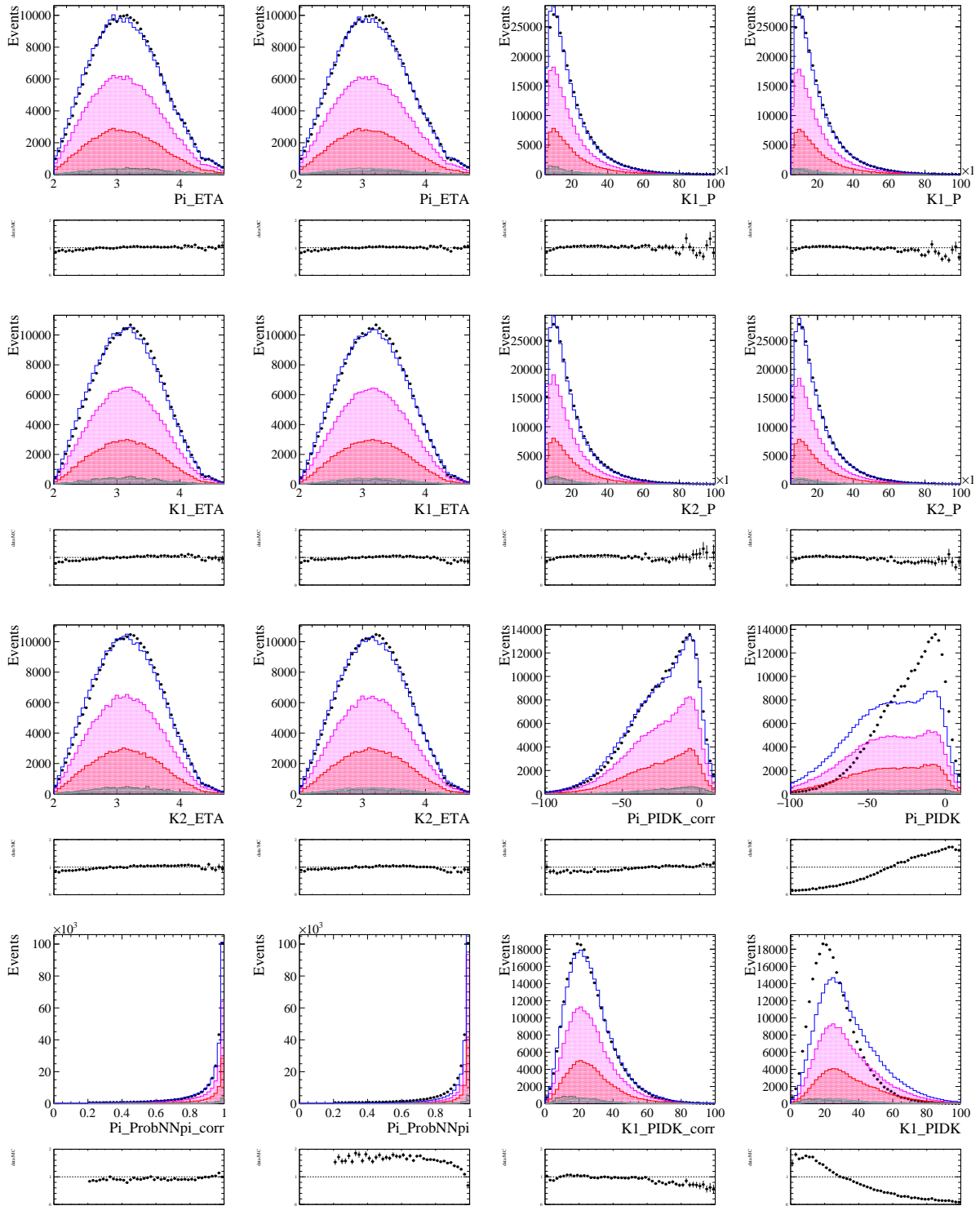
$$\mathcal{G}(0) = 1.073 \pm 0.037. \quad (\text{B.2})$$

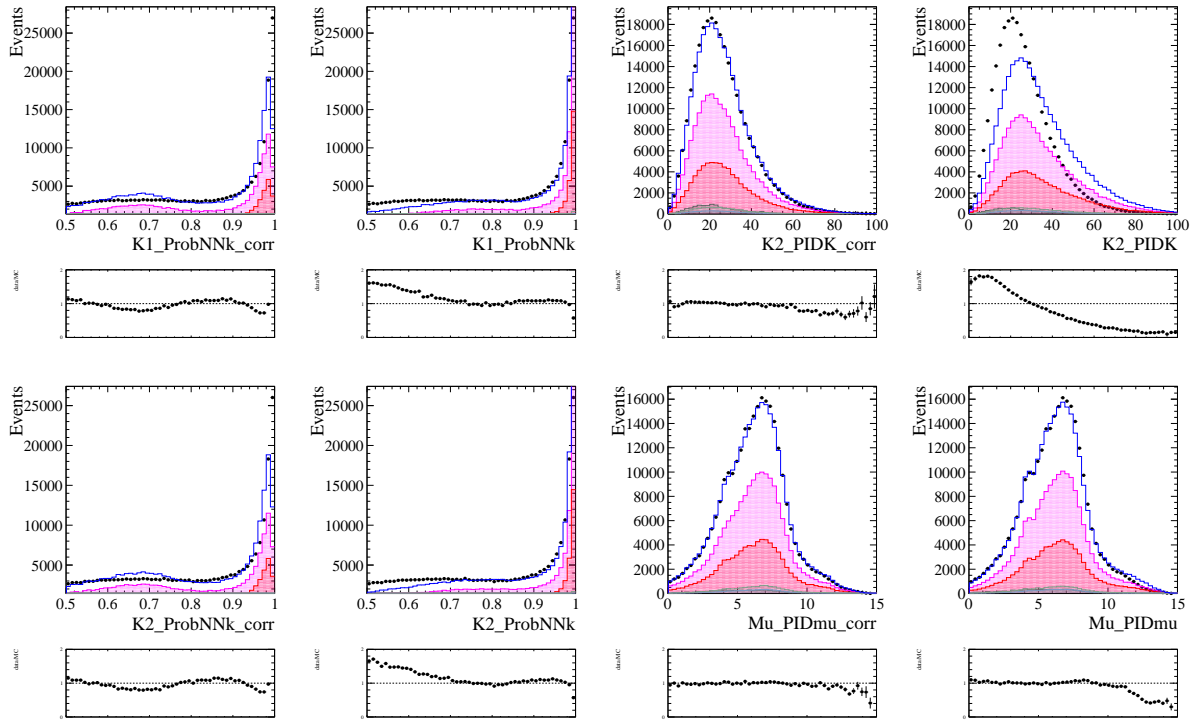
The correlation between the parameters is 0.842. Both values of ρ^2 and $\mathcal{G}(0)$ are in agreement with, and more precise than, an earlier calculation from HPQCD [209].

B.2 Data-simulation comparison

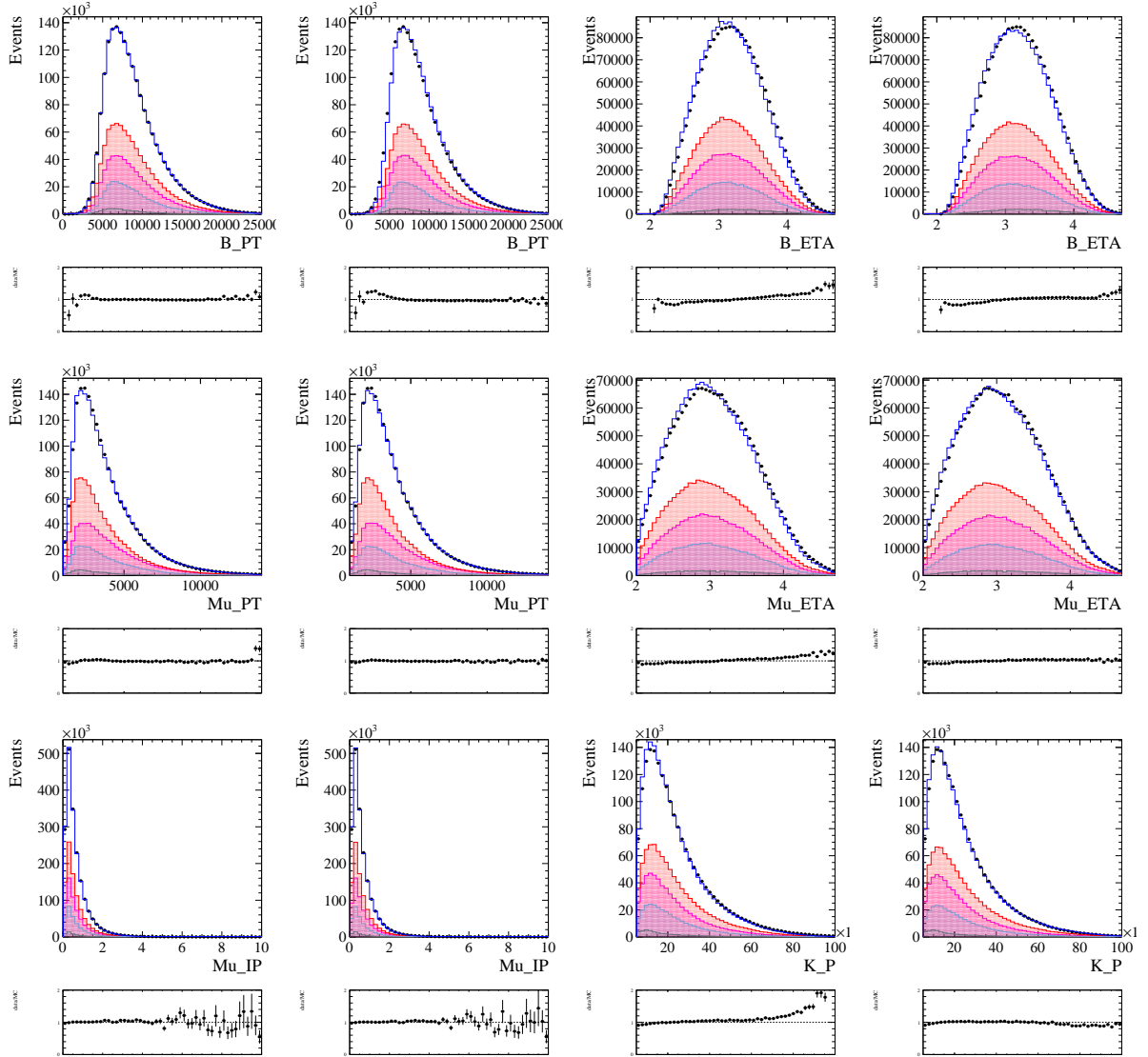
Post-fit data-simulation comparison of several distributions of the $B_s^0 \rightarrow D_s^-(\rightarrow K^+K^-\pi^-)\mu^+\nu_\mu X$ mode. For each pair of plots representing the same variable, in the left one the simulation includes all nominal corrections, while in the right one the simulation does not include any correction. In both cases, the simulation features the composition found from the fit of Sec. 4.3.4. The colours in the plots are the same used throughout the note and correspond to the following components: (magenta) $B_s^0 \rightarrow D_s^-\mu^+\nu_\mu$, (red) $B_s^0 \rightarrow D_s^{*-}\mu^+\nu_\mu$, (light blue) backgrounds from feed-down semimuonic B_s^0 decays and b hadron decays to a doubly charmed final state, (green) backgrounds from cross-feed semileptonic B decays and B_s^0 semitauonic decays and (gray) combinatorial background.

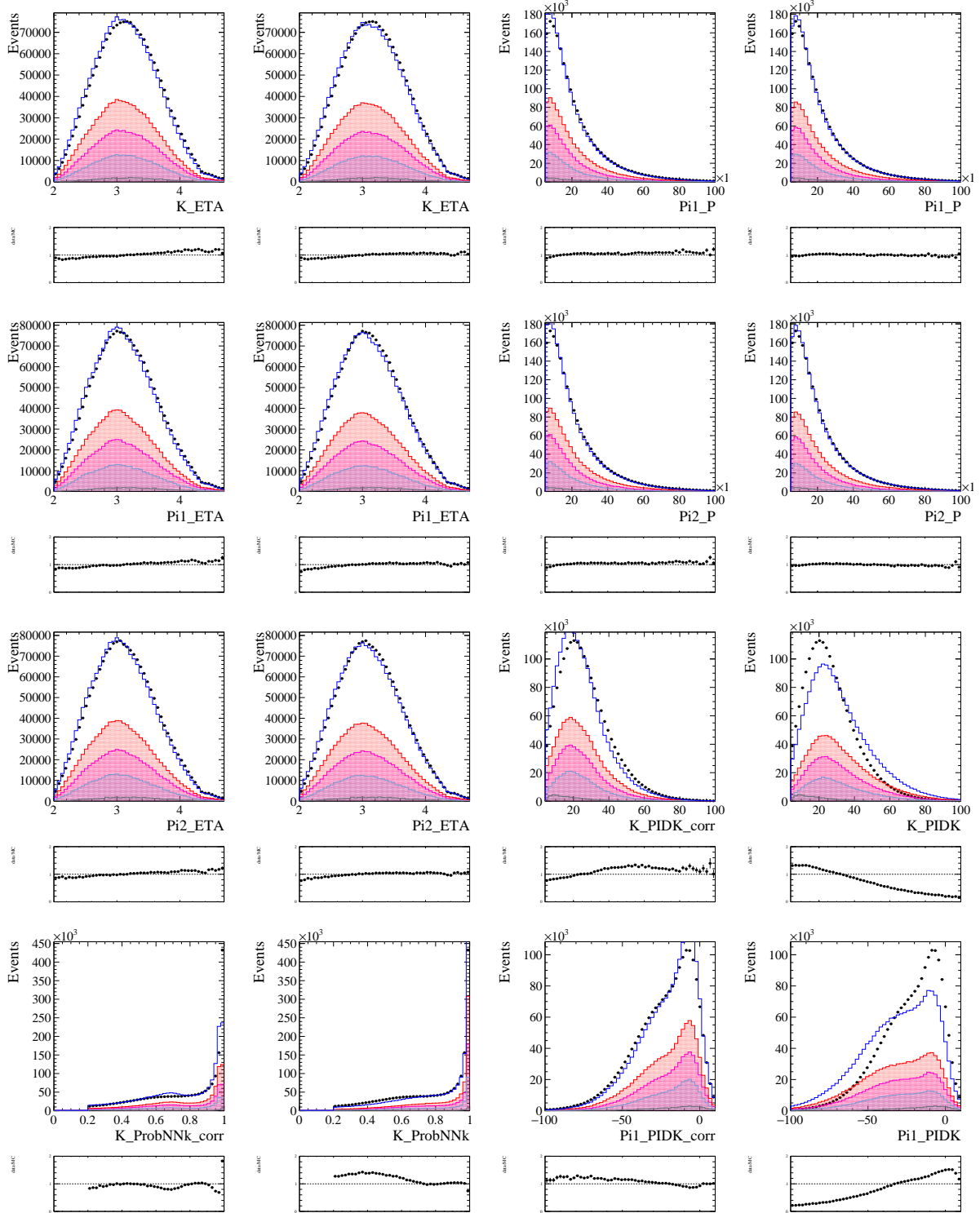


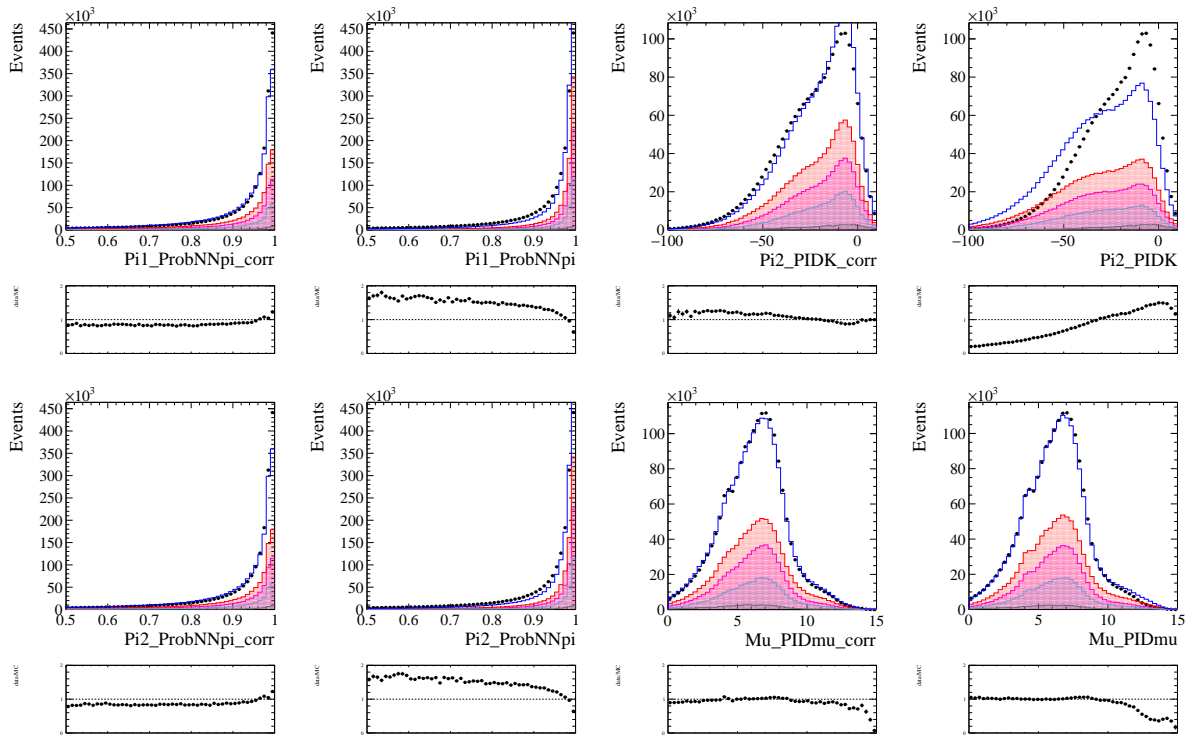




Post-fit data-simulation comparison of several distributions of the $B^0 \rightarrow D^-(\rightarrow K^+\pi^-\pi^-)\mu^+\nu_\mu X$ mode. For each pair of plots representing the same variable, in the left one the simulation includes all nominal corrections, while in the right one the simulation does not include any correction. In both cases, the simulation features the composition found from the fit of Sec. 4.4.2. The colours in the plots are the same used throughout the note and correspond to the following components: (magenta) $B^0 \rightarrow D^-\mu^+\nu_\mu$, (red) $B^0 \rightarrow D^{*-}\mu^+\nu_\mu$, (light blue) sum of B^0 and B^+ backgrounds and (gray) combinatorial background.

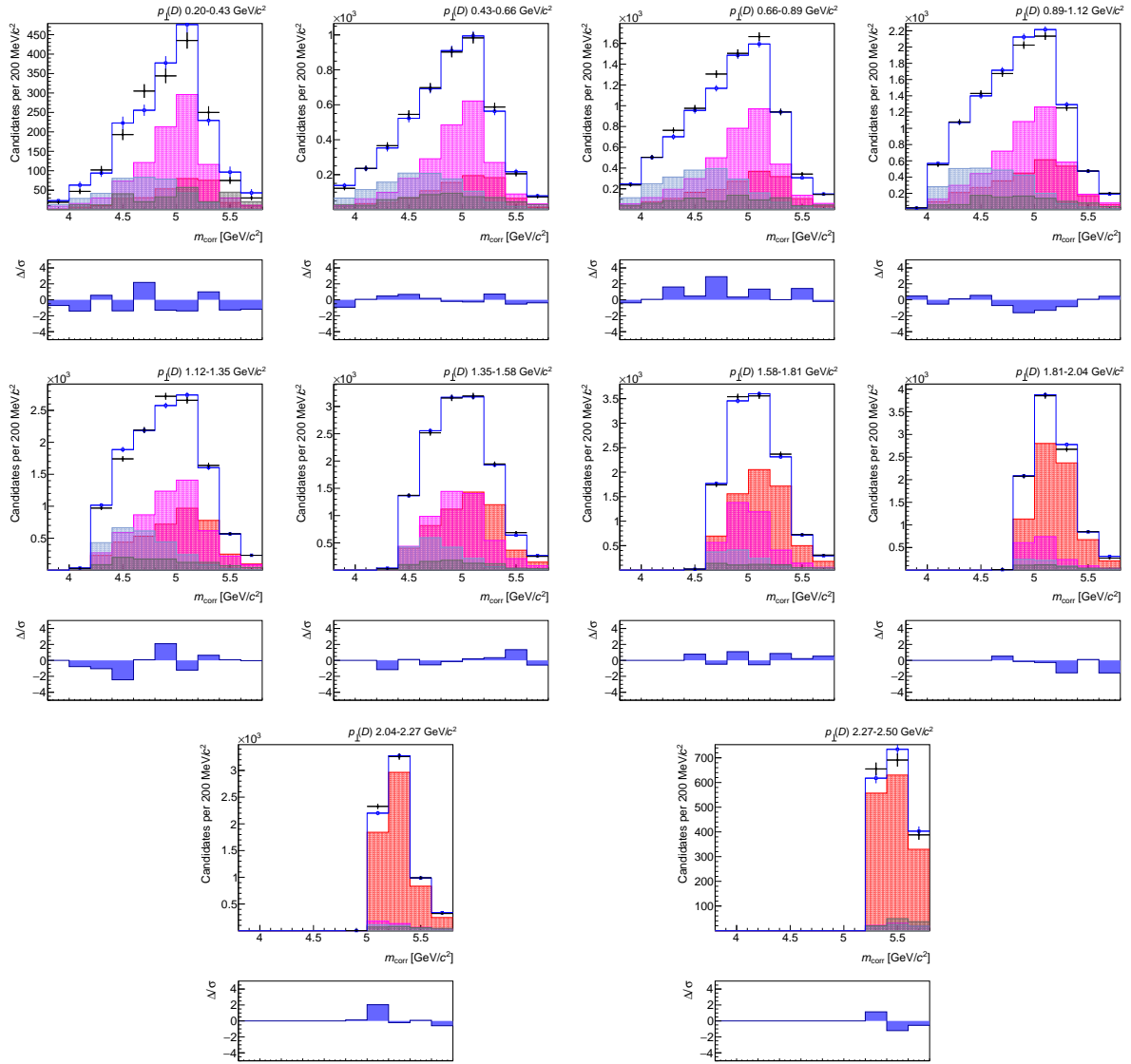




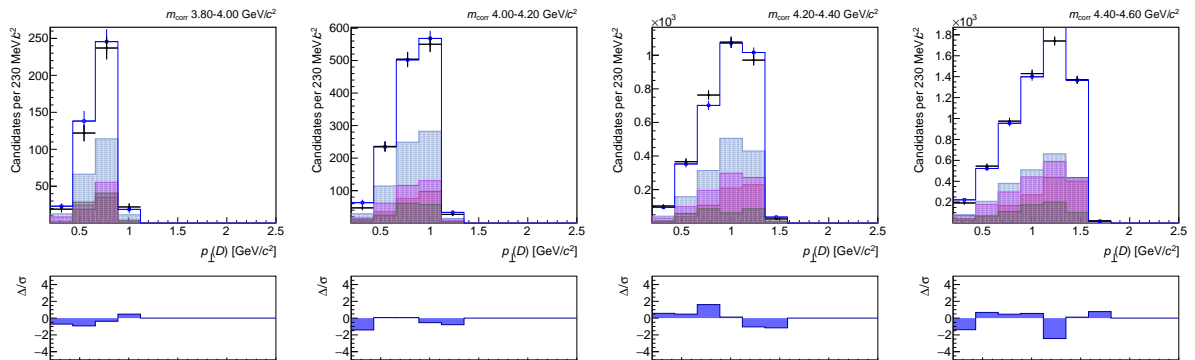


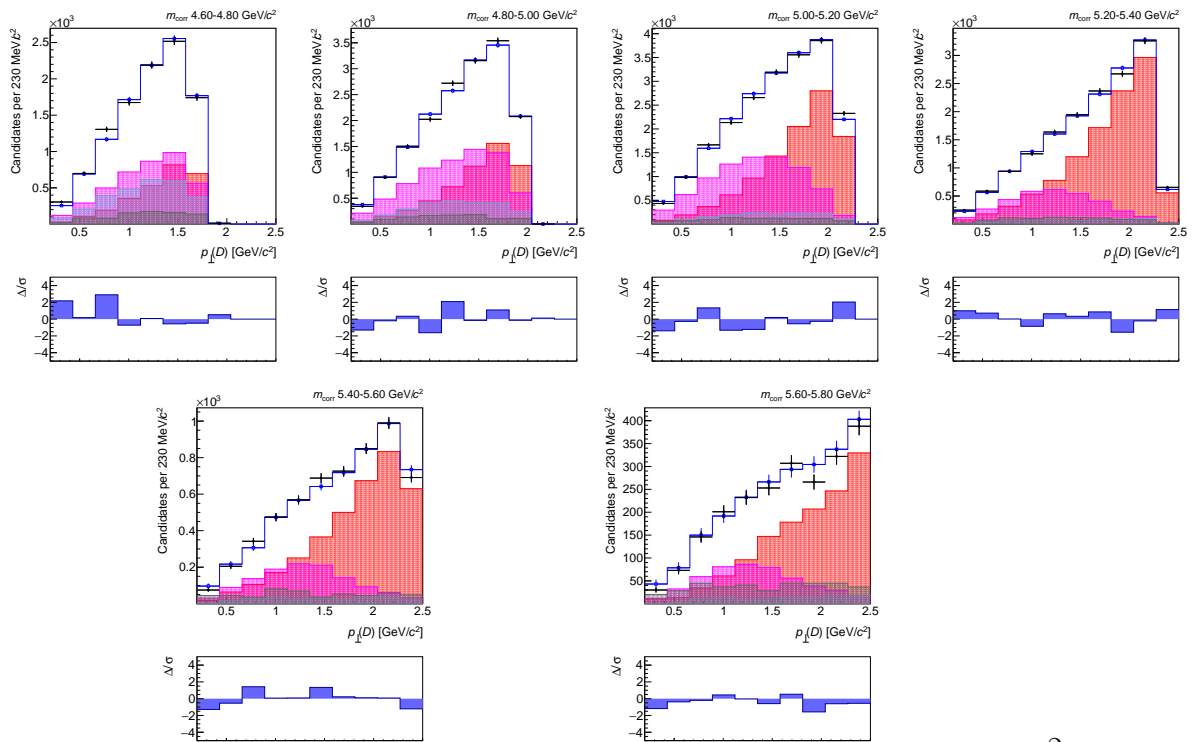
B.3 Reference sample fit projections

Distribution of m_{corr} in bins of p_{\perp} with fit projections overlaid.



Distribution of p_{\perp} in bins of m_{corr} with fit projections overlaid.

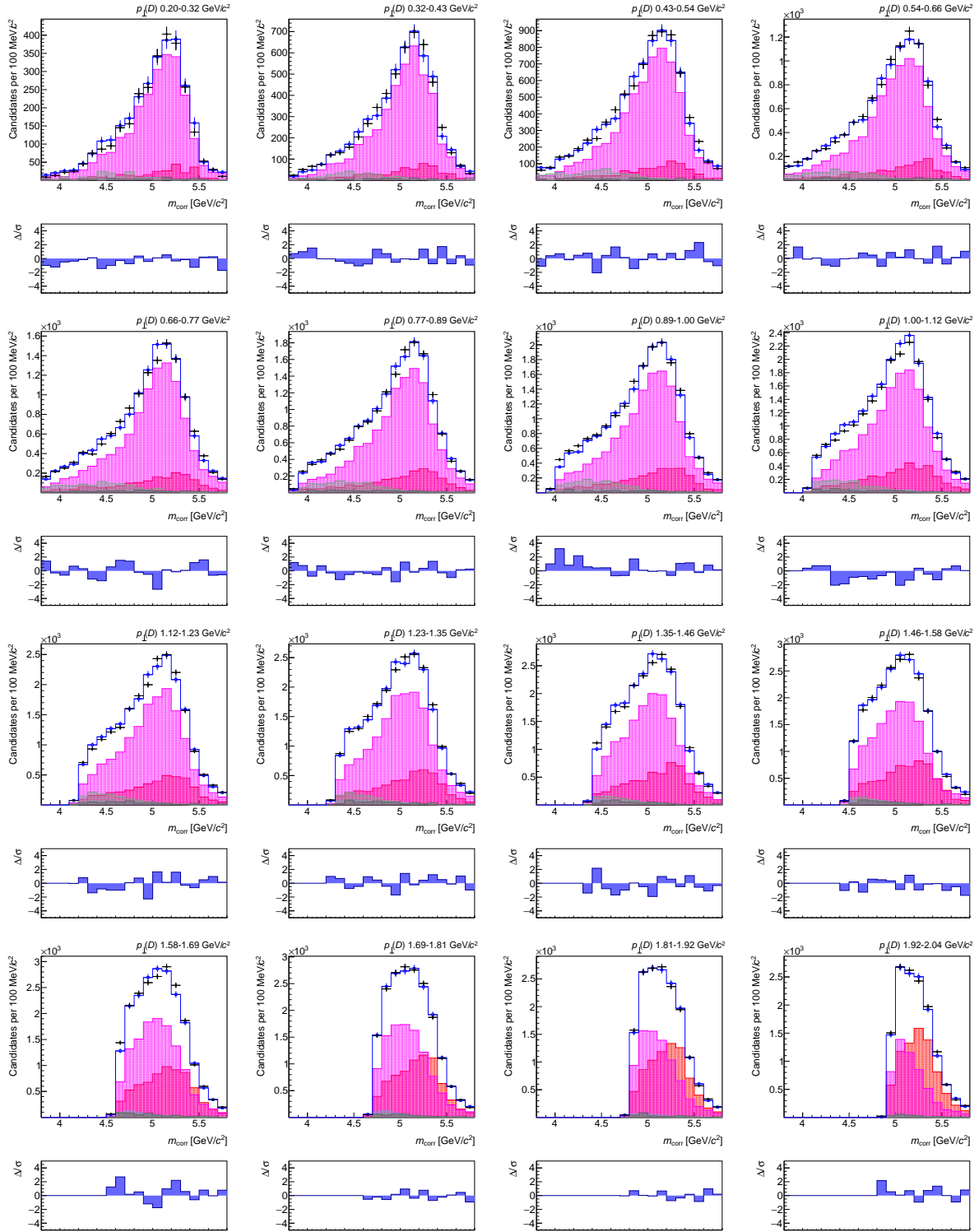


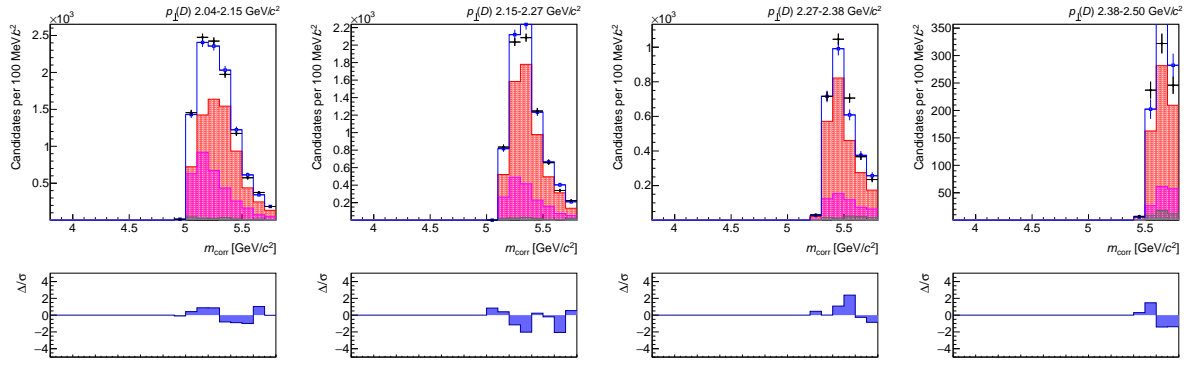


2

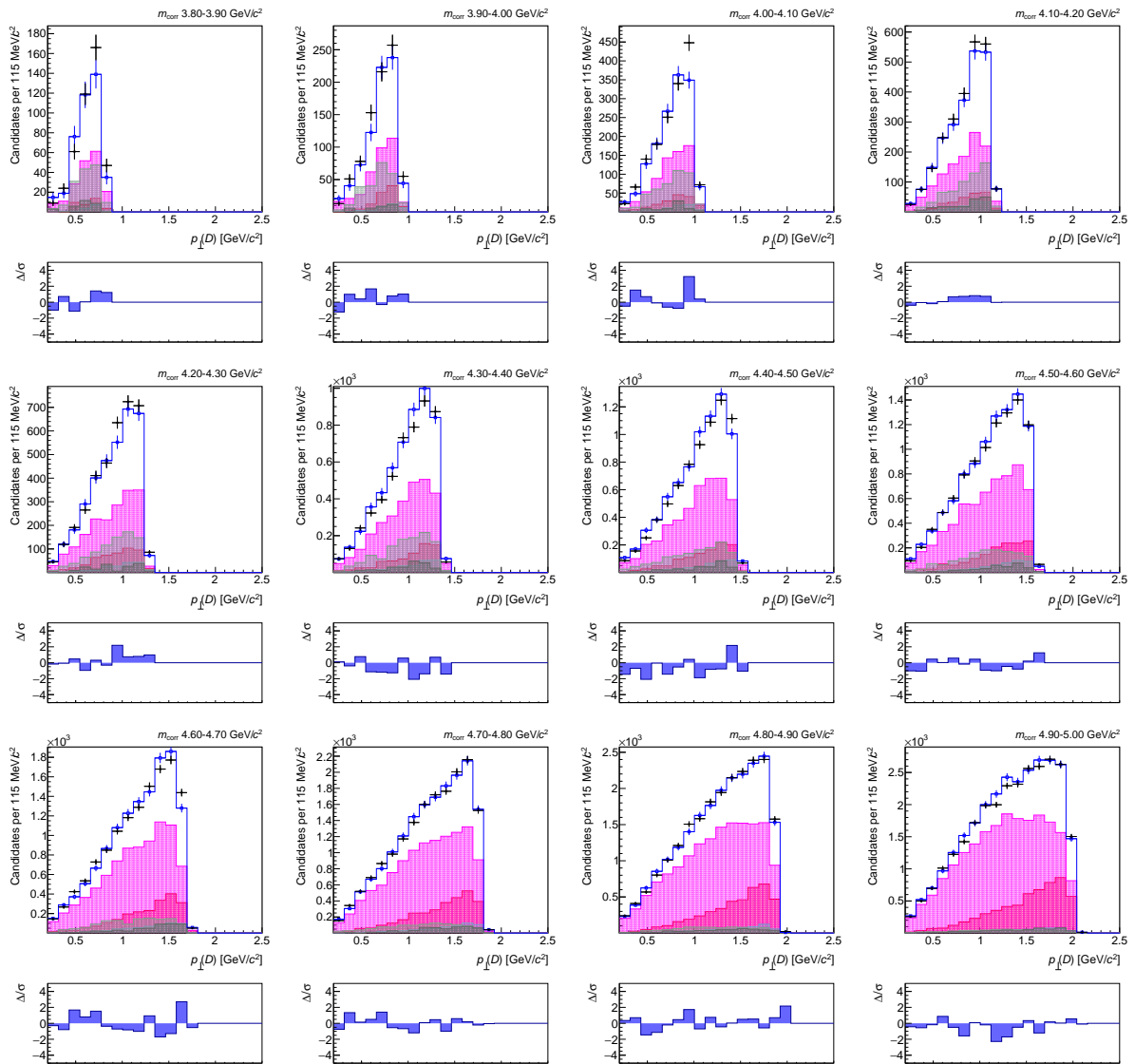
B.4 Signal sample fit projections

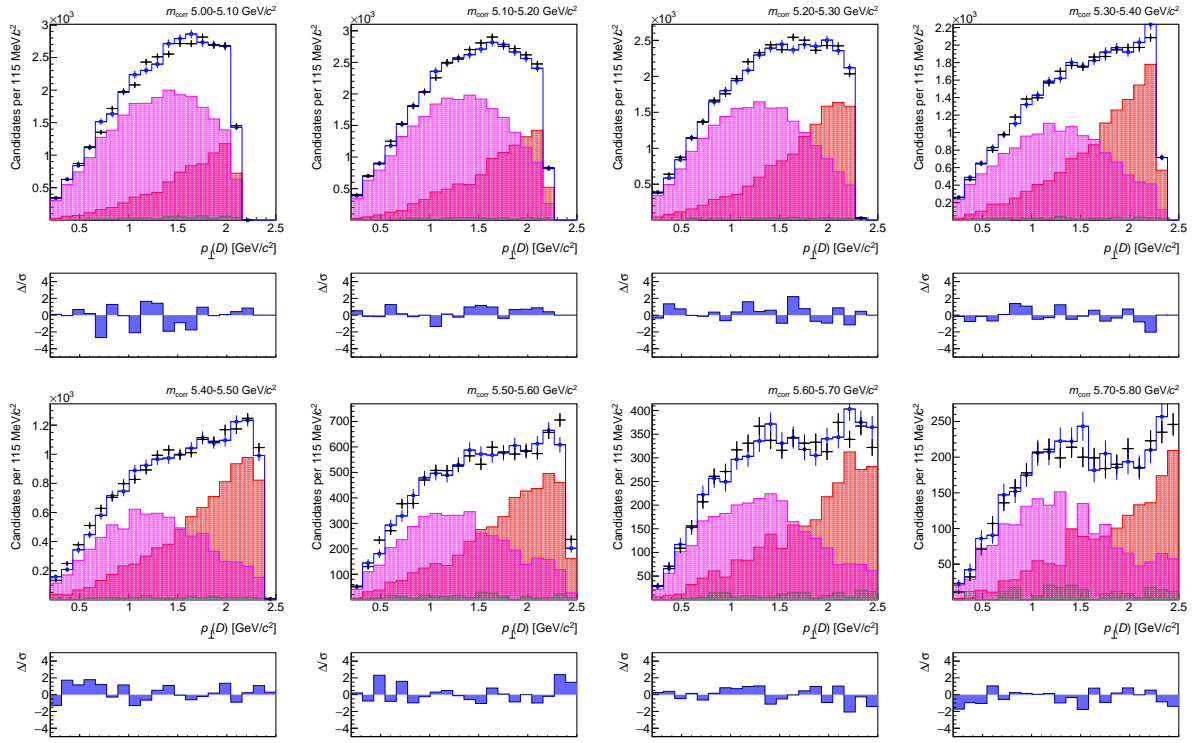
Distribution of m_{corr} in bins of p_{\perp} with fit projections overlaid for the nominal fit in the nominal CLN configuration.



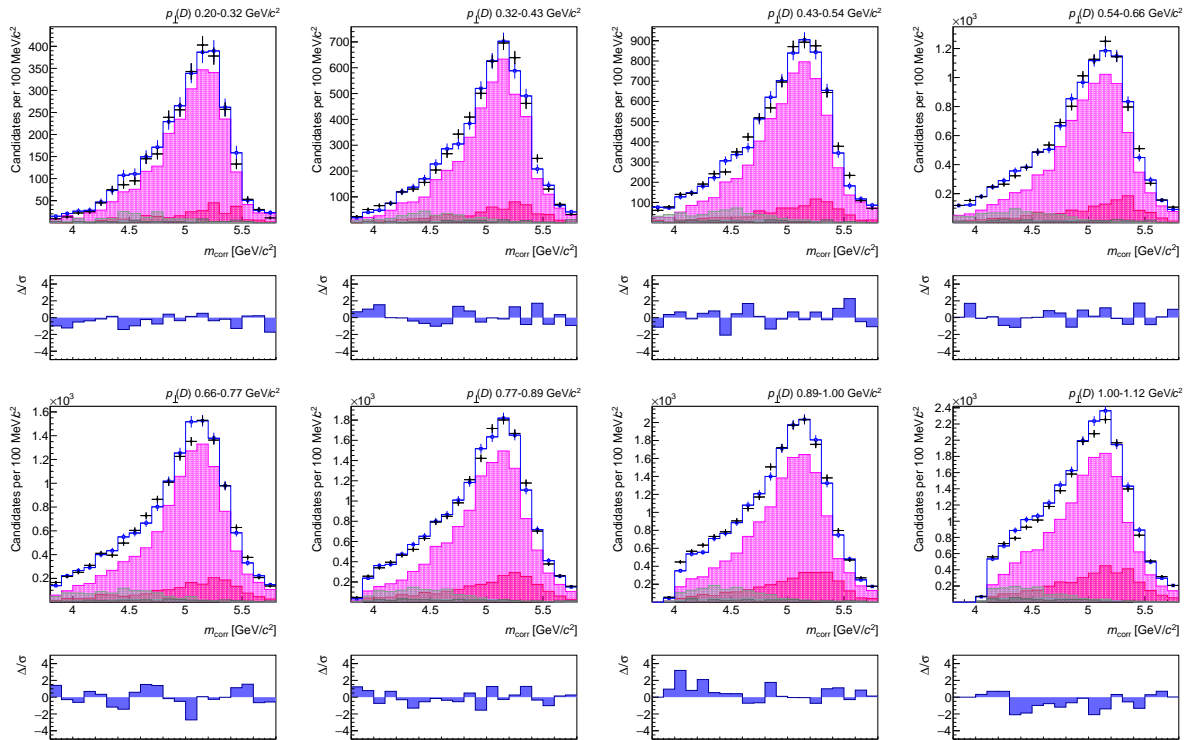


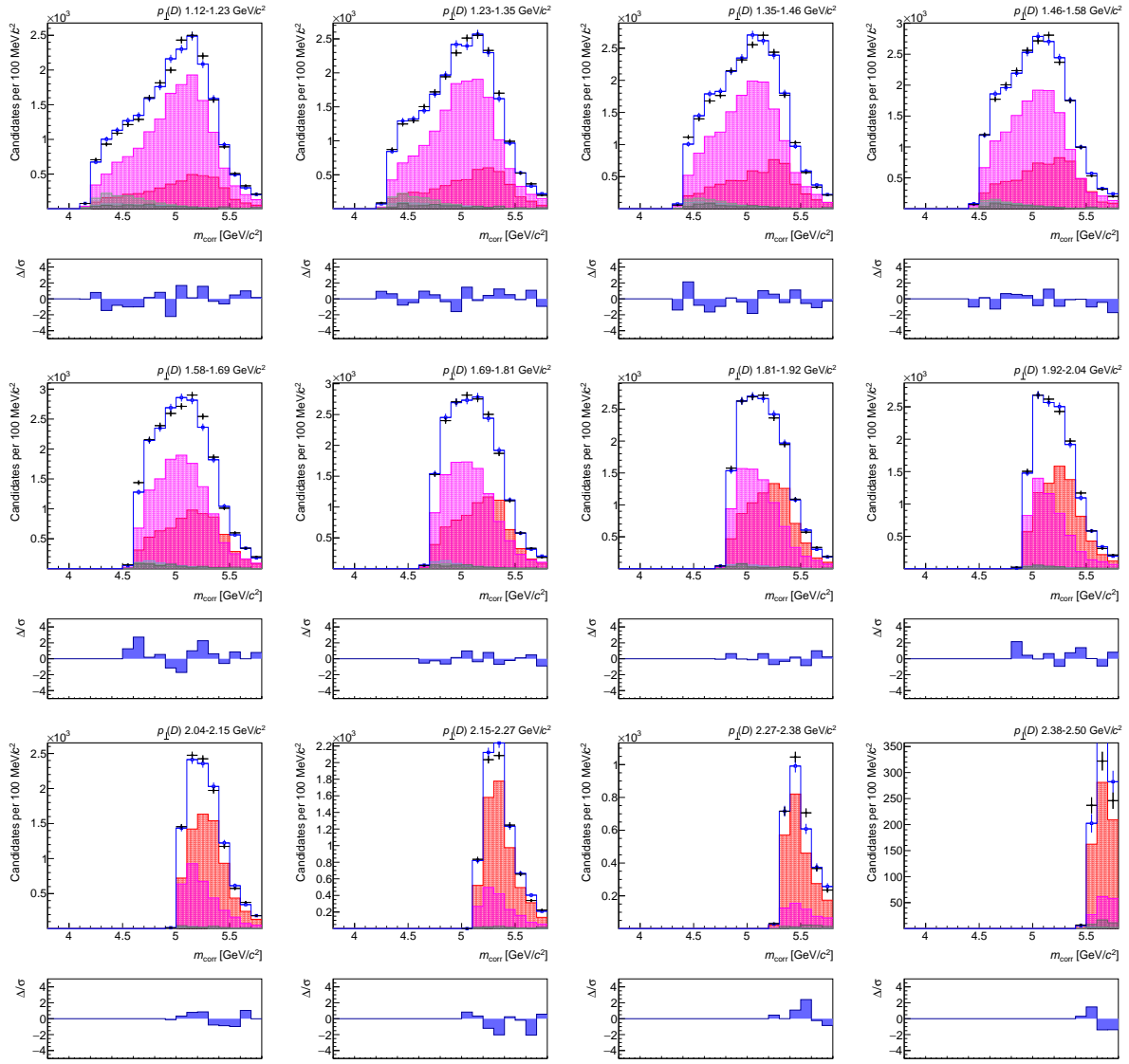
Distribution of p_{\perp} in bins of m_{CORR} with fit projections overlaid for the nominal fit in the nominal CLN configuration.



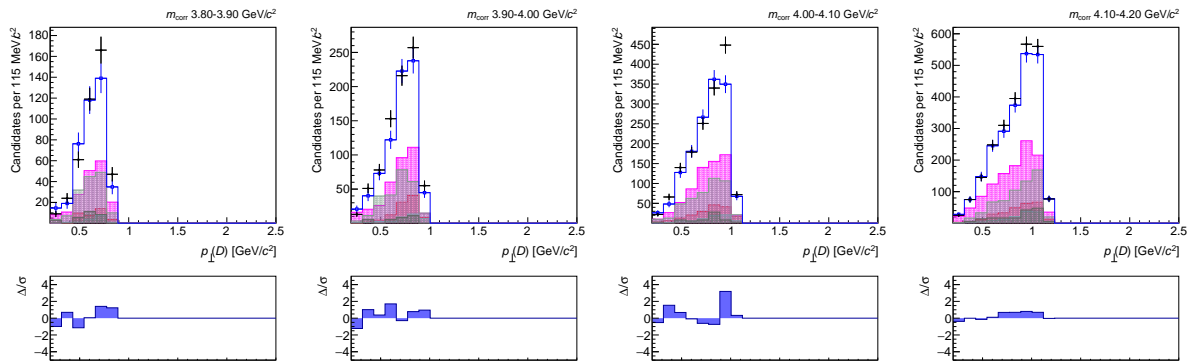


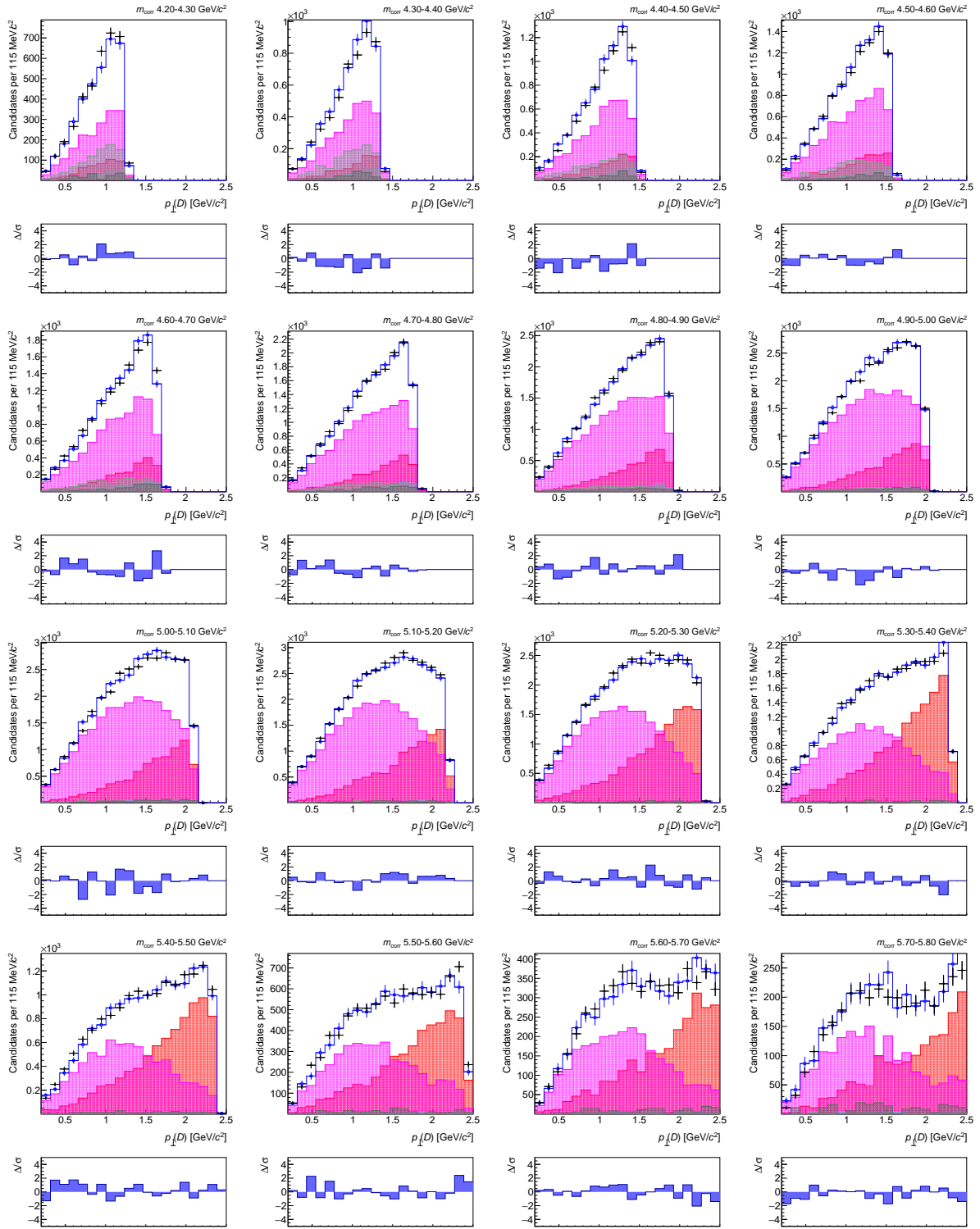
Distribution of m_{corr} in bins of p_{\perp} with fit projections overlaid for the nominal fit in the nominal BGL configuration.





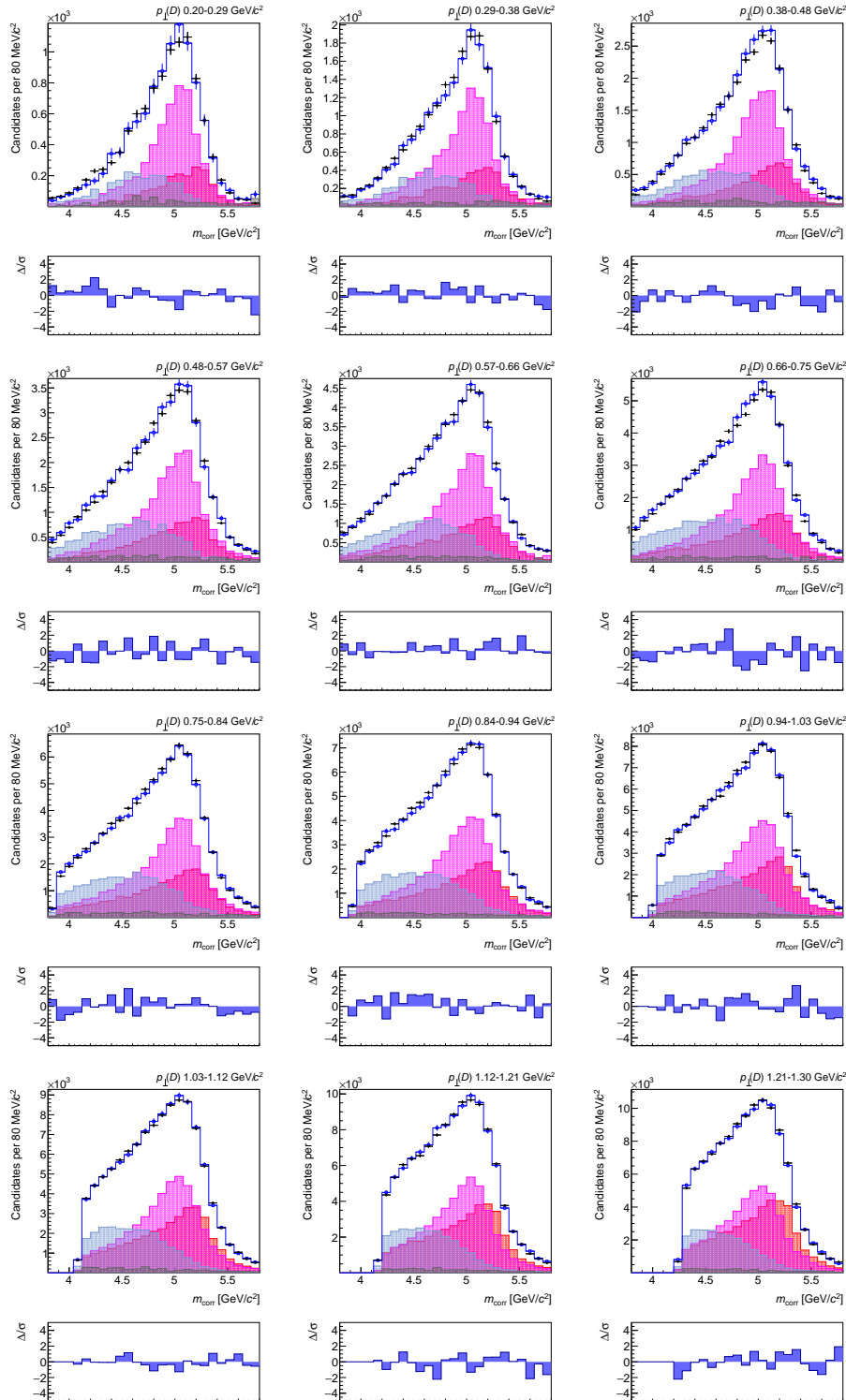
Distribution of p_{\perp} in bins of m_{corr} with fit projections overlaid for the nominal fit in the nominal BGL configuration.

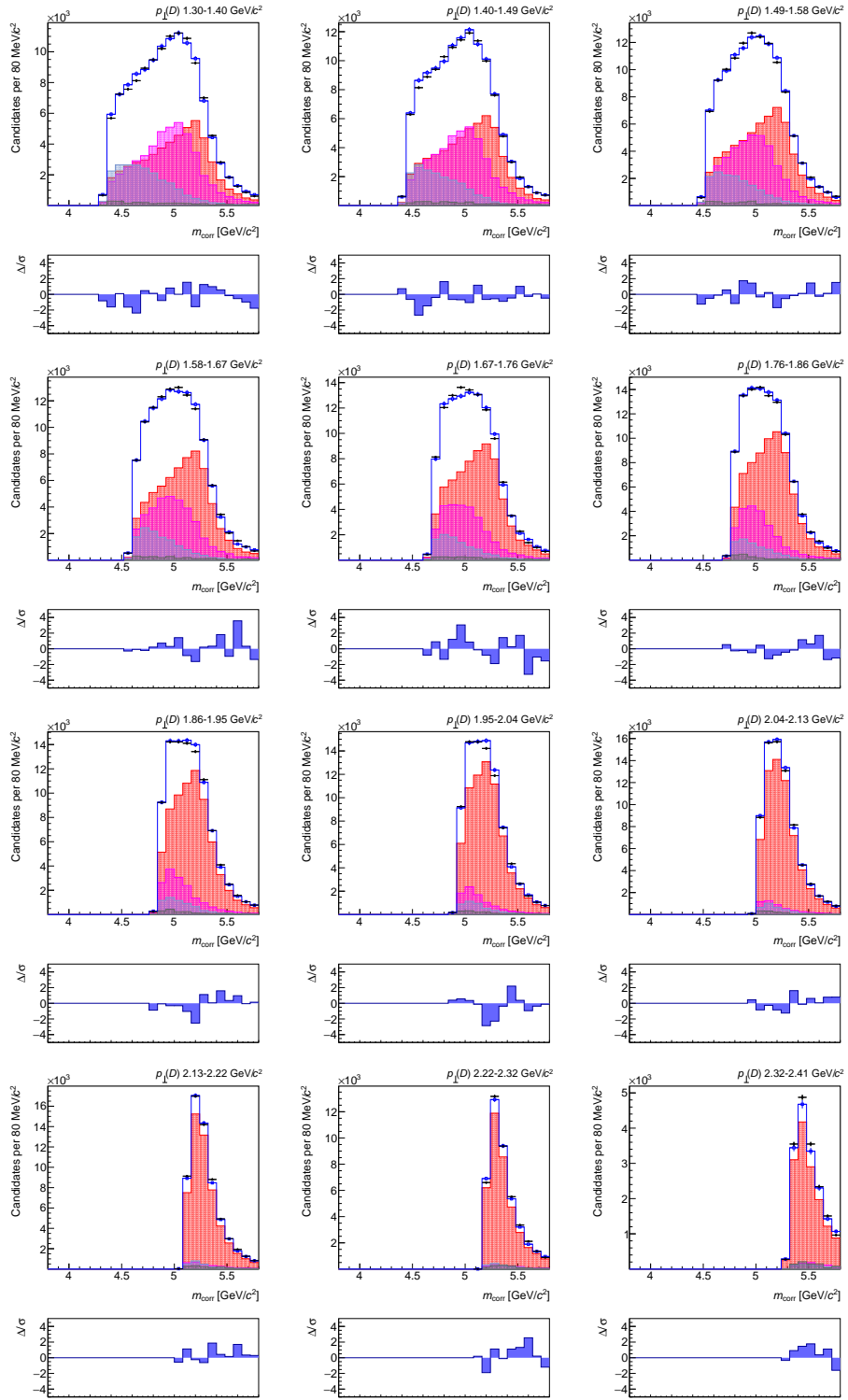




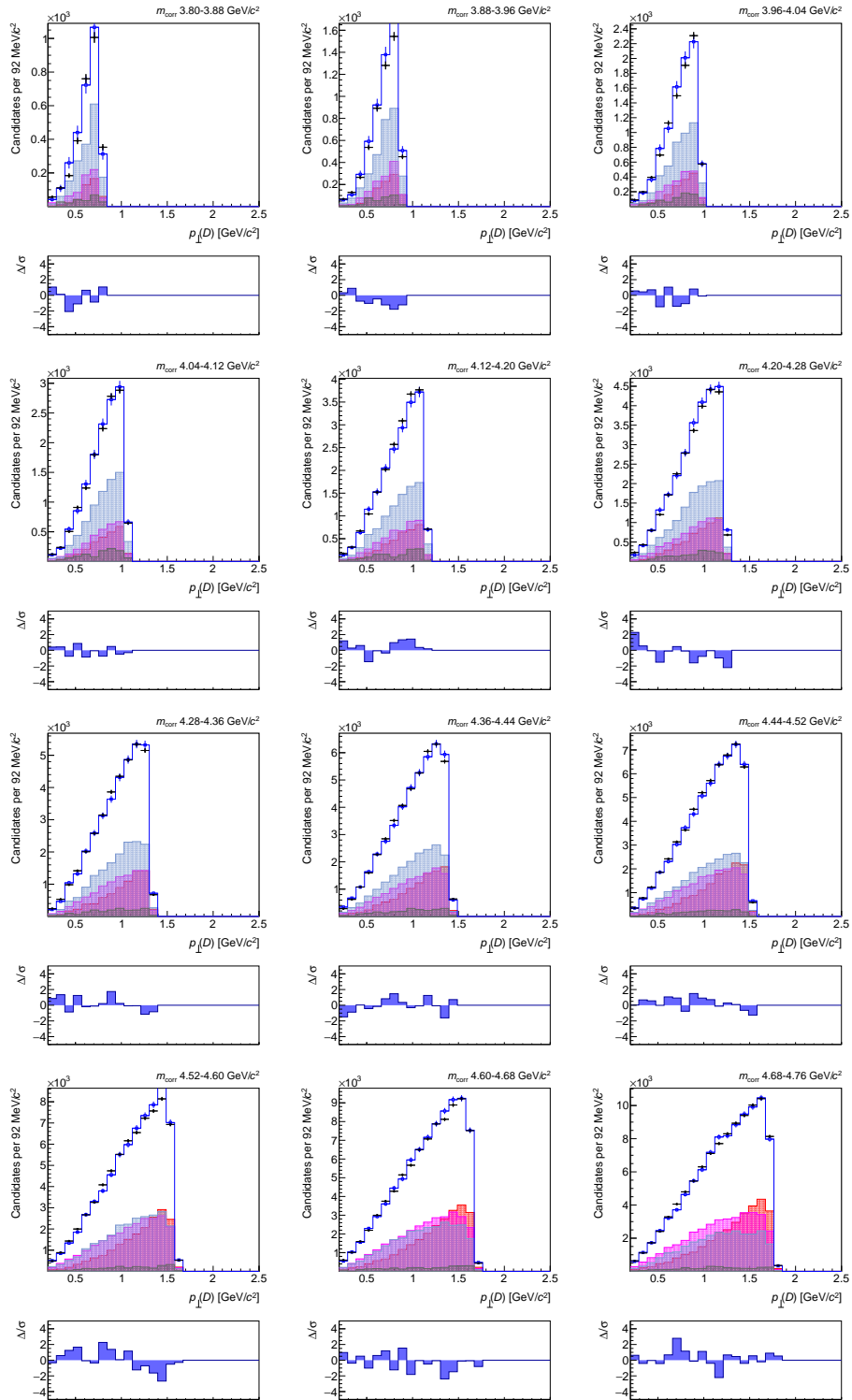
B.5 Control sample fit projections

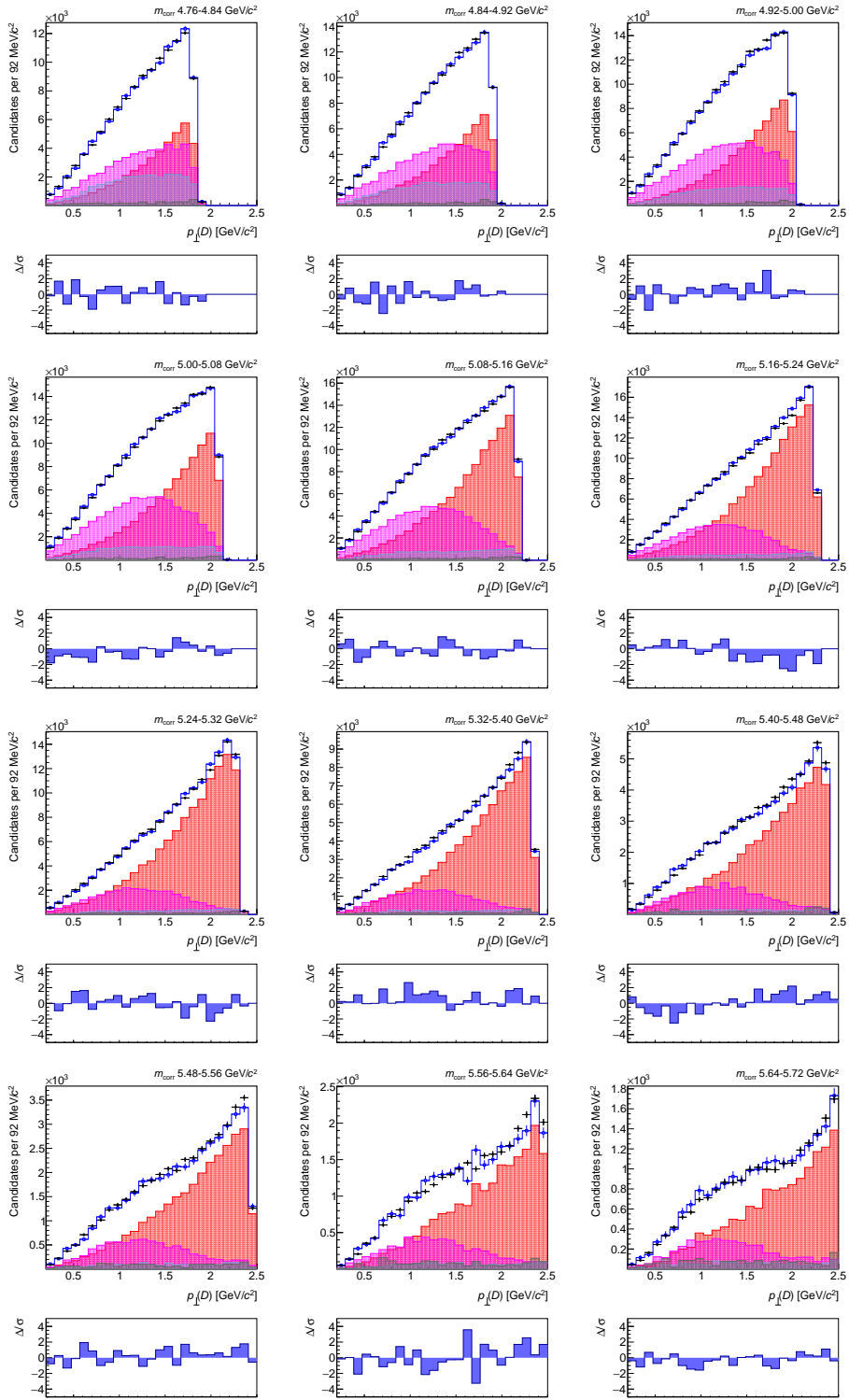
Distribution of m_{corr} in bins of p_{\perp} with fit projections overlaid for the CLN parametrisation.



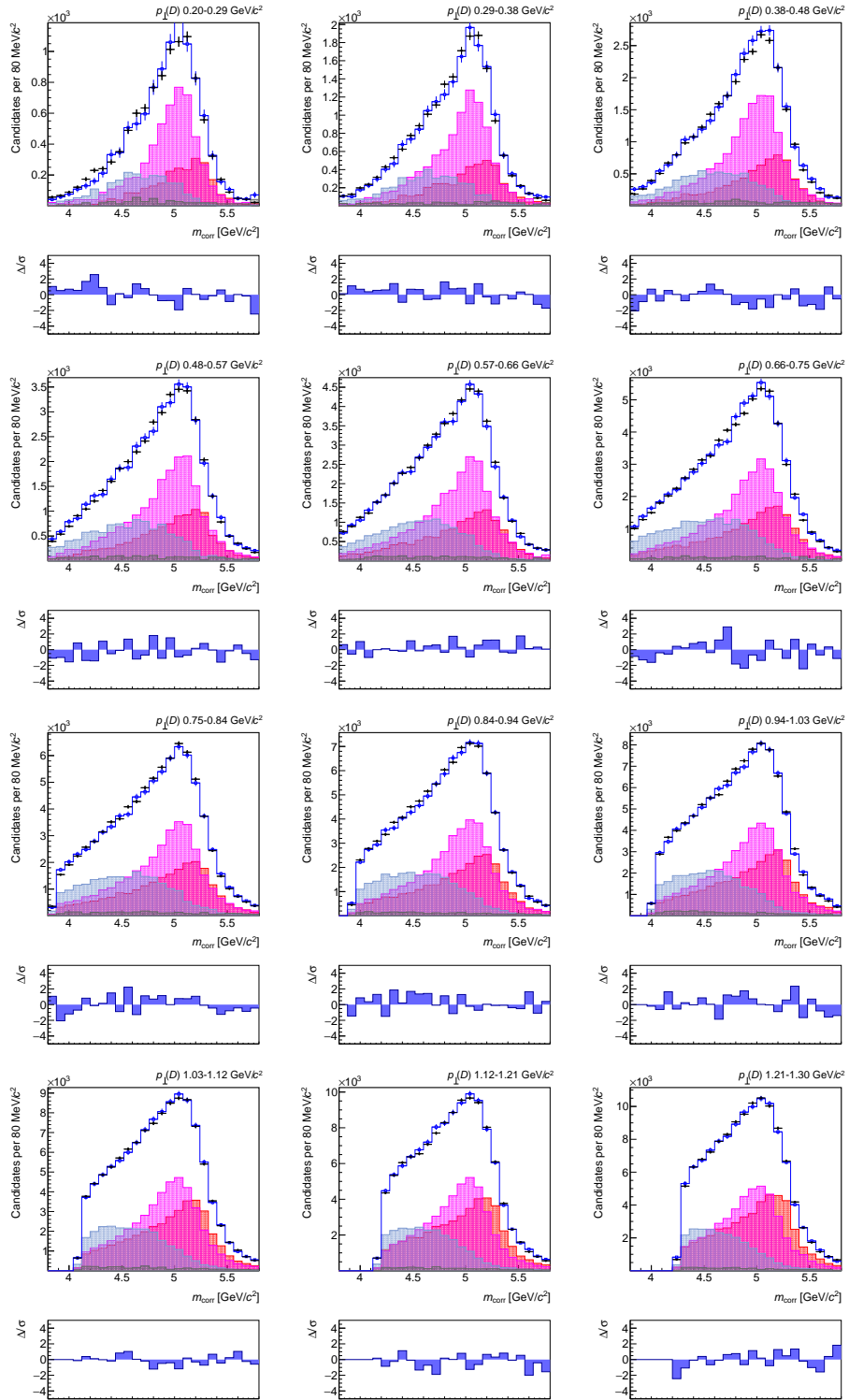


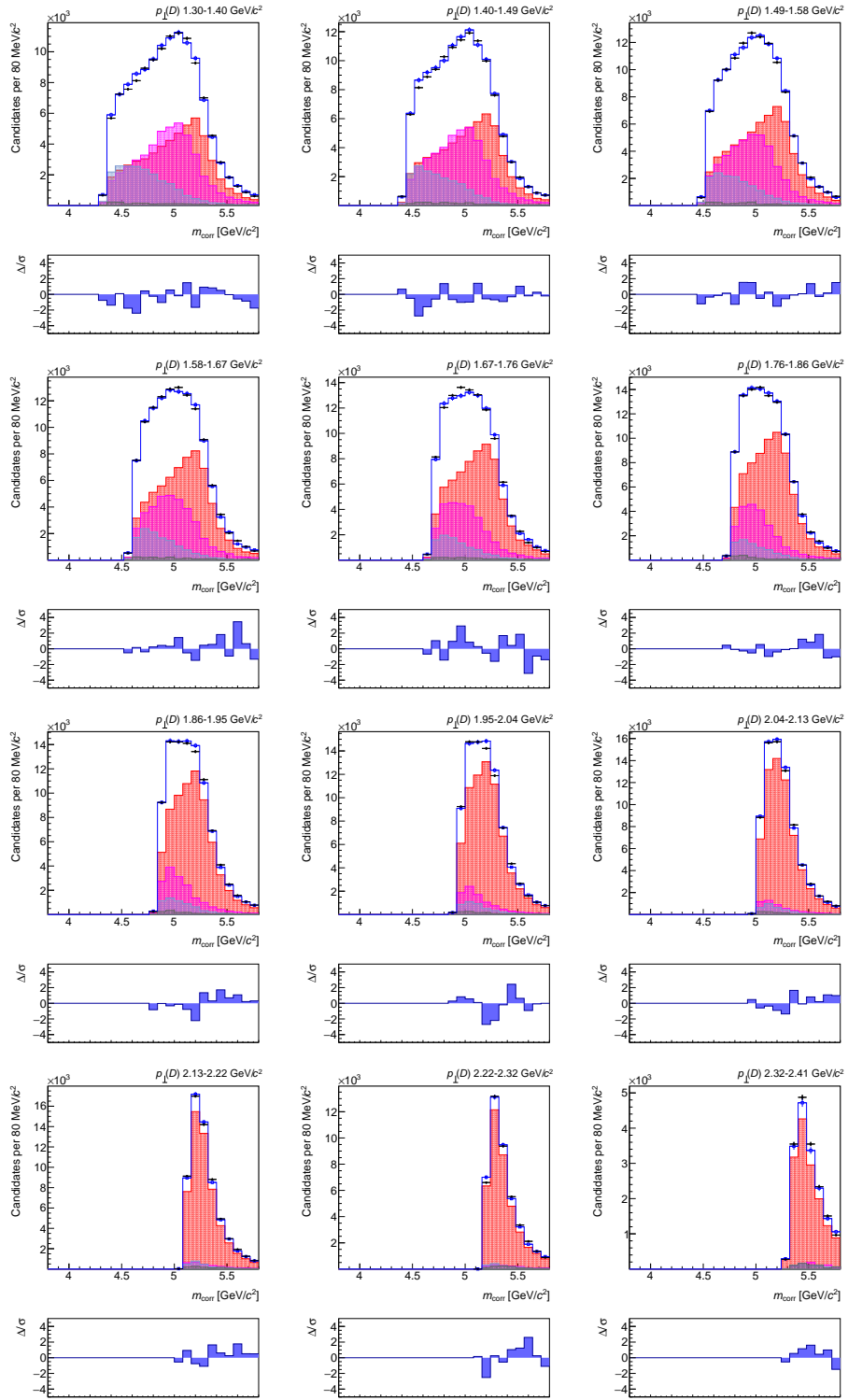
Distribution of p_{\perp} in bins of m_{corr} with fit projections overlaid for the CLN parametrisation.



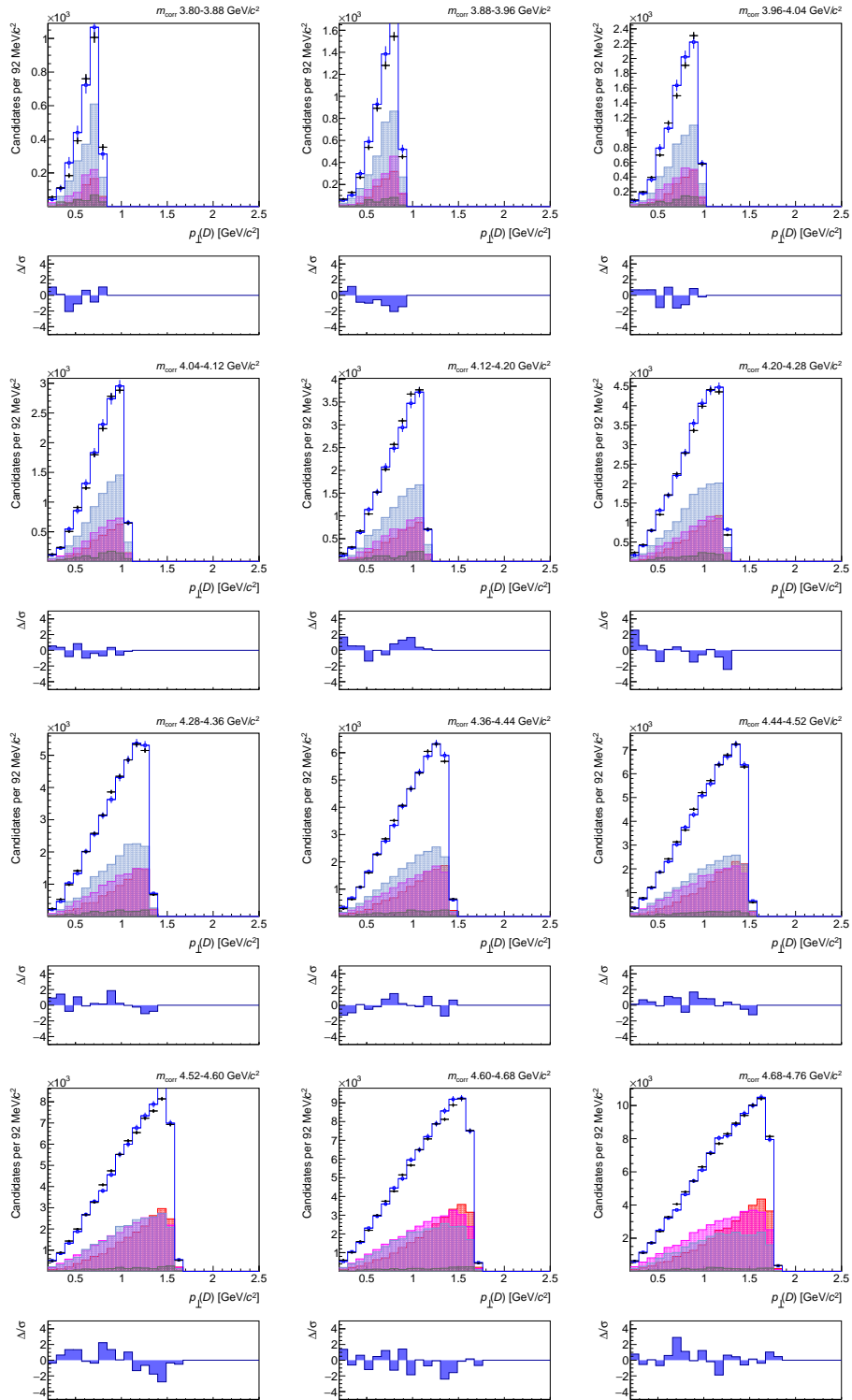


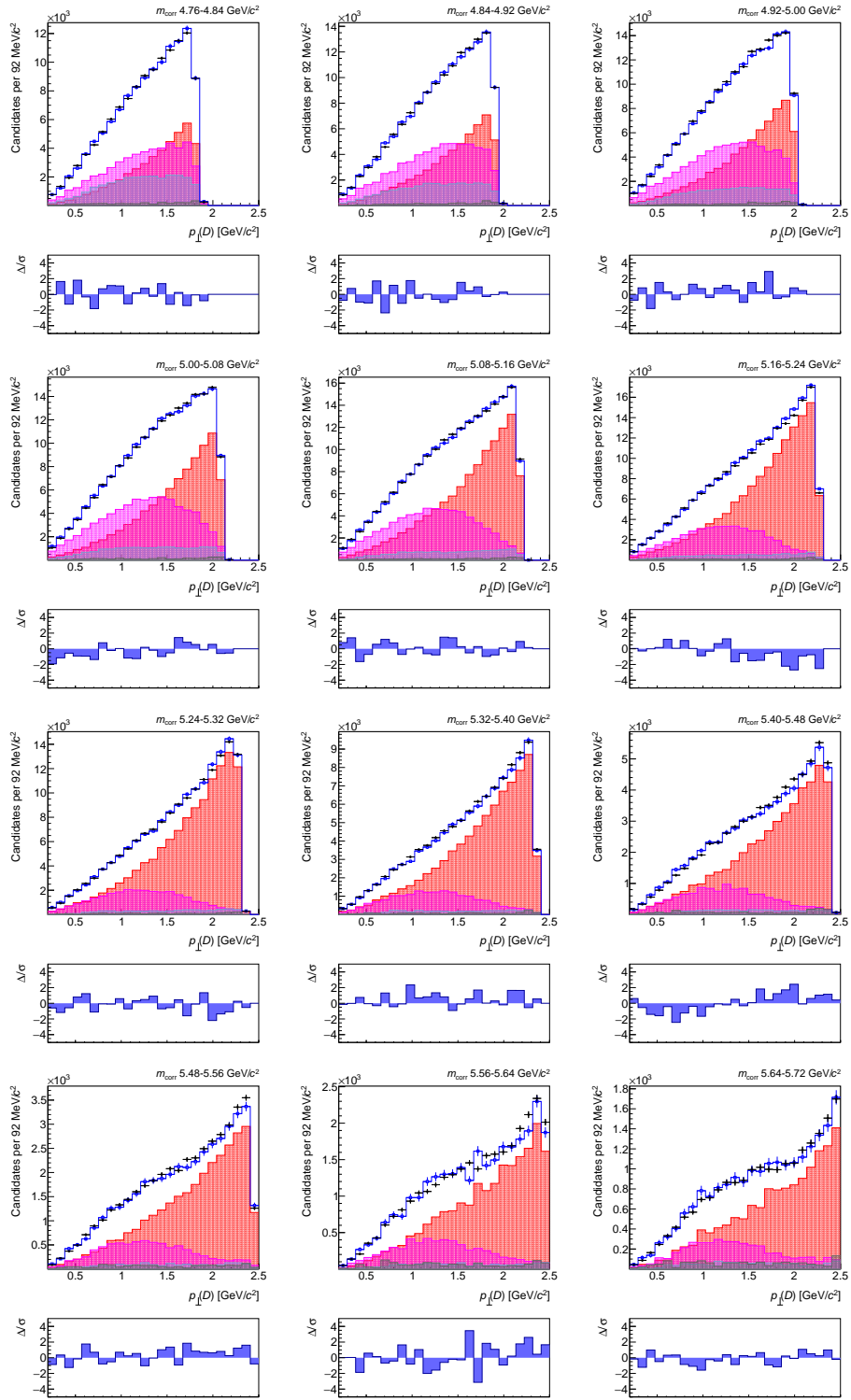
Distribution of m_{corr} in bins of p_{\perp} with fit projections overlaid for the BGL parametrization.





Distribution of p_{\perp} in bins of m_{corr} with fit projections overlaid for the BGL parametrisation.





Bibliography

- [1] P. A. M. Dirac, *The quantum theory of the electron*, Proceedings of the Royal Society of London. Series A, Containing Papers of a Mathematical and Physical Character **117** (1928) 610.
- [2] C. D. Anderson, *The apparent existence of easily deflectable positives*, Science **76** (1932) 238.
- [3] P. A. M. Dirac, *Theory of electrons and positrons*, in *Physics 1922-1941*, pp. 281–327. Elsevier, 2013. doi: 10.1016/B978-1-4831-9745-6.50016-7.
- [4] Particle Data Group, P. A. Zyla *et al.*, *Review of particle physics*, Prog. Theor. Exp. Phys. **2020** (2020) 083C01.
- [5] Particle Data Group, P. A. Zyla *et al.*, *Big-Bang Cosmology*, in Prog. Theor. Exp. Phys. **2020** (2020) 083C01.
- [6] I. Affleck and M. Dine, *A new mechanism for baryogenesis*, Nuclear Physics B **249** (1985) 361.
- [7] D. Toussaint, S. B. Treiman, F. Wilczek, and A. Zee, *Matter-antimatter accounting, thermodynamics, and black-hole radiation*, Phys. Rev. D **19** (1979) 1036.
- [8] S. Weinberg, *Cosmological production of baryons*, Phys. Rev. Lett. **42** (1979) 850.
- [9] V. A. Kuzmin, V. A. Rubakov, and M. E. Shaposhnikov, *On anomalous electroweak baryon-number non-conservation in the early universe*, Physics Letters B **155** (1985) 36.
- [10] M. Fukugita and T. Yanagida, *Baryogenesis without grand unification*, Physics Letters B **174** (1986) 45.
- [11] J. H. Christenson, J. W. Cronin, V. L. Fitch, and R. Turlay, *Evidence for the 2π decay of the K_2^0 meson*, Phys. Rev. Lett. **13** (1964) 138.
- [12] I. J. R. Aitchison and A. J. G. Hey, *Gauge theories in particle physics: A practical introduction. Vol. 1: From relativistic quantum mechanics to QED*, CRC Press, 2012; I. J. R. Aitchison and A. J. G. Hey, *Gauge theories in particle physics: A practical introduction. Vol. 2: Non-Abelian gauge theories: QCD and the electroweak theory*, CRC Press, 2012.
- [13] M. E. Peskin and D. V. Schroeder, *An Introduction to quantum field theory*, Addison-Wesley, Reading, USA, 1995.

- [14] N. Cabibbo, *Unitary symmetry and leptonic decays*, Phys. Rev. Lett. **10** (1963) 531.
- [15] M. Kobayashi and T. Maskawa, *CP-violation in the renormalizable theory of weak interaction*, Prog. Theor. Phys. **49** (1973) 652.
- [16] M. Gell-Mann, *A Schematic Model of Baryons and Mesons*, Phys. Lett. **8** (1964) 214; G. Zweig, *An SU_3 model for strong interaction symmetry and its breaking; Version 1* CERN-TH-401, CERN, Geneva, 1964.
- [17] A. D. Sakharov, *Violation of CP in variance, C asymmetry, and baryon asymmetry of the universe*, Phys. Usp. **34** (1991) 392.
- [18] M. B. Gavela *et al.*, *Standard model CP violation and baryon asymmetry. Part 2: Finite temperature*, Nucl. Phys. **B430** (1994) 382, arXiv:hep-ph/9406289.
- [19] M. B. Gavela, P. Hernandez, J. Orloff, and O. Pène, *Standard model CP violation and baryon asymmetry*, Mod. Phys. Lett. **A9** (1994) 795, arXiv:hep-ph/9312215.
- [20] P. Huet and E. Sather, *Electroweak baryogenesis and standard model CP violation*, Phys. Rev. **D51** (1995) 379, arXiv:hep-ph/9404302.
- [21] R. P. Feynman, *The theory of positrons*, Phys. Rev. **76** (1949) 749.
- [22] A. I. Vainshtein, V. I. Zakharov, and M. A. Shifman, *A possible mechanism for the $\Delta T = 1/2$ rule in nonleptonic decays of strange particles*, ZhETF Pisma Redaktsiiu **22** (1975) 123.
- [23] Heavy Flavor Averaging Group, Y. Amhis *et al.*, *Averages of b-hadron, c-hadron, and τ -lepton properties as of 2018*, Eur. Phys. J. **C81** (2021) 226, arXiv:1909.12524, updated results and plots available at <https://hflav.web.cern.ch>.
- [24] LHCb collaboration, R. Aaij *et al.*, *Observation of CP violation in two-body $B_{(s)}^0$ -meson decays to charged pions and kaons*, JHEP **03** (2021) 075, arXiv:2012.05319.
- [25] LHCb collaboration, *Physics case for an LHCb Upgrade II — Opportunities in flavour physics, and beyond, in the HL-LHC era*, arXiv:1808.08865.
- [26] T. Gershon and V. V. Gligorov, *Cp violation in the b system*, Reports on Progress in Physics **80** (2017) 046201.
- [27] R. A. Bertlmann and A. Zeilinger, eds., *Quantum unspeakables: From Bell to quantum information*, 2002.
- [28] R. A. Bertlmann, A. Bramon, G. Garbarino, and B. C. Hiesmayr, *Violation of a Bell inequality in particle physics experimentally verified?*, Phys. Lett. A **332** (2004) 355, arXiv:quant-ph/0409051.
- [29] LHCb collaboration, R. Aaij *et al.*, *Opposite-side flavour tagging of B mesons at the LHCb experiment*, Eur. Phys. J. **C72** (2012) 2022, arXiv:1202.4979.
- [30] LHCb collaboration, R. Aaij *et al.*, *B flavour tagging using charm decays at the LHCb experiment*, JINST **10** (2015) P10005, arXiv:1507.07892.

- [31] LHCb collaboration, R. Aaij *et al.*, *A new algorithm for identifying the flavour of B_s^0 mesons at LHCb*, JINST **11** (2016) P05010, [arXiv:1602.07252](https://arxiv.org/abs/1602.07252).
- [32] LHCb collaboration, R. Aaij *et al.*, *New algorithms for identifying the flavour of B^0 mesons using pions and protons*, Eur. Phys. J. **C77** (2017) 238, [arXiv:1610.06019](https://arxiv.org/abs/1610.06019).
- [33] R. P. Feynman, R. B. Leighton, M. Sands, and E. Hafner, *The Feynman Lectures on Physics; Vol. I*, vol. 33, AAPT, 1965.
- [34] T. D. Lee and L. Wolfenstein, *Analysis of CP-noninvariant interactions and the k_1^0, k_2^0 system*, Phys. Rev. **138** (1965) B1490.
- [35] T. D. Lee and C. S. Wu, *Weak interactions (second section) chapter 8: Decays of charged k mesons*, Annual Review of Nuclear Science **16** (1966) 471, [arXiv:https://doi.org/10.1146/annurev.ns.16.120166.002351](https://doi.org/10.1146/annurev.ns.16.120166.002351).
- [36] I. I. Bigi and A. I. Sanda, *CP Violation*, Cambridge University Press, 2 ed., 2009.
- [37] V. Weisskopf and E. P. Wigner, *Calculation of the natural brightness of spectral lines on the basis of Dirac's theory*, Z. Phys. **63** (1930) 54.
- [38] V. Weisskopf and E. Wigner, *Over the natural line width in the radiation of the harmonious oscillator*, Z. Phys. **65** (1930) 18.
- [39] M. Thomson, *Modern Particle Physics*, Cambridge University Press, 2013.
- [40] P. W. Higgs, *Broken symmetries, massless particles and gauge fields*, Phys. Lett. **12** (1964) 132; P. W. Higgs, *Broken symmetries and the masses of gauge bosons*, Phys. Rev. Lett. **13** (1964) 508.
- [41] G. S. Guralnik, C. R. Hagen, and T. W. B. Kibble, *Global conservation laws and massless particles*, Phys. Rev. Lett. **13** (1964) 585.
- [42] F. Englert and R. Brout, *Broken symmetry and the mass of gauge vector mesons*, Phys. Rev. Lett. **13** (1964) 321.
- [43] P. W. Anderson, *Plasmons, gauge invariance, and mass*, Phys. Rev. **130** (1963) 439.
- [44] J. Goldstone, *Field Theories with Superconductor Solutions*, Nuovo Cim. **19** (1961) 154.
- [45] Y. Nir, *CP violation in meson decays*, in *Les Houches Summer School on Theoretical Physics: Session 84: Particle Physics Beyond the Standard Model*, 79–145, 2006, [arXiv:hep-ph/0510413](https://arxiv.org/abs/hep-ph/0510413).
- [46] T. Jubb, M. Kirk, A. Lenz, and G. Tetlalmatzi-Xolocotzi, *On the ultimate precision of meson mixing observables*, Nuclear Physics B **915** (2017) 431–453; M. Artuso, G. Borissov, and A. Lenz, *Cp violation in the b_s^0 system*, 2019.
- [47] C. Jarlskog, *Commutator of the quark mass matrices in the standard electroweak model and a measure of maximal CP nonconservation*, Phys. Rev. Lett. **55** (1985) 1039.

- [48] L. Wolfenstein, *Parametrization of the kobayashi-maskawa matrix*, Phys. Rev. Lett. **51** (1983) 1945.
- [49] UTfit collaboration, M. Bona *et al.*, *The unitarity triangle fit in the standard model and hadronic parameters from lattice QCD: A reappraisal after the measurements of Δm_s and $BR(B \rightarrow \tau\nu_\tau)$* , JHEP **10** (2006) 081, arXiv:hep-ph/0606167, updated results and plots available at <http://www.utfit.org/>.
- [50] LHCb collaboration, R. Aaij *et al.*, *Search for CP violation in $\Lambda_b^0 \rightarrow pK^-$ and $\Lambda_b^0 \rightarrow p\pi^-$ decays*, Phys. Lett. **B784** (2018) 101, arXiv:1807.06544.
- [51] LHCb Collaboration, B. Adeva *et al.*, *Road map for selected key measurements from LHCb*, arXiv:0912.4179.
- [52] R. Fleischer, *New strategies to extract β and γ from $B^0 \rightarrow \pi^+\pi^-$ and $B_s^0 \rightarrow K^+K^-$* , Physics Letters B **459** (1999) 306–320.
- [53] R. Fleischer, *$B_{s,d} \rightarrow \pi\pi, \pi K, KK$: Status and Prospects*, Eur. Phys. J. C **52** (2007) 267, arXiv:0705.1121.
- [54] LHCb collaboration, R. Aaij *et al.*, *Determination of γ and $-2\beta_s$ from charmless two-body decays of beauty mesons*, Phys. Lett. **B739** (2015) 1, arXiv:1408.4368.
- [55] M. Ciuchini, E. Franco, S. Mishima, and L. Silvestrini, *Testing the Standard Model and Searching for New Physics with $B_d \rightarrow \pi\pi$ and $B_s \rightarrow KK$ Decays*, JHEP **10** (2012) 029, arXiv:1205.4948.
- [56] M. Gronau, O. F. Hernández, D. London, and J. L. Rosner, *Decays of bmesons to two pseudoscalars in broken $su(3)$ symmetry*, Physical Review D **52** (1995) 6356–6373.
- [57] M. Gronau, O. F. Hernández, D. London, and J. L. Rosner, *Electroweak penguin diagrams and two-body decays*, Physical Review D **52** (1995) 6374–6382.
- [58] M. Gronau, O. F. Hernández, D. London, and J. L. Rosner, *Decays of b mesons to two light pseudoscalars*, Phys. Rev. D **50** (1994) 4529.
- [59] N. G. Deshpande and X.-G. He, *Isospin structure of penguins and their consequences in B physics*, Phys. Rev. Lett. **74** (1995) 26, arXiv:hep-ph/9408404, [Erratum: Phys.Rev.Lett. 74, 4099 (1995)].
- [60] I. Caprini, L. Lellouch, and M. Neubert, *Dispersive bounds on the shape of $\bar{B} \rightarrow D^{(*)}\ell\bar{\nu}$ form-factors*, Nucl. Phys. **B530** (1998) 153, arXiv:hep-ph/9712417.
- [61] A. Sirlin, *Large m_W, m_Z behaviour of the $O(\alpha)$ corrections to semileptonic processes mediated by W*, Nucl. Phys. **B196** (1982) 83.
- [62] E. McLean, C. T. H. Davies, J. Koponen, and A. T. Lytle, *$B_s \rightarrow D_s\ell\nu$ Form Factors for the full q^2 range from Lattice QCD with non-perturbatively normalized currents*, arXiv:1906.00701.
- [63] Fermilab Lattice and MILC collaborations, J. A. Bailey *et al.*, *Update of $|V_{cb}|$ from the $\bar{B} \rightarrow D^*\ell\bar{\nu}$ form factor at zero recoil with three-flavor lattice QCD*, Phys. Rev. **D89** (2014) 114504, arXiv:1403.0635.

- [64] LHCb collaboration, A. A. Alves Jr. *et al.*, *The LHCb detector at the LHC*, JINST **3** (2008) S08005.
- [65] LHCb collaboration, R. Aaij *et al.*, *LHCb detector performance*, Int. J. Mod. Phys. **A30** (2015) 1530022, [arXiv:1412.6352](#).
- [66] *LHC Machine*, JINST **3** (2008) S08001.
- [67] M. Ferro-Luzzi, *Proposal for an absolute luminosity determination in colliding beam experiments using vertex detection of beam-gas interactions*, Nucl. Instrum. Meth. **A553** (2005) 388.
- [68] LHCb collaboration, R. Aaij *et al.*, *Measurement of the $B_s^0 \rightarrow \mu^+ \mu^-$ branching fraction and search for $B^0 \rightarrow \mu^+ \mu^-$ decays at the LHCb experiment*, Phys. Rev. Lett. **111** (2013) 101805, [arXiv:1307.5024](#).
- [69] LHCb collaboration, R. Aaij *et al.*, *Measurement of the $B_s^0 \rightarrow \mu^+ \mu^-$ branching fraction and effective lifetime and search for $B^0 \rightarrow \mu^+ \mu^-$ decays*, Phys. Rev. Lett. **118** (2017) 191801, [arXiv:1703.05747](#).
- [70] LHCb collaboration, R. Aaij *et al.*, *Observation of CP violation in $B^\pm \rightarrow DK^\pm$ decays*, Phys. Lett. **B712** (2012) 203, Erratum *ibid.* **B713** (2012) 351, [arXiv:1203.3662](#).
- [71] LHCb collaboration, R. Aaij *et al.*, *First observation of CP violation in the decays of B_s^0 mesons*, Phys. Rev. Lett. **110** (2013) 221601, [arXiv:1304.6173](#).
- [72] LHCb collaboration, R. Aaij *et al.*, *Observation of CP violation in two-body B_s^0 -meson decays to charged pions and kaons*, JHEP **03** (2021) 075, [arXiv:2012.05319](#).
- [73] LHCb collaboration, R. Aaij *et al.*, *Observation of CP violation in charm decays*, Phys. Rev. Lett. **122** (2019) 211803, [arXiv:1903.08726](#).
- [74] LHCb collaboration, R. Aaij *et al.*, *Observation of $J/\psi p$ resonances consistent with pentaquark states in $\Lambda_b^0 \rightarrow J/\psi p K^-$ decays*, Phys. Rev. Lett. **115** (2015) 072001, [arXiv:1507.03414](#).
- [75] LHCb collaboration, R. Aaij *et al.*, *Search for beautiful tetraquarks in the $\Upsilon(1S)\mu^+\mu^-$ invariant-mass spectrum*, JHEP **10** (2018) 086, [arXiv:1806.09707](#).
- [76] LHCb collaboration, R. Aaij *et al.*, *Study of the doubly charmed tetraquark T_{cc}^+* , [arXiv:2109.01056](#), submitted to journal.
- [77] LHCb collaboration, R. Aaij *et al.*, *Observation of an exotic narrow doubly charmed tetraquark*, [arXiv:2109.01038](#), submitted to journal.
- [78] LHCb collaboration, R. Aaij *et al.*, *Test of lepton universality using $B^+ \rightarrow K^+ \ell^+ \ell^-$ decays*, Phys. Rev. Lett. **113** (2014) 151601, [arXiv:1406.6482](#).
- [79] LHCb collaboration, R. Aaij *et al.*, *Measurement of the ratio of branching fractions $\mathcal{B}(\bar{B}^0 \rightarrow D^{*+} \tau^- \bar{\nu}_\tau) / \mathcal{B}(\bar{B}^0 \rightarrow D^{*+} \mu^- \bar{\nu}_\mu)$* , Phys. Rev. Lett. **115** (2015) 111803, Publisher's Note *ibid.* **115** (2015) 159901, [arXiv:1506.08614](#).

- [80] LHCb collaboration, R. Aaij *et al.*, *Measurement of the ratio of the $\mathcal{B}(B^0 \rightarrow D^{*-} \tau^+ \nu_\tau)$ and $\mathcal{B}(B^0 \rightarrow D^{*-} \mu^+ \nu_\mu)$ branching fractions using three-prong τ -lepton decays*, Phys. Rev. Lett. **120** (2018) 171802, [arXiv:1708.08856](#).
- [81] LHCb collaboration, R. Aaij *et al.*, *Test of lepton universality with $B^0 \rightarrow K^{*0} \ell^+ \ell^-$ decays*, JHEP **08** (2017) 055, [arXiv:1705.05802](#).
- [82] LHCb collaboration, R. Aaij *et al.*, *Tests of lepton universality using $B^0 \rightarrow K_S^0 \ell^+ \ell^-$ and $B^+ \rightarrow K^{*+} \ell^+ \ell^-$ decays*, [arXiv:2110.09501](#), submitted to PRL.
- [83] LHCb collaboration, R. Aaij *et al.*, *Test of lepton universality using $\Lambda_b^0 \rightarrow p K^- \ell^+ \ell^-$ decays*, JHEP **05** (2020) 040, [arXiv:1912.08139](#).
- [84] LHCb collaboration, R. Aaij *et al.*, *Measurement of the b -quark production cross-section in 7 and 13 TeV pp collisions*, Phys. Rev. Lett. **118** (2017) 052002, Erratum *ibid.* **119** (2017) 169901, [arXiv:1612.05140](#).
- [85] LHCb collaboration, R. Aaij *et al.*, *Prompt charm production in pp collisions at $\sqrt{s} = 7$ TeV*, Nucl. Phys. **B871** (2013) 1, [arXiv:1302.2864](#).
- [86] LHCb collaboration, R. Aaij *et al.*, *Measurements of prompt charm production cross-sections in pp collisions at $\sqrt{s} = 13$ TeV*, JHEP **03** (2016) 159, Erratum *ibid.* **09** (2016) 013, Erratum *ibid.* **05** (2017) 074, [arXiv:1510.01707](#).
- [87] F. Follin and D. Jacquet, *Implementation and experience with luminosity levelling with offset beam*, in *Proceedings, ICFA Mini-Workshop on Beam-Beam Effects in Hadron Colliders (BB2013): CERN, Geneva, Switzerland, March 18-22 2013*, 183–187, 2014, [arXiv:1410.3667](#).
- [88] LHCb collaboration, *Framework TDR for the LHCb Upgrade: Technical Design Report*, CERN-LHCC-2012-007, 2012.
- [89] LHCb collaboration, *LHCb VELO Upgrade Technical Design Report*, CERN-LHCC-2013-021, 2013.
- [90] LHCb collaboration, *LHCb PID Upgrade Technical Design Report*, CERN-LHCC-2013-022, 2013.
- [91] LHCb collaboration, *LHCb Tracker Upgrade Technical Design Report*, CERN-LHCC-2014-001, 2014.
- [92] LHCb collaboration, *LHCb Trigger and Online Upgrade Technical Design Report*, CERN-LHCC-2014-016, 2014.
- [93] I. Zurbano Fernandez *et al.*, *High-Luminosity Large Hadron Collider (HL-LHC): Technical design report*, doi: 10.23731/CYRM-2020-0010.
- [94] LHCb Collaboration, *Framework TDR for the LHCb Upgrade II Opportunities in flavour physics, and beyond, in the HL-LHC era*, CERN-LHCC-2021-012, 2021.
- [95] *LEP Design Report: Vol.2. The LEP Main Ring*, .

- [96] E. Mobs, *The CERN accelerator complex. Complexe des accélérateurs du CERN*, 2016.
- [97] LHCb collaboration, *LHCb VELO (VERTex LOcator): Technical Design Report*, CERN-LHCC-2001-011, 2001.
- [98] R. Aaij *et al.*, *Performance of the LHCb Vertex Locator*, JINST **9** (2014) P09007, arXiv:1405.7808.
- [99] LHCb collaboration, *LHCb inner tracker: Technical Design Report*, CERN-LHCC-2002-029, 2002.
- [100] LHCb collaboration, *LHCb outer tracker: Technical Design Report*, CERN-LHCC-2001-024, 2001.
- [101] R. Aaij *et al.*, *Selection and processing of calibration samples to measure the particle identification performance of the LHCb experiment in Run 2*, Eur. Phys. J. Tech. Instr. **6** (2019) 1, arXiv:1803.00824.
- [102] LHCb collaboration, *LHCb RICH: Technical Design Report*, CERN-LHCC-2000-037, 2000.
- [103] M. Adinolfi *et al.*, *Performance of the LHCb RICH detector at the LHC*, Eur. Phys. J. **C73** (2013) 2431, arXiv:1211.6759.
- [104] LHCb collaboration, *LHCb calorimeters: Technical Design Report*, CERN-LHCC-2000-036, 2000.
- [105] F. Archilli *et al.*, *Performance of the muon identification at LHCb*, JINST **8** (2013) P10020, arXiv:1306.0249.
- [106] LHCb collaboration, *LHCb trigger system: Technical Design Report*, CERN-LHCC-2003-031, 2003.
- [107] R. Fruhwirth, *Application of Kalman filtering to track and vertex fitting*, Nucl. Instrum. Meth. A **262** (1987) 444.
- [108] R. Aaij *et al.*, *Performance of the LHCb trigger and full real-time reconstruction in Run 2 of the LHC*, JINST **14** (2019) P04013, arXiv:1812.10790.
- [109] V. V. Gligorov, *A single track HLT1 trigger*, LHCb-PUB-2011-003, 2011.
- [110] R. Aaij *et al.*, *The LHCb trigger and its performance in 2011*, JINST **8** (2013) P04022, arXiv:1211.3055.
- [111] V. V. Gligorov and M. Williams, *Efficient, reliable and fast high-level triggering using a bonsai boosted decision tree*, JINST **8** (2013) P02013, arXiv:1210.6861.
- [112] T. Likhomanenko *et al.*, *LHCb topological trigger reoptimization*, J. Phys. Conf. Ser. **664** (2015) 082025.
- [113] V. V. Gligorov, C. Thomas, and M. Williams, *The HLT inclusive B triggers*, CERN, Geneva, 2011. LHCb-PUB-2011-016.

- [114] G. Dujany and B. Storaci, *Real-time alignment and calibration of the LHCb Detector in Run II*, J. Phys. Conf. Ser. **664** (2015) 082010.
- [115] LHCb collaboration, R. Aaij *et al.*, *Measurement of CP asymmetries in two-body $B_{(s)}^0$ -meson decays to charged pions and kaons*, Phys. Rev. D **98** (2018) 032004, arXiv:1805.06759.
- [116] BaBar collaboration, J. P. Lees *et al.*, *Measurement of CP Asymmetries and Branching Fractions in Charmless Two-Body B-Meson Decays to Pions and Kaons*, Phys. Rev. D **87** (2013) 052009, arXiv:1206.3525.
- [117] Belle collaboration, Y.-T. Duh *et al.*, *Measurements of branching fractions and direct CP asymmetries for $B \rightarrow K\pi$, $B \rightarrow \pi\pi$ and $B \rightarrow KK$ decays*, Phys. Rev. D **87** (2013) 031103, arXiv:1210.1348.
- [118] CDF collaboration, T. A. Aaltonen *et al.*, *Measurements of Direct CP -Violating Asymmetries in Charmless Decays of Bottom Baryons*, Phys. Rev. Lett. **113** (2014) 242001, arXiv:1403.5586.
- [119] Belle collaboration, I. Adachi *et al.*, *Measurement of the CP violation parameters in $B^0 \rightarrow \pi^+\pi^-$ decays*, Phys. Rev. D **88** (2013) 092003, arXiv:1302.0551.
- [120] S. Perazzini *et al.*, *Measurement of CP asymmetries in two-body $B_{(s)}^0$ -meson decays to charged pions and kaons with Run2 data at LHCb*, LHCb-ANA-2018-025, LHCb internal documentation, can be partially made available on request.
- [121] Perazzini, Stefano and Vagnoni, Vincenzo Maria and Fazzini, Davide and Carbone, Angelo and Ferrari, Fabio and Betti, Federico, *Measurement of CP asymmetries in two-body $B_{(s)}^0$ -meson decays to charged pions and kaons*, LHCb-ANA-2017-003, LHCb internal documentation, can be partially made available on request.
- [122] L. Breiman, J. H. Friedman, R. A. Olshen, and C. J. Stone, *Classification and regression trees*, Wadsworth international group, Belmont, California, USA, 1984.
- [123] Y. Freund and R. E. Schapire, *A decision-theoretic generalization of on-line learning and an application to boosting*, J. Comput. Syst. Sci. **55** (1997) 119.
- [124] A. Carbone, F. Ferrari, S. Perazzini, and V. Vagnoni, *Search for the $B^0 \rightarrow K^+K^-$ decay with $\int \mathcal{L} dt = 3 fb^{-1}$* , LHCb-ANA-2016-016, LHCb internal documentation, can be partially made available on request.
- [125] A. Hoecker *et al.*, *TMVA 4 — Toolkit for Multivariate Data Analysis with ROOT. Users Guide.*, arXiv:physics/0703039.
- [126] K. S. Cranmer, *Kernel estimation in high-energy physics*, Comput. Phys. Commun. **136** (2001) 198, arXiv:hep-ex/0011057.
- [127] ARGUS collaboration, H. Albrecht *et al.*, *Measurement of the polarization in the decay $B \rightarrow J/\psi K^*$* , Phys. Lett. **B340** (1994) 217.
- [128] M. Pivk and F. R. Le Diberder, *sPlot: A statistical tool to unfold data distributions*, Nucl. Instrum. Meth. **A555** (2005) 356, arXiv:physics/0402083.

- [129] L. Anderlini *et al.*, *Computing strategy for PID calibration samples for LHCb Run 2*, LHCb-PUB-2016-020.
- [130] O. Lupton, L. Anderlini, B. Sciascia, and V. Gligorov, *Calibration samples for particle identification at LHCb in Run 2*, LHCb-PUB-2016-005.
- [131] LHCb collaboration, R. Aaij *et al.*, *Measurements of the B^+ , B^0 , B_s^0 meson and Λ_b^0 baryon lifetimes*, JHEP **04** (2014) 114, arXiv:1402.2554.
- [132] H. G. Moser and A. Roussarie, *Mathematical methods for B^0 anti- B^0 oscillation analyses*, Nucl. Instrum. Meth. A **384** (1997) 491.
- [133] T. Skwarnicki, *A study of the radiative cascade transitions between the Upsilon-prime and Upsilon resonances*, PhD thesis, Institute of Nuclear Physics, Krakow, 1986, DESY-F31-86-02.
- [134] T. J. Rivlin, *The Chebyshev Polynomials*, John Wiley and Sons, 1 ed., 1974. Chebyshev polynomials were first presented in Chebyshev, P. L. (1854). “Théorie des mécanismes connus sous le nom de parallélogrammes”. Mémoires des Savants étrangers présentés à l’Académie de Saint-Pétersbourg (in French).
- [135] D. Fazzini, *Flavour Tagging in the LHCb experiment*, in *Proceedings, 6th Large Hadron Collider Physics Conference (LHCP 2018): Bologna, Italy, June 4-9, 2018*, LHCP2018 230, 2018.
- [136] Y. Xie, *sFit: a method for background subtraction in maximum likelihood fit*, arXiv:0905.0724.
- [137] Flavour Tagging working group, *EspressoPerformanceMonitor documentation*, , <https://gitlab.cern.ch/lhcb-ft/EspressoPerformanceMonitor/wikis/home>.
- [138] Heavy Flavor Averaging Group, Y. Amhis *et al.*, *Averages of b -hadron, c -hadron, and τ -lepton properties as of summer 2016*, Eur. Phys. J. **C77** (2017) 895, arXiv:1612.07233.
- [139] Davis, Adam and Dufour, Laurent and Ferrari, Fabio and Stahl, Sascha and Vesterinen, Mika Anton and Van Tilburg, Jeroen, *Measurement of the $K^-\pi^+$ two-track detection asymmetry in Run 2 using the Turbo stream*, LHCb-INT-2017-023, LHCb internal documentation, can be partially made available on request.
- [140] LHCb collaboration, R. Aaij *et al.*, *Measurement of CP asymmetry in $D^0 \rightarrow K^-K^+$ and $D^0 \rightarrow \pi^-\pi^+$ decays*, JHEP **07** (2014) 041, arXiv:1405.2797.
- [141] LHCb collaboration, R. Aaij *et al.*, *Updated measurement of time-dependent CP -violating observables in $B_s^0 \rightarrow J/\psi K^+K^-$ decays*, Eur. Phys. J. **C79** (2019) 706, Erratum *ibid.* **C80** (2020) 601, arXiv:1906.08356.
- [142] A. Bertolin *et al.*, *Precision measurement of the $B_s^0 - \bar{B}_s^0$ oscillation frequency with the $B_s^0 \rightarrow D_s^- \pi^+$ decays*, LHCb-ANA-2020-033, 2020, LHCb internal documentation, can be partially made available on request.

- [143] W. D. Hulsbergen, *Decay chain fitting with a Kalman filter*, Nucl. Instrum. Meth. **A552** (2005) 566, [arXiv:physics/0503191](https://arxiv.org/abs/physics/0503191).
- [144] U. c. M. Bona et al. *Standard model fit results: Summer 2018*, 2018.
- [145] CKMfitter group, J. Charles *et al.*, *Current status of the standard model CKM fit and constraints on $\Delta F = 2$ new physics*, Phys. Rev. **D91** (2015) 073007, [arXiv:1501.05013](https://arxiv.org/abs/1501.05013), updated results and plots available at <http://ckmfitter.in2p3.fr/>.
- [146] HPQCD collaboration, E. McLean, C. T. H. Davies, A. T. Lytle, and J. Koponen, *Lattice QCD form factor for $B_s^0 \rightarrow D_s^* \ell \nu$ at zero recoil with non-perturbative current renormalisation*, [arXiv:1904.02046](https://arxiv.org/abs/1904.02046).
- [147] HPQCD collaboration, J. Harrison, C. Davies, and M. Wingate, *Lattice QCD calculation of the $B_{(s)} \rightarrow D_{(s)}^* \ell \nu$ form factors at zero recoil and implications for $|V_{cb}|$* , Phys. Rev. **D97** (2018) 054502, [arXiv:1711.11013](https://arxiv.org/abs/1711.11013).
- [148] M. Atoui, V. Morénas, D. Bečirevic, and F. Sanfilippo, *$B_s \rightarrow D_s \ell \nu_\ell$ near zero recoil in and beyond the Standard Model*, Eur. Phys. J. **C74** (2014) 2861, [arXiv:1310.5238](https://arxiv.org/abs/1310.5238).
- [149] J. Flynn *et al.*, *Form factors for semi-leptonic B decays*, PoS **LATTICE2016** (2016) 296, [arXiv:1612.05112](https://arxiv.org/abs/1612.05112).
- [150] LHCb collaboration, R. Aaij *et al.*, *Measurement of b-hadron fractions in 13 TeV pp collisions*, Phys. Rev. **D100** (2019) 031102(R), [arXiv:1902.06794](https://arxiv.org/abs/1902.06794).
- [151] LHCb collaboration, R. Aaij *et al.*, *Measurement of f_s/f_u variation with proton-proton collision energy and B-meson kinematics*, Phys. Rev. Lett. **124** (2020) 122002, [arXiv:1910.09934](https://arxiv.org/abs/1910.09934).
- [152] D. Manuzzi, *Exclusive branching ratios of $B_s^0 \rightarrow D_s^{(*)} \mu \nu$ decays with Run 2 data*, talk at the Semileptonic WG meeting of 21/11/2018. LHCb internal documentation can be partially made available on request.
- [153] LHCb collaboration, R. Aaij *et al.*, *Measurement of B_s^0 and D_s^- meson lifetimes*, Phys. Rev. Lett. **119** (2017) 101801, [arXiv:1705.03475](https://arxiv.org/abs/1705.03475).
- [154] T. J. Boettcher *et al.*, *Measurement of the decay-width difference between the B_s^0 and B^0 mesons and the D_s and D mesons*, LHCb-ANA-2016-068, LHCb internal documentation, can be partially made available on request.
- [155] Archilli, Flavio and others, *Search for the $B^0 \rightarrow \mu^+ \mu^-$ decay and measurement of the $B_s^0 \rightarrow \mu^+ \mu^-$ branching fraction and effective lifetime*, LHCb-ANA-2016-038, LHCb internal documentation can be partially made available on request.
- [156] LHCb collaboration, R. Aaij *et al.*, *Measurement of the track reconstruction efficiency at LHCb*, JINST **10** (2015) P02007, [arXiv:1408.1251](https://arxiv.org/abs/1408.1251).
- [157] Correction tables for the tracking efficiencies available at <https://twiki.cern.ch/twiki/bin/viewauth/LHCbInternal/TrackingEffStatus2012S20>. LHCb internal documentation can be partially made available on request.

- [158] Anton Poluektov, *Correction of simulated particle identification response in LHCb using a kernel density estimation*, LHCb-INT-2017-007, LHCb internal documentation, can be partially made available on request.
- [159] A. Poluektov, *Kernel density estimation of a multidimensional efficiency profile*, JINST **10** (2015) P02011, arXiv:1411.5528.
- [160] LHCb collaboration, R. Aaij *et al.*, *A precise measurement of the B^0 meson oscillation frequency*, Eur. Phys. J. **C76** (2016) 412, arXiv:1604.03475.
- [161] P. Urquijo, *Semileptonic B decays branching fractions*, unpublished internal note available at https://indico.cern.ch/event/123574/contributions/95384/attachments/71997/103261/sl_br_int_note.pdf; J. Van Tilburg *et al.*, <https://twiki.cern.ch/twiki/bin/view/LHCbPhysics/SemileptonicCocktailMonteCarlo>, LHCb internal documentation can be partially made available on request.
- [162] S. Cali *et al.*, *Measurement of the shape of the $B_s^0 \rightarrow D_s^{*-} \mu^+ \nu$ differential distribution*, LHCb-ANA-2018-045, LHCb internal documentation, in preparation, can be partially made available on request.
- [163] G. Ciezarek, A. Lupato, M. Rotondo, and M. Vesterinen, *Reconstruction of semileptonically decaying beauty hadrons produced in high energy pp collisions*, JHEP **02** (2017) 021, arXiv:1611.08522.
- [164] Particle Data Group, M. Tanabashi *et al.*, *Review of particle physics*, Phys. Rev. **D98** (2018) 030001, and 2019 update.
- [165] E. McLean, C. T. H. Davies, A. T. Lytle, and J. Koponen, *Lattice QCD form factor for $B_s \rightarrow D_s^{*} l \nu$ at zero recoil with non-perturbative current renormalisation*, Phys. Rev. **D99** (2019) 114512, arXiv:1904.02046.
- [166] CLEO collaboration, S. Dobbs *et al.*, *Measurement of absolute hadronic branching fractions of D mesons and $e^+e^- \rightarrow D\bar{D}$ cross-sections at the $\psi(3770)$* , Phys. Rev. **D76** (2007) 112001, arXiv:0709.3783.
- [167] Internal LHCb discussion at the BSL WG meeting of 2019/09/04, can be partially made available on request.
- [168] Particle Data Group, M. Tanabashi *et al.*, *Review of particle physics*, Phys. Rev. **D98** (2018) 030001.
- [169] M. Jung, *Branching ratio measurements and isospin violation in B -meson decays*, Phys. Lett. **B753** (2016) 187, arXiv:1510.03423.
- [170] Belle-II collaboration, W. Altmannshofer *et al.*, *The Belle II Physics Book*, PTEP **2019** (2019) 123C01, arXiv:1808.10567, [Erratum: PTEP 2020, 029201 (2020)].
- [171] Belle collaboration, E. Waheed *et al.*, *Measurement of the CKM matrix element $|V_{cb}|$ from $B^0 \rightarrow D^{*-} \ell^+ \nu_\ell$ at Belle*, Phys. Rev. D **100** (2019) 052007, arXiv:1809.03290, [Erratum: Phys.Rev.D 103, 079901 (2021)].

- [172] BaBar collaboration, J. P. Lees *et al.*, *Extraction of form Factors from a Four-Dimensional Angular Analysis of $\bar{B} \rightarrow D^* \ell^- \bar{\nu}_\ell$* , Phys. Rev. Lett. **123** (2019) 091801, [arXiv:1903.10002](#).
- [173] LHCb collaboration, R. Aaij *et al.*, *Measurement of $|V_{cb}|$ with $B_s^0 \rightarrow D_s^{(*)-} \mu^+ \nu$ decays*, Phys. Rev. **D101** (2020) 072004, [arXiv:2001.03225](#).
- [174] I. Efthymiopoulos *et al.*, *LHCb Upgrades and operation at $10^{34} \text{ cm}^{-2} \text{ s}^{-1}$ luminosity — A first study*, CERN-ACC-NOTE-2018-0038, 2018.
- [175] J. Albrecht *et al.*, *Luminosity scenarios for LHCb Upgrade II*, LHCb-PUB-2019-001, CERN-LHCb-PUB-2019-001, CERN, Geneva, 2019.
- [176] J.-C. Brient, R. Salerno, and Y. Sirois, eds., *Proceedings, International Conference on Calorimetry for the High Energy Frontier (CHEF 2013): Paris, France, April 22-25, 2013*, (Palaiseau, France), LLR, 2013.
- [177] Y. Guz, *The LHCb calorimeter system: design, performance and upgrade*, JINST **12** (2017) C07024.
- [178] P. Jenni and P. Sonderegger, *The high resolution spaghetti hadron calorimeter*, https://inis.iaea.org/collection/NCLCollectionStore/_Public/19/028/19028958.pdf, 1987.
- [179] M. Lucchini *et al.*, *Test beam results with LuAG fibers for next-generation calorimeters*, JINST **8** (2013) P10017.
- [180] L. Martinazzoli, N. Kratochwil, S. Gundacker, and E. Auffray, *Scintillation properties and timing performance of state-of-the-art $Gd_3Al_2Ga_3O_{12}$ single crystals*, Nucl. Instrum. Meth. **A1000** (2021) 165231.
- [181] A. A. Derevshchikov *et al.*, *On possibility to make a new type of calorimeter: radiation resistant and fast*, <https://inspirehep.net/literature/300334>, Protvino 1990.
- [182] LAPPD collaboration, B. W. Adams *et al.*, *A Brief Technical History of the Large-Area Picosecond Photodetector (LAPPD) collaboration*, [arXiv:1603.01843](#).
- [183] Incom Inc. collaboration, *Large area picosecond photodetector*, <https://incomusa.com/lappd/>.
- [184] K. Matsuoka *et al.*, *Extension of the MCP-PMT lifetime*, Nucl. Instrum. Meth. **A876** (2017) 93, The 9th international workshop on Ring Imaging Cherenkov Detectors (RICH2016).
- [185] A. Lehmann *et al.*, *Tremendously increased lifetime of MCP-PMTs*, Nucl. Instrum. Meth. **A845** (2017) 570, Proceedings of the Vienna Conference on Instrumentation 2016.
- [186] M. Böhm *et al.*, *Performance of the most recent MCP-PMTs*, JINST **15** (2020) C11015.

- [187] A. Y. Barnyakov *et al.*, *Response of microchannel plates in ionization mode to single particles and electromagnetic showers*, Nucl. Instrum. Meth. **A879** (2018) 6.
- [188] A. Ronzhin *et al.*, *Direct tests of micro channel plates as the active element of a new shower maximum detector*, Nucl. Instrum. Meth. **A795** (2015) 52.
- [189] M. Clemencic *et al.*, *The LHCb simulation application, Gauss: Design, evolution and experience*, J. Phys. Conf. Ser. **331** (2011) 032023.
- [190] T. Sjöstrand, S. Mrenna, and P. Skands, *PYTHIA 6.4 physics and manual*, JHEP **05** (2006) 026, [arXiv:hep-ph/0603175](https://arxiv.org/abs/hep-ph/0603175).
- [191] I. Belyaev *et al.*, *Handling of the generation of primary events in Gauss, the LHCb simulation framework*, J. Phys. Conf. Ser. **331** (2011) 032047.
- [192] D. J. Lange, *The EvtGen particle decay simulation package*, Nucl. Instrum. Meth. **A462** (2001) 152.
- [193] N. Davidson, T. Przedzinski, and Z. Was, *PHOTOS interface in C++: Technical and physics documentation*, Comp. Phys. Comm. **199** (2016) 86, [arXiv:1011.0937](https://arxiv.org/abs/1011.0937).
- [194] Geant4 collaboration, J. Allison *et al.*, *Geant4 developments and applications*, IEEE Trans. Nucl. Sci. **53** (2006) 270; Geant4 collaboration, S. Agostinelli *et al.*, *Geant4: A simulation toolkit*, Nucl. Instrum. Meth. **A506** (2003) 250.
- [195] E. Shmanin, *GEANT4 simulation of energy resolution of the SPACAL electromagnetic calorimeter*, Journal of Physics: Conference Series **1439** (2020) 012007.
- [196] O. Deschamps *et al.*, *Photon and neutral pion reconstruction*, LHCb-2003-091, CERN, Geneva, 2003.
- [197] V. Breton, N. Brun, and P. Perret, *A clustering algorithm for the LHCb electromagnetic calorimeter using a cellular automaton*, LHCb-2001-123, CERN, Geneva, 2001.
- [198] D. A. Berninghoff, J. Albrecht, and V. Gligorov, *Bremsstrahlung Recovery of Electrons using Multivariate Methods*, LHCb-INT-2016-018, CERN, Geneva, 2016.
- [199] D. A. Roa Romero, *Study of charmless $B_{d,s}^0 \rightarrow h^+ h'^- \pi^0$ decays in LHCb*, 2013. Presented 24 May 2013.
- [200] Y. S. Amhis, C. Marin Benito, and M. Calvo Gomez, *State of the art of the Run 1 and 2 calorimeter reconstruction and towards the Upgrade*, CERN, Geneva, 2019. LHCb internal documentation, can be partially made available on request.
- [201] LHCb collaboration, R. Aaij *et al.*, *Tests of lepton universality using $B^0 \rightarrow K_S^0 \ell^+ \ell^-$ and $B^+ \rightarrow K^{*+} \ell^+ \ell^-$ decays*, [arXiv:2110.09501](https://arxiv.org/abs/2110.09501).
- [202] LHCb collaboration, R. Aaij *et al.*, *Search for lepton-universality violation in $B^+ \rightarrow K^+ \ell^+ \ell^-$ decays*, Phys. Rev. Lett. **122** (2019) 191801, [arXiv:1903.09252](https://arxiv.org/abs/1903.09252).
- [203] M. Gronau and D. London, *Isospin analysis of CP asymmetries in B decays*, Phys. Rev. Lett. **65** (1990) 3381.

- [204] UTfit collaboration, M. Bona *et al.*, *Improved Determination of the CKM Angle α from $B \rightarrow \pi\pi$ decays*, Phys. Rev. D **76** (2007) 014015, [arXiv:hep-ph/0701204](#).
- [205] J. Charles, O. Deschamps, S. Descotes-Genon, and V. Niess, *Isospin analysis of charmless B -meson decays*, Eur. Phys. J. C **77** (2017) 574, [arXiv:1705.02981](#).
- [206] LHCb collaboration, R. Aaij *et al.*, *Measurement of b -hadron branching fractions for two-body decays into charmless charged hadrons*, JHEP **10** (2012) 037, [arXiv:1206.2794](#).
- [207] LHCb collaboration, R. Aaij *et al.*, *Measurement of b hadron production fractions in 7 TeV pp collisions*, Phys. Rev. **D85** (2012) 032008, [arXiv:1111.2357](#).
- [208] Belle collaboration, A. Zupac *et al.*, *Measurement of the Branching Fraction \mathcal{B} ($\Lambda_c^+ \rightarrow pK^-\pi^+$)*, Phys. Rev. Lett. **113** (2014) 042002, [arXiv:1312.7826v](#).
- [209] C. J. Monahan *et al.*, *$B_s \rightarrow D_s \ell \nu$ Form Factors and the Fragmentation Fraction Ratio f_s/f_d* , Phys. Rev. **D95** (2017) 114506, [arXiv:1703.09728](#).